ASME
SETTING THE STANDARD

FLUIDS ENGINEERING DIVISION
Editor
J. KATZ (2009)
Assistant to the Editor
L. MURPHY (2009)

Associate Editors
M. J. ANDREWS (2009)
S. BALACHANDAR (2008)
A. BESKOK (2008)
S. L. CECCIO (2009)
D. DRIKAKIS (2008)
P. DUPONT (2010)
I. EAMES (2010)
C. HAH (2009)
T. J. HEINDEL (2010)
J. KOMPENHANS (2009)
J. A. LIBURDY (2010)
P. LIGRANI (2008)
R. MITTAL (2009)
T. J. O'HERN (2008)
U. PIOMELLI (2010)
Z. RUSAK (2010)
D. SIGINER (2008)
Y. ZHOU (2008)

PUBLICATIONS COMMITTEE
Chair, B. RAVANI

OFFICERS OF THE ASME
President, SAM Y. ZAMRIK
Executive Director, V. R. CARTER
Treasurer, T. D. PESTORIUS

PUBLISHING STAFF
Managing Director, Publishing
P. DI VIETRO
Manager, Journals
C. MCATEER
Production Coordinator
A. HEWITT

Transactions of the ASME, Journal of Fluids Engineering (ISSN 0098-2202) is published monthly by The American Society of Mechanical Engineers, Three Park Avenue, New York, NY 10016. Periodicals postage paid at New York, NY and additional mailing offices.
POSTMASTER: Send address changes to Transactions of the ASME, Journal of Fluids Engineering, c/o THE AMERICAN SOCIETY OF MECHANICAL ENGINEERS, 22 Law Drive, Box 2300, Fairfield, NJ 07007-2300.
CHANGES OF ADDRESS must be received at Society headquarters seven weeks before they are to be effective. Please send old label and new address.
STATEMENT from By-Laws. The Society shall not be responsible for statements or opinions advanced in papers or ... printed in its publications (B7.1, Par. 3).
COPYRIGHT © 2008 by the American Society of Mechanical Engineers. Authorization to photocopy material for internal or personal use under those circumstances not falling within the fair use provisions of the Copyright Act, contact the Copyright Clearance Center (CCC), 222 Rosewood Drive, Danvers, MA 01923, tel: 978-750-8400, www.copyright.com. Request for special permission or bulk copying should be addressed to Reprints/Permission Department.
Canadian Goods & Services Tax Registration #126148048.

Journal of Fluids Engineering

Published Monthly by ASME

VOLUME 130 • NUMBER 6 • JUNE 2008

RESEARCH PAPERS

Flows in Complex Systems

Fundamental Issues and Canonical Flows

Multiphase Flows

(Contents continued on inside back cover)

This journal is printed on acid-free paper, which exceeds the ANSI Z39.48-1992 specification for permanence of paper and library materials. ♾™
♻ 85% recycled content, including 10% post-consumer fibers.

Downloaded 03 Jun 2010 to 171.66.16.159. Redistribution subject to ASME license or copyright; see http://www.asme.org/terms/Terms_Use.cfm

(**Contents continued**)

Techniques and Procedures

TECHNICAL BRIEFS

The ASME Journal of Fluids Engineering is abstracted and indexed in the following:

Applied Science & Technology Index, Chemical Abstracts, Chemical Engineering and Biotechnology Abstracts (Electronic equivalent of Process and Chemical Engineering), Civil Engineering Abstracts, Computer & Information Systems Abstracts, Corrosion Abstracts, Current Contents, Ei EncompassLit, Electronics & Communications Abstracts, Engineered Materials Abstracts, Engineering Index, Environmental Engineering Abstracts, Environmental Science and Pollution Management, Excerpta Medica, Fluidex, Index to Scientific Reviews, INSPEC, International Building Services Abstracts, Mechanical & Transportation Engineering Abstracts, Mechanical Engineering Abstracts, METADEX (The electronic equivalent of Metals Abstracts and Alloys Index), Petroleum Abstracts, Process and Chemical Engineering, Referativnyi Zhurnal, Science Citation Index, SciSearch (The electronic equivalent of Science Citation Index), Shock and Vibration Digest, Solid State and Superconductivity Abstracts, Theoretical Chemical Engineering

Downloaded 03 Jun 2010 to 171.66.16.159. Redistribution subject to ASME license or copyright; see http://www.asme.org/terms/Terms_Use.cfm

Charles-Henri Bruneau
e-mail: bruneau@math.u-bordeaux1.fr

Iraj Mortazavi
e-mail: mortaz@math.u-bordeaux1.fr

Institut de Mathématiques de Bordeaux,
Université Bordeaux 1,
INRIA Bordeaux-Sud Ouest Team MC2,
CNRS UMR 5466,
351 Cours de la Libération,
F-33405 Talence, France

Patrick Gilliéron
Technocentre Renault,
Département Systémes Véhicles,
1 Avenue du Golf,
F-78288 Guyancourt, France
e-mail: patrick.gillieron@renault.com

Passive Control Around the Two-Dimensional Square Back Ahmed Body Using Porous Devices

The control of two-dimensional flows around the square back Ahmed body is achieved by using porous devices added on some parts of the body. The square back Ahmed body is considered either in an open domain or on top of a road. The modeling of the flow in different media is performed by means of the penalization method. A good choice of the location of the porous interfaces yields a significant improvement of the aerodynamic quantities, especially for the square back body. [DOI: 10.1115/1.2917423]

1 Introduction

The research developed today in car aerodynamics is carried out from the point of view of the durable development. Some car companies as Renault have the objective to develop control solutions able to reduce at least 30% of the aerodynamic drag of the vehicles without constraints on the design, the comfort, the storage, or the safety of the passengers [1]. Thus, it is necessary to locally modify the flow, to remove or delay the separation position, or to reduce the development of the recirculation zone at the back and of the separated swirling structures [2]. This can be mainly obtained by controlling the flow near the wall with or without additional energy by using active or passive devices [3,4]. The use of passive systems of control remains, however, always privileged for obvious reasons of cost. Significant results can be obtained by using simple techniques [5]. In practice, the flow control is obtained when the wall pressure distribution is successfully modified on the back and on the rear window, using various adapted devices, which locally change the geometry. Control experiments in wind tunnel on reduced or real ground vehicles are performed [6], and measurements of the wall static pressures and of the aerodynamic torque [7] allow to quantify the effect of the control [8]. However, due to the design constraints, the real gain is rather weak and so new control techniques have to be developed.

Among these new techniques in progress, separate devices located in front of or behind the vehicle can be used to reduce the development of the recirculation zone on the rear window or at the back and the interactions of the swirling wake structures. Reductions in the aerodynamic drag up to 97% are measured on the front part of a circular cylinder in Ref. [9]. Interesting results are also obtained with devices located streamwise or transverse to the upstream flow behind the back [10]. Another similar approach is to put devices along the wall to generate vortical structures in order to shift the separation line and to reduce the aerodynamic drag. The swirling structures increase the local turbulence of the flow and the energy transfers in the boundary layer. Therefore, the velocity increases near the wall. A drag reduction close to 40% is obtained on wing profiles in Ref. [11]. The extension of this technique to more complex geometries should be possible and could defer separation lines toward the back. Furthermore, significant reductions in drag up to 50% are obtained by using artificially rough surfaces [12]. Applied in the areas of weak curvature radius, this technique could decrease the aerodynamic drag.

Self-adapting surfaces made of special coatings can also be used to delay the turbulent laminar transition [13,14]. The impact of this control strategy remains, however, very weak in automobile aerodynamics because the flow is naturally turbulent and the contribution of the friction in the aerodynamic drag is very small (about 10%).

A simplified car as the Ahmed body [15] is a three-dimensional bluff body moving in the vicinity of the ground generating a turbulent flow. Several separations appear along the body from the front to the back. The resulting recirculation zones contribute to a significant part of the drag coefficient [16,6]. So, an objective of the control is to reduce the transverse separation area in the wake. The drag coefficient strongly changes with the angle α between the horizontal line and the rear window. For low angles smaller than 12 deg or large angles higher than 30 deg, the flow separates at the back and is mainly a two-dimensional base flow. Especially, experimental and numerical studies confirm the two-dimensional behavior of the detached near-wall flow at the base of the square back Ahmed body geometry [17,8,18]. On the contrary for angles between these two values of α, the flow is highly three dimensional over the rear window as there are two counter-rotary lateral vortices and an open separation bulb [6,8,17,19]. In this paper, we focus on the square back Ahmed body (α=90 deg) corresponding to simplified monospace cars or trucks and so a two-dimensional study is performed. The main objective is then to reduce the separated area at the back and thus the static and total pressure gradients that govern the aerodynamic drag. Two-dimensional computations cannot give the exact values of the drag around the three-dimensional Ahmed body but yield properly the effect of the passive control with respect to the uncontrolled case. However, the computational domain is restricted to a short area around the body as in any cases the wake flow is strongly three dimensional.

The use of porous interfaces is a new possibility that can

Contributed by the Fluids Engineering Division of ASME for publication in the JOURNAL OF FLUIDS ENGINEERING. Manuscript received November 3, 2006; final manuscript received March 19, 2008; published online May 19, 2008. Review conducted by Joseph Katz. Paper presented at the 2002 ASME Joint U.S.-European Fluids Engineering Conference (FEDSM2002), Montreal, Quebec, Canada, July 14–18, 2002.

Downloaded 03 Jun 2010 to 171.66.16.157. Redistribution subject to ASME license or copyright; see http://www.asme.org/terms/Terms_Use.cfm

modify the boundary layer behavior. This passive control technique moves the separation line, reduces the pressure gradients in the near wake, and therefore the aerodynamic drag of the vehicles is decreased. A numerical study on the effect of porous layer control on a 2D square cylinder has shown that significant gains on the drag coefficient can be achieved for an appropriate choice of the mechanical parameters (such as porous layer permeability and thickness) [20]. In addition, a drastic reduction in the vortex induced vibrations on a riser pipe has been obtained [21]. Here, the passive control is achieved by means of a porous medium layer, which is inserted between the flow and the body. This porous layer modifies the boundary layer effects as it changes the stress forces; indeed, the no-slip boundary condition is replaced by a mixed Fourier boundary condition on the walls [22,23]. The practical difficulty is to compute the flow in two different media, namely, the fluid and the porous medium, with different modeling. To overcome this difficulty, we use the penalization method that allows to simultaneously solve both flows with the same model. This method introduced in Ref. [24] is studied and validated in Ref. [25], and applied to turbulent flows in Ref. [26] and to flow control in Ref. [20]; it consists in adding a penalization term $\mathbf{U}/K$ in the incompressible Navier–Stokes equations, where $\mathbf{U}$ is the velocity vector and K is the nondimensional permeability coefficient. It was used as an immersed boundary method to avoid a body fitting and directly solve the flow around bluff bodies on Cartesian meshes. The parameter K is set to a very small value inside the body, which corresponds to solve Darcy equations with a very small intrinsic permeability. On the other hand, K is set to a very large value in the fluid domain in order to solve only the Navier–Stokes equations as the extra term vanishes. In our application, a third intermediate value of K is used to represent the porous medium where Brinkman equations are solved. In summary, we can solve the flow inside the three different media only by changing the value of the parameter K in the penalized Navier–Stokes equations. Besides, we avoid to fit the frontiers between the solid body, the porous layer, and the fluid.

The goal of this paper is to show how well positioned porous slices can modify the shedding and the near wake, in particular, the static pressure gradient to decrease the drag coefficient. In the following, we describe the modeling procedure that yields the penalized Navier–Stokes equations or Brinkman–Navier–Stokes equations and give a brief outline of the numerical approximation. Then, we give various results of the original flow or the controlled flow around the square back Ahmed body in an open domain or on top of a road. We carefully analyze these results and quantify the efficiency of the passive control by using a porous layer.

2 Modeling and Numerical Simulation

In this section, we show how an immersed boundary method can be successfully used to model three different media: a solid, a saturated porous medium, and an incompressible fluid, with the same equation. In a porous medium, the velocity in two dimensions $\mathbf{U}=(u,v)$ is given by Darcy law

$$\mathbf{U} = -\frac{k}{\mu\Phi}\nabla p \tag{2.1}$$

where p is the pressure, k is the intrinsic permeability, μ is the viscosity, and Φ is the porosity of the fluid. By assuming that the fluid saturating the porous medium is Boussinesq, we get from Brinkman's equation that is valid only for high porosities close to 1,

$$\nabla p = -\frac{\mu}{k}\Phi\mathbf{U} + \tilde{\mu}\Phi\Delta\mathbf{U} \tag{2.2}$$

by adding the inertial terms with the Dupuit–Forchheiner relationship [27], the Forchheiner–Navier–Stokes equations

$$\rho\partial_t\mathbf{U} + \rho(\mathbf{U}\cdot\nabla)\mathbf{U} + \nabla p = -\frac{\mu}{k}\Phi\mathbf{U} + \tilde{\mu}\Phi\Delta\mathbf{U} \tag{2.3}$$

where $\tilde{\mu}$ is Brinkman's effective viscosity. As Φ is close to 1, we can approximate $\tilde{\mu}\approx\mu/\Phi$ [28] and get the equation

$$\rho\partial_t\mathbf{U} + \rho(\mathbf{U}\cdot\nabla)\mathbf{U} + \nabla p = -\frac{\mu}{k}\Phi\mathbf{U} + \mu\Delta\mathbf{U} \tag{2.4}$$

Then, a nondimensionalization by using the usual substitutions including the mean velocity of the fluid $\bar{U}$ and the height of the domain H,

$$\rho = \rho'\rho, \quad \mathbf{U} = \mathbf{U}'\bar{U}, \quad x = x'H, \quad t = t'\frac{H}{\bar{\mathbf{U}}}, \quad p = p'\rho|\bar{U}|^2 \tag{2.5}$$

yields the penalized nondimensional Navier–Stokes equations or Brinkman–Navier–Stokes equations for the unknowns $(\mathbf{U}',p')$ denoted $(\mathbf{U},p)$ for the sake of simplicity,

$$\partial_t\mathbf{U} + (\mathbf{U}\cdot\nabla)\mathbf{U} - \frac{1}{\mathrm{Re}}\Delta\mathbf{U} + \frac{\mathbf{U}}{K} + \nabla p = 0 \quad \text{in } \Omega_T = \Omega\times(0,T) \tag{2.6}$$

$$\mathrm{div}\,\mathbf{U} = 0 \quad \text{in } \Omega_T \tag{2.7}$$

where $K=\rho k\Phi\bar{U}/\mu H$ is the nondimensional coefficient of permeability of the medium, $\mathrm{Re}=\rho\bar{U}H/\mu$ is the Reynolds number based on the height of the body, and Ω is the full domain including the porous layer and the solid body. This model is able to represent the three media as follows. In the fluid, the permeability coefficient goes to infinity, the penalization term vanishes, and we solve the nondimensional Navier–Stokes equations. In the solid body, the permeability coefficient goes to zero and it has been shown in Ref. [25] that solving these equations corresponds to solve Darcy's law in the solid and that the velocity is proportional to K. In the porous medium, Brinkman equations are recovered. For numerical simulations we set $K=10^{16}$ in the fluid and $K=10^{-8}$ in the solid body; the porous medium is represented by a range of intermediate values varying from $K=10^{-3}$ to $K=100$. Lower values correspond to porous media too close to the solid behavior to efficiently control the flow. On the opposite, upper values are almost dominated by the flow and thus are equivalent to reduce the size of the obstacle. All the numerical simulations presented in this paper have been performed with $K=10^{-1}$ that appears to be a good intermediate value referring to a parametric study on a wide range of K values [20]. The numerical simulation is performed by solving Eqs. (2.6) and (2.7), where K is set at the velocity points according to the medium they belong to. It was shown by different approaches that solving these equations is equivalent to solve the Navier–Stokes equations in the fluid with a Fourier-like boundary condition instead of the no-slip boundary condition (see, in particular, Refs. [29,30]). So, adding a porous layer between the solid body and the fluid induces a reduction in the shear effects in the boundary layer and thus allows to control the flow. In addition, as the pressure is computed inside the solid body, we can compute the drag and lift forces by integrating the penalization term on the volume of the body

$$F_D = -\int_{\text{body}}\partial_{x1}p\,dx + \int_{\text{body}}\frac{1}{\mathrm{Re}}\Delta u\,dx \approx \int_{\text{body}}\frac{u}{K}dx \tag{2.8}$$

$$F_L = -\int_{\text{body}}\partial_{x2}p\,dx + \int_{\text{body}}\frac{1}{\mathrm{Re}}\Delta v\,dx \approx \int_{\text{body}}\frac{v}{K}dx \tag{2.9}$$

where the body includes the porous layers. To quantify the effect of the control, we shall compare the following quantities; the

Downloaded 03 Jun 2010 to 171.66.16.157. Redistribution subject to ASME license or copyright; see http://www.asme.org/terms/Terms_Use.cfm

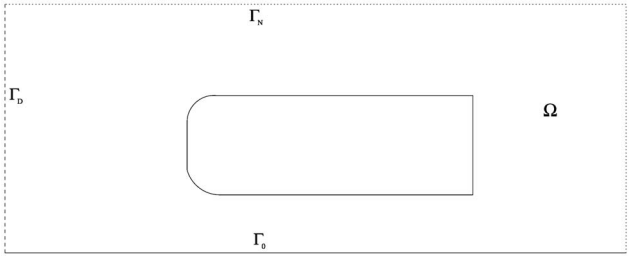

Fig. 1 Computational domain including the square back Ahmed body

static pressure coefficient C_p, the drag coefficient C_D, the root mean square of the lift coefficient $C_{L\text{rms}}$, and the enstrophy Z:

$$C_p = 2(p - p_0)/(\rho|\mathbf{U}|^2)$$

$$C_D = \frac{2F_D}{H}, \quad C_L = \frac{2F_L}{H}$$

$$C_{L\text{rms}} = \sqrt{\frac{1}{T}\int_0^T C_L^2 dt}, \quad Z = \frac{1}{2}\int_\Omega |\omega|^2 dx$$

where p_0 is the inlet static pressure and $\omega = \partial_{x1}v - \partial_{x2}u$ is the scalar vorticity in 2D. Let us note that the static pressure is set to zero at the downstream section of the computational domain.

The unsteady equations (2.6) and (2.6) are associated with an initial datum:

$$\mathbf{U}(x,0) = \mathbf{U}_0(x) \quad \text{in } \Omega$$

and the following boundary conditions:

$$\mathbf{U} = (1,0) \quad \text{on } \Gamma_D$$

$$\mathbf{U} = (1,0) \text{ on } \Gamma_0$$

$$\boldsymbol{\sigma}(\mathbf{U},p)n + \frac{1}{2}(\mathbf{U}\cdot n)^-(\mathbf{U} - \mathbf{U}_{\text{ref}}) = \boldsymbol{\sigma}(\mathbf{U}_{\text{ref}}, p_{\text{ref}})n \quad \text{on } \Gamma_N$$

where $\boldsymbol{\sigma}$ is the stress tensor and we use the notation $a = a^+ - a^-$. In this paper, we consider the flow around the body in an open domain and the flow around the body on top of a road. In the first case, the boundary is solely made up of the entrance section Γ_D and the far field boundary Γ_N everywhere else. In the second case, the road Γ_0 is added as in Fig. 1, and the same speed than the flow at infinity is given to the moving ground. The far field boundary condition is used to convey the vortices through the artificial frontiers without any reflection (see Ref. [31] for more details).

The system of Eqs. (2.6) and (2.7) is solved by a strongly coupled approach for the physical unknowns $(\mathbf{U}, p)$. The numerical simulation does not use any turbulence model. The time discretization in Eq. (2.6) is achieved by using a second-order Gear scheme with explicit treatment of the convection term. That means that $\partial_t \mathbf{U}$ is approximated at time $n\delta t$ by $(3\mathbf{U}^n - 4\mathbf{U}^{n-1} + \mathbf{U}^{n-2})/(2\delta t)$ and that the nonlinear convection term is computed on the right hand side on the form $2(\mathbf{U}^{n-1}\cdot\nabla)\mathbf{U}^{n-1} - (\mathbf{U}^{n-2}\cdot\nabla)\mathbf{U}^{n-2}$. All the linear terms are implicitly treated on the left hand side at time $n\delta t$ and discretized via a second-order centered finite difference scheme. The Courant–Friedrich–Levy (CFL) stability condition related to the convection term requires a time step of the order of magnitude of the space step as $U_\infty = (1,0)$, which is relevant to have a good accuracy of the evolution and does not induce too much CPU time. A third-order finite difference upwind scheme is used for the space discretization of the convection terms [32]. The efficiency of the resolution is obtained by a multigrid procedure by using a cell-by-cell relaxation smoother.

The numerical tests presented in this paper concern the flow around the square back Ahmed body without a road or on top of a road. The intermediate porous layers are set on various parts of the body, and the corresponding geometries are illustrated in Fig. 2 and referred as follows:

Case 0—Ahmed body without porous layer

Case 1—Ahmed body with a porous layer in the upper rounded part in front

Case 2—Ahmed body with a porous layer in the whole top

Case 3—Same as Case 1 but symmetric

Case 4—Same as Case 2 but symmetric

Case 5—Same as Case 4 with the additional front part

Case 6—Same as Case 5 with the additional back part

Case 7—Smaller Ahmed body corresponding to removing the porous part of Case 6

The nondimensioned length and height of Ahmed body are, respectively, $L = 3.625$ and $H = 1$. The computational domain without a road is $\Omega = (0,12H) \times (0,7H)$ and the body is centerd in height while the domain is $\Omega = (0,12H) \times (0,5H)$ when there is a road and then the body is located at a nondimensioned distance $l = 1$ from the road. The results are presented on 1536×896 and 1536×640 cell uniform meshes, respectively, in order to have a significant number of points in the porous layer of thickness h

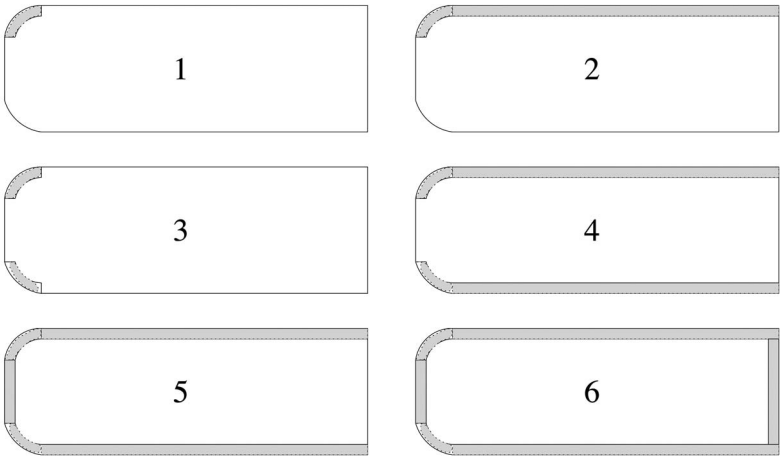

Fig. 2 Cases 1 (top left), 2 (top right), 3 (middle left), 4 (middle right), 5 (bottom left), and 6 (bottom right) corresponding to various porous device geometries

Downloaded 03 Jun 2010 to 171.66.16.157. Redistribution subject to ASME license or copyright; see http://www.asme.org/terms/Terms_Use.cfm

Table 1 Asymptotic values of C_{Lrms} and mean values of the drag coefficient for the square back Ahmed body in an open domain at Re=30,000

Grid size	C_{Lrms}	Drag coefficient
384×224	0.259	0.452
768×448	0.279	0.464
1536×896	0.274	0.469

$=0.1H$. In these computations, the space step is then $\delta x_1=\delta x_2=1/128=0.0078125$ and the related time step $\delta t=0.002$. The integration time over which the numerical simulations are performed is at least $T=100$ and the statistics are gathered when the permanent regime is well established over about ten shedding periods. The mean flows are obtained over at least 3000 snapshots recorded every five time steps; nevertheless, the vorticity contours are quite jagged because they are tabulated with low values around zero. In Ref. [20], a complete parametric study on the flow around a square cylinder has shown that the effect of the control is similar for a range of thickness of the porous layer ($0.05H\leqslant h\leqslant 0.2H$).

3 Numerical Results and Analysis of the Passive Control

To comment on the numerical results, we plot vorticity, fields at given times, the mean flow (vorticity, velocity and pressure fields) and the evolution along time of global quantities such as the enstrophy Z, the drag C_D, and the root mean square of the lift coefficient C_{Lrms} that reveals the regularity and steadiness of the flow. Let us note that up drag refers to the drag due to the front part of the body and down drag refers to the drag at the back. This permits to analyze more carefully the impact of the control. The numerical tests have been performed for the Reynolds number $\mathrm{Re}_r=\mathrm{Re}\times L=30{,}000$ based on the length of the Ahmed body to have a highly transitional flow that corresponds to the studies of literature [16]. Previous convergence studies have shown that grid convergence is achieved for such Reynolds numbers on the grids utilized in this study for a circular cylinder [21]. To confirm this assertion, we give in Table 1 the asymptotic values of the C_{Lrms} and the mean values of the drag coefficient on three consecutive grids for the square back Ahmed body. In addition, the results were then validated, comparing to experimental studies [21]. To have an accurate representation of the solutions, we have taken up to 13 points in the porous layers.

3.1 Flow Around the Square Back Ahmed Body in an Open Domain. As pointed out in the Introduction, the near-wall flow past the square back Ahmed body is mainly a two-dimensional base flow. So, this study is relevant and can properly describe the effect of the porous interfaces on the aerodynamic properties. The interest of the open domain is to have a symmetric geometry on which we can focus on the direct effect of the control procedure only on the body. First of all, we see in Fig. 3 that the unsteady flow is well captured by the numerical method, in particular, the alternate vortex shedding at the square back for the noncontrolled case is close to those observed in Ref. [17]. For the other case, it seems that the two porous layers modify the previous shedding generating a diffuse vortical zone in the near wake; we shall discuss the control effect below.

The effect of the porous layer is presented by illustrating a zoomed in view of the mean vorticity and mean velocity fields around the top circle (see Figs. 4 and 5, respectively). The flow velocity inside the porous layers is very low (less than 10% of the incoming flow velocity) and almost irrotational. For instance, in Case 2, there is a low speed laminar flow all along the upper porous layer that is expelled at the back in the near wake.

For Case 1, the abrupt discontinuity at the end of the porous layer creates a small vertical jet that increases the shedding. Indeed, the flow inside the porous slice is vertically expelled. This jet increases the transverse size of the wake and thus the drag increases with the pressure drag at the bottom (Figs. 6 and 7). This physical phenomenon is very well known in aerodynamics [6]. It increases the asymmetry and the unsteadiness too, so the C_{Lrms} and the enstrophy also increase (Table 2). The discontinuity between the porous layer and the solid obstacle induces positive pressure coefficients (the local static pressure is larger than the reference static pressure) as well as higher velocities and the front drag part increases. Both phenomena yield a 22% total drag increase.

To avoid the abrupt discontinuity at the end of the porous layer, we add a whole porous layer on top of the body in Case 2 (Fig. 2). Then, the vorticity at the interface between the fluid and the obstacle as well as inside the vortices in the near wake decreases. The flow inside the whole layer has two main consequences: It modifies the shear forces on the top boundary of the body and it induces a low horizontal jet at the back expelled into the wake. Each phenomenon partially contributes to the modification of body forces. It was already shown that the first one is equivalent to change the no-slip boundary condition to a Fourier condition [23,30] and so decreases the boundary layer effects. The influence of the jet at the back is the following: The velocity decreases and the negative mean pressure coefficient significantly increases, as shown in Fig. 7 and in Table 3. Consequently, the two phenomena drastically reduce the bottom drag coefficient. As the contribution of the front part is almost the same than without control (Table 2), a 45% reduction in the total drag coefficient is achieved.

To verify the jet effect of a continuous porous layer on the body end and to quantify it, we performed a new computation to control the flow without porous slices, adding a small uniform equivalent jet on the top back of the body. The results are presented in Fig. 8 and in Table 4; they show that the second phenomenon described above induces a 27% reduction in the pressure coefficient gradient

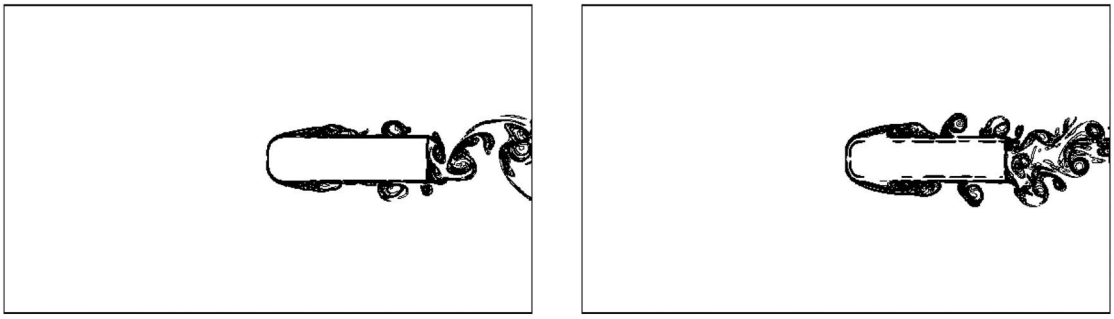

Fig. 3 Vorticity field around the square back Ahmed body in an open domain at Re=30,000; Cases 0 (left) and 5 (right)

Downloaded 03 Jun 2010 to 171.66.16.157. Redistribution subject to ASME license or copyright; see http://www.asme.org/terms/Terms_Use.cfm

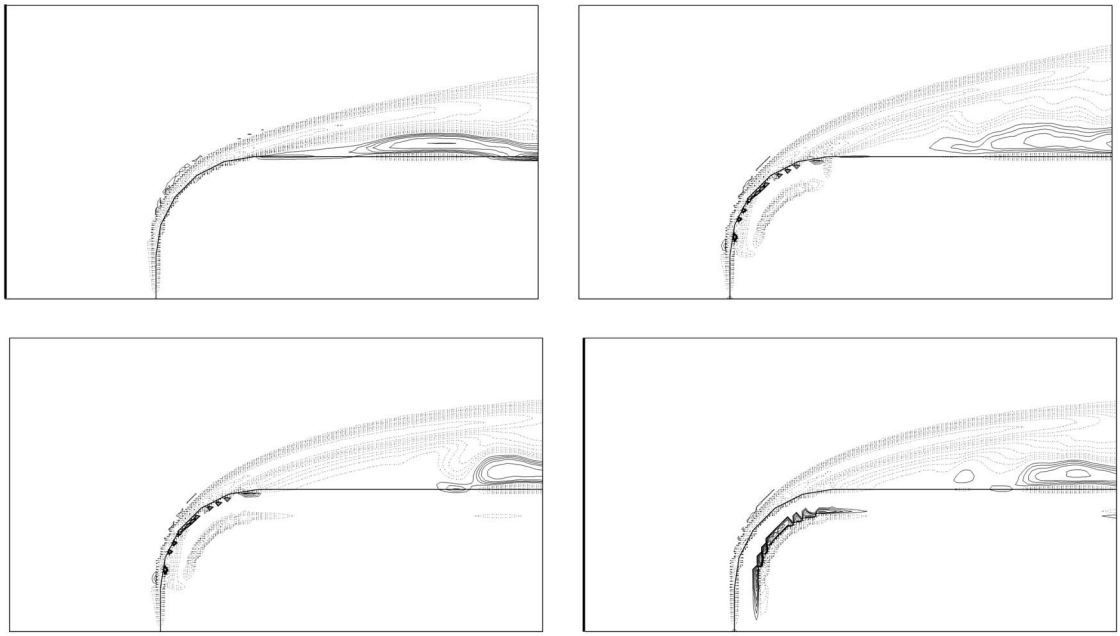

Fig. 4 Time-mean vorticity isolines of the flow near the top front section of a square back Ahmed body at Re =30,000. Cases 0 (top left), 1 or 3 (top right), 2 or 4 (bottom left), and 5 (bottom right). Dotted lines refer to negative values while solid lines refer to positive ones where the absolute values of the isolines are 1, 2, 3, 4, 6, 8, 10, 12, 15, 20, and 30.

at the back and consequently a 13% reduction in the drag. This study approximately quantifies the effect of the jet and shows that the modification of the shear forces on the whole top of the body contributes to a large part of the drag reduction.

For Case 3, the same comments than for Case 1 can be made (Fig. 2); nevertheless, we observe very different results with a significant decrease in the drag coefficient. These results suggest that the symmetry might change the vortex shedding mechanism at the base of the Ahmed body and consequently the static pressure is close to zero. The results for Case 4 should be, as we have shown above for Cases 1 and 3, better than for Case 2. However, the results are about the same as for Case 2. Indeed, due to the vertical jet, the symmetry is strongly failed in Case 1 whereas, Case 3 becomes symmetric again. The loss of symmetry drastically changes the alternate vortex shedding at the end of the body. On the contrary, in Cases 2 and 4, there is no vertical jet and the symmetry is almost conserved; thus, the decay is due both to the porous layers and to the small velocities at the end of the body.

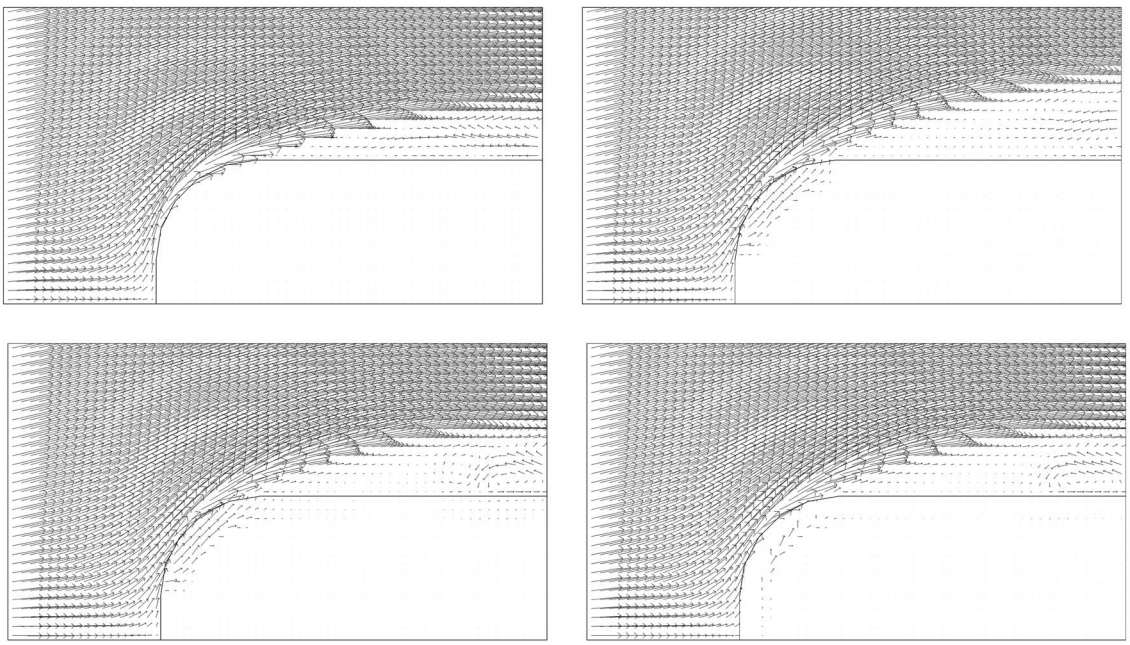

Fig. 5 Time-mean velocity vectors of the flow near the top front section of a square back Ahmed body at Re =30,000. Cases 0 (top left), 1 or 3 (top right), 2 or 4 (bottom left), and 5 (bottom right).

Downloaded 03 Jun 2010 to 171.66.16.157. Redistribution subject to ASME license or copyright; see http://www.asme.org/terms/Terms_Use.cfm

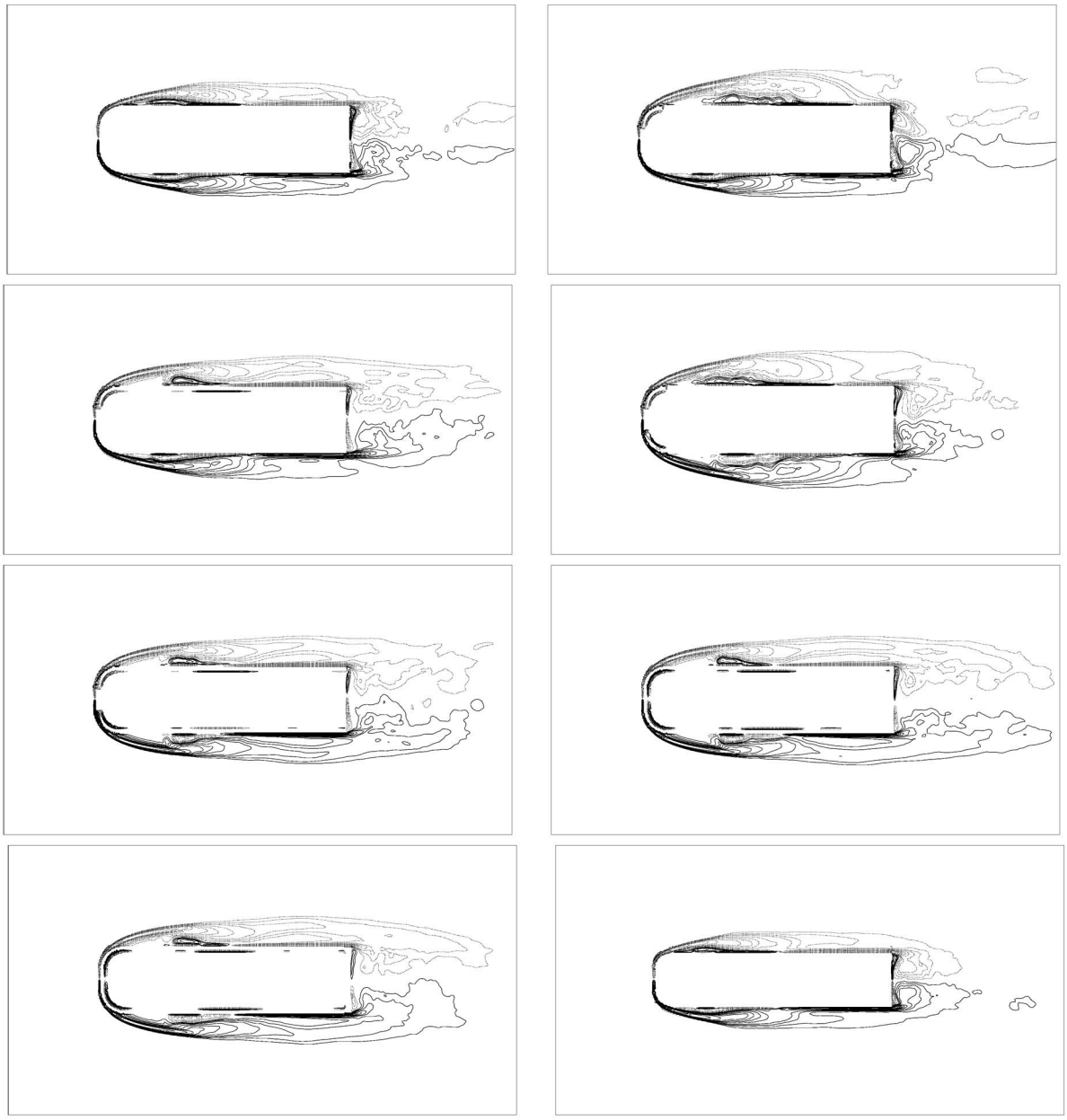

Fig. 6 Time-mean vorticity isolines for the flow around the square back Ahmed body in an open domain at Re =30,000. Cases 0 (top left), 1 (top right), 2 (middle-up left), 3 (middle-up right), 4 (middle-down left), 5 (middle-down right), 6 (bottom left), and 7 (bottom right). Dotted lines refer to negative values while solid lines refer to positive ones where the absolute values of the isolines are 1, 2, 3, 4, 6, 8, 10, 12, 15, 20, and 30.

Cases 5 and 6 give about the same results than Case 4; therefore, adding vertical devices has no significant effect on the whole flow even if the porous part in front (Case 5) reinforces the fluid flow in the porous layers and consequently the jet effect at the back (compare the values of the $C_{p_{\min}}$ in Table 3). All this study shows that, beyond the local action of the passive control by porous layers, there is also a global change linked to the topology of the vortex dynamics that can strongly affect the characteristics of the flow. The numerical experiments above suggest that this global change has a beneficial action in Case 3. The porous layer induces almost a slip property in the vicinity of the solid body and consequently reduces the shear forces acting on the body. Indeed, this is confirmed in Fig. 7 and Tables 2 and 3 as the gain obtained by the passive control using some porous devices is higher than the gain obtained by considering a smaller body completely removing the porous parts of Case 6 (called Case 7). It is clear that the flows corresponding to Cases 0 and 7 are very close to each other as the only difference comes from the size of the body. Whereas the flows obtained with porous devices are very different as the shear forces on the body and Darcy flow inside the porous interfaces change the whole flow.

Let us make some general comments on the various configurations. The large gradients of the mean vorticity fields correspond to the widest transverse eddy sizes and to the highest drag coefficients. This is in accordance to the results given in Ref. [6]. The best results for the aerodynamic drag are achieved when the mean vorticity is close to zero and almost constant at the back. The drag coefficient decreases when the static pressure gradients increase at the back (Fig. 7 and Table 3). This is a classical result for short bluff bodies.

Plotted in Fig. 9 is the time history of the drag and the enstrophy in Cases 0, 2, and 5. It is clear that the passive control de-

Downloaded 03 Jun 2010 to 171.66.16.157. Redistribution subject to ASME license or copyright; see http://www.asme.org/terms/Terms_Use.cfm

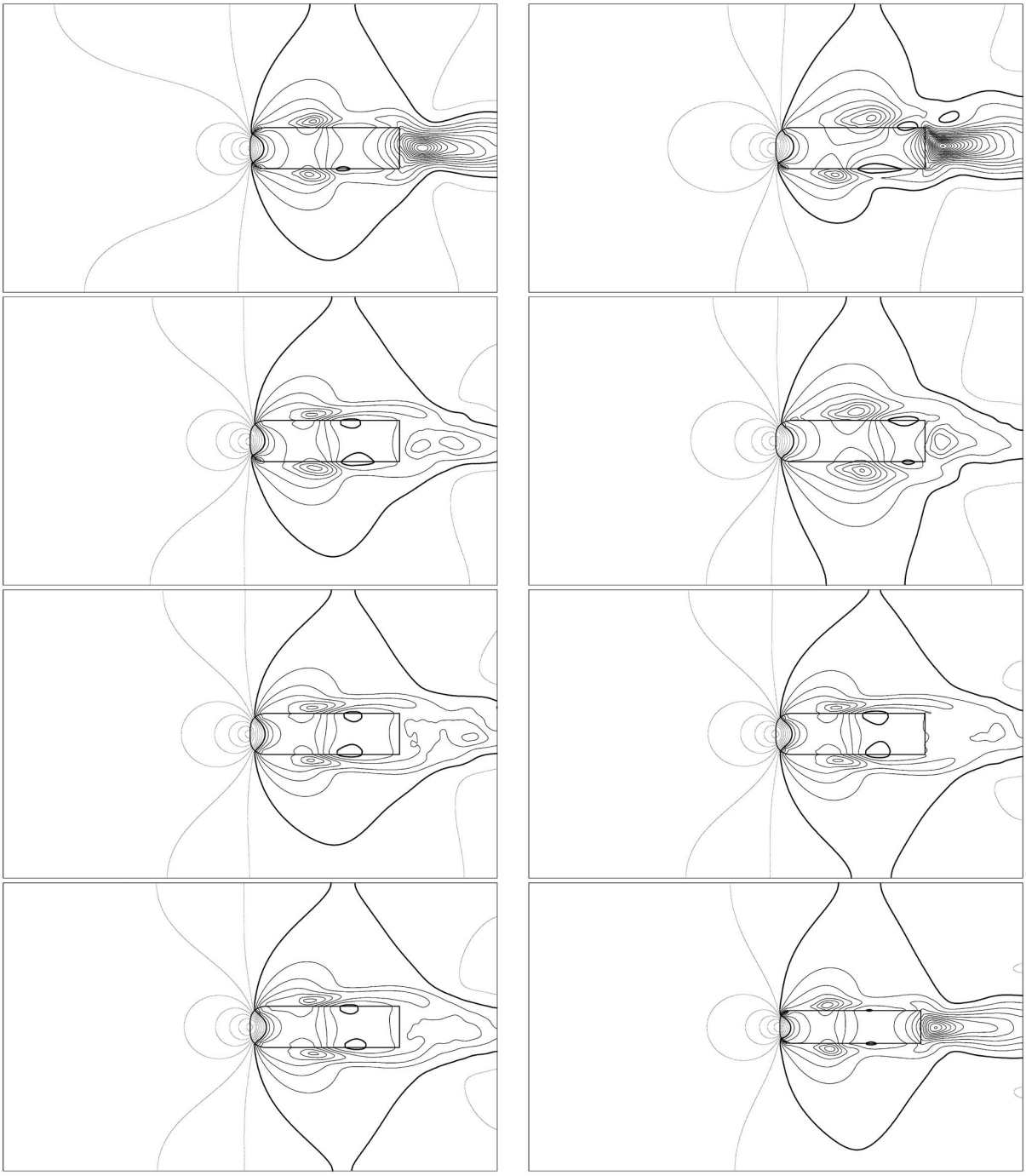

Fig. 7 Time-mean static pressure coefficient C_p isolines for the flow around the square back Ahmed body in an open domain at Re=30,000. Cases 0 (top left), 1 (top right), 2 (middle-up left), 3 (middle-up right), 4 (middle-down left), 5 (middle-down right), 6 (bottom left), and 7 (bottom right). Dotted lines refer to positive values while solid lines refer to negative ones where the change in the quantity between each subsequent isoline is equal to 0.2. The thick solid line refers to the isovalue 0.0.

Table 2 Asymptotic values of C_{Lrms} and mean values of the enstrophy and the drag coefficient for the square back Ahmed body in an open domain at Re=30,000

	C_{Lrms}	Enstrophy	Up drag	Down drag	Drag coefficient
Case 0	0.274	7911	0.133	0.329	0.469
Case 1	0.357 (+30%)	8174	0.200	0.370	0.573 (+22%)
Case 2	0.158 (−42%)	7877	0.130	0.120	0.257 (−45%)
Case 3	0.254 (−7%)	8117	0.176	0.161	0.338 (−28%)
Case 4	0.173 (−37%)	7827	0.163	0.104	0.276 (−41%)
Case 5	0.162 (−41%)	7876	0.185	0.088	0.281 (−40%)
Case 6	0.158 (−42%)	7862	0.169	0.109	0.286 (−39%)
Case 7	0.264 (−4%)	7561	0.096	0.221	0.322 (−31%)

Downloaded 03 Jun 2010 to 171.66.16.157. Redistribution subject to ASME license or copyright; see http://www.asme.org/terms/Terms_Use.cfm

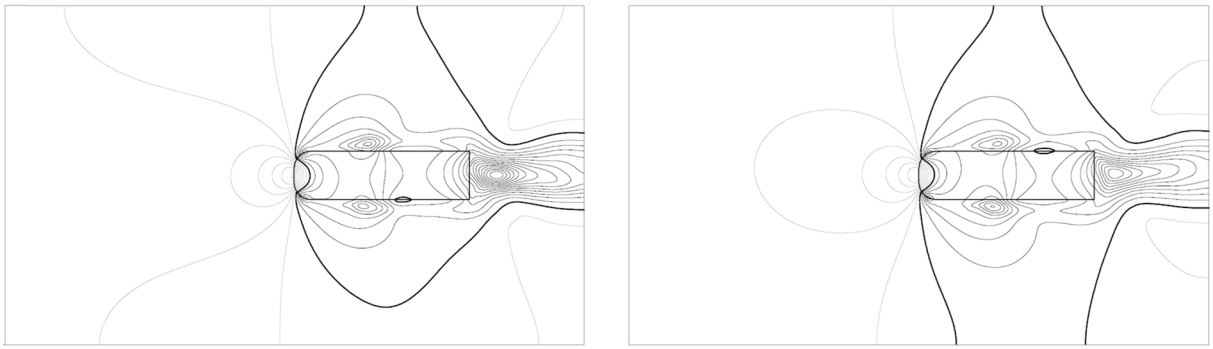

Fig. 8 Time-mean static pressure coefficient C_p isolines for the flow around the square back Ahmed body in an open domain at Re=30,000. Case without control (left) and case with control by a permanent jet on top of the back (right). Dotted lines refer to positive values while solid lines refer to negative ones where the change in the quantity between each subsequent isoline is equal to 0.2. The thick solid line refers to the isovalue 0.0.

creases these quantities as well as their amplitude, their frequency, and their irregularities. Table 2 shows that the mean values of the drag coefficient are significantly reduced (more than 40%) except in Cases 1 and 3 because of the vertical jet already pointed out. The time-mean values of the drag coefficient given in this table are very close to the root mean square of the drag coefficient $C_{D_{\text{rms}}}$ as the permanent regime is achieved and the drag coefficient is always positive. The flow is also regularized as there is also a significant reduction in the $C_{L_{\text{rms}}}$ for the same cases. Consequently, the vortex induced vibrations should be strongly reduced.

Table 3 The value and the location of the minimum of the mean static pressure coefficient C_p in the close wake of the square back Ahmed body in an open domain at Re=30,000

	$C_{p_{\text{min}}}$ value in the wake	$C_{p_{\text{min}}}$ location
Case 0	−2.983	(10.20, 3.52)
Case 1	−4.026	(10.06, 3.55)
Case 2	−0.728	(10.89, 3.47)
Case 3	−0.950	(10.02, 3.48)
Case 4	−0.657	(11.40, 3.42)
Case 5	−0.498	(11.38, 3.55)
Case 6	−0.589	(10.91, 3.56)
Case 7	−2.216	(9.89, 3.48)

In conclusion, it appears that the position of the porous slices is very sensible and that for a good choice, a significant improvement can be achieved by this passive control.

All the results obtained at Re=30,000 are confirmed by simulations with a higher Reynolds number Re=60,000, as it can be seen in Table 5 for Cases 2 and 4. The drag values depend on the Reynolds number but the drag reduction is in the same range. We notice that the results for the symmetric case are this time better.

3.2 Flow Around the Square Back Ahmed Body on Top of a Road. In this section, Cases 0–5 of the previous section are considered with the square back Ahmed body located on top of a road. As stated before, the road is represented by a moving ground having the same speed than the flow at infinity. The results are plotted in Figs. 10–12. The time history of the drag coefficient and the enstrophy are plotted in Fig. 13, and Table 6 summarizes the evolution of the three global quantities; The minimum of the mean static pressure in the near wake is given in Table 7. The enstrophy history shows both a strong reduction and a regularization. The same comments than in the previous section can be done, for instance, the vorticity fields plotted in Fig. 10 show again the negative effect of the small vertical jet in Case 1, and a porous layer on top of the whole roof gives again the best drag reduction. At the back for this last case, the static pressure coefficient gradients are weaker and the vorticity is close to zero (Table 7 and Fig.

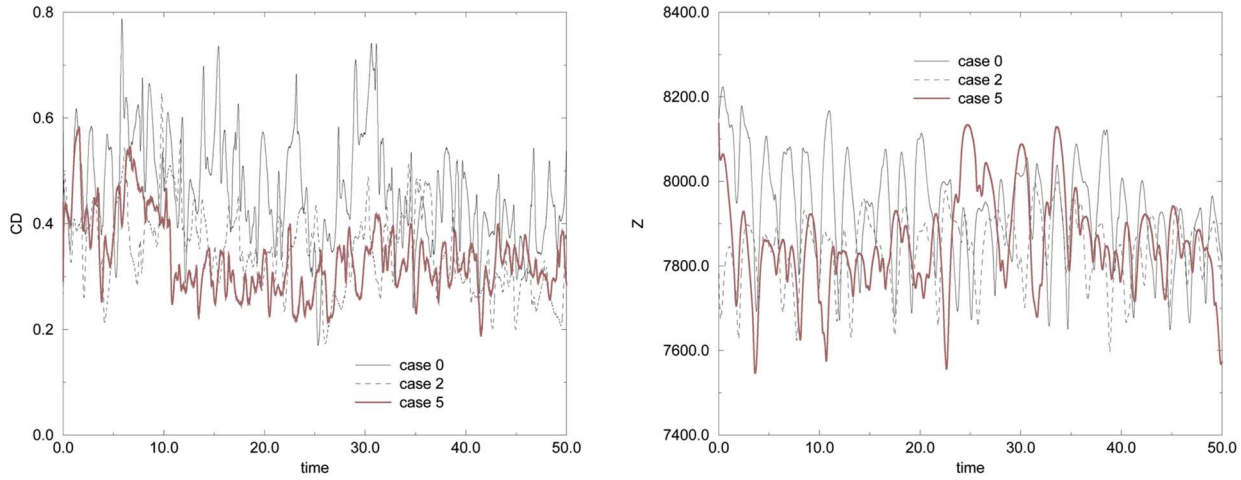

Fig. 9 Time history of the drag coefficient (left) and the enstrophy (right) for the flow around the square back Ahmed body in an open domain at Re=30,000

Downloaded 03 Jun 2010 to 171.66.16.157. Redistribution subject to ASME license or copyright; see http://www.asme.org/terms/Terms_Use.cfm

Table 4 The value of the mean drag coefficient and of the minimum of the mean static pressure coefficient C_p in the close wake of the square back Ahmed body in an open domain at Re=30,000

	Drag coefficient	$C_{p_{\min}}$ value in the wake
Without control	0.469	−2.983
With control by a jet	0.407 (−13%)	−2.165 (−27%)

Table 5 Asymptotic values of C_{Lrms} and mean values of the enstrophy and the drag coefficient for the square back Ahmed body in an open domain at Re=60,000

	C_{Lrms}	Enstrophy	Drag coefficient
Case 0	0.35	8268	0.549
Case 2	0.27 (−23%)	8011	0.354 (−35%)
Case 4	0.20 (−43%)	7931	0.310 (−44%)

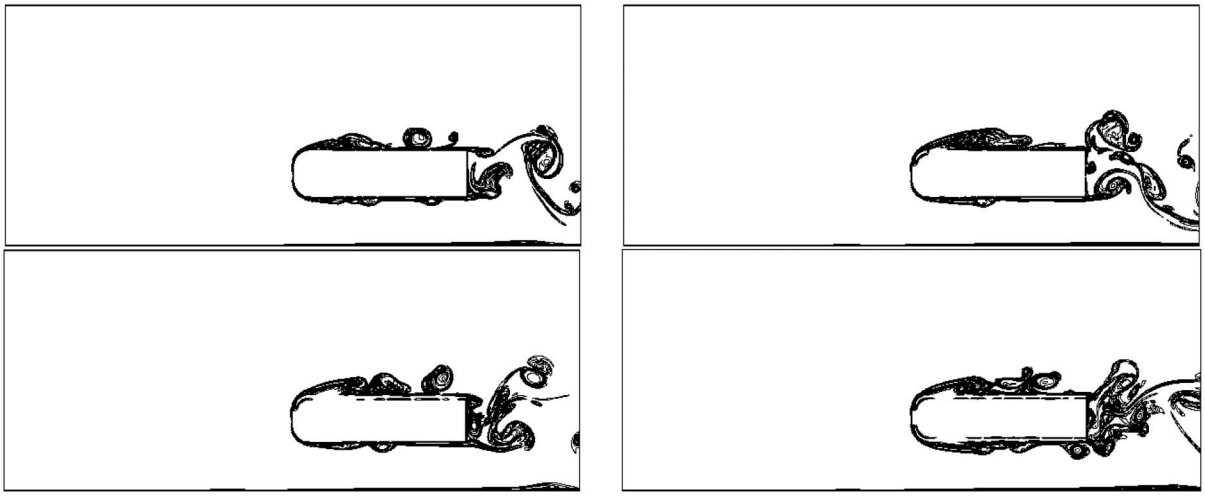

Fig. 10 Vorticity field around the square back Ahmed body on top of a road at Re=30,000; Cases 0 (top left), 1 (top right), 2 (bottom left), and 4 (bottom right)

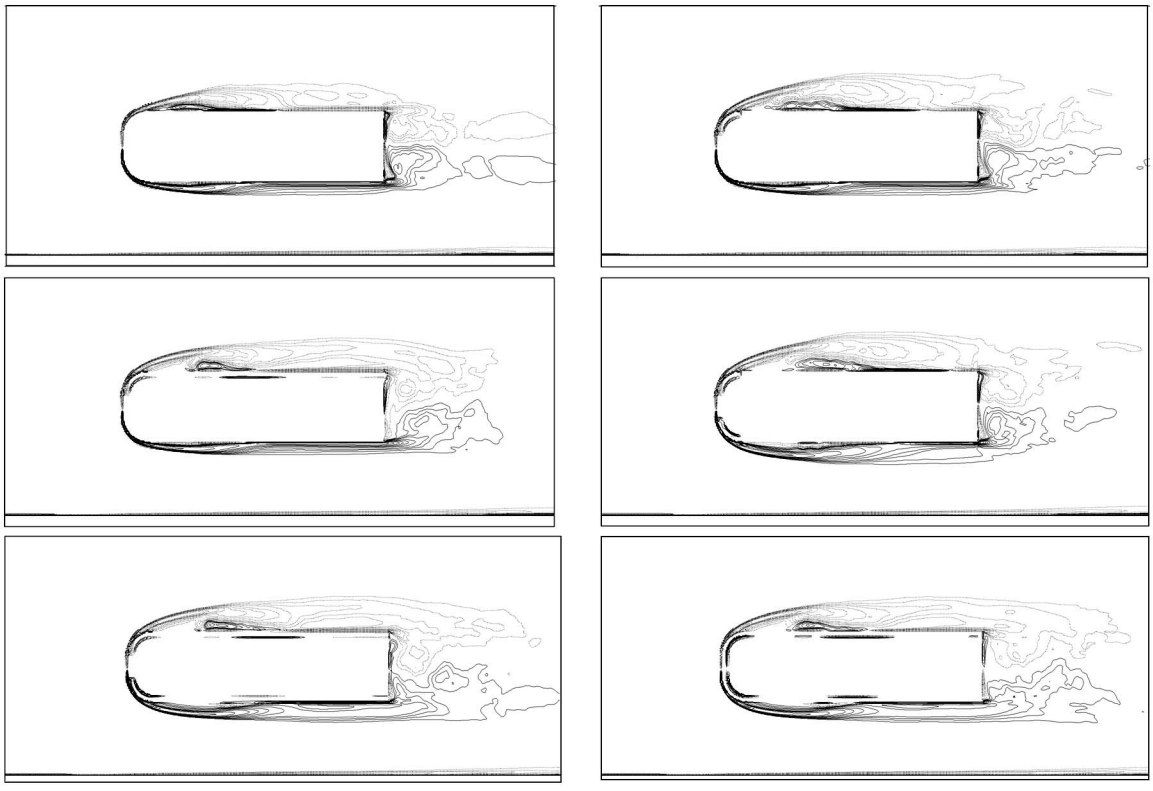

Fig. 11 Time-mean vorticity isolines for the flow around the square back Ahmed body on top of a road at Re =30,000. Cases 0 (top left), 1 (top right), 2 (middle left), 3 (middle right), 4 (bottom left), and 5 (bottom right). Dotted lines refer to negative values while solid lines refer to positive ones where the absolute values of the isolines are 1, 2, 3, 4, 6, 8, 10, 12, 15, 20, and 30.

Downloaded 03 Jun 2010 to 171.66.16.157. Redistribution subject to ASME license or copyright; see http://www.asme.org/terms/Terms_Use.cfm

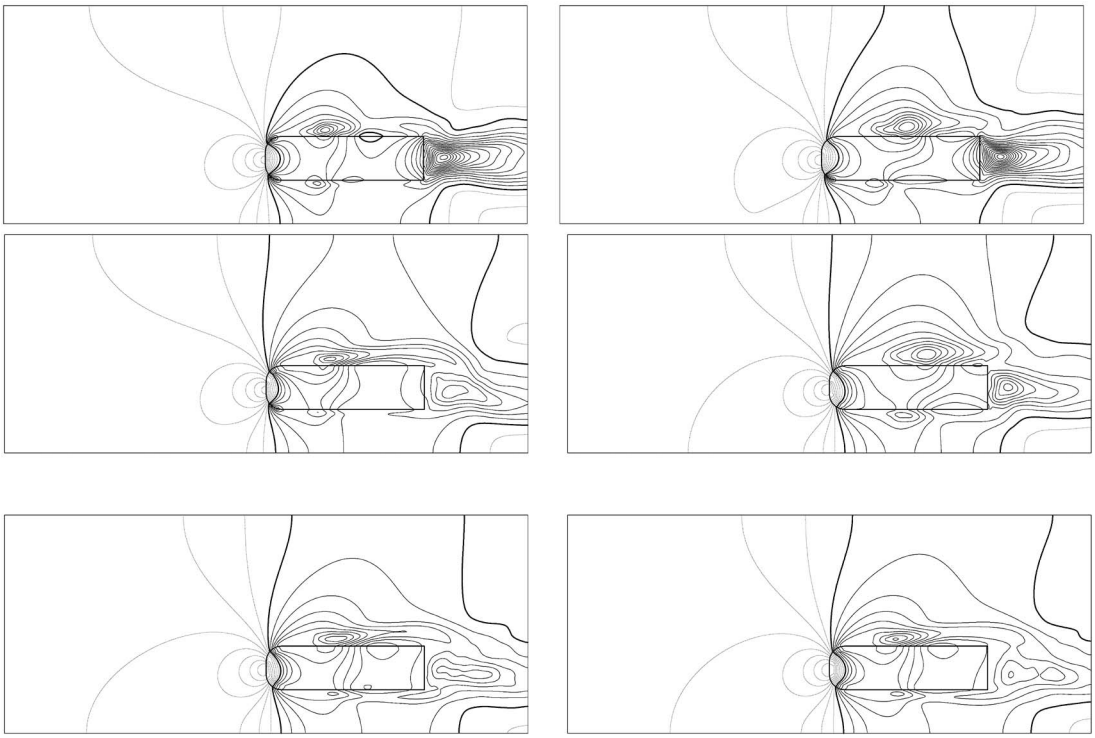

Fig. 12 Time-mean static pressure coefficient C_p isolines for the flow around the square back Ahmed body on top of a road at Re=30,000. Cases 0 (top left), 1 (top right), 2 (middle left), 3 (middle right), 4 (bottom left), and 5 (bottom right). Dotted lines refer to positive values while solid lines refer to negative ones where the change in the quantity between each subsequent isoline is equal to 0.2. The thick solid line refers to the isovalue 0.0.

11). This is in accordance with the previous results without a road. So, we focus on the effects due to the road. With the road, the aerodynamic forces are increased and the flow rate is larger on the upper part of the body. In Case 1, the porous layer on top of the rounded part of the body has two effects: First, the shedding angle is decreased (see Ref. [6]); second, the flow rate is increased on the upper part of the domain and thus decreased under the car. Consequently, the mean velocity under the car is lower and the aerodynamic power dissipated by the floor of the car is decreased [33]. Nevertheless, the vertical jet effect described in the open case yields an increase in the up drag. In summary, even if the drag is slightly increased, the loss of the aerodynamic performances is less important than in the open flow case (Table 6). Case 2 confirms the previous results and gives again the best results. Here, the up drag is decreased as the whole porous slice on top of the body induces a significant increase in the flow rate on top and a decrease in the flow rate under the car. In the other cases, the flow rate under the car increases and thus the up drag

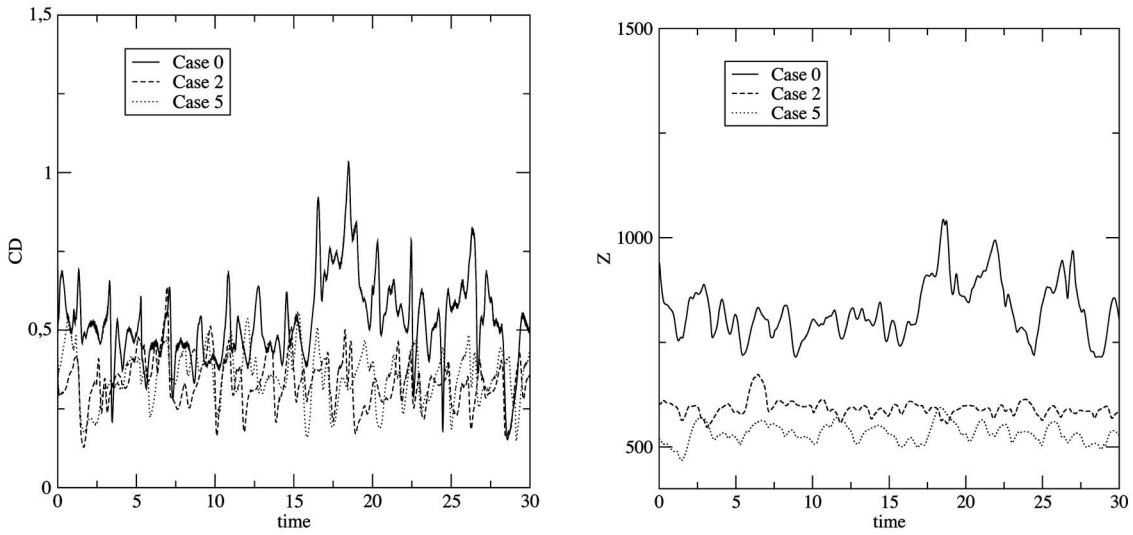

Fig. 13 Time history of the drag coefficient (left) and the enstrophy (right) for the flow around the square back Ahmed body on top of a road at Re=30,000

Downloaded 03 Jun 2010 to 171.66.16.157. Redistribution subject to ASME license or copyright; see http://www.asme.org/terms/Terms_Use.cfm

Table 6 Asymptotic values of C_{Lrms} and mean values of the enstrophy and the drag coefficient for the square back Ahmed body on top of a road at Re=30,000

	C_{Lrms}	Enstrophy	Up drag	Down drag	Drag coefficient
Case 0	0.517	827	0.173	0.343	0.526
Case 1	0.545 (+5%)	835 (+1%)	0.231	0.330	0.567 (+8%)
Case 2	0.396 (−23%)	592 (−28%)	0.156	0.166	0.332 (−37%)
Case 3	0.674 (+30%)	732 (−11%)	0.214	0.176	0.391 (−26%)
Case 4	0.381 (−26%)	541 (−35%)	0.213	0.139	0.362 (−31%)
Case 5	0.352 (−32%)	533 (−36%)	0.217	0.127	0.354 (−33%)

increases. However, the downstream jet effect under the car is beneficial to the down drag, and a global decrease in 30% is achieved as the mean static pressure coefficient strongly increases in the wake (Table 7). In Case 3, the jet effect on the upper part at the bottom of the body is responsible for the increase in the $C_{L_{\text{rms}}}$. This is mainly due to the oblique jet in the direction to the road that locally increases the pressure forces on the body underneath and thus increases the lift coefficient all along the time.

As in the previous section, these results show that the porous layer on the front of the body does not have a strong effect on the drag reduction. In the same way, the porous layer on the bottom is not very efficient as the gain on the down drag is compensated by a loss on the up drag. The effect of the porous layer is stronger than the effect of the road. As in the previous section, Cases 4 and 5 give the lowest static pressure coefficient gradients and Case 2 gives the best drag reduction.

4 Conclusions

A passive control technique by using a porous slice implemented on some parts of the two-dimensional square back Ahmed body is tested to reduce global quantities such as the drag coefficient, the enstrophy, or the $C_{L_{\text{rms}}}$ of the flow. Furthermore, the effect of the road on the control results is studied.

For every successful control configuration, the aerodynamic drag decreases with the rise of the static pressure and the decrease in the vorticity measured at the back. The drag reduction is also linked to the decrease in the wake transverse size. In most cases, the results show the beneficial effect of the porous layer implementation on the drag reduction. As an example, a porous layer placed on the upper front corner and roof considerably reduces the transverse section of the wake, and a drag reduction of about 45% is achieved. The symmetrization of the control devices generally improves the results but adding a porous slice to the vertical front wall does not change the control much. The presence of a road slightly decreases the efficiency of the control but does not alter the general tendency observed without the road.

In summary, this passive control approach is very promising as significant gains are obtained with a good choice of the layer location. Further work on coupling both passive and active control approaches will be performed on the three-dimensional Ahmed body as it is shown in Ref. [17] that the flow can be reattached by a suction jet on the top of the rear window.

Table 7 The value and the location of the minimum of the mean static pressure coefficient C_p in the close wake of the square back Ahmed body on top of a road at Re=30,000

	$C_{p_{\min}}$ value in the wake	$C_{p_{\min}}$ location
Case 0	−3.272	(10.11, 1.53)
Case 1	−3.515	(10.11, 1.53)
Case 2	−1.355	(10.22, 1.39)
Case 3	−1.681	(10.09, 1.52)
Case 4	−1.081	(10.89, 1.34)
Case 5	−1.017	(10.16, 1.34)

References

[1] Cooper, K. R., 1985, SAE Paper No. 850288.
[2] Gilliéron, P., Chometon, F., and Laurent, J., 2003, "Analysis of Hysteresis and Phase Shifting Phenomena in Unsteady Three-Dimensional Wakes," Exp. Fluids, **35**, pp. 117–129.
[3] Fiedler, H. E., and Fernholz, H. H., 1990, "On Management and Control of Turbulent Shear Flows," Prog. Aerosp. Sci., **27**, pp. 305–387.
[4] Gilliéron, P., 2002, "Flow Control Applied to the Car. State of the Art," Mécanique et Industrie, **3**, pp. 515–525.
[5] Roshko, A., and Koening, K., 1976, *Symposium on Aerodynamic Drag Mechanisms of Bluff Bodies and Road Vehicles*, General Motors Research Report.
[6] Onorato, M., Costelli, A., and Garonne, A., 1984, SAE Paper No. 840302.
[7] Reznicek, R., 1989, *Surface Tracing Methods*, Hemisphere, New York, 1989.
[8] Gilliéron, P., and Chometon, F., 1999, "Modelling of Stationary Three-Dimensional Detached Airflows Around an Ahmed Reference Body," ESAIM Proc., **7**, pp. 173–182.
[9] Mair, W. A., 1965, "The Effect of a Rear-Mounted Disc on the Drag of a Blunt-Based Body of Revolution," Aeronaut. Q., **16**, pp. 350–360.
[10] Gilliéron, P., 2003, "Detailed Analysis of the Overtaking Process," J. Mech. Eng., **53**, pp. 1–17.
[11] Bak, C., Fuglsang, P., Johansen, J., and Antoniou, I., 2000, Risoe National Laboratory, Technical Report No. Risoe-R-1193.
[12] Suzuki, Y., and Ijima, T., 1999, *Flucome 94*, Toulouse, pp. 379–384.
[13] Bearman, P. W., 1965, "Investigation of the Flow Behind a Two-Dimensional Model With a Blunt Trailing Edge With Splitter Plates," J. Fluid Mech., **21**, pp. 241–255.
[14] Bearman, P. W., and Harvey, J. K., 1993, "Control of Circular Cylinder Flow by the Use of Dimples," AIAA J., **31**, pp. 1753–1756.
[15] Ahmed, S. R., Ramm, G., and Falting, G., 1984, SAE Paper No. 840300.
[16] Gilliéron, P., and Spohn, A., 2002, *IUTAM Symposium Unsteady Separated Flows*, Toulouse, France.
[17] Rouméas, M., 2006, Ph.D. thesis, University of Toulouse III.
[18] Krajnovic, S., and Davidson, L., 2003, "Numerical Study of the Flow Around the Bus-Shaped Body," ASME J. Fluids Eng., **125**, pp. 907–918.
[19] Lienhart, H., Stoots, C., and Becker, S., 2000, *DGLR Fach Symposium Der AG STAB*, Stuttgart.
[20] Bruneau, C. H., and Mortazavi, I., 2004, "Passive Control of Flow Around a Square Cylinder Using Porous Media," Int. J. Numer. Methods Fluids, **46**, pp. 415–433.
[21] Bruneau, C. H., and Mortazavi, I., 2006, "Control of Vortex Shedding Around a Pipe Section Using a Porous Sheath," Int. J. Offshore Polar Eng., **16**, pp. 90–96.
[22] Caltagirone, J. P., 1994, "Sur L'interaction Fluide-Milieu Poreux: Application au Calcul des Efforts Exercés sur un Obstacle par un Fluide Visqueux," C. R. Acad. Sci. Paris, Série II, **318**, pp. 571–577.
[23] Achdou, Y., Pironneau, O., and Valentin, F., 1998, "Effective Boundary Conditions for Laminar Flows Over Periodic Rough Boundaries," J. Comput. Phys., **147**, pp. 187–218.
[24] Arquis, E., and Caltagirone, J. P., 1984, "Sur les Conditions Hydrodynamiques au Voisinage d'une Interface Milieu Fluide–Milieu Poreux: Application à la Convection Naturelle," C. R. Acad. Sci. Paris, Série II, **299**, pp. 1–4.
[25] Angot, Ph., Bruneau, C. H., and Fabrie, P., 1999, "A Penalization Method to Take Into Account Obstacles in Incompressible Viscous Flows," Numer. Math., **81**, pp. 497–520.
[26] Kevlahan, N., and Ghidaglia, J. M., 2001, "Computation of Turbulent Flow Past an Array of Cylinders Using a Spectral Method With Brinkman Penalization," Eur. J. Mech. B/Fluids, **20**, pp. 333–350.
[27] Nield, D., and Bejan, A., 1999, *Convection in Porous Media*, Springer, New York.

Downloaded 03 Jun 2010 to 171.66.16.157. Redistribution subject to ASME license or copyright; see http://www.asme.org/terms/Terms_Use.cfm

[28] Whitaker, S., 1999, *The Method of Volume Averaging*, Kluwer, Dordrecht.
[29] Beavers, G. D., and Joseph, D. D., 1967, "Boundary Conditions at a Naturally Permeable Wall," J. Fluid Mech., **30**, pp. 197–210.
[30] Carbou, G., 2007, "Brinkman Model and Double Penalization Method for the Flow Around a Porous Thin Layer," J. Math Fluid Mech., **10**, pp. 126–158.
[31] Bruneau, C. H., and Fabrie, P., 1994, "Effective Downstream Boundary Conditions for Incompressible Navier–Stokes Equations," Int. J. Numer. Methods Fluids, **19**, pp. 693–705.
[32] Bruneau, C. H., and Saad, M., 2006, "The 2D Lid-Driven Cavity Problem Revisited," Comput. Fluids, **35**, pp. 326–348.
[33] Chometon, F., and Gilliéron, P., 1996, "Modélisation des Écoulements Tridimensionnels Décolles Autour des Véhicules Automobiles à l'aide d'un Modèle à Zéro-Dimension," *Journée d'Étude Aérodynamique Automobile*, Courbevois-Paris 5, 960911.

Downloaded 03 Jun 2010 to 171.66.16.157. Redistribution subject to ASME license or copyright; see http://www.asme.org/terms/Terms_Use.cfm

Computational Investigation of Torque on Coaxial Rotating Cones

Steve Rapley

Carol Eastwick
e-mail: carol.eastwick@nottingham.ac.uk

Kathy Simmons

University Technology Centre for Gas Turbine Transmission Systems,
University of Nottingham,
University Park,
Nottingham NG7 2RD, United Kingdom

*This article looks at a modification of Taylor–Couette flow, presenting a numerical investigation of the flow around a shrouded rotating cone, with and without throughflow, using the commercial computational fluid dynamics code FLUENT 6.2 and FLUENT 6.3. The effects of varying the cone vertex angle and the gap width on the torque seen by the rotating cone are considered, as well as the effect of a forced throughflow. The performance of various turbulence models are considered, as well as the ability of common wall treatments/functions to capture the near-wall behavior. Close agreement is found between the numerical predictions and previous experimental work, carried out by Yamada and Ito (1979, "Frictional Resistance of Enclosed Rotating Cones With Superposed Throughflow," ASME J. Fluids Eng., **101**, pp. 259–264; 1975, "On the Frictional Resistance of Enclosed Rotating Cones (1st Report, Frictional Moment and Observation of Flow With a Smooth Surface)," Bull. JSME, **18**, pp. 1026–1034; 1976, "On the Frictional Resistance of Enclosed Rotating Cones (2nd Report, Effects of Surface Roughness)," Bull. JSME, **19**, pp. 943–950). Limitations in the models are considered, and comparisons between two-dimensional axisymmetric models and three-dimensional models are made, with the three-dimensional models showing greater accuracy. The work leads to a methodology for modeling similar flow conditions to Taylor–Couette.*
[DOI: 10.1115/1.2903518]

1 Introduction

The motivation for the work contained in this paper arose from an industrial problem. The problem was how could windage power loss (WPL) from rotating gears be reduced. Within many industries, gear box losses represent a major efficiency loss [4]. These losses can arise from many sources, one of which is the resistance or drag caused by the gear rotating in a fluid. At the University of Nottingham, experimental and computational projects are looking at this issue (Farrall et al. [5], Johnson et al. [6], and Rapley et al. [7]). As a first step in a computational project, a methodology relevant for a simplified situation that had experimental data available for validation was investigated. The simplified case undertaken was a shrouded rotating cone, which had physical similarity with a single shrouded spiral bevel gear, which was the first experimental case considered. The experimental data were taken from studies by Yamada and Ito [1–3].

A review of current literature is presented in Sec. 2, the computational fluid dynamics (CFD) methodology is presented in Sec. 3, with results and discussion in Sec. 4, and conclusions in Sec. 5.

1.1 Physical Background. The geometry in the physical setting is identical (except for an assumption on the inlet size) to that used by Yamada and Ito [1–3], and is shown in Fig. 1. It involves a cone of varying vertex angle rotating inside a conical shroud. The fluid used by Yamada & Ito was water. The water enters through an inlet, before impacting on the apex of the rotating inner cone. The physical cases modelled are described in Table 1.

2 Previous Work

This section describes previous work on basic and conical Taylor–Couette flow, which are of relevance to the work studied here. To commence, basic Taylor–Couette flow is considered (Sec. 2.1), as this provides the basis to the theory and knowledge utilized when considering any variations upon Taylor–Couette flow (Sec. 2.2). Throughflow effects are also considered, as they will be modeled in this study, so it is important to understand their potential impact on the flow structure (Sec. 2.3)

2.1 Taylor–Couette Flow. Much work has been conducted on basic Taylor–Couette flow, that is, the flow between two right cylinders[1] where the inner cylinder rotates and the outer cylinder remains stationary, see Wild et al. [8], Lathrop et al. [9], Dubrulle and Hersant [10], and Shiomi et al. [11]; these are discussed below.

Wild et al. [8] performed an experimental and computational assessment of windage losses in rotating machinery. This was achieved by studying Taylor–Couette flow experimentally and computationally, utilizing an earlier version of FLUENT (circa 1992). Their calculations made use of three turbulence models, the standard k-ϵ model [12], the RNG k-ϵ model [13,14], and the Reynolds stress model (RSM) model [15]. Wild et al. found that good agreement could be found between the standard k-ϵ model with their own experimental data.

Lathrop et al. [9] looked experimentally at Taylor–Couette flow at large Reynolds number, $10^3 < \mathrm{Re} < 10^6$. They observed a transition in the flow at $\mathrm{Re} = 1.3 \times 10^4$, and that while approximate relationships between the torque and Reynolds number could be given above and below this transition (respectivelly, $M_{\mathrm{disk}} \sim \mathrm{Re}^{1.3}$ and $M_{\mathrm{disk}} \sim \mathrm{Re}^{1.73}$), no global relationships could be defined.

Dubrulle and Hersant [10] looked at momentum transport and torque scaling in Taylor–Couette flow from an analogy with turbulent convection. They present two predictions as to the relationship between torque and Reynolds number for both low values of Re,

$$M_{\mathrm{disk}} = 1.46 \frac{T^{3/2}}{(1-T)^{7/4}} \mathrm{Re}^{3/2}$$

and larger values of Re,

Contributed by the Fluids Engineering Division of ASME for publication in the JOURNAL OF FLUIDS ENGINEERING. Manuscript received April 16, 2007; final manuscript received November 4, 2007; published online June 6, 2008. Assoc. Editor: Rajat Mittal.

[1] A "right" cylinder is one where the angle between the sides of the cylinder is 90 deg, a right angle.

 Copyright © 2008 by ASME

Downloaded 03 Jun 2010 to 171.66.16.157. Redistribution subject to ASME license or copyright; see http://www.asme.org/terms/Terms_Use.cfm

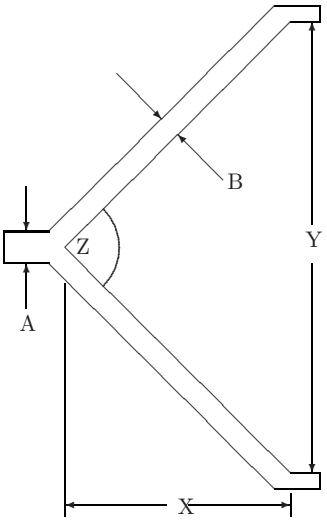

Fig. 1 Schematic of rotating cone geometry

$$M_{\text{disk}} = 0.5\frac{T^2}{(1-T)^{3/2}}\frac{\text{Re}^2}{\ln[T^2(1-T)\text{Re}^2 \times 10^{-4}]^{3/2}}$$

Dubrulle and Hersant [10] demonstrated good agreement between the predictions and experimental data.

To summarize, the literature indicates that basic Taylor–Couette flow can be modeled accurately, with torque levels relatively easy to predict. While global relationships between torque levels and Reynolds number may not exist, approximate relationships can be found.

2.2 Modified Taylor–Couette Flow. If we change the geometry of either cylinder, much more complex flows can occur. Wimmer [16] presented a comprehensive analysis of some of these variations on Taylor–Couette flow, describing the flow between combinations of cylinders, cones, or spheres, with thorough descriptions of when, where, and how the Taylor vortices occur, and looking at the influence of initial and boundary conditions have on the flow. It provides a first look at the possible flows that occur in the setting currently modelled.

Modifying Taylor–Couette flow by replacing the right cylinders by conical cylinders (which are also known as truncated cones), which may be known as conical Taylor–Couette flow, produces a complex flow pattern, as has been studied by Noui-Mehidi et al. [17–21]. For vertex angles close to 0 deg (close to a cylinder), the flow structure is very similar to Taylor–Couette flow, but, as the angle is increased toward 180 deg (close to a disk), the classic structure of vortex pairs starts to break down and eventually disappear. The flow starts to develop characteristics akin to disk flow for a vertex angle $\phi \sim 60$ deg [22]. Eventually, the flow starts to show similarities to the flow over a rotating disk. In general, the structure of conical Taylor–Couette flow is a lot more complicated than the basic Taylor–Couette flow, being dependent on gap width, cylinder height, rate of rotation, angle of conic, and rate of acceleration, with many different flows possible at the same angular velocities.

Wimmer [17] presented an experimental investigation of conical Taylor–Couette flow. The influence of initial and boundary conditions on the flow is seen to be considerable, producing a wide variety of possible vortex configurations. Wimmer observed, importantly, that a system of toroidal vortices can travel through a closed flow system, without any external influence. If there exist upward traveling vortices, their velocity decreases with increasing gap width, T. Wimmer also highlighted, importantly, that in "a rare case in fluid dynamics" unstable steady and transient flows can easily coexist in conical Taylor–Couette flow.

Noui-Mehidi [20] looked experimentally at the effect of acceleration on transition properties in a conical cylinder system, for which the vertex angle was $\phi = 16.38$ deg. Noui-Mehidi observed that the rate of acceleration of the rotating inner cone, $d\text{Re}/d\text{t}$, had a considerable effect on the final flow. If this acceleration rate was lower than 6.8, a helical motion (a pair of counter-rotating vortex tubes winding around the inner conical cylinder) was observed, whereas for accelerations higher than 6.8, an upward motion was observed in the vortices.

The helical motion has been investigated further by Noui-Mehidi et al. [21]. They considered the dynamics of the helical motion, looking at the transition from laminar helical motion to turbulent helical motion, highlighting yet more varieties in the flow field.

The acceleration rate can also have an influence on the number of vortices present. By looking at the mechanism of mode selection for conical Taylor–Couette flow, Noui-Mehidi et al. [18] observed that if $d\text{Re}/d\text{t} = 0.6$, six pairs of steady vortices develop at $\text{Re} = 340$, whereas if the acceleration is =1.3, seven pairs of steady vortices develop at $\text{Re} = 520$, and eight pairs of steady vortices develop at $\text{Re} = 730$.

Another mechanism, which will alter the number of vortices present, is varying the cone vertex angle, ϕ. Noui-Mehidi et al. [23] performed a numerical computation of this effect, by varying the cone vertex angle over the range $0 \text{ deg} \leq \phi \leq 8$ deg. This behavior was investigated experimentally over a greater range by Wimmer and Zierep [22], varying the vertex angle over the range $0 \text{ deg} \leq \phi \leq 180$ deg, that is all the way from a cylinder ($\phi = 0$ deg) to a disk ($\phi = 180$ deg). Some important observations as to the flow involved in the situation that will be modeled here were observed. Primarily, for cones with vertex angles of $\phi = 90$ deg and $\phi = 120$ deg (the same angles as considered numerically in the study), no Taylor vortices were observed. The flow that does occur is a spiral instability, which forms regular spiral patterns, which is similar to the flow observed on a rotating disk.

The gap width is another factor that can effect the vortices present in conical Taylor–Couette flow. Noui-Mehidi et al. [19] studied this effect and found that the vortices present in such a situation can reach sizes of up to 2.4 times the gap width.

Another possibility within conical Taylor–Couette flow is an Ekman boundary layer. Hoffman and Busse [24] looked at the instabilities of shear flows within this flow, observing a transition from Taylor vortex instabilities to Ekman-type instabilities at $\phi = 45$ deg.

Interesting flows also occur when only the inner cylinder is replaced with a cone. Pereira and Sousa [25] presented an extensive study of this flow, looking experimentally and numerically at the confined vortex breakdown generated by a rotating cone. They demonstrated that for some combinations of Reynolds number and gap ratio, a bubble type vortex breakdown can occur, and give some understanding as to the mechanism responsible for transition to transient flow.

Dependence, within the flow structure, on the vertex angle is clear, as the flow around a cone will be somewhat similar to the flow around either a cylinder or a disk. As the vertex angle increases, the moment on the cone loses its dependence on the vertex angle, and the flow becomes similar to that for a disk. Yamada and Ito [2] looked experimentally at the frictional resistance of shrouded rotating cones for vertex angles of $30 \text{ deg} \leq \phi \leq 270$ deg. They observed that, for very small spacing ratios (T/R_i), the theoretical equation

$$C_Y = \frac{\pi R_i}{T\text{Re}} \tag{1}$$

demonstrates good agreement with their experimental data, for any vertex angle ϕ. For $120 \text{ deg} \leq \phi \leq 180$ deg, C_Y shows little dependence, if any, on ϕ. However, when $\phi \leq 90$ deg, C_Y shows strong dependence on ϕ at the region where T/R_i is comparatively large. They also reported that at any of the vertex angles consid-

Downloaded 03 Jun 2010 to 171.66.16.157. Redistribution subject to ASME license or copyright; see http://www.asme.org/terms/Terms_Use.cfm

Table 1 Physical settings. Dimensions are as in Fig. 1.

Case	X (m)	Y (m)	Z (rad)	A (mm)	B (m)	Data source
1	0.06275	0.125	$\pi/2$	4	0.008	[1–3]
2	0.06275	0.125	$\pi/2$	4	0.016	[1–3]
3	0.03623	0.125	$2\pi/3$	4	0.016	[2–3]

ered, C_Y reaches a minimum at a certain value of T/R_i. The experimental data presented in Ref. [2] (along with Refs. [1,3]) will provide the experimental data to validate the numerical work presented in this paper.

To summarize, the literature indicates that many varied and interesting flows can be observed by making simple geometric changes to basic Taylor–Couette flow. Of most interest to the current study is the work concentrating upon conical Taylor–Couette flow, especially for vertex angles of 90 deg $\leq \phi \leq$ 120 deg, which has shown that we should not expect to see Taylor vortices in the flow.

2.3 Throughflow. Many authors have looked at the effect throughflow has on Taylor–Couette flow and on conical Taylor–Couette flow. When a throughflow is introduced into Taylor–Couette flow, the flow becomes a linear superposition of the Taylor–Couette flow and the imposed axial flow [26]. With conical Taylor–Couette flow, the location and direction of the throughflow affect the resulting flow pattern. If the throughflow enters tangentially, the flow is seen to snake around the cone, partially due to the orientation of the inlet with respect to the vertex of the cone. Noui-Mehidi et al. [27] studied the apex angle effects on the swirling flow between the cones induced by means of a tangential inlet. They observed that the location of the inlet has a considerable effect on the flow, with an increase in swirl intensity if the inlet is at the point of greatest radii compared to if the inlet is at the point of least radii. The geometry of the cone, in a similar manner as discussed in Sec. 2.1, also has considerable effect on the swirling flow [27].

In conical Taylor–Couette flow with throughflow, if the flow enters in an axial direction, the axial throughflow causes the transitions to unstable laminar flow and turbulent flow to occur at higher Reynolds number than for no axial throughflow. Yamada and Ito [3] investigated these phenomena. It was reported that, in the regions where the moment coefficient C_M with no throughflow is increased by the effect of Taylor type vortices, an increase in the throughflow rate C_Q results in a decrease in C_M, so long as C_Q is not too large. When the clearance ratio T/R_i and the Reynolds number Re are small, then the following relationship between C_M and Re holds:

$$C_M = \frac{\pi R_i}{T\mathrm{Re}}\left(1 + 0.186\left(C_Q\left(\frac{T}{R_i}\right)\sin\left(\frac{\phi}{2}\right)\right)^{0.8}\right)$$

The experimental data presented in Ref. [3] (along with Refs. [1,2]) will provide the experimental data to validate the numerical work presented in this paper.

A numerical simulation based on the experimental work of Yamada and Ito has also been conducted by May et al. [28]. They utilized two numerical methods, a momentum-integral method and a finite difference method. The finite difference method used simple turbulence modeling, making use of the mixing length hypothesis. It is worth highlighting that the resources available to May et al., by today's standards, were extremely limited. The grid utilized in the finite difference method was two-dimensional, using in the order of 4225 cells. The two dimensional results that will be presented here were conducted on grids of ~20,000–~100,000 cells. In order to reduce the computational expense, various assumptions about the flow were made by May et al. that would not be necessary today. The computational domain utilized assumed that the inflow was in a direction perpendicular to the axis of revolution. The domain was formed around a truncated cone. The outflow is through a narrow outlet, through which the flow is assumed to travel tangentially to the surface of the rotating cone. May et al., when utilizing the momentum-integral method, achieve good agreement with the experimental data of Yamada and Ito [1,2] for $\phi \geq 120$ deg. The finite difference scheme produces good agreement, though there are some discrepancies, which may well be due to the assumptions previously mentioned. The methods used by May et al. do not replicate the increase in C_M as ϕ decreases.

Of a similar vintage is the work of Moureh et al. [29], in which a similar experiment to that of Yamada and Ito is conducted, and modeled numerically through a finite volume code. The flow was assumed laminar. Reasonable agreement between numerical predictions and experimental results is again achieved in most cases presented.

To summarize, the effect of throughflow and basic and conical Taylor–Couette flow has been reviewed. Numerical simulations of these flows have been conducted by other authors, showing reasonable agreement between numerical and experimental predictions. It is felt that the assumptions made by these previous studies are not now necessary, resulting in greater accuracy and more detailed flow analysis, as will be demonstrated in this study.

3 CFD Methodology

Calculations of the fluid flow field (the fluid in question being water) and associated torques are obtained for a shrouded cone. The geometrical information for the shrouded cones used in the study is given in Table 1. The study uses two- and three-dimensional CFD to calculate the fluid flow and subsequent friction and turbulence losses for three configurations of shrouded cone. Computations have been carried out using two-dimensional and three-dimensional models. The two-dimensional models assume axisymmetry within the flow. Two different three-dimensional models were developed, one representing a rotationally periodic volume incorporating a 6 deg wedge on the shroud and cone, while the other represented the entire three-dimensional setting. The geometry (Fig. 1) matches that used in Yamada and Ito [1]. It was assumed that the inlet was of diameter 4 mm, as this dimension is not given in Refs. [1–3]. Steady state solutions for the single-phase fluid flow field have been obtained using the commercial CFD codes FLUENT 6.2.16 and FLUENT 6.3.17. Simulations are performed using a rotating frame of reference and the absolute velocity formulation. Computations correspond to rotation rates, Ω, within the range of 3 rad $s^{-1} \leq \Omega \leq 112$ rad s^{-1}. Turbulence is modeled using the standard k-ϵ model [30], as well as the RNG version [13,14], the shear-stress transport (SST) k-ω model [31], and the RSM [15,32,33]. The governing equations were discretized using a second order upwind differencing scheme. Near-wall behaviors were captured through the standard wall function [12] and the enhanced wall treatment [34], with comparisons made between the performances of each.

3.1 Viscous Models. In this section, the five types of viscous model used will be described. These are the k-ϵ turbulence models (standard and RNG, Sec. 3.1.1), the SST k-ω turbulence model (Sec. 3.1.2), and the RSM (Sec. 3.1.3).

Downloaded 03 Jun 2010 to 171.66.16.157. Redistribution subject to ASME license or copyright; see http://www.asme.org/terms/Terms_Use.cfm

3.1.1 k-ε Turbulence Models. FLUENT utilizes three versions of the k-ϵ turbulence model, these being the standard model [30], the RNG version [13,14], and a realizable model. The standard k-ϵ model has the form

$$\frac{\partial}{\partial t}(\rho k) + \frac{\partial}{\partial x_i}(\rho k u_i) = \frac{\partial}{\partial x_i}\left[\left(\mu + \frac{\mu_t}{\sigma_k}\right)\frac{\partial k}{\partial x_i}\right] + G_k + G_b - \rho\epsilon - Y_M \tag{2}$$

and

$$\frac{\partial}{\partial t}(\epsilon k) + \frac{\partial}{\partial x_i}(\epsilon k u_i) = \frac{\partial}{\partial x_i}\left[\left(\mu + \frac{\mu_t}{\sigma_\epsilon}\right)\frac{\partial \epsilon}{\partial x_i}\right] + C_{1\epsilon}\frac{\epsilon}{k}(G_k + C_{3\epsilon}G_b) - C_{2\epsilon}\rho\frac{\epsilon^2}{k} \tag{3}$$

In these equations, G_k represents the generation of turbulent kinetic energy due to the mean velocity gradients. G_b is the generation of turbulent kinetic energy due to buoyancy. Y_M represents the contribution of the fluctuating dilatation in compressible turbulence to the overall dissipation rate. $C_{1\epsilon}$, $C_{2\epsilon}$, and $C_{3\epsilon}$ are constants. σ_k and σ_ϵ are the turbulent Prandtl numbers for k and ϵ, respectively. The standard k-ϵ model has been used in one of the cases presented in this paper (90 deg vertex angle, nondimensional gap width s of 0.016, with a nondimensional throughflow C_Q of 1500), in order to investigate its performance relative to the RNG k-ϵ turbulence model.

The RNG k-ϵ model has a similar form to the standard k-ϵ turbulence model:

$$\frac{\partial}{\partial t}(\rho k) + \frac{\partial}{\partial x_i}(\rho k u_i) = \frac{\partial}{\partial x_i}\left(\alpha_k \mu_{\text{eff}}\frac{\partial k}{\partial x_i}\right) + G_k + G_b - \rho\epsilon - Y_M \tag{4}$$

and

$$\frac{\partial}{\partial t}(\epsilon k) + \frac{\partial}{\partial x_i}(\epsilon k u_i) = \frac{\partial}{\partial x_i}\left(\alpha_\epsilon \mu_{\text{eff}}\frac{\partial \epsilon}{\partial x_i}\right) + C_{1\epsilon}\frac{\epsilon}{k}(G_k + C_{3\epsilon}G_b) - C_{2\epsilon}\rho\frac{\epsilon^2}{k} - R \tag{5}$$

The quantities α_k and α_ϵ are the inverse effective Prandtl numbers for k and ϵ, respectively.

3.1.2 Shear-Stress Transport k-ω Model. FLUENT incorporates two versions of the k-ω turbulence model, these being the standard model [31] and the SST model [35]. Historically, the SST model was developed to try and incorporate the strengths of both standard k-ϵ and k-ω models. It is known that k-ϵ performs better than k-ω for high Re flow, but struggles with low Re (near wall) flows, for which wall functions have to be used. The SST k-ω model works by blending the two approaches together, in effect using the standard k-ω model as a wall function for the standard k-ϵ model (The k-ϵ model is transformed to use the variables k and ω). To this end, the standard k-ω model and the transformed k-ϵ model are both multiplied by a blending function and both models are added together. The blending function is designed to be one in the near-wall region, which activates the standard k-ω model, and zero at some point away from the surface, which activates the transformed k-ϵ model.

The SST k-ω model has a similar form to the standard k-ω model:

$$\frac{\partial}{\partial t}(\rho k) + \frac{\partial}{\partial x_i}(\rho k u_i) = \frac{\partial}{\partial x_j}\left(\Gamma_k \frac{\partial k}{\partial x_j}\right) + \tilde{G}_k - Y_k + S_k \tag{6}$$

and

$$\frac{\partial}{\partial t}(\rho\omega) + \frac{\partial}{\partial x_i}(\rho\omega u_i) = \frac{\partial}{\partial x_j}\left(\Gamma_\omega \frac{\partial \omega}{\partial x_j}\right) + G_\omega - Y_\omega + D_\omega + S_\omega \tag{7}$$

In these equations, $\tilde{G}_k$ represents the generation of turbulence kinetic energy due to the mean velocity gradients. G_ω represents the generation of ω. Γ_k and Γ_ω represent the effective diffusivity of k and ω, respectively. Y_k and Y_ω represent the dissipation of k and ω due to turbulence. D_ω represents the cross-diffusion term.

The SST k-ω model has been used in one of the cases presented in this paper (120 deg vertex angle with no throughflow), in order to investigate its performance relative to the RNG k-ϵ turbulence model.

3.1.3 RSM. The exact transport equations for the transport of the Reynolds stresses, $\rho\overline{u_i' u_j'}$, may be written as follows:

$$\begin{aligned}\frac{\partial}{\partial t}(\rho\overline{u_i u_j}) + \frac{\partial}{\partial x_k}(\rho U_k \overline{u_i u_j}) = &-\frac{\partial}{\partial x_k}[\rho\overline{u_i u_j u_k} + \overline{p(\delta_{kj}u_i + \delta_{ik}u_j)}] + \cdots \\ &+ \frac{\partial}{\partial x_k}\left[\mu\frac{\partial}{\partial x_k}(\overline{u_i u_j})\right] - \rho\left(\overline{u_i u_k}\frac{\partial U_j}{\partial x_k}\right. \\ &\left. + \overline{u_j u_k}\frac{\partial U_i}{\partial x_k}\right) - \rho\beta(g_i\overline{u_j\theta} + g_j\overline{u_i\theta}) + \cdots \\ &+ \overline{p\left(\frac{\partial u_i}{\partial x_j} + \frac{\partial u_j}{\partial x_i}\right)} - 2\mu\overline{\frac{\partial u_i}{\partial x_k}\frac{\partial u_j}{\partial x_k}} \\ &- 2\rho\Omega_k(\overline{u_j u_m}\epsilon_{ikm} + \overline{u_i u_m}\epsilon_{jkm})\end{aligned} \tag{8}$$

The RSM has been used in one of the cases presented in this paper (90 deg vertex angle, nondimensional gap width s of 0.016, with a nondimensional throughflow C_Q of 1500), in order to investigate its performance relative to the RNG k-ϵ turbulence model.

3.2 Wall Treatment. The standard wall functions in FLUENT are based on the proposal of Launder and Spalding [30], and have been most widely used for industrial flows. It utilizes two formulas for the stress-strain relationship, one a log law for the mean velocity (the so-called "law of the wall"),

$$U^* = \frac{1}{\kappa}\ln(9.793y^*) \tag{9}$$

(where κ is von Kármáns constant (=0.4187)), the other a laminar stress-strain relationship,

$$U^* = y^* \tag{10}$$

The log law is employed when $y^* > 11.225$, the laminar law is employed when $y^* < 11.225$. Reynolds' analogy between momentum and energy transport gives a similar logarithmic law for mean temperature.

The standard wall functions work reasonably well for a broad range of wall-bounded flows. However, they tend to become less reliable when the flow situations depart too much from the ideal conditions that are assumed in their derivation. Among others, the constant-shear and local equilibrium hypotheses are the ones that most restrict the universality of the standard wall functions.

Due to the restrictions mentioned above, in order to have a method that can extend its applicability throughout the near-wall region (i.e., laminar sublayer, buffer region, and fully turbulent outer region), it is necessary to formulate the law of the wall as a single wall law for the entire wall region. This is the enhanced wall treatment. FLUENT achieves this by blending linear (laminar) and logarithmic (turbulent) laws of the wall using a function suggested by Kader [34]:

$$u^+ = e^{\Gamma}u^+_{\text{lam}} + e^{1/\Gamma}u^+_{\text{turb}} \tag{11}$$

where the blending function is given by

Downloaded 03 Jun 2010 to 171.66.16.157. Redistribution subject to ASME license or copyright; see http://www.asme.org/terms/Terms_Use.cfm

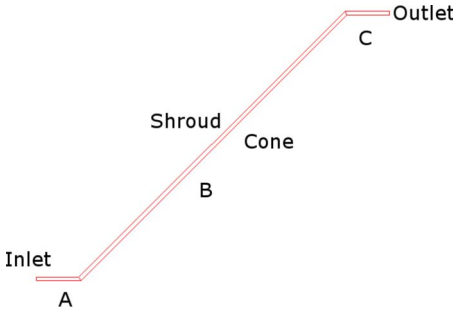

Fig. 2 Schematic diagram, showing a cross section of the model

$$\Gamma = -\frac{a(y^+)^4}{1+by^+} \tag{12}$$

where $a=0.01$ and $b=5$.

Similarly, the general equation for the derivative du^+/dy^+ is

$$\frac{du^+}{dy^+} = e^{\Gamma}\frac{du^+_{\text{lam}}}{dy^+} + e^{1/\Gamma}\frac{du^+_{\text{turb}}}{dy^+} \tag{13}$$

This approach allows the fully turbulent law to be easily modified and extended to take into account other effects, such as pressure gradients or variable properties. This formula also guarantees the correct asymptotic behavior for large and small values of y^+ and reasonable representation of velocity profiles in the cases where y^+ falls inside the wall buffer region $(3<y^+<10)$.

3.3 Boundary and Operating Conditions. In all cases, the flow is assumed to by steady state and isothermal. The fluid is assumed incompressible, as the tip velocity of the cone, even at the highest rotational rate, is only 0.0097 M.

A cross sectional view of the geometry is shown in Fig. 2. Water enters through a stationary inlet duct, passes through the shrouded cone, and exits axially through the outlet. A mass flow inlet, located 0.0214 m upstream of the cone vertex, is used at the upstream axial boundary to prescribe the flow entering the system. Turbulence quantities are calculated by turbulence intensity and hydraulic diameter. The intensity is chosen as 10%, the hydraulic diameter comes from the diameter of the inlet pipe, which is 4 mm. A pressure outlet is specified at the outlet. The cone is modeled as a rotating wall with a no-slip condition applied. The shroud is modeled as a stationary wall with a no-slip condition applied. For all cases, the flow is initialized to be stationary. The geometry is shown schematically in Fig. 2. Different meshes were used in order to demonstrate grid independence. These were as described in Table 2. While the apex of the inner cone appears to be a singularity point within the domain (Fig. 3), and caused numerous problems in meshing the three-dimensional models, it is not a problem numerically. The equations are solved in a rotating frame, so the flow over the apex becomes akin to flow round a corner. All the simulations, except those for Mesh 7, were computed on a computer with a Pentium 4, 3.40 GHz with 2.0 Gbytes of RAM. Calculations for Mesh 7 were computed on the High Performance Cluster installed at the University of Nottingham, running FLUENT in parallel on up to 18 computing nodes. Each node is a dual Opteron 248 processer, 2.2 GHz with 2.0 Gbytes of RAM. Mesh independence has been checked in two ways. First, the mesh is adapted on y^* until it is within acceptable levels $(0<y^*<4)$ for the use of enhanced wall functions, while checking whether the refinement has any effect on the moment reported. Second, to check that the solutions are independent of the style of grid used, for each mesh an individual throughflow rate has been chosen for which some of the work has been conducted using the two different meshes and the results compared. In each case, the overall difference between the different meshes has been negligible, so we can be confident of mesh independence.

4 Results

In this section, results will be presented, describing the various parameters used, and demonstrating the effect changing each parameter has on the moment coefficient. The results are split into four sections, those where the effect of throughflow has not been considered (Sec. 4.1), and those where their effect has been considered, first in two dimensions (Sec. 4.2), and then three dimensionally (Sec. 4.3). The final section presents details of the flow structure (Sec. 4.3.2).

4.1 No Throughflow. This section presents the results for which no throughflow was present. All the work in this section is from two-dimensional simulations.

Figure 4 presents a graph of rotating Reynolds number (Re)

Table 2 Mesh details

Name	ϕ	s	A	B	C	Cell count
Mesh 1	90 deg	0.016	Triangular	Quadrilateral, with boundary layer	Triangular	25,740
Mesh 2	90 deg	0.016	Triangular	Triangular, with boundary layer	Triangular, with boundary layer	24.482
Mesh 3	90 deg	0.008	Triangular	Triangular, with boundary layer	Triangular, with boundary layer	106,604
Mesh 4	90 deg	0.008	Quadrilateral	Quadrilateral, with boundary layer	Quadrilateral, with boundary layer	56.223
Mesh 5	120 deg	0.016	Triangular	Triangular, with boundary layer	Triangular, with boundary layer	36,324
Mesh 6 (3D, 6 deg wedge shape slice)	90 deg	0.016	Tetrahedral	Tetrahedral hybrid, with hexahedral core	Hexahedral map	1,343.856
Mesh 7 (3D, 360 deg)	90 deg	0.016	Hexahedral wedge	Tetrahedral hybrid, with hexahedral core	Hexahedral wedge	1,800.000

Downloaded 03 Jun 2010 to 171.66.16.157. Redistribution subject to ASME license or copyright; see http://www.asme.org/terms/Terms_Use.cfm

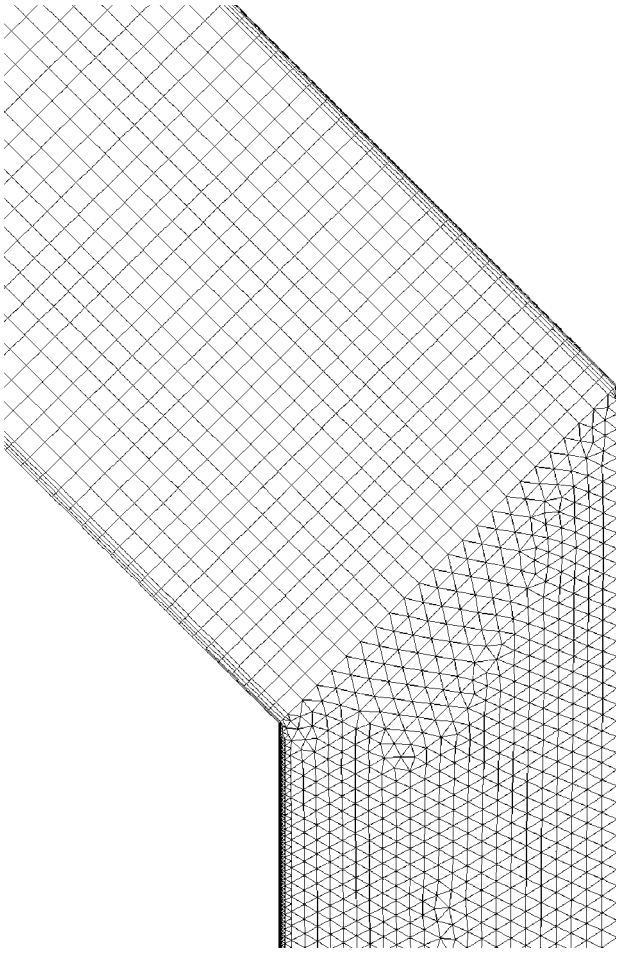

Fig. 3 Close up of mesh structure near cone vertex

against moment coefficient (C_M), for a vertex angle of ϕ =120 deg, a nondimensional gap width s=0.016 and no throughflow (C_Q=0), calculated on Mesh 5. A transition is visible in the experimental data over the range 249,000≤Re≤475,000. Before the transition, the quantitative agreement between the RNG k-ϵ turbulence model, with enhanced wall treatment, and the experimental data is weak, with the moment coefficient being consistently overestimated. The best agreement is found for Re =248,000, where the percentage difference, $C_{\%}$=33%. The worst

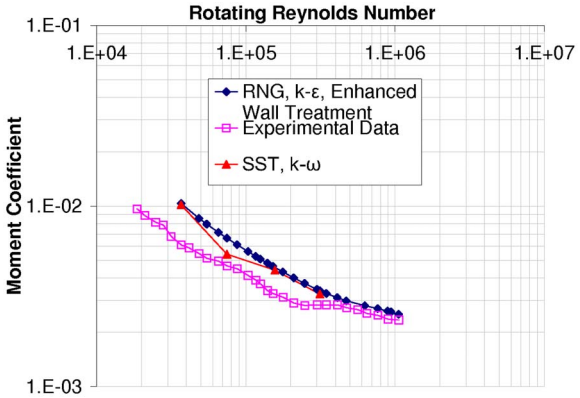

Fig. 4 Graph of rotating Reynolds number (Re) against moment coefficient (C_M), for a vertex angle of ϕ=120 deg, nondimensional gap width s=0.016, and no throughflow (C_q=0)

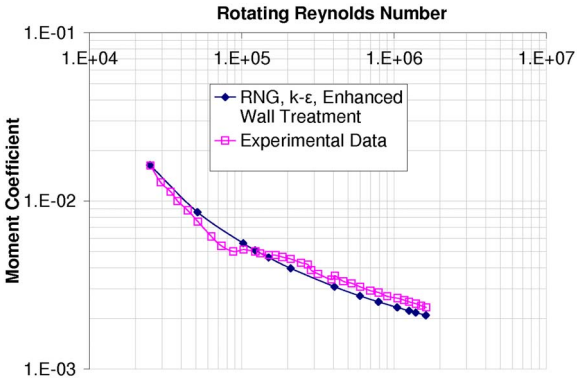

Fig. 5 Graph of rotating Reynolds number (Re) against moment coefficient (C_M), for a vertex angle of ϕ=90 deg, nondimensional gap width s=0.008, and no throughflow (C_Q=0)

agreement is found for Re=37,000, where the percentage difference is 70%. Before the transition, the quantitative agreement between the k-ω turbulence model and the experimental data is better than with the RNG k-ϵ turbulence model, with the moment coefficient being consistently overestimated. The best agreement is found for Re=75,000, where the percentage difference is 16%. The worst agreement is found for Re=37,000, where the percentage difference is 67%.

After the transition, the quantitative agreement between the RNG k-ϵ turbulence model, with enhanced wall treatment, and the experimental data greatly improves. The best agreement is found for Re=1,057,000, where the percentage difference is 7.8%. The worst agreement is found for Re=893,000, where the percentage difference is 11%. The k-ω turbulence model was not used for calculations after the transition in this case. As there are no experimental data available from Yamada and Ito [1–3] for the case of ϕ=120 deg with throughflow, the results are only presented for the case with no throughflow.

Figure 5 presents a graph of rotating Reynolds number (Re) against moment coefficient (C_M), for a vertex angle of ϕ =90 deg, nondimensional gap width s=0.008 and no throughflow (C_Q=0), calculated on Mesh 3. A transition is visible in the experimental data over the range 88,000≤Re≤210,000, in the same manner as that seen in Fig. 4. Across the entire range of the experimental data, the quantitative agreement between the RNG k-ϵ turbulence model, with enhanced wall treatment, and the experimental data is good. The best agreement is found for Re =25,000, where the percentage difference is 0.6%. The worst agreement is found for Re=406,000, where the percentage difference is 14%.

Figure 6 shows a graph of rotating Reynolds number (Re) against moment coefficient (C_M), for a vertex angle of ϕ =90 deg, nondimensional gap width s=0.016 and no throughflow (C_Q=0), calculated on Mesh 1. A transition is visible in the experimental data over the range 47,000≤Re≤110,000. Across the entire range of the experimental data, the quantitative agreement between the RNG k-ϵ turbulence model, with enhanced wall treatment, and the experimental data is good. The best agreement is found for Re=47,000, where the percentage difference is 2.7%. The worst agreement is found for Re=627,000, where the percentage difference is 17%.

To summarize, it has been shown that, for the cases with no throughflow and a 90 deg vertex angle, there is good numerical agreement between the CFD and the experimental data, with torque levels predicted to within 17% by the RNG k-ϵ turbulence model, with enhanced wall treatment. The agreement at the wider

Downloaded 03 Jun 2010 to 171.66.16.157. Redistribution subject to ASME license or copyright; see http://www.asme.org/terms/Terms_Use.cfm

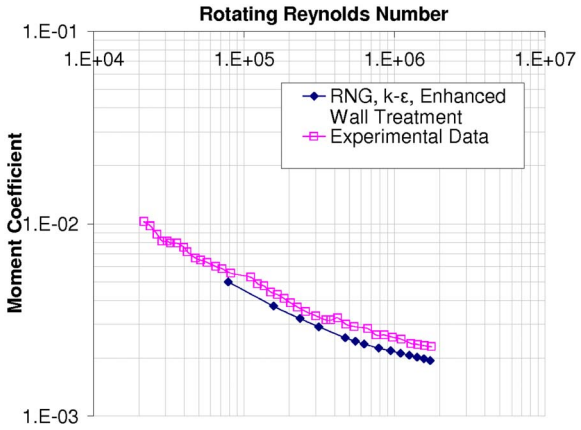

Fig. 6 Graph of rotating Reynolds number against moment coefficient, for a vertex angle of ϕ=90 deg, nondimensional gap width s=0.016, and no throughflow (C_Q=0)

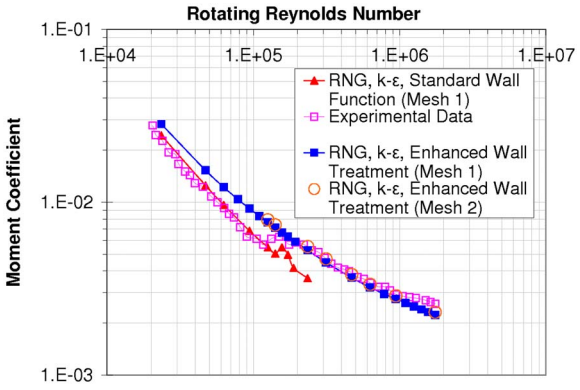

Fig. 8 Graph of moment coefficient (C_M) against rotating Reynolds number (Re), for a vertex angle of ϕ=90 deg, nondimensional gap width s=0.016, and nondimensional throughflow C_Q=1500

vertex angle is not so good, with torque levels predicted by the RNG k-ϵ turbulence model, with enhanced wall treatment, within 70% of the experimental data.

4.2 Throughflow, Two-Dimensional Models. This section presents the results for which throughflow was present.

Figure 7 presents a graph of moment coefficient (C_M) against rotating Reynolds number (Re), for a vertex angle of ϕ=90 deg, nondimensional gap width s=0.008, and nondimensional throughflow C_Q=1500, Calculated on meshes 3 and 4. A transition is visible in the experimental data over the range 200,000≤Re≤464,000. Before the transition, the quantitative agreement between the RNG k-ϵ turbulence model, with enhanced wall treatment, and the experimental data is weak, with the moment coefficient being consistently overestimated. The best agreement is found for Re=78,000, where the percentage difference is 39%. The worst agreement is found for Re=196,000, where the percentage difference is 62%. Before the transition, the quantitative agreement between the RNG k-ϵ turbulence model, with standard wall functions, and the experimental data is strong. The best agreement is found for Re=30,000, where the percentage difference is 0.6%. The worst agreement is found for Re=78,000, where the percentage difference is 12%.

After the transition, the quantitative agreement between the RNG k-ϵ turbulence model, with enhanced wall treatment, and the experimental data greatly improves. The best agreement is found for Re=470,000, where the percentage difference is 4%. The worst agreement is found for Re=1,567,000, where the percentage difference is 9.4%. The RNG k-ϵ turbulence model, with standard wall functions, was not used for calculations after the transition in this case.

In order to see if the results are independent of the mesh used (Mesh 3), an alternative mesh (Mesh 4) was used to replicate the work performed by the original mesh (Mesh 3), using the RNG k-ϵ turbulence model, with enhanced wall treatment. It can be observed (Fig. 7) that the behavior of these models is very similar. Before the transition, the quantitative agreement between the RNG k-ϵ turbulence model, with enhanced wall treatment, and the experimental data is weak, with the moment coefficient being consistently overestimated. The best agreement is found for Re=78,000, where the percentage difference is 39%. The worst agreement is found for Re=157,000, where the percentage difference is 53%.

After the transition, the quantitative agreement between the RNG k-ϵ turbulence model, with enhanced wall treatment, and the experimental data greatly improves. The best agreement is found for Re=2,022,000, where the percentage difference is 4.2%. The worst agreement is found for Re=1,254,000, where the percentage difference is 7.6%.

Figure 8 presents a graph of moment coefficient (C_M) against rotating Reynolds number (Re), for a vertex angle of ϕ=90 deg,

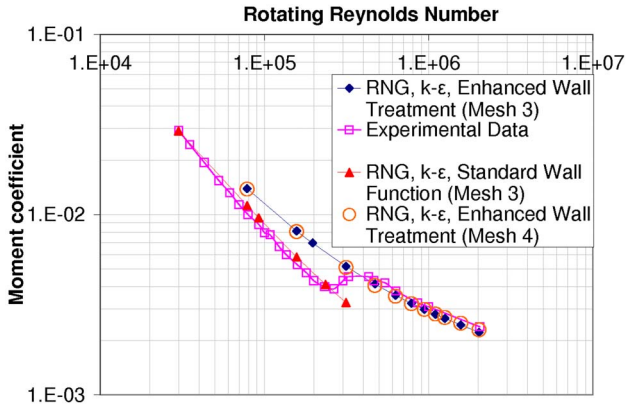

Fig. 7 Graph of moment coefficient (C_M) against rotating Reynolds number (Re), for a vertex angle of ϕ=90 deg, nondimensional gap width s=0.008 and nondimensional throughflow C_Q=1500

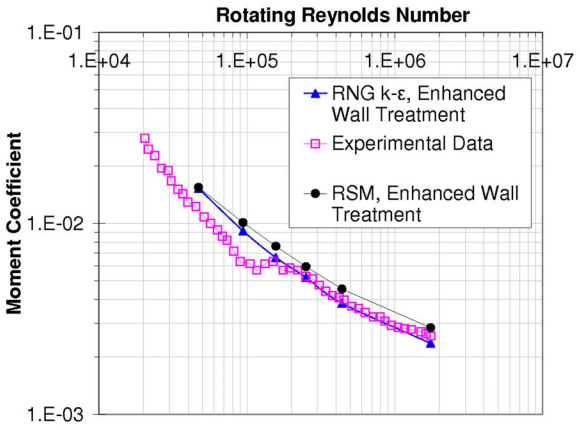

Fig. 9 Graph of moment coefficient (C_M) against rotating Reynolds number (Re), for a vertex angle of ϕ=90 deg, a nondimensional gap width of s=0.016, and a nondimensional throughflow of C_Q=1500, showing the effect of using different turbulence models

Downloaded 03 Jun 2010 to 171.66.16.157. Redistribution subject to ASME license or copyright; see http://www.asme.org/terms/Terms_Use.cfm

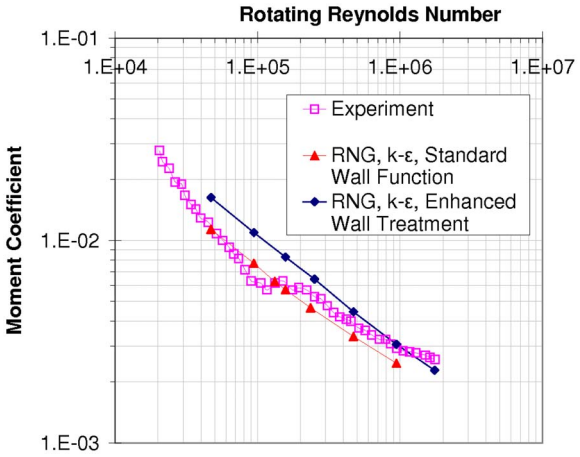

Fig. 10 Graph of moment coefficient (C_M) against rotating Reynolds number (Re), for a vertex angle of ϕ=90 deg, a nondimensional gap width of s=0.016, and a nondimensional throughflow of C_Q=1500, showing the effect of using different turbulence models

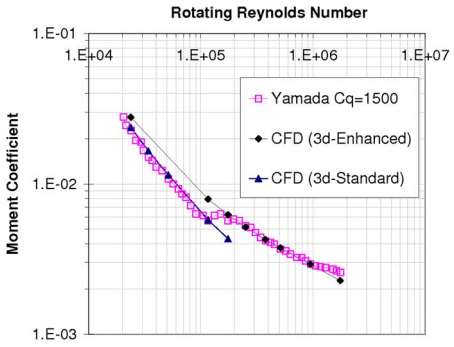

Fig. 12 Graph of moment coefficient (C_M) against rotating Reynolds number (Re), to show the performance of the three-dimensional model (Mesh 6), for a vertex angle of ϕ=90 deg, nondimensional gap width s=0.016, and nondimensional throughflow C_Q=1500

nondimensional gap width s=0.016, and nondimensional throughflow C_Q=1500, calculated on Meshes 1 and 2. A transition is visible in the experimental data over the range 117,000≤Re≤221,000. As in Fig. 7, before the transition, the quantitative agreement between the RNG k-ϵ turbulence model, with enhanced wall treatment, and the experimental data is weak, with the moment coefficient being consistently overestimated. The best agreement is found for Re=24,000, where the percentage difference is 25%. The worst agreement is found for Re=78,000, where the percentage difference is 45%. Before the transition, the quantitative agreement between the RNG k-ϵ turbulence model, with standard wall functions, and the experimental data is strong. The best agreement is found for Re=63,000, where the percentage difference is 4.1%. The worst agreement is found for Re=94,000, where the percentage difference is 13%.

After the transition, as before, the quantitative agreement between the RNG k-ϵ turbulence model, with enhanced wall treatment, and the experimental data greatly improves. The best agreement is found for Re=470,000, where the percentage difference is 4.6%. The worst agreement is found for Re=1,746,000, where the percentage difference is 14%. The RNG k-ϵ turbulence model, with standard wall functions, was not used for calculations after the transition in this case.

In order to see if the results are independent of the mesh used (Mesh 1), an alternative mesh (Mesh 2) was used to replicate the work performed by the original mesh (Mesh 1), using the RNG k-ϵ turbulence model, with enhanced wall treatment. It can be observed (Fig. 8) that the behavior of these models is very similar, with a maximum percentage difference in moment coefficient of 3%. After the transition, the quantitative agreement between the RNG k-ϵ turbulence model, with enhanced wall treatment, and the experimental data is good. The best agreement is found for Re=470,000, where the percentage difference is 0.6%. The worst agreement is found for Re=1,746,000, where the percentage difference is 10%.

In Fig. 9, the relative performance of the RSM and the RNG k-ϵ turbulence model, with enhanced wall treatment, is presented, calculated on Mesh 1, for the same case presented in Fig. 8. Over the entire range of the experimental data, it can be observed that RSM model, with enhanced wall treatment, does not perform as well as the RNG k-ϵ turbulence model, with enhanced wall treatment. Before the transition, the quantitative agreement between the RSM model, with enhanced wall treatment, and the experimental data is weak, with the moment coefficient being consistently overestimated. After the transition, the quantitative agreement between the RSM model, with enhanced wall treatment, and the experimental data greatly improves. The best agreement is found for Re=1,746,000, where the percentage difference is 10%. The worst agreement is found for Re=439,000, where the percentage difference is 14%. Its performance, in terms of accuracy, over the speed range considered, is similar to the RNG k-ϵ turbulence model, though it can also be observed that with increasing Reynolds num-

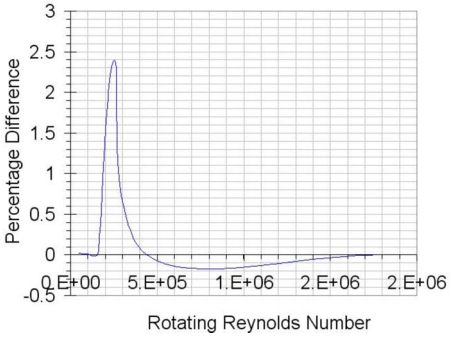

Fig. 11 Graph of percentage difference between standard and RNG k-ϵ turbulence models, for a vertex angle of ϕ=90 deg, nondimensional gap width s=0.016, and nondimensional throughflow C_Q=1500

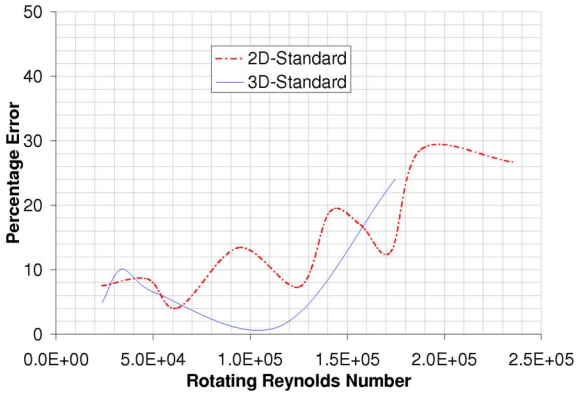

Fig. 13 Graph of rotating Reynolds number against percentage error, to show the performance of the three-dimensional model, relative to that of the two-dimensional model, using the RNG k-ϵ turbulence model, with standard wall function

Downloaded 03 Jun 2010 to 171.66.16.157. Redistribution subject to ASME license or copyright; see http://www.asme.org/terms/Terms_Use.cfm

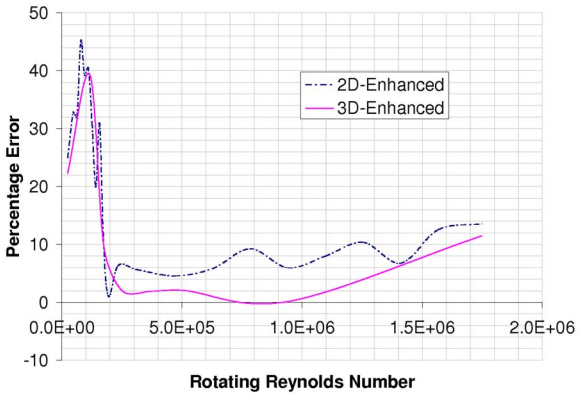

Fig. 14 Graph of rotating Reynolds number against percentage error, to show the performance of the three-dimensional model relative to that of the two-dimensional model, using the RNG k-ϵ turbulence model, with enhanced wall treatment

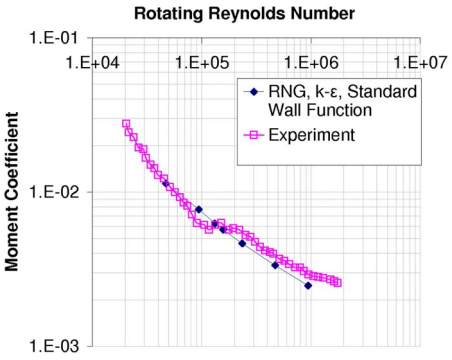

Fig. 15 Graph of rotating Reynolds number against moment coefficient, to show the performance of the three-dimensional model

ber (Re), the performance of the RSM model improves.

In Fig. 10, the relative performance of the standard k-ϵ and the RNG k-ϵ turbulence models, with enhanced wall treatment, is presented. As will be shown in Fig. 11, there is little difference in the results obtained with the two models. As in Fig. 8, a transition is visible in the experimental data over the range $117{,}000 \leq \mathrm{Re} \leq 221{,}000$. Before the transition, the quantitative agreement between the standard k-ϵ turbulence model, with enhanced wall treatment, and the experimental data is weak, with the moment coefficient being consistently overestimated. After the transition, the quantitative agreement between the standard k-ϵ turbulence model, with enhanced wall treatment, and the experimental data greatly improves. The best agreement is found for $\mathrm{Re}=251{,}000$, where the percentage difference is 3.6%. The worst agreement is found for $\mathrm{Re}=1{,}746{,}000$, where the percentage difference is 8.4%.

Overall, little difference is observable between the results obtained with the two different versions of the k-ϵ model, as can be observed by looking at the percentage difference between the two cases (Fig. 11). A similar lack of difference between the performance of these two different versions of the k-ϵ model has been reported in Modeling other variations on Taylor–Couette flow by Shiomi et al. [11].

To summarize, it has been demonstrated that, with the presence of throughflow, the numerical modeling can produce results that agree well with the experimental data, but neither of the wall treatments used performs consistently across the speed range. A transition that is present in the experimental data has not been captured numerically, but the torque levels before and after this transition can be predicted using (respectively) the standard wall function or the enhanced wall treatment. The RNG k-ϵ turbulence model, with standard wall functions, predicts the torque levels to within 13% before the transition, and with enhanced wall treatment, predicts the torque levels to within 14% after this transition.

4.3 Throughflow, Three-Dimensional Models

4.3.1 Torque Levels To check the accuracy of the two-dimensional models in capturing any three dimensionality of the flow, two three-dimensional models were created, the initial model representing a 6 deg wedge shape section. Subsequently, due to an increase in computing resources available, a fully three-dimensional model was developed. In this section, a comparison with experimental torque values is discussed, while the flow structure is discussed in Sec. 4.3.2

In Fig. 12, we see the results from the wedge shaped model, which is equivalent to Fig. 8 in Sec. 4.2. A transition is visible in

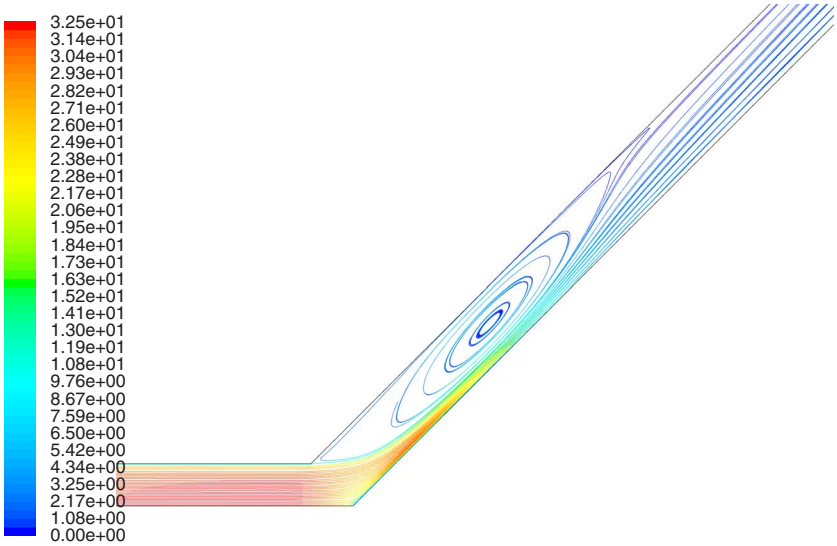

Fig. 16 Streamlines, between the shroud and the cone, colored by velocity magnitude, to show vortex. Computed using Mesh 3, $\Omega=28$ rad s^{-1}, $C_Q=1500$.

Downloaded 03 Jun 2010 to 171.66.16.157. Redistribution subject to ASME license or copyright; see http://www.asme.org/terms/Terms_Use.cfm

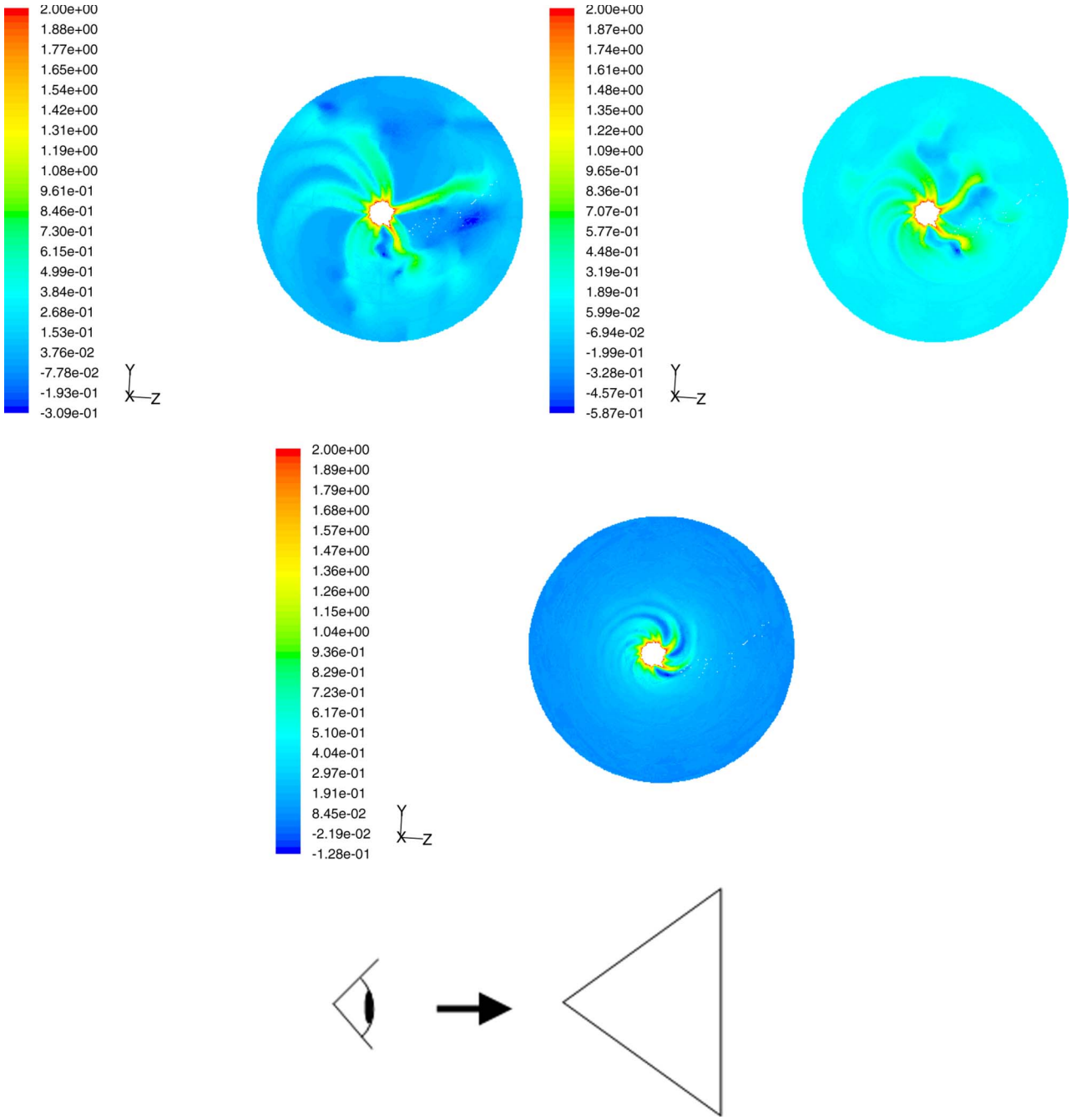

Fig. 17 Contours of axial velocity on the cone surface, for 3 rad $s^{-1} \leq \Omega \leq 30$ rad s^{-1}

the experimental data over the range $117{,}000 \leq Re \leq 221{,}000$. Before the transition, as for the two dimensional cases, the quantitative agreement between the RNG k-ϵ turbulence model, with standard wall function, and the experimental data is strong. The best agreement is found for Re=24,000, where the percentage difference is 4.9%. The worst agreement is found for Re=34,000, where the percentage difference is 10%.

After the transition, again, as for the two-dimensional cases, the quantitative agreement between the RNG k-ϵ turbulence model, with enhanced wall treatment, and the experimental data is good. The best agreement is found for Re=946,000, where the percentage difference is 0.2%. The worst agreement is found for Re =1,747,000, where the percentage difference is 11%.

Overall, the three-dimensional wedge model is more accurate than the two-dimensional model, as can be seen in Figs. 13 and 14. Figure 13 shows the percentage error (relative to the experimental data) in the 2D and 3D models, using the standard wall functions [12]. Figure 14 shows the percentage error (relative to the experimental data) in the 2D and 3D models, using the enhanced wall treatment [34]. The increase in the accuracy of the predictions produced by the three dimensional wedge model, over the two-dimensional model, compared to the experimental data of Yamada and Ito [1], is of the order of between 5% and 7%.

In Fig. 15, we see the results from the fully three-dimensional model. A transition is visible in the experimental data over the range $117{,}000 \leq Re \leq 221{,}000$. In a notable change from the two-dimensional model results, it can be observed that, across the entire experimental range, the quantitative agreement between the RNG k-ϵ turbulence model, with standard wall function, and the experimental data is strong. The best agreement is found for Re =132,000, where the percentage difference is 2.0%. The worst agreement is found for Re=12,000, where the percentage differ-

Downloaded 03 Jun 2010 to 171.66.16.157. Redistribution subject to ASME license or copyright; see http://www.asme.org/terms/Terms_Use.cfm

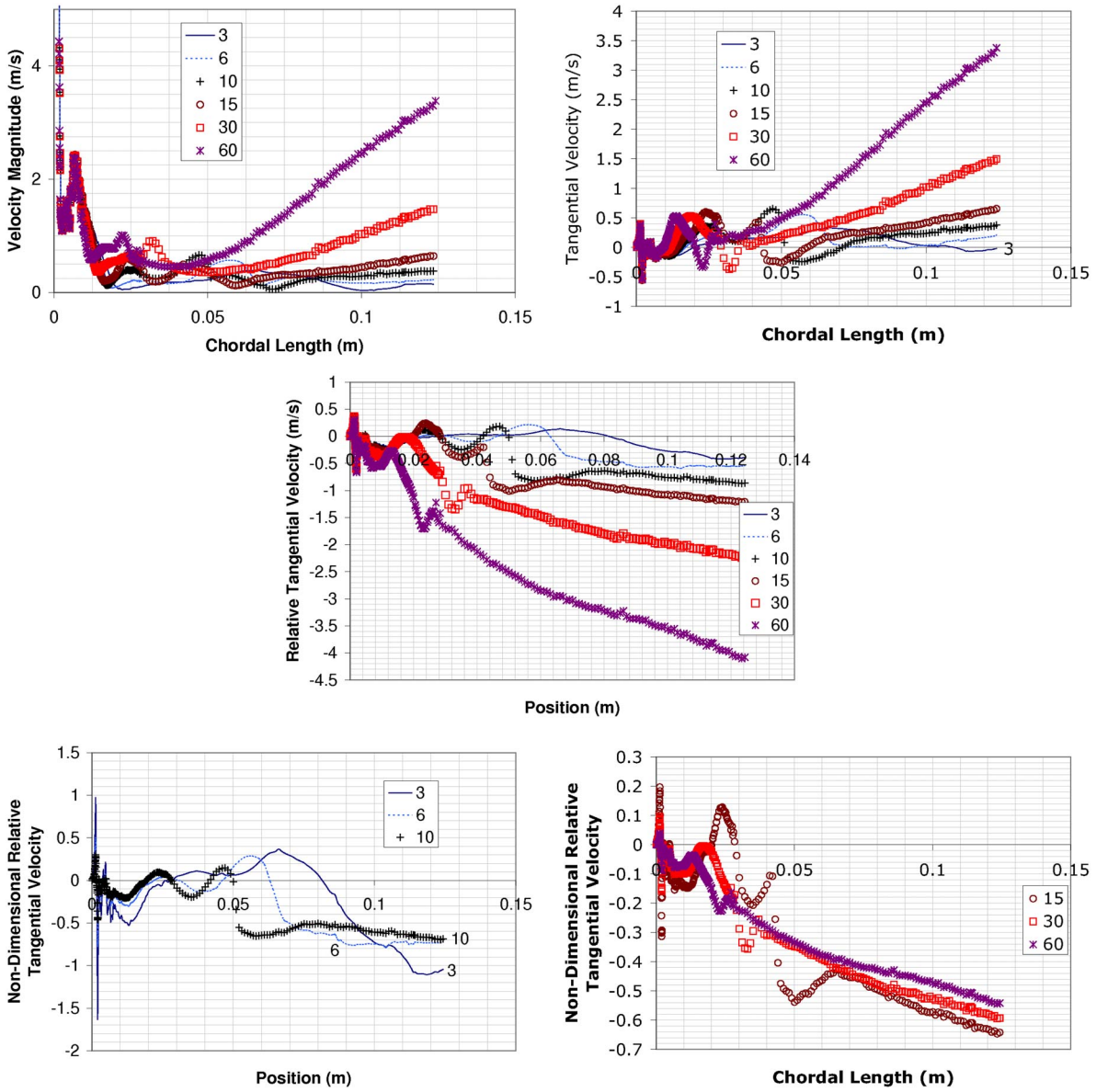

Fig. 18 Graphs of velocity components against chordal length (along a chord situated in the middle of the annulus) for a variety of rotational speeds (rad s^{-1})

ence is 22%. While the transition seen in the experimental data is not replicated, the results show significant differences from the two-dimensional models (Sec. 4.2) and the three-dimensional wedge model.

4.3.2 Flow Structure. This section looks at the flow structure and its dependence on rotational speed and throughflow conditions. First, we look at the two-dimensional flow fields with throughflow. The first case is at a rotational speed of $\Omega = 28$ rad s^{-1}, $C_Q = 1500$, with Fig. 16 depicting streamlines between the shroud and the cone, colored by radial velocity, showing a vortex contained between the shroud and the cone near to the inlet pipe. This is present for all rotation speeds where throughflow is present, giving clear evidence of the behavior Pereira and Sousa described [25], with a vortex trapped between the outer cone and the more dominant throughflow. As the rate of throughflow is increased, the size of the vortex is seen to increase, with its center being seen to travel away from the inlet (in the positive axial direction). Increasing the rate of rotation while maintaining the throughflow rate constant causes the area of interaction between the vortex and the throughflow to increase, which could explain the decrease in moment coefficient as Ω increases. In Figs. 17(*a*)–17(*c*), we can see the effect of increasing rotation on the flow structure. It can be seen that the increasing rotation is having a noticeable effect on the axial flow. By looking at how the flow structure changes with increasing rotational speed in the fully three-dimensional model, we can see that the flow is not axisymmetric in nature, although there is clear rotational periodicity in the flow. Indeed, the spiral patterns described by Wimmer and Zierep [22] appear to be occurring. By studying the velocity magnitude in the annulus (Fig. 18(*a*)), it can be observed that with increasing rotational velocity, the velocity magnitude in the annulus increases. A similar behavior can be observed through looking at the tangential velocity, as shown in Fig. 18(*b*). It is more interesting to look at the tangential velocity relative to the rotating surface. It can be observed from Fig. 18(*c*) that as the rotational rate is increased, the relative tangential velocity decreases. Through nondimensionalization of the relative tangential

Downloaded 03 Jun 2010 to 171.66.16.157. Redistribution subject to ASME license or copyright; see http://www.asme.org/terms/Terms_Use.cfm

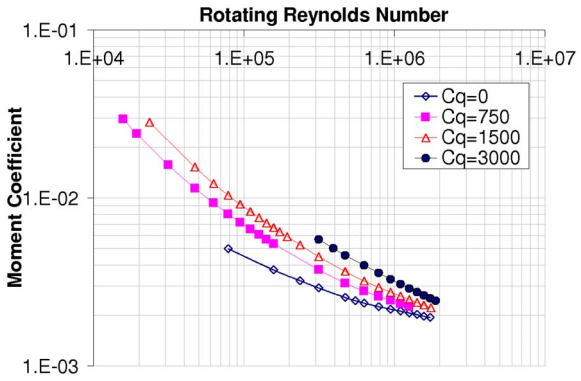

Fig. 19 Graph of moment coefficient (C_M) against rotating Reynolds number (Re), for a vertex angle of ϕ=90 deg and a nondimensional gap width s=0.016, for increasing nondimensional throughflow rates (C_Q)

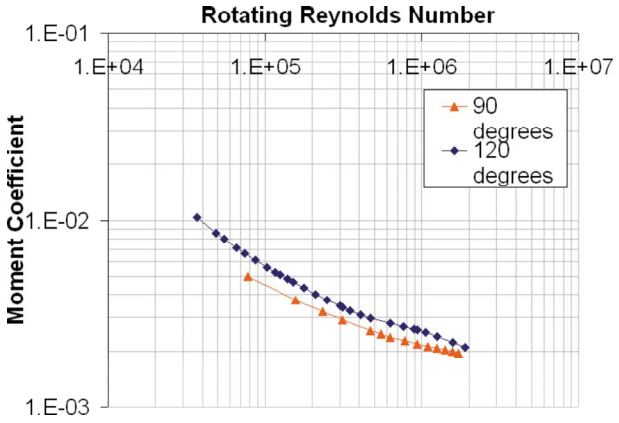

Fig. 20 Graph of moment coefficient (C_M) against rotating Reynolds number (Re), to show the effect of increasing vertex angle (ϕ) for a constant, nondimensional gap width (s=0.016)

velocity as in Eq. (14), the curves shown in Figs. 18(*d*) and 18(*e*) can be obtained:

$$v_n = \frac{v_r}{\Omega R_i} \tag{14}$$

From this, an explanation for the difference in the behavior before and after the transition can be approached at. Before the transition, the relative tangential velocity is positive for at least the first third of the cone, whereas after the transition the relative tangential velocity is negative for most of the region. If the relative velocity is positive, this means the flow is rotating slightly faster than the cone, whereas if it is negative, the flow is rotating slower. If the flow is slower than the cone, then it will be retarding the cone, which will create a greater moment about the cone surface.

To summarize, in this section, it has been shown that three-dimensional modeling, either when rotationally periodicity is applied on the solution domain or the entire situation is modeled, results in greater accuracy compared to two-dimensional models. Physically, the flow is expected to be nonaxisymmetric [22], which has been replicated numerically (Fig. 17), and so modeling the entire situation is the only way of capturing such phenomena.

4.4 Overall Effects of Increasing Throughflow and Geometrical Changes. Figure 19 presents a graph of moment coefficient (C_M) against rotating Reynolds number (Re), for a vertex angle of ϕ=90 deg and a nondimensional gap width s=0.016, for increasing nondimensional throughflow rates (C_Q). In Fig. 19, it can be observed that increasing the throughflow rate causes an increase in the moment coefficient calculated by the CFD, which is consistent with the experimental data of Yamada and Ito [1]. So as to be consistent, all of these data points were calculated using the RNG k-ϵ turbulence model, with enhanced wall treatment.

Figure 20 presents a graph of moment coefficient (C_M) against rotating Reynolds number (Re), for a nondimensional throughflow rates (C_Q), a nondimensional gap width s=0.016, and increasing vertex angle ϕ. In Fig. 20, it can be observed that increasing the vertex angle causes an increase in the moment coefficient calculated by the CFD, which is consistent with the experimental data of Yamada and Ito [1]. So as to be consistent, all of these data points were calculated using the RNG k-ϵ turbulence model, with enhanced wall treatment.

Figure 21 presents a graph of moment coefficient (C_M) against rotating Reynolds number (Re), for a nondimensional throughflow rates (C_Q), a vertex angle ϕ, and increasing nondimensional gap width s. In Fig. 21, it can be observed that increasing the gap width causes a decrease in the moment coefficient calculated by the CFD, which is consistent with the experimental data of Yamada and Ito [1].

To summarize, the numerical modeling has shown that increasing C_Q, increasing the vertex angle ϕ, or decreasing the gap width s lead to increases in the moment coefficient, which agrees with the experimental trends observed by Yamada and Ito [1–3].

5 Conclusions

In simulations of the flow where no forced throughflow is present, calculations from two-dimensional models computed using the RNG k-ϵ or SST k-ω turbulence models have been presented for different vertex angles and gap widths. These show good agreement with the experimental data of Yamada and Ito [1–3] for a vertex angle of ϕ=90 deg. The transition that is present in all the cases is relatively weak when there is no throughflow, and as such the enhanced wall treatment is seen to predict the torque levels consistently across the speed range in these cases. For the cases with a larger vertex angle (ϕ =120 deg), the performance of the model is far worse, with torque levels consistently overpredicted by between 33% and 70% in comparison with the experimental data. Additionally, a computation was conducted using the SST k-ω turbulence model, which was seen to perform slightly better, though still overpredicting torque levels by between 16% and 67%.

The effect of throughflow on the flow has also been considered in both two-dimensional and three-dimensional simulations. In these cases, the experimental transition is far more distinct. Again, these show good agreement with the experimental data of Yamada and Ito, except for in the transitional regime. Three different treatments for viscosity effects were utilized, and comparisons made between their performances, the RNG k-ϵ turbulence model, the standard k-ϵ turbulence model, and the RSM. Little difference was found between the results from the RNG k-ϵ turbulence model and the standard k-ϵ turbulence model, nor between the RNG k-ϵ turbulence model and the RSM. More significant differences were found by varying the wall function utilized in each case. The two-dimensional models have been unable to offer any insight into the mechanism behind the transition. This is due to the fact that while the two different wall approaches (standard wall functions and enhanced wall treatment) give very good agreement, respectively, before and after the transition, neither approach performs with equal accuracy both sides of the transition when used in these models.

The situation has been modeled in three dimensions for one geometrical setting (ϕ=90 deg, s=0.016), utilizing a rotationally periodic, 6 deg wedge shaped model and also a full 360 deg simulation. Turbulence modeling in these models has concentrated on

Downloaded 03 Jun 2010 to 171.66.16.157. Redistribution subject to ASME license or copyright; see http://www.asme.org/terms/Terms_Use.cfm

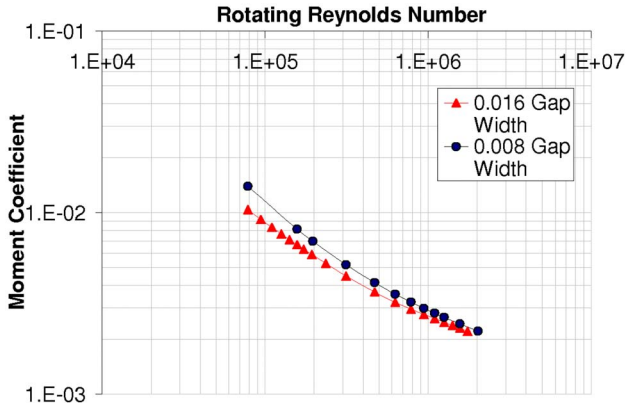

Fig. 21 Graph of moment coefficient (C_M) against rotating Reynolds number (Re), to show the effect of increasing gap width (s), for a constant vertex angle (ϕ=90 deg), and a constant, nondimensional throughflow (C_Q=0)

utilizing the RNG k-ϵ model. Similar to the two-dimensional simulations, the transition is not well captured by the rotationally periodic model. This supports the notion that the mechanism behind the transition is incorporated in the nonaxisymmetricity of the flow, as discussed in Sec. 4.4. The full simulations still fail to capture the transition. However, the performance of the turbulence model used (RNG k-ϵ with standard wall function) is consistent with the experimental data across the speed range.

This investigation has produced a methodology for the modeling of the flow around a bevel gear, and has highlighted some shortcomings in the two-dimensional numerical modeling. It has also shown that using a three-dimensional model produces more accurate results. However, to clearly see whether a flow is axisymmetric or not, the entire situation needs to be modeled. In doing this, a much clearer understanding of the flow has been obtained, and it is possible to use the CFD to explain differences in the flow field.

Nomenclature

u, v, w = x-, y-, z-velocities (ms^{-1})
p = pressure (Pa)
A = area (m^2)
R = radius (m)
$T=R_o-R_i$ = radial gap width (m)
Ω = Angular velocity (rad s^{-1})
M = moment transmitted by rotating surface (N m)
$\mathrm{Re}=\Omega R_i^2/\nu$ = rotating Reynolds number
ϕ = cone vertex angle (deg)
$C_M=\lvert M_{\mathrm{cone}}\sin(\phi/2)/(1/2)\rho\Omega^2R_i^5\rvert$ = torque or moment coefficient
$C_Y=\lvert M_{\mathrm{cone}}/(1/2)\rho\Omega^2R_i^3(A/\pi)\rvert$ = moment coefficient used in Ref. [2]
Q = mass flow rate (kg s^{-1})
$C_q=Q/R_i\nu$ = nondimensional throughflow rate
$s=T/R_i$ = nondimensional radial gap width
v_n = nondimensional relative tangential velocity
v_r = relative tangential velocity
$U^*=U_PC_\mu^{1/4}k_P^{1/2}/\tau_w/\rho$ = nondimensional velocity at point P
$y^*=\rho C_\mu^{1/4}k_P^{1/2}y_P/\mu$ = nondimensional value of y_P
k = turbulent kinetic energy
y = distance to the wall (m)
$u_\tau=\sqrt{\tau_{\mathrm{wall}}/\rho}$ = friction velocity
U = mean velocity
$C_{\%}=100(1-C_{M_{\mathrm{CFD}}}/C_{M_{\mathrm{expt}}})$ = percentage difference in moment coefficients

Greek Letters

ρ = density (kg m^{-3})
ν = kinematic viscosity (m^2/s)
μ = dynamic viscosity (kg m^{-1} s^{-1})
ϵ = turbulence dissipation rate
ω = specific dissipation rate

Subscripts

P = values at point P
CFD = values from CFD
expt = values from experimental data [1–3]

References

[1] Yamada, Y., and Ito, M., 1979, "Frictional Resistance of Enclosed Rotating Cones With Superposed Throughflow," ASME J. Fluids Eng., **101**, pp. 259–264.
[2] Yamada, Y., and Ito, M., 1975, "On the Frictional Resistance of Enclosed Rotating Cones (1st Report, Frictional Moment and Observation of Flow With a Smooth Surface)," Bull. JSME, **18**, pp. 1026–1034.
[3] Yamada, Y., and Ito, M., 1976, "On the Frictional Resistance of Enclosed Rotating Cones (2nd Report, Effects of Surface Roughness)," Bull. JSME, **19**, pp. 943–950.
[4] Lord, A., 1998, "An Experimental Investigation of Geometric and Oil Flow Effects on Gear Windage and Meshing Losses," Ph.D. thesis, University of Wales, Swansea.
[5] Farrall, M., Simmons, K., Hibberd, S., and Young, C., 2005, "Computational Investigation of the Airflow Through A Shrouded Bevel Gear," *ASME Turbo Expo 2005*, ASME.
[6] Johnson, G., Simmons, K., Stables, R., and Young, C., 2006, "Reduction in Aeroengine Transmission Gear Windage Loss by Shrouding," Performance Enhancing Technologies for Transmission Systems.
[7] Rapley, S., Simmons, K., and Eastwick, C., 2007, "The Application Of CFD To Model Windage Power Loss From A Spiral Bevel Gear," *ASME Turbo Expo 2007, ASME*.
[8] Wild, P. M., Djilali, N., and Vickers, G., 1996, "Experimental and Computational Assessment of Windage Lossed in Rotating Machinery," ASME J. Fluids Eng., **118**, pp. 116–122.
[9] Lathrop, D. P., Fineberg, J., and Swinney, H. L., 1992, "Turbulent Flow Between Concentric Rotating Cylinders at Large Reynolds Number," Phys. Rev. Lett., **68**(10), pp. 1515–1518.
[10] Dubrulle, B., and Hersant, F., 2002, "Momentum Transport and Torque Scaling in Taylor–Couette Flow From an Analogy With Turbulent Convection," Eur. Phys. J. B, **26**, pp. 379–386.
[11] Shiomi, Y., Nakanishi, S., and Kutsuna, H., 2000, "CFD Calculation for Two-Phase Flow in Concentric Annulus With Rotating Inner Cylinder," *PHOENICS Users Conference Proceedings*, Phoenix.
[12] Launder, B., and Spalding, D., 1974, "The Numerical Computation of Turbulent Flows," Comput. Methods Appl. Mech. Eng., **3**, pp. 269–289.
[13] Wilson, K., 1971, "Renormalization Group and Critical Phenomena. I Renormalization Group and the Kandoff Scaling Picture," Phys. Rev. B, **4**, pp. 3174–3183.
[14] Wilson, K., 1971, "Renormalization Group and Critical Phenomena. II Phase-Space Cell Analysis of Critical Behaviour," Phys. Rev. B, **4**, pp. 3184–3205.
[15] Launder, B., Reece, G., and Rodi, W., 1975, "Progress in the Development of a Reynolds-Stress Turbulence Closure," J. Fluid Mech., **68**, pp. 537–566.
[16] Wimmer, M., 2000, "Taylor Vortices at Different Geometries," Lect. Notes Phys., **549**, pp. 194–212.
[17] Wimmer, M., 1995, "An Experimental Investigation of Taylor Vortex Flow Between Conical Cylinders," J. Fluid Mech., **292**, pp. 205–227.
[18] Noui-Mehidi, M. N., Ohmura, N., and Kataoka, K., 2002, "Mechanism of Mode Selection for Taylor Vortex Flow Between Coaxial Conical Rotating Cylinders," J. Fluids Struct., **16**, pp. 247–262.
[19] Noui-Mehidi, M. N., Ohmura, N., and Kataoka, K., 2002, "Gap Effect on Taylor Vortex Size Between Rotating Conical Cylinders," *15th Australasian Fluid Mechanics Conference*, The University of Sydney, Sydney, Australia, Dec.
[20] Noui-Mehidi, M. N., 2005, "Effect of Acceleration on Transition Properties in a Conical Cylinder System," Exp. Therm. Fluid Sci., **29**, pp. 447–456.
[21] Noui-Mehidi, M. N., Ohmura, N., and Kataoka, K., 2005, "Dynamics of the

Downloaded 03 Jun 2010 to 171.66.16.157. Redistribution subject to ASME license or copyright; see http://www.asme.org/terms/Terms_Use.cfm

Helical Flow Between Rotating Conical Cylinders," J. Fluids Struct., **20**, pp. 331–344.
[22] Wimmer, M., and Zierep, J., 2000, "Transition From Taylor Vortices to Cross-Flow Instabilities," Acta Mech., **140**, pp. 17–30.
[23] Noui-Mehidi, M. N., Ohmura, N., and Kataoka, K., 2002, "Numerical Computation of Apex Angle Effects on Taylor Vortices in Rotating Conical Cylinder Systems," J. Chem. Eng. Jpn., **35**, pp. 22–31.
[24] Hoffman, N. P., and Busse, F. H., 1999, "Instabilities of Shear Flows Between Two Coaxial Differentially Rotating Cones," Phys. Fluids, **11**, pp. 1676–1678.
[25] Pereira, J. C. F., and Sousa, J. M. M., 1999, "Confined Vortex Breakdown Generated by a Rotating Cone," J. Fluid Mech., **385**, pp. 287–323.
[26] Wereley, S. T., and Lueptow, R. T., 1999, "Velocity Field for Taylor–Couette Flow With an Axial Flow," Phys. Fluids, **11**, pp. 3637–3649.
[27] Noui-Mehidi, M. N., Salem, A., Legentilhomme, P., and Legrand, J., 1999, "Apex Angle Effects on the Swirling Flow Between Cones Induced by Means of a Tangential Inlet," Int. J. Heat Fluid Flow, **20**, pp. 405–413.
[28] May, N. E., Chew, J. W., and James, P. W., 1994, "Calculation of Turbulent Flow for an Enclosed Rotating Cone," ASME J. Turbomach., **116**, pp. 548–554.
[29] Moureh, J., Flick, D., and Larrieu, P. L., 1996, "Etude hydrodynamique et thermique d'un échangeur de chaleur à noyau tournant conique," Rev. Gen. Therm., **35**(414), pp. 402–407.
[30] Launder, B., and Spalding, D., 1972, *Lectures in Mathematical Models of Turbulence*, Academic, New York.
[31] Wilcox, D., 1998, "Turbulence Modeling for CFD," DCW Industries, Inc., La Canada, California.
[32] Gibson, M. M., and Launder, B., 1978, "Ground Effects on Pressure Fluctuations in the Atmospheric Boundary Layer," J. Fluid Mech., **86**, pp. 491–511.
[33] Launder, B., 1989, "Second-Moment Closure: Present…and Future?," Int. J. Heat Fluid Flow, **10**, pp. 282–300.
[34] Kader, B., 1981, "Temperature and Concentration Profiles in Fully Turbulent Boundary Layers," Int. J. Heat Mass Transfer, **24**, pp. 1541–1544.
[35] FLUENT 6.2 User's Guide.

Downloaded 03 Jun 2010 to 171.66.16.157. Redistribution subject to ASME license or copyright; see http://www.asme.org/terms/Terms_Use.cfm

Identification of Flow Structures on a LP Turbine Blade Due to Periodic Passing Wakes

S. Sarkar
Department of Mechanical Engineering,
Indian Institute of Technology,
Kanpur 208016, India
e-mail: subra@iitk.ac.in

The paper describes the flow structures on the suction surface of a highly cambered low-pressure turbine (LPT) blade (T106 profile) subjected to periodic convective wakes. A separation bubble on the rear half of the suction side of the blade was found to form under the operating condition due to the highly diffusive boundary layer. Interactions of migrating wakes with this separated boundary layer trigger rollup of the shear layer leading to transition and the appearance of coherent vortices. To characterize the dynamics of these large-scale structures, a proper orthogonal decomposition is pursued on both the fluctuating velocity and the vorticity fields generated by large-eddy simulations (LESs) of wake passing over the LPT blade for a Reynolds number $Re = 1.6 \times 10^5$. *The first two modes clearly depict the rollup of the unstable shear layer and formation of large-scale vortex loops that contain a major fraction of the fluctuation energy. The present LES, at least in a qualitative sense, illustrates the large-scale motions in the outer layer and dynamics of vortical structures in a separated boundary layer excited by external perturbations.* [DOI: 10.1115/1.2911682]

Keywords: blade-wake interactions, LPT blade, flow structures, POD, LES

1 Introduction

Transition, in general, and its applications to turbomachinery flows, in particular, have been the subject of much research. Transition arising from a separated boundary layer is quite common and plays an important role in engineering applications. In a modern jet engine, the low-pressure turbine (LPT) supplies power to the fan and the first stages of the compressor. As the LPT is relatively heavy consisting of a large number of stages, small improvements of its efficiency have a significant effect on the overall efficiency of an engine and thus the fuel consumption. Therefore, there are continued efforts toward the generation of "high-lift" blade profiles that help to reduce the number of blades leading to the reduction in weight and cost of LPT. However, the reduction in the number of blades comes up against the problem of boundary layer separation on the suction surface due to the increased blade loading. Wakes shed from the upstream vane rows interact with the separated boundary layer on the suction surface of downstream blades, resulting in a highly unsteady flow. Under such an environment, the flow configuration depends on the receptivity to external disturbances and the internal growth mechanisms of the shear layer [1]. One could possibly find a combination of bypass transition and separation-induced transition depending on the wake-frequency and Reynolds number. Considerable progress has been made over the past three decades in understanding the behavior of a separated boundary layer under the influence of unsteady wakes [2–8]. It was indicated that apart from the wake kinematics, small-scale fluctuations carried by the convective wake influence the transition to turbulence of the highly diffusive boundary layer on the suction surface [9,10]. The present work aims to elucidate the dynamics of unsteady-flow structures during the evolution of turbulence in a separated boundary layer under the influence of periodic passing wakes.

The problem of wake-induced transition over a turbine blade is not only of engineering interest but also fundamental in nature from the viewpoint of flow instability. A few relevant studies on the instability mechanism of a separation bubble under the influence of freestream turbulence were reported through experiments [11], direct numerical simulation (DNS) [12], and large eddy simulation (LES) [13]. It was observed [14,15] that boundary layers that separate in laminar state behave differently from those that are already transitional or highly unstable (pretransitional) at separation. Downstream of separation, the *Kelvin–Helmholtz* (KH) instability sets in; the rollup vortex periodically forms, grows, pairs, and finally interacts with the wall. The basic information about how transition originates and develops in separated boundary layers are described in Refs. [4,11]. Correlations of intermittency within the separated region are provided by the turbulent spot theory with a high spot production rate. Reference [12] demonstrated the transition mechanism occurring in a short laminar separation bubble that was characterized by the breakdown of Λ-vortices. The entire transition process leading to breakdown to turbulence of a leading-edge separated layer was elucidated in Ref. [13]. The primary two-dimensional instability originates from the free shear layer in the separated bubble via KH waves, which grow downstream and start to develop three-dimensional spanwise disturbances around the mean reattachment point. Vortex shedding from the separated layer was also observed with a considerable fluctuation of the reattachment point.

A few relevant studies [16–18] on the instability mechanism of a separation bubble under the influence of periodic artificial disturbances have been reported. The correlations for predicting transition length in turbomachinery applications have been extended in Refs. [16,17]. However, the physics of transition, owing to the interactions of the convective wake and the separation bubble, was not very complete. Watmuff [18] illustrated that the instability mechanism governing the amplification of the wave packet in a separated bubble is predominantly inviscid. In the vicinity of the reattachment, the nonlinear interaction and the rollup of the shear layer evolve large-scale vortex loops (*coherent structures*) that retain their presence far downstream of separation.

A DNS of low Reynolds number flow in a LPT cascade with incoming wakes has become feasible, owing to recent advancement of computing power, although it is still very expensive and not suitable for engineering analyses. Such a simulation was per-

Contributed by the Fluids Engineering Division of ASME for publication in the JOURNAL OF FLUIDS ENGINEERING. Manuscript received August 27, 2007; final manuscript received December 29, 2007; published online June 9, 2008. Assoc. Editor: Chunill Hah.

Downloaded 03 Jun 2010 to 171.66.16.157. Redistribution subject to ASME license or copyright; see http://www.asme.org/terms/Terms_Use.cfm

formed for a Reynolds number $Re=1.48\times10^5$ in Ref. [7]. The focus of the paper was on induced longitudinal vortical structures along the downstream half of the pressure side by straining of migrating wakes within the blade passage. The experiments [8], DNS [19], and LES [9] at a lower Reynolds number illustrate some interesting differences in the flow characteristics with a separation bubble on the suction surface. Perturbations created by the convective wake develop coherent vortices by rollup of the separated boundary layer. These vortices are identified as the source of pressure fluctuations over the rear half of the suction surface. Sarkar [20] illustrated that transition during the wake-induced path is governed by a mechanism that involves the formation and convection of large-scale vortices followed by the production of turbulent kinetic energy inside the KH rolls. Thus, an understanding of the dynamics of coherent structures and their nonlinear interactions is the key to comprehension of the concerned flow transition.

The proper orthogonal decomposition (POD) of spatial velocity correlations was originally suggested by Lumley [21] to extract organized large-scale structures from turbulent flows. This approach leads to the eigenfunction-eigenvalue problem. Since the introduction of POD, it has been applied to many kinds of flows such as boundary layers [22,23], shear layers [24–26], turbulent jets [27–29], and bounded flows [30,31]. In most of these cases, it has been found that first few modes contain a high percentage of energy. The method has been proved to be a powerful tool in recognizing coherent structures in turbulent flows. The POD analysis of fluctuating flow field obtained from a LES of wake passing within a high-lift LPT cascade is performed. An attempt is made to describe the flow instability and also to identify and characterize the flow structures during transition of a separated boundary layer on the suction surface of the LPT blade under the influence of periodic convective wakes. The eddy motions and their nonlinear interactions are expected to be resolved in the process of evolution of turbulence on the suction surface through the LES. A DNS would have been ideal for the problem, but it is extremely costly and Reynolds-averaged Navier–Stokes calculations will not provide the answer. Hence, LES can be pursued as an alternative means with the benefit being a considerably lower computational effort.

2 Cascade Geomentry and Numerical Details

The cascade geometry considered here is that of the high-lift LPT blade, T106 profile experimentally studied in different laboratories [8,32]. According to Ref. [8], the blade aspect (span-to-pitch) ratio was 1.89 with a chord of 198 mm and thus the flow at the midspan can be considered two dimensional. This allows a three-dimensional simulation to be performed under the assumption of a homogeneous flow in the spanwise direction. The pitch-to-chord ratio was 0.799. The blade stagger angle λ, the inlet flow angle β_1, and the exit flow angle β_2 are 30.7 deg, 37.7 deg, and −63.2 deg, respectively, as shown in Fig. 1. The effects of an upstream row of vanes have been traditionally studied through experiments by sweeping a row of wake-generating bars upstream of a cascade. The moving cylinders ahead of the cascade are also shown in Fig. 1. LES of wake passing over the T106 profile in a cascade is performed at a Reynolds number of 1.6×10^5 (based on the chord and the isentropic exit velocity) and the flow coefficient $\phi=V_{X1}/U_b$ of 0.83. The bar pitch matches the cascade pitch that yields a reduced blade passing frequency $f_r=fC/V_{2is}$ of 0.68, f being the frequency. This allows using a single cascade channel to replace the large number of blades in a cascade by periodic condition on the pitchwise boundaries and makes a DNS or LES affordable.

The moving row of wake-generating bars is replaced by a precursor LES of the flow past a thin cylinder, D being 2% of the blade chord. The wake data are collected from a plane $5.25D$ downstream of the cylinder and are interpolated at the inlet plane of cascade considering the kinematics of flow by matching the velocity triangles. Thus, the present LES uses coupled simulations of flow around a cylinder for the generation of a wake, providing inflow conditions for successor simulations of wake interactions with the blade. The wake data that are kinematically transferred to the cascade inlet have a maximum mean wake deficit of $0.25V_1$, a wake half-width of $0.02C_x$, and a level of turbulence intensity of about 10%.

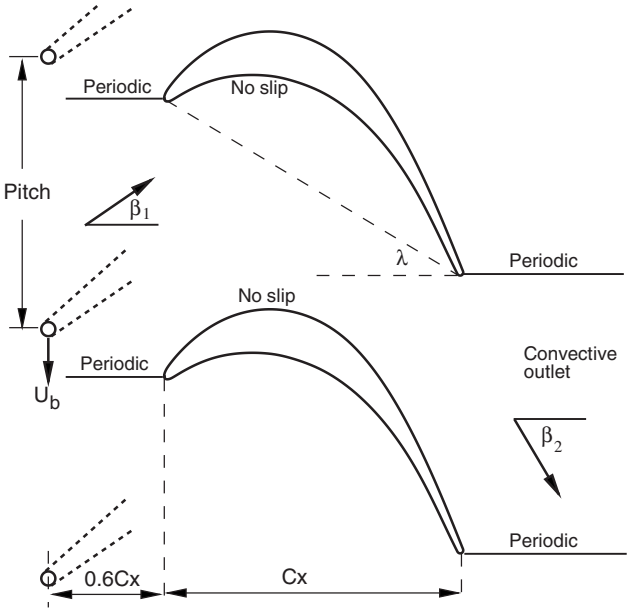

Fig. 1 Geometry of T106 low-pressure cascade and a schematic of a row of wake-generating cylinders sweeping at a speed U_b ahead of cascade

The filtered, time-dependent, incompressible mass and momentum equations in fully covariant form are solved on a staggered grid using a symmetry-preserving finite difference scheme of second-order spatial and temporal accuracy. The details of mathematical formulations and numerical methods in general curvilinear coordinates used in the present study have already been reported [33,13]. The momentum advancement is explicit using the second-order Adams–Bashforth scheme except for the pressure term that is solved by a standard projection method. The pressure equation is discrete Fourier transformed in one dimension (in which periodicity of the flow and so uniformity of the geometry are imposed) and is iteratively solved by using multigrid acceleration in the other two dimensions. The computational details and the subgrid model are the same as used in the earlier study [20] that describes the unsteady pressure and the separation-induced transition on the suction surface. The LES uses 3.05×10^6 points for the cylinder and 2.4×10^6 points for the cascade with the near wall mesh resolution as $5<\Delta x^+<80$, $5<\Delta z^+<20$, and $1<\Delta y^+<3.5$. In order to validate, the results from the present LES were compared to the experiment [8,32] and the DNS [19] and were presented in Ref. [20]. This indicated that the LES data could be qualitatively used to describe the evolution of the boundary layer perturbed by passing wakes on the suction surface.

3 Results and Discussion

Results from the LES are presented to illustrate the dynamics of coherent vortices formed due to excitation of a separated boundary layer on the suction surface of a LPT blade by migrating wakes and turbulence generated thereafter by breakdown of these vortices. The distortion of a wake segment (characterized by bowing, reorientation, elongation, and stretching) as it convects within the LPT passage is illustrated in Fig. 2 by instantaneous isosurface of vorticity magnitude $|\omega|$. After being segmented at the leading

Downloaded 03 Jun 2010 to 171.66.16.157. Redistribution subject to ASME license or copyright; see http://www.asme.org/terms/Terms_Use.cfm

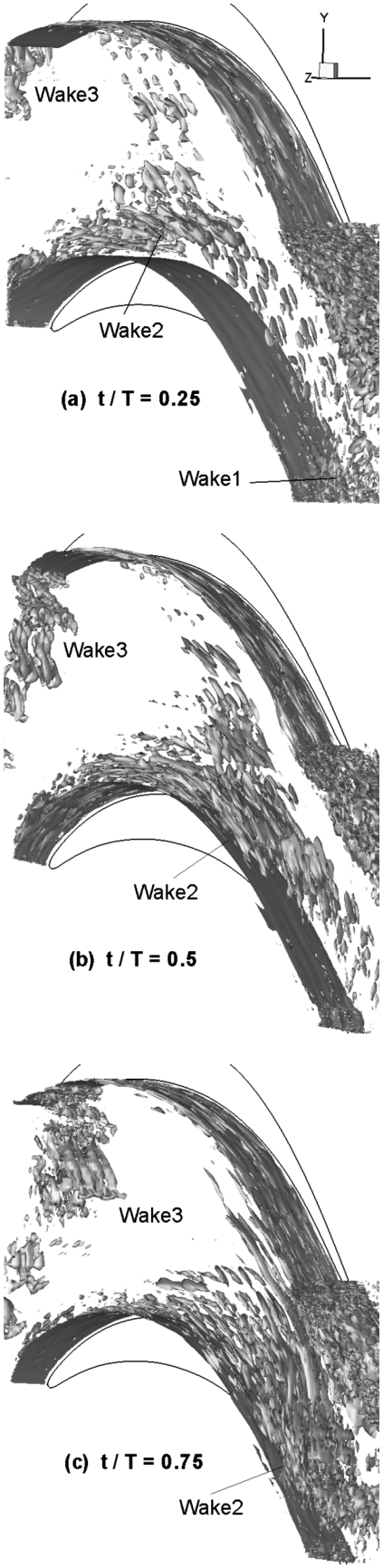

Fig. 2 Instantaneous isosurface of vorticity $|\omega|$ at three equal time intervals during the wake passing cycle

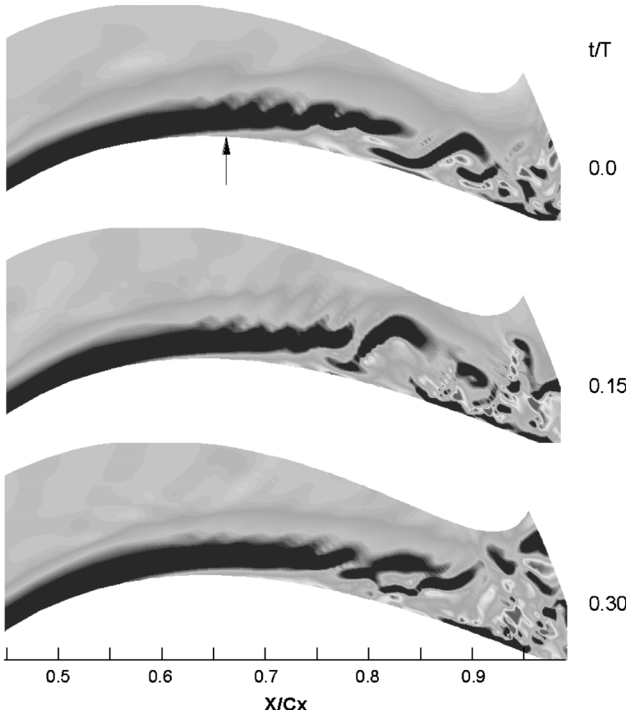

Fig. 3 Snapshots of instantaneous spanwise vorticity when the wake is ahead of the separation region over the rear half of the suction surface (the location of separation is marked by an arrow)

edge, the suction- and the pressure-side wakes differently behave. Straining of wakes near the suction surface has started from the stagnation point, but these are quickly broken down to random small-scale structures (Wake2 in Fig. 2(*a*)). The pressure-side wake suffers from severe stretching and thinning with the decay of turbulence (Wake2 in Fig. 2(*b*)). A bow forms between the pressure- and suction-side wakes owing to different convective speeds. In the apex region (Figs. 2(*b*) and 2(*c*)) of the distorted wake, enhancement of turbulence occurs with growing random small-scale structures and loss of preferred orientation. Sharp turning of the turbine passage causes the pressure-side wake to descend toward the wall over the downstream half of the pressure surface, whereas the suction-side wake after warping around the leading edge travels relatively above the surface. This highly strained wake fluid and generated small-scale structures periodically interact with the inflectional boundary layer over the suction surface, an example of complex interactions between spatial and temporal scales of turbulent eddies with an unsteady boundary layer. In the following sections, the growth mechanisms of the shear layer due to receptivity to the external disturbances along the suction side of the LPT will be described.

3.1 Flow Structure on the Suction Surface. A laminar separation bubble was observed [32] over the rear half of the suction surface for flow without passing wakes. The bubble started at $S/S_0=0.6$ and extended to $S/S_0=0.8$, where the separated layer underwent transition and reattached by $S/S_0=0.9$. To visualize the flow structure during the wake passing cycle, snapshots of isocontours of spanwise vorticity and streamlines along the midspan for the rear half of the suction surface are presented in Figs. 3 and 4. Although part of the vorticity plot was reported in Ref. [9], it is further illustrated here to correlate the dynamics of large-scale structure with POD modes that will be discussed later. Prior to t/T at about 0.5 (Fig. 3), when the wake center is ahead of the steady-flow separation (referred to as the separated region without the wake passing), isocontours of the spanwise vorticity depict the development of a cat's eye pattern, typical to the KH instability,

Downloaded 03 Jun 2010 to 171.66.16.157. Redistribution subject to ASME license or copyright; see http://www.asme.org/terms/Terms_Use.cfm

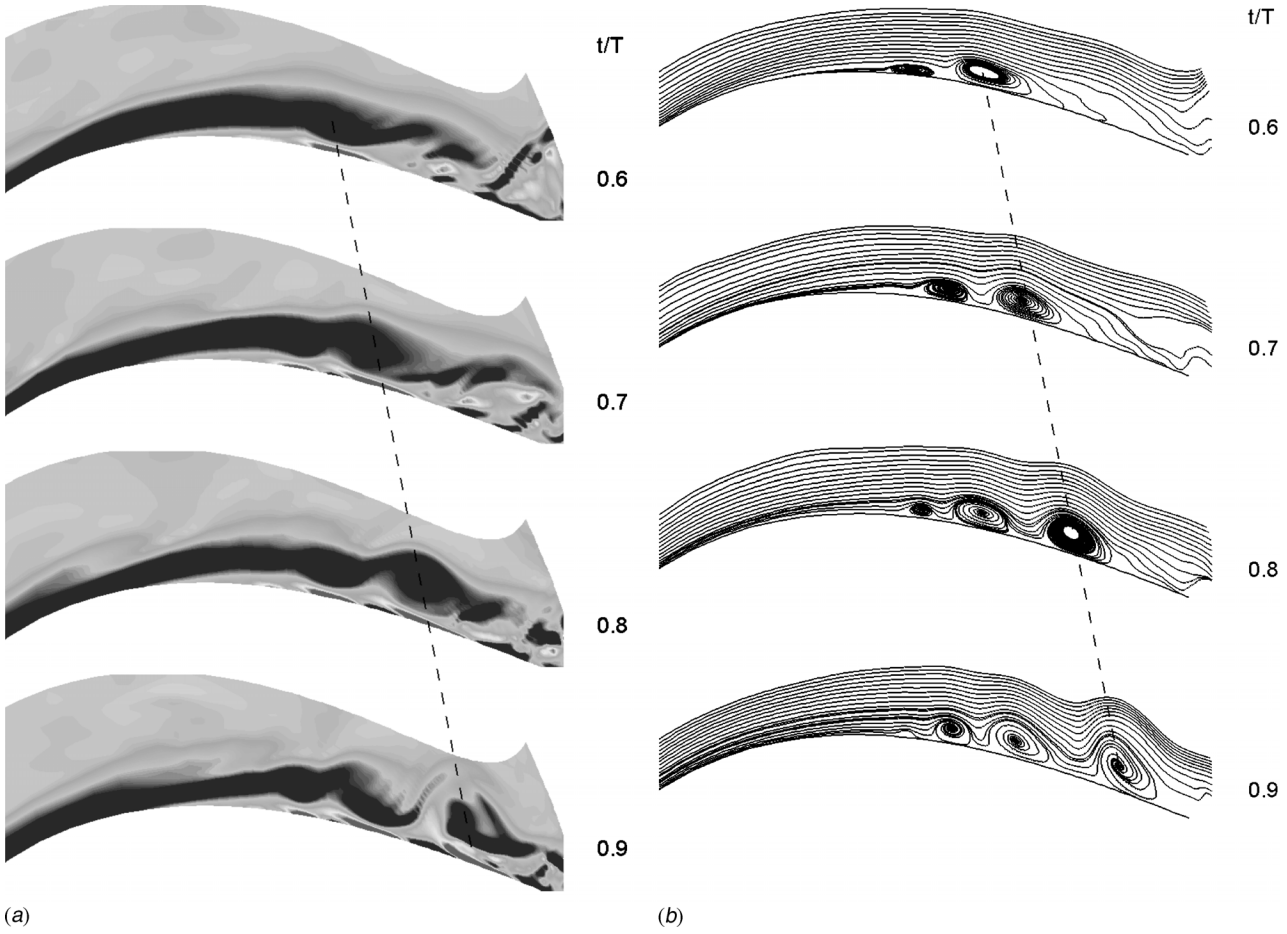

Fig. 4 Snapshots of (*a*) instantaneous spanwise vorticity and (*b*) streamlines as the wake passes over the separation region of the suction surface

just downstream of the separation. The approximate location of the separation (although it shifts with time) during $t/T=0.0-0.4$ is marked by an arrow. Thus, the instability of the boundary layer occurs through an inviscid mechanism because of the enhanced receptivity of perturbations associated with the separated boundary layer that finally breaks down to the turbulent flow downstream of $S/S_0=0.9$.

A migrating wake can be modeled as a negative jet, which impinges on the blade and splits in two streams; one pointing downstream that accelerates the flow downstream of the approaching wake and the other pointing upstream that retards the flow after the wake has passed. As the wake approaches the region of steady-flow separation ($t/T>0.5$), the negative-jet effect of the wake initiates a rollup of the separated boundary layer, and a large vortex associated with instantaneous backflow appears, as shown by the vorticity contours (Fig. 4(*a*)) and streamlines (Fig. 4(*b*)). Once a vortex appears, it grows and convects downstream at a speed approximately 37% of the local freestream [9]. The dotted line joining instantaneous locations of a vortex core illustrates its traveling speed. Thus, the wake, which convects with the freestream, moves ahead of these structures and perturbs the separated layer further downstream. This process generates further rollup vortices downstream. Thus, a train of apparently three prominent coherent vortices appears as the wake moves past the separated region and these vortices retain their presence far downstream before breakdown (Fig. 4(*b*)). These convective vortex rolls formed by excitation of the shear layer remarkably change the steady-flow separation. Once the influence of the passing wake subsides, the boundary layer again begins to separate. The instability mechanism, the nonlinear interaction, and the rollups of the shear layer evolving large-scale vortex loops (coherent structures) are very similar to those observed by Watmuff [18] in a study of the instability mechanism governing the amplification of a wave packet in a separated boundary layer. The large amplitude of pressure fluctuations observed on the rear half ($0.7<S/S_0<0.95$) of the suction surface is due to the formation of these rollup vortices as the wake passes over the separated boundary layer [8,9].

Power spectrum. Figures 5(*a*) and 5(*b*) show the power spectra evaluated from the pressure histories at four locations designated by P1–P4, near the suction surface at $S/S_0=0.45$, 0.80 and downstream of the trailing edge at $X/C_X=0.06$, 0.24. The slope of the resolved inertial range appears to follow $-5/3$ power law correlation between the energy and the frequency. The resolution seems to be good. Figure 5(*a*) illustrates that vortex shedding is present at $S/S_0=0.80$ (rear half of the blade) and is not periodic with a single frequency. The shedding process seems to happen within a range of frequency of roughly $2.4(V_{2is}/C)-4.0(V_{2is}/C)$ (the Strouhal number based on the isentropic exit velocity and the blade chord). Power spectra for the location $S/S_0=0.45$ do not show such fluctuations, indicating the absence of vortices. Figure 5(*b*) depicts a wider range of shedding frequency with more energetic high-frequency harmonics. This is due to vortex shedding from the trailing edge of the blade. A peak at a lower frequency of $0.68(V_{2is}/C)$ is apparent in the power spectra from all the locations. This is connected to the wake passing frequency. However, a subharmonic of that with another peak of frequency of about $1.5(V_{2is}/C)$ appears; the cause is not very well understood. This low-frequency flapping of the shear layer may be attributed to the occurrence of large-scale vortices from amalgamation of vortices

Downloaded 03 Jun 2010 to 171.66.16.157. Redistribution subject to ASME license or copyright; see http://www.asme.org/terms/Terms_Use.cfm

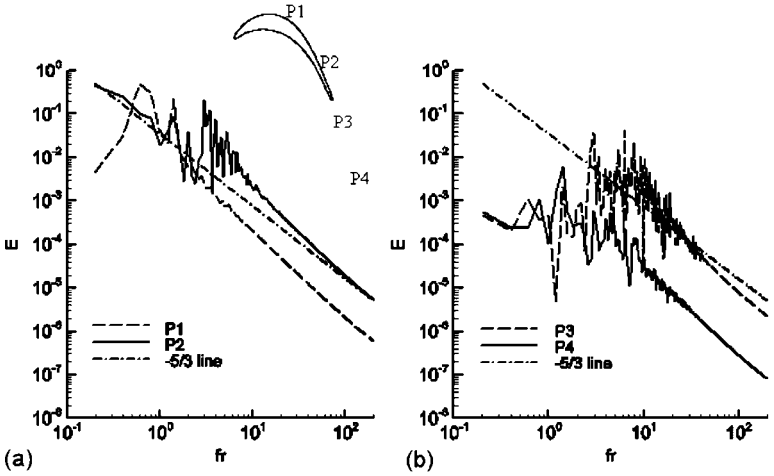

Fig. 5 Power spectrum of pressure histories from different points, $f_r = fC/V_{2is}$

formed due to instability of the shear layer and wake passing [34,13].

3.2 Instability Mechanism and Breakdown to Turbulence. To clarify whether the instability of the boundary layer over the rear half of the suction surface in the present study is indeed the KH instability, we will consider the KH instability mechanism in more detail. Let the two uniform incompressible inviscid fluids of densities ρ_1 and ρ_2 and velocities U_1 and U_2 be separated by a horizontal boundary layer. As stated by Chandrasekhar [35], for a given difference in velocity U_2-U_1, no matter how small it is, the KH instability occurs for all wave numbers larger than a critical value. To clarify whether the KH instability is due to the sharp discontinuities in ρ and U, Chandrasekhar assumed the case of continuous variation of U and a certain distribution of ρ (characterized by the Richardson number). He concluded that for any value of Richardson number, there are always bands of wavelengths for which the KH instability occurs. In particular, when the Richardson number is zero, i.e., for constant density, the condition for the KH instability to occur is $0<Kh<1.2785$, where K is the wave number and h is the shear layer thickness.

The time-averaged velocity profiles with their derivatives at different streamwise locations along the rear half of the suction surface are shown in Fig. 6, depicting the nature of the boundary layer under periodic passing wakes. The mean flow tends to be inflectional over the region $0.70<S/S_0<0.85$, relaxes from the inflectional layer downstream of $S/S_0=0.85$, and becomes a fully developed profile from $S/S_0=0.95$. In the present study, the shear layer thickness h at a location $S/S_0=0.80$, where the unsteadiness is very apparent, is about $0.027C$ (estimated from the vorticity profile) and hence the unstable region for K is $0<K<47.4/C$. In other words, the KH instability will not occur in the present study for wave numbers larger than $47.4/C$ or wavelength smaller than $2\pi/K=0.1325C$. Figure 5(*a*) shows the power spectra for pressure at $S/S_0=0.80$. It is apparent from the spectra that the characteristics frequency $f_r=fC/V_{2is}$ varies in the range 2.4–4.0. The velocity profile at this location illustrates that the wave speed v_w is about $0.45V_\infty$, which is equal to the velocity at the critical layer (i.e., the streamwise velocity at the inflection point $d^2V/d\eta^2=0$, which roughly occurs at $\eta/C=0.01$ for the velocity profile at $S/S_0=0.80$, Fig. 6). This finally becomes $v_w=0.55V_{2is}$. Therefore, the maximum wave number from the simulated result is $K_{max}=2\pi f_{max}/v_w=45.7/C$, corresponding to a wavelength of $0.1375C$, which satisfies the KH instability criterion for the present study $(0<K<47.4/C)$. Thus, it can be concluded that the boundary layer over the rear half of the suction surface is most likely to become unstable via the KH mechanism.

The growth of disturbances and development of three-dimensional motions can be monitored by the evolutions of velocity fluctuations. The streamwise, blade-normal, and spanwise components of the time-averaged velocity fluctuations (rms) at three sections of the boundary layer along the rear half of the suction surface are shown in Fig. 7. It should be noted that the mean boundary layer thickness over the rear half of the suction surface varies from 3% to 5% of the chord. A few representative phase-averaged velocity fluctuations (streamwise) at $t/T=0.6$, 0.8, and 0.933 as the wake convects over the inflectional region are superimposed. Upstream of $S/S_0=0.75$, the rms values of velocity fluctuations tend to have the same level of the freestream, indicating the flow to be laminar. The velocity fluctuations rapidly increase in the second half of the steady-flow separation $0.80<S/S_0<0.90$, reaching a maximum at $S/S_0=0.92$, near the point of mean reattachment, indicating that three-dimensional motion and nonlinear interaction lead to breakdown to turbulence in the second half of the separated boundary layer. The velocity fluctuations tend to slowly drop downstream of $S/S_0=0.92$, reflecting the

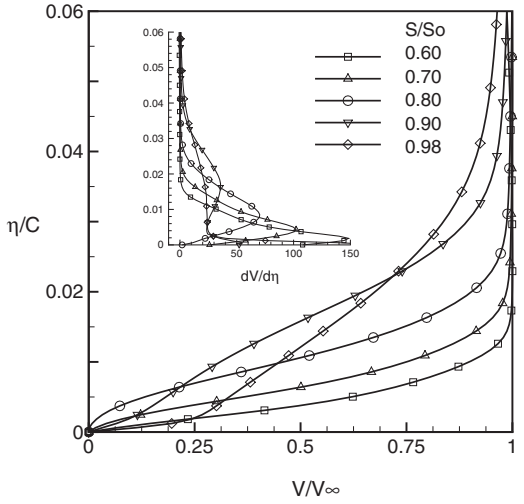

Fig. 6 Time-averaged velocity profiles and their derivatives at different sections along the rear half of the suction surface

Downloaded 03 Jun 2010 to 171.66.16.157. Redistribution subject to ASME license or copyright; see http://www.asme.org/terms/Terms_Use.cfm

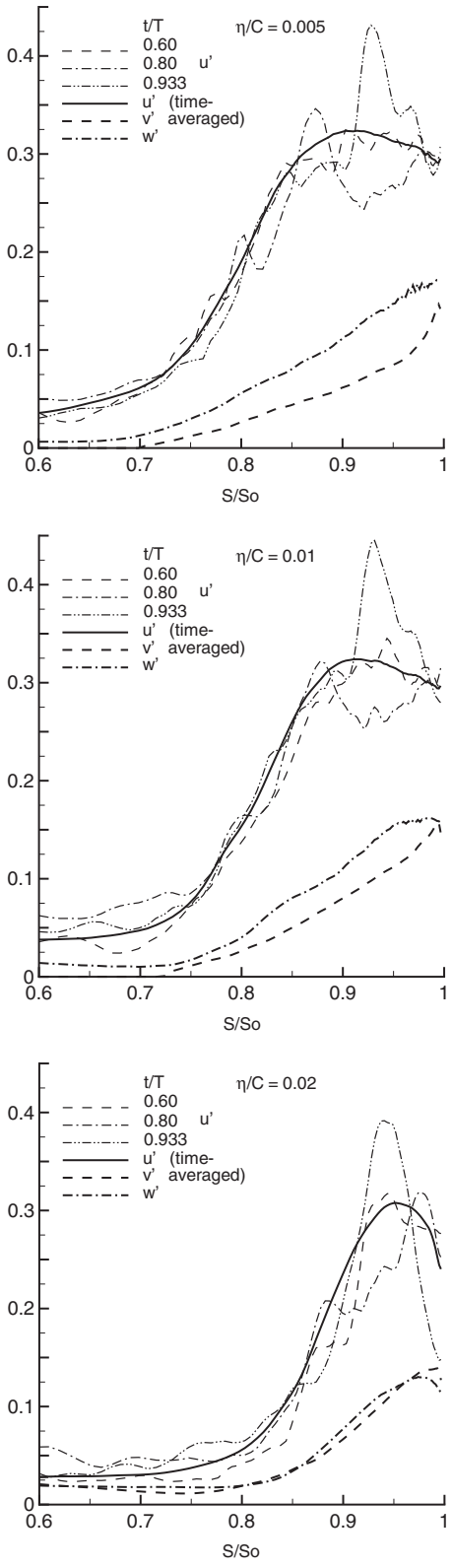

Fig. 7 Velocity fluctuations (rms and phase averaged) at three sections of the boundary layer along the rear half of the suction surface

end of transition [4,5]. Thus, the velocity fluctuations (rms values) elucidate that the mean boundary layer influenced by wake passing is transitional in $0.75 < S/S_0 < 0.92$ and then it becomes turbulent. Anisotropy is high within the inner part of the shear layer

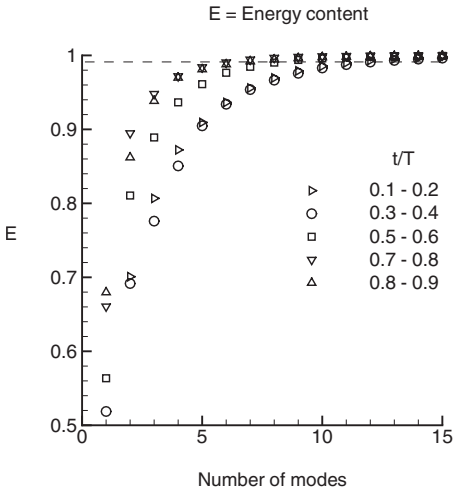

Fig. 8 Sum of eigenvalues divided by their total sum, indicating energy content

with a very prominent streamwise component of velocity fluctuation; a similar trend was reflected in a DNS [7]. What is interesting is the streamwise evolutions of phase-averaged velocity fluctuations, which demonstrate large oscillations as the wake migrates over the steady-flow separated region. This is attributed to the appearance of the large-scale rollup vortices via excitation of the shear layer. Once these vortices are formed, they convect

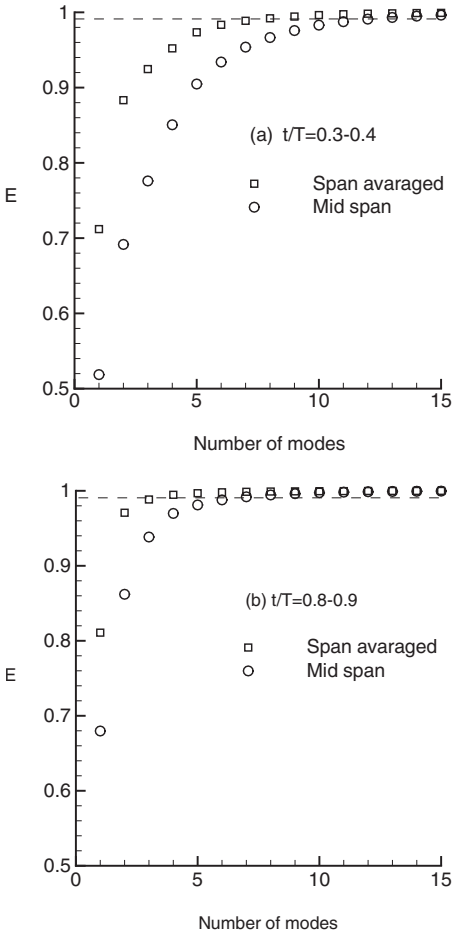

Fig. 9 Sum of eigenvalues divided by their total sum, indicating energy content for the midspan and span-averaged data

Downloaded 03 Jun 2010 to 171.66.16.157. Redistribution subject to ASME license or copyright; see http://www.asme.org/terms/Terms_Use.cfm

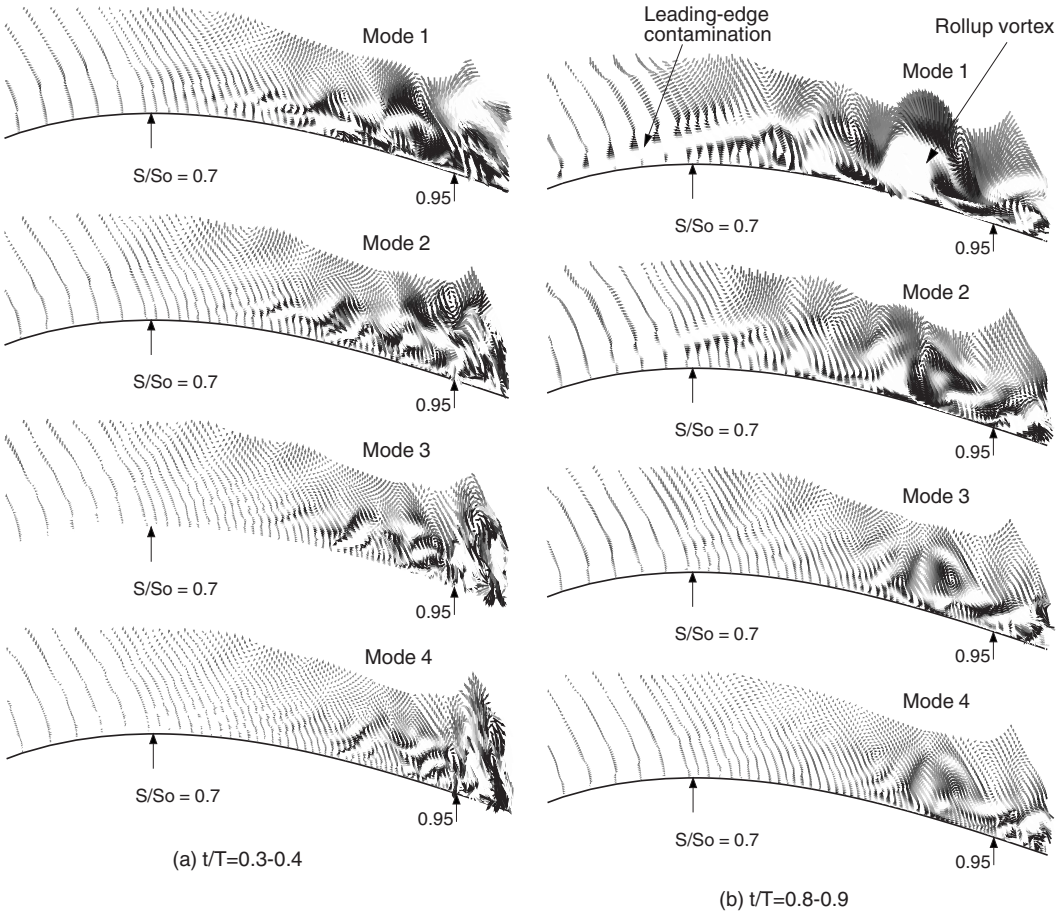

Fig. 10 First four eigenvectors of velocity disturbances for the midspan data during the wake-passing cycle: (*a*) indicates the shear layer instability via the KH mechanism and (*b*) illustrates the formation of large-scale vortex loops and the leading-edge contamination

downstream, start growing, and thus progressively enhance turbulence. This illustrates a strong influence of the rollup vortices on generation of turbulence along the suction surface of a high-lift LPT blade, the effect of interaction of the passing wake with the separated boundary layer.

It is noteworthy that a LES is grid dependent and a DNS is mandatory for an accurate prediction of transitional flow. However, the present study indicates that a LES, even with its limitations, is still capable of qualitatively describing the flow structures and transition because of the interactions of passing wakes and the separating boundary layer in a LPT. There is a scope for refinement of the grid and the subgrid model at the cost of computational time.

3.3 Coherent Structures and POD Analysis. To visualize the special and temporal behavior of energetic large-scale structures on the suction surface of a LPT blade during the wake passing cycle, a POD analysis following Sirovich [36] is pursued. The method of snapshots by Sirovich alleviates the difficulties of handling an autocorrelation matrix of large dimensions and it is most appropriate to perform POD for a realistic flow domain. In the present study, 21 frames of velocity perturbations along the midspan section on the suction surface have been used over time span of $0.1T$.

The energy associated with different eigenmodes for a flow field is represented in their corresponding eigenvalue λ. Figure 8 shows the fraction of the total fluctuation energy contained by a specific number of leading eigenmodes. The fractional energy content is given by the sum of the eigenvalues divided by their total sum. Figure 8 indicates the relative importance of eigenmodes at different time intervals during the wake passing cycle and illustrates the characteristics of flow structures. During the time interval $t/T=0.1-0.2$ or 0.3–0.4, when the wake is away from the inflectional region and the boundary layer relaxes to its pretransitional state as the stimulus for early transition is removed, about 12 eigenmodes contain 99% of the total disturbance energy. It should be noted that during these times, the flow is governed by the inviscid instability of the separated boundary layer due to enhanced receptivity of freestream disturbances and appearance of relatively smaller eddies. During $t/T=0.5-0.6$, when the wake approaches the steady-flow separation region, the first eight modes contain 99% of the total energy. During $t/T=0.7-0.8$ or 0.8–0.9, when the wake passes over the inflectional region and the flow is characterized by the large-scale structures because of the negative-jet effect, the first six modes are sufficient to capture 99% of the total energy. Even during this time interval, the first three leading modes contain about 95% of the total fluctuation energy supporting the appearance of larger coherent structures by the rollup of the separated boundary layer on the suction surface. Thus, using three modes for reconstruction of flow during the time interval would be sufficient for a good representation of the flow field [26,37].

To characterize and understand the coherent structure further, the POD is performed on the instantaneous velocity field, which is averaged over the homogeneous spanwise direction. Figure 9 compares the cumulative energy of the eigenmodes for the span-averaged data and that for the midspan plane. This indicates that fewer modes capture a significant percent of the total energy for the span-averaged data. For example, during $t/T=0.8-0.9$, the

Downloaded 03 Jun 2010 to 171.66.16.157. Redistribution subject to ASME license or copyright; see http://www.asme.org/terms/Terms_Use.cfm

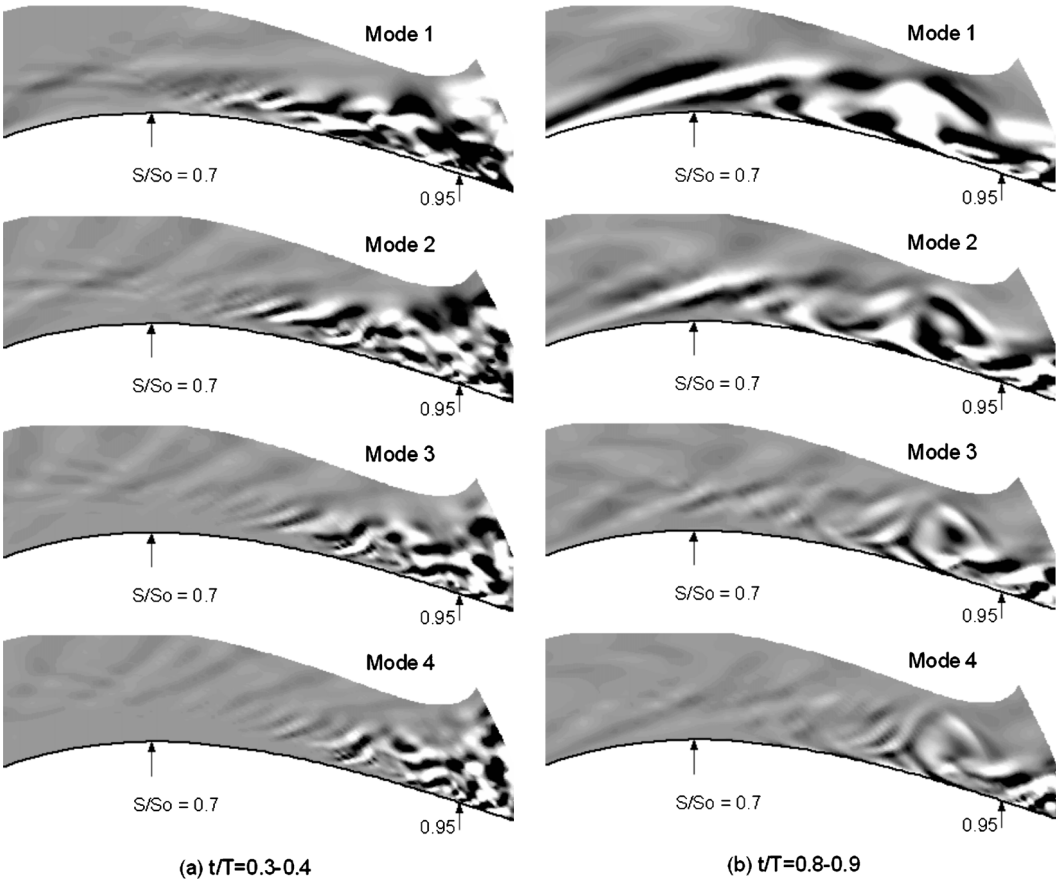

Fig. 11 First four eigenvectors of disturbances of vorticity for the midspan data during the wake-passing cycle

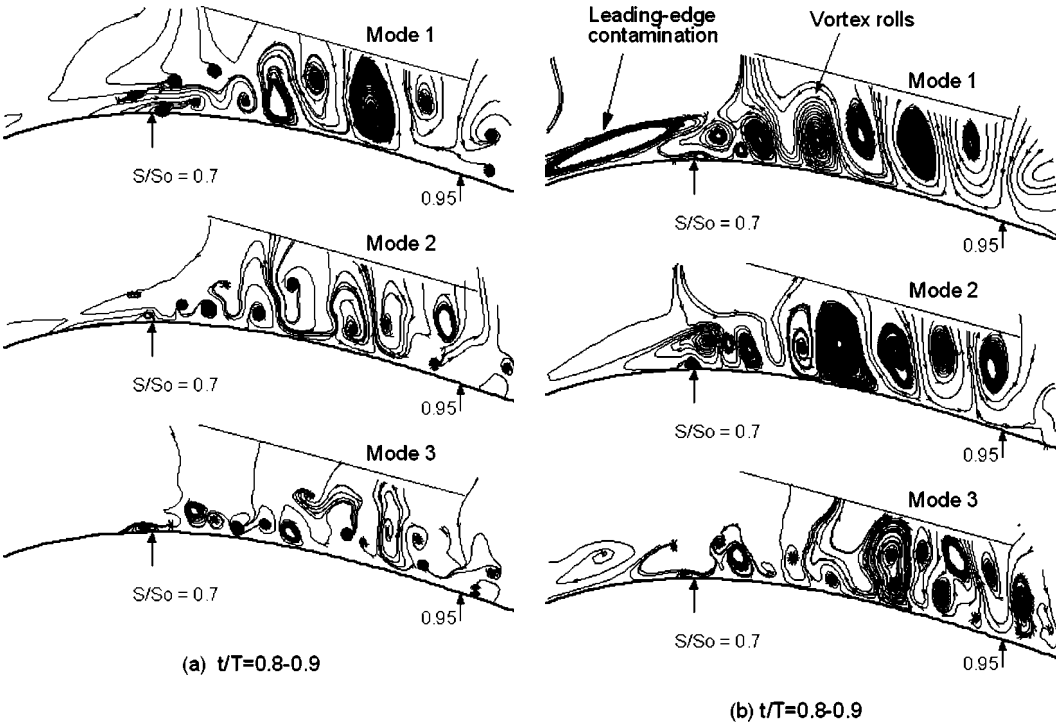

Fig. 12 First three eigenvectors of velocity disturbances (streamlines) during the wake-passing cycle: (*a*) for the midspan data and (*b*) for the span-averaged data

Downloaded 03 Jun 2010 to 171.66.16.157. Redistribution subject to ASME license or copyright; see http://www.asme.org/terms/Terms_Use.cfm

first three leading modes contain about 99% of the total fluctuation energy of the span-averaged field as compared to six modes in the case of the midspan flow field. This elucidates that the span averaging eliminates random fluctuations in the lateral direction, retaining deterministic coherent structures.

The characteristics of the POD modes are now examined to understand the dynamics of large-scale structures that appear on the suction surface of the LPT due to excitation of passing wakes (unless stated, mode shapes are presented for the midspan flow field). Figures 10(*a*) and 10(*b*) present the first four eigenmodes of velocity disturbances during $t/T=0.3-0.4$ and 0.8–0.9, respectively. During $t/T=0.3-0.4$, when the wake is ahead of the inflectional region (Fig. 10(*a*)), the first two modes clearly depict the formation of vortices over the separated boundary layer via KH instability. Higher modes are associated with small-scale structures. During $t/T=0.8-0.9$, as the wake passes over the inflectional region, the rollup of the unstable separated boundary layer and the formation of large-scale vortex loops are reflected in the first two eigenmodes (Fig. 10(*b*)). The first two modes also carry the information of instabilities experienced at the leading edge (known as the *leading-edge contamination*) due to the passing wakes. Higher modes carry the information of high-frequency small-scale eddies created due to the nonlinear interactions and breakdown to turbulence downstream. The POD modes of vorticity presented in Fig. 11 have the very similar information illustrating the shear layer instability and large-scale vortex loops formation as the wake is ahead of and passes over the separated boundary layer. The instantaneous spanwise vorticity presented in Figs. 3 and 4 during the same periods has very close resemblance to the mode shapes. Thus, the mode shapes are patterns that may have some relationship with the physics of large-scale structures.

Figure 12 compares the shape of the first three eigenmodes (streamline) for the midspan and span-averaged data during $t/T=0.8-0.9$. The span-averaged data depict more vivid pattern illustrating perturbations from the leading edge due to the migrating wake, the leading-edge contamination, and multiple vortex loops produced by rollup of the shear layer on the suction surface. This further explains that the span averaging eliminates random fluctuations in the lateral direction and retains deterministic coherent structures.

4 Conclusions

The receptivity of the boundary layer over the suction surface of a high-lift LPT blade subjected to the periodic passing wakes is presented through LES. The time-mean velocity profiles detect an inflectional layer over the rear half of the suction surface. The spectral analysis of the numerical results illustrates that the shear layer instability just downstream of separation occurs via the KH mechanism. The evolution of velocity fluctuations elucidates a growth of disturbances that starts at about $S/S_0=0.75$. These disturbances seem to rapidly increase with development of three-dimensional motions in the second half of the steady-flow separation, leading to the breakdown to turbulence downstream of $S/S_0=0.92$, the point of mean reattachment. When the wake convects over the rear half of the suction surface, the rollup of the separated boundary layer occurs evolving the large-scale vortex loops that play an important role in the generation of turbulence.

A POD analysis also supports the insight of the flow physics depicting the shear layer instability with occurrence of relatively smaller-scale vortices when the wake is ahead of the separated region. It further indicates that as the wake moves past the region of separation, the first three leading modes of eigenfunction contain about 95% of the total fluctuation energy, illustrating the appearance of larger rollup vortices. Higher modes carry the information of high-frequency small-scale eddies created due to nonlinear interaction and breakdown of the KH rolls downstream. The averaging in the homogeneous direction retains the deterministic coherent structures by eliminating random fluctuations.

Nomenclature

C = chord
C_X = axial chord
D = bar diameter
f = bar passing frequency
Re = Reynolds number$=V_{2\text{is}}C/\nu$
S = distance along the blade surface
S_0 = suction surface length
t = time
T = bar passing period
u',v',w' = velocity fluctuations (rms)
U_b = bar speed or blade speed
V = velocity
V_x = axial velocity
x,y,z = Cartesian coordinates
Δx^+, Δy^+, Δz^+ = mesh size in wall units
η = wall-normal axis
ν = kinematic viscosity

Subscripts

0 = total
1 = inlet
2 = exit
is = isentropic
∞ = freestream

References

[1] Hunt, J. C. R., and Durbin, P. A., 1999, "Perturbed Vortical Layers and Shear Sheltering," Fluid Dyn. Res., **24**, pp. 375–404.
[2] Halstead, D. E., Wisler, D. C., Okiishi, T. H., Walker, G. J., Hodson, H. P., and Shin, H.-W., 1997, "Boundary Layer Development in Axial Compressors and Turbines—Part 1 of 4: Composite Picture; Part 2 of 4: Compressors; Part 3 of 4: LP Turbines; Part 4 of 4: Computations and Analyses," ASME J. Turbomach., **119**, pp. 114–127, **119**, pp. 426–444, **119**, pp. 225–237, **119** pp. 128–139.
[3] Walker, G. J., 1993, "The Role of Laminar Turbulent Transition in Gas Turbine Engines: A Discussion," ASME J. Turbomach., **115**, pp. 207–217.
[4] Mayle, R. E., 1991, "The Role of Laminar Turbulent Transition in Gas Turbine Engines," ASME J. Turbomach., **113**, pp. 509–537.
[5] Wu, X., Jacobs, R. G., Hunt, J. R. C., and Durbin, P. A., 1999, "Simulation of Boundary Layer Transition Induced by Periodically Passing Wakes," J. Fluid Mech., **398**, pp. 109–153.
[6] Schulte, V., and Hodson, H. P., 1998, "Unsteady Wake-Induced Boundary Layer Transition in High Lift LP Turbine," ASME J. Turbomach., **120**, pp. 28–35.
[7] Wu, X., and Durbin, P. A., 2001, "Evidence of Longitudinal Vortices Evolved from Distorted Wakes in Turbine Passage," J. Fluid Mech., **446**, pp. 199–228.
[8] Stieger, R., Hollis, D., and Hodson, H., 2003, "Unsteady Surface Pressures Due to Wake Induced Transition in Laminar Separation Bubble on a LP Turbine Cascade," ASME Paper No. GT2003–38303.
[9] Sarkar, S., and Voke, P. R., 2006, "Large-Eddy Simulation of Unsteady Surface Pressure Over a LP Turbine Due to Interactions of Passing Wakes and Inflexional Boundary Layer," ASME J. Turbomach., **128**, pp. 221–231.
[10] Wissink, J. G., Rodi, W., and Hodson, H., 2006, "Influence of Disturbances Carried by Periodically Incoming Wakes on the Separating Flow Around a Turbine Blade," Int. J. Heat Fluid Flow, **27**, pp. 721–729.
[11] Malkiel, E., and Mayle, R. E., 1996, "Transition in a Separation Bubble," ASME J. Turbomach., **118**, pp. 752–759.
[12] Alam, M., and Sandham, N. D., 2000, "Direct Numerical Simulation of Short Laminar Separation Bubbles With Turbulent Reattachment," J. Fluid Mech., **410**, pp. 1–28.
[13] Yang, Z. Y., and Voke, P. R., 2001, "Large-Eddy Simulation of Boundary Layer Separation and Transition at a Change of Surface Curvature," J. Fluid Mech., **439**, pp. 305–333.
[14] Hatman, A., and Wang, T., 1998, "Separated-Flow Transition, Part 1—Experimental Methodology, Part 2—Experimental Results, Part 3—Primary Modes and Vortex Dynamics," ASME Paper Nos. 98-GT-461, 98-GT-462, and 98-GT-463.
[15] Hatman, A., and Wang, T., 1999, "A Prediction Model for Separated-Flow Transition," ASME J. Turbomach., **121**, pp. 594–602.
[16] D'Ovidio, A., Harkins, J. A., and Gostelow, J. P., 2001, "Turbulent Spot in Strong Adverse Pressure Gradient: Part 1—Spot Behaviour," ASME Paper No. 2001-GT-0194.
[17] D'Ovidio, A., Harkins, J. A., and Gostelow, J. P., 2001, "Turbulent Spot in Strong Adverse Pressure Gradient: Part 2—Spot Propagation and Spreading Rates," ASME Paper No. 2001-GT-0407.
[18] Watmuff, J. H., 1999, "Evolution of a Wave Packet Into Vortex Loops in a Laminar Separation Bubble," J. Fluid Mech., **397**, pp. 119–169.
[19] Wissink, J. G., 2003, "DNS of Separating, Low Reynolds Number Flow in a

Downloaded 03 Jun 2010 to 171.66.16.157. Redistribution subject to ASME license or copyright; see http://www.asme.org/terms/Terms_Use.cfm

Turbine Cascade With Incoming Wakes," Int. J. Heat Fluid Flow, **24**, pp. 626–635.
[20] Sarkar, S., 2007, "The Effects of Passing Wakes on a Separating Boundary Layer Along a Low-Pressure Turbine Blade Through Large-Eddy Simulation," Proc. Inst. Mech. Eng., Part A, **221**, pp. 551–564.
[21] Lumley, J. L., 1967, "The Structure of Inhomogeneous Turbulent Flows," *Atmospheric Turbulence and Wave Propagation*, Nauka, Moscow.
[22] Aubry, N., Holmes, P., Lumley, J. L., and Stone, E., 1988, "The Dynamics of Coherent Structures in the Wall Region of a Turbulent Boundary Layer," J. Fluid Mech., **192**, pp. 115–173.
[23] Rempfer, D., 1996, "Investigations of Boundary Layer Transition Via Galerkin Projections on Empirical Eigenfunctions," Phys. Fluids, **8**, pp. 175–188.
[24] Payne, F. R., and Lumley, J. L., 1967, "Large Eddy Structure of the Turbulent Wake Behind a Circular Cylinder," Phys. Fluids, **10**, pp. 194–196.
[25] Delville, J., Ukeiley, L., Cordier, L., Bonnet, J. P., and Glauser, M., 1999, "Examination of Large-Scale Structures in a Turbulent Plane Mixing Layer. Part 1. Proper Orthogonal Decomposition," J. Fluid Mech., **391**, pp. 91–122.
[26] Rajaee, M., Karlsson, S. K. F., and Sirovich, L., 1994, "Low-Dimensional: Description of Free Shear Flow Coherent Structures and Their Dynamical Behaviour," J. Fluid Mech., **258**, pp. 1–29.
[27] Gordeyev, S., and Thomas, F., 2000, "Coherent Structure in the Turbulent Planar Jet. Part 1. Extraction of Proper Orthogonal Decomposition Eigenmodes and Their Self-Similarity," J. Fluid Mech., **414**, pp. 145–194.
[28] Citriniti, J., and George, W., 2000, "Reconstruction of the Global Velocity Field in the Axisymmetric Mixing Layer Utilizing the Proper Orthogonal Decomposition," J. Fluid Mech., **418**, pp. 137–166.
[29] Gordeyev, S., and Thomas, F., 2002, "Coherent Structure in the Turbulent Planar Jet. Part 2. Structural Topology Via POD Eigenmode Projection," J. Fluid Mech., **160**, pp. 349–380.
[30] Moin, P., and Moser, R. D., 1989, "Characteristic Eddy Decomposition of Turbulence in a Channel," J. Fluid Mech., **200**, pp. 471–509.
[31] Ball, K. S., Sirovich, L., and Keefe, L. R., 1991, "Dynamical Eigenfunction Decomposition of Turbulent Channel Flow," Int. J. Numer. Methods Fluids, **12**, pp. 585–604.
[32] Stadtmüller, P., 2001, "Investigation of Wake-Induced Transition on the LP Turbine Cascade T106 A-EIZ," DFG-Verbundproject Fo 136/11, Version 1.0, University of the Armed Forces Munich, Germany.
[33] Yang, Z., and Voke, P. R., 2000, "Large-Eddy Simulation of Separated Leading-Edge Flow in General Coordinate," Int. J. Numer. Methods Eng., **49**, pp. 681–696.
[34] Kiya, M., and Sasaki, K., 1985, "Structure of Large-Scale Vortices and Unsteady Reverse Flow in the Reattaching Zone of a Turbulent Separation Bubble," J. Fluid Mech., **154**, pp. 463–491.
[35] Chandrasekhar, S., 1961, *Hydrodynamic and Hydromagnetic Stability*, Clarendon, Oxford.
[36] Sirovich, L., 1987, "Turbulence and the Dynamics of Coherent Structures Part-1: Coherent Structures," Q. Appl. Math., **14**(3), pp. 561–571.
[37] Moreno, D., Krothapalli, A., Alkislar, M. B., and Lourenco, L. M., 2004, "Low-Dimensional Model of a Supersonic Rectangular Jet," Phys. Rev. E, **69**, p. 026304.

Downloaded 03 Jun 2010 to 171.66.16.157. Redistribution subject to ASME license or copyright; see http://www.asme.org/terms/Terms_Use.cfm

Valery Ponyavin
e-mail: ponyavin@nscee.edu

Yitung Chen
e-mail: uuchen@nscee.edu

Department of Mechanical Engineering,
University of Nevada, Las Vegas,
4505 Maryland Parkway,
Las Vegas, NV 89154-4027

James Cutts
e-mail: jcutts@ceramatec.com

Merrill Wilson

Ceramatec, Inc.,
2425 South 900 West,
Salt Lake City, UT 84119
e-mail: wilson@ceramatec.com

Anthony E. Hechanova
Harry Reid Center for Environmental Studies,
University of Nevada, Las Vegas,
4505 Maryland Parkway,
Las Vegas, NV 89154-4009
e-mail: hechanova@unlv.nevada.edu

Calculation of Fluid Flow Distribution Inside a Compact Ceramic High Temperature Heat Exchanger and Chemical Decomposer

Numerical analysis of flow distribution inside a compact ceramic high temperature heat exchanger and chemical decomposer (thereafter, heat exchanger), which will be used for hydrogen production, wherein the sulfur iodine thermochemical cycle is performed. To validate the numerical model, experimental investigation of the heat exchanger is accomplished. The study of the flow distribution in the base line design heat exchanger shows that the design has large-flow maldistribution and the reverse flow may occur at poor inlet and outlet manifold configurations. To enhance uniformity of the flow rate distribution among the heat exchanger internal channels, several improved designs of the heat exchanger manifolds and supply channels are proposed. The proposed designs have a sufficiently uniform flow rate distribution among the internal channels, with an appropriate pressure drop. [DOI: 10.1115/1.2911680]

Keywords: CFD, pressure drop, fluid flow distribution, channel flow, gross flow maldistribution

1 Introduction

Crudely designed heat exchangers often have lower performance and higher operating costs than more accurate designs. One of the most important factors influencing the performance is uniformity of the flow rate distribution inside the heat exchanger. Flow maldistribution among the heat exchanger channels can decrease chemical decomposition and increase pumping power. The uniformity of flow distribution depends on inlet manifold geometry, internal channel configuration, and flow regimes.

The problem of flow maldistribution in heat exchangers has been recognized for a long time. A number of experimental investigations of the problem are possible to find in literature, for example, in Refs. [1–7]. Flow characteristics of a flow field in the entrance of a plate-fin heat exchanger have been investigated by means of particle image velocimetry (PIV) [1]. The experimental results indicate that performance of fluid maldistribution in conventional entrance configuration is very serious, while the improved entrance configuration can effectively improve the performance of fluid flow distribution in the entrance. The flow inside a heat exchanger, which is a component developed for cooling a high-current protons linear accelerator, has been experimentally investigated by Faure et al. [2]. The study focused on velocity distribution between the heat exchanger tubes. It is found that for the range of investigated inlet Reynolds numbers, velocity distribution among the tubes does not depend on the flow rate. Shell side cross-flow velocity measurements have been made within the horizontal pass partition lane of an E-type cylindrical shell and tube heat exchanger using a particle tracking technique [3]. It was found that the cross-flow velocity variation in a baffle space within a shell and tube heat exchanger increases with increasing distance between the upstream and downstream baffles. Jiao and Baek [4] and Jiao et al. [5] obtained a correlation of the dimensionless flow maldistribution parameter and the Reynolds number under different distributor configuration parameters. The experimental studies prove that the performance of flow distribution in heat exchangers can be effectively improved by the optimum design of the distributor's configuration parameter. The flow maldistribution due to the port-to-channel flow, which has a severe effect on the heat exchanger thermal performance, has been experimentally investigated by Rao et al. [6]. The authors have conducted an experimental study on the port-to-channel-flow maldistribution in a small package of a 37 channel plate heat exchanger by creating the flow maldistribution while inserting a reduced cross-sectional area of a wooden mandrel in both the inlet and outlet ports of the heat exchanger. Ranganayakulu et al. [7] investigated the effect of two-dimensional nonuniform inlet fluid flow distribution on both hot and cold fluid sides of a cross-flow plate-fin heat exchanger, using a finite element model. Moreover, it was found that the performance deteriorations and variations in pressure drops are quite significant in some typical applications, due to the fluid flow nonuniformity.

Computational studies of fluid flow distributions in inlet manifolds of heat exchangers have been performed in Refs. [8–11]. Zhang and Li [8] numerically investigated the fluid flow distribution in plate-fin heat exchangers. In this paper, two modified headers with a two-stage-distributing structure are proposed and simulated. The numerical investigation of the effects of the inlet-equivalent diameters for the two-stage structures has been conducted and also compared to experimental measurement. It

Contributed by the Fluids Engineering Division of ASME for publication in the JOURNAL OF FLUIDS ENGINEERING. Manuscript received June 14, 2007; final manuscript received December 12, 2007; published online June 12, 2008. Review conducted by Malcolm J. Andrews.

Downloaded 03 Jun 2010 to 171.66.16.157. Redistribution subject to ASME license or copyright; see http://www.asme.org/terms/Terms_Use.cfm

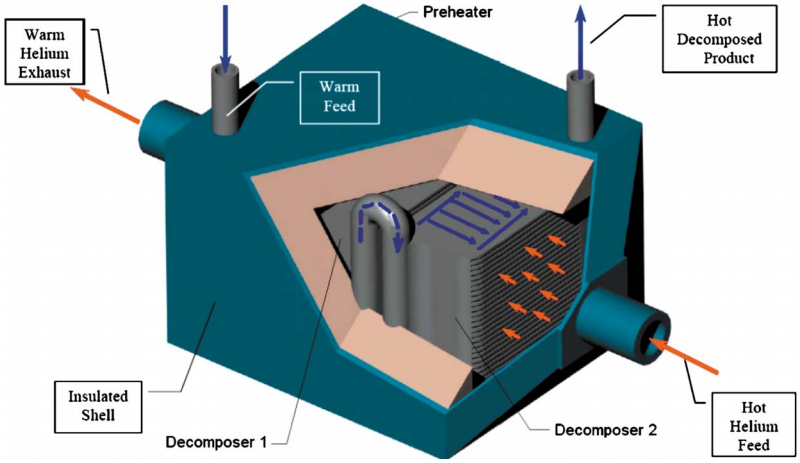

Fig. 1 Shell and plate heat exchanger

was verified that the flow distribution in plate-fin heat exchangers is more uniform if the ratios of outlet and inlet-equivalent diameters for both headers are equal. Dynamic behavior of plate heat exchangers with flow maldistribution from the port to channel was reported by Srihari et al. [9]. Fluid axial dispersion characterizes back mixing and other notable deviations from plug flow through the heat exchanger. Variations of the heat transfer coefficient, due to the nonuniform distribution of fluid velocity throughout the channels, were also reported. Solutions were obtained with Laplace transforms and numerical inversion from the frequency domain. Predicted results show that the dynamic response and thermal performance deteriorate with flow maldistribution. A steady state analysis was presented by Rao et al. [6] on the effect of flow distribution to the channels on the thermal performance of the heat exchanger. Lalot and Florent [10] studied the gross flow maldistribution in an electrical heater and found that the perforated grid can improve the fluid flow distribution. Wen [11] employed the computational fluid dynamics (CFD) technique to simulate and analyze the performance of fluid flow distribution and pressure drop in the header of the plate-fin heat exchanger. A baffle with small-size holes is a recommended installation in the header in order to improve the performance of flow distribution.

This paper represents an examination of flow distribution in the cross section of the microchannel heat exchanger for the decomposition of sulfuric acid as part of the hydrogen producing sulfur iodine thermochemical cycle [12]. This compact heat exchanger utilizes microchannels to enhance the heat transfer while maintaining low pressure drops within the system. The high thermal performance of the heat exchanger will intensify the chemical reaction of sulfuric trioxide decomposition to form sulfuric dioxide.

The common repeat unit within the heat exchanger is the heat transfer plate. These are made using planar processes that can be easily automated. These plates are then stacked and sealed together into monolithic robust ceramic modules, which have gas headers for feed and product flows. During the assembly of these modules, the plates are stacked with narrow gaps that define the flow channels for the external heat transfer fluid (helium). These stacking and joining processes also lend themselves well to automated processes, potentially reducing the cost of these heat exchangers.

The base line design of the shell and plate heat exchanger is shown in the Fig. 1. The hot helium from nuclear reactor ($T=975^\circ$C) is used to heat the sulfuric acid feed components (H_2O, H_2SO_4, SO_3) to get appropriate conditions for the decomposition reaction ($T>850^\circ$C). The heat exchanger consists of four main parts: preheater, Decomposer 1, Decomposer 2, and insulated shell (Fig. 1). The geometries of the preheater, Decomposer 1, and Decomposer 2 are the same; therefore, this paper addresses the analysis only of Decomposer 1 and the obtained results for the Decomposer 1 can be applicable to the preheater and Decomposer 2.

Some study of the base line design using the single channel model with the chemical reaction presence have been already completed at the University of Nevada, Las Vegas, and the obtained results are shown in Refs. [13,14].

2 Calculation Domain and Dimensions

Due to the existence of a symmetry plane, the developed calculation domain contains one-half of the heat exchanger layers. The domain includes only the fluid part of the heat exchanger. The calculating geometry for the base line design is shown in Fig. 2 (Case A). The dimensions of the calculation domain are shown in Table 1. The distance between internal channels is 0.762 mm.

The preliminary calculations of the base line designs show that the flow distribution in the internal channels is nonuniform; therefore, three other geometries with different design of the manifolds and supply channels are chosen to make the flow distribution among the internal channels more uniform.

The computation domain for Case B (Fig. 2) has the same dimensions as the base line design with the exception of inlet manifold shape. The manifold shape and dimensions are shown in the Fig. 3. The new manifold has three wide plates of the same thickness (0.45 mm) and flow separators (grooves on Fig. 3), which are located opposite the channels. The separators redistribute flow to obtain more uniform flow distribution, as compared to the original design. Each separator has a different size to improve uniformity of the flow rate among the channels. The width of the separators for the each channel (Fig. 2, Case C): Channels 1–15, 1.64 mm; Channel 16, 1.16 mm; Channel 17, 1.06 mm; Channel 18, 0.98 mm; Channel 19, 0.98 mm; Channel 20, 0.91 mm; Channel 21, 0.55 mm; Channel 22, 0.4 mm; Channel 23, 0.25 mm; Channels 24 and 25, 0.36 mm.

The computation domain for Case C (Fig. 2) has the same dimensions as Case B; only the outlet manifold is longer than that of the original design. The length of the modified outlet manifold is 11.3 mm.

The computation domain for Case D (Fig. 2) has the same dimensions as Case C, with the exception of the inlet supply channel and outlet channel, which are twice as wide, compared to the original design (i.e., 4.064 mm).

3 Numerical Model and Boundary Conditions

The calculations of fluid flow are performed using FLUENT software version 6.2.16 [15]. The shear-stress transport (SST) k-ω

Downloaded 03 Jun 2010 to 171.66.16.157. Redistribution subject to ASME license or copyright; see http://www.asme.org/terms/Terms_Use.cfm

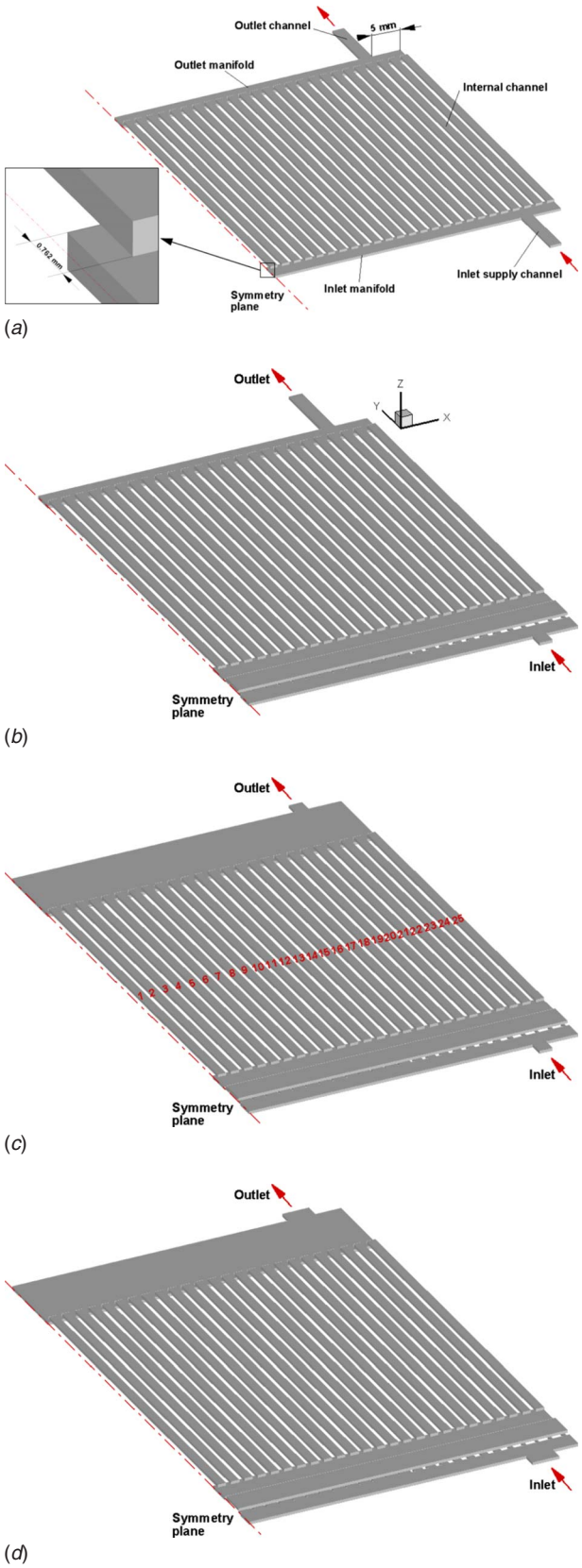

Fig. 2 Four different cases of the calculation domain

turbulence model was used since the Reynolds number, higher than 5000 in the manifolds region. The model has wall functions for the near wall treatment. The governing equations were as follows:

Table 1 Dimensions for the base line design

Geometric characteristic	Length, mm	Width, mm	Height, mm
Internal channels	52.324	1.27	0.424
Inlet and outlet manifolds	3.175	50.419	0.45
Inlet supply channel and outlet channel	10.16	2.032	0.45

In mass conservation,

$$\frac{\partial u_i}{\partial x_j} = 0 \tag{1}$$

In momentum conservation,

$$\rho u_j \frac{\partial u_i}{\partial x_j} = -\frac{\partial p}{\partial x_i} + \frac{\partial}{\partial x_j}\left(\mu\left(\frac{\partial u_i}{\partial x_j} + \frac{\partial u_j}{\partial x_i}\right) - \rho u_i' u_j'\right) \tag{2}$$

where

$$-\rho u_i' u_j' = \mu_T\left(\left(\frac{\partial u_i}{\partial x_j} + \frac{\partial u_j}{\partial x_i}\right)\right) - \frac{2}{3}\rho k \delta_{ij} \tag{3}$$

In transport equations for the SST k-ω model,

$$\rho \frac{\partial}{\partial x_i}(k u_i) = \frac{\partial}{\partial x_j}\left(\Gamma_k \frac{\partial k}{\partial x_j}\right) + \tilde{G}_k - Y_k \tag{4}$$

$$\rho \frac{\partial}{\partial x_i}(\omega u_i) = \frac{\partial}{\partial x_j}\left(\Gamma_\omega \frac{\partial \omega}{\partial x_j}\right) + G_\omega - Y_\omega + D_\omega \tag{5}$$

The governing equations are solved in the Cartesian coordinate system with a control volume finite difference method similar to that introduced by Patankar [16]. The general purpose CFD code FLUENT [15] is used as a numerical solver for the present three-dimensional simulation. A nonstaggered grid storage scheme is adapted to define the discrete control volumes. In this scheme, the same control volume is employed for the integration of all conservation equations, and all variables were stored at the control volume's cell center. The numerical scheme used in this study is a power-law differencing scheme, and the solver used is a segregated solver. The SIMPLE algorithm is used to resolve the coupling between pressure and velocity. The governing equations, which were discrete and nonlinear, are linearized using an implicit technique with respect to a set of dependent variables. The algebraic equations are iteratively solved, using an additive correction multigrid method with a Gauss–Seidel relaxation procedure.

The grid independence studies are performed for each investigated geometry to check the dependence of the calculated parameters (pressure, velocities) on mesh size. The grid systems are refined until the calculated parameters become independent from the grid size. As result of the grid independence studies, the following grid sizes have been chosen: Case A: 508,920 cells, 607,612 nodes; Case B: 1,025,271 cells, 1,230,764 nodes; Case C: 1,098,671 cells, 1,272,877 nodes; Case D: 1,100,149 cells, 1,292,249 nodes. The calculation time for all of the cases until full convergence was no more than 3 h.

The mass flow inlet boundary condition was applied to the inlet of the computation domain and the pressure outlet boundary condition was used to the outlet (Fig. 4). The symmetry boundary condition is applied for the symmetry plane (see Fig. 4). The nonslip boundary conditions are used for all of the walls. The mass flow inlet for the base line conditions is 0.0001574 kg/s.

The density and dynamic viscosity for the mixture are calculated for the conditions:

$T=1086.5$ K; $p=1.5$ MPa; $X_{SO_1}=0.40815$; $X_{SO_2}=0.32652$; $X_{O_2}=0.08163$; $X_{H_3O}=0.1837$.

For these conditions, $\rho=7.2374$ kg/m^3; $\mu=1.5\times10^{-5}$ kg(m s)—using ideal gas mixing law.

Downloaded 03 Jun 2010 to 171.66.16.157. Redistribution subject to ASME license or copyright; see http://www.asme.org/terms/Terms_Use.cfm

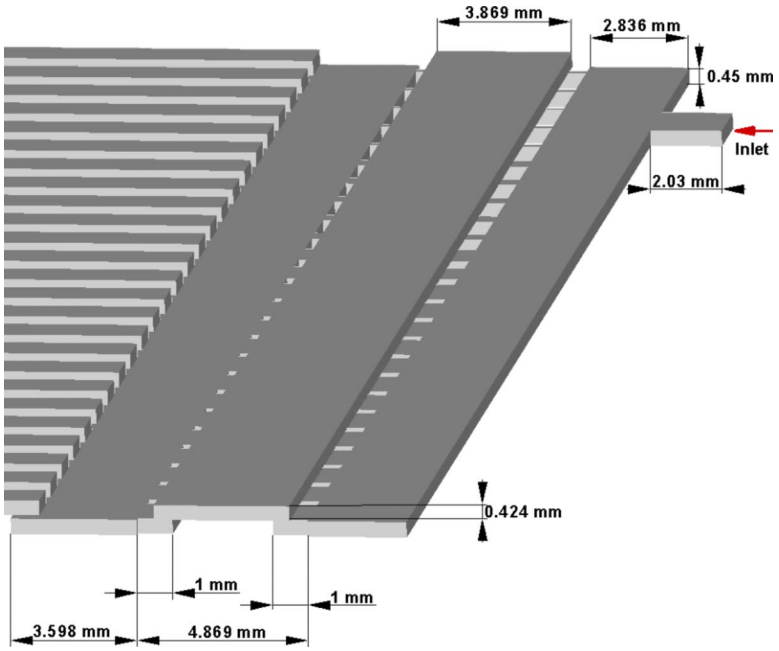

Fig. 3 Geometry and dimensions of the modified inlet manifold

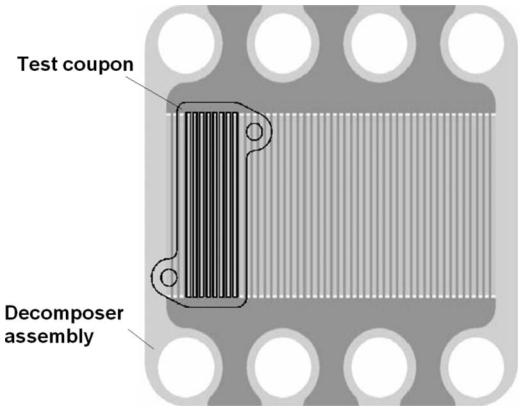

Fig. 4 Comparison of test coupon geometry with heat exchanger assembly

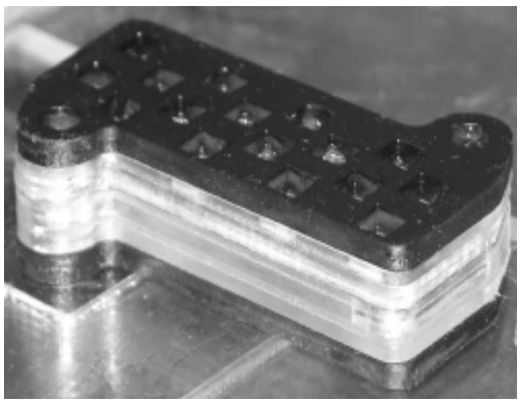

Fig. 5 Plexiglas test coupon

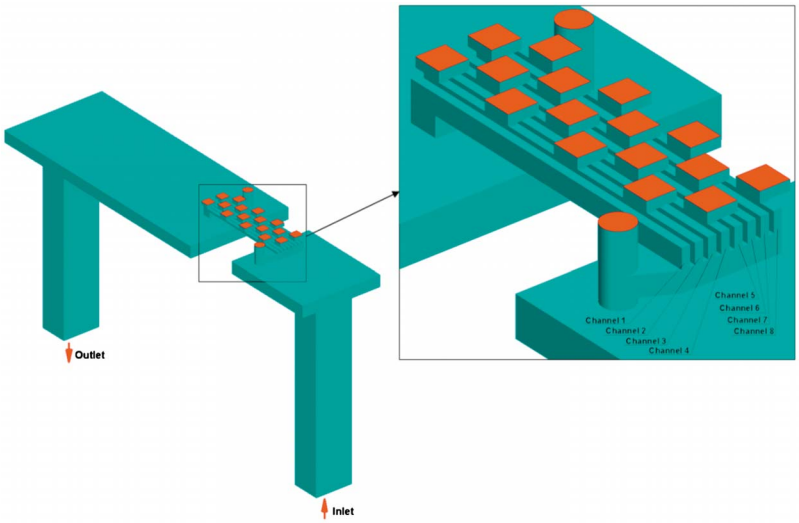

Fig. 6 Calculation geometry and channel numbering for the test coupon model

Downloaded 03 Jun 2010 to 171.66.16.157. Redistribution subject to ASME license or copyright; see http://www.asme.org/terms/Terms_Use.cfm

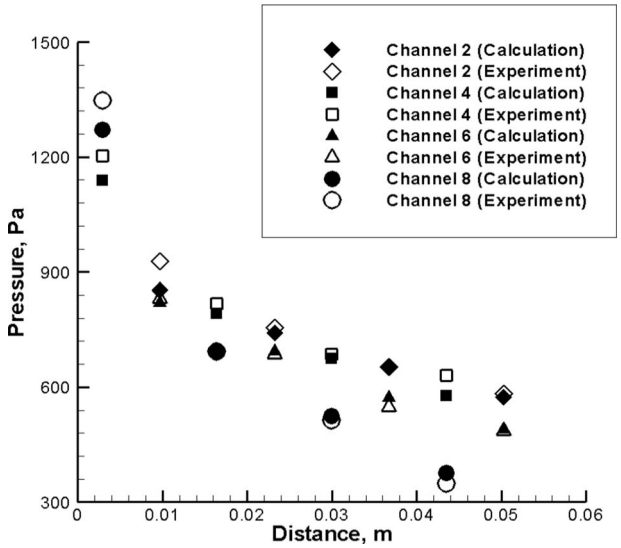

Fig. 7 Pressures for the Re=870

4 Experimental Validation

The fluid flow in the test coupon, which has the same internal channel dimensions as the heat exchanger assembly (Fig. 4), has been experimentally studied, and the measured data are compared to the computed results.

The test coupon is manufactured using Plexiglas parts (Fig. 5), instead of the more brittle and expensive ceramic coupons. A metal cap covers the coupon. This cap is machined to incorporate an array of 18 pressure taps, in order to measure the local pressure inlet and exit, and along the length of various channels. The pressure measurements have been taken using a dynamic pressure mat that has been calibrated to allow for precise measurements of the flow data. The pressure values on each pressure tap have been calculated as the average of all of the pressure sensors on the tap. The test coupon was tested using room temperature compressed air at various flow rates. The accuracy of the measurements is within $\pm 10\%$.

The pressure measurements were performed at four Reynolds numbers in the internal channels: 1160, 870, 580, and 435. The Reynolds numbers have been calculated using: [6]

$$\mathrm{Re} = \frac{\rho u_{\mathrm{ave}} d_h}{\mu} \tag{6}$$

where u_{av} is the mean velocity through the internal channels and d_h is the hydraulic diameter of the internal channels.

The results of the pressure measurement were compared to the CFD calculations. The calculation geometry is shown in Fig. 6. The geometry has exactly the same dimensions as the experiment, including the inlet and outlet manifolds and pressure tabs. The red color on the figures designates the pressure measurement areas.

Comparison between the calculated pressures on the pressure taps with experimental data for the Re=870 is shown in the Fig. 7. The difference between the measured and experimental data is within $\pm 10\%$. The same difference takes place for the Reynolds

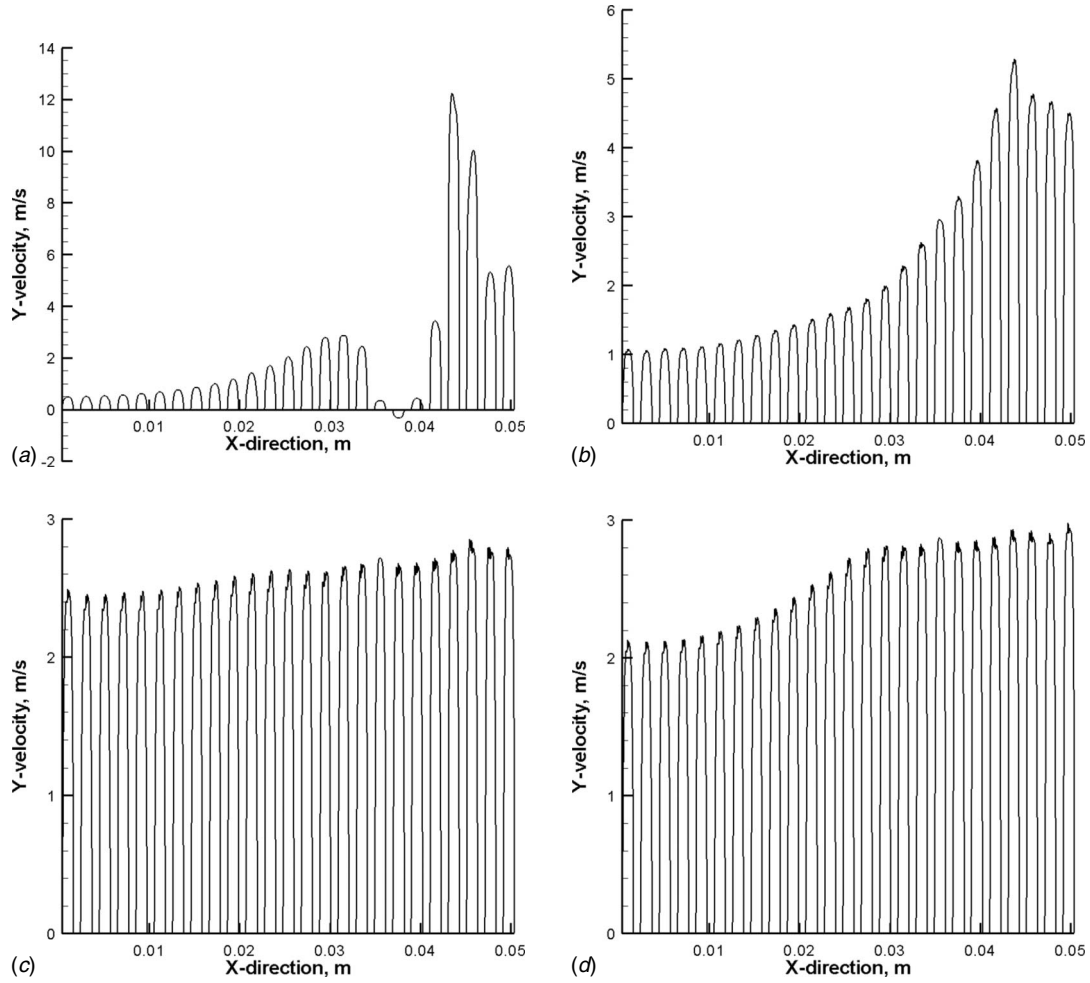

Fig. 8 *y*-velocity distribution at the midsection of the channels, m/s

Downloaded 03 Jun 2010 to 171.66.16.157. Redistribution subject to ASME license or copyright; see http://www.asme.org/terms/Terms_Use.cfm

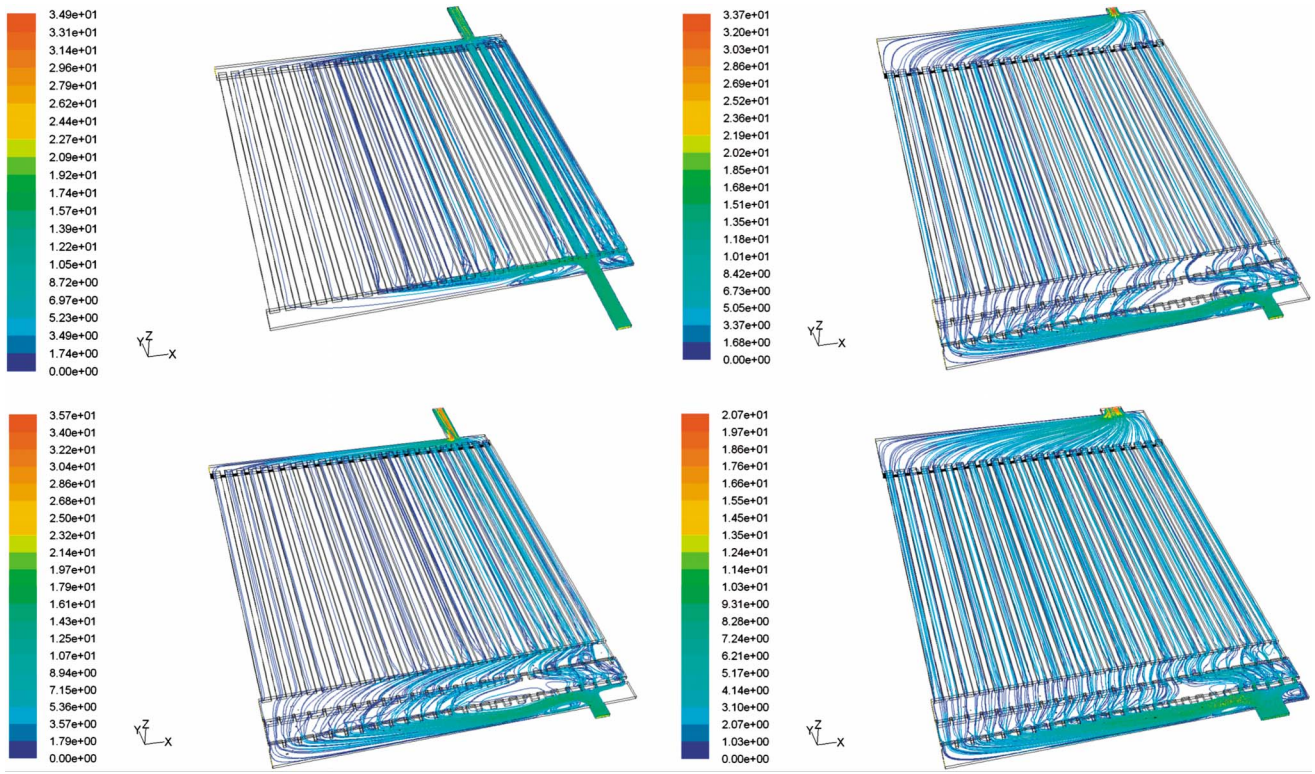

Fig. 9 Streamlines, colored by velocity magnitude, m/s

numbers (1160, 580, and 435). So, it can be concluded that the computational model is capable of closely predicting the fluid distribution.

5 Calculation Results and Discussion

The fluid flow calculations for the base line conditions ($\dot{m} = 1.574 \times 10^{-4}$ kg/s) for all of the four designs have been accomplished. The mean Reynolds number in internal channels for the conditions is 497. The y-velocity distributions at the midsection of the channels are shown in Fig. 8. According to calculation, the velocity distribution among the internal channels is not uniform for the base line design (Fig. 8, Case A) and there is backflow in the seventh channel from the right side. For the case, the maximal flow rates take place in the third and fourth channels from the right side. That sort of behavior is obvious when the inlet channel of a heat exchanger is small compared to the global size of the inlet header, and the fluid tends to preferentially go into the channels that face the inlet channel [17].

For Case B, the velocity distribution is more uniform than that for Case A, and there are not channels with backflow. However, there is still large velocity maldistribution for the case (Fig. 8, Case B). For the case, the velocity ratio (ratio of the highest velocity in the internal channels to the lowest velocity, used in Ref. [10]) is equal to 5.

The velocity maldistribution for Cases C and D is much smaller than that for Cases A and B. This is because the outlet manifold is much wider for the cases, as compared to Cases A and B, and tremendously affects the velocity distribution among the internal channels. The velocity distribution for Case C is more uniform than that of Case D (the velocity ratio for Case D is 1.41, for the case C is 1.17).

Figure 9 represents the flow pattern (streamlines) inside the calculation domains. According to the figure (Case A), the major part of the flow directly goes from the inlet manifold to the internal channels without the redistribution. For Cases B, C, and D, the main portion of the flow from the inlet supply channel turns left in the inlet manifold to be redistributed among the internal channels. Also, for Case A, there are two large vortices in the inlet manifold on the right and on the left sides from the inlet supply channel. Most of the streamlines for the case pass through the third and fourth channels. For Cases B and C, the flow patterns look alike: There is a small vortex in the inlet manifold on the left side, as seen from the inlet supply channel. The flow pattern of the inlet manifold for Case D has the additional vortex on the right side from the inlet supply channel.

The pressure drops for the all of the geometries are shown in Fig. 10. The overall pressure drop for Case A is 7.27 kPa, Case B 8.61 kPa, Case C 7.49 kPa, and Case D 3.37 kPa. The data show that the largest pressure drop for the design takes place in the inlet supply channel and outlet channel. Increasing the flow area for the inlet supply channel and outlet channel, twice for Case D, decreased the overall pressure drop more than twofold.

The parametric study of the four designs for different Reynolds numbers has been completed. Dependence of flow nonuniformity in the channels from the Reynolds number has been investigated. The flow nonuniformity for the individual channel and the sum of flow nonuniformity for the cross section have been calculated using formulas from Ref. [8]. In flow nonuniformity for the individual channel,

$$S_i = (g_i - g_a)/g_a \tag{7}$$

In sum of flow nonuniformity for the cross section,

$$S = \sum_{i=1}^{25} |(g_i - g_a)/g_a| \tag{8}$$

where g_i and g_a represent the local mass flow rate for internal channel i and mean mass flow rate for the cross section.

Figure 11 represents the relation of flow nonuniformity (S) to Reynolds number for all of the four cases. The Reynolds number influences flow nonuniformity for all of the four cases, but the highest influence takes place for Cases C and D. For Case A flow,

Downloaded 03 Jun 2010 to 171.66.16.157. Redistribution subject to ASME license or copyright; see http://www.asme.org/terms/Terms_Use.cfm

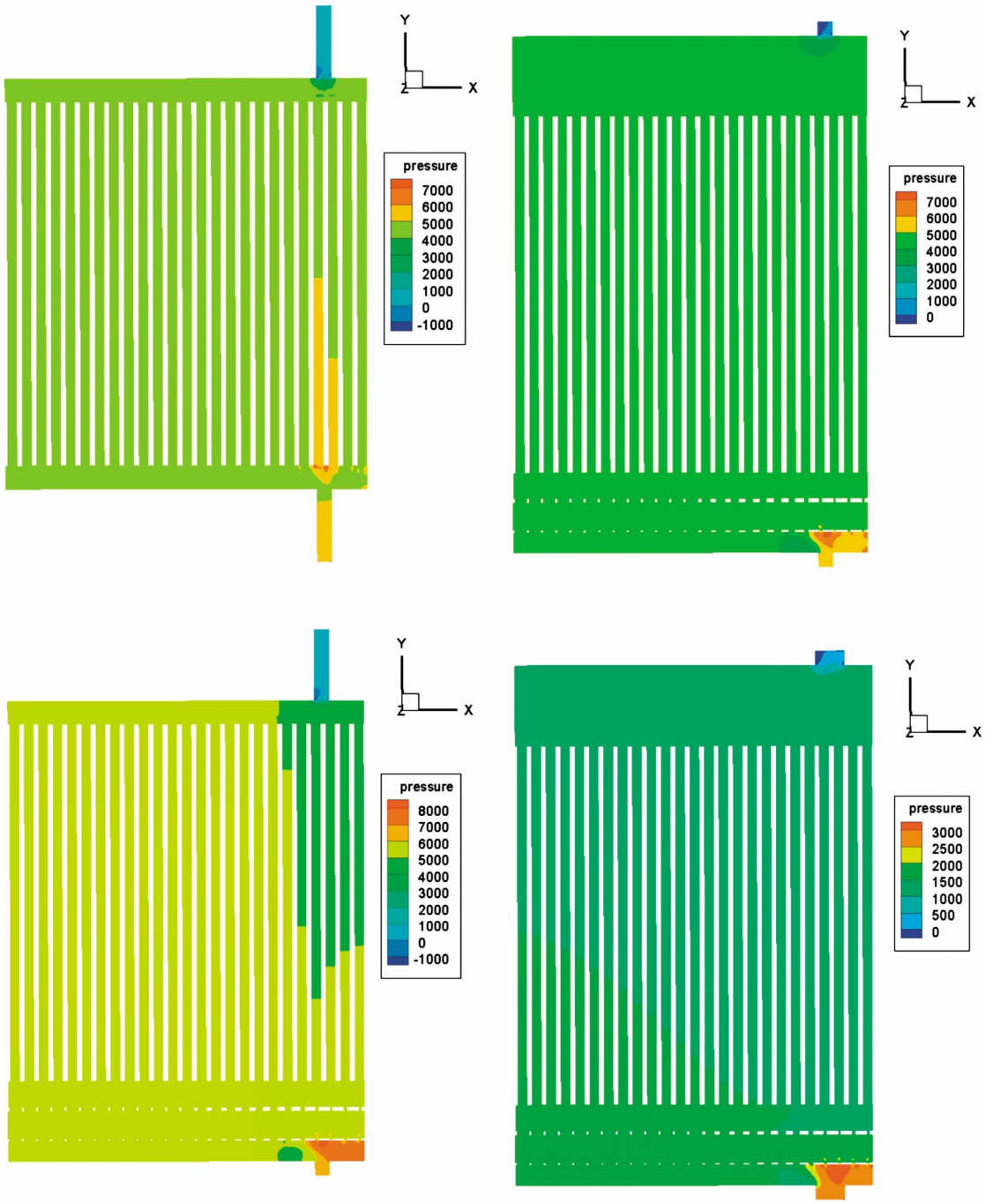

Fig. 10 Pressure distribution, Pa

maldistribution increases with increasing Re. Cases B and C have lower peaks for the dependence. For Case D, flow maldistribution decreases with increasing Re. The lowest maldistribution takes place for Cases C and D.

Figure 12 shows the dependence of the overall pressure drop to Reynolds number for all of the four cases. The overall pressure drop increases with increasing Reynolds number for all the four cases. Case D has the least pressure drop among all the cases.

6 Conclusions

Numerical study of flow distribution inside a compact ceramic high temperature heat exchanger, which will be used for hydrogen production within the sulfur iodine thermochemical cycle, is performed. To validate the numerical model, experimental investigation of the heat exchanger is accomplished. The numerical results are in good agreement with those from experiments.

The base line design of the heat exchanger has been investigated. It was found that the flow maldistribution in the heat exchangers is very serious, and the reverse flow occurs due to the improper inlet and outlet manifold configurations.

Because of nonuniformity of the flow distribution among the channels for the base line design, three improved plate and manifold designs of heat exchanger have been proposed and investigated. The flow calculations in the improved designs show that the flow rate distributions in the improved designs are more uniform among the channels than that in the base line design. The parametric study of the base line design and the improved designs of the heat exchanger for the different inlet Reynolds numbers has

Downloaded 03 Jun 2010 to 171.66.16.157. Redistribution subject to ASME license or copyright; see http://www.asme.org/terms/Terms_Use.cfm

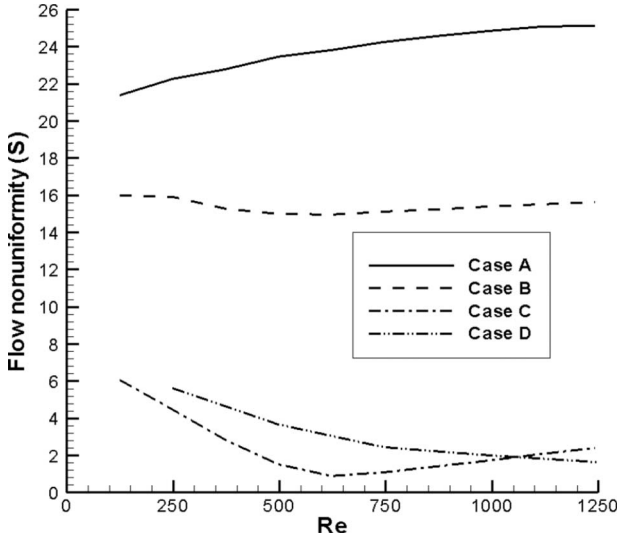

Fig. 11 Dependence of the flow nonuniformity parameter from Re

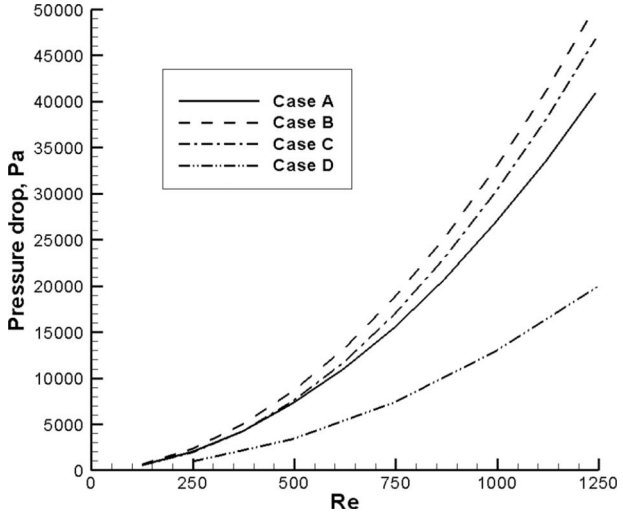

Fig. 12 Overall pressure drop from Re

been accomplished. It was concluded that the most preferable design is Case D because the design has a small nonuniformity parameter with smallest overall pressure drop.

Acknowledgment

This work was funded by the U.S. Department of Energy under Contract No. DE-FG04-01AL67356.

Nomenclature

D_ω = cross-diffusion term
$\tilde{G}_k$ = generation of turbulence kinetic energy due to the mean velocity gradients, kg m^{-1} s^{-3}
G_ω = generation of specific dissipation rate, kg m^{-3} s^{-2}
K = kinetic energy of turbulence, m^2 s^{-2}
$\dot{m}$ = mass flow rate, kg s^{-1}
p = static pressure, Pa
S = sum of flow nonuniformity
S_i = single channel flow nonuniformity
t = time, s
T = static temperature, K
U = velocity magnitude
u_i = mean velocity component (i=1,2,3), m s^{-1}
u_i' = fluctuating velocity components (i=1,2,3), m s^{-1}
X_i = mass concentration of species i
x_j = length coordinate j (x,y,z), m
Y_k = dissipation of k, kg m^{-1} s^{-3}
Y_ω = dissipation of ω, kg m^{-3} s^{-2}
Γ_k = effective diffusivity of k, kg m s^{-2}
Γ_ω = effective diffusivity of ω, kg m^{-1} s^{-1}
δ_{ij} = delta function
μ_T = dynamic viscosity, kg m^{-1} s^{-1}
μ_t = turbulent viscosity, kg m^{-1} s^{-1}
ρ = density, kg m^{-3}
ω = specific dissipation rate, s^{-1}

References

[1] Wen, J., Li, Y., Zhou, A., Zhang, K., and Wang, J., 2006, "PIV Experimental Investigation of Entrance Configuration on Flow Maldistribution in Plate-Fin Heat Exchanger," Cryogenics, **46**(1), pp. 37–48.
[2] Faure, T. M., Lusseyran, F., Gougat, P., and Launay, F., 2006, "Experimental Investigation of the Flow Distribution Inside a Tubular Heat Exchanger," ASME J. Fluids Eng., **128**(6), pp. 1218–1227.
[3] Pekdemir, T., Davies, T. W., Haseler, L. E., and Diaper, A. D., 1993, "Flow Distribution on the Shellside of a Cylindrical Shell and Tube Heat Exchanger," Int. J. Heat Fluid Flow, **14**(1), pp. 76–85.
[4] Jiao, A., and Baek, S., 2005, "Effects of Distributor Configuration on Flow Maldistribution in Plate-Fin Heat Exchangers," Heat Transfer Eng., **26**(4), pp. 19–25.
[5] Jiao, A., Zhang, R., and Jeong, S., 2003, "Experimental Investigation of Header Configuration on Flow Maldistribution in Plate-Fin Heat Exchanger," Appl. Therm. Eng., **23**(10), pp. 1235–1246.
[6] Rao, B. P., Sunden, B., and Das, S. K., 2005, "An Experimental and Theoretical Investigation of the Effect of Flow Maldistribution on the Thermal Performance of Plate Heat Exchangers," ASME J. Heat Transfer, **127**(3), pp. 332–343.
[7] Ranganayakulu, C., Seetharamu, K. N., and Sreevatsan, K. V., 1996, "The Effects of Inlet Fluid Flow Nonuniformity on Thermal Performance and Pressure Drops in Crossflow Plate-Fin Compact Heat Exchangers," Int. J. Heat Mass Transfer, **40**(1), pp. 27–38.
[8] Zhang, Z., and Li, Y., 2003, "CFD Simulation on Inlet Configuration of Plate-Fin Heat Exchangers," Cryogenics, **43**(12), pp. 673–678.
[9] Srihari, N., Prabhakara Rao, B., Sunden, B., and Das, S. K., 2005, "Transient Response of Plate Heat Exchangers Considering Effect of Flow Maldistribution," Int. J. Heat Mass Transfer, **48**(15), pp. 3231–3243.
[10] Lalot, S., Florent, P., Lang, S. K., and Bergles, A. E., 1999, "Flow Maldistribution in Heat Exchangers," Appl. Therm. Eng., **19**(8), pp. 847–863.
[11] Wen, J., and Li, Y., 2004, "Study of Flow Distribution and Its Improvement on the Header of Plate-Fin Heat Exchanger," Cryogenics, **44**(11), pp. 823–831.
[12] Brown, L., Besenbruch, G., Lentsch, R., Schultz, K., Funk, J., Pickard, P., Marshall, A., and Showalter, S., 2003, "High Efficiency Generation of Hydrogen Fuels using Nuclear Power—Final Technical Report for the Period August, 1, 1999 through September, 30, 2002," Prepared under the Nuclear Energy Research Initiative (NERI) Program Grant No. DE-FG03–99SF21888 for the US Department of Energy, Jun.
[13] Ponyavin, V., Chen, Y., Mohamed, T., Trabia, M., Wilson, M., and Hechanova, A. E., 2006, "Modeling and Parametric Study of a Ceramic High Temperature Heat Exchanger and Chemical Decomposer," *Proceedings of IMECE2006, ASME International Mechanical Engineering Congress and Exposition*, Chicago, IL.
[14] Ponyavin, V., Chen, Y., Mohamed, T., Trabia, M., Hechanova, A. E., and Wilson, M., 2006, "Parametric Study of Sulfuric Acid Decomposer for Hydrogen Production," *Second COE-INES International Symposium on Innovative Nuclear Energy Systems, INES-2*, Tokyo, Japan.
[15] FLUENT, Inc., 2005, FLUENT 6.2 User's Guide, Lebanon, NH.
[16] Patankar, S. V., 1980, *Numerical Heat Transfer and Fluid Flow*, Hemisphere, New York.
[17] Rohsenow, W. M., Hartnett, J. P., and Ganic, E. N., 1985, *Handbook of Heat Transfer, Applications*, McGraw-Hill, New York.

Downloaded 03 Jun 2010 to 171.66.16.157. Redistribution subject to ASME license or copyright; see http://www.asme.org/terms/Terms_Use.cfm

Effect of Interfacial Waves on Turbulence Structure in Stratified Duct Flows

M. Fernandino
e-mail: maria.fernandino@ntnu.no

T. Ytrehus

Department of Energy and Process Engineering,
Norwegian University of Science and Technology,
N-7491 Trondheim, Norway

Stratified flows are encountered in many industrial applications. The determination of the flow characteristics is essential for the prediction of pressure drop and holdup in the system. The aim of this study is to gain insight into the interaction of a gas and a liquid phase flowing in a stratified regime, with especial focus on the effect of interfacial waves on the turbulence structure of the liquid phase. Measurements of mean velocities and turbulent intensities in the liquid phase of a stratified air-water duct flow are performed. Mean velocity profiles and turbulence structure are affected differently for different wave amplitudes. The effect of small amplitude waves is restricted to the near-interface region, resembling the effect of increasing shear rate on a flat interface. On the other hand, large amplitude waves modify the flow structure throughout the whole liquid depth. The mean velocity is greatly enhanced, resulting in a higher bulk velocity. Turbulent intensities are also significantly enhanced especially in the interface region. This big difference in flow structure is not observed after the appearance of the first waves but rather when a certain critical wave amplitude is triggered, indicating that the prediction of this critical wave type turns out to be more important than the determination of the transition from a smooth to a stratified wavy regime. [DOI: 10.1115/1.2928295]

1 Introduction

Contrary to turbulence in the wall region, which has been intensively studied over the past two decades, turbulence near fluid-fluid interfaces has not been studied with the same detail due to the difficulties that lie on the measurements near this interface and on the simulation of flows with deformable interfaces. With the accessibility of new experimental techniques, such as laser Doppler velocimetry (LDV), more and more data of the flow structure close to gas-liquid interfaces are now becoming available.

Free-surface flows have been studied experimentally and numerically. In the LDV experiments from Nezu and Rodi [1], the mean velocity profile was found to deviate from the logarithmic behavior near the free surface (for $\mathrm{Re}_h > 10{,}000$). According to the authors, as the Reynolds number becomes larger, such deviation cannot be neglected for $y/h_L > 0.6$, and they suggested the use of the Coles wake law as the more convenient way to account for this deviation. Contrary to the findings of Nezu and Rodi [1], Rashidi and Banerjee [2] did not observe any deviation from the logarithmic law near the interface. They attributed this fact to the lower Reynolds numbers that were used in their study as compared to those in the work of Nezu and Rodi [1]. Near a shear-free surface, vertical fluctuations are damped due to gravity and surface tension, resembling the behavior of a solid boundary. At the same time, streamwise and spanwise fluctuations are enhanced in the interfacial region [2,3]. The direct numerical simulation (DNS) of free-surface flows performed by Komori et al. [4] and Pan and Banerjee [5] confirm these experimental results.

When an interfacial shear is applied, the interface region becomes an active one, where structures can form and even attach to the interface as opposed to what happens at a solid wall [6–8]. For low shear rates, bursts coming from the wall region are responsible for scalar transport, whereas for high enough shear rates, the fluid structures originating in the interface region dominate the process.

Under the condition of small shear rates, small amplitude (SA) waves form on the interface. SA disturbances do not significantly influence the flow structure, and the interface can be treated as a rigid slip wall in numerical simulations [4,8]. This is because in this case, the shear rate appears to be more important than the nature of the boundary conditions in determining such structures [7]. For this case of small disturbances, the mean velocity profile follows the logarithmic law near the wall, with higher values of the summation constant A with increasing interfacial shear [7]. The mean velocity profiles from and near the sheared interface also follow a logarithmic profile from the center of the flow up to $y_i^+ \approx 20-30$ according to the experimental study of Rashidi and Banerjee [7]. No outer region was seen to exist since both logarithmic regions (wall and interface) interact with each other.

When significant shear is imposed on the liquid surface, the surface is no longer "free" and entirely different structures result. The presence of larger amplitude interfacial waves changes the kinematic and turbulence structure of the liquid phase close to the sheared interface (see, for example, Ref. [9]). Fabre et al. [10] observed an increase in turbulent intensities close to the wavy interface. However, no description of the wave structure was provided. Streamwise and vertical turbulent fluctuations were also seen to increase substantially under the presence of waves by Kemp and Simons [11]. Rashidi et al. [12] superimposed SA gravity waves on a turbulent liquid layer via a wave maker, with a maximum wave amplitude to liquid film height ratio of $h_w/h_L = 0.16$. For an increasing wave amplitude, the value of the wall shear velocity u_τ was seen to increase under wave crests and to decrease under wave troughs, resulting in a nearly constant mean value. Mean velocities were seen to be higher near the interface and near the wall for an increasing wave amplitude, and, therefore, a small deviation from the logarithmic law was observed for those cases. Similar observations were reported by Kemp and Simons [11]. The intensity of turbulent fluctuations showed a similar behavior as in free-surface flows although their intensity was increased by the presence of superficial waves. The frequency of bursts originating at the wall was increased by the occurrence of waves, implying that the transport of turbulent energy from the wall to the interface region was altered when waves were present. Reynolds stresses in the wall region were amplified also due to the

Contributed by the Fluids Engineering Division of ASME for publication in the JOURNAL OF FLUIDS ENGINEERING. Manuscript received August 29, 2006; final manuscript received March 11, 2008; published online May 19, 2008. Assoc. Editor Phillip M. Ligrani.

 Copyright © 2008 by ASME

Downloaded 03 Jun 2010 to 171.66.16.157. Redistribution subject to ASME license or copyright; see http://www.asme.org/terms/Terms_Use.cfm

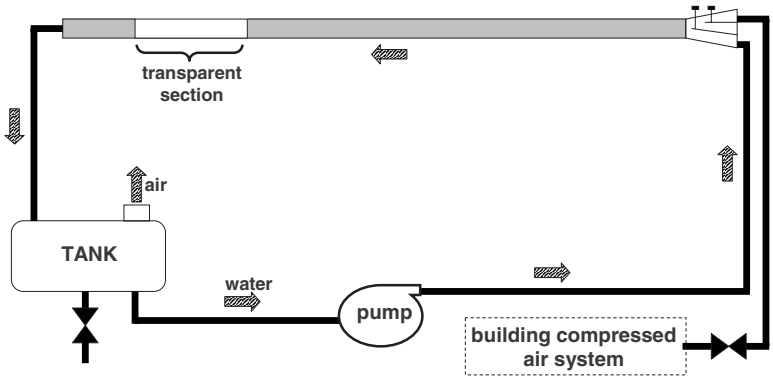

Fig. 1 Experimental facility

change in wall ejection frequency. These effects would be more important for the large amplitude (LA) waves usually found in stratified flows in industrial applications.

Interfacial waves are also known to induce secondary currents both in the gas and the liquid phase of a stratified flow, having important effects on the flow structure in each of the two phases [13–15]. The variation in wave amplitude across the width of the duct is an important source for the mean secondary flow [15]. The measurements in duct flow from Suzanne [13] show two counter-rotating vortices in the duct cross-section area in the liquid phase. The flow goes up along the lateral walls and comes down along the duct center plane. This flow is responsible for the maximum streamwise velocity occurring just below the interface. Similar secondary motions were reported in the numerical simulations of a rectangular duct flow by Nordsveen [15] and the pipe flow measurements of Andreussi and Persen [16]. For a duct aspect ratio of 6, Nordsveen [15] reported that wave-induced secondary currents were much more important than turbulence-induced ones. The former formed in all the duct cross-section areas (but mainly along the interface), and the latter only close to the walls and corners. For an aspect ratio of 2, both effects were of the same order.

Even when the number of results reported in the literature regarding wave-turbulence interaction has increased during the past years, much work still needs to be done before we can really understand the dynamics of interaction and transport phenomena occurring between a gas and a liquid flowing in a stratified regime. In particular, the effect of LA waves on turbulence structure has not been largely documented in the literature, mainly due to the difficulties involved both in numerical simulations and in laboratory measurements. Furthermore, while some authors claim to have studied LA wave effect on a flow structure, we have not found any work where the ratio of wave amplitude to liquid film height was as large as the one considered in this work. In this work, wave-turbulence interaction in a stratified air-water duct flow is studied. LDV measurements of mean velocity and turbulence structure in the liquid phase for different kinds of interfacial waves are presented. A comparison of LA waves and liquid film heights is included in this study.

2 Description of the Experiments

The experiments were carried out in a horizontal 9 m long duct, with a square cross-section area of 7×7 cm^2. The duct was made of stainless steel, and an acrylic transparent section was introduced approximately 6 m from the entrance, where velocity measurements were performed. Figure 1 shows a schematic diagram of the flow loop.

The study was performed using air and water at atmospheric pressure as working fluids. The duct inlet had three entrances intended for the injection of gas, water, and oil into the duct. Water was injected through the bottom entrance, and air through the top one. The air was supplied by the laboratory compressed-air system and was regulated by a manual valve. The water was recirculated by a manually regulated screw pump from a tank connected to the outlet of the channel. The water flow rate was monitored by an electromagnetic flow meter, and the air flow rate by a mass flow meter operating on the principle of heat transfer along a laminar flow device. Both fluids entered the channel through a square–cross-section converging nozzle with two inlets, one above the other (see Fig. 1). The water was introduced through the bottom of the nozzle, and the air through the top half.

The pressure drop along the channel and the test section was measured using a double positive dp-cell. A Pt100 probe placed at the end of the transparent test section was used to record the temperature of the water phase.

Measurements of the liquid velocity and turbulent fluctuations were performed using LDV. The laser used was a TSI two-component argon-ion laser with wavelengths of 514.4 nm and 488.0 nm. The laser was mounted on a traverse mechanism capable of shifting positions in the vertical and horizontal (streamwise) directions. It was pointing at the transparent section perpendicularly from the side of the duct.

The measurements were performed for liquid superficial velocities of $U_{LS}=0.068$ m/s and $U_{LS}=0.136$ m/s, resulting in mean liquid heights of $h_L=21$ mm and $h_L=31$ mm, respectively. The gas superficial velocities were varied from 0 m/s to 3.5 m/s. The parameters for each measured case are shown in Table 1. The laser was aimed at the center plane of the duct from the side. In order to ensure the two dimensionality of the measurements, the laser was aligned by measuring the distance from the laser outer diameter (from two opposite points of its diameter, pointing upstream and downstream from the measuring point) to the lateral wall of the duct. Velocity measurements were performed in the liquid phase throughout the whole liquid film depth.

Laser data acquisition was made simultaneously in both channels, thus being able to directly measure Reynolds stresses. Near the interface and near the wall, the beams corresponding to the vertical velocity measurements were obstructed by the bottom wall or were above the water surface. Therefore, the acquisition was no longer simultaneous in both channels, resulting in measurements only of streamwise velocity components in these regions.

During the velocity measurements, interfacial waves were characterized by the spectra obtained from the LDV measurement of vertical fluctuations close to the interface. The method is described in detail in Fernandino and Ytrehus [17]. Basically, three subregimes were identified with this method and will be considered in this work: (i) stratified smooth (SS) waves, (ii) SA waves, and (iii) 2D LA waves (two dimensional at the centerline of the duct, away from the lateral walls). The SS regime is characterized by a flat spectrum. In turn, the SA regime presented one dominant frequency at 12–14 Hz. Two dominant frequencies (two peaks)

Downloaded 03 Jun 2010 to 171.66.16.157. Redistribution subject to ASME license or copyright; see http://www.asme.org/terms/Terms_Use.cfm

Table 1 Combination of air and water flow rates used during this study, with U_{LS} as the water superficial velocity, U_L the mean water velocity, h_L the mean liquid film height and corresponding Reynolds number Re_L based on the mean velocity and mean liquid depth, U_{GS} the gas superficial velocity, Re_{GS} the gas phase Reynolds number based on the superficial, velocity, and h_w the mean wave amplitude. The SS, SA, and LA (wave regimes) are classified according to Fernandino and Ytrehus [17].

	U_{LS} (m/s)	U_L (m/s)	h_L (mm)	Re_L	U_{GS} (m/s)	Re_{GS}	h_w (mm)
Run 2a	0.068	0.34	21	7140	0	0	0 (SS)
Run 2b	0.068	0.34	21	7140	1.24	5748	0 (SS)
Run 2c	0.068	0.34	21	7140	1.69	7834	~1 (SS)
Run 2d	0.068	0.34	21	7140	1.83	8483	2–3 (SA)
Run 2e	0.068	0.34	21	7140	1.96	9086	2–4 (SA)
Run 2f	0.068	0.35	21	7350	2.19	10,152	4–5 (SA)
Run 2g	0.068	0.35	21	7350	2.53	11,728	5–6 (SA)
Run 2h	0.068	0.38	21	7980	2.92	13,536	8–10 (LA)
Run 2i	0.068	0.41	21	8610	3.25	15,066	~10 (LA)
Run 3a	0.136	0.44	31	13,640	0	0	0 (SS)
Run 3b	0.136	0.47	31	14,570	1.23	5702	1–2 (SA)
Run 3c	0.136	0.48	31	14,880	1.72	7973	4–6 (SA)
Run 3d	0.136	0.48	31	14,880	2.21	10,245	7–9 (LA)
Run 3e	0.136	0.48	31	14,880	2.41	11,172	9–10 (LA)
Run 3f	0.136	0.53	31	16,430	2.87	13,305	~10 (LA)
Run 3g	0.136	0.60	31	18,600	3.31	15,344	10–12 (LA)

appeared in the spectrum when the air flow was further increased and led the way almost immediately to one dominant frequency, this time at 7 Hz. The latter was designated as the LA waves. Mean velocities and turbulent fluctuations were characterized based on this subregime classification.

3 Results and Discussion

3.1 Mean Velocity. Mean velocities and turbulent fluctuations presented in this section are nondimensionalized with the wall shear velocity $u_\tau \equiv \sqrt{\tau_w/\rho_L}$, with τ_w as the mean wall shear stress and ρ_L the liquid density. Different methods for obtaining the wall shear velocity were analyzed, namely, obtaining the wall shear velocity from the velocity gradient at the wall, from the measured mean velocity profile and the logarithmic law, from the measured pressure drop, from the measured Reynolds stresses, and from the expression $\tau_w = f_L \rho_L U_L^2/2$ and the Blasius formula $f_L = 0.0559 Re_L^{-0.22}$, with f_L as the liquid wall friction factor (the methods were described and compared in detail in Ref. [18]). The latter option seemed to be the most appropriate and is the one used in this work.

Figure 2 shows the measured mean velocity profile for a free-surface condition. Here, $y^+ = y u_\tau/\nu_L$, where y represents the distance from the wall. The profile presents a logarithmic region for $y^+ \geqslant 70$, in accordance with the empirical log law for an open channel flow, with the von Karman's constant $\kappa = 0.41$ and the summation constant $A = 5.5$ [1,2]. A small deviation from the logarithmic behavior is observed close to the interface for Run 2a for $y/h_L \geqslant 0.8$. For Run 3a, the deviation is more significant and the profile shows a zero shear region close to the interface.

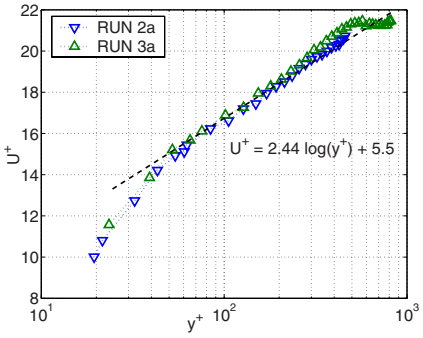

Fig. 2 The measured mean velocity profile for the free-surface duct flow compared to the empirical log law of the wall for the open channel flow

Mean velocity profiles for different air superficial velocities are shown in Fig. 3. The horizontal black lines indicate the mean interface level. The dashed line is the mean level corresponding to the more wavy interfaces, where the position of the interface could not be located accurately but just visually (the wave amplitude varied throughout the duct width). Therefore, the profiles from Run 2f and Run 3d onward show the same mean water level. The filled rounded dots in Fig. 3 indicate the reference free-surface profile (Runs 2a and 3a).

As the air flow is increased (always by the same constant amount), the velocity profiles are enhanced close to the interface, while the rest of the bulk flow is nearly undisturbed (Runs 2b–2e and 3a–3c). In these cases, the result of increasing the interfacial shear rate translates into increasing the profile slope close to the sheared surface only. However, if the air flow is increased a little more (Runs 2f and 2g and 3d and 3e), the velocity in the bulk region of the flow is also increased, forming a kind of belly in the profile in that region. For higher air flows (Runs 2h and 2i and 3f and 3g), mean velocities are enhanced near the interface and near the wall as well, while they seem to decrease in the center region with respect to the wall and interface values, resulting in an s-shaped profile. This s-shaped velocity profile accompanied by a significant increase in bulk velocity was also observed by Suzanne [13] during rectangular duct flow measurements and by Strand [14] during stratified pipe flow experiments. This means that the s-shaped profile with higher bulk velocity is not a consequence of the rectangular cross section but of the flow itself. It is worth remembering here that the s-shaped profile was observed (both in this work and in the mentioned previous studies) in the duct/pipe centerline. As one comes close to the lateral walls of the duct or the point of contact of the liquid film with the walls of the pipe, it is expected that the flow in those regions could experience some backward recirculations caused by the direct interaction of the waves with the solid walls. Some three-dimensional effects from the lateral walls are also expected for the studied liquid film height to duct width ratio.

It can be seen that the effect of a shear imposed on the interface is restricted to the near-interface region only for low shear rates.

Downloaded 03 Jun 2010 to 171.66.16.157. Redistribution subject to ASME license or copyright; see http://www.asme.org/terms/Terms_Use.cfm

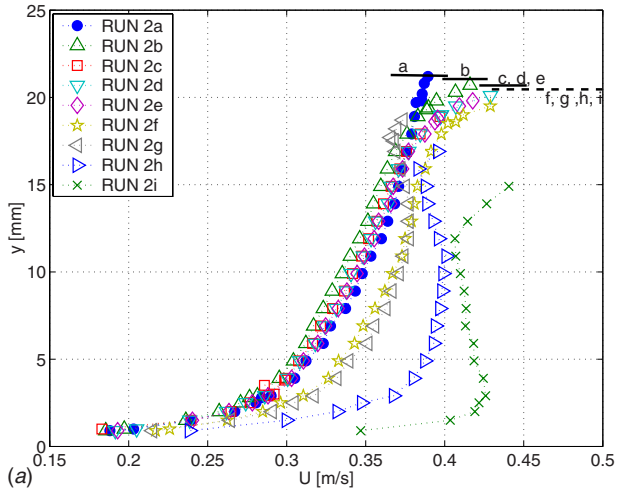

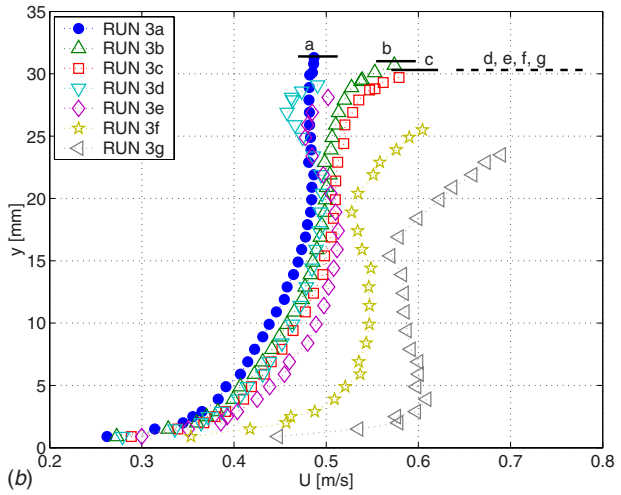

Fig. 3 Mean streamwise velocity profiles for different air superficial velocities and corresponding wave patterns: (*a*) Run 2 and (*b*) Run 3. The black lines indicate the interface position.

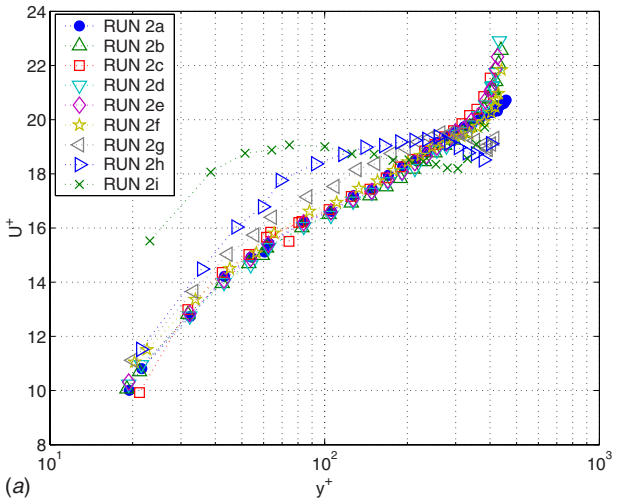

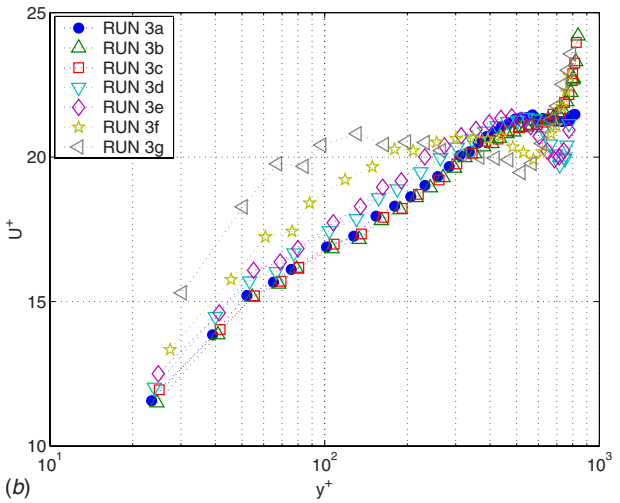

Fig. 4 Nondimensional mean stremaiwse velocity profiles for different air superficial velocities and corresponding wave patterns: (*a*) Run 2 and (*b*) Run 3

On the other hand, for a sufficiently high shear rate, the shape of the mean velocity profiles is affected also in the bulk region of the flow, while the near wall region seems to remain unaltered. When the shear is enough to trigger the appearance of LA waves on the interface, an s-shaped profile and an apparent significant increase in the liquid bulk velocity is observed.

Figure 4 shows the same profiles as in Fig. 3, but they are nondimensionalized with the inner variables ν_L and shear velocity u_τ. The profiles corresponding to free-surface flow are plotted with filled dots. In all cases, a deviation from the logarithmic profile is observed near the interface. However, for $50<y^+<200$, almost all profiles coincide with the empirical logarithmic law for the open channel flow, except the ones corresponding to LA waves on the interface (Runs 2h and 2i and 3f and 3g). Regarding Runs 2g and 3d and 3e, a logarithmic region seems to exist although the summation constant appears to be larger.

The large increase in bulk velocity when LA waves appear on the interface indicates an overall decrease in wall shear and corresponds to a significant increase in pressure drop in the gas phase [17]. It is not clear from these measurements why the velocity profile is shifted so much to the front. One hypothesis is related to the effect of drag reduction. Waves are known to significantly influence the number of bursting events (sweeps and ejections) in the wall region [12]. These sweep events are particularly important for drag reduction because they are responsible for the generation of turbulent wall shear stress [19]. Thus, drag reduction is achieved by the suppression of streamwise vortex formation [20]. Therefore, it is possible that the wave motion attenuates the formation of streaks close to the walls (bottom and/or lateral one) and in this way produces an overall reduction in skin friction. Wave-induced secondary currents can also be a way of explaining the significant enhancement of mean velocity in the bulk region when LA waves are present. Secondary currents in the liquid phase of a stratified rectangular duct flow were measured by Suzanne [13] and obtained in numerical simulations by Nordsveen [15]. In both cases, the secondary motion consisted of two big vortices in the duct cross-section area, with flow going up near the lateral walls and coming down along the duct center plane. The latter is responsible for carrying high speed fluid from the center of the duct to the wall region, possibly resulting in this way in an acceleration of the flow in the near wall region.

The described wave-induced secondary flow is evident from measurements of the mean vertical velocity, as shown in Fig. 5. For Runs 2i, 3f, and 3g, there is a mean downward flow motion, indicating the presence of wave-induced secondary motion in the middle of the duct cross-section area. The magnitude of this secondary flow is around 2–5% of the mean streamwise velocity. For Runs 2h and 3f, the flow from the interface toward the bottom of the duct is rather small as compared to that for Runs 2i and 3g. However, for these two cases, the streamwise mean velocity pro-

Downloaded 03 Jun 2010 to 171.66.16.157. Redistribution subject to ASME license or copyright; see http://www.asme.org/terms/Terms_Use.cfm

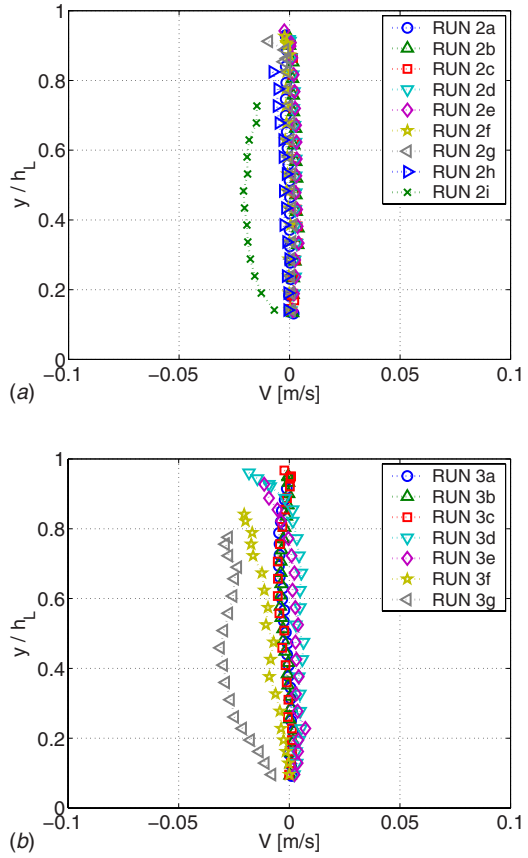

Fig. 5 Mean vertical velocity profiles for different air superficial velocities and corresponding wave patterns: (*a*) Run 2 and (*b*) Run 3. Positive mean vertical velocity implies an upward movement of the flow.

files are already significantly enhanced, as seen in Fig. 3. Therefore, some other effect rather than the secondary flow alone can be responsible for this enhancement. However, more measurements—probably with some other experimental techniques that allow for the visualization of the whole flow field in the duct cross-section area, for instance, particle image velocimetry (PIV) or simply some flow visualization technique—would be needed in order to determine the cause of this increase in bulk velocity under the presence of LA waves.

3.2 Turbulence Structure. Figures 6 and 7 show the measurements of streamwise ($u' \equiv \sqrt{\overline{u'^2}}$) and vertical ($v' \equiv \sqrt{\overline{v'^2}}$) turbulent fluctuation and Reynolds stress ($-\overline{u'v'}$) profiles for the two liquid flow rates considered.

It is seen in these figures that vertical fluctuations for the free surface flow (Runs 2a and 3a) are damped close to the wall and close to the free surface due to gravity and surface tension in the latter case. On the other hand, streamwise fluctuations peak in the near wall region, and contrary to what happens in a solid boundary, they do not vanish as the interface is approached, as expected for free-surface flows [1,3].

As the shear rate is increased, streamwise fluctuations are enhanced close to the interface (Runs 2b–2e, and 3b and 3c), while vertical fluctuations in the same region are not allowed to increase that much due to gravity and surface tension effects. Reynolds stresses for Runs 2b–2e are not affected by the applied interfacial shear or the SA waves on the interface, indicating why the mean velocity profiles for these Runs remain unaltered throughout the flow depth.

For Runs 2f and 2g, the streamwise fluctuation profiles are more similar to the unsheared interface case, with a pronounced peak as the interface is approached, giving the profile a "c" shape. The streamwise fluctuations are completely undisturbed for $y/h_L \leq 0.6$. An akin behavior is shown in the vertical intensities, where the latter are enhanced very close to the interface and remain unaltered for $y/h_L \leq 0.4$, coinciding in this region with the nonsheared case of Run 2a instead of showing a continuous deformation following Runs 2b–2e for an increasing shear rate. A sudden increase in vertical fluctuations is observed for Run 2g though, reaching a value 35% higher close to the interface than for smaller shear rates. Both streamwise and vertical fluctuations peak close to the interface just below the wave troughs. The peak magnitude increases for higher shear rates. Reynolds stresses $-\overline{u'v'}$ are decreased for both cases, with smaller values for Run 2g. For $y/h_L \leq 0.2$, turbulent intensities scale with the wall shear velocity, so that turbulence at the wall appears to be independent of what happens to the rest of the flow.

For Runs 2h and 2i, LA waves are generated by the wind shear. As a result, the bulk velocity was greatly enhanced. Streamwise turbulent intensities for these Runs peak close to the wall and just under the wave trough, apparently reducing their magnitude as the interface is approached. For higher wave amplitudes, the peak in streamwise fluctuations occurs in deeper locations and almost at the same distance down from the wave trough. Therefore, this peak is probably related to the balance between generation and dissipation of the wave-induced fluctuations as one gets away from the interface. Vertical fluctuations also peak close to the interface, decreasing their magnitude with a constant downslope until close to the wall. Here, we see how the region $y/h_L \leq 0.2$ is apparently affected by the wavy motion in both Runs. However, this is not enough reason to assume that wall turbulence and, therefore, the shear at the wall are indeed affected since measurements within the viscous sublayer would be needed to probe this assumption. Vertical fluctuations have to vanish when the wall is reached due to the physical restriction the latter imposes on the flow. The Reynolds stresses $-\overline{u'v'}$ are significantly reduced for $y/h_L \leq 0.5$ due to the LA wave motion. For Runs 2i and 3g, Reynolds stresses take a strange shape, being negative at $0.1 \leq y/h_L \leq 0.55$. In principle, the negative Reynolds stresses could be due to the fact that our experimental technique did not distinguish between wave-induced fluctuations and turbulence-induced fluctuations. The coupling between these two could be the reason for the observed negative values. At the same time, in the same depth range as the Reynolds stresses become negative, the mean velocity profile shows a negative slope, leaving the production term $-\overline{u'v'}\partial U/\partial y$ positive.

Looking at the measurements for Runs 2 and 3, the effects of applying an interfacial shear can be summarized as follows. For a free interface (open duct flow), the flow structure was similar to an open channel flow, with the mean velocity profile described by a logarithmic profile. As the interfacial shear increased, SA waves were formed on the interface. Under these conditions, the effect on the flow structure in the liquid phase was the same as that produced by an increasing shear rate on a flat interface. The wavy motion did not show any effect in the bulk flow structure, and turbulent fluctuations were enhanced continuously close to the interface as the shear increased. Mean velocity profiles were still represented by the log law of the wall. Consequently, it can be said that the interface actually acts as a flat surface with a shear imposed on it and could be treated as such in numerical simulations. These results confirm the previous suggestions by the numerical simulations of Lam and Banerjee [6], Komori et al. [4] and Lombardi et al. [21]. However, the effect of a shear imposed on the interface is restricted to the near-interface region only for low shear rates. When the shear rate was large enough to trigger a certain wave amplitude, turbulent fluctuations were suddenly enhanced close to the interface. From that moment and for increasing wave amplitudes the effect of the interface motion affected the bulk flow structure as well. Mean velocity profiles were no longer described by a logarithmic region, and turbulent fluctuations were

Downloaded 03 Jun 2010 to 171.66.16.157. Redistribution subject to ASME license or copyright; see http://www.asme.org/terms/Terms_Use.cfm

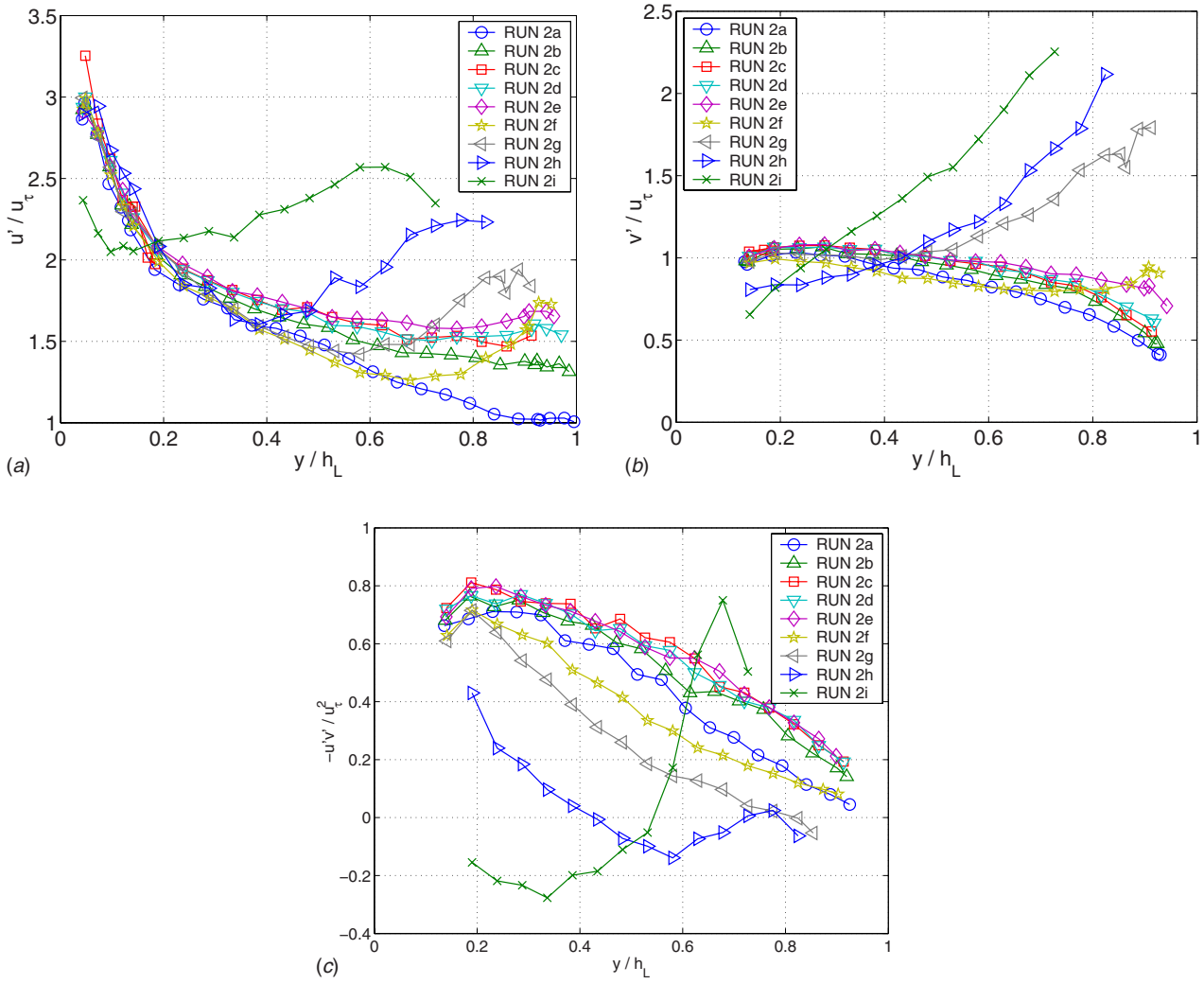

Fig. 6 Turbulent intensity profiles versus normal distance to the wall for Run 2, where $u' \equiv \sqrt{\overline{u'^2}}$ are streamwise fluctuations, $v' \equiv \sqrt{\overline{v'^2}}$ are vertical fluctuations, and $-\overline{u'v'}$ are Reynolds stresses

continuously enhanced. In both cases (for both liquid film heights considered here), the appearance of these critical waves was characterized by a wave amplitude to liquid film height ratio of approximately $h_w/h_L \geqslant 0.2$. The difference in flow structure observed before and after the appearance of these waves or of critical wave amplitudes indicates that, at some point, wave-induced fluctuations begin to be more important than turbulence-induced fluctuations. These wave-induced fluctuations could be responsible for modifying the flow structure near the bottom wall, but, again, more measurements are needed in order to try to relate the interface dynamics with the bursts and events in the wall boundary layer.

According to the previous observations, predicting the transition from a stratified smooth to a stratified wavy regime, i.e., the appearance of the first waves, is not so important as to be able to predict the emergence of the critical wave amplitudes that have a significant influence on the flow structure. The experimental technique used in this work for wave characterization [17] was not able to distinguish the appearance of this kind of waves. The technique, however, was intended to produce an objective way of characterizing the interface while velocity measurements were performed. In order to determine a more accurate technique for detecting these critical waves, more measurements of wave parameters, such as wavelength and wave amplitude, would be needed.

4 Summary and Conclusions

Streamwise mean velocity and turbulent stress profiles in the liquid phase were measured using LDV. The measurements were performed in the duct center plane, from the bottom wall to the interface. Two different liquid film heights were used, and in both cases, the effect of shear on the interface had similar results.

For a free surface (zero gas flow), the interface remained smooth, with vertical fluctuations and Reynolds stresses vanishing at the interface. The mean velocity profile was described by the log law of the wall for an open channel. SA waves resulted in an increase in the streamwise velocity close to the interface due to the higher interfacial shear rate. The latter were enhanced continuously as the gas flow rate increased, while vertical fluctuations remained close to zero in that region. This is an indication that with the presence of SA waves, the interface can still be treated as a sheared flat interface in numerical simulations. Numerical simulations found in the literature contribute to this idea by showing that treating the interface as flat with a shear imposed on it gives accurate results.

On the other hand, LA waves have a great impact on flow structure. The mean velocity showed an s-shaped profile, and the bulk velocity was increased. This apparent increase in bulk velocity was attributed either to wave-generated secondary flows or to an effect of drag reduction produced by the change in bursting

Downloaded 03 Jun 2010 to 171.66.16.157. Redistribution subject to ASME license or copyright; see http://www.asme.org/terms/Terms_Use.cfm

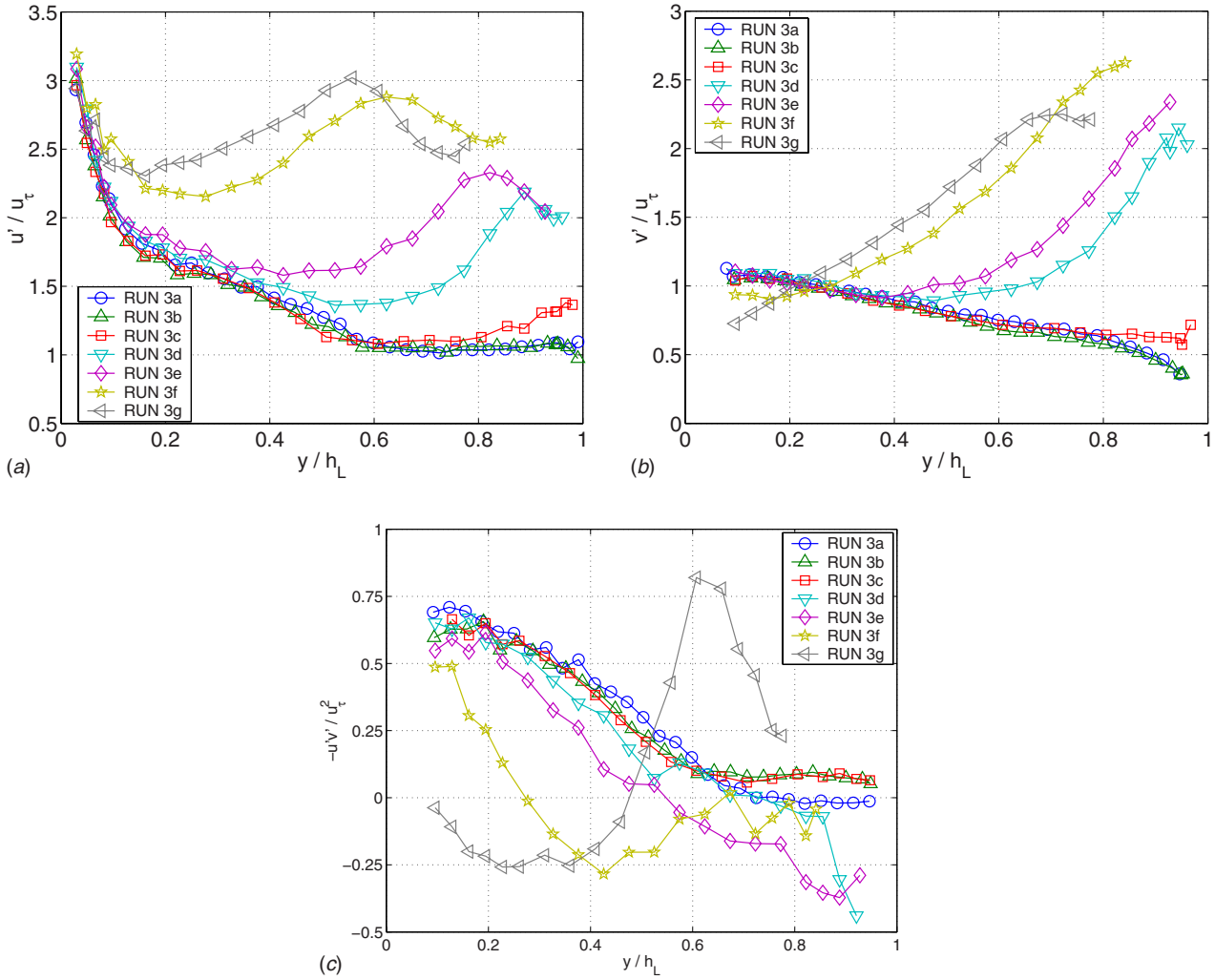

Fig. 7 Turbulent intensity profiles versus normal distance to the wall for Run 3 (wall at $y/h_L=0$, interface at $y/h_L=1$), where $u' \equiv \sqrt{\overline{u'^2}}$ are streamwise fluctuations, $v' \equiv \sqrt{\overline{v'^2}}$ are vertical fluctuations, and $-\overline{u'v'}$ are Reynolds stresses

frequency in the wall region due to the interfacial oscillations. However, this is just a hypothesis that could not be verified in the present work. More measurements, probably using another experimental technique, should be carried out in order to determine the real cause of change in the flow structure. No logarithmic region was observed in the mean velocity profile. Both streamwise and vertical fluctuations were greatly enhanced in the interface region, presenting maximum values close to the interface and close to the wall, while vertical fluctuations peaked close to the interface and decreased almost linearly to the wall. Reynolds stresses showed a completely different behavior compared to that in the SA wave regime. Their values were decreased throughout the flow depth, and some negative values were measured. Both the mean flow and turbulent stresses appeared to be modified close to the wall when LA disturbances were present. However, since the LDV measurements were performed outside the viscous sublayer, this assumption of LA waves modifying the wall turbulence could not be confirmed.

The big difference in flow structure was not observed after the appearance of the first waves but rather when a certain critical wave amplitude was triggered. Therefore, the prediction of the critical wave amplitude and wavelength, which had a significant influence on the flow and turbulence structure, seems more important than the usual determination of the transition from a smooth to a stratified wavy regime. More work should be dedicated to the characterization of this critical wave height and the prediction of its appearance.

Acknowledgment

This work was made possible, thanks to the financial support of the Norwegian Research Council through CARPET Strategic University Program.

References

[1] Nezu, I., and Rodi, W., 1986, "Open-Channel Flow Measurements With Laser Doppler Anemometer," J. Hydraul. Eng., **112**, pp. 335–355.
[2] Rashidi, M., and Banerjee, S., 1988, "Turbulence Structure in Free-Surface Channel Flows," Phys. Fluids, **31**, pp. 2491–2503.
[3] Komori, S., Ueda, H., Ogino, F., and Mizushina, T., 1982, "Turbulence Structure and Transport Mechanism at the Free Surface in an Open Channel Flow," Int. J. Heat Mass Transfer, **25**, pp. 513–521.
[4] Komori, S., Nagaosa, R., Murakami, Y., Chiba, S., Ishii, K., and Kuwahara, K., 1993, "Direct Numerical Simulation of Three-Dimensional Open-Channel Flow With Zero-Shear Gas-Liquid Interface," Phys. Fluids A, **5**, pp. 115–125.
[5] Pan, Y., and Banerjee, S., 1995, "A Numerical Study of Free-Surface Turbulence in Channel Flow," Phys. Fluids, **7**, pp. 1649–1664.
[6] Lam, K., and Banerjee, S., 1992, "On the Condition of Streak Formation in a Bounded Turbulent Flow," Phys. Fluids A, **4**, pp. 306–320.
[7] Rashidi, M., and Banerjee, S., 1990, "Streak Characteristics and Behavior Near Wall and Interface in Open Channel Flows," ASME J. Fluids Eng., **112**,

Downloaded 03 Jun 2010 to 171.66.16.157. Redistribution subject to ASME license or copyright; see http://www.asme.org/terms/Terms_Use.cfm

pp. 164–170.
[8] Kumar, S., Grupta, R., and Banerjee, S., 1998, "An Experimental Investigation of the Characteristics of Free-Surface Turbulence in Channel Flow," Phys. Fluids, **10**, pp. 437–456.
[9] Lorencez, C., Nasr-Esfahany, C. L. M., Kawaji, M., and Ojha, M., 1997, "Liquid Turbulence Structure at a Sheared and Wavy Gas-Liquid Interface," Int. J. Multiphase Flow, **23**, pp. 205–226.
[10] Fabre, J., Marodon, D., and Suzanne, L. M. C., 1984, *Turbulence Structure of Wavy Stratified Air-Water Flow*, Gas Transfer at Water Surfaces, W. Brutsaert and G. H. Jirka, eds., Reidel Publishing Company, Dordrecht, Holland, pp. 113–123.
[11] Kemp, P., and Simons, R., 1982, "The Interaction Between Waves and a Turbulent Current: Waves Propagating With the Current," J. Fluid Mech., **116**, pp. 227–250.
[12] Rashidi, M., Hetsroni, G., and Banerjee, S., 1992, "Wave-Turbulence Interaction in Free-Surface Channel Flows," Phys. Fluids A, **4**, pp. 2727–2737.
[13] Suzanne, C., 1985, "Structure de l'Ecoulement Stratifié de Gaz et de Liquide en Canal Rectangulaire," Ph.D. thesis, Institut National Polytechnique de Toulouse, France.
[14] Strand, O., 1993, "An Experimental Investigation of Stratified Two-Phase Flow in Horizontal Pipes," Ph.D. thesis, University of Oslo, Norway.
[15] Nordsveen, M., 1995, "Modelling of Wave and Turbulence Induced Secondary Currents in Stratified Duct Flow," Ph.D. thesis, University of Oslo, Norway.
[16] Andreussi, P., and Persen, L., 1987, "Stratified Gas-Liquid Flow in Downwardly Inclined Pipes," Int. J. Multiphase Flow, **13**, pp. 565–575.
[17] Fernandino, M., and Ytrehus, T., 2006, "Determination of Flow Sub-Regimes in Stratified Air-Water Channel Flow Using LDV Spectra," Int. J. Multiphase Flow, **32**, pp. 436–446.
[18] Fernandino, M., 2006, "Experimental and Numerical Characterization of Turbulence Structure in Stratified Horizontal Air-Water Duct Flow," Ph.D. thesis, Norwegian University of Science and Technology, Norway.
[19] Choi, K.-S., 1989, "Near-Wall Structure of Turbulent Boundary Layer With Riblets," J. Fluid Mech., **208**, pp. 417–458.
[20] Schoppa, W., and Hussain, F., 1998, "A Large-Scale Control Strategy for Drag Reduction in Turbulent Boundary Layers," Phys. Fluids, **10**, pp. 1049–1051.
[21] Lombardi, P., Angelis, V. D., and Banerjee, S., 1996, "Direct Numerical Simulation of Near-Interface Turbulence in Coupled Gas-Liquid Flow," Phys. Fluids, **8**, pp. 1643–1665.

Downloaded 03 Jun 2010 to 171.66.16.157. Redistribution subject to ASME license or copyright; see http://www.asme.org/terms/Terms_Use.cfm

Influence of Upstream Conditions and Gravity on Highly Inertial Thin-Film Flow

Roger E. Khayat
Department of Mechanical and Materials Engineering,
The University of Western Ontario,
London, ON, N6A 5B9, Canada
e-mail: rkhayat@uwo.ca

Steady two-dimensional thin-film flow of a Newtonian fluid is examined in this theoretical study. The influence of exit conditions and gravity is examined in detail. The considered flow is of moderately high inertia. The flow is dictated by the thin-film equations of boundary layer type, which are solved by expanding the flow field in orthonormal modes in the transverse direction and using Galerkin projection method, combined with integration along the flow direction. Three types of exit conditions are investigated, namely, parabolic, semiparabolic, and uniform flow. It is found that the type of exit conditions has a significant effect on the development of the free surface and flow field near the exit. While for the parabolic velocity profile at the exit, the free surface exhibits a local depression, for semiparabolic and uniform velocity profiles, the height of the film increases monotonically with streamwise position. In order to examine the influence of gravity, the flow is studied down a vertical wall as well as over a horizontal wall. The role of gravity is different for the two types of wall orientation. It is found that for the horizontal wall, a hydraulic-jump-like structure is formed and the flow further downstream exhibits a shock. The influence of exit conditions on shock formation is examined in detail. [DOI: 10.1115/1.2928387]

1 Introduction

This study focuses on the influence of exit conditions and gravity on the high-speed thin-film flow of a Newtonian fluid emerging from a channel and moving on a flat stationary substrate. The problem is of close relevance to a wide variety of industrial processes. Details of these processes can be found in textbooks [1,2]. The characteristic feature of this flow is that the cross-sectional area of the film changes as the fluid emerges from the channel. The problem consists of obtaining the shape of the free surface and the flow field inside the domain. The flow is induced by the pressure gradient maintained inside the channel. Three types of exit conditions are assumed, namely, parabolic, semiparabolic, and uniform. Given the small thickness of the film compared to the film length and local curvature, the thin-film approximation will be used.

Many theoretical analyses of the thin-film flow over a substrate have been presented in literature. The lubrication approximation and asymptotic long-wave theory have been used with great success for flows at low Reynolds numbers [3]. For moderate Reynolds numbers, however, it is important to take both inertial and viscous effects into account [4]. Attempts have been made to extend the classical Reynolds equation to include the effect of fluid inertia in thin-film theory [5]. In the review article on fiber coating, Quere discussed the effect of inertia on rapid coating and droplet expulsion [6]. The steady two-dimensional flow between sliding sheets at finite Reynolds number was determined for a flow where viscous and inertial forces are comparable [7]. The flow was obtained approximately on the basis of an ad hoc linearization of the convective term. At higher Reynolds number, inertia is better accounted for through the "boundary layer" (BL) approximation, which includes the effect of depthwise flow [4]. Watson [8] examined much earlier the steady laminar and turbulent radial spreading of a liquid jet over a horizontal plane, including the special case of two-dimensional flow. Far from the source, a similarity solution of the laminar BL equation was sought. In particular, Watson found that for two-dimensional flow, the steady (dimensionless) shape of the free surface is given by $h_s = \pi x/\sqrt{3}\mathrm{Re} = 1.81x/\mathrm{Re}$, where x is the distance from the source, and Re is the (modified) Reynolds number [9]. The steady surface profile was obtained in the absence of gravity and surface tension. It constitutes an important limit form against which nonlinear film flow formulations may be validated (see below).

The major difference between the original Navier–Stokes and BL equations is the hydrostatic variation of the pressure across the film depth. As a result, only the depthwise momentum equation is eliminated, but the convective terms are retained in the remaining equations, and the number of boundary conditions is reduced. However, the solution of the BL equations remains essentially as difficult to obtain as that of the Navier–Stokes equations [10]. A depthwise integration of the momentum equation(s) in the lateral direction(s) is usually performed by assuming a self-similar semiparabolic flow profile in the depthwise direction, as was proposed by Shkadov [11]. Although the depth-averaged equations are only of second order in time, they yield plausible results, at least qualitatively, but they remain fundamentally questionable because of the semiparabolic profile assumption [10]. A measure of the error involved may be inferred by computing the free-surface profile (dimensionless) in the absence of gravity and surface tension, and comparing it to Watson's result given above. The parabolic approximation is widely used in literature, and its validity was established experimentally [12]. In addition to high-inertia flow, other flow conditions that restrict the range of validity of the semiparabolic profile include the presence of end effects, turbulent flow, and (most likely) nonlinear effects stemming from shear-thinning or viscoelastic effects [13,14].

When gravity is taken into account, the flow over a flat horizontal wall exhibits new features. The fluid flowing in a thin layer from the source experiences at some distance downstream an abrupt increase in the thickness of the film, which is called a hydraulic jump. Experiments on the circular hydraulic jump have been carried out by many researchers [8,15,16]. In these experiments, the hydraulic jump is formed by the jet impinging on a flat

Contributed by the Fluids Engineering Division of ASME for publication in the JOURNAL OF FLUIDS ENGINEERING. Manuscript received February 19, 2007; final manuscript received December 3, 2007; published online May 19, 2008. Review conducted by Joseph Katz.

 Copyright © 2008 by ASME

Downloaded 03 Jun 2010 to 171.66.16.157. Redistribution subject to ASME license or copyright; see http://www.asme.org/terms/Terms_Use.cfm

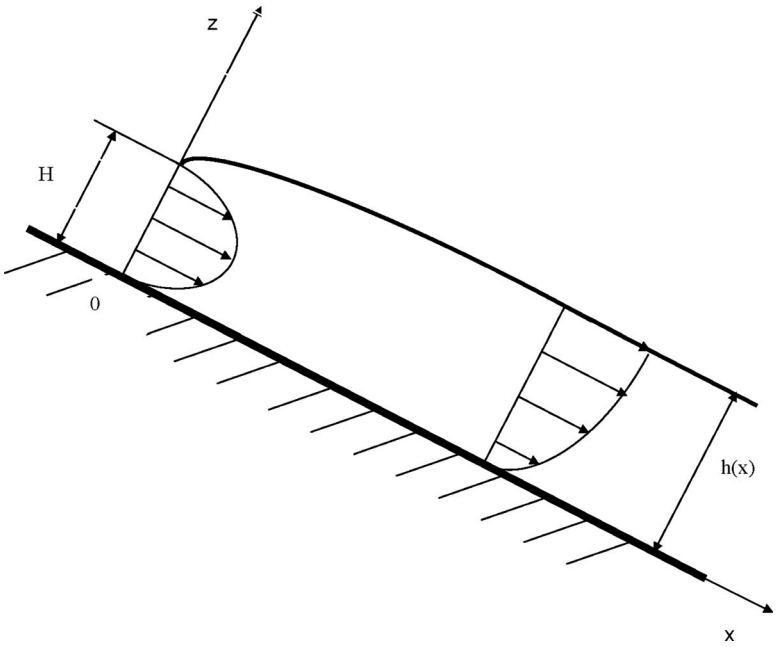

Fig. 1 Schematic of two-dimensional thin-film flow emerging from a channel. The figure also shows the dimensionless notations used in the formulation.

disk with a circular rim. It has been reported that the flow contains an eddy beyond the jump, a separation bubble [15,16]. When the rim is small, the jump is stable. However, as the rim height increases, a flow transition takes place, resulting in another state of flow [17,18]. In this case, the flow has an additional eddy, called a surface roller.

Considering a momentum balance on a flow across the jump, Watson [8] derived a relationship between the streamwise position of the jump and the depth downstream. Comparison with experimental results showed that the data agree reasonably well with the predicted behavior [8]. Recently, Bush and Aristoff [19] extended Watson's theory of the hydraulic jump by including the curvature force. They report that the correction is generally small in laboratory settings, but appreciable for jumps of small radius and height. Bowles and Smith [20] examined the flow in the neighborhood of the planar jump by the BL analysis. Their model predicts the thickness profile in the neighborhood of the jump, but uses the position of the jump from the experiments of Craik et al. [16]. as input data to their model. Higuerra [21] numerically solved such a system of BL equations, and predicted the position of the jump and the thickness of the film at the downstream edge of the flow. Watanabe et al. [22] included an additional degree of freedom in the velocity profile to make it non-self-similar, as in the Karman–Pohlhausen method for the usual BL theory. The resulting model can reproduce the flow with the hydraulic jump and the separation bubble. Chippada et al. [23] solved the two-dimensional unsteady Navier–Stokes equations using the finite-element method. They found that the surface roller and a small recirculation zone near the foot of the jump influence the characteristics of the jump significantly.

In this study, a unified spectral approach is proposed to model the pressure-gravity-driven flow of a Newtonian thin film. Given the importance of inertia, the BL formulation rather than long-wave approximation will be used. Surface tension is not considered. In the film flow problems, surface tension tends to bring the film shape to a smooth straight profile. However, the influence of surface-tension effects decreases with inertia [24]. Watanabe et al. [22] estimated the Weber number, and found $\mathrm{We} \approx 0.01$ at $\mathrm{Re} = 18$ for a stationary state of a liquid spreading over a flat plate. Since the current work focuses on high-inertia flow, it is concluded that surface-tension effects can be neglected in this case. The flow equations are first mapped onto the rectangular domain, and a formal expansion of the velocity field is introduced in terms of orthonormal basis functions. The formulation is similar to the one used previously [13,14,25–27], which led to excellent agreement with Watson's similarity solution for liquid spreading. The method follows closely and generalizes the formulation of Zienkiewicz and Heinrich [28], which emphasizes water flow over extended areas. There are, however, two major simplifying assumptions adopted by Zienkiewicz and Heinrich [28], which will be relaxed in the present study. First, the depthwise velocity component and its derivative will not be neglected in the momentum equation. Second, despite the long-wave approximation, the variation in surface height will not be neglected in the momentum equation. The Galerkin projection method is used to generate the equations that govern the expansion coefficients. The spectral method, and, particularly, the low-dimensional description of flow, has emerged as an effective alternative to conventional methods [29]. Although this method has predominantly been used for simple flow, recent developments have included complex geometry [30] and complex fluids [31–34]. Unlike the depth-averaging method, the proposed spectral methodology becomes particularly suited for highly nonlinear thin-film flow. Details of the free surface and flow field can be captured explicitly as well as in the mean sense.

2 Problem Formulation

Consider the flow of an incompressible Newtonian fluid of density ρ and viscosity μ. The fluid emerges from a channel of depth H and flows over a flat plate inclined by the angle α, as illustrated in Fig. 1. The flow is induced by a pressure gradient inside the channel and gravity. Surface tension is assumed to be negligible. Let L and H be the reference length and thickness in the streamwise and depthwise directions, respectively, with x and z being the corresponding dimensionless coordinates. The reference length L is yet undetermined. The streamwise and depthwise velocity components are scaled by V and HV/L, respectively, where V is a reference velocity, which is taken as an average velocity inside the channel. The pressure is scaled by $\mu VL/H^2$. The scaling for the

Downloaded 03 Jun 2010 to 171.66.16.157. Redistribution subject to ASME license or copyright; see http://www.asme.org/terms/Terms_Use.cfm

pressure is chosen to ensure the balance between pressure and viscous forces. The dimensionless shape of the free surface is given by $z=h(x,t)$, which is scaled by H. The fluid is assumed to occupy the domain $\Omega(x,z)$, which is partly bounded by the channel exit ($x=0$), the free surface $z=h(x)$, and the plate ($z=0$). There are three important dimensionless groups that emerge, namely, the Reynolds number Re, Froude number Fr, and the aspect ratio ε:

$$\mathrm{Re}=\frac{\rho VH^2}{L\mu},\quad \mathrm{Fr}=\frac{V}{\sqrt{Lg}},\quad \varepsilon=\frac{H}{L} \tag{1}$$

where g is the gravitational acceleration in the downward vertical direction. L is determined after the aspect ratio of the problem is chosen. Assuming steady state conditions and neglecting terms of $O(\varepsilon^2)$ and higher, the dimensionless governing equations, namely, the continuity equation and the momentum equation in the x direction, reduce to

$$u_{,x}+w_{,z}=0 \tag{2}$$

$$uu_{,x}+wu_{,z}=-\varepsilon\frac{\cos\alpha}{\mathrm{Fr}^2}h_{,x}+\frac{1}{\mathrm{Re}}u_{,zz}+\frac{\sin\alpha}{\mathrm{Fr}^2} \tag{3}$$

where $u(x,z)$ and $w(x,z)$ are streamwise and depthwise velocity components, respectively. A subscript after a comma denotes partial differentiation. Re is sometimes referred to as the modified Reynolds number in BL or lubrication theory. Equation (3) was obtained upon combining the momentum conservation equations in the streamwise and depthwise directions. It is interesting to note that ε appears as similarity parameter for any inclination except for a flow down a vertical plane ($\alpha=\pi/2$).

The shape of the free surface is dictated by the kinematic condition

$$w(x,z=h)=u(x,z=h)h_{,x} \tag{4}$$

The relevant dynamic condition reads

$$u_{,z}(x,z=h)=0 \tag{5}$$

Note that another dynamic condition is the vanishing of the pressure at the free surface. The no-slip and no-penetration conditions at the wall give

$$u(x,z=0)=w(x,z=0)=0 \tag{6}$$

Flow conditions at the channel exit are assumed to be known. The condition on velocity is generally given by $u(x=0,z)=u_0(z)$. Three types of exit conditions on the velocity will be examined, namely, parabolic, semiparabolic, and uniform velocity profiles across the channel exit, which are given, respectively, by

$$u(x=0,z)=6z(1-z) \tag{7a}$$

$$u(x=0,z)=\frac{3}{2}z(2-z) \tag{7b}$$

$$u(x=0,z)=1 \tag{7c}$$

The film height is assumed to be fixed at the channel exit. Thus,

$$h(x=0)=1 \tag{8}$$

Equation (3) is of "BL" type, which must be solved subject to condition (6), one of the conditions (7*a*)–(7*c*) and condition (8).

3 Solution Procedure

Given the small thickness of the film, the governing equations are customarily depth averaged across the thickness. This step is justified on the basis that the flow field should not vary significantly in the z direction. However, the presence of the nonlinear convective terms in Eq. (3) prohibits the conduction of an exact averaging process. The key difficulty, of course, is the explicit z dependence of the velocity components. Even if the x and z dependencies are assumed to be decoupled, with a separation of variable-type argument becoming possible, the question remains as to the type of z dependence that u and w must have. Several types and levels of approximations have been used in literature, the most prominent of which is the assumption of the similarity solution semiparabolic profile [35]. Expectedly, the similar profile loses its validity when inertia becomes important. In this case, more formal treatments in the form of flow expansion in the z direction were suggested. In this work, Eq. (3) is further reduced by expanding the flow field in terms of appropriately chosen orthonormal modes in the z direction. Galerkin projection method is applied to generate the equations that govern the expansion coefficients. The procedure includes the depth-averaging technique as a limit case. The first step involves the mapping of a physical domain onto a straight strip. The following transformation is introduced, namely,

$$\chi(x,z)=x,\quad \xi(x,z)=\frac{z}{h(x)} \tag{9}$$

The physical domain $[0,x_e]\times[0,h(x)]$ is mapped onto a rectangular strip $[0,\chi_e]\times[0,1]$. Here, x_e is the length of the domain. The mapped governing equations become

$$hu_{,\chi}-h_{,\chi}\xi u_{,\xi}+w_{,\xi}=0 \tag{10}$$

$$u(hu_{,\chi}-h_{,\chi}\xi u_{,\xi})+wu_{,\xi}=-\varepsilon\frac{h}{\mathrm{Fr}^2}h_{,x}\cos\alpha+\frac{1}{h\,\mathrm{Re}}u_{,\xi\xi}+\frac{h}{\mathrm{Fr}^2}\sin\alpha \tag{11}$$

The streamwise velocity component u is represented in terms of orthonormal basis functions, $\Phi_i(\xi)$, such that

$$u(\chi,\xi)=\sum_{i=1}^{M}U_i(\chi)\Phi_i(\xi) \tag{12}$$

where M is the number of modes and $U_i(\chi)$ are the unknown expansion coefficients. The shape functions are taken to satisfy conditions (5) and (6) as well as orthonormality. Thus,

$$\Phi_i(\xi=0)=\Phi_{i,\xi}(\xi=1)=0,\quad \langle\Phi_i\Phi_j\rangle=\delta_{ij},\quad \forall\, i,j\in[1,M] \tag{13}$$

where δ_{ij} is the Kronecker delta and $\langle\ \rangle$ denotes the integral over $\xi\in[0,1]$. In this work, simple polynomials are used as shape functions. It has been previously proven that polynomial shape functions lead to high rate of convergence and fast accuracy [36]. First, four simple polynomials that satisfy conditions (13) are

$$\begin{aligned}
\Phi_1&=\sqrt{\frac{15}{8}}\xi(\xi-2)\\
\Phi_2&=\sqrt{\frac{42}{13}}\left(8\xi^3-61\xi^2+\frac{13}{2}\xi\right)\\
\Phi_3&=\sqrt{\frac{13}{22}}\left(105\xi^4-\frac{3108}{13}\xi^3+\frac{4293}{26}\xi^2-33\xi\right)\\
\Phi_4&=\sqrt{\frac{12{,}204{,}867}{22}}\left(-\frac{1056}{2017}\xi^5+\frac{2865}{2017}\xi^4-\frac{2692}{2017}\xi^3+\frac{1}{2}\xi^2-\frac{121}{2017}\xi\right)
\end{aligned} \tag{14}$$

The depthwise velocity component is obtained by substituting Eq. (12) into Eq. (10) and integrating the latter over the interval $[0,\xi]$ to give

Downloaded 03 Jun 2010 to 171.66.16.157. Redistribution subject to ASME license or copyright; see http://www.asme.org/terms/Terms_Use.cfm

$$w(\chi,\xi)=\sum_{i=1}^{M}\left[h_{,\chi}(\xi\Phi_i-\varphi_i)U_i-h\varphi_i U_{i,\chi}\right] \tag{15}$$

where $\varphi_i(\xi)=\int_0^\xi \Phi_i d\xi$. Upon use of expressions (12) and (15), the kinematic condition (4) becomes

$$h_{,\chi}=-\frac{h\Sigma_{i=1}^{M}U_{i,\chi}\langle\Phi_i\rangle}{\Sigma_{i=1}^{M}U_i\langle\Phi_i\rangle} \tag{16}$$

A hierarchy of equations is obtained for the coefficients $U_i(\chi)$, when expressions (12), (15), and (16) are substituted into the momentum equation (11), which is then multiplied by $\Phi_{i\geq 1}$ and integrated over $\xi\in[0,1]$. Thus, the set of equations is

$$\sum_{k=1}^{M}\left[\sum_{j=1}^{M}\langle\Phi_i(\Phi_j\Phi_k-\Phi_{j,\xi}\varphi_k)\rangle U_j + \frac{\langle\Phi_k\rangle}{\Sigma_{m=1}^{M}\langle\Phi_m\rangle U_m}\left(\sum_{j=1}^{M}\sum_{r=1}^{M}\langle\Phi_i\varphi_j\Phi_{r,\xi}\rangle U_r U_j - \frac{\varepsilon\langle\Phi_i\rangle}{\mathrm{Fr}^2}h\cos\alpha\right)\right]U_{k,\chi}=\frac{1}{h^2\,\mathrm{Re}}\sum_{j=1}^{M}\langle\Phi_i\Phi_{j,\xi\xi}\rangle U_j+\frac{\langle\Phi_i\rangle}{\mathrm{Fr}^2}\sin\alpha \tag{17}$$

Equations (16) and (17) reflect a system of nonlinear differential equations with $M+1$ degrees of freedom. The boundary conditions are deduced from Eqs. (7*a*)–(7*c*), (8), and (12), leading to

$$U_i(\chi=0)=6\langle\xi(1-\xi)\Phi_i\rangle \tag{18a}$$

$$U_i(\chi=0)=\frac{3}{2}\langle\xi(2-\xi)\Phi_i\rangle \tag{18b}$$

$$U_i(\chi=0)=\langle\Phi_i\rangle \tag{18c}$$

$$h(\chi=0)=1 \tag{19}$$

The solution of systems (16) and (17) subject to conditions (18*a*)–(18*c*) and (19) is solved by using a sixth order Runge–Kutta integration in the streamwise direction. The solution procedure is validated in the next section by assessing the convergence of expansions (12) and (15). A more direct comparison with results based on conventional methods, such as the finite-element method, would be difficult because of the small thickness of the film. An excessively large number of mesh elements is needed to ensure a reasonable aspect ration and avoid ill conditioning.

4 Results and Discussion

The methodology above is now applied to determine the flow field and film profile. The validity and accuracy of the solution procedure are first assessed by examining a simplified problem for which an exact solution exists. Some further numerical validation is then carried out for the full film flow problem. The effect of exit conditions on the flow is then examined in some detail. The influence of gravity is particularly emphasized in this study for film flow over horizontal and vertical walls.

4.1 Numerical Validation: A Test Problem. In order to validate the proposed numerical method, a simplified test problem is first examined where an exact solution is possible to obtain. This test problem is based on a simplified version of Eq. (3). It is assumed that the depthwise velocity component w is negligible everywhere. Gravity is also assumed to be negligible. With these assumptions, Eq. (3) reduces to

$$uu_{,x}=\frac{1}{\mathrm{Re}}u_{,zz} \tag{20}$$

The equation is of the convective-diffusive type. Note that the continuity and momentum conservation equations are decoupled in this case. Equation (20) is solved subject to the following boundary conditions:

$$u(x,z=0)=u_{,z}(x,z=1)=0,\quad u(x=0,z)=1 \tag{21}$$

Unlike in the full film flow problem, the physical domain is here a rectangle $[0,10]\times[0,1]$ in the x and z directions, respectively. Thus, $h(x)=1$. The Reynolds number is set to be equal to 100. The influence of the number of modes is illustrated in Fig. 2, where $u(x=10,z)$ is plotted against the height, z, for the range $M\in[1,7]$. The exact solution obtained using MATLAB (solver PDEPE) is included for comparison. The figure shows that the solution based on $M=1$ leads only to qualitative agreement. The rate of convergence is found to be rapid, except perhaps near the boundary $z=1$. The difference between successive solutions decreases rapidly and becomes essentially negligible for $M=3$ and 4.

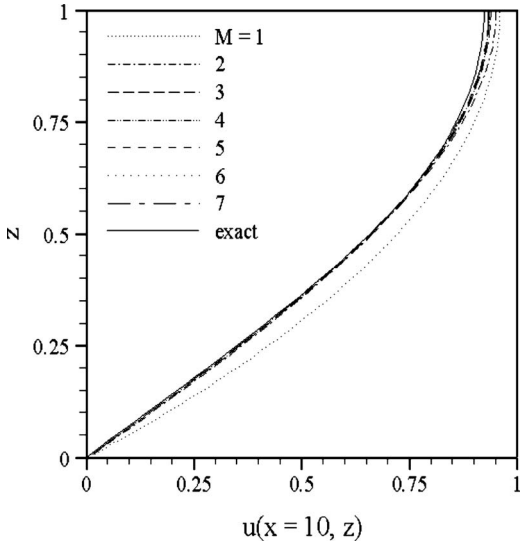

Fig. 2 Influence of the number of modes on the streamwise flow. The figure shows *u* profiles across the thickness of the film at *x*=10. Exact solution obtained by MATLAB is also included.

In order to assess the rate of convergence, the criterion for convergence is set up with regard to the kinetic energy contained in the flow field. The kinetic energy of the streamwise component of velocity field, E_u, is defined as

$$E_u=\left|\int_0^{10}\left[\int_0^{h(x)}u^2(x,z)dz\right]dx\right|^{1/2} \tag{22}$$

The contribution of the number of modes to the kinetic energy defined in Eq. (22) can be measured by the ratio

$$I_u^M=\frac{E_u^M}{E_u} \tag{23}$$

where

$$E_u^M=\left|\int_0^{10}\left[\int_0^{h(x)}u_M^2(x,z)dx\right]dz\right|^{1/2} \tag{24}$$

u_M being the streamwise velocity based on M modes. In this case, E_u is taken as exact. If M tends to infinity, I_u^M will approach 1. Therefore, $I_u^M=1$ is taken as the convergence criterion for the flow, and will be referred to as the energy ratio criterion. This criterion is conservative as it gives relative error control and guarantees that the relevant characteristics of the flow field are calculated with high accuracy. In general, E_u is unknown, but it can be determined approximately by taking a large enough number of modes and computing E_u^M until the difference between two suc-

Downloaded 03 Jun 2010 to 171.66.16.157. Redistribution subject to ASME license or copyright; see http://www.asme.org/terms/Terms_Use.cfm

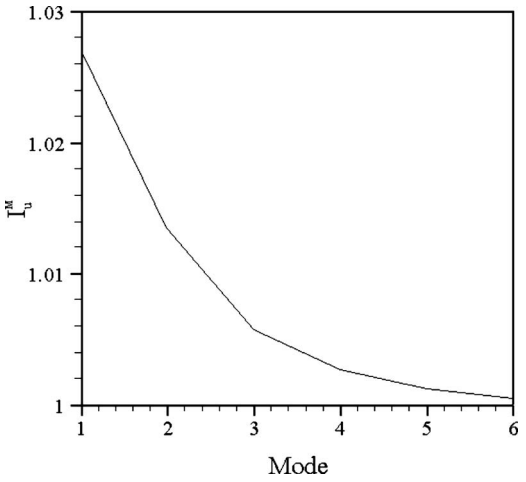

Fig. 3 Convergence assessment based on the energy ratio criterion. The figure shows the relationship between velocity *u* convergence criterion I_u^M and the mode number *M*.

cessive values is small: $|E_u^M - E_u^{M-1}| \leq \delta$, where δ is small and positive. In this work, δ is set to be equal to 0.01. Convergence of results of the spectral method is illustrated in Fig. 3, which is based on the energy ratio criterion. In the figure, the ratio I_u^M is plotted against the mode number M. With an increase in the number of modes, I_u^M exponentially approaches 1 as expected. The advantage of the convergence assessment using energy ratio criterion is that the criterion provides the information regarding the entire flow domain and not only in part as shown in Fig. 2, where the convergence is demonstrated for certain location. Moreover, Fig. 3 accounts directly for the weight of the mode number in the convergence. For example, one can obtain the information that as $M=2$, the streamwise velocity u overestimates its actual value by 1.3%; as M increases to 4, the error reduces to 0.2%; and as $M=6$, the actual value is overestimated by less than 0.01%. The validation of the current method is further assessed below when thin-film flow is examined.

4.2 Influence of Exit Conditions. Consider now the steady state flow emerging from the channel as illustrated schematically in Fig. 1, with the inclination angle α set equal to zero. Assume high-inertia flow with negligible gravity. The velocity profile at the channel exit is either parabolic (condition (7*a*)), semiparabolic (condition (7*b*)), or uniform (condition (7*c*)) across the channel. These three exit conditions can be encountered in industrial processes such as coating and extrusion. In general, the velocity profile of a fluid exiting a channel under a pressure gradient is parabolic. The semiparabolic velocity profile represents the velocity of a fluid exiting a channel, with its upper wall lubricated. If both upper and lower walls are lubricated, the resulting flow across the channel is uniform. Alternatively, a free jet impinges on the solid substrate with uniform velocity. The film profile and flow field are calculated from the channel exit onward. The influence of exit conditions on the flow is now examined. The solution is based on six modes. It is shown below that this level of truncation leads to acceptable accuracy.

Consider first the flow of a film with parabolic velocity profile at $x=0$, as given by condition (7*a*). The influence of inertia on such flow is illustrated in Fig. 4. The thickness profiles are plotted against position for $\mathrm{Re} \in [25, 100]$ (Fig. 4(*a*)). The flow strength and shear-stress distributions are shown for $\mathrm{Re}=25$ in Figs. 4(*b*) and 4(*c*), respectively. Figure 4(*a*) shows that the film experiences a depression near the channel exit and then monotonically increases in thickness with position further downstream. The depression is the result of the jump in u at $x=0$, which in turn leads to a drop in w from zero, causing the film surface to contract. For

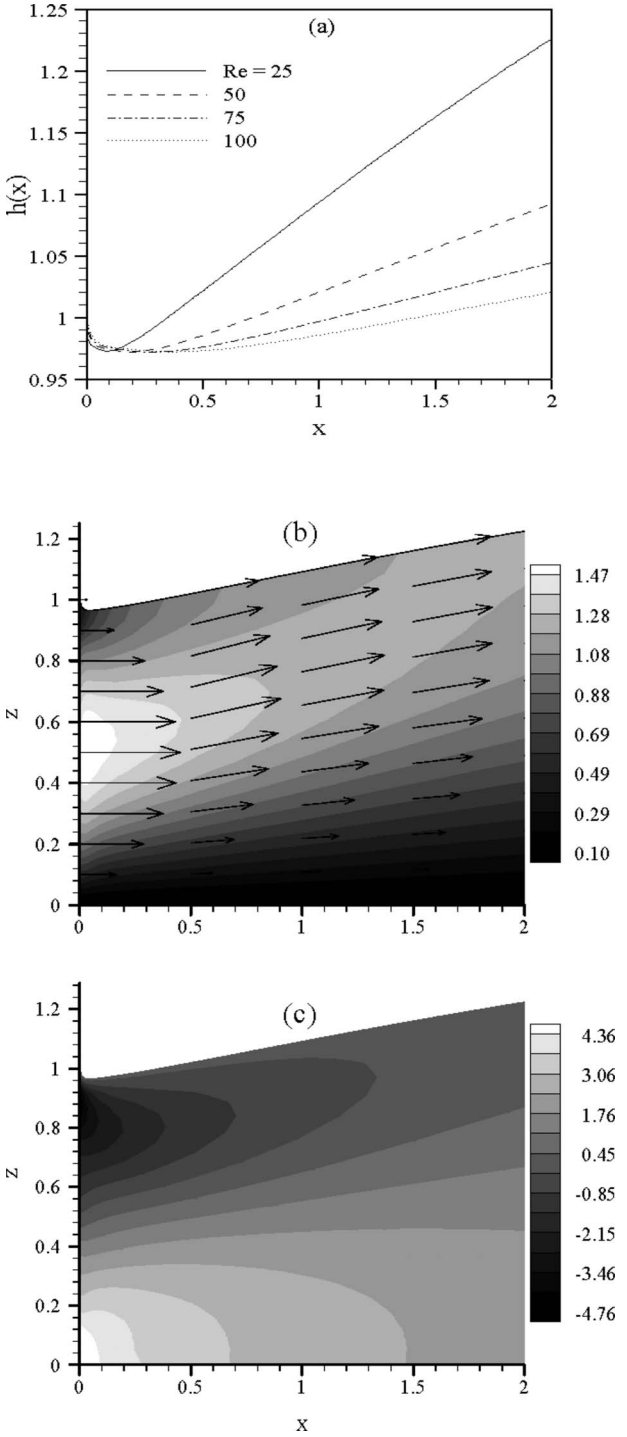

Fig. 4 Influence of inertia on the film height of the flow at Re $\in$ [25,100] subject to the parabolic exit condition (*a*). Flow field with contours of the velocity magnitude (*b*) and shear-stress distribution (*c*) at Re=25. Gravity is neglected.

flow with higher inertia, the jump in velocity becomes less significant, leading to weaker minimum in surface depression and further shift from the exit. Expectedly, with an increase in inertia, the slope of the height downstream of the depression decreases. This simultaneously demonstrates that a film with weak inertia tends to accumulate near the exit. Figure 4(*b*) indicates that the maximum in velocity tends to remain in the middle of the film near the channel exit, and slightly increases near the channel exit as a result of film contraction. As the fluid moves further down-

Downloaded 03 Jun 2010 to 171.66.16.157. Redistribution subject to ASME license or copyright; see http://www.asme.org/terms/Terms_Use.cfm

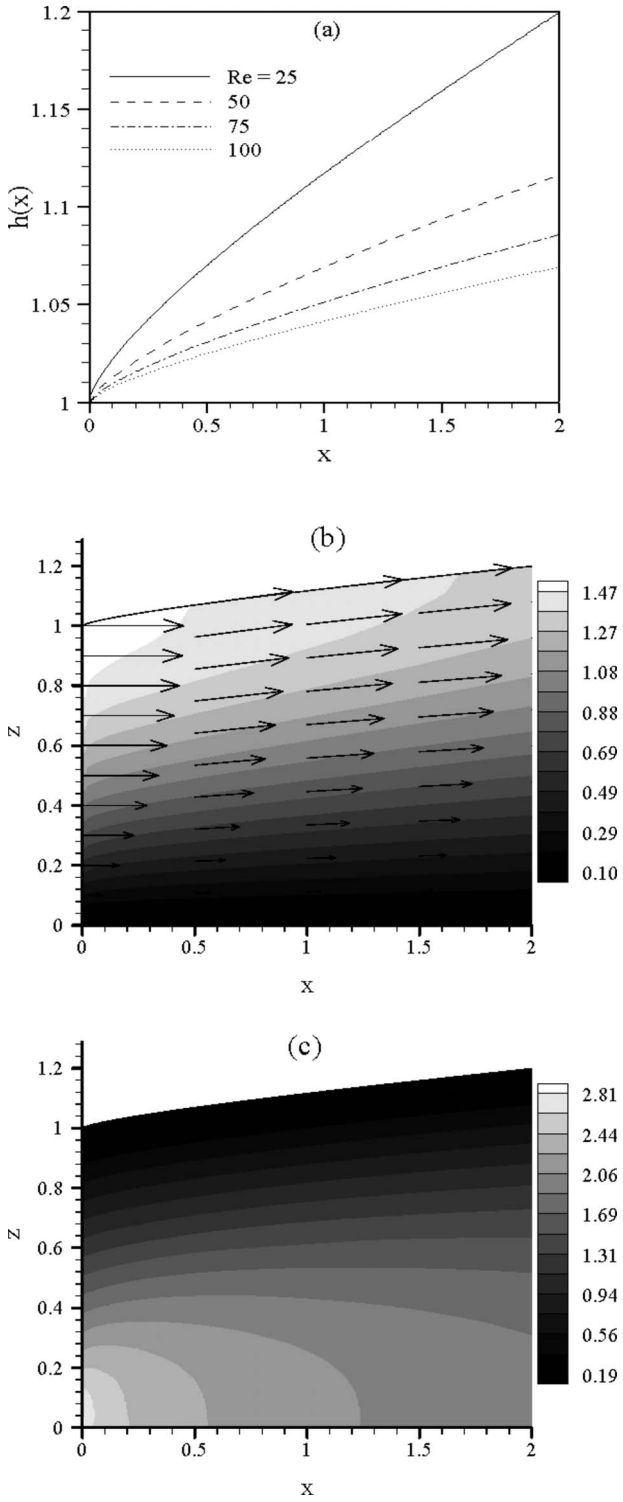

Fig. 5 Influence of inertia on the film height of the flow at Re $\in[25,100]$ subject to the semiparabolic exit condition (*a*). Flow field with contours of the velocity magnitude (*b*) and shear-stress distribution (*c*) at Re=25. Gravity is neglected.

stream, the velocity profile gradually changes from parabolic to semiparabolic, and the velocity maximum moves toward the free surface. This change in position is also reflected in the shear-stress distribution depicted in Fig. 4(*c*). While values of shear stress at the exit are positive in the lower region and negative in the upper region of the film, with distance they become positive across the whole film, suggesting that for a given position x the streamwise velocity does not decrease with z.

Some changes in flow are observed, compared to the previous case, when the velocity profile at the exit is assumed to be semiparabolic, as given by condition (7*b*). The film height, velocity, and stress distributions are shown in Fig. 5 for the same range of Reynolds number as before. In contrast to the case with condition (7*a*), the height of the film increases monotonically with distance from the exit. It is found that in the case with condition (7*b*), the film is generally thinner, except near the channel exit. The absence of film contraction is due to the relatively mild jump in u at $x=0$. In fact, there is a weak drop in $u(x=0,z)$ with x, which causes the swell. In this case, the maximum velocity is always at the free surface. Values of the shear stress are positive anywhere in the flow domain, and not only far downstream as in the previous case. The shear stress decreases with increasing z for any x position. In fact, the shear stress is highest at $z=0$, similar to BL flow over a flat plate.

Figure 6 shows the profiles for the uniform exit velocity across channel, as given by condition (7*c*), of the film height along x, flow field, and shear-stress distribution. Similar to the case with condition (7*b*), the film height monotonically increases, while the slope of the free surface decreases with distance, eventually reaching a constant value far from the channel exit. It is observed that the slope in all three cases reaches essentially the same value far downstream from the channel exit. However, the growth in height near the channel exit is significantly larger compared to both cases with condition (7*a*) and (7*b*). In contrast to the two previous cases, the film height near the channel exit is mostly influenced by elongational effect in the flow at the lower wall. The jump in flow velocity at the free surface does not seem to have a significant influence. Since the velocity profile at the exit is uniform (plug flow), the streamwise velocity experiences a sudden drop at $x=z=0$, which in turn causes a jump in the depthwise velocity, and thus an abrupt increase in film height near the channel exit. The slope of the film thickness at $x=0$ is therefore greater than in the two previous cases. It is observed from the flow field displayed in Fig. 6(*b*) that the maximum velocity in the domain is 1.09, which is the smallest of the three cases (compare with Figs. 4(*b*) and 5(*b*)). The abrupt change in velocity causes the shear stress to experience a strong and localized maximum at $x=z=0$ (see Fig. 6(*c*)), which is one order of magnitude higher than in the two previous cases.

So far, all flow results reported are based on six modes. The accuracy assessment of the test problem solution in Sec. 4.1 indicates that this level of truncation is expected to be acceptable. Convergence of the solution for the full flow problem is now examined using the energy ratio criterion defined earlier and the conservation of mass criterion. The results for the three exit conditions are displayed in Fig. 7. In Fig. 7(*a*), where I_u^M is plotted against the number of modes, for $M\in[1,6]$. The fastest convergence is observed in the case with condition (7*b*), and the slowest convergence is found when condition (7*c*) is used. While the relative error in the case with condition (7*b*) is less than 1% for solution based on as few as two modes, a comparable accuracy for the case with condition (7*c*) is obtained upon including at least six modes. It is also interesting to note from the figure that while convergence is monotonic in cases of semiparabolic and uniform exit conditions, it is oscillatory when the exit condition is parabolic.

Further assessment of accuracy is made by examining the conservation of mass. The exact volume flow rate at the channel exit is compared to the numerically obtained value at the end of the computational domain. Figure 7(*b*) shows the relative error resulting from the lack of mass conservation for $M\in[1,7]$. In general, the error monotonically decreases with M for all three exit conditions. The results confirm the presence of a strong correlation with the results in Fig. 7(*a*). The least accurate solution is again the one corresponding to condition (7*c*), exhibiting a relative error of 1.28% for a solution based on seven modes. Results for the case

Downloaded 03 Jun 2010 to 171.66.16.157. Redistribution subject to ASME license or copyright; see http://www.asme.org/terms/Terms_Use.cfm

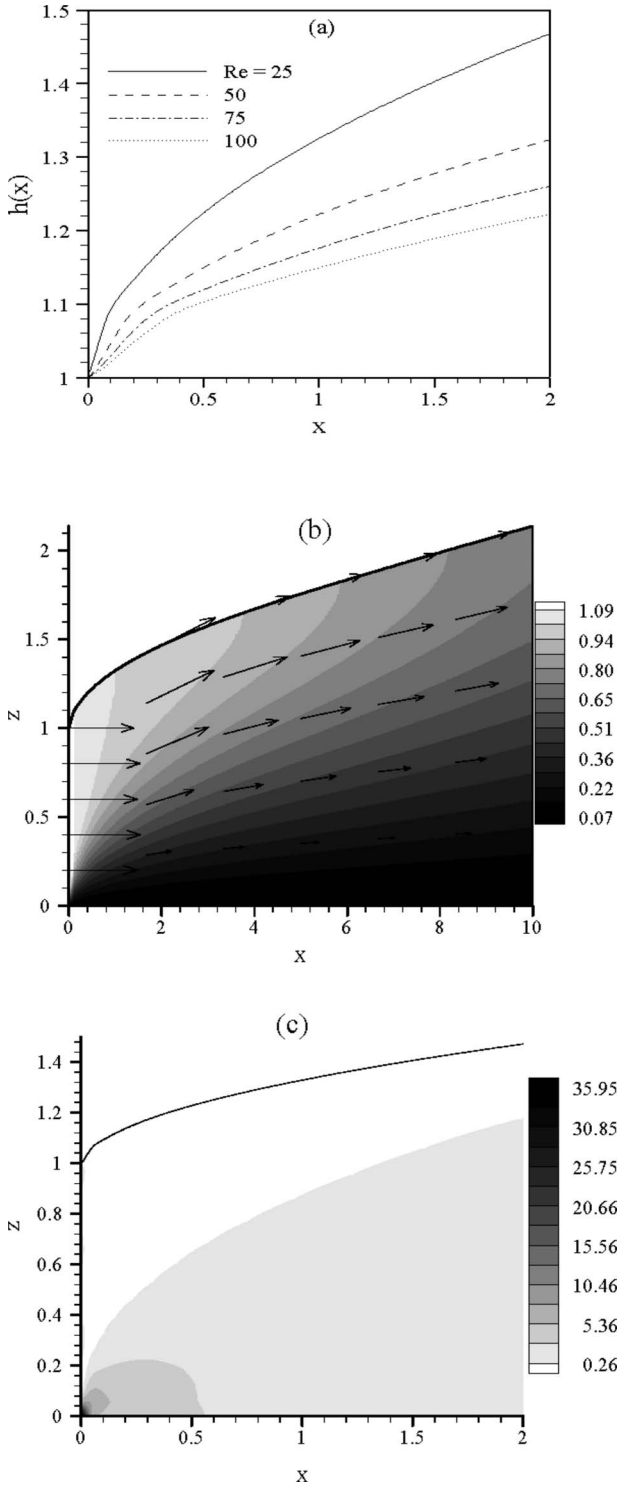

Fig. 6 Influence of inertia on the film height of the flow at Re $\in[25,100]$ subject to the uniform exit condition (*a*). Flow field with contours of the velocity magnitude (*b*) and shear-stress distribution (*c*) at Re=25. Gravity is neglected.

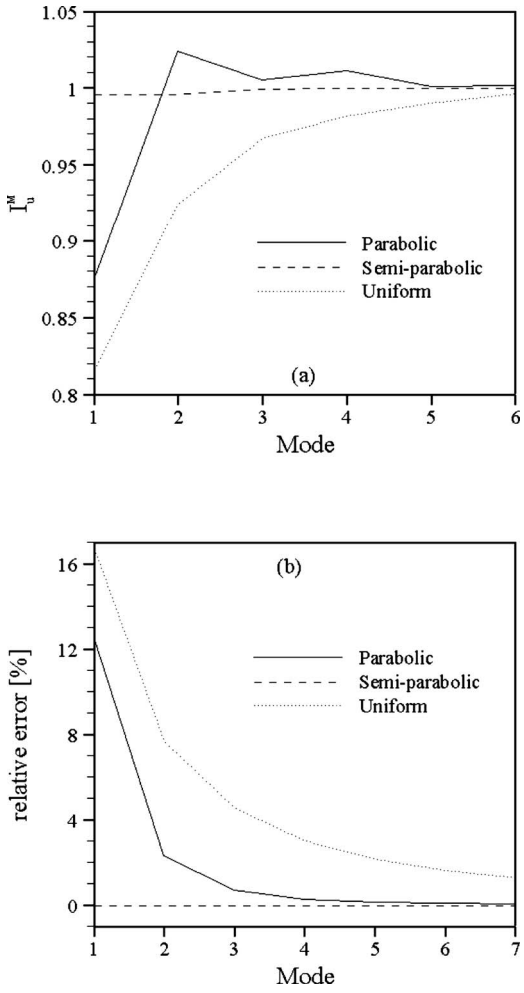

Fig. 7 Convergence assessment based on the energy ratio criterion. The figure shows the relationship between velocity *u* convergence criterion I_u^M and the mode number *M* for the parabolic, semiparabolic, and uniform exit conditions (*a*). Error assessment based on the conservation of mass (*b*).

with condition (7*a*) are considerably more accurate, reflecting a relative error of only 0.03%. The relative error due to the loss of mass for the case with condition (7*b*) is less than 0.01%, which is, expectedly, the most accurate of all three cases.

Finally, assessment of accuracy can be made by comparing the results against Watson's similarity solution [8]. Watson examined the spreading of a liquid jet impinging on a flat solid substrate. The two-dimensional similarity solution is assumed to be valid far from the channel exit. The slope of the free surface predicted by Watson is 1.813. Khayat and Welke [25] calculated the value of slope of the height far downstream from the channel exit (for parabolic velocity profile at the exit) and compared it with Watson's result. Their solution overestimated Watson's by 7%. The present calculations indicate that the slope of the height far downstream based on seven modes is in good agreement with that of Watson [8] for all three exit conditions. More specifically, for the cases with conditions (7*a*) and (7*b*), the slope of the height far downstream is 1.814 (relative error of 0.06%), and for the case with condition (7*c*), it is 1.834 (relative error of 1.16%). The error is found to decrease further if a higher number of modes is included.

Based on the convergence and accuracy tests above, it is concluded that not more than six modes are needed to secure a reasonably accurate solution. Therefore, all the results reported in this study are based on $M=6$ unless stated otherwise.

4.3 Influence of Gravity. The role of gravity is now examined for a flow with relatively high inertia. Gravity is found to have an intricate effect on the film flow, as will be seen below. Results of the converged solution will be first examined for the flow down a vertical wall. The solution based on one mode is then obtained analytically, and will then be examined in detail in order

Downloaded 03 Jun 2010 to 171.66.16.157. Redistribution subject to ASME license or copyright; see http://www.asme.org/terms/Terms_Use.cfm

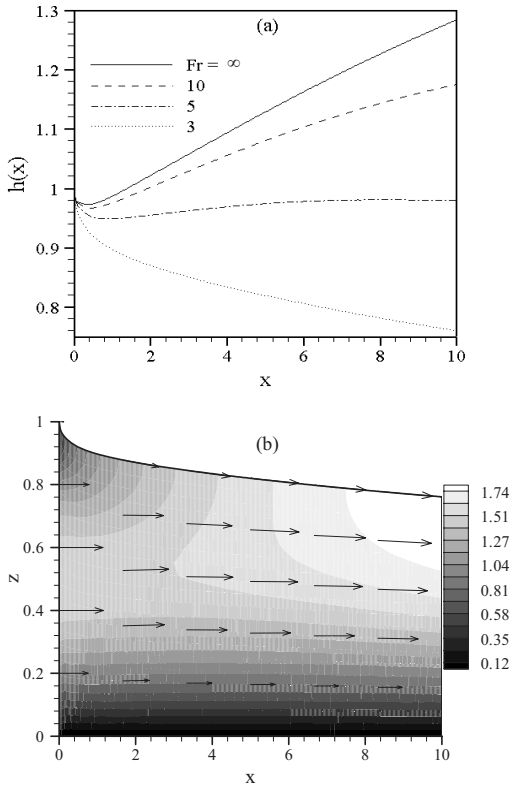

Fig. 8 Influence of gravity on the film height for $Fr \in [3, \infty)$, Re=100, and $\alpha = \pi/2$ (*a*). Flow field with contours of the velocity magnitude for Fr=3 (*b*). The exit condition is parabolic.

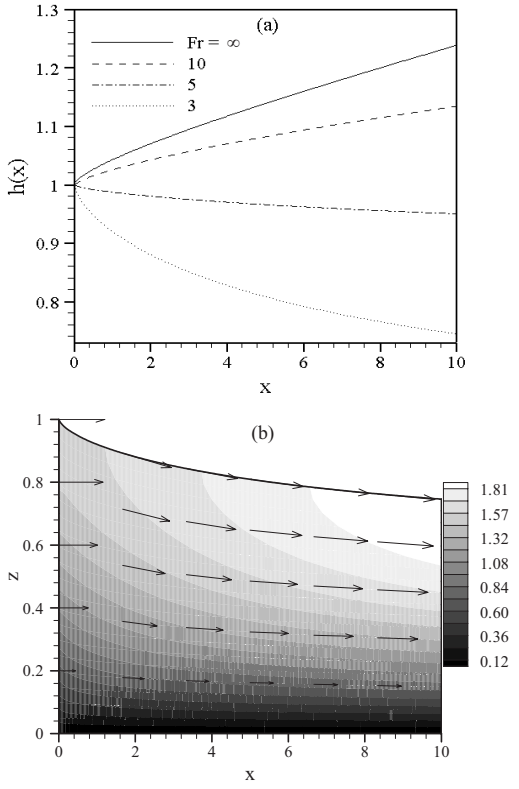

Fig. 9 Influence of gravity on the film height for $Fr \in [3, \infty)$, Re=100, and $\alpha = \pi/2$ (*a*). Flow field with contours of the velocity magnitude for Fr=3 (*b*). The exit condition is semiparabolic.

to decipher the origin of the intricate effect that gravity has on film flow over a horizontal wall. Analysis of results based on the converged solution is then carried out. The interplay between the influence of exit conditions and gravity on the two types of flow is also examined.

4.3.1 Flow Down a Vertical Wall. Consider the flow down a vertical wall ($\alpha = \pi/2$) at relatively high inertia (Re=100). Recall that ε is not a relevant parameter in this case. The influence of gravity on such flow is first examined subject to condition (7*a*). Results calculated based on the converged solution are shown in Fig. 8. The film height is shown for $Fr \in [3, \infty)$ in Fig. 8(*a*) and the flow field is shown for Fr=3 in Fig. 8(*b*). Figure 8(*a*) indicates that the film experiences a contraction in thickness for any Froude number. In the absence of gravity, the contraction is localized near the channel exit in the form of a minimum in film height; the film thickness increases with position further downstream. As gravity effect increases, the minimum weakens, and the film thickness is considerably reduced with gravity. It is interesting to note that the slope of the surface at the exit does not change significantly with gravity. Thus, gravity tends to inhibit the growth of the film height with position. At some critical value (roughly Fr=5), the film tends to remain flat with position, particularly further downstream from the channel exit. When $3 < Fr < 10$, the profile of the film height exhibits a maximum at a position downstream from the channel exit (here illustrated by the Fr=5 curve). When Fr decreases further, the local maximum weakens and eventually disappears as it is shown for Fr=3 in the figure. Unlike for higher Fr, the behavior of the film thickness with distance is monotonic in the whole domain. The flow field displayed in Fig. 8(*b*) for Fr =3 shows a gradual change of the velocity profile from parabolic at the exit to semiparabolic at $x \approx 4$. Expectedly, the velocity of the film increases with gravity. Upon comparing Figs. 8(*b*) and 4(*b*), the velocity maximum is seen to have increased as a result of the contraction, and is no longer located at the channel exit.

Figure 9 depicts the situation corresponding to the flow subject to condition (7*b*). Figure 9(*a*) shows that, in contrast to the flow in Fig. 8, the slope of the film height at the channel exit changes significantly with gravity; the film contraction is experienced right at $x=0$ for Fr less than 5. As a result, the film thickness changes with position monotonically for any value of the Froude number. Figure 9(*b*) shows that the velocity profile across the film is essentially self-similar. Compared with the previous case, the maximum velocity is slightly higher as a result of higher film contraction.

Consider finally the flow subject to condition (7*c*), which is depicted in Fig. 10. When gravity is negligible or very small ($Fr > 10$), Fig. 10(*a*) shows that the height increases monotonically with distance similarly as in the case with condition (7*b*). However, for Fr=5, as opposed to the two previous cases, the height of the film rises from the exit until it reaches a maximum at $x \approx 2$ and then gradually decreases. When gravity effect is even further enhanced (Fr=3), the maximum decreases in magnitude and shifts upstream ($x \approx 0.5$). The flow field for Fr=3 is depicted in Fig. 10(*b*) and should be compared with Figs. 8(*b*) and 9(*b*), corresponding to conditions (7*a*) and (7*b*), respectively. Figure 10(*b*) shows that the velocity profile changes gradually from uniform to semiparabolic. The swelling near the exit slows down the flow in the streamwise direction. Thus, when compared with the two previous cases, the flow is slowest; the maximum velocity is only 1.63 compared to 1.74 and 1.81. In summary, for a film subject to gravity in the streamwise direction, the effect of exit conditions is only felt close to the exit. Generally, gravity tends to always contract the flow downstream from the exit.

Downloaded 03 Jun 2010 to 171.66.16.157. Redistribution subject to ASME license or copyright; see http://www.asme.org/terms/Terms_Use.cfm

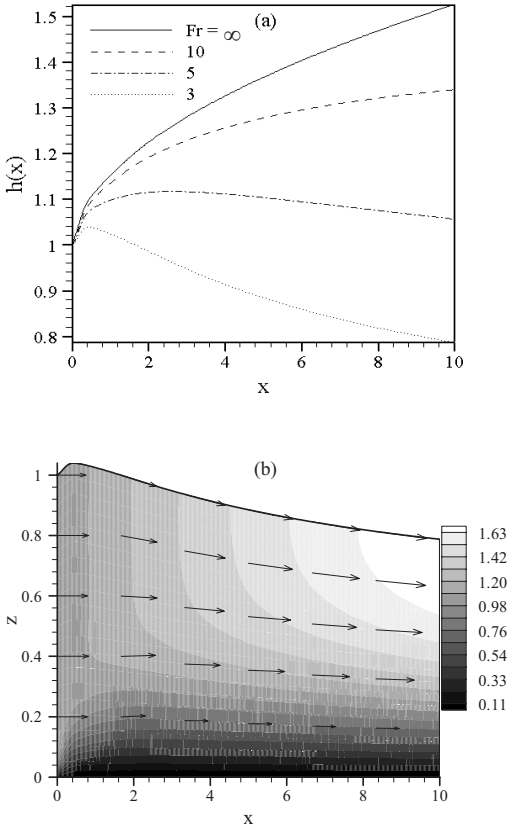

Fig. 10 Influence of gravity on the film height for $\mathrm{Fr}\in[3,\infty)$, $\mathrm{Re}=100$, and $\alpha=\pi/2$ (*a*). Flow field with contours of the velocity magnitude for $\mathrm{Fr}=3$ (*b*). The exit condition is uniform.

4.3.2 Leading-Order Solution. It was established above that, in the absence of gravity, only few modes are needed to secure convergence and reasonable accuracy. In particular, the solution based on one mode is qualitatively similar to the converged solution. However, in the presence of gravity, the solution exhibits sharp gradients in flow velocity and film shape, leading to flow singularity for pressure-driven horizontal film flow. In order to investigate the nature of this singularity, the solution based on one mode will be considered in some detail since an analytical solution is possible to obtain. This allows a preliminary exploration of the qualitative interplay between gravity and driving pressure. Consider first the one-mode solution for a flow subject to any inclination. In this case, $U_{i>1}(x)$ are set equal to zero, and the equations for $h(x)$ and $U(x)\equiv U_1(x)$ are obtained by keeping only one mode in Eqs. (16) and (17), which reduce to

$$h_{,x}=-\frac{hU_{,x}}{U} \tag{25}$$

$$\left[\langle\Phi\Phi\Phi\rangle U-\frac{\varepsilon\langle\Phi\rangle}{U\mathrm{Fr}^2}h\cos\alpha\right]U_{,x}=\frac{1}{h^2\,\mathrm{Re}}\langle\Phi\Phi_{,\xi\xi}\rangle U+\frac{\langle\Phi\rangle}{\mathrm{Fr}^2}\sin\alpha \tag{26}$$

where $\Phi\equiv\Phi_1$. Equation (25) is readily integrated to give a relation between $U(x)$ and the film height $h(x)$, namely,

$$h(x)=\frac{\langle u_0(z)\Phi\rangle}{U(x)} \tag{27}$$

where boundary condition (19) is applied. The numerator on the right-hand side of Eq. (27) is a constant and represents the mean velocity at the channel exit. This constant will be further denoted as K. Note that K is different for each of the exit conditions considered. The equation that governs $U(x)$ is obtained upon integrating Eq. (26) and using Eq. (27), namely,

$$K^2\,\mathrm{Re}\left[\frac{\varepsilon\cos\alpha}{K\,\mathrm{Re}\,U\sin\alpha}+(\varepsilon C\cos\alpha+AK\,\mathrm{Re}\sin\alpha)\mathrm{Fr}^2\left(-\frac{1}{3}\frac{\ln\left(U+\frac{K^2\,\mathrm{Re}\sin\alpha}{\mathrm{Fr}^2C}\right)^{1/3}}{\mathrm{Fr}^2C\left(\frac{K^2\,\mathrm{Re}\,B\sin\alpha}{\mathrm{Fr}^2C}\right)^{1/3}}\right.\right.$$
$$\left.\left.+\frac{1}{6}\frac{\ln\left(U^2-U\left(\frac{K^2\,\mathrm{Re}\,B\sin\alpha}{\mathrm{Fr}^2C}\right)^{1/3}+\left(\frac{K^2\,\mathrm{Re}\,B\sin\alpha}{\mathrm{Fr}^2C}\right)^{2/3}\right)}{\mathrm{Fr}^2C\left(\frac{K^2\,\mathrm{Re}\,B\sin\alpha}{\mathrm{Fr}^2C}\right)^{1/3}}+\frac{\sqrt{3}}{3}\frac{a\tan^{-1}\left(\frac{\sqrt{3}}{3}\left(\frac{2U}{\left(\frac{K^2\,\mathrm{Re}\,B\sin\alpha}{\mathrm{Fr}^2C}\right)^{1/3}}-1\right)\right)}{\mathrm{Fr}^2C\left(\frac{K^2\,\mathrm{Re}\,B\sin\alpha}{\mathrm{Fr}^2C}\right)^{1/3}}\right)\Bigg/(K\,\mathrm{Re}\sin\alpha)\Bigg]$$
$$=x+D \tag{28}$$

where $A=\langle\Phi\Phi\Phi\rangle=919/783$, $B=\langle\Phi\rangle=461/505$, $C=\langle\Phi\Phi_{,\xi\xi}\rangle=-2.5$, and D is an integration constant. For horizontal flow ($\alpha=0$), the solution (28) is considerably simplified and reduces to

$$K^2\left(\frac{1}{4}\frac{\varepsilon BK}{\mathrm{Fr}^2U^4}-\frac{A}{U}\right)=\frac{C}{\mathrm{Re}}x+\frac{1}{4}\frac{\varepsilon B}{K\mathrm{Fr}^2}-AK \tag{29}$$

The relation between the film height h and streamwise position x is obtained upon substitution of Eq. (27) into Eq. (29):

Downloaded 03 Jun 2010 to 171.66.16.157. Redistribution subject to ASME license or copyright; see http://www.asme.org/terms/Terms_Use.cfm

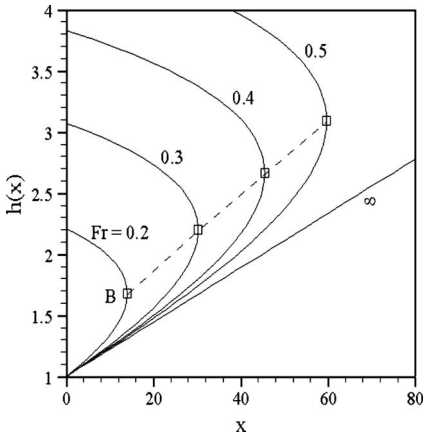

Fig. 11 Influence of gravity on the film height for $\mathrm{Fr} \in [0.2, \infty)$, $\mathrm{Re}=100$, $\alpha=0$, and $\varepsilon=0.01$. The exit condition is parabolic. The solution is based on one mode.

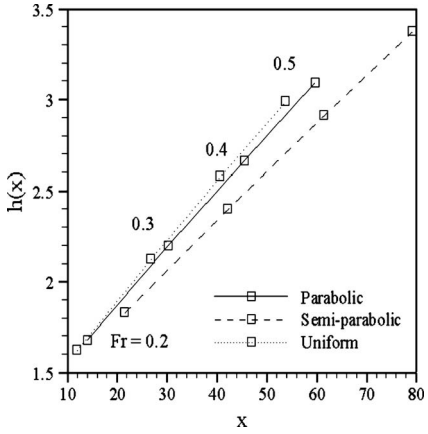

Fig. 12 Influence of gravity on position of a turning point for $\mathrm{Re}=100$, $\alpha=0$, and $\varepsilon=0.01$. The exit conditions are parabolic, semiparabolic, and uniform. The solution is based on one mode.

$$\frac{1}{4}\frac{\varepsilon B}{\mathrm{Fr}^2 K}h^4 - AKh = \frac{C}{\mathrm{Re}}x + \frac{1}{4}\frac{\varepsilon B}{\mathrm{Fr}^2 K} - AK \tag{30}$$

Note that, if gravity is neglected ($\mathrm{Fr}\to\infty$), the expression for film height can be obtained explicitly:

$$h = 1 - c\frac{x}{\mathrm{Re}} \tag{31}$$

where $c=B/AC=-2.22$. This expression is comparable to the similarity solution of Watson [8] for two-dimensional flow. In Watson's case, $c=-\pi/\sqrt{3}=-1.813$, which is smaller than the current value (based on one-mode only). It is evident from Eq. (31) that the film height grows linearly with distance. The situation is very different when gravity effect is considered. Although Eq. (30) is quartic, only two real solution branches exist.

Figure 11 illustrates the influence of gravity on film height for $\mathrm{Re}=100$, $\varepsilon=0.01$, and $\mathrm{Fr}\in[0.2,\infty)$. Although the results in the figure are based on condition (7*a*), other exit conditions lead to the same qualitative behavior. For finite Froude number, each curve in the figure displays a bifurcation diagram with a bifurcation or turning point, reflecting a nontrivial solution in h. The turning point divides the solution into two branches. Only the lower branch is expected to be physical. The upper branch leads to an unrealistic boundary condition at the channel exit ($x=0$). Thus, from a nonlinear dynamics perspective, the lower branch is expected to be stable and the upper branch unstable. The thickness of the film increases with distance as suggested by the lower branch. The film thickness at the turning points grows linearly with streamwise position. It is anticipated that the presence of the turning point indicates a significant change in the flow, which will be confirmed later when a more accurate solution is sought. The one-mode solution tends to give an accurate description of the flow when only the lower branch is focused on. As Fr increases, the turning point moves downstream and increases in height. The lower branches appear to be tangent at $x=0$ to the curve that corresponds to infinite Froude number. The film height decreases with Fr, reflecting the tendency of gravity to prohibit the film from flowing downstream from the channel exit.

Regarding the turning point, it is possible to obtain its locus analytically from Eq. (29):

$$h_B = \left(\frac{AK^2\mathrm{Fr}^2}{\varepsilon B}\right)^{1/3} \tag{32}$$

$$x_B = \frac{\mathrm{Re}}{C}\left(\frac{1}{4}\frac{\varepsilon B}{\mathrm{Fr}^2 K}\left(\left(\frac{AK^2\mathrm{Fr}^2}{\varepsilon B}\right)^{4/3} - 1\right) + AK\left(1 - \left(\frac{AK^2\mathrm{Fr}^2}{\varepsilon B}\right)^{4/3}\right)\right) \tag{33}$$

It is interesting to note that the film thickness at the turning point does not depend on Reynolds number cas suggested by Eq. (32). Figure 12 shows location of turning points in the h-x space for $\mathrm{Fr}\in[0.2,0.5]$ when parabolic, semiparabolic, and uniform exit conditions are considered. It is found that for a given Froude number, the distance of a turning point from the channel exit as well as the height is the largest for the flow with condition (7*b*) followed by turning points of flows with conditions (7*a*) and (7*c*) successively. Also, the slope of lines connecting turning points varies with exit conditions, being the largest for the flow with the uniform exit condition, followed by flows with parabolic and semiparabolic exit conditions successively. Influence of inertia on the film height is displayed in Fig. 13. The figure shows the situation for the flow with $\mathrm{Re}\in[25,100]$, $\mathrm{Fr}=0.4$, subject to exit condition (7*a*). While the height slope at the exit decreases, the downstream position of the turning point increases with Reynolds number. Equation (33) indicates that the streamwise position of a turning point depends on Re linearly. The picture is qualitatively the same for the other two exit conditions; thus, it is not included.

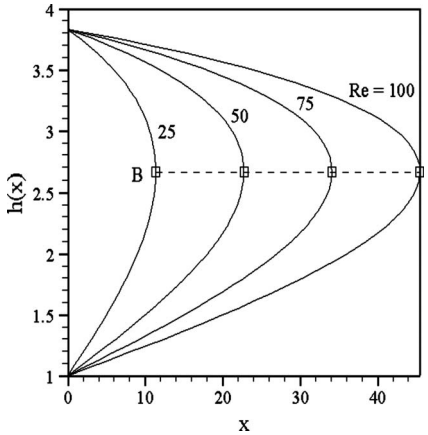

Fig. 13 Influence of inertia on the film height for $\mathrm{Re}\in[25,100]$ $\mathrm{Fr}=0.4$, $\alpha=0$, and $\varepsilon=0.01$. The exit condition is parabolic. The solution is based on one mode.

Downloaded 03 Jun 2010 to 171.66.16.157. Redistribution subject to ASME license or copyright; see http://www.asme.org/terms/Terms_Use.cfm

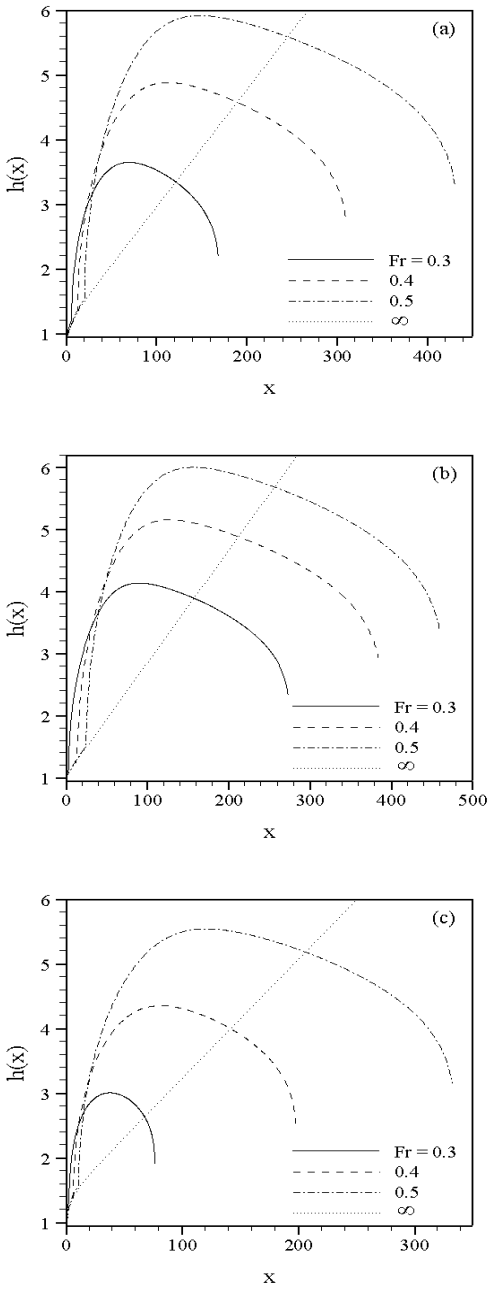

Fig. 14 Influence of gravity on the film height for $\mathrm{Fr} \in [0.3, \infty)$, $\mathrm{Re}=100$, $\alpha=0$, and $\varepsilon=0.01$. The exit conditions are (*a*) parabolic, (*b*) semiparabolic, and (*c*) uniform. The solution is based on six modes.

4.3.3 Flow Over a Horizontal Wall. The influence of gravity on the flow over a horizontal wall ($\alpha=0$) is now examined more accurately with the solution based on six modes. The aspect ratio ε is set equal to 0.01 and Re is fixed at 100, as in the leading-order solution above. The three types of exit conditions (7*a*)–(7*c*) are considered again. The film flow beyond the turning point, predicted by the leading-order solution, is examined. In fact, when higher-order modes are included, the turning point is "smoothed out" giving way to a jump in height. Figure 14 shows the film profile for $\mathrm{Re}=100$ and $\mathrm{Fr} \in [0.3, \infty)$ subject to exit conditions (7*a*)–(7*c*). In general, the flow exhibits the same qualitative behavior regardless of the exit condition used. However, there is a significant change in film shape resulting from gravity effect, which becomes particularly obvious upon comparing profiles that correspond to finite and infinite Froude numbers in Fig. 14. The film thickness increases linearly with x over most of the film domain when gravity effect is neglected. However, for finite Froude number, the film experiences a jump in thickness at some distance downstream from the channel exit. This jump corresponds to the turning point predicted by the leading-order solution. With higher number of modes, the jump location shifts upstream. Instead of exhibiting a turning point, the film continues to grow in height with streamwise position, forming a hydraulic jump. With distance, the slope of the height diminishes and the film height eventually experiences a weak maximum. Further downstream, the flow exhibits a shock, which is reflected by a sudden drop in film thickness. There are two distinct regions for flow behavior. In the region close to the exit, the film thickness increases significantly with gravity, and the location of the jump point shifts toward the channel exit as gravity effect increases. At some distance downstream $20 < x < 30$, the curves intersect, resulting in the reverse order. In the region far from the exit, the film height decreases with gravity, but the maximum in height tends to strengthen.

As mentioned earlier, the type of exit condition does not seem to affect the qualitative behavior of the flow; this is clear upon comparing Figs. 14(*a*)–14(*c*). The effect of exit condition is particularly noticeable in the location, x_{shock}, of the shock for a given Fr. For example, for $\mathrm{Fr}=0.5$, $x_{\mathrm{shock}} \approx 430$, 460, and 330 for flows subject to conditions (7*a*)–(7*c*), respectively. These values are in correlation with the position of the turning point in Fig. 12. A similar but much less noticeable effect is observed regarding the value of maximum height $h_{\max}$. Figure 15 shows the dependence of $h_{\max}$ (Fig. 15(*a*) and x_{shock} (Fig. 15(*b*)) on gravity and exit condition. Both maximum thickness and shock location exhibit an almost linear response against the Froude number.

The detailed flow field is typically illustrated in Fig. 16 for $\mathrm{Fr}=0.4$. The flow field and velocity contours, and the streamlines and shear-stress contours, for the flow subject to condition (7*a*), are displayed in Figs. 16(*a*) and 16(*b*), respectively. Figure 16(*a*) depicts a strong upward flow, right downstream from the jump point below the maximum height, which causes a significant decrease in streamwise flow. The flow regains strength further downstream as a result of film contraction. Not surprisingly, the shear stress varies mostly near the channel exit, over the range $0 < x < 50$, as suggested by Fig. 16(*b*). Particularly interesting is the region where the height rapidly increases, and where the shear stress across the film exhibits a maximum close to the free surface (and not at the rigid wall boundary), which suggests that the streamwise velocity component lost its semiparabolic character. The shear-stress distribution clearly suggests that downstream from the jump point, there is a region of maximum shear stress at about $\frac{3}{4}$ of the film thickness. In fact, as the streamlines in Fig. 16(*b*) indicate, recirculation (separation bubble) takes place at the jump. With distance, the maximum shear stress moves to the bottom of the film and it exhibits little variation with height.

The presence of the separation bubble is surprising at first, as it is not expected to be predicted by thin-film flow theory. This is certainly the case for sudden variation in bottom topography where the flow is of purely two-dimensional nature (see for instance, Kalliadasis et al. [37] and Khayat and Welke [25]). However, Kalliadasis et al. [37] solved the evolution equation for the film height derived from Stokes equations. They considered the surface-tension effect but neglected gravity. As a result, the pressure remains constant across the film for the thin-film flow. The pressure gradient is therefore also constant across the film, which eliminates the possibility of flow recirculation. To solve the flow over a bump, Khayat and Welke [25] used the same methodology as presented in this work. They included the effect of gravity and neglected the surface-tension effect. The streamwise velocity profile in their case consists of only one mode (parabolic); thus, the recirculation cannot be observed. An adverse pressure gradient

Downloaded 03 Jun 2010 to 171.66.16.157. Redistribution subject to ASME license or copyright; see http://www.asme.org/terms/Terms_Use.cfm

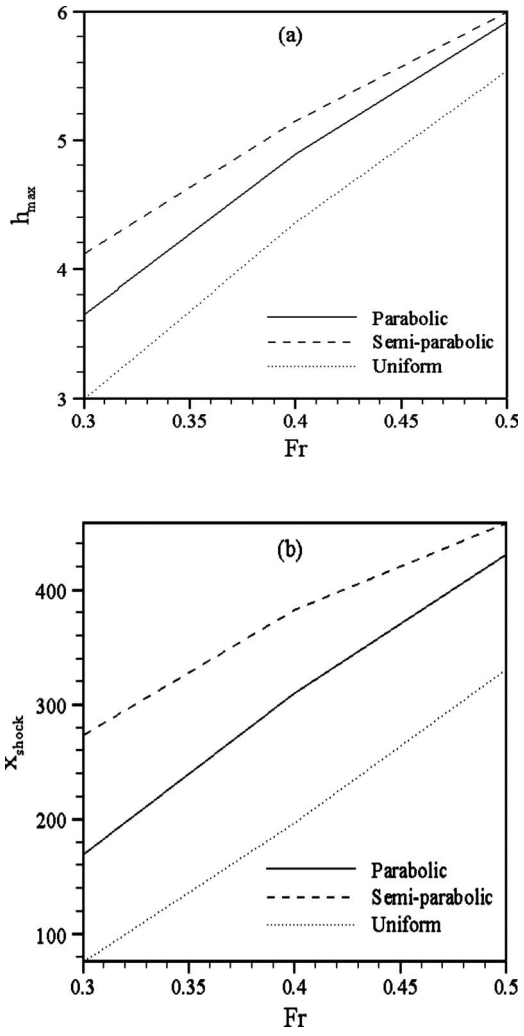

Fig. 15 Influence of gravity on position of (*a*) maximum height h_{max} and (*b*) shock x_{shock} for Re=100, α=0, and ε=0.01. The exit conditions are parabolic, semiparabolic, and uniform. The solution is based on six modes.

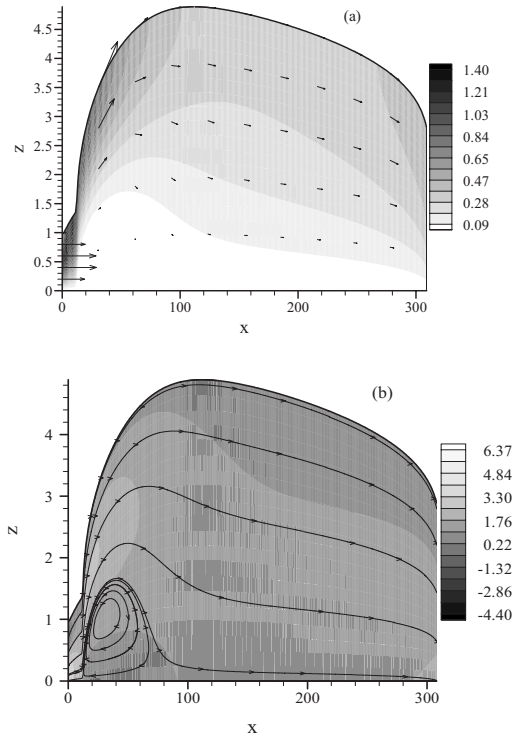

Fig. 16 Flow field and contours of velocity magnitude (*a*) and shear-stress distribution and streamlines (*b*) of flow at Re =100, Fr=0.4, α=0, and ε=0.01. The exit condition is parabolic.

5 Conclusion

Influence of exit boundary conditions and gravity on high-inertia flow is examined in this study. Thin-film flow of a Newtonian fluid over a flat plate is assumed for moderately high inertia. The flow emerges from a channel with parabolic, semiparabolic, or uniform flow conditions prevailing inside the channel. The thin-film equations are solved by expanding the flow field in orthonormal modes over the depth. The Galerkin projection is applied to generate the governing equations for the expan-

that causes the recirculation in the flow can be observed in the present results because of the gravity effect, and at the same time, the streamwise velocity profile allowing an inflection point.

Finally, the interplay between gravity and inertia effects is examined. In order to assess the effect of inertia, comparison is made against the results above for flow with strong gravity effect. Figure 17 shows the thickness distribution for $\mathrm{Re} \in [25, 100]$, and Fr=0.4, when the exit velocity is given by condition (7*a*). It is evident from the figure that the inertia has an opposite effect as gravity. The jump moves away from the channel exit as the inertia increases, which correlates with the position of the turning point in the leading-order analysis (compare with Fig. 13). Also, the change in the inertia of flow does not have any influence on the maximum thickness of the film, as the leading-order analysis indicated. The streamwise position of shock x_{shock} versus Reynolds number is plotted in Fig. 18 for the three types of exit conditions. Of the three cases for a given Re, x_{shock} occurs farthest from the channel exit for the flow with condition (7*b*), followed by the flows with conditions (7*a*) and (7*c*). The dependence of x_{shock} on Reynolds number is in all three cases linear as it is evident from the figure. Different slopes of lines in the figure suggest that the rate of change of x_{shock} with Re is largest for the flow subject to condition (7*b*) followed by flows subject to conditions (7*a*) and (7*c*).

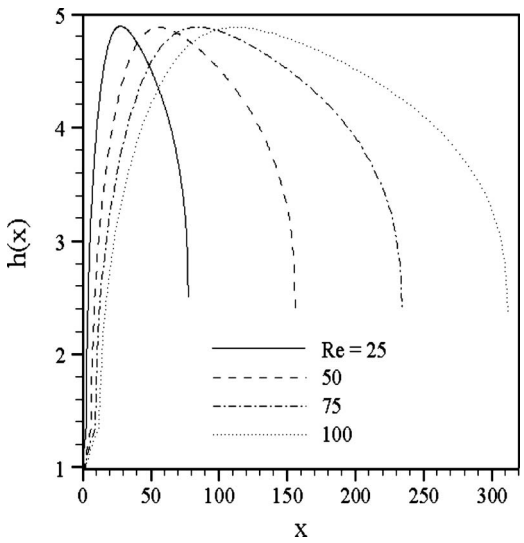

Fig. 17 Influence of inertia on the film height for Re $\in$[25,100], Fr=0.4, α=0, and ε=0.01. The exit condition is parabolic. The solution is based on six modes.

Downloaded 03 Jun 2010 to 171.66.16.157. Redistribution subject to ASME license or copyright; see http://www.asme.org/terms/Terms_Use.cfm

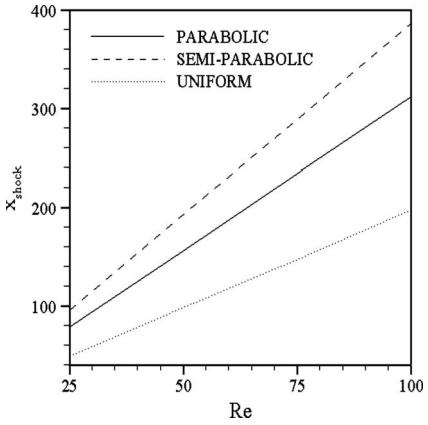

Fig. 18 Influence of inertia on position of x_{shock} for Re=100, α=0, and ε=0.01. The exit conditions are parabolic, semiparabolic, and uniform. The solution is based on six modes.

sion coefficients. A test problem of the convective-diffusive type is solved in order to compare results of the method proposed in this work. The accuracy and convergence are assessed by monitoring the conservation of mass as well as kinetic energy contained in the domain. The three considered channel exit conditions predict different behaviors of the flow, particularly near the channel exit. While for the parabolic velocity at the exit, the flow experiences near the exit a local contraction in the thickness, for the semiparabolic and uniform velocity profiles, the film thickness monotonically increases over the whole computational domain. The effect of gravity is examined on the flow over a horizontal and vertical walls. It is found that in the former case, the gravity always reduces the film thickness. In the latter case, the behavior of the flow is very different. The film height of the flow initially increases with distance for any Froude number. At some position downstream, the flow exhibits a jump, abruptly increases in film height, and forms a recirculation bubble near the wall. The flow experiences a shock far downstream from the channel exit. It is found that the jump shifts toward the exit and reduces in size as the gravity effect increases.

References

[1] Pearson, J. R. A., 1985, *Mechanics of Polymer Processing*, Elsevier Applied Sciences, New York.

[2] Middleman, S., 1977, *Fundamentals of Polymer Processing*, McGraw-Hill, New York.

[3] Oron, A., Davis, S. H., and Bankoff, S. G., 1997, "Long-Scale Evolution of Thin Liquid Films," Rev. Mod. Phys., **69**(3), pp. 931–980.

[4] Chang, H.-C., and Demekhin, E. A., 2002, *Complex Wave Dynamics on Thin Films*, Elsevier Sciences B. V., Amsterdam.

[5] Szeri, A. Z., 1987, "Some Extensions of the Lubrication Theory of Osborne Reynolds," Trans. ASME, J. Tribol., **109**(1), pp. 21–36.

[6] Quere, D., 1999, "Fluid Coating on a Fiber," Annu. Rev. Fluid Mech., **31**, pp. 347–384.

[7] Tuck, E. O., and Bentwitch, M., 1983, "Sliding Sheets: Lubrication With Comparable Viscous and Inertia Forces," J. Fluid Mech., **135**, pp. 51–69.

[8] Watson, E. J., 1964, "The Radial Spread of a Liquid Jet Over a Horizontal Plane," J. Fluid Mech., **20**, pp. 481–499.

[9] Hamrock, B. J., 1994, *Fundamentals of Fluid Film Lubrication*, McGraw-Hill, New York.

[10] Takeshi, O., 1999, "Surface Equation of Falling Film Flows With Moderate Reynolds Number and Large but Finite Weber Number," Phys. Fluids, **11**(11), pp. 3247–3269.

[11] Shkadov, V. Ya., 1967, "Wave Condition of Flow in a Thin Viscous Layer Under the Action of Gravitational Forces," Izv. Akad. Nauk SSSR, Mekh. Zhidk. Gaza, **1**, pp. 43–51.

[12] Alekseenko, S. V., Nakoryakov, V. E., and Pokusaev, B. G., 1985, "Wave Formation on a Vertical Falling Liquid Film," AIChE J., **31**, pp. 1446–1460.

[13] Kim, K., and Khayat, R. E., 2002, "Transient Coating Flow of a Thin Non-Newtonian Fluid Film," Phys. Fluids, **14**(7), pp. 2202–2215.

[14] Khayat, R. E., 2000, "Transient Two-Dimensional Coating Flow of a Viscoelastic Fluid Film on a Substrate of Arbitrary Shape," J. Non-Newtonian Fluid Mech., **95**, pp. 199–233.

[15] Nakoryakov, V. E., Pokusaev, B. G., and Troyan, E. N., 1978, "Impingement of an Axisymmetric Liquid Jet on a Barrier," Int. J. Heat Mass Transfer, **21**, pp. 1175–1184.

[16] Craik, A. D. D., Latham, R. C., Fawkes, M. J., and Gribbon, P. W. F., 1981, "The Circular Hydraulic Jump," J. Fluid Mech., **112**, pp. 347–362.

[17] Bohr, T., Ellegaard, C., Hansen, A. E., and Haaning, A., 1996, "Hydraulic Jump, Flow Separation and Wave Breaking: An Experimental Study," Physica B, **228**, pp. 1–10.

[18] Bohr, T., Ellegaard, C., Hansen, A. E., Hansen, K., Haaning, A., Putkaradze, V., and Watanabe, S., 1998, "Separation and Pattern Formation in Hydraulic Jumps," Physica A, **249**, pp. 111–117.

[19] Bush, J. W. M., and Aristoff, J. M., 2003, "The Influence of Surface Tension on the Circular Hydraulic Jump," J. Fluid Mech., **489**, pp. 229–238.

[20] Bowles, R., and Smith, F., 1992, "The Standing Hydraulic Jump: Theory, Computations and Comparisons With Experiments," J. Fluid Mech., **242**, pp. 145–168.

[21] Higuerra, F., 1994, "The Hydraulic Jump in a Viscous Laminar Flow," J. Fluid Mech., **274**, pp. 69–92.

[22] Watanabe, S., Putkaradze, V., and Bohr, T., 2003, "Integral Methods for Shallow Free Surface Flows With Separation," J. Fluid Mech., **480**, pp. 233–265.

[23] Chippada, S., Jue, T. C., Joo, S. W., Wheeler, M. F., and Ramaswamy, B., 1996, "Numerical Simulation of Free-Boundary Problems," Int. J. Comput. Fluid Dyn., **7**, pp. 91–118.

[24] Lee, J.-J., and Mei, C. C., 1996, "Stationary Waves on an Inclined Sheet of Viscous Fluid at High Reynolds and Moderate Weber Numbers," J. Fluid Mech., **307**, pp. 191–229.

[25] Khayat, R. E., and Welke, S., 2001, "Influence of Inertia, Gravity and Substrate Topography on the Two-Dimensional Transient Coating Flow of a Thing Newtonian Fluid Film," Phys. Fluids, **13**(2), pp. 355–367.

[26] Siddique, M. R., and Khayat, R. E., 2002, "Influence of Inertia and Topography in Thin-Cavity Flow," Phys. Fluids, **14**(5), pp. 1703–1719.

[27] Khayat, R. E., 2001, "Influence of Inertia on the Transient Axisymmetric Free-Surface Flow Inside Thin Cavities of Arbitrary Shape," Phys. Fluids, **13**(12), pp. 3636–3651.

[28] Zienkiewicz, O. C., and Heinrich, J. C., 1979, "A Unified Treatment of Steady-State Shallow Water and Two-Dimensional Navier-Stokes Equations—Finite-Element Penalty Function Approach," Comput. Methods Appl. Mech. Eng., **17/18**, pp. 673–698.

[29] Sell, G. R., Foias, C., and Temam, R., 1993, *Turbulence in Fluid Flows: A Dynamical Systems Approach*, Springer-Verlag, New York.

[30] Deane, A. E., Kevrekidis, I. G., Karniadakis, G. E., and Orszag, S. A., 1991, "Low-Dimensional Models for Complex Geometry Flows: Application to Grooved Channels and Circular Cylinders," Phys. Fluids A, **3**(10), pp. 2337–2354.

[31] Khayat, R. E., 1999, "Finite-Amplitude Taylor-Vortex Flow of Viscoelastic Fluids," J. Fluid Mech., **400**, pp. 33–58.

[32] Ashrafi, N., and Khayat, R. E., 2000, "A Low-Dimensional Approach to Nonlinear Plane-Couette Flow of Viscoelastic Fluids," Phys. Fluids, **12**(2), pp. 345–365.

[33] Khayat, R. E., and Ashrafi, N., 2002, "A Low-Dimensional Approach to Nonlinear Plane-Poiseuille Flow of Viscoelastic Fluids," Phys. Fluids, **14**(5), pp. 1757–1767.

[34] Khayat, R. E., 2000, "Transient Free-Surface Flow Inside Thin Cavities of Viscoelastic Fluids," J. Non-Newtonian Fluid Mech., **91**, pp. 15–29.

[35] Chang, H.-C., 1994, "Wave Evolution on a Falling Film," Annu. Rev. Fluid Mech., **26**, pp. 103–136.

[36] Muhammad, T., and Khayat, R. E., 2004, "Effect of Substrate Movement on Shock Formation in Pressure-Driven Coating Flow," Phys. Fluids, **16**(5), pp. 1818–1821.

[37] Kalliadasis, S., Bielarz, C., and Homsy, G. M., 2000, "Steady Free-Surface Thin Film Flows Over Topography," Phys. Fluids, **12**(8), 1889–1898.

Downloaded 03 Jun 2010 to 171.66.16.157. Redistribution subject to ASME license or copyright; see http://www.asme.org/terms/Terms_Use.cfm

On the Flutter and Drag Forces on Flexible Rectangular Canopies in Normal Flow

Antonio Filippone
School of Mechanical, Aerospace and Civil Engineering,
The University of Manchester,
George Begg Building,
P.O. Box 88,
Manchester M60 1QD, UK
e-mail: a.filippone@manchester.ac.uk

The paper presents results of experimental investigations on flexible rectangular canopies fixed at two edges (tapes). Data are presented for the aerodynamic drag as a function of the planform area, the slenderness, and the Reynolds number. The slenderness varies from 3.3 to 30. The Reynolds number is limited to 2×10^6. The wind speed is in the range 6–19 m/s. The results show that the drag decreases with the increasing aspect ratio. The dominant parameter is the slenderness; a second dominant factor is the planform area. The drag is only weakly dependent on the Reynolds number. The analysis of the drag data indicates that a proper scaling parameter is the crosswise length scale. When normalization is done, the data tend to collapse into a single curve. A further study addressed the drag characteristics of the canopies with perforated planforms. Perforation of up to 6% of the planform area has been considered. Corrections for air permeability of the fabric are introduced. The drag is reduced roughly linearly with perforated area. A detailed study into the flutter characteristics of the canopies in the turbulent wind is presented. The investigation has highlighted different modes of oscillations, including deformations through folding and twisting, vertical flapping, rotations, and cross-type oscillations. [DOI: 10.1115/1.2928431]

1 Introduction

This paper presents the results of experimental investigations on flexible membranes made of cloth and attached at two vertical edges. The edges are separated by a fixed distance, as shown in Fig. 1. The term "tape" will be used to denote this device, which creates large drag, is subject to complicated flutter movements at high speeds, and creates turbulence by self-reinforced deformations. Since the aerodynamic forces are mostly horizontal and the weight is parallel to the support rods, a perturbation is always forced on the tape; hence, the tape tends to move up and down in an attempt to restore the balance disrupted by the deformations. For cases when the deformations are inhibited, high drag-to-weight ratios are established, and the tape remains stable in the wind. Tapes of varying slenderness and planform areas have been considered. Interim results, highlighting some flutter properties, have been published earlier by Carruthers and co-worker [1,2].

In contrast to streamers and banners that have axially oriented canopies, a tape is oriented across the flow. Therefore, it is suitable for a range of applications, including space probe recovery, personnel drops, inflatable life rafts, and street advertising banners. Holes can be distributed over the canopy for drag reduction and stabilization purposes, as shown by Foreman [3]. Although the device looks like a parafoil, the tape does not require canopy inflation, and has no thickness at all (if one excludes the thickness of the fabric itself). Once the tape is turned at 90 deg to the incoming wind, the lift effectively disappears if the tape is stable and does not show any flutter. Modern parafoils have slenderness $l/b \simeq 2.5$. Their glide ratio is in the order of $L/D \simeq 3$, as reported by Matos et al. [4]. Their aerodynamic coefficients are $C_D \simeq 0.14$ and $C_L \simeq 0.45$ at free flight conditions, although the lift and drag are generally dependent on the airfoil's cross section. The leading edge has a series of air gaps that allow inflation of the device.

A tape tightly fixed at its short edges operates as a flat plate in normal flow. However, there remains the problem of defining an effective reference area. This problem will be highlighted in the analysis of the wind tunnel data. A number of complicating factors intervene. Flutter, or even a slight rotation of the membrane, may produce some lift, pitch, and roll. Therefore, a cross-coupling of aerodynamic forces is possible, although the drag is by far the largest force.

2 Experimental Arrangement

The research was carried out in low-speed wind tunnel at the University of Manchester. This is a suction wind tunnel with a working section of 0.92×0.92 m^2 and length of 3.66 m. The velocity range is between 6 m/s and 19 m/s, and was measured by a Pitot-static probe upstream the working section inlet. The probe gave a dynamic pressure output, read by a digital manometer. The probe provided accuracies of ±0.1 Pa at $U=6$ m/s and ±18 Pa at 19 m/s. The corresponding velocity accuracies at the test section are between ±0.01 m/s and ±0.08 m/s, respectively.

The arrangement of the model in the wind tunnel test section is shown in Fig. 2. The horizontal mounting rod had a 6 mm diameter rod fitted to a 12 mm diameter rod. The larger rod was held by the collet of the force balance; the step between the two diameters was positioned to lie flush with the wind tunnel walls. The 6 mm rod, once fitted to the larger diameter rod, spanned half the tunnel width. The O-rings ensured that the luff was held taut. The two vertical rods are separated by a fixed distance of 0.420 m. The rod was relatively heavy, compared with the range of aerodynamic forces that had to be measured. Therefore, a counterbalance, as illustrated in Fig. 2, was designed in order to relieve the force balance. In fact, the balance becomes insensitive to small changes in aerodynamic forcing once a heavy weight has already been applied. One weight was placed outside the wind tunnel, hung from the rod arm that extended through the collet. The second weight lifted the entire system upward through a seesaw, place on the wind tunnel roof.

The drag measurements were done by taking time series readings at each data point (2048 samples over 2 s, once the condition

Contributed by the Fluids Engineering Division of ASME for publication in the JOURNAL OF FLUIDS ENGINEERING. Manuscript received December 6, 2006; final manuscript received August 20, 2007; published online May 19, 2008. Assoc. Editor: Hamid Johari.

 Copyright © 2008 by ASME

Downloaded 03 Jun 2010 to 171.66.16.157. Redistribution subject to ASME license or copyright; see http://www.asme.org/terms/Terms_Use.cfm

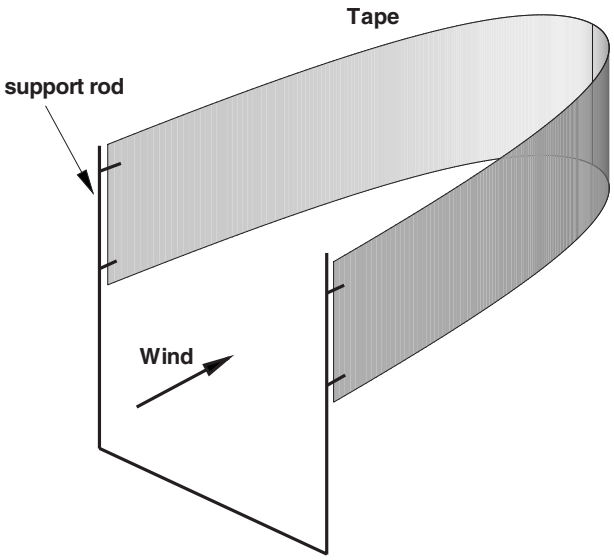

Fig. 1 Example of tape, stable in the wind

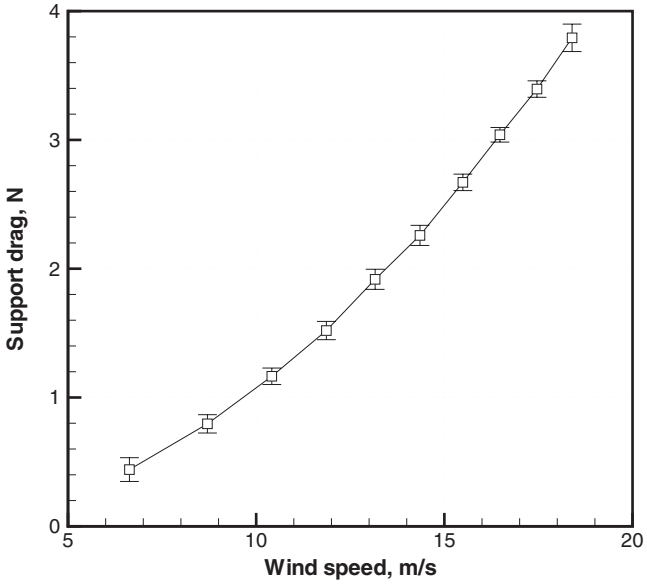

Fig. 3 Support drag for force calibration

in the test section was stabilized). The voltage output was converted into a force reading through a calibration. The drag force is an average of the time series at each test point.

A drag-velocity curve was drawn for the rods, Fig. 3. From this curve, the drag of the rod could be interpolated at all wind speeds. It was found that by moving the U-shaped rod sideways, a notable alteration in drag occurred. This result is justified by the presence of a greater portion of the rod facing the wind. The mounting rod was moved to the center of the working section, so that the tapes were also centrally positioned. The horizontal rod has a low drag over the entire range of wind speeds, while the U-shaped rod (in both positions) shows a more dramatic increase in drag with the wind speed. This drag was subtracted from the actual reading.

The devices tested were rectangles with areas $A=0.025$ m^2, 0.050 m^2, and 0.075 m^2, and slenderness $l/b=3,10,20,30$. The longest tape was 1.5 m. Table 1 is a summary of the geometries tested. It is noted that the flat plate approximation in normal flow holds for tapes whose length is about 0.5 m. Tapes subject to large-amplitude flutter are fully flexible canopies for which a suitable drag model has not been found.

The fabric used for these experiments was cotton. Essential properties of the fabrics are listed in Table 2. The bending rigidity B_r is the resistance of a fabric to deformations; higher values of bending rigidity indicate stiffer fabrics. The bending hysteresis B_h denotes the recovery of a fabric following a large deformation; higher values of bending hysteresis indicate a fabric with poor shape recovery. The permeability μ is the resistance of the fabrics to through flow. It is usually given at a specified pressure value. Specifically, this is 0.250 m of water head.

The four corners of each canopy were punched with 3 mm diameter eyelets. The eyelets were fastened to the mounting rod via short lengths of string connected to the rubber O-rings.

The blockage is estimated at about 1.5–7.5%, not accounting for the deformation of the slender tapes. The data presented are not corrected for blockage effects. Most of the correction methods require additional information, such as pressure data, which could not be collected during the experiments. The drag data discussed in this paper are the average of six tests taken over 2 days, with correction for temperature effects in the laboratory. Error bars are added to the presentation of the data when relevant.

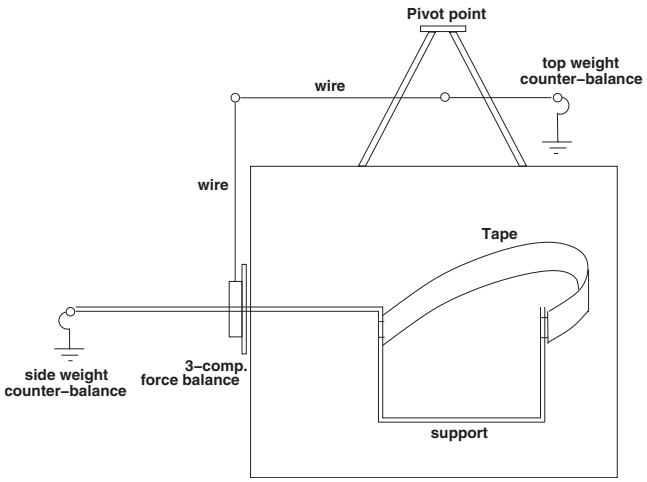

Fig. 2 Experimental arrangement

Table 1 Summary of canopy geometries tested

Area	l/b	b	l
0.025	10	0.050	0.500
	20	0.036	0.707
	30	0.029	0.866
0.050	3.3	0.123	0.406
	10	0.070	0.700
	20	0.050	1.000
	30	0.041	1.225
0.075	3.3	0.150	0.500
	10	0.087	0.866
	20	0.061	1.225
	30	0.050	1.500

Table 2 Physical properties of the canopies tested

Material	W (kg)	t (mm)	B_r (10^{-5} kg m)	B_h (10^{-3} kg)	μ (m/s)
Cotton	0.177	0.3	0.0642	0.0446	2.6

Downloaded 03 Jun 2010 to 171.66.16.157. Redistribution subject to ASME license or copyright; see http://www.asme.org/terms/Terms_Use.cfm

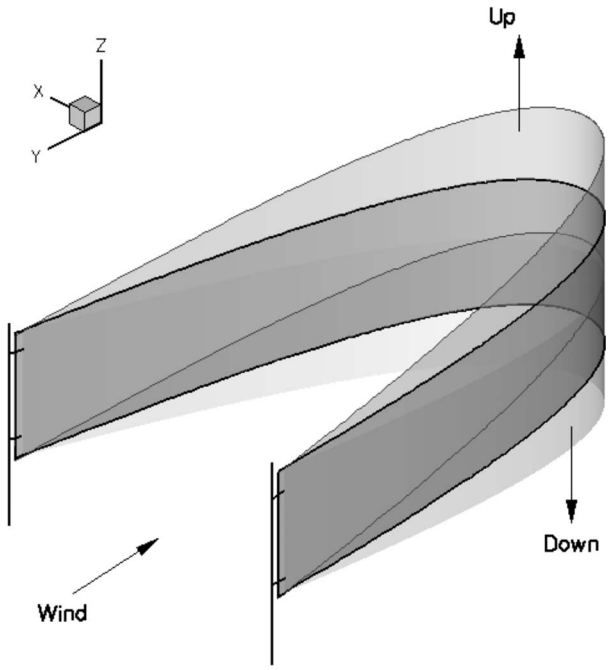

Fig. 4 Rigid rotation, up and down movement

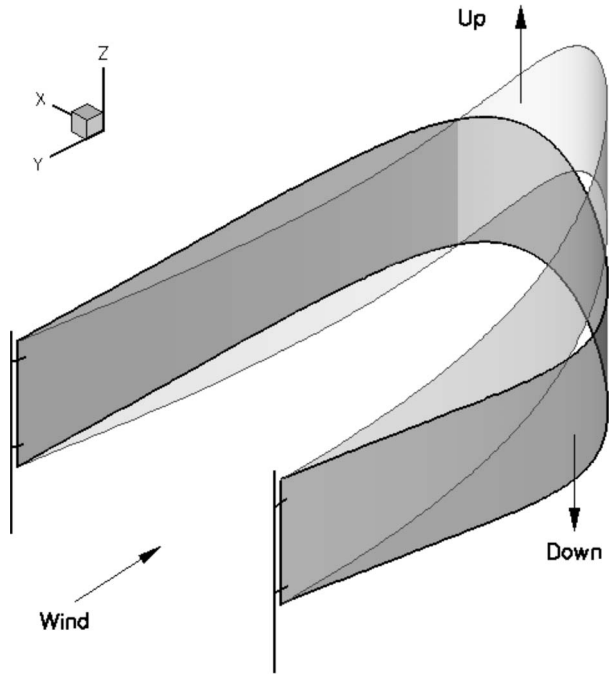

Fig. 5 Alternate flutter mode

3 Flutter Modes

The flutter is characterized by flapping and rotational modes. Due to the constraints at the edge, the flutter is strongly dependent on the slenderness l/b.

Consider first the case of low slenderness ($l/b=3.3$) and low planform area ($A=0.025$ m^2, $A=0.050$ m^2). These tapes were not long enough to allow large-scale deformations. Therefore, they operated essentially as flat plates in normal flow. In fact, these tapes required longer and tighter attachment threads in order to fit to the mounting struts. Vortex shedding has been observed to occur from the edges. Flow is entrained from the edges and sustains an area of unsteady low pressure on the downstream side. As the Reynolds number is increased, the vortices produced by flow separation become more vigorous, and greater pressure variations are produced between the upstream and downstream sides. The low-speed Strouhal number was estimated at $\mathrm{St}\simeq 0.15$. The vortex shedding frequencies indicate an increase in frequency with the wind speed.

The basic deformation mode, observed at low speed and for moderately slender canopies, is that of a rigid cable under its own weight. Thus, the deformed canopy in steady-state conditions would be similar to a catenary. We will refer to a "catenary" to indicate the stable low-speed deformation of the canopy, and is similar to the geometry shown in Fig. 1. Rotational modes, introduced by a combination of wind speed and the tape's own weight, create a disturbance to the basic deformation shape. This is possible only because the aerodynamic drag is a factor of 10^2 of the canopy's weight, as discussed further below. The rotational modes only appear on slender tapes at high speeds, when the flexibility of the tape, coupled with transient conditions on the wind speed, contributes to large deformations. At Reynolds numbers below $\mathrm{Re}=5\times 10^5$, a catenary is formed with vertical "rigid" oscillations occurring in the x-z plane, as indicated in Fig. 4. As the Reynolds number is increased further, rotational and vertical oscillations are observed in the movement of the canopy.

One flutter mechanism identified is the alternate up and down motion, as sketched in Fig. 5. In this case, as one section moves up, the other moves down, and vice versa. The opposing tendencies are caused by rotations in the same direction and vertical oscillations in the opposite sense, as if there were a half-cycle phase shift between the two sections of the canopy. The center section remains relatively still. Seen from the x-z plane (e.g., the plane normal to the wind), the tape loops and traces a bow-tie shape. The alternate up and down flutter is coherent and has a low frequency.

The second flutter mechanism is the *folding*. This is shown schematically in Fig. 6. This mechanism is enhanced by the slenderness at medium to high wind speeds. The section of the tape furthest from the attachment folds on itself and eventually assumes an upside-down position. The folding is smooth and persistent. As a consequence, the planform area offered to the wind is smaller than the actual planform area. A detailed geometrical analysis based on high-speed photography would allow to calculate the effective area.

The third flutter mechanism involves *twisting*. This mode appears on very slender tapes at high wind speeds, and makes the wind tunnel testing difficult. The canopy appears segmented, as shown in Fig. 7. No twisting is observed at slenderness below 20. Thus, the rotational mode still operates cyclically in respect to its influence over the flapping mode. Each end of the tape acts separately as a streamer, although its downstream movement is influenced by the movement of the other end. The net effect is to cause an alternation of the flapping motion, so that one side moves upward, while the other side moves downward. Therefore, at the leech of the tape, a cross or bow-tie-like shape is traced out.

Fig. 6 Folding of slender tape

Downloaded 03 Jun 2010 to 171.66.16.157. Redistribution subject to ASME license or copyright; see http://www.asme.org/terms/Terms_Use.cfm

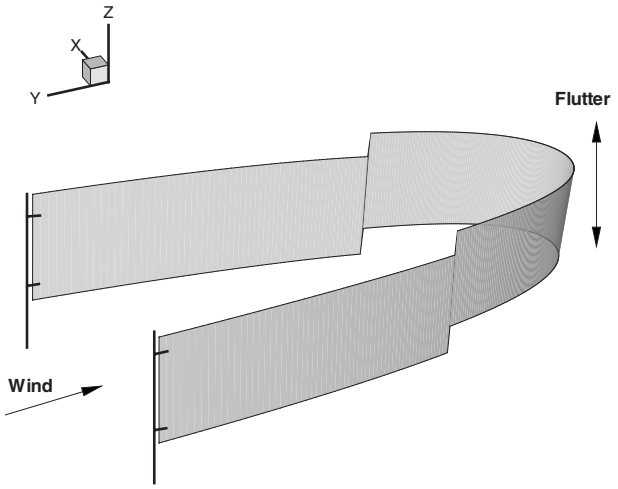

Fig. 7 Canopy deformation by twisting

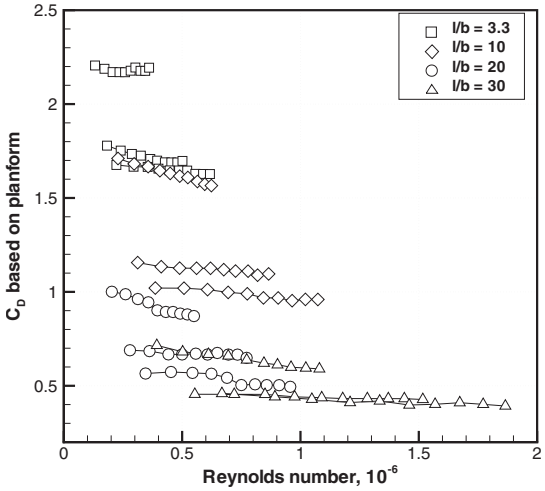

Fig. 9 C_D based on planform area for all tapes

The most slender tapes are more susceptible to twisting at the low wind speed. The rotational mode has the most dominant influence. Wind tunnel testing of these tapes was performed from the highest wind speed to the lowest, because the twisting at low speeds made testing impossible. Even at the high speeds, some manual adjustments were required to unwrap tapes that would otherwise tend to be ineffective. Twisting of the canopy does not cause complete loss of planform area. The canopy will fold over and find a new stable equilibrium. It was concluded that this tape would only be suitable for high velocity and impact conditions. Investigations into the flutter frequencies were made too difficult by the oscillations, and could not be taken. However, an important qualitative conclusion, arising from observation, is that tapes of low slenderness are subject to high-frequency, low amplitude oscillations; tapes of high slenderness are subject to low-frequency, high amplitude motion.

A summary of these flutter modes is shown in Fig. 8. In the graph, we have plotted the dimensional quantity $C_D L$ versus the slenderness l/b. This is the dominant parameter, as discussed further. The data points nearly collapse at a given value of l/b and A. The Reynolds number does intervene, particularly for the large slenderness, where the transition from one mode to another takes place. The chart shows the dominant modes, as they could be observed in the wind tunnel, but it is possible that in the Reynolds number range at a given slenderness and planform area, two modes coexist. The nomenclature for the various modes is given in the figure. The symbol for twisting (T) refers to both twisting and folding.

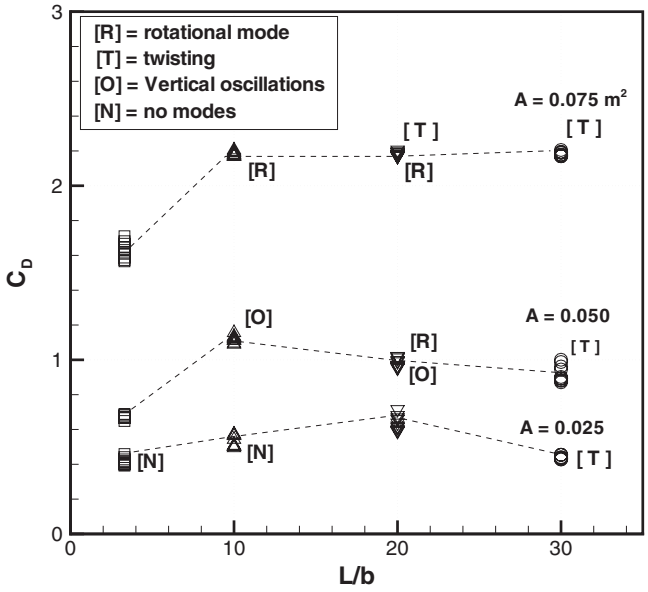

Fig. 8 Summary of flutter modes as a function of slenderness and planform area

4 Aerodynamic Drag

On investigating the drag, we are led to decide which reference area is suitable for the normalization of the data, and hence to the calculation of the C_D. The problem is not ambiguous if fixed reference surfaces can be found. However, in the present context, suitable areas are the planform, the wetted area, an effective area based on the width of the canopy, and the distance between the support rods. Furthermore, different reference lengths can be chosen, such as the distance between the rods, the length of the canopy, the width of the canopy, and even the integral turbulence length scale. A further complication arises from the air permeability of the tape. This is discussed separately.

In cases of ambiguity, the fraction D/q (drag over dynamic pressure) must be plotted. This is proportional to the drag coefficient $C_D A$, which can be rescaled as needed. Accordingly, the drag data are plotted against the Reynolds number.

Figure 9 shows the C_D calculated in terms of the planform area. Each symbol denotes one slenderness. As the planform area increases, the C_D decreases. There is a step change from $A=0.025$ m^2 to $A=0.050$ m^2; increasing the planform area from $A=0.050$ m^2 is not a clear determinant, as the data seem to collapse onto a single curve. However, the slenderness is the key factor, because the C_D ranges from about 0.35 to over 2.2. The vertical scale of the graph tends to reduce the importance of the Reynolds number and hence the wind speed.

Comparison of drag at different slenderness ratios shows considerable differences, mostly attributed to the geometrical shape of the tape and its flutter characteristics. The dependence on the Reynolds number is rather weak.

The planform area can be normalized by using the span r between the rods (fixed) and the width of the canopy; therefore, $A_e=A/br$. Since A_e is a fixed quantity (except the case $A=0.025$ m^2, $A=0.050$ m^2, with $l/b=3.3$), the data can be plotted against the Reynolds number. However, this method is hardly useful, because it does not highlight the drag properties of canopies of increasing slenderness.

Downloaded 03 Jun 2010 to 171.66.16.157. Redistribution subject to ASME license or copyright; see http://www.asme.org/terms/Terms_Use.cfm

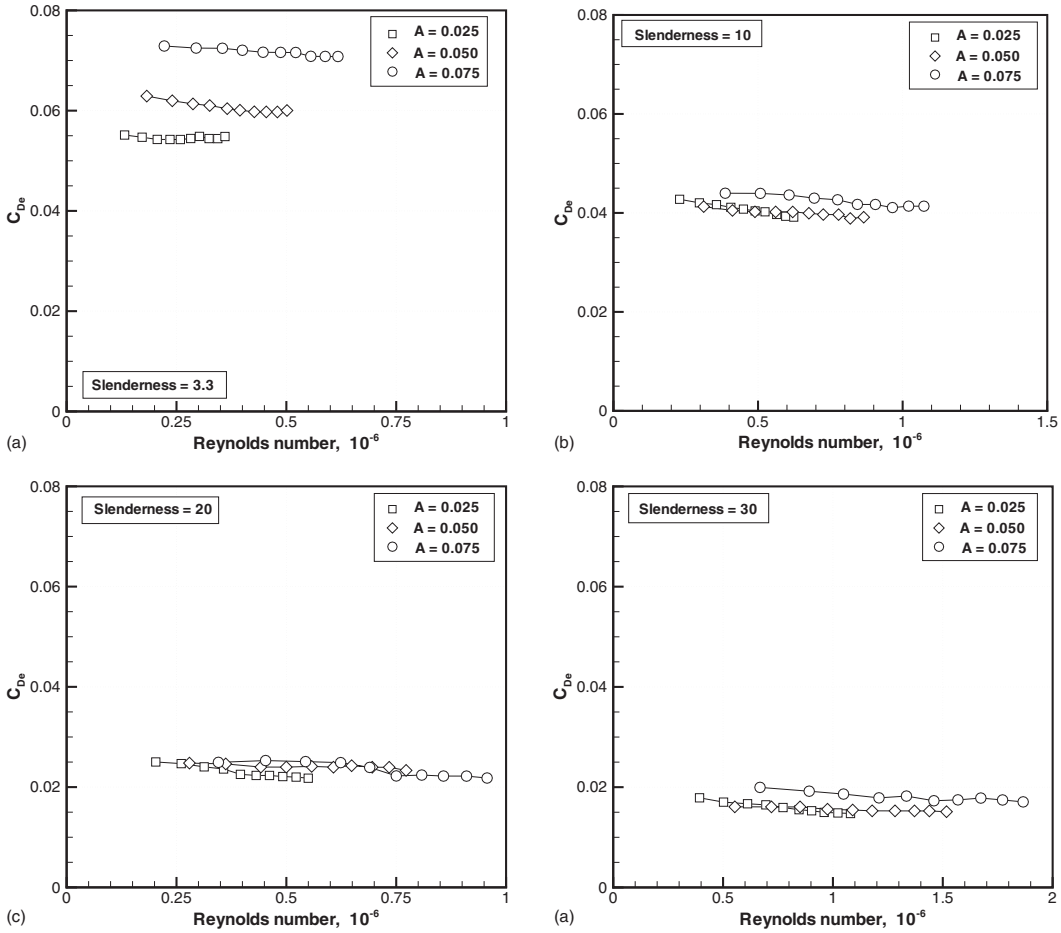

Fig. 10 Drag coefficient based on $A_e = D/qb$

An alternative dimensional analysis is proposed. The parametric space investigated included the wind speed, the slenderness, and the planform area. Hence, the ratio D/q is

$$\frac{D}{q} = f(l, b, \rho, \mu, A, L_x, \sqrt{\overline{u^2}}) \tag{1}$$

where L_x is the integral turbulence length scale and $\sqrt{\overline{u^2}}$ is the turbulence intensity. The turbulence intensity was not varied in the wind tunnel, while the integral length scale is a property of the flow; L_x is dependent on the crosswise reference length of the tape facing the wind. Therefore, a proper scaling is L_x/b, and the drag area becomes a function like

$$\frac{D}{q} = C_D A = f(\mathrm{Re}, L_x/b) \tag{2}$$

Most of the data points gathered are only weakly dependent on the Reynolds number but strongly dependent on the tape's geometry. Hence, a further approximation can be done to make the drag dependent on L_x/b only,

$$\frac{D}{q} = C_D A \simeq f(L_x/b) \tag{3}$$

Calculation of the integral length scale could not be done directly in the wind tunnel. We assume in this context that L_x is independent of the canopy. If this is the case, we scale the factor D/q with the width of the tape, the data almost collapse onto a single line. The new correlation is

$$C_{D_e} = D/qb \tag{4}$$

which is a drag coefficient per unit length of the canopy. Note that by increasing the planform area from 0.025 m^2 to 0.050 m^2, the width increases by a factor of 1.4; the D/q of this tape is then divided by 1.4; when the area is increased to 0.075 m^2, the width has increased by a factor of 1.74. This analysis is shown in Fig. 10. The procedure is repeated for all the slenderness tested, and shows a good correlation, except for the slenderness $l/b = 3.3$. However, this was a special case, because in at least one case, the length of the tape was considerably shorter than the distance between support rods. Hence, it seems reasonable to assume that the integral turbulence length scale is not affected by the canopy by a great deal.

Interpretation of the data produced by Bearman [5] for the flat plate indicates that the Reynolds number is not a clear determinant for rigid flat plates in normal turbulent flows (as in the present case) and that the values of the average C_D are more dependent on the ratio L_x/b between integral turbulence length scale and a reference dimension of the plate (again, in agreement with the present case).

From the data in Fig. 10, we find that $D/qb = f(l/b)$ is only weakly dependent on the Reynolds number. The drag coefficient can also be written as

$$C_D = \frac{D}{qA} = \frac{D}{qb}\frac{b}{A} = \left(\frac{b}{A}\right) f(l/b) = \left(\frac{1}{L}\right) f(l/b) \tag{5}$$

or $C_D L = f(l/b)$. Therefore, the data are now plotted against the slenderness in Fig. 11. There is a correlation of the data on a linear

Downloaded 03 Jun 2010 to 171.66.16.157. Redistribution subject to ASME license or copyright; see http://www.asme.org/terms/Terms_Use.cfm

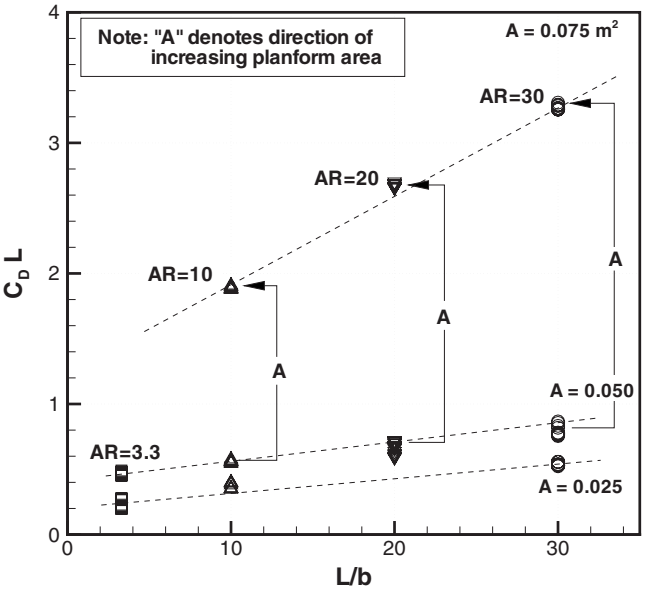

Fig. 11 Effects of slenderness at fixed planform area

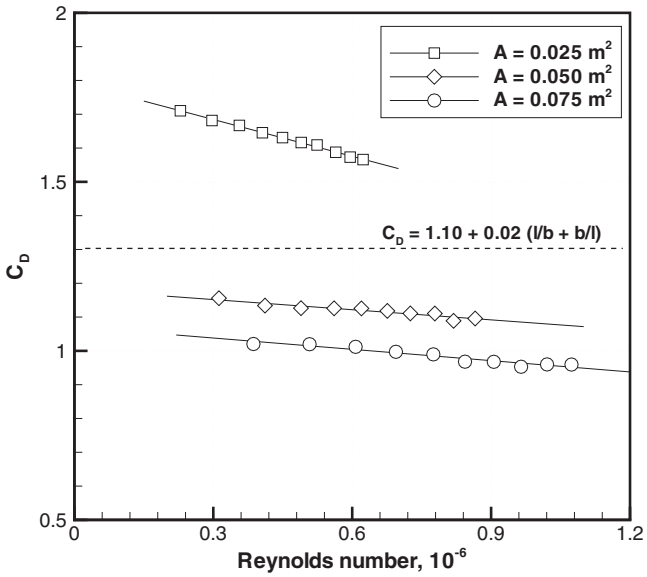

Fig. 12 C_D for tapes of slenderness $l/b=10$, and comparison with semiempirical formula for normal flat plates

regression for a constant planform area. Thus, we conclude that

$$C_D L \simeq k_p\left(\frac{l}{b}\right) \tag{6}$$

The factor k_p is the slope of the line in Fig. 11 that depends on the planform area only.

If we compare the data plotted in Fig. 11 with the same data plotted in Fig. 8 (flutter modes), we see that the correlation makes good sense. In fact, in Fig. 11, it is not possible to see a clear effect of the slenderness.

5 Drag Models

Experimental results, a summary of which is outlined by Hoerner [6], suggest that the drag coefficient may reach as high as $C_D=2$ for a two dimensional plate. This result was explained by direct measurement of the wake. The problem is considerably complicated if the device is not rigid and responds to the aerodynamic loads with large-amplitude, low-frequency flutter.

The first experimental investigations on the effects of turbulence on normal flat plates were published by Schubauer and Dryden [7]. Engineering correlations of aerodynamic forces and moments on plates of various configurations (rectangular, circular, in ground effect, perforated, etc.) are given by the Engineering Sciences Data Units (ESDU) [8] on the basis of experimental data gathered over 60 years. Relevant references on the subject are given in that document.

A suitable expression for the aerodynamic drag of a flat plate in a low-turbulence wind is

$$C_D = 1.10 + 0.02\left(\frac{l}{b} + \frac{b}{l}\right) \tag{7}$$

The correction for turbulence effects is

$$C_{D_t} = C_D(1 + k_1 k_2) \tag{8}$$

where k_1 is a function of the turbulence intensity and k_2 is a factor depending on the integral scale of turbulence through the term L_x/b (the ratio between the turbulence length scale and the width of the tape). Suitable approximations are

$$k_1 = \frac{\sqrt{\overline{u^2}}}{U_\infty}, \quad \frac{\sqrt{\overline{u^2}}}{U_\infty} < 0.10 \tag{9}$$

$$k_2 = \frac{3}{2}\,\mathrm{erfc}\left(\frac{1}{\tau}\frac{L_x}{b}\right) \tag{10}$$

with $\tau \simeq 0.74$ a relax factor and "erfc" the complementary error function.

Although the turbulence level in the wind tunnel is relatively low, turbulence around the canopies and in the wake is greatly enhanced by the flutter. Therefore, application of the above correlations lacks a physical basis where large-amplitude fluctuations occur. In practice, this means that one can attempt to associate the tapes with $l/b=3.3$ to flat plates in normal flow.

For a slenderness $l/b=3.3$, Eq. (8) provides a $C_D \simeq 1.17$, a value close to the square flat plate in normal flow. However, this estimate is off by a factor of 2 on the low planform area. Turbulence corrections for this case are estimated as follows: $k_1 \simeq 0.05$ (typical of the turbulence in the wind tunnel test section) and $k_2 \simeq 0.99$ (with $L_x/b \simeq 0.23$). Even in this case, the measured drag is far higher, because the equivalent flat plate drag coefficient would be $C_D \simeq 1.20$.

The analysis was repeated for the tapes of $l/b=10$, with similar results, and is shown in Fig. 12. A proper analysis of the relative turbulence length scale L_x/b would require detailed measurements of the wake. Bearman [5] showed that $L_x \simeq 0.07-0.1$ m behind a normal flat plate in turbulent flow. Changes in average C_D measured by Bearman are of the order of 0.1 or less. Even if parametric changes in the integral length scale are done on a spreadsheet, only relatively small changes in the C_D are found in our case (of the same order as Bearman's). Therefore, the flat plate model essentially defaults in the present context. Clearly, the turbulence level is greatly affected downstream, whether flutter occurs or not.

6 Effects of Surface Perforation

The perforation was simulated by introducing holes in the canopy. The perforation level was defined as the ratio of the hole area to the total area. The case selected was a canopy of area $A=0.050$ m^2 and slenderness $l/b=10$. Canopies with a total perforated area up to 4% had holes distributed on a rectangular grid; other canopies had holes distributed on a triangular grid pattern. One such perforated tape in the wind tunnel test section is shown in the photograph of Fig. 13.

In summary, the cases considered are given in Table 3; d is the hole diameter, A_p/A is the perforated area in percent, and N is the total number of holes. The results of the wind tunnel testing are

Downloaded 03 Jun 2010 to 171.66.16.157. Redistribution subject to ASME license or copyright; see http://www.asme.org/terms/Terms_Use.cfm

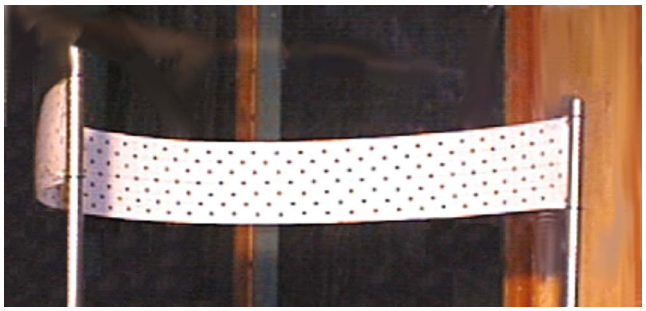

Fig. 13 Perforated tape in the wind tunnel, $A=0.050$ m^2, $l/b=10$, $A_p/A=0.06$, and $U=11.0$ m/s

shown in Fig. 14. The symbols denote the measured points; the lines are exponential line fits of the points. The error bars are shown for the case with no perforation to indicate the uncertainty of the measurements. The error tends to increase toward the low wind speeds. The Reynolds number is a weak parameter in the speed range tested (up to 1×10^6).

The results depend on the thickness and type of fabrics, in particular, on the air permeability. Original theoretical studies of the drag coefficient of a porous flat plate are due to Taylor [9,10]. However, the correlations provided are well below the wind tunnel data (maximum $C_D\simeq1$, independent of turbulence intensity). A suitable extrapolation of the data published by ESDU [8] is

$$C_D \simeq 1.14 - 0.035\left(1 - \frac{A_p}{A}\right) \tag{11}$$

for a squared plate and is

$$C_D \simeq 1.197 - 0.0405\left(1 - \frac{A_p}{A}\right) \tag{12}$$

for a plate of slenderness $l/b=5$. A least-squares fit of the wind tunnel data, uncorrected for residual air permeability of the fabric, is

$$C_D = 1.108 - 0.0355\left(1 - \frac{A_p}{A}\right) \tag{13}$$

The results of this analysis are shown in Fig. 15 for an average Reynolds number. Error bars are shown in the wind tunnel data. Although the drag level is slightly lower than the one predicted by ESDU, the slope of the curve is nearly the same. This indicates that (1) the effect of the perforated tape on the drag is the same as the effect of a perforated solid flat plate, although the data must be corrected for the air permeability (see data in Table 2), and (2) the comparison between tapes and flat plates is fair, but it also shows how small-amplitude flutter can affect the aerodynamic loads on the canopy.

The correction for air permeability is done as follows. From the definition of μ, the corresponding wind speed is

$$U_\infty = \sqrt{2\frac{\rho_w g h}{\rho}} = 63.28 \text{ m/s} \tag{14}$$

With this speed, the residual velocity through the canopy would be about $U=2.6$ m/s. If the air permeability were a constant

Table 3 Distribution of holes

d (mm)	A_p/A (%)	N
4.0	1.0	39
	2.0	81
	3.4	136
	4.3	170
	6.0	238

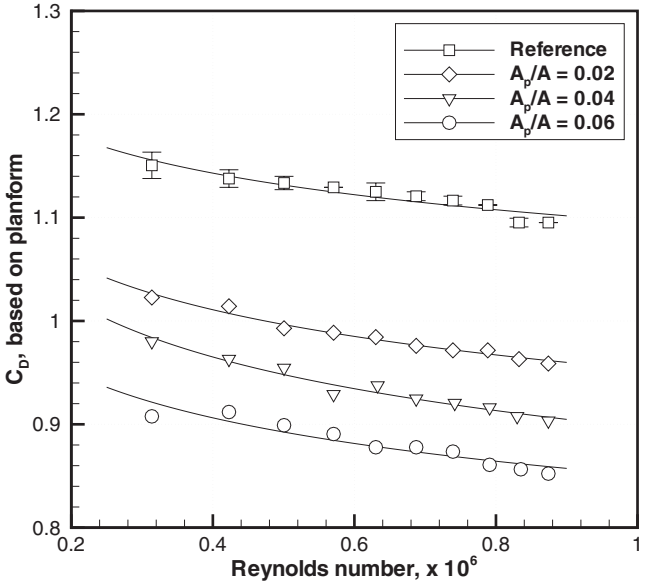

Fig. 14 Effects of perforated area on drag

throughout the range of wind speeds, then the correction would be an increase in effective porosity by

$$0.04\left(1 - \frac{A_p}{A}\right)$$

In general, the effective mass flow rate through a tape not affected by flutter can be described by

$$\dot{m} = A_e U = k(\Delta p)^m \tag{15}$$

where k and m are two terms that depend on the fabric and its air permeability. These coefficients can be measured with appropriate equipment for all types of modern fabrics. In the absence of more accurate data on the effects of air permeability, and pressure measurements on the downstream side of the tapes, the correction consists of a shift by the amount indicated above with respect to the original data. The shift is considerable, and brings the C_D to a level higher than the one corresponding to perforated flat plates, perhaps as a result of some residual flutter.

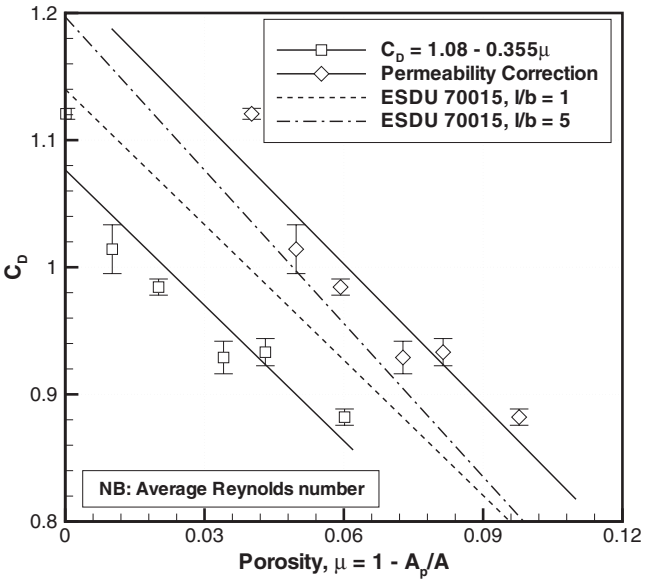

Fig. 15 Effects of perforated tapes on drag coefficient (corrected)

Downloaded 03 Jun 2010 to 171.66.16.157. Redistribution subject to ASME license or copyright; see http://www.asme.org/terms/Terms_Use.cfm

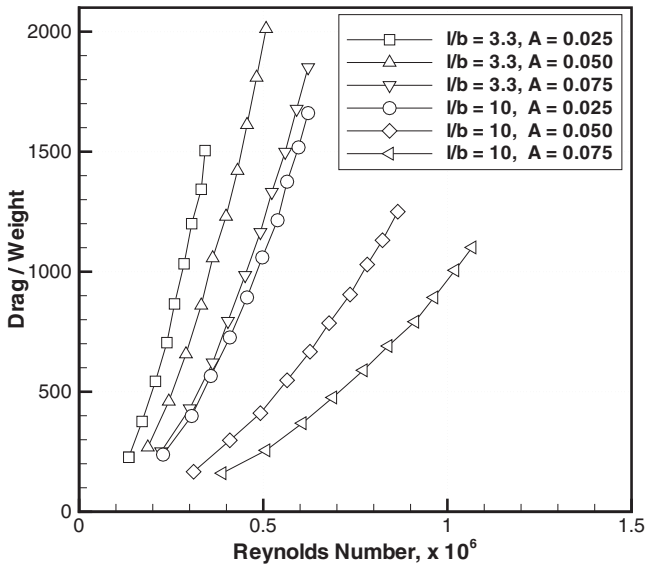

Fig. 16 Drag/weight for selected tapes

7 Decelerator Efficiency

When the tape is used as decelerator, it is a high-drag device. For this purpose, it is necessary that the canopy be free of major oscillations, such as wrapping and twisting. Therefore, from the flutter analysis, we define a cut-off point at a slenderness ratio $l/b \cong 3.3$. The efficiency itself is the ratio D/W, e.g., a. nondimensional quantity. This quantity is plotted in Fig. 16 against the Reynolds number. Only tapes that have some degree of flutter stability have been plotted. In particular, we concluded that tapes of slenderness $l/b=3.3$ can be used as decelerators; tapes of higher slenderness are not suitable because of their instability.

The tape of $l/b=3.3$ and $A=0.025$ m^2 was not long enough to stretch the full width of the vertical rods. Likewise, the tape with $l/b=3.3$ and $A=0.025$ m^2 was just as long as the distance between the rods. In these cases, the tapes operate nearly as flat plates at 90 deg to the wind. Their decelerator efficiency reaches values above 2000.

8 Conclusions

Highly flexible canopies fixed at vertical edges have been investigated in a low-speed wind tunnel. The canopies were fixed at the edges to simplify the parametric space of the experimental investigations. Practical applications may require additional considerations on the effects varying distance between the fixed edges. The effects of the payload in a decelerator application can only be studied in drop tests due to the difficulty of designing a measurement technique in a wind tunnel.

The investigations included the flutter modes, the aerodynamic drag, the effects of surface porosity, and the decelerator efficiency. The parametric space analyzed included slenderness, planform area, and Reynolds numbers. No drag breakdown has been detected in the range of Reynolds numbers tested. All the data indicate that the Reynolds number is a secondary parameter. Unlike all rigid systems, the drag of the flexible tapes can be plotted in a variety of methods; each method highlights a different aspect of the device. However, it was shown that a suitable length scale for the normalization of the drag is the width of the tape, e.g., a reference length normal to the flow. This result appears to be in line with the characteristics of normal flat plates. Drag force normalization with the planform area results in drag coefficients variable between 0.4 and 2.2. Furthermore, it was shown that the product between the drag coefficient and the length of the canopy is a linear function of the slenderness for all the cases tested. This is the most important result of the drag analysis.

A number of flutter modes have been identified, including rotations, oscillations, folding, warping, and twisting. The modes increase in complexity if both the wind speed and the slenderness increase. Tapes that are sufficiently short assume a stable configuration. Tapes fixed tightly at the supports behave like flat plates in normal flow, although they present some degree of vibration. For tapes that are allowed to deform, the shape of the canopy between supports is approximately a catenary. Also, these tapes operate in a similar fashion as normal flat plates. Differences arise due to small self-sustained deformations, small interference due to the support rods, and air permeability. These tapes are shown to perform well as decelerators or high-drag devices, since they are lightweight and easy to deploy.

The flutter characteristics are more critical, since the large-scale deformations give rise to further flow instabilities. These tapes cannot be used efficiently as decelerators, because their response is unsteady; wrap-up is likely. Furthermore, the ratio between drag and own weight is relatively low for slender canopies. A slenderness $l/b \simeq 3-4$ creates some oscillations; more slender canopies can be subject to the whole range of flutter phenomena illustrated in this study.

Nomenclature

A = planform area
A_p = area of perforated tape
b = tape's width
B_h = bending hysteresis
B_r = bending rigidity
C_D = drag coefficient
C_{D_e} = effective drag coefficient
d = hole diameter
D = drag force
k = air permeability factor, Eq. (15)
k_1 = turbulence intensity factor, Eq. (8)
k_2 = turbulence length-scale factor, Eq. (8)
k_p = slope in the linear drag correlation, Eq. (6)
l = tape's length
L_x = integral turbulence length scale
N = number of perforated holes
Re = Reynolds number
q = dynamic pressure
$\overline{u^2}$ = square of mean velocity perturbation
U_∞ = wind speed
W = weight

References

[1] Carruthers, A. C., 2005, "Experimental Studies on the Drag and Flutter of Aerodynamic Decelerators," Ph.D. thesis, The University of Manchester, Manchester, UK.
[2] Carruthers, A. C., and Filippone, A., 2005, "The Aerodynamic Drag of Parafoils," J. Aircr., **42**(4), pp. 1081–1083.
[3] Foreman, E. J., 1982, "An Investigation Into the Performance of Sea Anchors for Inflatable Liferafts," National Maritime Institute, Technical Report No. NMI R-127.
[4] Matos, C., Mahalingam, R., Ottinger, G., Klapper, J., Funk, R., and Komerath, N., 1998, "Wind Tunnel Measurements of Parafoil Geometry and Aerodynamics," AIAA Paper No. 98-0606.
[5] Bearman, P., 1971, "An Investigation of the Forces on Flat Plates Normal to a Turbulent Flow," J. Fluid Mech., **46**(1), pp. 177–198.
[6] Hoerner, S. F., 1965, *Fluid Dynamic Drag*.
[7] Schubauer, G. B., and Dryden, H. L., 1935, "The Effect of Turbulence on the Drag of Flat Plates," NACA, Technical Report No. 546.
[8] ESDU, 1972, "Fluid Forces and Moments on Flat Plates," ESDU, Technical Report No. 70015.
[9] Taylor, G. I., and Davies, R. M., 1944, "The Aerodynamics of Porous Sheets," *ARC R&M 2237, Republished in the Scientific Papers of Sir Geoffrey Ingram Tailor*, Vol. III(45), pp. 391–405.
[10] Taylor, G. I., 1944, "Air Resistance of a Flat Plate of Very Porous Material," *ARC R&M 2236, Republished in the Scientific Papers of Sir Geoffrey Ingram Tailor*, Vol. III(43), pp. 383–386.

Downloaded 03 Jun 2010 to 171.66.16.157. Redistribution subject to ASME license or copyright; see http://www.asme.org/terms/Terms_Use.cfm

Investigation of Combined Electro-Osmotic and Pressure-Driven Flow in Rough Microchannels

Prashant R. Waghmare
e-mail: prashant.waghmare@iitb.ac.in

Sushanta K. Mitra[1]
e-mail: skmitra@me.iitb.ac.in

Department of Mechanical Engineering,
Indian Institute of Technology Bombay,
Mumbai 400076, India

The present study is carried out to investigate the influence of surface roughness in combined electro-osmotic and pressure-driven flow in microchannel. Two-dimensional theoretical model is developed to predict the behavior of velocity profiles in rough microchannel. The concept of surface roughness-viscosity model is used to account the effect of surface roughness. The pluglike velocity profile for electro-osmotic flow and the parabolic velocity profile for pressure-driven flow with delay in attaining the centerline velocity are observed. It is found that for electro-osmotic flow, the deviation in velocity profile from a flow in a smooth channel occurs near the wall, whereas in pressure-driven flow, such deviation is dominant in the core region. A superposition of pluglike and parabolic velocity profiles is found in combined electro-osmotic and pressure-driven flow. It is also observed that in the case of combined flow, the deviation in velocity profile from the smooth channel case reduces gradually with the distance from the wall.
[DOI: 10.1115/1.2928333]

Keywords: electro-osmotic flow, microchannel, surface roughness

1 Introduction

Microchannels are integral part of microfluidic devices, which are used for various applications such as lab-on-chip, bio-MEMS (MEMS denotes microelectromechanical system) based sensors, etc. These microchannels are used for seamless integration of sample collection, separation, and detection of various biological and chemical species on a single chip with fluidic pumps and valves integrated with the system. Fundamental understanding of liquid flow through microchannels is important to predict the performance and behavior of microfluidic devices [1,2]. Depending on the manufacturing technique [3] or by adhesion of biological particles from the liquids, the channel surface has certain degree of roughness. The surface roughness ranges from 0.1 μm to 2 μm and this surface roughness of microfluidic channel affects the flow characteristics in the channel [4,5].

A variety of numerical models and experimental studies have been presented to investigate surface roughness effect on fluid flow behavior. Morani [6] has provided an extensive review of literature related to the experimental study of flow in the microchannel, which shows that surface roughness plays an important role in the measured value of pressure drop and heat transfer. Mala and Li [7] observed experimentally that for a fixed volume flow rate, the pressure gradient required to force the liquid through microtube is higher than that predicted by conventional theory. They also found that the frictional factor and friction constant (product of friction factor and Reynolds number) values are higher than that predicted by the conventional theory. They proposed a surface roughness-viscosity model (RVM) to account the surface roughness and showed good agreement with the experimental measurement. Que et al. [5] used a similar concept for trapezoidal silicon microchannel. They also found good agreement with experimental results after considering the surface RVM in their theoretical study. Kandlikar et al. [8] studied the effect of surface roughness by using a constricted flow model for lower values of roughness pitch. Three new parameters (maximum profile peak height, mean spacing of profile irregularities, and floor distance to mean line) have been proposed to characterize the surface roughness. Rawool et al. [9] studied the effect of surface roughness for higher values of surface roughness pitch with rectangular, triangular, and trapezoidal obstructions. They found that pressure drop decreases with an increase in the obstruction pitch. The variations in velocity profiles across the channel for different surface roughness values have not been presented in both the studies. Hence, it is observed that in order to study the effect of surface roughness on velocity profile and to predict the experimental trends in the microchannel, it is important to include an appropriate RVM in the analysis.

Generally, electrokinetic effects are used in combination of pressure-driven flows for better fluid handling and species transport in the fluidic device. Electrokinetic effects are often used in separation and transport of species in microfluidic devices [10]. Electro-osmotic (EO) flow is an important type of electrokinetic flow and it is often preferred over pressure-driven flow. Electro-osmosis is the bulk movement of liquid near a stationary surface due to an externally applied electric field. Although EO flow was first reported in 1809 by Reuss, Dutta and Beskok [11] developed a numerical model for combined EO and pressure-driven flow in a straight channel and in *T*-junction geometry. They observed a combination of pluglike and parabolic profile for adverse as well as favorable pressure gradients. Reviews of development of experimental and theoretical studies in EO/pressure-driven flow can be found in Ref. [1]. Reza et al. [12] studied variation in velocity profiles in a rectangular microchannel under different EO operating conditions. With KCl solution as an electrolyte, their results indicate that the variation in potential becomes steeper and the thickness of electric double layer (EDL) decreases considerably with the increase in the solution concentration.

Hu et al. [13] developed a three-dimensional finite-volume-based numerical model to simulate EO transport in a microchannel with 3D roughness elements. These elements are produced by photolithography to enhance biochemical reactions on sensing

[1]Corresponding author.

Contributed by the Fluids Engineering Division of ASME for publication in the JOURNAL OF FLUIDS ENGINEERING. Manuscript received July 30, 2007; final manuscript received March 23, 2008; published online May 22, 2008. Assoc. Editor: Ali Beskok.

 Copyright © 2008 by ASME

Downloaded 03 Jun 2010 to 171.66.16.157. Redistribution subject to ASME license or copyright; see http://www.asme.org/terms/Terms_Use.cfm

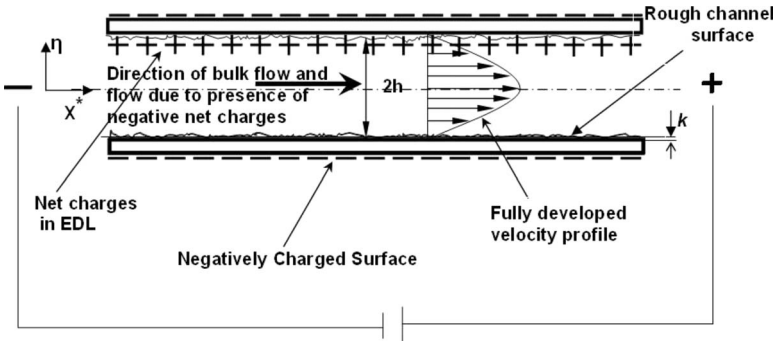

Fig. 1 Schematic of rectangular channel with distribution of charges due to EO flow

surfaces. They observed that the roughness elements make the central flow velocity smaller than that in the near-wall region and hence significantly reduce the flow rate through the rough microchannel. There are several reports regarding the effect of surface heterogeneity in microchannels. A recent review on the effect of different surface heterogeneity on electrokinetics can be found in Ref. [14]. Molecular dynamics simulation is performed by Kim and Darve [15] to compute EO flow in nanochannels of different types of surface roughness. They concluded that with an increase in the surface roughness, the flow rate across the channel decreases. Recently, Wang et al. [16] studied the surface roughness and cavitation's effects in EO flows. They have simplified the surface roughness as a group of rectangles on the lower channel wall. The results across the middle section of roughness element shows the reduction in flow rate and change in velocity profiles as the roughness element height increases.

The existing literature suggests that the effect of surface roughness is usually considered either in EO flow or in pressure-driven flow. It is important to study the effect of surface roughness on the distribution of velocity for a combined EO and pressure-driven flow. Hence, the objective of the present work is to investigate theoretically the behavior of combined flow in rough microchannels.

2 Physical Model and Mathematical Formulation

Figure 1 shows the schematic of a two-dimensional rough microchannel with surface charges on both walls of the channel and subjected to an applied electric field. The channel height (h) is assumed to be much smaller than the width and therefore, the flow can be treated as two dimensional. It is assumed that the fluid is single phase and Newtonian. The flow is considered to be laminar and the distribution of charges, ion concentration, and permittivity is uniform.

2.1 Mathematical Model and Solution. Ion distribution due to EDL is characterized by using an electrokinetic potential (ψ). The value of ψ at the edge of the stern layer is known as zeta potential (ζ). For most practical cases, the zeta potential is used to describe electrokinetic flows rather than the wall potential (ψ_0). Ion distribution in the diffuse layer results in a net electric charge, which can be related to the electrokinetic potential using Poisson distribution.

$$\nabla^2\psi = \frac{-\rho_e}{\varepsilon_r} \tag{1}$$

where ρ_e is the electric charge density and ε_r is the dielectric permittivity.

$$\rho_E = F\sum z_i c_i \tag{2}$$

where z is the valence and c is the ionic concentration far away from the surface. The subscript i indicates the ith species.

If one assumes a symmetric electrolyte of equal valence electric charge density, Eq. (1) leads to a Boltzmann distribution and finally, the governing equation becomes Poisson–Boltzmann equation, which can be written as

$$\frac{\partial^2\psi}{\partial y^2} = \frac{Fzc}{\varepsilon_r}\sinh\left(\frac{Fz\psi}{K_BT}\right) \tag{3}$$

where F is Faraday's constant. The effect of EDL can be approximately estimated by Debye–Huckle parameter (ω),

$$\omega = \frac{1}{\lambda_D} = \sqrt{\frac{e^2z^2c}{\varepsilon_r K_B T}} \tag{4}$$

where e is the electron charge and λ_D is the Debye length. Assuming symmetric electrolyte for $c=10^{-1}M$, $10^{-5}M$, and $10^{-6}M$, the Debye length comes $\lambda_D=3$ nm, 100 nm, and 300 nm, respectively.

Furthermore, the nondimensional form of Eq. (3) is obtained, where electric potential (ψ) and y coordinate are normalized with zeta potential (ζ) and half width of the channel (h), respectively.

Finally, the nondimensional form of the governing equation is

$$\frac{\partial^2\psi^*}{\partial\eta^2} = \beta\sinh(\alpha\psi^*) \tag{5}$$

where the nondimensional parameters are $\psi^*=\psi/\zeta$; $\eta=y/h$ and α is the ionic energy parameter, which can be written as

$$\alpha = \frac{ez\zeta}{K_BT} \tag{6}$$

For $\zeta=25.4$ mV and $T=20°$C, $\alpha=1$. The variable β relates the ionic energy parameter α and the characteristic flow dimension (channel width).

$$\beta = \frac{\omega h^2}{\alpha} \tag{7}$$

The potential at the wall is approximately the zeta potential and away from the wall in the center, it is zero. Considering these boundary conditions, the final form of the governing equation is

$$\psi^*(\eta) = \frac{4}{\alpha}\tan h^{-1}\left[\tanh\left(\frac{\alpha}{4}\right)\exp(-\eta\sqrt{\alpha\beta})\right] \tag{8}$$

The electric charge distribution in the EDL and the externally applied electric field generate electrokinetic body force. The Navier–Stokes equation for the combined flow is given as

$$\nabla p = \mu\nabla^2\mathbf{v} + f_{\mathrm{EK}} \tag{9}$$

The equation for electrokinetic body force for incompressible medium with constant electric permittivity can be written as

Downloaded 03 Jun 2010 to 171.66.16.157. Redistribution subject to ASME license or copyright; see http://www.asme.org/terms/Terms_Use.cfm

$$f_{EK} = \rho_e E \tag{10}$$

where ρ_e is the charge density, p is the pressure, E is the externally applied electric field, and f_{EK} is the electrokinetic body force. For combined EO and pressure-driven flow, the momentum equation can be written as

$$\frac{\partial p}{\partial x} = \mu \frac{\partial^2 u}{\partial y^2} + \rho_e E_x \tag{11}$$

Using Eq. (1), one can rewrite Eq. (11) as

$$\frac{\partial p}{\partial x} = \mu \frac{\partial^2 u}{\partial y^2} - \varepsilon_r E_x \frac{\partial^2 \psi}{\partial y^2} \tag{12}$$

When externally applied pressure gradient is absent, the viscous diffusion term is balanced by the EO forces. This results in Helmholtz–Smoluchowski EO velocity (u_{HS}),

$$u_{HS} = -\frac{\zeta \varepsilon E_x}{\mu} \tag{13}$$

The nondimensional form of Eq. (12) is

$$\frac{\partial p^*}{\partial x^*} = \frac{\partial^2 u^*}{\partial \eta^2} + \frac{\partial^2 \psi^*}{\partial \eta^2} \tag{14}$$

where the nondimensional parameters are as follows:

$$p^* = \frac{ph}{\mu u_{HS}}, \quad x^* = \frac{x}{h}, \quad u^* = \frac{u}{u_{HS}}, \quad \psi^* = \frac{\psi}{\zeta} \tag{15}$$

To incorporate the surface roughness effect, as proposed by Mala and Li [7], an additional viscosity term is introduced in the analysis. This is done via a roughness-viscosity μ_r term, which is similar to the eddy-viscosity concept in the turbulent flow model. μ_r has higher value near the wall and it gradually diminishes toward the center of the channel. It is also proportional to the Reynolds number. The ratio of the roughness viscosity to the fluid viscosity, as proposed by Mala and Li [7], is

$$\frac{\mu_r}{\mu} = A \, \mathrm{Re}_k \frac{r}{k}\left[1 - \exp\left(-\frac{\mathrm{Re}_k}{\mathrm{Re}}\frac{r}{k}\right)\right]^2 \tag{16}$$

Here, Re_k is calculated using the formula of Merkle et al. [17]. According to their study, the velocity at the top of the roughness element (U_k) is given by

$$U_k = \left(\frac{\partial u}{\partial r}\right)_{r=R} k \tag{17}$$

and the corresponding roughness Reynolds number (Re_k), which is defined as the Reynolds number at the tip of the average surface roughness height, can be written as

$$\mathrm{Re}_k = \frac{U_k k}{\nu}\left(\frac{\partial u}{\partial r}\right)_{r=R}\frac{k^2}{\nu} \tag{18}$$

With the introduction of the roughness viscosity, Eq. (12) becomes

$$\frac{\partial p}{\partial x} = \mu_e \frac{\partial^2 u}{\partial y^2} - \varepsilon_r E_x \frac{\partial^2 \psi}{\partial y^2} \tag{19}$$

where μ_e is the effective viscosity, which is the summation of dynamic viscosity and roughness viscosity (μ_r). In Eq. (16), all the parameters can be calculated from operating flow condition except the coefficient A. To determine A, experimental results and an iterative procedure are needed. By assuming an initial value of the coefficient A in the momentum equation, a velocity distribution in the microchannel with known pressure drop dp/dx value is obtained. Once the velocity profile is known, the volume flow rate can be calculated. At the same time, the volume flow rate and pressure gradient are measured. The value of A is adjusted until the percentage difference between the theoretical volume flow rate and the measured volume flow rate is minimum. Mala and Li [7] and Qu et al. [5] considered the criteria for difference in theoretical and experimental flow rate as $\pm 2\%$. The empirical relationship for A in the case of microtubes of radius R was obtained by Mala and Li [7] as follows:

$$A = 0.1306\left(\frac{R}{k}\right)^{0.3693} \exp\left\{\mathrm{Re}\left[6 \times 10^{-5}\left(\frac{R}{k}\right) - 0.0029\right]\right\} \tag{20}$$

This method suggests that determination A requires experimental inputs and is valid for a given microchannel geometry. Furthermore, experimental studies need to be conducted for accurate determination of A for combined flow in the microchannel.

Existing literature suggests that correlation for A is not available for combined EO and pressure-driven flow. It is to be noted that the empirical correlation for μ_r in Eq. (13) suggests that the roughness viscosity is an exponential function and it varies with surface roughness as well as Reynolds number. Therefore, instead of experimental correlation which are derived only for pressure-driven flow, simple exponential function is suggested here for roughness-viscosity function (μ_r/μ), which can be written as

$$\frac{\mu_r}{\mu} = \exp\left[\frac{\mathrm{Re}_k}{\mathrm{Re}}\frac{k}{y}\right] - 1.0 \tag{21}$$

After nondimensionalizing the average surface roughness height (k) with half channel width (h), Reynolds number at the tip of surface roughness (Re_k) with Reynolds number of the stream flow (Re), and surface roughness viscosity (μ_r) with viscosity of fluid (μ), the nondimensional form of Eq. (21) is given below,

$$\mu_r^* = \exp\left[\mathrm{Re}_{\mathrm{eff}}\frac{\varepsilon_r}{\eta}\right] - 1.0, \quad R_{\mathrm{eff}} = \mathrm{Re}_k/\mathrm{Re} \tag{22}$$

For practical applications, it is expected that μ_r^* should be maximum near the wall and decreases gradually to zero at the core of the channel. The variation of μ_r^* for different surface roughness values across the microchannel is available in literature [7].

Figure 2 shows the comparison of roughness-viscosity function; proposed function predicts the trend as available in Ref. [7]. The value of $\mathrm{Re}_{\mathrm{eff}}=0.3$ satisfies the required behavior of μ_r^*; therefore, in the present analysis, $\mathrm{Re}_{\mathrm{eff}}$ is taken as 0.3.

Considering this roughness parameter, the nondimensional form of Eq. (19) is

$$\frac{\partial p^*}{\partial x^*} = (1 + \mu_r^*)\frac{\partial^2 u^*}{\partial \eta^2} + \frac{\partial^2 \psi^*}{\partial \eta^2} \tag{23}$$

where

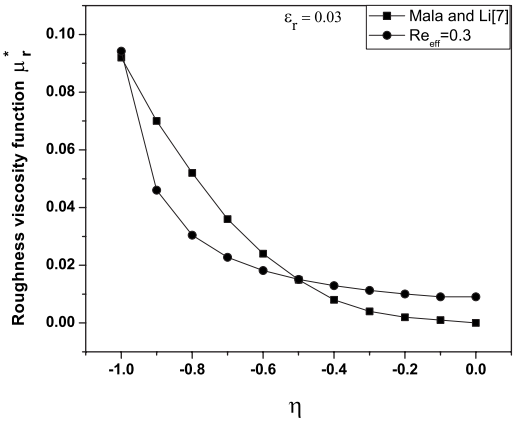

Fig. 2 Comparison of proposed roughness-viscosity function with Mala and Li's [7] function

Downloaded 03 Jun 2010 to 171.66.16.157. Redistribution subject to ASME license or copyright; see http://www.asme.org/terms/Terms_Use.cfm

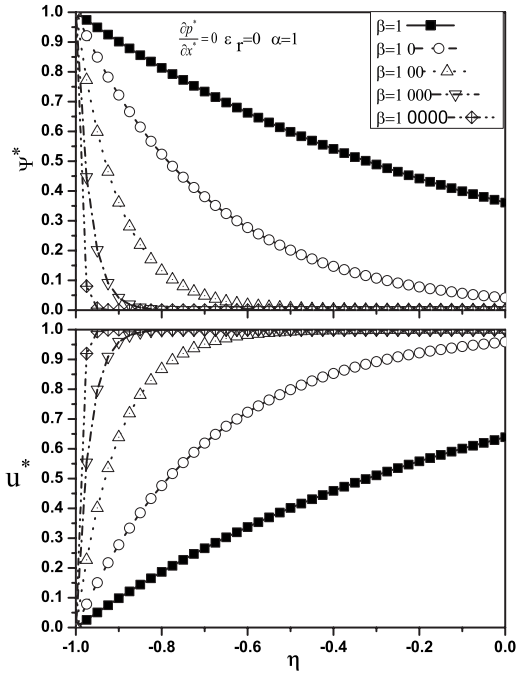

Fig. 3 Variation of nondimensional EO potential Ψ^* and velocity u^* across half channel for various values of β at $\alpha=1$

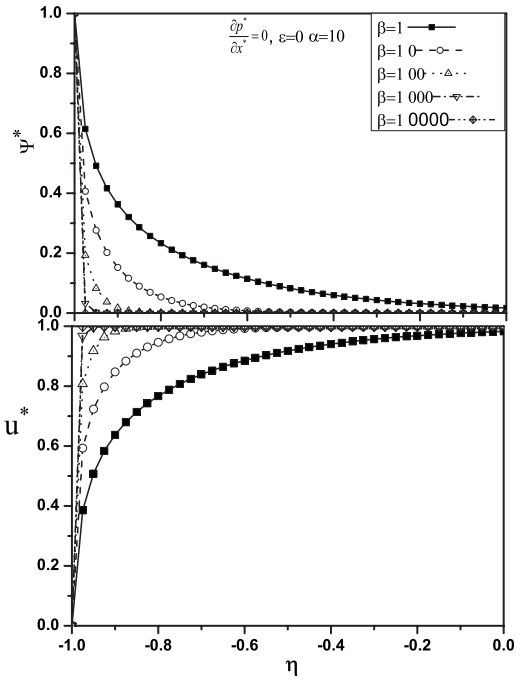

Fig. 4 Variation of nondimensional EO potential Ψ^* and velocity u^* across half channel for various values of β at $\alpha=10$

$$\mu_r^* = \frac{\mu_r}{\mu}, \quad \varepsilon_r = \frac{k}{h} \tag{24}$$

Considering no slip boundary condition ($u^*=0$) at the wall and maximum velocity in the center ($\partial u^*/\partial y=0$), the final governing equation for distribution of velocity is as follows:

$$u^*(\eta) = -\frac{1}{2(1+\mu_r^*)}\left\{\frac{\partial p^*}{\partial x_*}[1-\eta^2] + 1.0 - \psi^*(\eta)\right\} \tag{25}$$

where μ_r^* corresponds to the nondimensional surface roughness of the channel given in Eq. (22). By substituting the solution for ψ^* from Eq. (8), velocity distribution is obtained across the channel for different operating conditions. The $dp^*/dx^*=0$ corresponds to a pure EO flow, and $dp^*/dx^*<0$ and $dp^*/dx^*>0$ correspond to favorable and adverse pressure gradients, respectively. In this analysis, only favorable pressure gradient is considered.

3 Results and Discussion

After computing the electric potential distribution, the nondimensional velocity profile in the presence of surface roughness is obtained for different operating and surface roughness conditions. Initially, for smooth channel, results are plotted for different values of β at $\alpha=1$ [11]. Figure 3 shows that the potential and velocity are mirror image of each other. For the higher values of β ($\beta>100$), the EDL is very thin and below this value, it covers the entire channel. Similarly, in the case of higher β values, the velocity profiles attain Helmholtz–Smouluchowski quickly. For lower values of β ($\beta<10$), the maximum velocity due to pure EO flow is in the core region, whereas for higher values, it is near the wall. In short, as the value of the zeta potential and hence the value of ionic energy parameter increase, the thickness of EDL and velocity distribution across the channel increases. For $\alpha=10$ with the same range of β, the results are plotted in Fig. 4. It is observed that for the same value of β, the decay is faster. As the value of ε_r is considered zero in all cases, the results are shown here to be the same as that of Dutta and Beskok [11].

Figure 5 shows the distribution of velocity across the channel in pure EO flow for various surface roughness values. The effective Reynolds number in this analysis is taken to be 0.3, the reason behind which has been already discussed in Fig. 2. The result shown in the inset plot of Fig. 5 reveals that the impact of surface roughness is dominant within the EDL only, whereas in the core region, the velocity profile distribution tries to attain the velocity of a smooth surface ($\varepsilon_r=0$). A pluglike velocity in each case is observed but attainment of maximum velocity (i.e., centerline) is delayed due to surface roughness. Although the centerline velocity across the channel is approximately constant, the average velocity is reduced. The delay in attainment of centerline velocity reduces the average velocity, which is due to surface roughness and is termed as damping. The velocity damping is a function of the average height of surface roughness k. As the surface roughness increases, the damping increases. For $\varepsilon_r=0.02$, it covers the entire channel, i.e., surface roughness affects the centerline velocity,

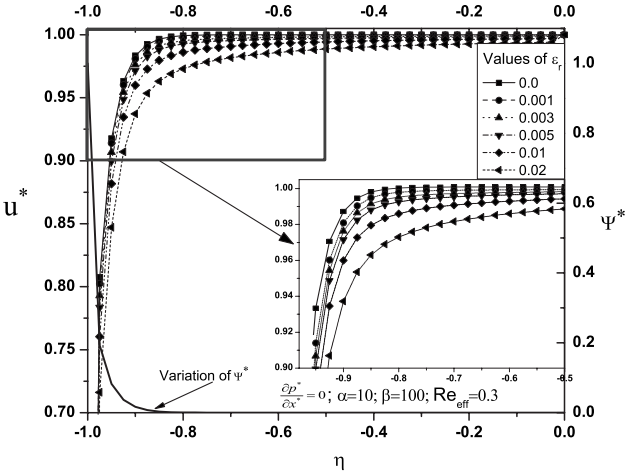

Fig. 5 Variation of nondimensional velocity u^* and EO potential Ψ^* in pure EO flow for various values of ε_r at $\beta=100$

Downloaded 03 Jun 2010 to 171.66.16.157. Redistribution subject to ASME license or copyright; see http://www.asme.org/terms/Terms_Use.cfm

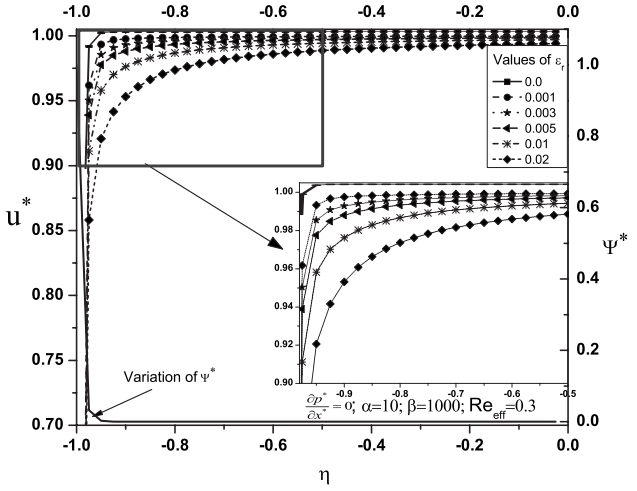

Fig. 6 Variation of nondimensional velocity u^* and EO potential Ψ^* in pure EO flow for various values of ε_r at β=1000

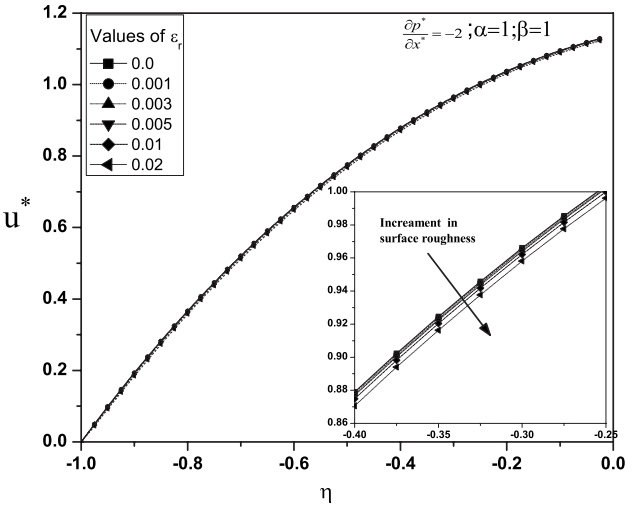

Fig. 7 Variation of nondimensional velocity u^* for various values of ε_r in PD flow at $\partial p^*/\partial x^*=-2$

whereas for ε_r=0.001, the effect is near the wall only. However, in both these cases, the average channel velocity is less as compared to the smooth channel (ε_r=0.0). Comparison of β=100 and β=1000 for the same value of ε_r indicates that there is a faster increment in velocity for higher value of β, as shown in Fig. 6. For higher value of β, faster decay in EO potential is observed in Figs. 3 and 4, due to which a faster increment in the velocity near the wall is observed. An equal amount of deviation for higher as well as lower values of β is observed. The distribution of electric potential across the channel is shown in Figs. 3 and 4 for various values of surface roughness. It is observed that the distribution of electric potential across the channel is independent of the surface roughness. Wang et al. [16] reported that across the middle section of the roughness element, the velocity maximum increases as the surface roughness increases. The increment in maximum velocity was observed across the middle section of the roughness element. After an increase in height of the roughness element, the effective cross section area will decrease across that section and it is a known fact that to maintain the same flow rate, velocity has to increase.

The changes in velocity profiles presented are not for constant cross section area; therefore, it is not clear that for a constant cross sectional area, the effect of surface roughness increases or decreases the velocity maximum in pure EO flow. However, from the flow rate variation results from their analysis, it is clear that after an increase in surface roughness, the flow rate decreases.

Figure 7 shows the velocity distributions for pressure-driven flow. As literature suggests [6], there is a deviation in friction factor and friction number in laminar flow due to surface roughness, which reduces the average velocity. However, the surface roughness values, which have been used in all these studies, are for metal microchannels like steel. The EO effect is widely used in MEMS devices, which are generally nonmetallic and hence in this analysis, the maximum value of surface roughness considered is ε_r=0.002. In pressure-driven flow, the effect of surface roughness across the channel is approximately the same. The deviation in the velocity from a smooth surface is zero at the wall, it increases toward the center, and remains constant after some distance across the channel, as shown in the inset plot in Fig. 7. For higher pressure drop, the centerline velocity is more but at the same time, the relevant damping is also more as compared to lower pressure drop condition. As shown in Fig. 8, the magnitude of velocity is higher due to large pressure drop but the behavior of attainment of the centerline velocity is similar to that of a standard parabolic profile. A large pressure drop increases the flow momentum across the channel, which results in an increase in the effect of surface roughness. The results from Figs. 7 and 8 exhibit similar trend and deviation as observed by Mala and Li [7].

Figure 9 shows the velocity distribution for different flow conditions: EO flow in a smooth channel, EO flow in a rough channel (EO+μ_r), pressure-driven flow in a smooth channel (PD), pressure-driven flow in a rough channel (PD+μ_r), combined pressure-driven and EO flow in a smooth channel (PD+EO), and combined pressure-driven and EO flow in a rough channel (PD+EO+μ_r). The standard velocity profiles are observed for EO as well as for PD flow in the smooth channel. In combined (PD+EO) flow, it is observed that the behavior is a combination of pluglike and parabolic velocity profile.

For EO and PD+EO operating conditions, the relevant damping is observed near the wall, whereas in the core region, the velocity profile attains the maximum centerline velocity. The amount of damping is the same for both the cases. In combined flow (PD+EO+μ_r), the damping is maximum near the wall and reduces slowly toward the center of the channel. This reduction in damping from the wall to the channel center is very less across the channel but in the case of (EO+μ_r), the attainment of the center-

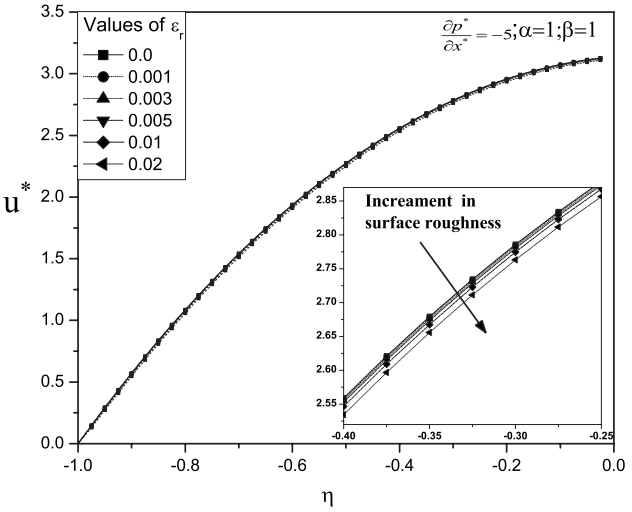

Fig. 8 Variation of nondimensional velocity u^* for various values of ε_r in high PD flow at $\partial p^*/\partial x^*=-5$

Downloaded 03 Jun 2010 to 171.66.16.157. Redistribution subject to ASME license or copyright; see http://www.asme.org/terms/Terms_Use.cfm

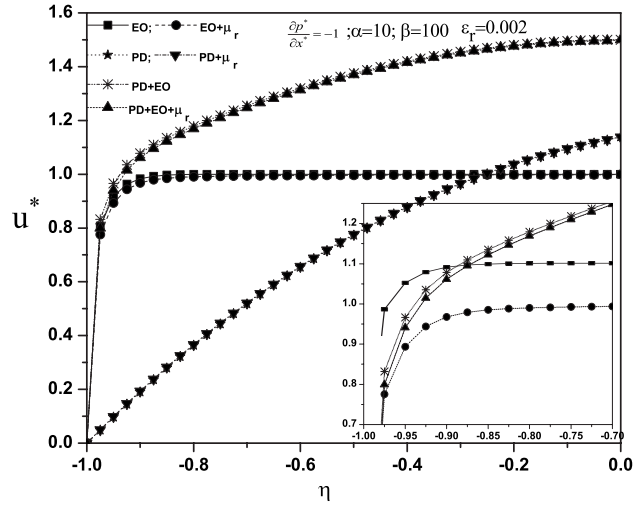

Fig. 9 Variation of nondimensional velocity u^* for various values of ε_r in different operating conditions

line velocity is very sharp. Figure 10 shows the effect of roughness for a combined flow (PD+EO+μ_r). The velocity profile within the EDL follows the pluglike profile but beyond EDL, the parabolic velocity component due to PD flow is added. As shown in the inset plot, the damping increases as the surface roughness is increased. The amount of damping is more near the wall region and decreases with the distance from the wall.

As observed earlier, there is always a damping in velocity across the channel due to surface roughness, which cannot be avoided by using conventional microfabrication processes for microfluidic devices. Surface roughness influences the hydrodynamic flow, which in turn affects the electrokinetic phenomena in a microchannel. However, by introducing appropriate electric potential, such damping effect can be partially nullified in the core region but may not be possible near the wall. Hence, combined EO and PD flow is an attractive proposition for microfluidic devices with an inherent roughness in the channel walls.

4 Conclusions

The effect of surface roughness on velocity profiles for combined EO and PD flow is studied here. Surface roughness is accounted using modified surface RVM. In pure EO flow, a pluglike velocity profile with delay in attaining the centerline velocity is observed. The deviation in the velocity profile across the microchannel due to the surface roughness is found to be dominant within the EDL. In PD flow, the deviation increases with distance from the wall and remains constant after a certain distance from the wall. Within the core region of the flow, the magnitude of damping in the case of PD force is more than EO flow. In combined EO and PD flow, a combination of pluglike and parabolic velocity profiles is observed. It is found that in combined flow, damping reduces slowly across the channel. It is suggested that in a combined EO and PD flow, the EO pumping may be an alternative means to reduce the effect of surface roughness in the core region of the flow.

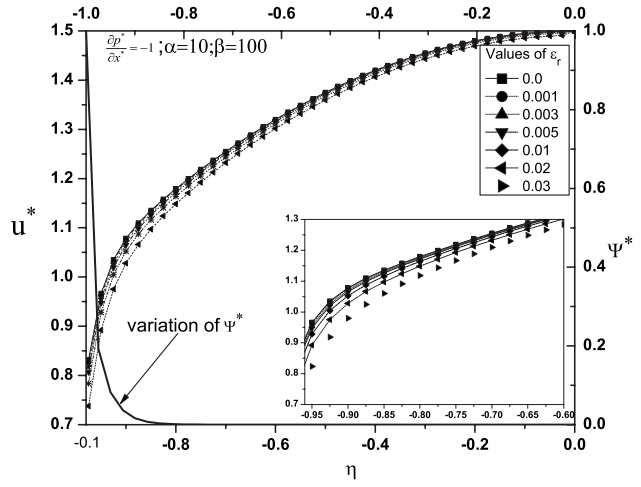

Fig. 10 Variation of nondimensional velocity u^* for various values of ε_r in combined EO and PD flow

Nomenclature

B = width of the channel
E_x = electric field intensity in the direction of flow
F = Faraday's constant
K_B = Boltzmann constant
P = pressure
Re = Reynolds number
Re_k = roughness Reynolds number
$\mathrm{Re}_{\mathrm{eff}}$ = effective Reynolds number
T = absolute temperature
U_k = roughness velocity
c = ionic concentration in bulk solution
f_{EK} = electrokinetic body force
k = average surface roughness height
u = velocity component in the x-direction
u_{HS} = Helmholtz–Smoluchowski electro-osmotic velocity
$\mathbf{v}$ = velocity vector
x = coordinate variable in the x-direction
y = coordinate variable in the y-direction
z = valence number of univalent fluid
α = nondimensional ionic energy parameter
ε_r = dielectric constant of fluid
ε_r = ratio of average surface roughness height and width of channel
ζ = zeta potential
η = nondimensional coordinate variable in the y-direction
λ_D = debye length
μ = viscosity of fluid
μ_r = viscosity due to the surface roughness
μ_e = effective viscosity
ρ = density of fluid
ρ_e = charge density
ϕ = applied potential
ϕ_0 = wall potential
ψ = potential due to electrical double layer
ω = Debye–Huckle parameter

Superscript

$*$ = nondimensional parameter

References

[1] Karniadakis, G., Beskok, A., and Aluru, N., 2004, *Microflows and Nanoflows Fundamentals and Simulation*, Springer, New York, pp. 255–292.
[2] Nguyen, N., and Wereley, S., 2006, *Fundamentals and Applications of Microfluidics*, Artech House, Boston.
[3] Heng, Q., Tao, C., and Tie-chuan, Z., 2006, "Surface Roughness Analysis and Improvement of Microfluidic Channel With Excimer Laser (Short Communication)," Microfluid. Nanofluid., **2**, pp. 357–360.
[4] Croce, G., and D'Agaro, P., 2004, "Numerical Analysis of Roughness Effect on Microtube Heat Transfer," Superlattices Microstruct., **35**, pp. 601–616.
[5] Que, W., Mohiuddin, M. G., and Dongqing, L., 2000, "Pressure-Driven Water Flows in Trapezoidal Silicon Microchannels," Int. J. Heat Mass Transfer, **43**, pp. 353–364.
[6] Morani, G., 2004, "Single-Phase Convective Heat Transfer in Microchannels: A Review of Experimental Results," Int. J. Therm. Sci., **43**, pp. 631–651.
[7] Mala, M., and Li, D., 1999, "Flow Characteristics of Water in Microtubes,"

Downloaded 03 Jun 2010 to 171.66.16.157. Redistribution subject to ASME license or copyright; see http://www.asme.org/terms/Terms_Use.cfm

Int. J. Heat Mass Transfer, **20**, pp. 142–148.
[8] Kandlikar, S., Schmitt, D., Carrano, A., and Taylor, J., 2005, "Characterization of Surface Roughness Effects on Pressure Drop in Single-Phase Flow in Microchannels," Phys. Fluids, **17**, p. 100606.
[9] Rawool, A. S., Mitra, S. K., and Kandlikar, S. G., 2006, "Numerical Simulation of Flow Through Microchannel With Designers Surface Roughness," Microfluid. Nanofluid., **2**, pp. 215–221.
[10] Rawool, A. S., Mitra, S. K., and Kandlikar, S. G., 2006, "Numerical Simulation of Electroosmotic Effect in Serpentine Channels," Microfluid. Nanofluid., **2**, pp. 261–269.
[11] Dutta, P., and Beskok, A., 2001, "Analytical Solution of Combined Electroosmotic/Pressure-Driven Flows in Two-Dimensional Straight Channels: Finite Debye Layer Effects," Anal. Chem., **75**, pp. 57–70.
[12] Reza, M., Mehradad, T., and Manzari, M., 2007, "Analysis of Combined Pressure-Driven Electroosmotic Flow Through Square Microchannel (Short Communication)," Microfluid. Nanofluid., **3**, pp. 123–126.
[13] Hu, Y., Wernera, C., and Li, D., 2006, "Influence of the Three-Dimensional Heterogeneous Roughness on Electrokinetic Transport in Microchannels," J. Colloid Interface Sci., **15**, pp. 527–536.
[14] Zembla, M., 2004, "Electrokinetics of Heterogeneous Surface," Adv. Colloid Interface Sci., **112**, pp. 59–92.
[15] Kim, D., and Darve, E., 2006, "Molecular Dynamics Simulation of Electro-Osmotic Flows in Rough Wall Nanochannels," Phys. Rev. E, **73**, p. 051203.
[16] Wang, M., Wang, J., and Chen, S., 2007, "Roughness and Cavitation's Effects on Electro-Osmotic Flows in Rough Microchannels Using Lattice Poisson-Boltzmann Methods," J. Comput. Phys., **226**, pp. 836–851.
[17] Merkle, C., Kubato, C., and Ko, T., 1974, "An Analytical Study of the Effects of Surface Roughness on Boundary-Layer Transition," AF Office of Science Res. Space and Missile System Org.AD/004786.

Downloaded 03 Jun 2010 to 171.66.16.157. Redistribution subject to ASME license or copyright; see http://www.asme.org/terms/Terms_Use.cfm

Donald M. McEligot[1]
Aerospace and Mechanical Engineering Department,
University of Arizona,
Tucson, AZ 85721;
Institute für Kernenergetik und Energiesysteme (IKE),
University of Stuttgart,
D-70569 Stuttgart, Deutschland;
Idaho National Laboratory (INL),
Idaho Falls, ID 83415-3885

Edmond J. Walsh
Stokes Research Institute,
Mechanical and Aeronautical Engineering Department,
University of Limerick,
Limerick, Ireland

Eckart Laurien
Institute für Kernenergetik und Energiesysteme (IKE),
University of Stuttgart,
D-70569 Stuttgart, Deutschland

Philippe R. Spalart
Boeing Commercial Airplanes,
Seattle, WA 98124-2207

Entropy Generation in the Viscous Parts of Turbulent Boundary Layers

The local (pointwise) entropy generation rate per unit volume S''' is a key to improving many energy processes and applications. Consequently, in the present study, the objectives are to examine the effects of Reynolds number and favorable streamwise pressure gradients on entropy generation rates across turbulent boundary layers on flat plates and—secondarily—to assess a popular approximate technique for their evaluation. About two-thirds or more of the entropy generation occurs in the viscous part, known as the viscous layer. Fundamental new results for entropy generation in turbulent boundary layers are provided by extending available direct numerical simulations. It was found that, with negligible pressure gradients, results presented in wall coordinates are predicted to be near "universal" in the viscous layer. This apparent universality disappears when a significant pressure gradient is applied; increasing the pressure gradient decreases the entropy generation rate. Within the viscous layer, the approximate evaluation of S''' differs significantly from the "proper" value but its integral, the entropy generation rate per unit surface area S''_{ap}, agrees within 5% at its edge. [DOI: 10.1115/1.2928376]

Keywords: turbulent boundary layer, entropy generation, viscous layer, dissipation, direct numerical simulation, pressure gradient

1 Introduction

The local (pointwise) entropy generation rate per unit volume S''' is a key to improving many energy processes and applications [1]. In developing his reciprocal relations for irreversible processes, Onsager [2] extended Lord Rayleigh's "principle of least dissipation of energy" and indicated that the rate of increase of entropy plays the role of a potential. Thus, entropy generation (or "production" [3]) may be used as a parameter to measure a system's departure from reversibility. Bejan [1] has suggested that real systems, which owe their thermodynamic imperfections to fluid flow, heat transfer, and mass transfer irreversibilities, be optimized by minimizing their entropy generation. This approach has been applied to compact heat exchangers, power plants, natural convection, rotating bodies, enhanced heat transfer surfaces, impinging jets, convection in general, and other thermal systems.

Understanding of the distribution of entropy generation rate is important for several reasons, including those indicated above. Kock and Herwig [4] suggested that predicting the efficient use of energy in thermal systems requires accounting for the second law of thermodynamics since the loss of available work [5] is proportional to the amount of entropy produced (e.g., via the Gouy [6]–Stodola [7] theorem cited by Bejan). Therefore, apparatus producing less entropy by irreversibilities destroys less available work, increasing the efficiency and, in turn, reducing the fuel consumption and waste products. In turbomachinery and other applications, definitions of loss coefficients differ depending on the components considered; evaluation of entropy generation rate provides a universal measure of loss, irrespective of how or where it occurs and allows direct comparisons of loss rates from friction, heat transfer, and other irreversible processes. Kock and Herwig and others are using computational fluid dynamics (CFD) codes to predict entropy generation for optimization by minimizing it. Since S''' determines the localized contribution to energy losses or reduction in the availability of energy [8,9], insight into the dominant loss sources and their locations can allow reducing them intelligently, thereby improving efficiency. These CFD studies seek to identify the regions of maximum entropy production so they may be attacked and reduced.

In the present study, we examine the entropy generation due to shear stresses in "unheated, two-dimensional" *turbulent boundary layers*. Geometry is constrained to the classical smooth flat plate but both negligible and favorable pressure gradients are considered in the streamwise direction. Fluid properties are idealized as constant.

We concentrate on the viscous part, known as the viscous layer, because it is typically the region where the largest gradients occur and the production of turbulence is greatest. Following Bradshaw [10], we are here defining the viscous layer as the region where viscous effects are significant, but not necessarily dominant, typically to y^+ about 30 in a classical zero-pressure gradient case (it includes the "laminar" and buffer sublayers in some investigators's terminology). The major resistances to momentum, energy, and mass transfer occur in this layer, and the pointwise entropy generation rate is greatest here as well [1,11]. While we concentrate on the viscous layer, the analyses are not limited to this region but extend to the edge of the turbulent boundary layer.

The *objectives* of the present study are to obtain fundamental new results for the effects of Reynolds number and favorable streamwise pressure gradients on entropy generation rates across turbulent boundary layers, particularly in the viscous layer, and secondarily to assess a popular approximate technique for their evaluation. Key relations for evaluating entropy generation rates are presented in Sec. 2, which follows. Related literature is discussed there and also through the remainder of the text where

[1]Corresponding author.

Contributed by the Fluids Engineering Division of ASME for publication in the JOURNAL OF FLUIDS ENGINEERING. Manuscript received October 30, 2006; final manuscript received February 4, 2008; published online June 5, 2008. Assoc. Editor: Paul Durbin.

 Copyright © 2008 by ASME

Downloaded 03 Jun 2010 to 171.66.16.157. Redistribution subject to ASME license or copyright; see http://www.asme.org/terms/Terms_Use.cfm

pertinent. The results of the direct numerical simulations (DNS) by Spalart [12,13] are extended to determine the distributions of entropy generation rates. They are applied first for the classical case of a negligible streamwise pressure gradient (referred to as zpg=zero pressure gradient) and then to favorable pressure gradients, approaching laminarization. Since the turbulent dissipation rate can be difficult to measure and to predict, an approximate approach suggested by Rotta is next evaluated. We then summarize with concluding remarks. These new results should be useful for optimization analyses.

2 Background

Entropy appears in the second law of thermodynamics, which can be written for a flowing open system, in terms of the "rate of creation" of entropy by London [14], as

$$\mathrm{RoC}(S) = S_{\mathrm{out}} + (dS_{\mathrm{cv}}/dt) - S_{\mathrm{in}} \geq \sum (\dot{Q}/T) \tag{1}$$

where $S_{\mathrm{in/out}}$ is the rate of entropy convection into or out of the system, S_{cv} is the entropy stored in the control volume, t is time, $\dot{Q}$ is the rate of heat transfer into the control volume, and T is the absolute temperature of the thermal reservoir from which this heat transfer comes. As a measure of the irreversibility, Bejan [1] and others defined an entropy generation rate or rate of production of entropy [15]

$$S_{\mathrm{gen}} = \Sigma(\dot{m}s)_{\mathrm{out}} + (dS_{\mathrm{cv}}/dt) - \Sigma(\dot{m}s)_{\mathrm{in}} - \Sigma(\dot{Q}/T) \geq 0 \tag{2}$$

which can be seen to be the inequality, if any, between RoC(S) and the reversible portion of entropy transfer with heat into the system. Possible irreversible processes are recognized to include friction, heat transfer with significant temperature gradients, combustion, etc.

For an isothermal, laminar pipe flow with no external heating imposed, Bejan [1] and others suggested that the volumetric entropy generation rate S''' can be estimated by evaluating the viscous dissipation function Φ for the flow

$$S'''\{y\} = (\mu\Phi/T) = \mu(\partial U/\partial y)^2/T \tag{3}$$

The braces $\{\}$ are used to indicate that S''' is considered to be a function of y. In the remainder of this paper, the symbol S will refer to the entropy generation rate, not to the extensive entropy itself.

The time-mean value of $\mu\Phi$ at a point in a flow with turbulent fluctuations may be expanded to $\mu\Phi+\rho\varepsilon$ where the former represents viscous dissipation of mean-flow kinetic energy (called "direct dissipation") and the latter represents dissipation of turbulent kinetic energy into thermal energy ("indirect" or turbulent dissipation) [16–19],

$$\rho\varepsilon = 2\mu\left[\overline{\left(\frac{\partial u}{\partial x}\right)^2} + \overline{\left(\frac{\partial v}{\partial y}\right)^2} + \overline{\left(\frac{\partial w}{\partial z}\right)^2}\right] + \mu\left[\overline{\left(\frac{\partial u}{\partial y} + \frac{\partial v}{\partial x}\right)^2} + \overline{\left(\frac{\partial v}{\partial z} + \frac{\partial w}{\partial y}\right)^2} + \overline{\left(\frac{\partial w}{\partial x} + \frac{\partial u}{\partial z}\right)^2}\right] \tag{4}$$

One might question the physical meaning of splitting entropy generation into two parts (direct and turbulent). Since—in reality—the mean profile never occurs, the direct part might only be described as "something that would exist if the flow were steady and laminar with a profile like the turbulent mean one." Comparable concerns have been presented by Brodkey et al. [20,21] and Bradshaw [22] concerning the idea of "instantaneous production" of turbulent kinetic energy. However, in the present study, we follow the customary approach [23] of identifying so-called mean and turbulent dissipation individually as is often done via Reynolds averaging in turbulent flows in general [11]. Then one may benefit from earlier studies, which, for example, specifically defined turbulent dissipation of turbulence kinetic energy in the same manner and examined it.

When expressed in wall units, the pointwise entropy generation rate for a two-dimensional boundary layer can be written as

$$(S'''\{y^+\})^+ = [(\partial U^+/\partial y^+) + (\partial V^+/\partial x^+)]^2 + 2[(\partial U^+/\partial x^+)^2 + (\partial V^+/\partial y^+)^2] + \varepsilon^+ \tag{5}$$

where $(S''')^+$ is defined as $T\nu S'''/(\rho u_\tau^4)$ and ε^+ is $\nu\varepsilon/u_\tau^4$. For a laminar boundary layer on a flat plate without freestream turbulence, S''' and its integrals can be calculated from the Blasius or Pohlhausen solutions [24].

The prediction of pointwise $(S'''\{y^+\})^+$ is desired to identify regions where most losses occur (large values of S''') and to deduce the entropy generation rate per unit surface area—and, ultimately, S' or S over the entire surface. In wall coordinates, the entropy generation rate per unit surface area value can be evaluated as

$$(S''\{y^+\})^+ = (TS''/(\rho u_\tau^3)) = \int_0^{y^+} (S'''\{y^+\})^+ dy^+ \tag{6}$$

Based on definitions, continuity and momentum equations, and empirical relations, one can form approximate relations between some of the nondimensional parameters suggested as governing flows with streamwise pressure gradients. Streamwise acceleration is often represented by an acceleration parameter [25] defined as

$$K_v = (\nu/U_\infty^2) dU_\infty/dx \tag{7}$$

For a boundary layer flow, one can show $K_v = -(c_f/2)^{3/2} K_p$, where c_f is the skin friction coefficient, defined as $2\tau_w/(\rho U_\infty^2)$, and $K_p = (\nu/\rho u_\tau^3) dp/dx$ is the nondimensional streamwise pressure gradient.

The likelihood of streamwise pressure gradients affecting the viscous layer was discussed by McEligot and Eckelmann [26]. The governing momentum equation may be written as

$$U^+(\partial U^+/\partial x^+) + V^+(\partial U^+/\partial y^+) = -K_p + (\partial \tau^+/\partial y^+) \tag{8}$$

Near the wall, the solution for the total shear stress variation can be approximated as in Eq. (11.35) by Rotta [11] and as by Julien et al. [27] and Finnicum and Hanratty [28] as

$$\tau^+\{y^+\} = (\tau\{y^+\}/\tau_w) \approx 1 + K_p y^+ \left[1 - (c_f/(2y^+)) \int_0^{y^+} (U^+)^2 dy^+\right] \tag{9}$$

For the effect of a favorable pressure gradient to be negligible in the viscous layer, one could establish a 5% criterion that τ^+ still be greater than 0.95 or such at its edge (say $y^+ \approx 30$). This constraint translates to requirements such as $-K_p < 0.0017$, $\mathrm{Re}_\tau > 600$ and, for tubes or ducts, $\mathrm{Re}_{D,h} > 46{,}000$. McEligot and Eckelmann suggested that, for the viscous layer behavior to be similar in various geometries and flows, one needs (1) the viscous layer to be small relative to geometric scales in the flow and (2) to have the same distribution of $\partial\tau^+\{y^+\}/\partial y^+$ through the viscous layer. In a comparable study, Nieuwstadt and Bradshaw [29] showed that viscous layer statistics can be expected to be approximately equivalent in different geometries if their values of Re_τ are the same, i.e., $\tau^+\{y^+\}$ would be about the same in both geometries. In deriving inner scaling for wall flows subject to large pressure gradients, Nickels [30] presented comparable arguments.

From analysis and application of boundary layer assumptions for asymptotic high-Reynolds-number zpg and of measurements by Klebanoff [31] at $\delta^+ \approx 2200$, Rotta [11] concluded that almost 60% of the dissipation (and therefore entropy generation) occurs within y^+ less than about 20. The rate of direct dissipation alone amounts to 40% of the total energy loss and nearly 20% is converted into turbulent energy in the same region. Measurements by deGraaff and Eaton [32] for negligible pressure gradients at Re_θ from 1430 to 31,000 correspond to these conditions and provide mean velocity data to y^+ as low as unity. Their results are gener-

Downloaded 03 Jun 2010 to 171.66.16.157. Redistribution subject to ASME license or copyright; see http://www.asme.org/terms/Terms_Use.cfm

ally in agreement with those of Spalart [13], which will be presented in the next section. By assuming the three-layer von Karman "universal velocity profile," Bejan [1] derived comparable results for fully developed turbulent pipe flow at high Reynolds numbers. The assumption of an asymptotic high-Reynolds-number profile is equivalent to considering a low streamwise pressure gradient and a constant shear layer $\tau\{y\}$ near the wall.

Rotta, for boundary layers, and then Bejan [1] and Laadhari [33], for fully-developed duct flows, have provided estimates of direct or mean dissipation for high Reynolds numbers. Likewise Jovanovic et al. [34] presented measurements for channel flows at $\mathrm{Re}_\tau \approx 600$ and 810 (essentially high Reynolds numbers) emphasizing turbulent dissipation. Information on variation of indirect or turbulent dissipation is available *for fully developed channel flow*, which, by definition, does not have streamwise acceleration although it can have significant streamwise pressure gradients [35,36]. From the DNS predictions of Kawamura and co-workers for the channel flows [37,38], one can infer that direct dissipation will increase and turbulent dissipation will decrease as a favorable pressure gradient is increased but the total or net dissipation is not presented in their papers so one cannot tell whether $(S''')^+$ will increase or decrease. Likewise, with their 2-1/2 D model for the viscous layer Finnicum and Hanratty [28] have forecasted, that, relative to a zpg boundary layer, a near-laminarizing pressure gradient will yield an increase in direct dissipation and will lower indirect dissipation but they did not present the effects on their sum (i.e., S''') either.

Equilibrium turbulent boundary layers with strongly adverse pressure gradients have been measured by Skare and Krogstad [39] with data for U^+ to y^+ as low as 2. However, the Reynolds stresses could not be measured nearer than $y^+ \approx 20-30$ so there are no data for turbulent dissipation (or production) in the viscous layer. Aubertine and Eaton [40] conducted an experiment on development of turbulence structure in nonequilibrium boundary layers over a range about $3000 < \mathrm{Re}_\theta < 6700$, emphasizing a mildly adverse pressure gradient but including a few stations with negligible or slightly favorable pressure gradients. Direct dissipation was not presented as such but presumably could be calculated from their $U^+\{y^+\}$ data with some uncertainty near the wall; however, at their strongest favorable pressure gradient ($K_p \approx -0.006$), the authors seem less confident about the results. Jones et al. [41] measured sink flow boundary layers with mild favorable pressure gradients at $1800 < \mathrm{Re}_\theta < 3000$ but their first data are at y^+ about 12–55, depending on location and acceleration. For strong favorable pressure gradients, Jones and Launder [42] conducted experiments at $K_v \approx 1.5\times10^{-6}$, 2.5×10^{-6}, and 3×10^{-6}, corresponding to the DNS of Spalart [12] to be extended in a later section; however, they were not able to measure dissipation in the viscous layers of their boundary layers.

Apparently missing for the dominant viscous layers of turbulent boundary layers are (1) quantitative variations—without pressure gradients and *at lower-than-asymptotic Reynolds numbers*—of direct dissipation, details of turbulent dissipation, and, therefore, pointwise and areal entropy generation rates plus (2) the same fundamental results *for* cases with *significant favorable pressure gradients*. Only limited DNS or experimental results related to those items are readily available. While expected to be qualitatively comparable to channel flows, the quantitative results are likely to differ for pressure gradients greater than $|K_p|$ of about 0.002 or so.

3 Entropy Generation With Negligible Pressure Gradients

The simulations of Spalart [13] allow examination of the effects of Reynolds number on entropy generation in turbulent boundary layers without significant streamwise pressure gradients. The geometry was a smooth flat plate with a constant freestream velocity. He solved the three-dimensional time-dependent Navier–Stokes equations using a spectral method with up to 10^7 grid points. Periodic spanwise and streamwise conditions were applied and a multiple-scale procedure was employed to approximate the slow streamwise growth of the boundary layer. Freestream turbulence was negligible. Details of the governing equations, assumptions, and numerical procedures are provided in his original paper and an earlier one [12], which used essentially the same computer program. His results provide tabulations at $\mathrm{Re}_\theta = 300$, 670, and 1410 with approximate boundary layer thicknesses of $\delta^+ \approx 150$, 325, and 650, respectively. The highest of these should be close to having asymptotically high-Reynolds-number behavior in its viscous layer. With $-K_p \approx 0$, the x-momentum equation reduces to $\tau^+\{y^+\} \approx 1$ near the wall, i.e., the constant shear layer assumption becomes valid, provided the boundary layer thickness is "large" enough.

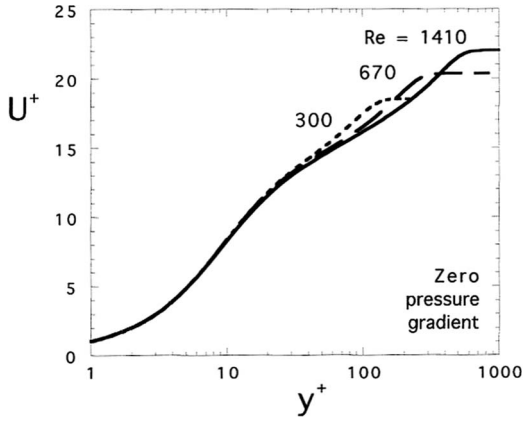

Fig. 1 Streamwise mean velocity profiles for turbulent boundary layers with negligible pressure gradients; the Reynolds number is based on momentum thickness [13]

From the background considerations above, one sees that profiles of mean velocity and the mean dissipation of turbulence kinetic energy are needed in order to calculate the pointwise entropy generation rate. Figure 1 demonstrates that—relative to the Reynolds number—there is a very little variation of the mean profile in the viscous layer. At $y^+ = 30$, there is less than 3% difference between the lowest and highest Reynolds numbers. The main divergence between these mean profiles begins near y^+ of 40–50. From these results, one can infer that in the viscous layer the contribution of the *mean motion* to the entropy generation—given by terms such as $(\partial U^+/\partial y^+)^2$—will be approximately independent of Reynolds number. One comes to the same conclusion from the presentation of the quantity $y^+\partial U^+/\partial y^+$ in Fig. 5(b) of Spalart [13]. Toward the edges of the boundary layers in the so-called wake regions, the profiles do vary obviously with Reynolds number; however, by then—as will be seen later—the entropy generation rate is very small. Rotta [11], Bejan [1], and Laadhari [33] presented the variation of direct dissipation versus y^+ but only for asymptotically high Reynolds numbers. For turbulent dissipation, Spalart [13] commented that there was a weak trend with Reynolds number but "noticeable" enhancement for y^+ less than 10.

Under boundary layer approximations, the term $(\partial U^+/\partial y^+)^2$ dominates the contribution to "direct dissipation" or entropy production from the mean flow field so the pointwise entropy generation rate may be calculated as

$$(S''')^+ \approx (\partial U^+/\partial y^+)^2 + \varepsilon^+ \tag{10}$$

Spalart and others tabulate the "pseudodissipation" ε_u^+ (in the terms of Gersten and Herwig [17]); citing Hinze [43], the desired dissipation ε^+ is called the "true dissipation" by Wilcox [44]. For a two-dimensional boundary layer, the difference is provided by some terms common with viscous diffusion,

Downloaded 03 Jun 2010 to 171.66.16.157. Redistribution subject to ASME license or copyright; see http://www.asme.org/terms/Terms_Use.cfm

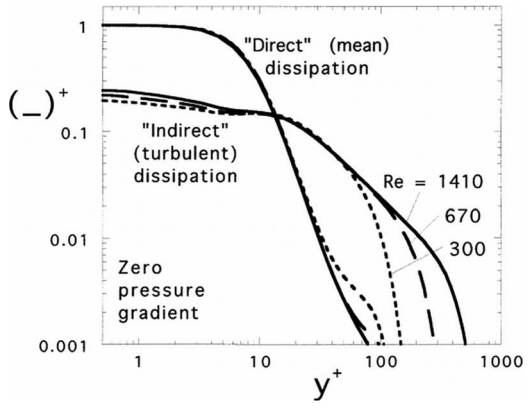

Fig. 2 Relative magnitudes of contributions to entropy generation in turbulent boundary layers with negligible pressure gradients ($Re_\theta \approx 1410$, solid curves; $Re_\theta \approx 670$, dashes; $Re_\theta \approx 300$, short dashes)

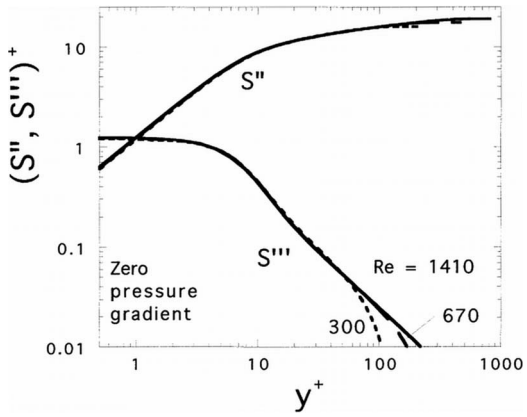

Fig. 3 Pointwise and areal entropy generation rates across turbulent boundary layers with negligible pressure gradients (curves denoted as in Fig. 2)

$$\varepsilon - \varepsilon_u = \nu\{(\partial^2\overline{u^2}/\partial x^2) + 2(\partial^2\overline{uv}/\partial x\partial y) + (\partial^2\overline{v^2}/\partial y^2)\} \qquad (11)$$

which, therefore, cancel in the governing equation for turbulence kinetic energy. In a boundary layer, the third term on the right-hand side would be dominant. From the DNS of Kim et al. [45] *for channel flow* at $-K_p \approx 0.006$, Bradshaw and Perot [46] showed that the contribution of viscous diffusion is everywhere less than about 2% of the dissipation rate and conclude that the difference between the true dissipation rate and the pseudodissipation rate "can be ignored for all purposes of computation and discussion." This difference is also addressed by Antonia et al. [35].

In the present study, we formed ε^+ by calculating the second derivative of $(\overline{v^2}\{y^+\})^+$ from Spalart's tabulations and adding it to ε_u^+, which is listed directly. Spalart [12,13] tabulated and presented the terms for the balance of twice the turbulence kinetic energy (sum of the Reynolds normal stresses) so we divide by two to obtain ε_u^+. His numerical technique does not provide the streamwise gradients so only the dominant third term is included in the calculation of viscous diffusion. The other two terms involve streamwise derivatives (equation for $\varepsilon - \varepsilon_u$ above) and, under standard boundary layer approximations, can be expected to be much smaller. This third term is positive near the wall and becomes negative near y^+ about 14–15 and positive again at $y^+ > 80$. The resulting maximum difference between "true" and pseudodissipation is about 3% at y^+ near 5, where it is small relative to direct dissipation from the mean motion anyhow. (Thus, a significant error in evaluating this contribution from the viscous diffusion term would have only a negligible effect on the resulting total entropy generation rate.) A maximum negative value of this difference is about 1.6% near the edge of the viscous layer.

The direct dissipation and the turbulent dissipation ε^+ are compared for the three cases from low to "high" Reynolds numbers in Fig. 2. The logarithmic representation emphasizes the viscous layer while still giving indication of results well outside it. Logarithmic coordinates also make it easy to estimate percent differences and, therefore, relative importance of terms. As implied by Fig. 1, the direct dissipation differs only slightly with Reynolds number within the viscous layer. Since the turbulent dissipation term ε^+ dominates beyond y^+ of 30, the effect of Reynolds number variation in the *mean motion on the total* entropy generation rate becomes negligible at larger distances. The turbulent dissipation varies with Reynolds number about 20% in the so-called "linear layer" near the wall ($y^+ < \sim 5$) but there the contribution from the mean motion dominates. From y^+ of 10 to about 50, ε^+ is almost independent of the Reynolds number. These observations are qualitatively comparable to those for channel flow [36]; Spalart also noted that his near-wall results were similar to those of Moser and Moin [47] for a channel.

In wall coordinates, the contribution of direct (mean) dissipation is unity at the wall. It dominates near the wall while turbulent dissipation contributes about 20% to the total. Consequently, the difference between true and pseudodissipation corresponds to less than 1/2% of the total in this region. Both direct and turbulent dissipation decrease as y^+ increases but the reduction of direct dissipation is more rapid with respect to y than the turbulent dissipation—so they become of about equal magnitude near $y^+ \approx 14$ or so. For larger values of y^+, turbulent dissipation becomes progressively more dominant. By the edge of the viscous layer, the contribution of the mean motion is almost negligible. Both direct and turbulent dissipation are seen to decrease rapidly beyond this region. Through the typical logarithmic layer and wake region, the total dissipation and therefore the entropy generation are essentially provided by the turbulent dissipation.

The resulting entropy generation rates S''' are presented in Fig. 3 for the three different Reynolds numbers. For closer comparisons, a few values are listed in Table 1. Since it is the sum of direct and turbulent dissipation, in wall coordinates $(S'''\{y^+\})^+$ is of *order* unity in the linear layer. It then undergoes a sharp reduction through the rest of the viscous layer. In accordance with the key observations from Fig. 2, there is almost no effect of Reynolds number in the viscous layer and for some distance beyond. The results are *near* "universal." By y^+ of 30 the volumetric rate S''' is reduced to about 8% of its value at the wall and continues to decrease rapidly further in the boundary layer. Consequently, as shown by the integration $S''\{y^+\}^+$ for entropy generation per unit surface area, about two-thirds or more (depending on Reynolds number) occurs in the viscous layer. This result agrees qualitatively with the approximate predictions of Rotta [11] for a high-Reynolds-number boundary layer and of Bejan [1] for a fully developed, high-Reynolds-number pipe flow; as noted by McEligot and Eckelmann [26], this pipe flow would correspond to a low value of $-K_p$, the nondimensional streamwise pressure gradient. Direct dissipation is reduced to less than 1% of the wall value of total dissipation by $y^+ \approx 40$ but by then ε^+ is an order of magnitude greater than the direct dissipation so $(S''')^+ \approx \varepsilon^+$ there.

As noted in Sec. 2, the integral with respect to y of the pointwise entropy generation rate gives the entropy generation rate per unit surface area (S''), which would be sought by thermal fluid engineers. Figure 3 demonstrates the increase of $(S''\{y^+\})^+$ through the viscous layer. Since $(S''')^+$ ranges only from about 1.2 to 0.9 in the linear layer ($y^+ < \sim 5$), the integral increases *nearly* linearly with respect to y in that region. About 30% of the entropy generation occurs in this layer. Beyond $y^+ \approx 5$, S''' decreases sharply with respect to y. By $y^+ \approx 20$, the turbulent dissipation is significantly greater than the direct dissipation due to the mean motion

Downloaded 03 Jun 2010 to 171.66.16.157. Redistribution subject to ASME license or copyright; see http://www.asme.org/terms/Terms_Use.cfm

Table 1 Effects of Reynolds number and streamwise acceleration on entropy generation rates in turbulent boundary layers

Re_θ	300	670	1410	690	415	380
K_v	0	0	0	1.5×10^{-6}	2.5×10^{-6}	2.75×10^{-6}
$-K_p$	0	0	0	0.0120	0.0187	0.0202
δ^+	150	325	650	505	310	270
$U^+\{30\}$	13.28	13.19	13.00	13.59	14.50	14.59
$(S'''\{30\})^+$	0.1002	0.09467	0.09497	0.07457	0.06613	0.06023
$(S'''\{50\})^+$	0.05220	0.05256	0.05265	0.03388	0.02604	0.02357
$(S'''\{100\})^+$	0.01223	0.02375	0.02430	0.01031	0.006052	0.005298
$(S''\{30\})^+$	12.768	12.716	12.680	11.921	11.796	11.623
$(S''\{50\})^+$	14.210	14.113	14.078	12.929	12.627	12.379
$(S''\{100\})^+$	15.646	15.850	15.835	13.877	13.283	12.970
$(S''\{\delta\})^+$	15.920	17.495	19.078	14.497	13.534	13.167

so the contribution to S'' is then primarily from turbulent dissipation. For these conditions, the total $(S''\{\delta^+\})^+$ is about 16–19; by the edge of the viscous layer at $y^+\approx30$, approximately two-thirds or more has appeared (and about three-quarters or more by $y^+\approx50$). Beyond $y^+\approx100$, the distance to the edge of the boundary layer is still large in wall units, but $(S''')^+$ is small so the additional contribution to entropy generation per unit surface area $(S'')^+$ is likewise small.

From Table 1, one sees a variation of $(S'''\{30\})^+$ from maximum to minimum of about 6% but the integration to $(S''\{30\})^+$ gives a range of less than 1%. The range of $(S''\{50\})^+$ likewise is only about 1%. The integral across the boundary layer $(S''\{\delta^+\})^+$ shows a weak dependence on Reynolds number, about $\mathrm{Re}_\theta^{1/8}$, as δ^+ increases. This variation is consistent with the trend of a dissipation coefficient of Rotta (Eq. (22.17) of Schlichting [24] but defined differently) when converted to wall coordinates. Since the integral $(S''\{30\})^+$ is *almost* constant, one could form $(S''\{\delta^+\})^+ = (S''\{30\})^+ + (S''\{\delta^+-30\})^+$ with the second term representing the boundary layer beyond the viscous layer; its small contribution varies approximately as $\mathrm{Re}_\theta^{0.43}$ for these three zpg cases. A kind reviewer has suggested correlating the results for the benefit of analysts conducting design optimization on the basis of entropy generation. However, only the results for $\mathrm{Re}_\theta=300$ are at a sufficiently low Reynolds number to differ significantly from near asymptotic conditions; thus, for the intermediate results, detailed variations as functions of Reynolds number are lacking. The overall entropy generation rate for turbulent boundary layers with negligible pressure gradients can be very approximately correlated as

$$(S''\{\delta^+\})^+ \approx 12.7 + 0.28\mathrm{Re}_\theta^{0.43} \quad \text{for} \quad 300 < \mathrm{Re}_\theta < 1410 \tag{12}$$

but we would be hesitant to apply this relation beyond its specified range without further confirmation.

In summary, variation of Reynolds number does not have much effect on entropy generation rates in the viscous layer of turbulent boundary layers *with negligible pressure gradients*.

4 Entropy Generation With Favorable Pressure Gradients

Previous studies of turbulent flows with favorable streamwise pressure gradients have been summarized by Narasimha and Sreenivasan [48], Spalart [12], McEligot and Eckelmann [26], and others. From integral analyses and an assumption that the integral of the turbulent dissipation is a function only of a shape parameter, Rotta [11] has presented a total dissipation coefficient as a function of the skin friction coefficient and a shape factor (therefore indirectly a function of the pressure gradient).

Spalart [12] provided DNS of sink-flow turbulent boundary layers with negligible freestream turbulence having streamwise acceleration parameters of $K_v=1.5\times10^{-6}$, 2.5×10^{-6}, and 2.75×10^{-6}, yielding pressure gradients $-K_p$ of about 0.012, 0.019, and 0.020, respectively. The experimental geometry represented is a "sink" formed by contraction of opposing flat plates; details of the governing equations, assumptions, and numerical procedures are provided in his original paper. The first of these pressure gradients corresponds to some experiments by McEligot and Eckelmann with "moderate" pressure gradients while the last was near the value for their highest, nearing laminarization. (Nickels [30] defined a case where K_p exceeds 0.005 as a "strong" pressure gradient.) However, McEligot and Eckelmann could not measure turbulent dissipation with their single X-probe. The range of δ^+ in the accelerated simulations (270–505) falls within the range covered by the zpg results (150–650). The present study extends the limited discussion of the effect of pressure gradient on turbulent dissipation by Spalart [12].

From the momentum equation, one sees the distribution of $\partial\tau^+\{y^+\}/\partial y^+$ will be a function of K_p alone provided the convective terms are zero or negligible. Fully developed flows in tubes, channels, and parallel plate ducts inherently satisfy this requirement. In the study by McEligot and Eckelmann [49], the effect of the convective terms was found to increase as y^+ and/or $|K_p|$ increase. One sees the magnitude of the convective term in τ^+ will be less than $K_p y^+ c_f (U^+)^2/2$; taking one-half this value as an order-of-magnitude approximation, we can estimate that the effect of the convective terms will be 5% or less provided that $-K_p$ is about 0.006 or less. So, for lower $|K_p|$ and higher δ^+, results for accelerating flows should agree approximately with those from fully developed results in the viscous layer at the same value of K_p. As $|K_p|$ increases to higher values, the results should diverge as the convective terms become more important; the trends with K_p should be the same but magnitudes would differ at the same K_p. Above this level, a given value of K_p for an accelerating flow would correspond to a lower value for fully developed duct flow, since the convective terms counter the pressure gradient in the expression for τ^+. McEligot and Eckelmann [49] indirectly evaluated sensitivity to the convective term by conducting evaluations with and without it when applying their procedure for deducing the wall shear stress. When using data from $y^+\approx25$ at $-K_p\approx0.011$, they found the difference in deduced friction velocity u_τ to be less than 1%. (One may reach a comparable conclusion by examining Fig. 11.12 by Rotta [11].) Therefore, the effect of the convective term on $\tau^+\{30\}$ will be small relative to that due to the streamwise pressure gradient.

The variation of $\tau^+\{y+\}$ in the viscous layer is indicated by evaluating the term $-y^+K_p$ at $y^+=30$. While countered slightly by

Downloaded 03 Jun 2010 to 171.66.16.157. Redistribution subject to ASME license or copyright; see http://www.asme.org/terms/Terms_Use.cfm

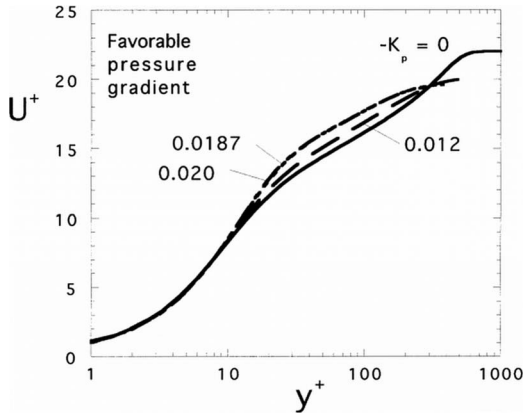

Fig. 4 Streamwise mean velocity profiles for turbulent boundary layers with favorable pressure gradients [12,13]: $-K_p=0$, solid curve; $-K_p\approx0.0120$, long dashes; $-K_p\approx0.0187$, short dashes; $-K_p\approx0.0202$, "centerline" curve

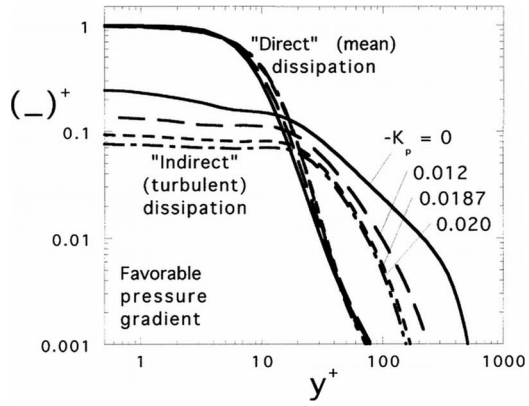

Fig. 5 Relative magnitudes of contributions to entropy generation in turbulent boundary layers with favorable pressure gradients; symbols as in Fig. 4

the effect of acceleration on the advective term as noted, this pressure gradient term dominates in the viscous layer. For the three cases, $-30K_p$ has magnitudes of 0.36, 0.561, and 0.606 as the pressure gradient increases, i.e., the constant shear layer approximation would not be valid in the viscous layer. For the highest pressure gradient, the reduction in τ^+ is already about 10% by $y^+=5$, the edge of the "linear layer."

The works of Senecal [50], Patel [51], McEligot et al. [52], Spalart [12], and others have shown that the level of the mean velocity profile in wall coordinates increases with acceleration or a favorable pressure gradient. Figure 4 demonstrates this effect for the three DNS runs with acceleration [12] when compared to the calculation for $\mathrm{Re}_\theta=1410$ with zero pressure gradient [13]. All three show an increase in the viscous layer beginning near y^+ of 10 and differing from the zpg reference by up to 12% by $y^+\approx30$. Consequently, the contribution of direct dissipation from the mean motion can be expected to be greater with a favorable pressure gradient than without. While the effect of the term $-K_py^+$ decreases the direct dissipation in the linear layer (via $\partial U^+/\partial y^+$), one sees from the slope of the mean velocity profile at larger y^+ that this effect is more than compensated by reduction of turbulent momentum transfer as the pressure gradient increases.

For a two-dimensional boundary layer, the terms for production in the governing equation for turbulence kinetic energy are

$$-\rho[\overline{u^2}(\partial U/\partial x)-\overline{v^2}(\partial V/\partial x)+\overline{uv}\{(\partial U/\partial y)+(\partial V/\partial x)\}] \quad (13)$$

As indicated by Hinze [43], for a flow with velocity increasing in the x direction the first term promotes a decrease in turbulence kinetic energy. (Since $\overline{u^2}$ is greater than $\overline{v^2}$ near the wall [12], the magnitude of the first term more than counters the second term.) With less production, there is less turbulence kinetic energy to dissipate and the turbulent dissipation term can be expected to decrease as well. For the terms in the balances of Reynolds stresses near the wall, Spalart [12] noted *qualitatively* that the general levels were lower in sink flow as implied. So the turbulent dissipation should be reduced (no direct comparisons of mean or turbulent dissipation were presented in his original paper).

Antonia et al.[35] examined turbulent dissipation and models thereof for *turbulent channel flows* at $\mathrm{Re}_\tau=180$ and 395 ($-K_p\approx0.0056$ and 0.0025, respectively) as predicted by the DNS algorithm of Kim et al. [45]. These results have been extended to evaluate entropy generation over a wider range of pressure gradients in a recent paper by McEligot et al. [36]. The results of Antonia et al. show that, for this limited range, ϵ^+ decreased as $|K_p|$ increased, consistent with the observations of Spalart [12] for boundary layers. Indirectly, in a study of anisotropy of turbulence, Jovanovic and Hillerbrand [53] have demonstrated that the turbulent dissipation rate at the wall decreases as a favorable pressure gradient increases. This trend corresponds to an approach to their "one-component turbulence limit" and accompanying suppression of small-scale turbulence in near-wall layers.

The effects of favorable pressure gradients on the two contributions to entropy generation *for turbulent boundary layers* are demonstrated in Fig. 5. As implied by the mean velocity profile behavior, direct dissipation from the mean motion increases with respect to pressure gradient in the viscous layer. Near $y^+\approx18$, it is about 40% greater for $K_v=2.75\times10^{-6}$ than for the zpg reference. However, the contribution from turbulent dissipation decreases as K_v increases (presumably, if K_v were large enough, say, greater than $(3-4)\times10^{-6}$ or so [25], the boundary layer would begin to laminarize and turbulent production and dissipation would eventually disappear). While there is little effect on direct dissipation from the increase of K_v from 2.5×10^{-6} to 2.75×10^{-6} (or $-K_p$ from 0.0187 to 0.0202), there is an observable but small effect on the indirect or turbulent dissipation.

The trends of the dissipation with respect to y^+ are the same as the pressure gradient varies but differ in magnitude. At each value of y^+, the turbulent dissipation decreases as pressure gradient increases. The turbulent dissipation ε^+ decreases slightly across a region from the wall to $y^+\approx15$. Then it decreases more sharply with y^+. For the low pressure gradient (lpg) cases, by $y^+\approx20$, the turbulent dissipation is greater than the direct dissipation due to the mean motion; for the higher pressure gradients the two are of the *same order* until nearer the edge of the viscous layer. Again direct dissipation is reduced to less than 1% of the wall value of total dissipation by $y^+\approx40$ but by then ε^+ is almost an order of magnitude greater than the direct dissipation so $(S''')^+$ becomes approximately equal to ε^+. Beyond $y^+\approx100$, the distance to the edge of the boundary layer may still be large in wall units, but $(S''')^+$ is small so the contribution to entropy generation per unit surface area $(S'')^+$ is likewise small.

The consequences of the countering effects on the two types of dissipation are plotted in terms of $(S''')^+$ and $(S'')^+$ in Fig. 6 and some key values are listed in Table 1. In general, one sees that the pressure gradient *does* affect entropy generation in the viscous layer but not to a large extent. As functions of y^+, the trends and orders of magnitude are the same as for negligible pressure gradients but quantitatively they differ. Since the trends with respect to pressure gradient are in opposing directions for the mean and turbulent dissipations, the variations of $(S''')^+$ are less than of its individual components. Moreover, these variations lead to convergence of the curves for $(S'''\{y^+\})^+$ so they become nearly equal (crossing) while still within the viscous layer.

Again S''' drops to less than 10% of its wall value by $y^+=30$ and, for these values of K_p, over 80% of the entropy generation

Downloaded 03 Jun 2010 to 171.66.16.157. Redistribution subject to ASME license or copyright; see http://www.asme.org/terms/Terms_Use.cfm

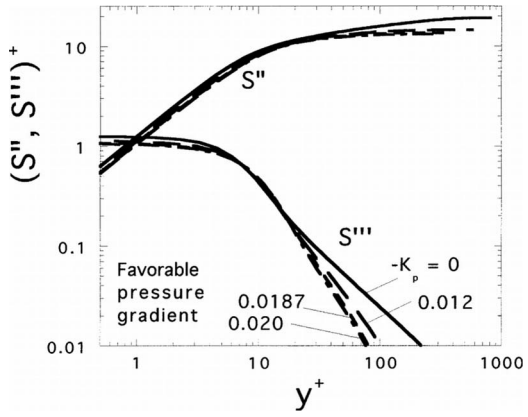

Fig. 6 Pointwise and areal entropy generation rates across turbulent boundary layers with favorable pressure gradients; symbols as in Fig. 4

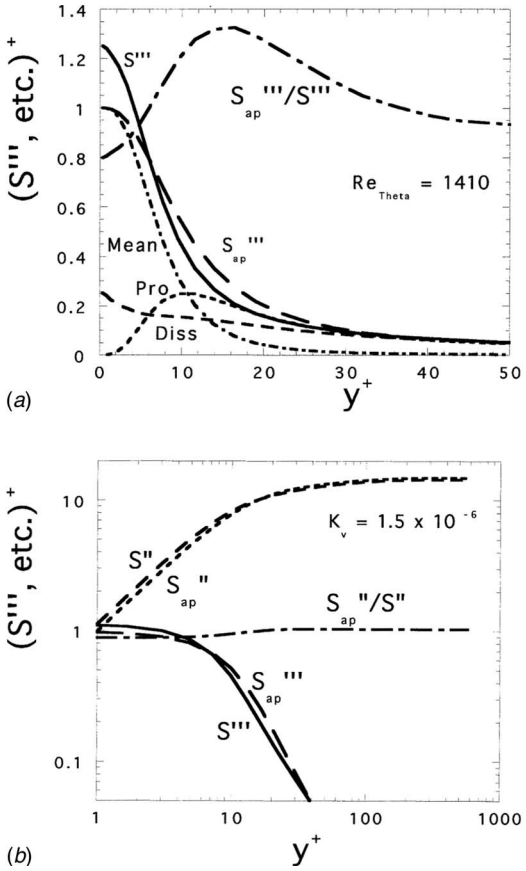

Fig. 7 Examples of approximate and exact approaches to calculating entropy generation rates in turbulent boundary layers from DNS with (*a*) a zero pressure gradient ($\mathrm{Re}_\theta \approx 1410$) and (*b*) a favorable pressure gradient ($-K_p \approx 0.012$, $K_v \approx 1.5\times10^{-6}$, $\mathrm{Re}_\theta \approx 690$)

occurs in this viscous layer. The total entropy generation rate in the boundary layer $(S''\{\delta\})^+$ decreases with increasing pressure gradient; for the simulated conditions, the decrease is about 30% relative to the zpg reference. From Table 1, one sees a variation of $(S'''\{30\})^+$ from maximum to minimum of about 20% but the integration to $(S''\{30\})^+$ gives a range of about 8%. In contrast to the zpg behavior, the range of $(S''\{50\})^+$ is about 14% (i.e., 12.38 $\rightarrow$14.08). This last observation has import for CFD analysts predicting entropy generation rates.

The values of $(S''\{\delta\})^+$ for the accelerated runs are smaller than for the zpg results and appear to have a slightly stronger variation with Re_θ (particularly when presented in terms of $(S''\{\delta^+-30\})^+$). However, for the accelerated cases, an increase in Re_θ corresponds to a decrease in the pressure gradient $-K_p$. If one examines the variation of $(S''\{\delta\})^+$ with respect to pressure gradient, one sees a steady decrease from the zpg results as $-K_p$ is increased and δ^+ decreases. This reduction occurs across the boundary layer, both in the region where $y^+<30$ and beyond as shown in Table 1; most of the reduction is in the turbulent region beyond $y^+\approx30$. (However, the viscous layer may be considered to "thicken" beyond $y^+\approx30$ for situations with strong pressure gradients, as indicated by McEligot and Eckelmann [26].)

As suggested by Kock and Herwig [4,23], the DNS for the viscous layer can be employed in conjunction with those CFD codes which use wall functions and solve a partial differential equation for turbulent dissipation (ε_u here). As fair approximations from Table 1, one can represent the predictions at the nominal edge of the viscous layer ($y^+=30$) for boundary layers with $-K_p<\sim0.020$ as pointwise entropy generation rate,

$$(S'''\{30\})^+ \approx 0.095 + 1.7K_p \tag{14}$$

and areal entropy generation rate,

$$(S''\{30\})^+ \approx 12.65 + 50K_p \tag{15}$$

Ultimately, the thermal designer desires to predict S'', the entropy generation rate per unit surface area, for the turbulent flow of interest. A CFD code can provide $\partial U\{y\}/\partial y$ and $\varepsilon_u\{y\}$ beyond the node where the wall function is anchored; from these quantities, $S'''\{y\}$ can be predicted beyond this node. The desired value is then given by

$$(S''\{y^+\})^+ = (S''\{y_1^+\})^+ + \int_{y_1^+}^{y^+} (S'''\{y^+\})^+ dy^+ \tag{16}$$

The value of S'' needed for an initial node at $y_1^+=30$ is given by the correlation. If the code anchors its wall function at a node closer than $y^+=30$, the required values of $\partial U/\partial y$ and ε_u can be estimated at $y^+=30$ by suitable interpolation (spline, logarithmic, quadratic, or such) and then the integration can proceed to larger y^+. For $30<{y_1}^+<100$, approximate values for $(S''\{{y_1}^+\})^+$ can be interpolated from Table 1.

We conclude that entropy generation in the viscous layer is affected by a favorable pressure gradient but apparently is not significantly a function of Reynolds number.

5 Approximate Prediction or Measurement of Entropy Generation

By application of boundary layer and other approximations, Rotta has suggested that dissipation in a turbulent boundary layer may be evaluated as

$$\mu\Phi \approx [\mu(\partial U/\partial y) - \rho\overline{uv}](\partial U/\partial y) \tag{17}$$

(reported as Eq. (23.8d) in the Schlichting text [24]) so that the volumetric entropy generation rate can be calculated *approximately* as

$$(S'''_{\mathrm{ap}})^+ \approx (\partial U^+/\partial y^+)^2 - (\overline{uv})^+(\partial U^+/\partial y^+) \tag{18}$$

One sees his turbulent dissipation term to be equivalent to the main contributor to production of turbulent kinetic energy. Several investigators have adopted this idea to measure or predict entropy generation (e.g., Moore and Moore [54], O'Donnell and Davies [55], Stieger and Hodson [56], and Hyhlik and Marsik [57]). While the approximation that production is equal to turbulent dissipation may be reasonable in the typical logarithmic layer beyond $y^+\approx30$, Fig. 7(*a*) and Rotta [11] remind us that they can differ

Downloaded 03 Jun 2010 to 171.66.16.157. Redistribution subject to ASME license or copyright; see http://www.asme.org/terms/Terms_Use.cfm

Table 2 Comparisons of entropy generation rates predicted by approximate and "exact" approaches

Re_θ	300	670	1410	690	415	380
K_v	0	0	0	1.5×10^{-6}	2.5×10^{-6}	2.75×10^{-6}
$-K_p$	0	0	0	0.0120	0.0187	0.0202
δ^+	150	325	650	505	310	270
Maximum						
S'''_{ap}/S'''	1.299	1.329	1.326	1.309	1.331	1.336
at y^+	14.6	16.1	16.4	16.7	20.3	18.9
$S'''_{ap}\{30\}/S'''$	1.030	1.065	1.083	1.126	1.192	1.187
$S'''_{ap}\{50\}/S'''$	0.9804	0.9124	0.9339	0.9735	0.9259	0.8979
$S'''_{ap}\{100\}/S'''$	1.008	1.089	0.962	1.010	0.9045	0.9090
$S''_{ap}\{30\}/S''$	1.031	1.034	1.026	1.035	1.042	1.045
$S''_{ap}\{50\}/S''$	1.026	1.028	1.023	1.035	1.043	1.045

significantly in the viscous layer. In the linear layer ($y^+ < \sim 5$), production (labeled "Pro") is nearly negligible whereas turbulent dissipation (labeled "Diss") is significant. Then at its peak, the production is 60–90% greater than turbulent dissipation.

Conceptually, one might suggest that the root source of entropy generation is the production of turbulence kinetic energy, which is later dissipated as thermal energy. Furthermore, the approximate representation $S'''_{ap}\{y\}$ is much easier to predict or measure than the more complete version of Cebeci and Bradshaw [16], Gersten and Herwig [17], and others. The Reynolds shear stress ($-\rho\overline{uv}$) can be measured at a point by single-slanted or dual-crossed hot-wire or hot-film probes and comparable laser Doppler velocimetry systems and, in some situations, it can be deduced from mean velocity profile data (e.g., pitot tubes). However, for the "exact" treatment, one needs to measure the *instantaneous gradients*, i.e., values of the individual components at two points simultaneously. Tanaka and Eaton [58] have recently examined the difficulty in measuring turbulent dissipation, even in simple flows. For example, Hinze [43] suggested three techniques for deducing dissipation from hot-wire measurements but all depend on isotropic assumptions, which are not valid close to a wall.

For prediction of ε^+ with turbulence models, one needs solution of a dissipation equation (which corresponds to pseudo dissipation ε_u) plus at least solution for the Reynolds normal stress in the wall-normal direction to evaluate the dominant contribution to viscous diffusion. In contrast, even a reasonable van Driest mixing length model can be adequate to predict the Reynolds shear stress in the viscous layer and, therefore, the production of turbulence kinetic energy [59,60]. So the question becomes how well (or poorly) do the two approaches (exact and approximate) agree.

Alternate approaches to estimating turbulent dissipation rates have been examined by other investigators. Antonia et al. [35] applied DNS results for *channels* at $\mathrm{Re}_\tau \approx 180$ and 395 ($-K_p \approx 0.0056$ and 0.0025) primarily to examine evaluation of dissipation and vorticity in the viscous layer. In addition to presentation of the magnitudes for individual terms in the definition, "homogeneous," "isotropic," "axisymmetric," and other approximations were treated. The isotropic approximation "grossly underestimates" ε^+ for $y^+ < 60$. The homogeneous approximation (essentially $\varepsilon_u{}^+$ of Gersten and Herwig [17]) agrees closely but has the same measuring difficulties; however, it is effectively the quantity predicted by k-ε turbulence models. Reasonable agreement with the exact treatment was found with an empirical approximation, which involves calculation or measurement of four terms involving instantaneous gradients, $(\partial u/\partial y)$, $(\partial w/\partial y)$, $(\partial u/\partial z)$, and $(\partial u/\partial x)$. Antonia et al. noted that these terms can be measured with a 1-1/2 X-probe (also called an A_xI-probe) as by George and Hussein [61] but they imply likely difficulties for the viscous layer where this approximation could be an improvement to the suggestion of Rotta; prediction of the mean values of fluctuating gradients near the wall remains a problem. Khoo et al. [62] compared their own careful data for isotropic approximations to the DNS results for the "true" values by Antonia et al. at $\mathrm{Re}_\tau \approx 395$. As one would expect, poor agreement was demonstrated for $y^+ < 80$.

One sees from the discussion of Fig. 7(*a*) above that, in the linear layer near the wall, the approximate volumetric entropy generation rate $S'''_{ap}\{y\}$ will be less than $S'''\{y\}$. Then as production exceeds dissipation and direct dissipation decreases to the same order of magnitude as turbulent dissipation, $S'''_{ap}\{y\}$ will become greater than $S'''\{y\}$ until they become approximately equal (production $\approx$ dissipation) beyond the viscous layer. At larger distances in the typical logarithmic layer and beyond, both approaches give small values compared to their magnitudes in the viscous layer.

As an example, Fig. 7 compares the DNS predictions of S''' and its integral S'' and related quantities by the two approaches for turbulent boundary layers with (a) a zero pressure gradient ($\mathrm{Re}_\theta = 1410$) and (b) $-K_p \approx 0.012$, a "moderate" favorable pressure gradient ($K_v = 1.5\times10^{-6}$). Figure 7(*a*) uses linear coordinates and Fig. 7(*b*) employs logarithmic coordinates; each has its advantage for the reader. Behavior of the other four cases is qualitatively the same. Figure 7(*a*) shows the relation of S'''_{ap} to S''' to be consistent with the reasoning above. It is seen that the distributions in the viscous layer differ between the two approaches as production and dissipation differ considerably there. Near the wall, the ratio S'''_{ap}/S''' is about 0.88 but it increases to about 1.31 near $y^+ \approx 17$ before decreasing to *near* unity in the usual "logarithmic" region as seen in both figures. Near the "edge" of the viscous layer at $y^+ = 30$, it is still about 13% high. These results vary slightly with Reynolds number and pressure gradient so a few key values are listed in Table 2 to demonstrate the ranges and possible trends.

Based on a scaling analysis (or boundary layer approximations) for turbulent boundary layers with negligible pressure gradients, Hinze [43] concluded that in the fully turbulent region beyond the viscous layer, a state of energy equilibrium of the turbulence should occur where production approximately equals turbulent dissipation. (He indicated that further from the wall in his outer region, convective transport by mean motion and diffusion by turbulent motion would become important.) Since the contribution to entropy generation from the mean motion is the same for S'''_{ap} and S''', this observation by Hinze would imply that $S'''_{ap} \approx S'''$ in the region beyond the viscous layer. Table 2 and the centerline

Downloaded 03 Jun 2010 to 171.66.16.157. Redistribution subject to ASME license or copyright; see http://www.asme.org/terms/Terms_Use.cfm

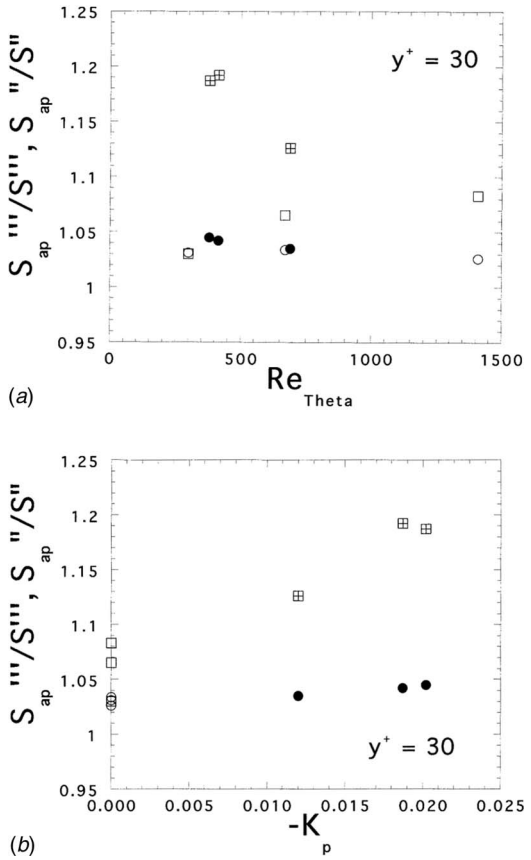

Fig. 8 Comparisons of entropy generation rates predicted by approximate and exact approaches near the edges of the viscous layers: (*a*) variation with Reynolds number based on momentum thickness and (*b*) variation with streamwise pressure gradient (S'''_{ap}/S''': zpg, open squares; favorable pressure gradient, crossed squares; S''_{ap}/S'': zpg, open circles; favorable pressure gradient, solid circles)

curve in Fig. 7(*a*) present the ratio S'''_{ap}/S''' to examine this suggestion; as y^+ increases, this ratio becomes equivalent to the ratio production/dissipation because the contribution from the mean motion becomes negligible. One sees that the two are approximately equal (say, within 10–15%) in this region but differ in detail. These detailed differences are best seen by examining this ratio as in Fig. 7(*a*) and Table 2.

To the unaided eye, it appears that in Fig. 7(*a*) the areas under the curves for S'''_{ap} and S''' are approximately equal in the range $0<y^+<30$. In the integration to obtain $S''\{y\}$, the higher value of S''' near the wall counters S'''_{ap}, which is higher in most of the viscous layer, to give agreement within 5% by $y^+=30$. Ultimately, the integrations across the boundary layer (e.g., $S''\{\delta\}$) should be approximately equal, differing only by the advection of turbulence kinetic energy to be dissipated further downstream. Thus, one sees the asymptote $S''_{ap}\{\delta\}$ to be larger than $S''\{\delta\}$, consistent with the production of turbulence kinetic energy across the boundary layer being slightly greater than its turbulent dissipation. In Fig. 7(*b*), the curve denoted by long dashes provides the ratio S''_{ap}/S'' to quantify agreement (or disagreement) of S''_{ap} with S''. Beyond the viscous layer, the ratio is almost constant and near unity (but differs slightly from case to case); Table 2 indicates that the differences for the six cases would be about 2–5% in the range $30<y^+<50$.

To examine possible trends with respect to Reynolds number and pressure gradient, Figs. 8(*a*) and 8(*b*) are constructed from Table 2 for $y^+=30$. By comparison of the two figures, one sees there is not a clear trend with Reynolds number or pressure gradient alone. There is greater variation of these measures of "agreement" for S''' (squares) than for S'' (circles), about 15% versus a bit less than 2%. For $S''_{ap}\{30\}/S''\{30\}$, there seems to be slightly more effect of the variation of pressure gradient than Reynolds number over the ranges covered.

These comparisons demonstrate that while the approximate approach can give pointwise errors of $S'''_{ap}\{y\}$ up to 30% in the viscous layer, the integrals over the viscous layer agree somewhat more closely (i.e., within 5%).

6 Concluding Remarks

The local (pointwise) entropy generation rate per unit volume S''' is a key to improving many energy processes and applications. Thus, CFD studies seek to identify the regions of maximum entropy production so they may be attacked and reduced. Apparatus producing less entropy by irreversibilities destroys less available work, increasing the efficiency and—in turn—reducing fuel consumption and waste products.

By employing available direct numerical simulations, it has been possible to obtain new fundamental results for entropy generation in the viscous layers of turbulent boundary layers on flat plates, with and without significant favorable pressure gradients. Entropy generation due to friction occurs from viscous dissipation of mean-flow kinetic energy (called "direct dissipation") and dissipation of turbulent kinetic energy into thermal energy ("indirect" or turbulent dissipation). We concentrate on the viscous layer because it is typically the region where the largest gradients occur and the production of turbulence is greatest; major resistances to momentum, energy, and mass transfer occur in this layer, and the pointwise entropy generation rate is greatest here as well.

In wall coordinates, the contribution of direct (mean) dissipation is unity at the wall. It dominates near the wall while turbulent dissipation contributes about 10–20% to the total. Both direct and turbulent dissipations decrease as y^+ increases but the reduction of direct dissipation is more rapid with respect to y than the turbulent dissipation—so they become about equal within the viscous layer. For larger values of y^+, turbulent dissipation becomes progressively more dominant. By the edge of the viscous layer, the contribution of the mean motion is negligible. At low pressure gradients, about 30% of the entropy generation rate per unit surface area S'' occurs in the linear layer ($y^+<\sim 5$) and about two-thirds or more occurs within the viscous layer.

With *negligible pressure gradients*, results presented in wall coordinates are predicted to be *near universal* in the viscous layer. This apparent universality disappears when a *significant pressure gradient* is applied. The variations of $(S''')^+$ due to pressure gradients are less than of its individual components. Increasing the pressure gradient increases the direct dissipation and decreases the turbulent dissipation, giving a net decrease in integrated entropy generation rate $(S'')^+$ at the edge of the viscous layer as well as at the edge of the boundary layer. As functions of y^+, the trends and orders of magnitude are the same as for the low pressure gradients but the quantitative results differ.

In the viscous layer, an *approximate* estimate of S''' (based on a suggestion of Rotta [24]) *does not agree* with the result from the more exact evaluation of the turbulent dissipation whereas reasonable agreement is found beyond the viscous layer where mechanical equilibrium (production $\approx$ dissipation) is approached. The observation of fair agreement between $S''_{ap}\{30\}$ and $S''\{30\}$ (within 5% overall and within 1% for negligible pressure gradients) may be useful in the development of CFD predictions of entropy generation rate per unit surface area $(S''\{\delta\})$ but such extension is beyond the scope of the present study. Alternate models for estimating the distribution of $\varepsilon^+\{y^+\}$ in channels have been suggested and examined by Antonia, Kim, and Browne [35] and Khoo,

Downloaded 03 Jun 2010 to 171.66.16.157. Redistribution subject to ASME license or copyright; see http://www.asme.org/terms/Terms_Use.cfm

Chew, and Teo [62]; however, they are less useful than the approximate approach of Rotta.

For the *viscous layer*, DNS calculations for $\mathrm{Re}_\theta \approx 1410$ with a zpg are close to asymptotically high-Reynolds-number conditions. The thickness δ^+ is about 650 so the viscous layer is small relative to the overall scale of the boundary layer and, therefore, is not expected to be affected significantly by the boundary condition away from the wall. The nondimensional total shear stress $\tau^+\{y^+\}$ is only reduced about 1–1/2 percent by the nominal edge of the viscous layer at $y^+ \approx 30$. This situation is close to the constant shear layer idealization, which applies for high-Reynolds-number flows. Thus, its distributions of $(S'''\{y^+\})^+$ and $(S''\{y^+\})^+$ would be approximately valid universally for the viscous layer of smooth wall flows at *higher* Reynolds numbers—as well as for developed internal turbulent flows with *high* $\mathrm{Re}_{\mathrm{Dh}}$=low $|K_p|$ (perhaps say $\mathrm{Re}_\tau > \sim 2000$ giving $-K_p < \sim 0.0005$). The results for S'' in Figs. 3 and 6 demonstrate that the correlation suggested by Kock and Herwig [23] can be expected to predict the entropy generation rates within the viscous layer $(S''\{30\})^+$ reasonably for high Reynolds numbers and low pressure gradients although their value of $-K_p \approx 0.0025$ (Re_τ=395) is not quite an asymptotic situation. (Their nondimensional quantity is comparable to our $(S'')^+$ but is defined differently.)

It was shown that the streamwise pressure gradient controls the variations of direct and indirect dissipations in the viscous layer. As noted by a kind reviewer, this knowledge is a very important tool for efficient design of energy systems, especially with application of second law analysis for optimization. Further study involving optimization of the budgets of dissipations in entropy production would be desirable. Jovanovic [63] has reported some progress in this direction in order to deduce an optimum surface configuration. However, many applications such as turbine stages involve high freestream turbulence and extensive transitional regions; further understanding of entropy generation behavior for these situations with both transition and laminarization will be needed for complete surface optimization.

Concerning the idea of reducing entropy generation rate and, therefore, lost work, while the results show some variation of $(S'')^+$ with pressure gradient, this variation is not large. From the definition of $(S'')^+$, the main variation of entropy generation rate S'' in physical terms (e.g., $\mathrm{W}/(\mathrm{m}^2\,\mathrm{K})$) is approximately as $U_\infty^3 (c_f)^{3/2}$. The skin friction coefficient varies slightly with Reynolds number (and possibly pressure gradient) and therefore with freestream velocity. So reducing the upstream velocity and/or reducing freestream velocity by adjusting the surface shape can reduce the physical entropy generation rate. Some drag reduction techniques might be considered to reduce c_f, provided they do not involve other irreversible phenomena which increase entropy generation rates more (e.g., possibly wall temperature control schemes). Frohnapfel et al. [64] examined predictions from DNS of a number of drag-reducing phenomena, such as fibers, surfactants, riblets, highly accelerated flows, and supersonic flows. They concluded that the most effective is the addition of long-chain polymers. Jovanovic et al. [34] conducted analyses and experiments for this case and showed the DNS results of Dimitropoulos et al. [65] as a demonstration of the effect. These DNS predictions indicate that the dominant streamwise vorticity (and therefore the turbulent dissipation) is reduced in the viscous layer and the direct dissipation is increased—as with our predictions for a favorable streamwise pressure gradient. The net dissipation was not presented so it is not clear whether $(S''')^+$ would decrease but the reduction in skin friction coefficient should reduce S'' in physical terms.

Acknowledgment

Dr. Suad Jakirlic of the Technische Universität Darmstadt kindly provided tabulations of the DNS results from Spalart [12,13]. The study reported here was partly supported through Science Foundation Ireland and by programs at Idaho National Engineering and Environmental Laboratory and later at INL under DoE Idaho Operations Office Contracts DE-AC07-99ID13727 and DE-AC07-05ID14517, respectively. The United States Government retains and the publisher, by accepting this article for publication, acknowledges that the United States Government retains a nonexclusive, paid-up, irrevocable, worldwide license to publish or reproduce the published form of this manuscript, or allow others to do so, for United States Government purposes. We thank the Director of IKE at Universität Stuttgart, Professor Dr. G. Lohnert, for his kind encouragement and support.

Nomenclature

$\{\}$ = function of
A_{cs} = flow area
D_h = hydraulic diameter, $4A_{\mathrm{cs}}/P_w$
g_c = units conversion factor, e.g., 1 kg m/(N s^2), 32.1739 lbm ft/(lbf s^2)
G = mean mass flux, $\dot{m}/A_{\mathrm{cs}}$
$\dot{m}$ = mass flow rate
P = perimeter; P_w, wetted perimeter
p = pressure
$\dot{Q}$ = heat transfer rate
s = specific entropy (i.e., per unit mass)
S = entropy, entropy generation rate
T = temperature
t = time
U,V = mean velocity components in streamwise and wall-normal directions, respectively
u,v,w = velocity fluctuations about means in streamwise, wall-normal and spanwise directions, respectively
u_τ = friction velocity, $(g_c \tau_w/\rho)^{1/2}$
$\overline{uv}$ = mean fluctuation product in Reynolds shear stress $(-\rho\,\overline{uv})$
x,y,z = coordinates in streamwise, wall-normal and spanwise directions, respectively

Nondimensional Quantities

c_f = skin friction coefficient, $2g_c\tau_w/(\rho U_\infty^2)$
K_p = streamwise pressure gradient, $(\nu/\rho u_\tau^3)dp/dx$
K_v = acceleration parameter, $(\nu/U_\infty^2)dU_\infty/dx$
Re = Reynolds number; Re_{D_h}, based on hydraulic diameter, GD_h/μ; Re_θ, based on momentum thickness, $U_\infty\theta/\nu$
Re_τ = distance from wall to centerplane, centerline, etc., $y_c u_\tau/\nu$
$(S'')^+$ = entropy generation rate per unit surface area, $TS''/(\rho u_\tau^3)$
$(S''')^+$ = pointwise volumetric entropy generation rate, $T\nu S'''/(\rho u_\tau^4)$
y^+ = wall-normal coordinate, $y\,u_\tau/\nu$
δ^+ = boundary layer thickness, $\delta\,u_\tau/\nu$
ε^+ = turbulent dissipation of turbulent kinetic energy, $\nu\varepsilon/u_\tau^4$
τ^+ = pointwise shear stress, $\tau\{y^+\}/\tau_w$

Greek Symbols

δ = boundary layer thickness
ε = dissipation of turbulence kinetic energy; ε_u, pseudodissipation [17]
Φ = viscous dissipation function
μ = absolute viscosity
ν = kinematic viscosity, μ/ρ
ρ = density
τ = shear stress; τ_w, wall shear stress

Downloaded 03 Jun 2010 to 171.66.16.157. Redistribution subject to ASME license or copyright; see http://www.asme.org/terms/Terms_Use.cfm

θ = momentum thickness

Superscripts

$()^+$ = normalization by wall units, ν and u_τ
$()'$ = per unit length
$()''$ = per unit surface area
$()'''$ = per unit volume
$\overline{()}$ = time mean value

Subscripts

ap = approximate
b = bulk or mixed-mean quantity (one-dimensional)
c = centerplane, centerline
cs = cross section
cv = control volume
D_h, D,h = evaluated with hydraulic diameter
gen = generation
in = evaluated at inlet, entry
out = outflow
w = wall
∞ = freestream value

References

[1] Bejan, A., 1982, *Entropy Generation Through Heat and Fluid Flow*, Wiley, New York.
[2] Onsager, L., 1931, "Reciprocal Relations in Irreversible Processes. I," Phys. Rev., **37**, pp. 405–426.
[3] Prigogine, I., 1978, "Time, Structure and Fluctuations," Science, **201**, pp. 777–785.
[4] Kock, F., and Herwig, H., 2005, "Entropy Production Calculation for Turbulent Shear Flows and Their Implementation in CFD Codes," Int. J. Heat Fluid Flow, **26**, pp. 672–680.
[5] Kestin, J., 1980, "Availability: The Concept and Associated Terminology," Energy Intl. J., **5**, pp. 679–692.
[6] Gouy, M., 1889, "Sur l'energie Utilisable," J. Phys., **8**, pp. 501–518.
[7] Stodola, A., 1910, *Steam and Gas Turbines*, McGraw-Hill, New York.
[8] Clausius, R., 1887, *Die Mechanische Wärmetheorie*, Vieweg, Braunschweig.
[9] Lichty, L. C., 1936, *Thermodynamics*, McGraw-Hill, New York.
[10] Bradshaw, P., 1975, *An Introduction to Turbulence and Its Measurement*, 2nd ed., Pergamon, Oxford.
[11] Rotta, J. C., 1962, "Turbulent Boundary Layers in Incompressible Flow," *Progress in Aeronautical Sciences*, A. Ferri, D. Küchemann, and L. H. G. Sterne, eds., Pergamon, Oxford, Vol. 2, pp. 1–219.
[12] Spalart, P. R., 1986, "Numerical Study of Sink-Flow Boundary Layers," J. Fluid Mech., **172**, pp. 307–328.
[13] Spalart, P. R., 1988, "Direct Simulation of a Turbulent Boundary Layer up to Re_θ=1410," J. Fluid Mech., **187**, pp. 61–98.
[14] London, A. L., 1960, *Advanced Thermodynamics*, Stanford University, Palo Alto, CA., Course ME 233.
[15] Reynolds, W. C., and Perkins, H. C., 1970, *Engineering Thermodynamics*, McGraw-Hill, New York.
[16] Cebeci, T., and Bradshaw, P., 1984, *Physical and Computational Aspects of Convective Heat Transfer*, Springer, New York.
[17] Gersten, K., and Herwig, H., 1992, *Strömungsmechanik*, Vieweg, Braunschweig.
[18] Schlichting, H., and Gersten, K., 1997, *Grenzschicht-Theorie, 9., Völlig Neubearbeitete und Erweiterte Auflage*, Springer, Berlin.
[19] Schlichting, H., and Gersten, K., 2000, *Boundary Layer Theory*, 8th revised ed., Springer, Berlin.
[20] Brodkey, R. S., Nychas, S. G., Taraba, J. L., and Wallace, J. M., 1973, "Turbulent Energy Production, Dissipation and Transfer," Phys. Fluids, **16**, pp. 2010–2011.
[21] Brodkey, R. S., Taraba, J. L., Nychas, S. G., and Wallace, J. M., 1974, "Reply To Comments By P. Bradshaw," Phys. Fluids, **17**, p. 2150.
[22] Bradshaw, P., 1974, "Comments on Turbulent Energy Production, Dissipation and Transfer," Phys. Fluids, **17**, pp. 2149.
[23] Kock, F., and Herwig, H., 2004, "Local Entropy Production in Turbulent Shear Flows: A High-Reynolds Number Model With Wall Functions," Int. J. Heat Mass Transfer, **47**, pp. 2205–2215.
[24] Schlichting, H., 1968, *Boundary Layer Theory*, 6th ed. McGraw-Hill, New York.
[25] Kline, S. J., Reynolds, W. C., Schraub, F. A., and Rundstadler, P. W., 1967, "The Structure of Turbulent Boundary Layers," J. Fluid Mech., **30**, pp. 741–773.
[26] McEligot, D. M., and Eckelmann, H., 2006, "Laterally Converging Duct Flows. Part 3. Mean Turbulence Structure in the Viscous Layer," J. Fluid Mech., **549**, pp. 25–59.
[27] Julien, H. L., Kays, W. M., and Moffat, R. J., 1969, "The Turbulent Boundary Layer on a Porous Plate: Experimental Study of the Effects of A Favorable Pressure Gradient," Stanford University, Palo Alto, Technical Report HMT-4.
[28] Finnicum, D. S., and Hanratty, T. J., 1988, "Effect of Favorable Pressure Gradients on Turbulent Boundary Layers," AIChE J., **34**, pp. 529–540.
[29] Nieuwstadt, F. T. M., and Bradshaw, P., 1997, "Similarities and Differences in Turbulent Boundary-Layer, Pipe and Channel Flows," *Boundary-Layer Separation in Aircraft Aerodynamics*, R. A. W. M. Henkes and P. G. Bakker, eds., Delft University Press, Delft, pp. 15–22.
[30] Nickels, T. B., 2004, "Inner Scaling for Wall-Bounded Flows Subject to Large Pressure Gradients," J. Fluid Mech., **521**, pp. 217–239.
[31] Klebanoff, P. S., 1955, "Characteristics of Turbulence in a Boundary Layer With Zero Pressure Gradient," NACA Report 1247, pp. 1135–1153.
[32] deGraaff, D. B., and Eaton, J. K., 2000, "Reynolds-Number Scaling of the Flat-Plate Turbulent Boundary Layer," J. Fluid Mech., **422**, pp. 319–346.
[33] Laadhari, F., 2007, "Reynolds Number Effect on the Dissipation Function in Wall-Bounded Flows," Phys. Fluids, **19**(3), pp. 038101-1–038101-4.
[34] Jovanovic, J., Pashtrapanska, M., Frohnapfel, B., Durst, F., Koskinen, J., and Koskinen, K., 2006, "On the Mechanism Responsible for Turbulent Drag Reduction by Dilute Addition of High Polymers: Theory, Experiments, Simulations and Predictions," ASME J. Fluids Eng., **128**, pp. 118–130.
[35] Antonia, R. A., Kim, J., and Browne, L. W. B., 1991, "Some Characteristics of Small-Scale Turbulence in a Turbulent Duct Flow," J. Fluid Mech., **233**, pp. 369–388.
[36] McEligot, D. M., Nolan, K. P., Walsh, E. J., and Laurien, E., 2008, "Effect of Pressure Gradients on Entropy Generation in the Viscous Layers of Turbulent Wall Flows," Int. J. Heat Mass Transfer, **51**, pp. 1104–1114.
[37] Abe, H., Kawamura, H., and Matsuo, Y., 2001, "Direct Numerical Simulation of a Fully Developed Turbulent Channel Flow With Respect to the Reynolds Number Dependence," ASME J. Fluids Eng., **123**, pp. 382–393.
[38] Tsukahara, T., Seki, Y., Kawamura, H., and Tochio, D., 2005, "DNS of Turbulent Channel Flow at Very Low Reynolds Numbers," *Proceedings of the Fourth International Symposium Turbulent Shear Flow Phenomena*, Williamsburg, VA, Jun. 27–29, pp. 935–940.
[39] Skare, P. E., and Krogstad, P.-A., 1994, "A Turbulent Equilibrium Boundary Layer Near Separation," J. Fluid Mech., **272**, pp. 319–348.
[40] Aubertine, C. D., and Eaton, J. K., 2005, "Turbulence Development in a Non-Equilibrium Turbulent Boundary Layer With Mild Adverse Pressure Gradient," J. Fluid Mech., **532**, pp. 345–364.
[41] Jones, M. B., Marusic, I., and Perry, A. E., 2001, "Evolution and Structure of Sink-Flow Turbulent Boundary Layers," J. Fluid Mech., **428**, pp. 1–27.
[42] Jones, W. P., and Launder, B. E., 1972, "Some Properties of Sink Flow Turbulent Boundary Layers," J. Fluid Mech., **56**, pp. 337–351.
[43] Hinze, J. O., 1975, *Turbulence*, 2nd ed., McGraw-Hill, New York.
[44] Wilcox, D. C., 1998, *Turbulence Modeling for CFD*, 2nd ed., DCW Industries, La Canada, CA.
[45] Kim, J., Moin, P., and Moser, R. D., 1987, "Turbulent Statistics in Fully Developed Channel Flow at Low Reynolds Number," J. Fluid Mech., **177**, pp. 133–166.
[46] Bradshaw, P., and Perot, J. B., 1993, "A Note on Turbulent Energy Dissipation in the Viscous Wall Region," Phys. Fluids A, **5**(12), pp. 3305–3306.
[47] Moser, R. D., and Moin, P., 1987, "Direct Numerical Simulation of Curved Turbulent Channel Flow," J. Fluid Mech., **175**, pp. 479–510, also NASA TM-85974.
[48] Narasimha, R., and Sreenivasan, K. R., 1979, "Relaminarization of Fluid Flows," Adv. Appl. Mech., **19**, pp. 221–309.
[49] McEligot, D. M., and Eckelmann, H., 2003, "Effects of Laterally Converging Flows on Mean Turbulence Structure in the Viscous Layer," Idaho National Engineering and Environmental Laboratory, Technical Report INEEL/EXT-2002-697.
[50] Senecal, V. E., 1952, "Fluid Flow in the Transition Zone," Carnegie Institute of Technology, Ph.D. thesis.
[51] Patel, V. C., 1965, "Calibration of the Preston Tube and Limitations on Its Use in Pressure Gradients," J. Fluid Mech., **23**, pp. 185–208.
[52] McEligot, D. M., Ormand, L. W., and Perkins, H. C., 1966, "Internal Low Reynolds Number Turbulent and Transitional Gas Flow With Heat Transfer," ASME J. Heat Transfer, **88**, pp. 239–245.
[53] Jovanovic, J., and Hillerbrand, R., 2005, "On Peculiar Property of the Velocity Fluctuations in Wall-Bounded Flows," J. Therm. Sci., **9**(1), pp. 3–12.
[54] Moore, J., and Moore, J. G., 1983, "Entropy Production Rates From Viscous Flow Calculations. Part I. A Turbulent Boundary Layer Flow," ASME Paper No. 83-GT-70.
[55] O'Donnell, F. K., and Davies, M. R. D., 1999, "Measurements of Turbine Blade Aerodynamic Entropy Generation Rate," Third European Conference Turbomachinery, London, pp. 43–53.
[56] Stieger, R. D., and Hodson, H. P., 2003, "Unsteady Dissipation Measurements on a Flat Plate Subject to Wake Passing," Proc., Inst. Mech. Eng., Part A, **217**, pp. 413–419.
[57] Hyhlik, T., and Marsik, F., 2006, "New Approach to Turbulence Model Testing Based on the Entropy Production and the Analysis of Simple Wall Flows," *Turbulence, Heat And Mass Transfer 5*, K. Hanjalic, Y. Nagano, and S. Jakirlic, eds., Begell House, New York, pp. 377–380.
[58] Tanaka, T., and Eaton, J. K., 2007, "A Correction Method for Measuring Turbulence Kinetic Energy Dissipation Rate by PIV," Exp. Fluids, **42**, pp. 893–902.
[59] Huffman, G. D., and Bradshaw, P., 1972, "A Note on Von Karman's Constant in Low Reynolds Number Turbulent Flows," J. Fluid Mech., **53**, pp. 45–60.
[60] McEligot, D. M., 1985, "Measurement of Wall Shear Stress in Favorable Pres-

Downloaded 03 Jun 2010 to 171.66.16.157. Redistribution subject to ASME license or copyright; see http://www.asme.org/terms/Terms_Use.cfm

sure Gradients," Lect. Notes Phys., **235**, pp. 292–303.
[61] George, W. K., and Hussein, H. J., 1991, "Locally Axisymmetric Turbulence," J. Fluid Mech., **233**, pp. 369–388.
[62] Khoo, B. C., Chew, Y. T., and Teo, C. J., 2000, "On Near-Wall Hot-Wire Measurements," Exp. Fluids, **29**, pp. 448–460.
[63] Jovanovic, J., 2006, Personal electronic communication, Lehrstuhl für Strömungsmechanik, Uni. Erlangen, Oct. 11.
[64] Frohnapfel, B., Lammers, P., Jovanovic, J., and Durst, F., 2007, "Interpretation of the Mechanism Associated With Turbulent Drag Reduction in Terms of Anisotropy Invariants," J. Fluid Mech., **577**, pp. 457–466.
[65] Dimitropoulos, C. D., Sureshkumar, R., and Beris, A. N., 1998, "Direct Numerical Simulation of Viscoelastic Turbulent Channel Flow Exhibiting Drag Reduction: Effects of the Variation of Rheological Parameters," J. Non-Newtonian Fluid Mech., **79**, pp. 433–468.

Downloaded 03 Jun 2010 to 171.66.16.157. Redistribution subject to ASME license or copyright; see http://www.asme.org/terms/Terms_Use.cfm

PIV Study of Separated and Reattached Open Channel Flow Over Surface Mounted Blocks

Martin Agelinchaab

Mark F. Tachie
e-mail: tachiemf@cc.umanitoba.ca

Department of Mechanical and Manufacturing,
University of Manitoba,
Winnipeg, MB R3T 5V6, Canada

A particle image velocimetry is used to study the mean and turbulent fields of separated and redeveloping flow over square, rectangular, and semicircular blocks fixed to the bottom wall of an open channel. The open channel flow is characterized by high background turbulence level, and the ratio of the upstream boundary layer thickness to block height is considerably higher than in prior experiments. The variation of the Reynolds stresses along the dividing streamlines is discussed within the context of vortex stretching, longitudinal strain rate, and wall damping. It appears that wall damping is a more dominant mechanism in the vicinity of reattachment. In the recirculation and reattachment regions, profiles of the mean velocity, turbulent quantities, and transport terms are used to document the salient features of block geometry on the flow. The flow characteristics in these regions strongly depend on block geometry. Downstream of reattachment, a new shear layer is formed, and the redevelopment of the shear layer toward the upstream open channel boundary layer is studied using the boundary layer parameters and Reynolds stresses. The results show that the mean flow rapidly redeveloped so that the Clauser parameter recovered to its upstream value at 90 step heights downstream of reattachment. However, the rate of development close to reattachment strongly depends on block geometry. [DOI: 10.1115/1.2911677]

1 Introduction

Separated and reattached turbulent flows occur in diverse technological and environmental applications. In the reattachment region, the shear layer may be overwhelmingly distorted so that the usual thin layer approximations are not valid. In this regard, separated and reattaching turbulent flows can be used as prototypical flows to conduct fundamental research on complex turbulent shear flows and to study the effects of extra strains produced by separation and reattachment on the flow characteristics and the subsequent redevelopment to an equilibrium state. Given their diverse practical and fundamental importance, geometry-induced separated turbulent flows have been quite extensively studied in the past [1–3]. Prior experimental studies have been reviewed by Bradshaw and Wong [4] and Eaton and Johnston [5]. The characteristics of flow downstream a backward facing step are well documented in the literature [6,7]. Uniform flows downstream a normal flat plate [8,9] and a blunt plate [10] have also been used to study the characteristics of separated turbulent flow. Surface mounted obstacles, such as rectangular and square prisms attached to a ground plane, have been studied by Tillman [11], Bergeles and Athanassiadis [12], and Antoniou and Bergeles [13]. For these configurations, multiple separations and reattachments may occur depending on the longitudinal span (b) to height (h) ratio, b/h.

Irrespective of the specific geometry, the flow field can be divided into the following four zones (Figs. 1(b) and 1(c)): (i) the shear layer, (ii) separation bubble or recirculation region beneath the shear layer, (iii) reattachment region, and (iv) recovery region where a new boundary layer develops. The shear layer bears some resemblance to a plane mixing layer [9,10], and in this region, the appropriate velocity scale is $\Delta U = U_{\max} - U_{\min}$. Prior separated flows generated by different obstacles [9,10] have shown that the vorticity thickness, $\delta_\omega = \Delta U / (\partial U / \partial y)_{\max}$, linearly grows and at a rate similar to that of mixing layer. The maximum turbulence intensity, $u_{\max}$, is typically higher than for mixing layer but appears to vary somewhat from one flow type to another. For example, $u_{\max} = 20-30\%$ of the upstream freestream velocity for a blunt plate [10] and 30–34% for a normal flat plate [8].

The characteristics of flow separation and curvature of mean dividing streamline depend very much on the upstream flow and specific geometry used to perturb the approach flow. Consequently, the recirculation zone beneath the shear layer and the reattachment region are unique to the specific geometry of the obstacle and upstream flow conditions. For example, the size of the separation bubble may vary from $x/h \approx 6.8$ for a backward facing step [7] to $x/h \approx 17$ for a normal flat plate [8]. The strength of the separation bubble, degree of distortion induced by the pressure field at reattachment, and subsequent redevelopment downstream of reattachment point are also a strong function of geometry of the obstacle. Unfortunately, this is the region where reliable measurements are lacking owing to flow reversal and relatively high turbulence levels that make measurement techniques, such as Pitot tube and standard hot wires, inappropriate in this region. Beyond reattachment point, a new shear layer develops and given sufficient development length, the new shear layer may return to a standard turbulent boundary layer. Bradshaw and Wong [4] suggested that the flow just downstream of reattachment bears very little resemblance to a plane mixing layer or any other thin shear layer. Return of the mean flow to equilibrium, which is usually assessed by comparing values of the Clauser parameter G to its "equilibrium" value, is nonmonotonic and may take several hundred step heights to be achieved [4]. The recovery process, in general, may strongly depend on upstream and initial condition, e.g., geometry of obstacle and upstream boundary layer.

All the experimental studies cited above were conducted in zero pressure gradient (ZPG) and closed channels. It appears that no detailed investigations of separated and reattached flow in an open channel have been made with the possible exception of the laser Doppler anemometry (LDA) measurements downstream of a forward facing step [14]. Such flows can be used to model many important engineering fluid flow phenomena, such as flow over pipelines on a seabed. It should also be noted that the character-

Contributed by the Fluids Engineering Division of ASME for publication in the JOURNAL OF FLUIDS ENGINEERING. Manuscript received August 24, 2007; final manuscript received January 15, 2008; published online June 12, 2008. Assoc. Editor: Steven Ceccio. Paper presented at the 5th Joint ASME/JSME Fluids Engineering Conference, San Diego, CA, July 30–August 2, 2007.

 Copyright © 2008 by ASME

Downloaded 03 Jun 2010 to 171.66.16.157. Redistribution subject to ASME license or copyright; see http://www.asme.org/terms/Terms_Use.cfm

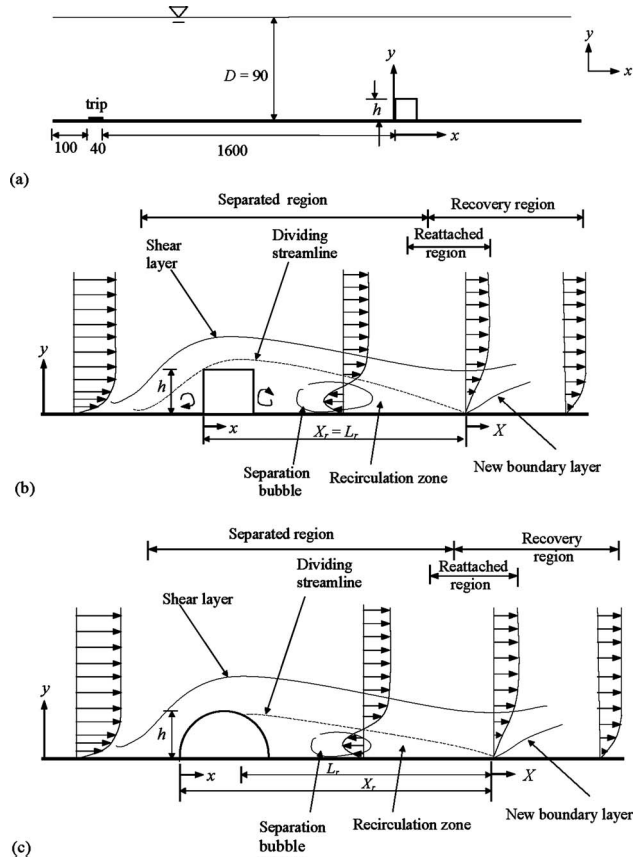

Fig. 1 Schematic diagram of experimental setup and coordinate system: (*a*) side view of test section, (*b*) and (*c*) are sketches showing dividing streamlines and the various flow regions for square and semicircular blocks, respectively. All dimensions are in mm. X_r is the reattachment length, and L_r is length of separation bubble.

istic high background turbulence levels in open channel flows, among others, differentiate them from ZPG turbulent boundary layers. Thus, the objective of this study is to investigate separated flow over the two-dimensional transverse blocks of square, rectangular, and semicircular cross sections in an open channel. The heights of all the blocks are kept constant, and the upstream conditions are kept similar so that differences in the flow structure can be solely attributed to the geometries of the blocks. The particle image velocimetry (PIV) technique is used to conduct the measurements because it is well suited for measuring velocity in reverse flows and also estimating derived quantities, such as vorticity and the various terms in the transport equations for turbulent kinetic energy and Reynolds stresses. The comprehensive data from the present study will also be invaluable for the purpose of turbulence model validation.

2 Experimental Setup and Measurement Procedure

The experiments were performed in a recirculating open channel flow. The channel is constructed using Plexiglas to facilitate optical access. The test section of the channel is 2500 mm long, 200 mm wide, and 200 mm deep. Figure 1(*a*) shows a schematic of the test section, a typical surface mounted (square) block, and the Cartesian coordinate system adopted in this work. The streamwise and wall-normal directions are denoted by x and y, respectively; $x=0$ corresponds to the upstream edge of the block and $y=0$ corresponds to the floor of the channel. The mean and fluctuating velocities will be denoted by the upper and lower cases, respectively. For example, U is the mean velocity in the streamwise direction and u and v are the fluctuating components in the streamwise and wall-normal directions, respectively. As shown in Fig. 1(*a*), a 40 mm wide strip of 1 mm sand grains spanning the width of the channel was placed 100 mm from the entrance of the water tunnel to enhance a rapid development of the boundary layer.

Two-dimensional transverse blocks of square, rectangular, and semicircular cross sections glued onto a 4 mm thick acrylic sheet using a double-sided tape were used to induce flow separation. The acrylic sheet, which spans the entire width and length of channel, was then tightly screwed onto the bottom wall of the channel. The average height of each block was $h=6$ mm. Figures 1(*b*) and 1(*c*) show the various flow regions as well as sketches of the mean velocity profiles in these regions. For the rectangular block (not shown), the ratio of longitudinal span to height was $b/h=6$. As shown in the figures, the flow separates at the upstream edge of the square but downstream of the crest of the semicircular block. The distance between the upstream edge of the block ($x=0$) and the reattachment point is denoted as X_r while the length of separation bubble, defined as the distance between the points of separation and reattachment, is denoted by L_r. The streamwise distance measured relative to the reattachment point is denoted by X whereas x' denotes streamwise distance relative to the mean separation point.

The flow was seeded with polyamide seeding particles having mean diameters of 5 μm and specific gravity of 1.03. A Nd-YAG (yttrium aluminum garnet), 120 mJ/pulse laser ($\lambda=532$ nm) was used to illuminate the flow. The laser sheet was located at the midplane of the channel and the flow field was imaged using a 12 bit 2048×2048 pixel charge coupled device (CCD) camera with a 7.4 μm pixel pitch. The camera was fitted with 60 mm Nikkor lens combined with a bandpass filter. The instantaneous images were processed using adaptive correlation and moving average validation options of FLOWMANAGER (commercial software developed by Dantec Dynamics Inc). The adaptive correlation uses a multipass fast Fourier transform (FFT) cross-correlation algorithm to determine the average particle displacement within an interrogation area. A three-point Gaussian curve fit was used to determine particle displacement with subpixel accuracy. The mean and turbulent statistics reported in this work were obtained using 2500 instantaneous images. Interrogation area side of 32×32 pixels with 50% overlap was employed. The particle image diameter was estimated to be $d_p=15.0$ μm (2.03 pixels), which is in good agreement with the value of 2.0 recommended by Raffel et al. [15] to minimize peak locking. During the image acquisition, the PIV parameters were optimized to satisfy the condition that the maximum particle displacement is less than one-quarter of the interrogation area used. Depending on the streamwise location, the interrogation area size in wall units varied from $l_y^+=5.5$ to 9.8. Based on the results from previous experiments specifically conducted to study the PIV spatial resolution effects in near-wall turbulent flow, we conclude that the present interrogation area sizes are sufficient to reliably measure all the mean velocity and turbulent quantities subsequently reported.

For each block shape, detailed measurements were made at seven different x-y planes along the flow in the separated and reattached regions and also in the redeveloping region down to 130 block heights downstream of reattachment point. Measurements were also made upstream of the blocks and data were extracted at $x=-250$ mm in order to obtain the characteristics of the approach turbulent boundary layer. The pertinent boundary layer parameters for the approach flow are summarized in Table 1, where D is the water depth, U_e is the freestream velocity, δ is the boundary layer thickness, δ^* is the displacement thickness, θ is the momentum thickness, H is the shape factor, G is the Clauser parameter, U_τ is the friction velocity, C_f is the skin friction coefficient, h is the height of blocks, w is the width of channel, and Re_D and Re_θ are the Reynolds number based on the water depth and momentum thickness, respectively. The turbulence level mea-

Downloaded 03 Jun 2010 to 171.66.16.157. Redistribution subject to ASME license or copyright; see http://www.asme.org/terms/Terms_Use.cfm

Table 1 Summary of upstream boundary layer parameters

$D=90$ mm	$U_r=0.315$ m/s	$\delta=55$ mm	$\delta^*=8.45$ mm	$\theta=5.79$ mm	$H=1.46$
$\delta/h=9.3$	$w/h=33.3$	$U_\tau=0.0142$ m/s	$G=6.8$	$C_f=0.0043$	$\mathrm{Re}_D=28{,}000$
$\mathrm{Re}_\theta=1800$	$\mathrm{Re}_h=1920$	$U_{(y=h)}=0.69U_e$	$H=\delta^*/\theta$	$G=\sqrt{2/C_f}(H-1)/H$	
$C_f=2(U_\tau/U_e)^2$		$\delta^*=\int_0^\delta(U_e-U)dy/U_e$		$\theta=\int_0^\delta U(U_e-U)dy/U_e^2$	

sured at $y=\delta$ is 5% and the mean velocity at $y=h$ (or 6 mm above the floor), which corresponds to the top plane of the obstacles is $U_{(y=h)}=0.69U_e$. The ratio $\delta/h=9.3$, and based on Bradshaw and Wong's [4] terminology, the present perturbation may be classified as a weak one. Figures 2(*a*) and 2(*b*) show the mean velocity profile in the outer and inner coordinates, respectively. The data shown in Fig. 2(*b*) follow the classical log law ($U^+=\kappa^{-1}\ln y^+ +C$, where $U^+=U/U_\tau$, $y^+=yU_\tau/\nu$, ν is kinematic viscosity, $\kappa=0.41$, and $C=5.0$ are log law constant) reasonably well. Figure 2(*b*) reveals a weak wake component that is typical of open channel flows [16,17]. Figure 2(*c*) shows that, for the approach boundary layer, variation of U_e with x is much smaller than the measurement uncertainty so that the acceleration parameter $K=\nu/U_e^2(dU_e/dx)$ is considered negligible. The peak values of the normalized turbulent intensities and Reynolds shear stress are $u^+_{\max}=2.7$ (i.e., $u^+=u/U_\tau$), $v^+_{\max}=1.0$ and $-\langle u^+v^+\rangle_{\max}=0.6$. These are in good agreement with the values of $u^+_{\max}=2.75$, $v^+_{\max}=1.1$ and $-\langle u^+v^+\rangle_{\max}=0.65$ obtained in open channel flow with a high resolution LDA [17]. However, the level of turbulence is higher in the present study and the profile of the transverse turbulence intensity v^+ is nearly flat over the boundary layer because of the high background turbulence level. Following the methodologies outlined by Coleman and Steele [18] and Forliti et al. [19], the uncertainty in the mean velocities at 95% confidence level was determined to be $\pm 2\%$. The uncertainties in turbulence intensities and Reynolds shear stress were estimated to be $\pm 7\%$ and $\pm 10\%$, respectively. In some of the graphs subsequently shown, the error bars are used to indicate the measurement uncertainties at 95% confidence level.

3 Results and Discussion

The results in this study will be discussed in three parts. The characteristics of the separated shear layer will be discussed in Sec. 3.1, while the profiles of the mean velocities, turbulent statistics, and transport terms in the recirculation and redevelopment regions are discussed in Sec. 3.2. The block height, $h=6$ mm and the freestream or reference velocity, $U_r=0.315$ m/s, will be used as the length and velocity scales, respectively. In Sec. 3.3, the boundary layer parameters and profiles of the mean velocity and turbulent quantities in inner coordinates downstream of the reattachment point will be used to provide insight into the evolution of the flow toward equilibrium.

3.1 Separated Shear Layer. The streamlines close to the blocks are shown in Fig. 3. Two pairs of separations and reattachments were found for the square block (Fig. 3(*a*)), one for the semicircular block (Fig. 3(*b*)) and three for the rectangular block (Fig. 3(*c*)). A small separation bubble on top of rectangular block is also evident close to the upstream edge (Fig. 3(*c*)). Figure 3 also immediately reveals the characteristic corner counter-rotating vortices behind the square and rectangular blocks. Unlike the rectan-

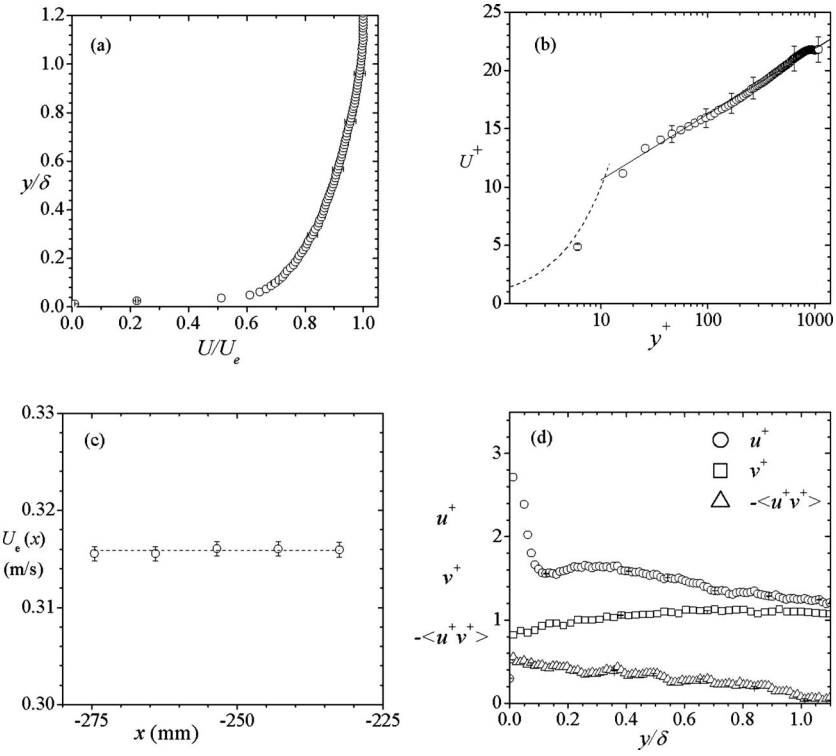

Fig. 2 Characteristics of upstream boundary layer: mean velocity profiles in outer (*a*) and inner (*b*) coordinates; (*c*) variation of the freestream velocity, U_e with x; (*d*) profiles of u^+, v^+, and $-\langle u^+v^+\rangle$. Dotted line in (*b*) is $U^+=y^+$, and solid line is $U^+=2.44\ln y^+ +5$.

Downloaded 03 Jun 2010 to 171.66.16.157. Redistribution subject to ASME license or copyright; see http://www.asme.org/terms/Terms_Use.cfm

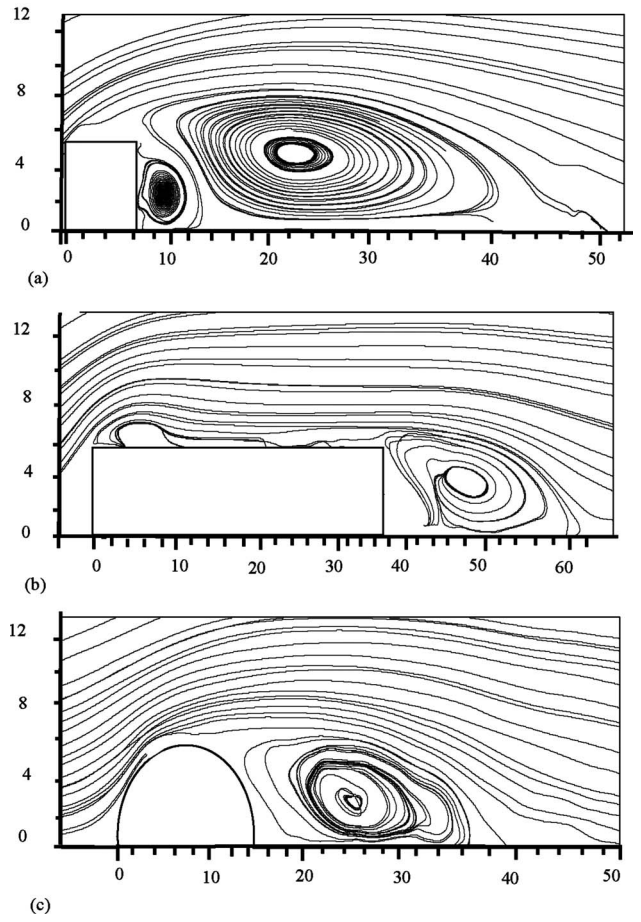

Fig. 3 Streamlines in recirculation zone: (*a*) square, (*b*) rectangular, and (*c*) semicircular blocks

gular and semicircular blocks, the dividing streamline for the square block is substantially deflected upward from the block. Consequently, the separation bubbles for the rectangular and semicircular blocks are much shallower than for the square block. It is evident that the square block increased the size and intensity of the separation bubble.

The reattachment point was found by determining the x-location where the streamwise component of the mean velocity $U \approx 0$ and where the dividing streamline reattaches on the floor. The values obtained from the two methods differ by $0.5h$ or less (which is within measurement uncertainty ($\pm 0.5h$) in locating the reattachment point). As noted earlier, the reattachment length, X_r, is defined as the distance between the upstream edge of the obstacle ($x=0$) and reattachment point, whereas the length of separation bubble, L_r, is defined as the distance between points of mean separation and reattachment. The values of X_r/h and L_r/h determined from the streamlines for the three blocks are summarized in Table 2. The values of L_r and X_r are similar for the square block because separation occurred at the upstream edge of the square. L_r is largest for the square block and least for the rectangular block. The present values of $X_r=8.5h$ for the square block

Table 2 Summary of length of reattachment (X_r) and separation bubble (L_r) for the blocks

Model	Square	Semi-circular	Rectangular
X_r/h	8.5	6.7	10.1
L_r/h	8.5	5.0	4.1

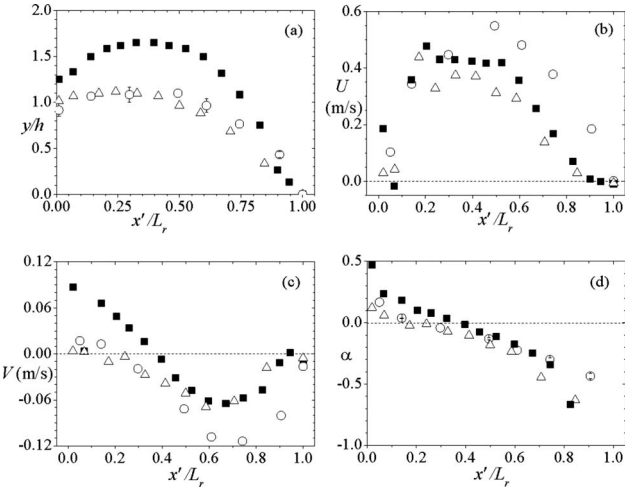

Fig. 4 (*a*) Loci of the dividing streamlines, (*b*) mean streamwise velocity (U) along the dividing streamlines, (*c*) mean transverse velocity (V) along the dividing streamlines, and (*d*) flow angle V/U along the dividing streamlines. Note that $x'=0$ at separation point. Symbols: square block, ■; semicircular block, ○; rectangular block, △.

are 35% and 25%, respectively, lower than values reported by Tillman [11] and Bergeles and Athanassiadis [12]. For the rectangular block, the present value ($X_r=10.1h$) is only 10% higher than that reported by Bergeles and Athanassiadis [12]. The disparity may be partly due to the differences in upstream boundary condition, such as Reynolds number, boundary layer thickness, and turbulence level or measurement uncertainty.

The y-locations at which the dividing streamline occurs at various x-locations in the recirculation region were determined and plotted in Fig. 4(a) for the three blocks. While the y-values for the rectangular block almost monotonically decrease with x, the values for the semicircular and square blocks initially increase before decreasing to $y=0$ at reattachment. The dividing streamline for the semicircular and rectangular blocks are closer to the wall than for the square block. The shear-layer direction could be defined, among others, along the y-locations where the local mean velocity is ($0.67\Delta U+U_{\min}$), along the lines of maximum kinetic energy, and along the dividing streamline [2]. Although the shear-layer directions from the different definitions did not exactly coincide, it was found that those defined along ($0.67\Delta U+U_{\min}$) and the dividing streamline favorably compared for $x'/L_r \leq 0.7$ [2]. The variations of the mean velocities (U and V) and the flow angle ($\alpha = V/U$) along the dividing streamlines are shown in Figs. 4(b), 4(b), and 4(c), respectively. Figure 4(b) shows that U increases from zero at $x'/L_r=0$, peaks, and then decreases to zero at $x'/L_r \approx 1$, whereas V initially decreases from zero, to a minimum (negative) value before increasing to zero at reattachment point. It is evident from Fig. 4(d) that the flow angle α is positive for $x'/L_r \leq 0.15$ ($x'/L_r \leq 0.4$ for square block) and negative beyond this location. The trend in Fig. 4(d) is similar to those reported by Castro and Haque [2] for a normal flat plate.

The variations of the velocity difference across the shear layer ($\Delta U=U_{\max}-U_{\min}$) and the maximum slope $(\partial U/\partial y)_{\max}$ with x'/L_r are shown in Fig. 5(a). The velocity difference increases from its value at separation point ($x'=0$) to a maximum value at $x'/L_r \approx 0.5$ and then decreases toward a value of unity beyond reattachment. The trend is similar to those obtained in prior studies; however, the peak value of $\Delta U/U_r \approx 1.26$ is lower than a value of 1.5 obtained for a normal flat plate [2,9] but higher than 1.1 for backward facing step [7]. As expected, $(\partial U/\partial y)_{\max}$ generally decreases along the flow. The vorticity thickness, δ_ω, shown in Fig. 5(b) is not consistent with a linear growth rate documented for a plane

Downloaded 03 Jun 2010 to 171.66.16.157. Redistribution subject to ASME license or copyright; see http://www.asme.org/terms/Terms_Use.cfm

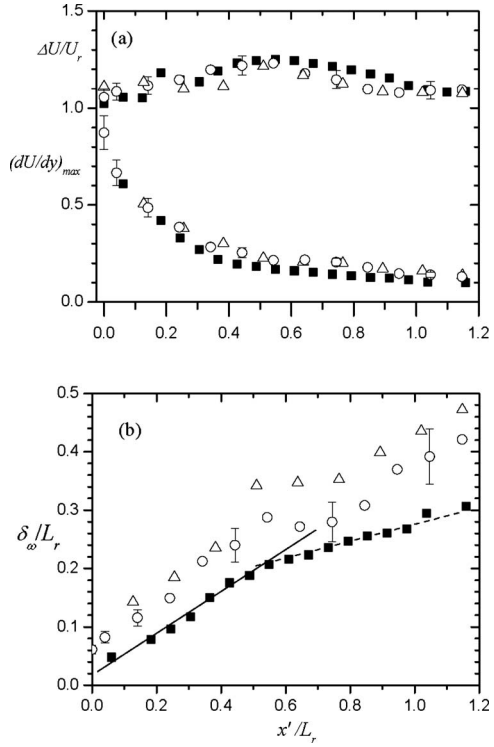

Fig. 5 The variation of (*a*) velocity difference $\Delta U = U_{max} - U_{min}$, maximum slope $\partial U/\partial y_{max}$, and (*b*) vorticity thickness δ_ω in recirculating and reattachment regions. In (*b*), the solid line is $d\delta_\omega/dx = 0.33$ and the dash line is $d\delta_\omega/dx = 0.15$. Symbols are as in Fig. 4.

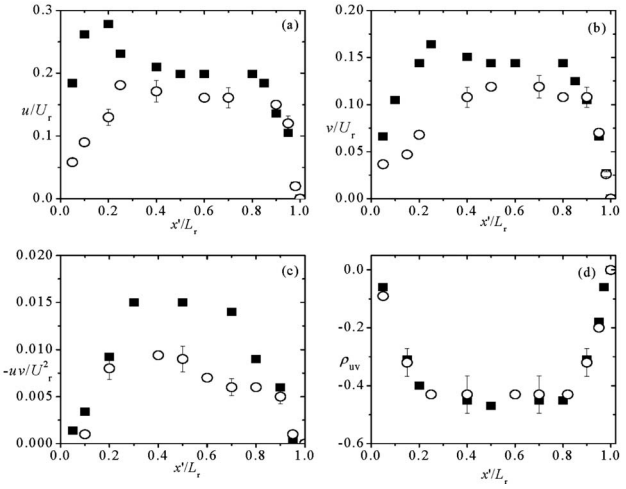

Fig. 6 Distributions of turbulence intensities, Reynolds shear stress, and correlation coefficient along the dividing streamlines for the square (■) and semicircular (○) blocks. (*a*) u/U_r, (*b*) v/U_r, (*c*) $-\langle uv\rangle/U_r^2$, and (*d*) ρ_{uv}.

mixing layer. With reference to their experimental data [2], it was suggested that there is no reason why, in this complex flow, the shear layer should linearly grow. Jovic [7] argued that the separated shear layer cannot be expected to exactly resemble the plane mixing layer because the former is influenced by a strong adverse pressure gradient, short reattachment length, and high turbulent recirculating flow beneath it. The data reported for a normal flat plate [2,8] and a blunt plate [10] indeed show that the initial shear-layer growth is higher than for the plane mixing layer. The growth rate in the region next to this and extending to the reattachment point is much slower than in the initial shear-layer region. For the present data, the growth rate in the first half of the recirculation region is $d\delta_\omega/dx = 0.33$, which is substantially higher than the values in the range of 0.145 and 0.22 reported for a plane mixing layer [20]. For the square block, $d\delta_\omega/dx = 0.15$, obtained in the second half of recirculating region is consistent with growth rate for a plane mixing layer.

The variation of the turbulence intensities, Reynolds shear stress, and correlation coefficient along the dividing streamlines (Fig. 4(*a*)) for the square and semicircular blocks is shown in Fig. 6. It should be emphasized that the plots in Fig. 6 are those along the dividing streamline and should not be confused with the peak values in the shear layer. The turbulence levels rapidly increase along the streamline over the first 20–30% of the separation bubble. Beyond this region, the turbulence intensities and Reynolds shear stress nearly remain constant over a range and then rapidly decrease toward a nominal value of zero at reattachment point. The region of rapid turbulent reduction approximately corresponds to the region of rapid flow acceleration. Although the turbulence intensities and Reynolds shear stress along the dividing streamlines are higher for the square block, the correlation coefficient is independent of block geometry. In their backward facing step experiments, Etheridge and Kemp [21] showed that both u and v increase along the dividing streamline and then rapidly drop as the reattachment point is approached. Thus, their results are consistent with the present ones. Etheridge and Kemp [21] also argued that a vortex line along a streamline is rotated and stretched by the rate of strain $\partial U/\partial y$, and as a consequence, the Reynolds shear stress should be enhanced along the dividing streamline. The sharp increase in $-\langle uv\rangle$ along the streamline supports this view. The dramatic reduction in $-\langle uv\rangle$ as the wall (or reattachment) is approached is consistent with the notion that the Reynolds shear stress should decrease along the dividing streamline near reattachment [4]. The dramatic reduction in $-\langle uv\rangle$ close to reattachment can also be explained by attenuation of v and a reduced correlation between u and v in this region. The variation of u along the streamline may be partly explained by turbulence production due to the vortex stretching $\partial U/\partial y$ ($-\langle uv\rangle \partial U/\partial y$) and the extra production due to the longitudinal strain $\partial U/\partial x$ ($-u^2 \partial U/\partial x$). Since u^2 is positive, the sign of $\partial U/\partial x$ determines whether the extra production term makes a positive or negative contribution. It should be noted that the region over which u^2 increases corresponds to region of flow deceleration (positive contribution), while the region of decreasing u^2 corresponds to region of flow acceleration (negative contribution).

3.2 Profiles in the Recirculation and Redevelopment Regions

3.2.1 Mean Velocity Field. Since only a minute fraction of the large volume of velocity data acquired can be presented, it was decided to concentrate most of the plots in the recirculating region and immediately downstream of reattachment where reliable data sets are scarce. In the recirculating region, data will be presented at $x'/L_r = 0.25$, 0.50, 0.75, and 1.0. In addition to these locations, data will be plotted at the crest of the semicircular block, which is located upstream of the separating point. For the square and rectangular blocks, additional data will be plotted at x-locations corresponding to top of block ($x/h = 0.5$ and $x/h = 3$, for the square and rectangular blocks, respectively) and center of corner counter-rotating vortices behind the blocks. In the redeveloping region, data will be shown at $X/h = 2$, 4, 6, 10, 20, and 30, where $X = 0$ corresponds to the reattachment point. For convenience, x-locations corresponding to crest/top of block and center of counter-rotating vortex will be denoted by S1 and S2, while $x'/L_r = 0.25$, 0.50, 0.75, and 1.0 will be denoted by S3, S4, S5, and S6, respectively. Similarly, $X/h = 2$, 4, 6, 10, 20, and 30 will be denoted by SA, SB, SC, SD, SE, and SF, respectively.

Figures 7(*a*) and 7(*b*) show the streamwise mean velocity profiles in the recirculation and redeveloping regions, respectively. As

Downloaded 03 Jun 2010 to 171.66.16.157. Redistribution subject to ASME license or copyright; see http://www.asme.org/terms/Terms_Use.cfm

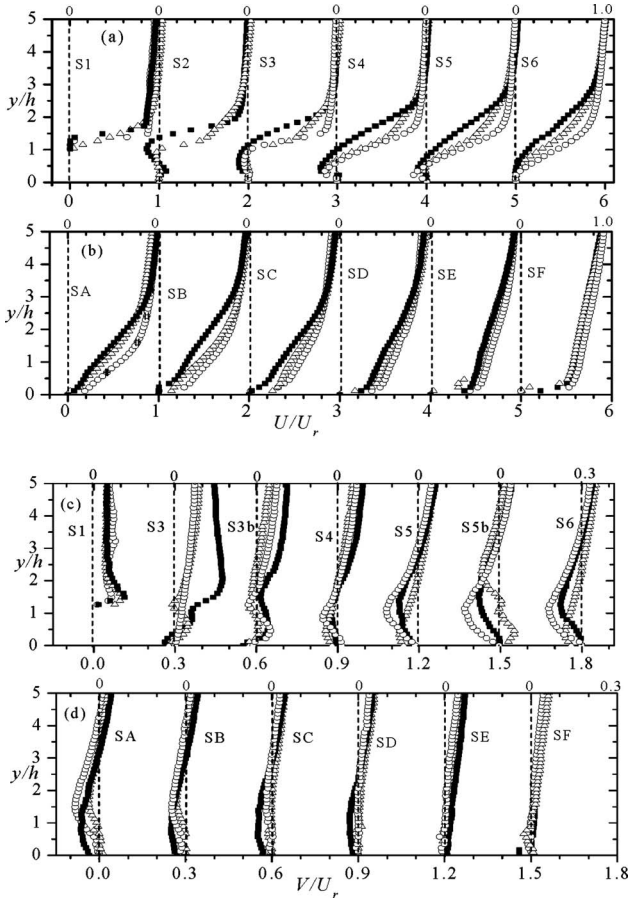

Fig. 7 Mean velocity profiles: streamwise components in (*a*) recirculation and (*b*) reattachment regions; wall-normal components in (*c*) recirculation and (*d*) reattachment regions. Symbols as in Fig. 4. Definition of the stations is provided in text.

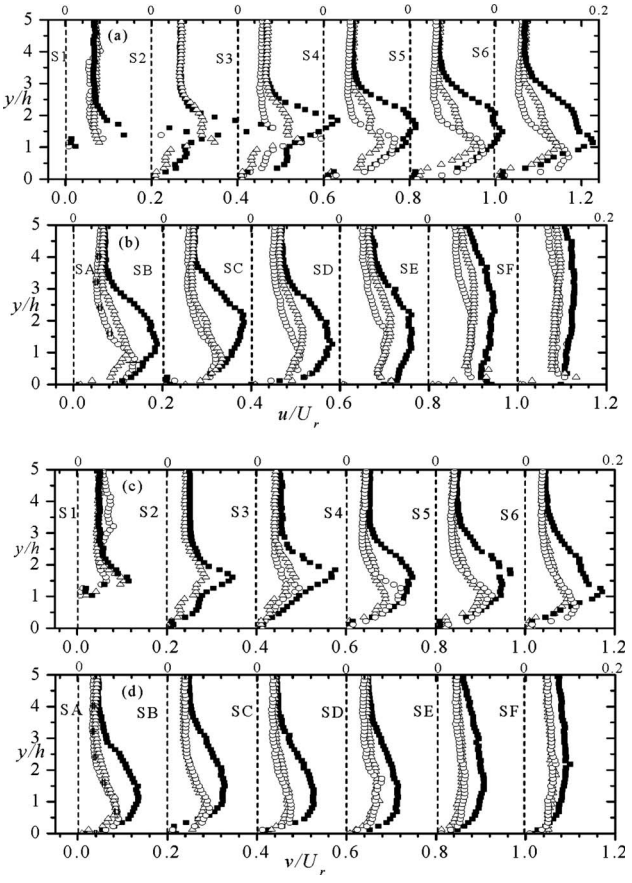

Fig. 8 Profiles of turbulence intensities: streamwise component in (*a*) recirculation and (*b*) recovery regions; wall-normal component in (*c*) recirculation and (*d*) recovery regions. Symbols are as in Fig. 4.

expected, the velocity profiles in the recirculation region deviate from the upstream profile. The mean flow close to the floor is most distorted by the square block, partly because the dividing streamline is significantly deflected away from the block. The magnitude of maximum backflow velocity was found to be 20%, 14%, and 10% of the reference velocity for the square, semicircular, and rectangular blocks, respectively. These values are within the range of 10% to more than 20% reported for backward facing step [5,7] and 30% for a normal flat plate [2] and a bluff flat plate [10]. Similarity with upstream profile improves with increasing streamwise distance and at $X/h=30$ (SF), the profile begins to resemble the upstream profile. Distribution of the wall-normal component of the mean velocity V in the recirculating region is rarely reported. Profiles of V for the three blocks are shown in Figs. 7(*c*) and 7(*d*). The magnitudes of the maximum negative values are approximately 8–12% of reference upstream velocity. These values are comparable to maximum backflow velocities so that the classical thin shear-layer assumption that V is small compared to U is not valid close to the wall in the recirculating region.

3.2.2 Turbulent Intensity and Reynolds Shear Stress. The profiles of u, v, and $-\langle uv\rangle$ in the recirculating and reattachment regions are shown in Figs. 8 and 9. The profiles are lower than the upstream profile close to the wall but higher than the upstream profile away from the wall. The profiles for the square block are significantly higher than those for the rectangular and semicircular blocks. Because the dividing streamline for the square block is initially deflected away from the wall, the locations of $u_{\max}$, $v_{\max}$, and $-\langle uv\rangle_{\max}$ initially increase with x/h before decreasing. Downstream of reattachment where the new shear layer develops, the locations of peak values increasingly move up. As a result of the mixing and spreading of the new shear layer, the levels of u, v, and $-\langle uv\rangle$ monotonically decrease and the profiles become more uniform as x increases. Furthermore, the turbulence intensities and Reynolds shear stress nearly linearly increase from their wall

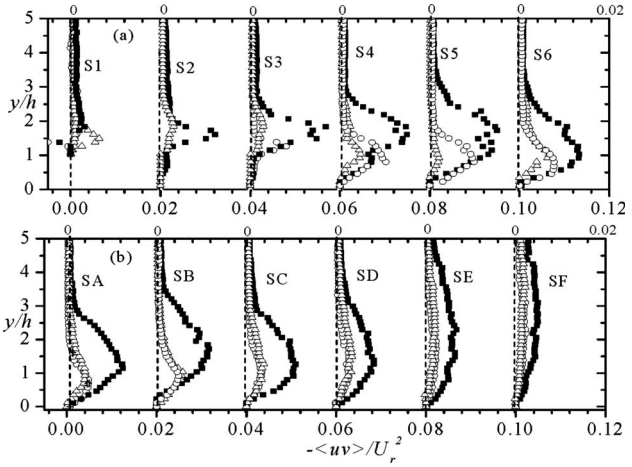

Fig. 9 Profiles of $-\langle uv\rangle$ in (*a*) recirculation and (*b*) recovery regions. Symbols are as in Fig. 4.

Downloaded 03 Jun 2010 to 171.66.16.157. Redistribution subject to ASME license or copyright; see http://www.asme.org/terms/Terms_Use.cfm

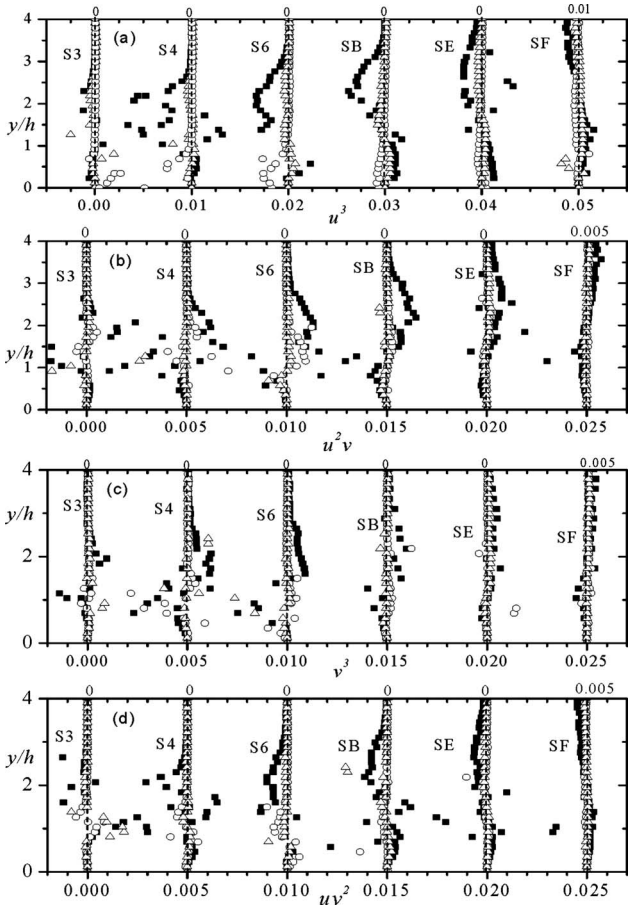

Fig. 10 Distributions of triple products (normalized by U_r^3) at selected *x*-locations: (*a*) u^3, (*b*) u^2v, (*c*) v^3, and (*d*) uv^2. Symbols are as in Fig. 4.

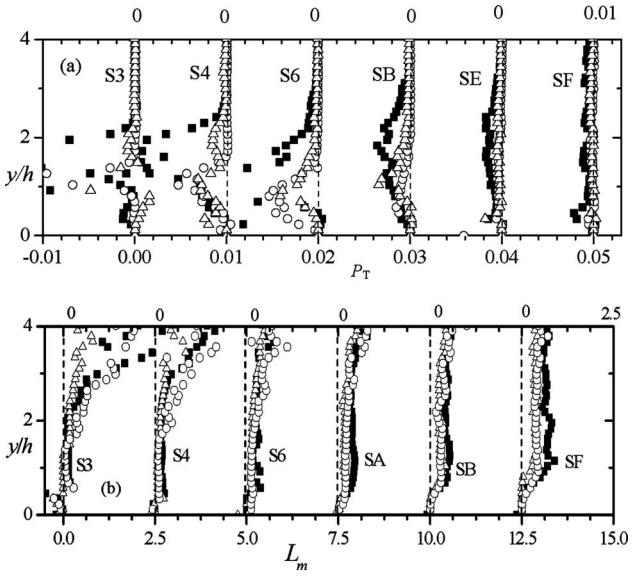

Fig. 11 Production and mixing length at selected *x*-locations: (*a*) total production, $P_T=[u^2\partial U/\partial x+v^2\partial V/\partial y]+[\langle uv\rangle(\partial U/\partial y+\partial V/\partial x)]$; (*b*) mixing length, $L_m=(-\langle uv\rangle)^{1/2}/\partial U/\partial y$. Symbols are as in Fig. 4.

value to their respective peak values. Antoniou and Bergeles [13] reported u data downstream of square and rectangular blocks and came to a similar conclusion.

3.2.3 Triple Products and Turbulent Diffusion. The triple products (u^3, uv^2, u^2v, and v^3) are shown in Fig. 10. The values of u^3 are higher than uv^2, u^2v, and v^3. Both u^3 and uv^2 are generally positive close to the wall and negative farther out, whereas u^2v and v^3 are negative close to the wall and positive away from the wall. These trends are the same as in flow downstream of backward facing step [7]. With regard to turbulence transport, it is the gradients of these quantities (not their magnitudes) that are important. It is evident that $[\partial(u^2v)/\partial y+\partial(v^3)/\partial y]$, which corresponds to diffusion or transport of turbulence kinetic energy in the wall-normal direction, is negative close to the wall and positive farther out. The exact regions of positive and negative diffusion rate depend on block geometry and vary along the flow. The magnitude of diffusion rate is not negligible compared to the other terms in the energy budget. Jovic [7] made similar observations in his measurements downstream of a backward facing step, and negative diffusion rates have been reported on the low velocity side of mixing layers [22]. Simpson et al. [23] concluded that diffusion plays a major role in transporting the turbulent kinetic energy in separated flows from the middle part of the layer, where it is mainly produced, to the outer region and region near the wall. The magnitude of $[\partial(u^2v)/\partial y+\partial(v^3)/\partial y]$ is largest for the square block. It should be noted that the profiles of u^2v and v^3 become more uniform as the flow evolves downstream of reattachment. Thus, turbulence diffusion rate will diminish as it redevelops toward an equilibrium turbulent boundary layer.

3.2.4 Production of Turbulence Kinetic Energy and Mixing Length. The production of turbulent kinetic energy, $P_T=[u^2\partial U/\partial x+v^2\partial V/\partial y]+[\langle uv\rangle(\partial U/\partial y+\partial V/\partial x)]$, consists of contribution from normal stresses (first two terms on the right hand side) and shear stresses (last two terms). All the four production terms were directly estimated from the measured data. Since $\partial U/\partial y>\partial V/\partial x$ over most of the shear layer, production by the shear stress is well approximated by $P_s=\langle uv\rangle\partial U/\partial y$. Similarly, production by the normal stresses may be approximated by $P_n\approx(u^2-v^2)\partial U/\partial x$ (since $\partial U/\partial x\approx-\partial V/\partial y$). The magnitudes of $u^2\partial U/\partial x$ and $v^2\partial V/\partial y$ are individually high; however, their sum is smaller than the individual terms. Figure 11(*a*) shows P_T at typical locations in the recirculation and redeveloping regions of the square and semicircular blocks. The P_T values are negligible very close to the wall but rise to a maximum between $y/h=1$ and 2 and becomes negligible again after $y/h=2.5$. The values for square block are higher than those of the semicircular and rectangular blocks but at station SF they collapsed. Unlike classical near-wall turbulent flows, the bulk of turbulence in separated flows is produced in midlayer and transported to the inner and outer layers. Figure 11(*b*) shows that the values of $L_m(=(-\langle uv\rangle)^{1/2}/\partial U/\partial y)$ rapidly increased from a nominal value of zero at the wall to a maximum value at $y/h<1$, and approximately stay flat before increasing again. The flat portion of L_m is relatively narrower in the recirculation region (S3, S4, S6) than in the redevelopment region (SA, SB, SF). Furthermore, the rise in L_m beyond the flat portion is more dramatic in the recirculation region.

3.3 Return to Equilibrium. Consideration is now turned to the redeveloping region. The main focus is to document how the mean flow and fluctuating components evolve toward a typical turbulent boundary layer. For the mean flow, we make this assessment by comparing the momentum thickness θ, shape factor H, skin friction coefficient C_f, and Clauser parameter G, at various x-locations to their corresponding upstream values. Since direct measurement of skin friction coefficient C_f was not made in the present study, the C_f values downstream of reattachment were consistently estimated using the Ludwieg–Tillman formula: $C_f=0.246\times10^{0.678H}\mathrm{Re}_\theta^{-0.268}$. This formula has been used in prior separated and reattached flows and values obtained from it favorably compared with those obtained from other reliable skin fric-

Downloaded 03 Jun 2010 to 171.66.16.157. Redistribution subject to ASME license or copyright; see http://www.asme.org/terms/Terms_Use.cfm

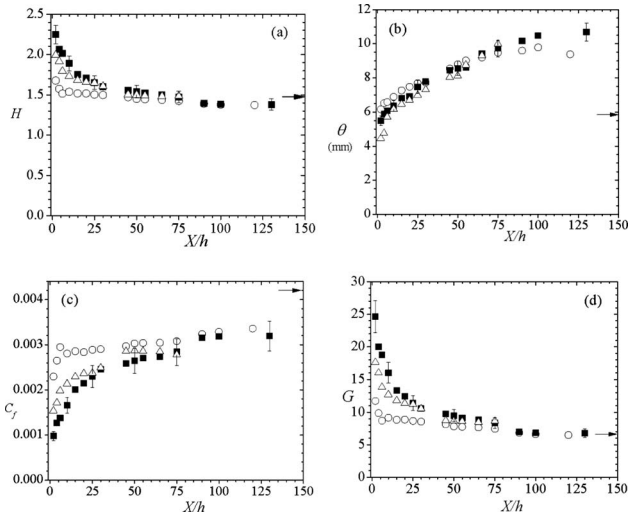

Fig. 12 Variation of the boundary layer parameters with *X*/*h*: (*a*) shape factor *H*, (*b*) momentum thickness θ, (*c*) skin friction coefficient C_f, and (d) Clauser parameter *G*. Symbols are as in Fig. 4.

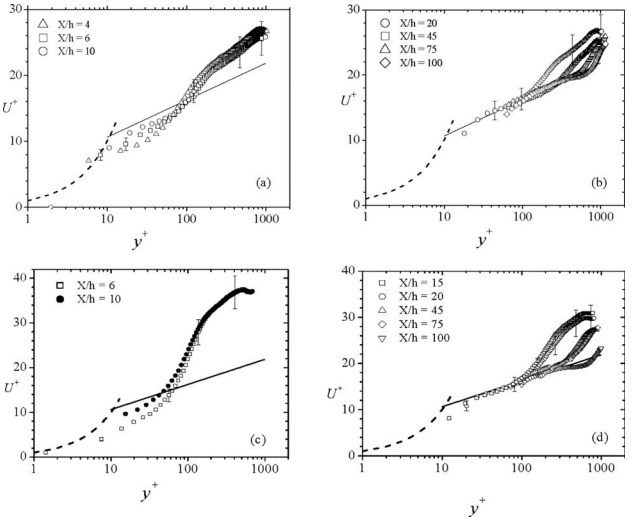

Fig. 13 Typical mean profiles in inner coordinates at selected locations for ((*a*) and (*b*)) semicircular block and ((*c*) and (*d*)) square block. The dashed lines are $U^+ = y^+$, the solid lines are $U^+ = 2.44 \times \ln y^+ + 5$.

tion techniques. For example, the maximum difference between the C_f values obtained behind a backward facing step from Ludwieg–Tillman formula and Preston tubes is less than 10% [4]. The C_f values obtained downstream surface mounted obstacles [13] and a wall fence in an adverse pressure gradient turbulent boundary layer [24] using the log law and the Ludwieg–Tillman formula were found to be within $\pm 5-10\%$ of each other. The uncertainty estimates are $\pm 5\%$ for H and θ, and $\pm 10\%$ for C_f and G.

The variations of θ, H, C_f, and G with X are shown in Fig. 12. In these plots, the arrows indicate the upstream values for the particular parameter. Because the square block distorted the mean flow most, the parameters obtained immediately downstream of reattachment for the square block deviate most from the upstream value. Similar to the results of Antoniou and Bergeles [13], the C_f values for square block are lower than those for the rectangular block immediately downstream of reattachment ($X/h < 25$), while the G values are higher for the square than for the rectangular block. At similar X/h in the region $X/h < 25$, the present G values for the square block favorably compare with those in Ref. [11] but higher than those reported in Ref. [13]. Since the present value of δ/h is comparable to that in Ref. [11] but an order of magnitude higher than in Ref. [13], the results are consistent with the notion that G increases with δ/h. As noted earlier, δ/h was kept constant in the present experiments, and so we may conclude from Fig. 12 that G, C_f, H, and θ strongly depend on block geometry over the first 25–50 block heights downstream of reattachment. These parameters fairly rapidly readjust and beyond 50 block heights downstream of reattachment they are almost independent of block crosssection. The evolution of the shape factor H and Clauser parameter G toward the upstream value appears to be monotonic. At approximately $X/h = 90$, H and G are within 5% of the corresponding upstream values and C_f is 21% lower than the upstream value and θ is almost twice as high as the corresponding upstream value.

Figure 13 shows the typical mean velocity profiles in the inner coordinates. The friction velocity obtained from the C_f values estimated from Ludwieg–Tillman formula is used in normalizing U and y. In the region $X/h \geq 15$, the profiles follow the log law fairly well. Closer to reattachment point ($X/h \leq 10$), however, the experimental data fall below the log law. These observations are consistent with numerous earlier experiments (e.g., Refs. [4,8,25]) but at variance with the backward facing step study of Ref. [17] and over surface mounted obstacles [13] in which the dip below the log law was not immediately observed downstream of reattachment point. Note that in Ref. [13], the friction velocity was varied to force a collapse of measured data onto the log law. This was not done in the present study since we are not certain of the validity of the log law very close to reattachment. Similar to previous results, the wake component is very large compared to the characteristic values of 0.55 and 0.1, respectively, for ZPG turbulent boundary layer and open channel flow. As the flow develops downstream, the wake component substantially diminishes.

The Reynolds normal stresses (u^2 and v^2) and shear stress ($-\langle uv \rangle$) obtained at $X/h = 25$ and 45 or 50 downstream the reattachment point for the square and semicircular blocks are compared to the upstream profiles in Fig. 14. The downstream profiles, particularly those for the square block, are significantly higher than the upstream profiles over most of the boundary layer. For the square block, the peak values at $X/h = 50$ are considerably lower than those at $X/h = 25$. Furthermore, the position of the peak values at $X/h = 50$ is further away from the wall than for $X/h = 25$. For the semicircular block, there is only a little variation between the profiles at $X/h = 25$ and 45, an indication that several step heights will be required for the profiles to collapse onto the upstream profiles, if that is possible at all.

4 Conclusions

A PIV technique was used to provide extensive data sets to document the salient features of separated and reattached open channel flow downstream of surface mounted blocks of square, rectangular, and semicircular cross sections. The benchmark data presented in this study will also be useful for assessing the ability of turbulence models to reproduce the behavior of separated and reattached open channel flows. The major observations are as follows:

1. The curvature of dividing streamline and the separation bubble beneath it are larger for the square block than for the rectangular and semicircular blocks. As a result, the interaction between the shear layers is most intense downstream of the square block. The Reynolds stresses and correlation coefficient rapidly increase along the dividing streamline and then rapidly decrease as the reattachment point is approached. The rate of reduction of the streamwise component of turbulent kinetic energy by stretching of longitudinal strain rate is somewhat lower than the reduction of the wall-normal component by wall blocking.

Downloaded 03 Jun 2010 to 171.66.16.157. Redistribution subject to ASME license or copyright; see http://www.asme.org/terms/Terms_Use.cfm

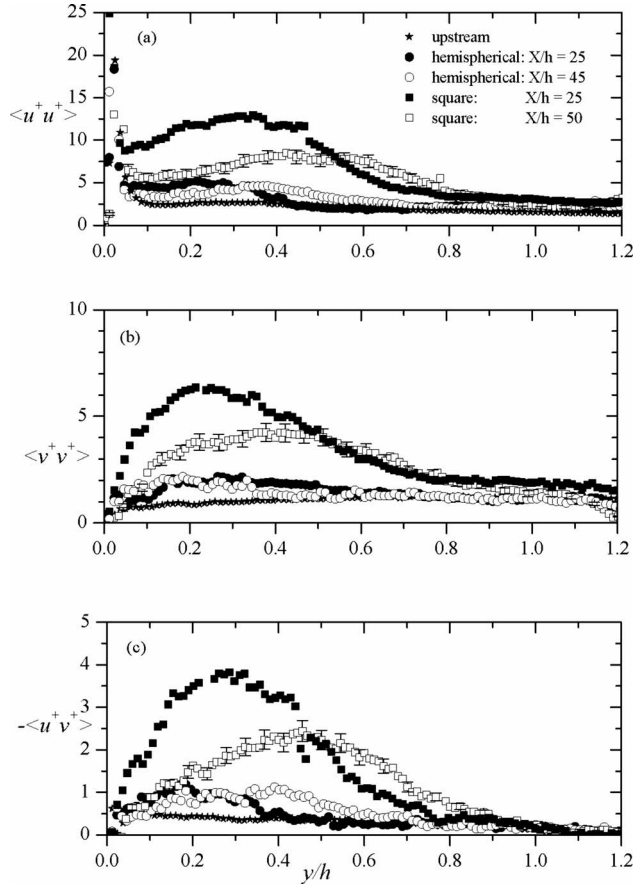

Fig. 14 Profiles of (*a*) $\langle u^+u^+\rangle$, (*b*) $\langle v^+v^+\rangle$, and (*c*) $-\langle u^+v^+\rangle$ for upstream boundary layer and at selected *X*-locations for square and semicircular blocks

2. Similarity between the separated shear layer in an open channel and the plane mixing layer is more limited than implied in some previous studies. This is based on the premise that the initial growth rate of the vorticity thickness is significantly larger than typical values reported for the plane mixing layer.
3. The shape factor, skin friction coefficient, momentum thickness, and Clauser parameter strongly depend on geometry of the blocks over the first 25–50 block heights downstream of reattachment. However, beyond 50 block heights downstream of reattachment, they are almost independent of block cross section. It is anticipated that a very long redevelopment length will be required for the skin friction coefficient, momentum thickness, and profiles of the Reynolds stresses to collapse onto their corresponding upstream values.

Acknowledgment

The support of this work by the Natural Sciences and Engineering Research Council of Canada and The Canada Foundation for Innovation is gratefully acknowledged.

References

[1] Castro, I. P., 1979, "Relaxing Wakes Behind Surface-mounted Obstacles in Rough Wall Boundary Layers," J. Fluid Mech., **93**, pp. 631–659.
[2] Castro, I. P., and Haque, A., 1987, "The Structure of a Turbulent Shear Layer Bounding a Separation Region," J. Fluid Mech., **179**, pp. 439–468.
[3] Driver, D. M., and Seegmiller, H. L., 1985, "Features of a Reattaching Turbulent Shear Layer in Divergent Channel Flow," AIAA J., **23**, pp. 83–1712.
[4] Bradshaw, P., and Wong, F. Y. F., 1972, "The Reattachment and Relaxation of a Turbulent Shear Layer," J. Fluid Mech., **52**, pp. 113–135.
[5] Eaton, J. K., and Johnston, J. P., 1981, "A Review of Research on Subsonic Turbulent Flow Reattachment," AIAA J., **19**, pp. 1093–1100.
[6] Jovic, S., and Driver, D. M., 1995, "Reynolds Number Effects on the Skin Friction in Separated Flow Behind a Backward Facing Step," Exp. Fluids, **18**, pp. 464–467.
[7] Jovic, S., 1996, "An Experimental Study of a Separated/Reattached Flow Behind a Backward Facing Step. Re_h=37000," NASA Technical Memorandum 110384.
[8] Ruderich, R., and Fernholz, H. H., 1985, "An Experimental Investigation of a Turbulent Shear Flow with Separation, Reverse Flow and Reattachment," J. Fluid Mech., **163**, pp. 53–73.
[9] Hancock, P. E., 2002, "Low Reynolds Number Two-Dimensional Separated and Reattaching Turbulent Flow," J. Fluid Mech., **410**, pp. 101–122.
[10] Djilali, N., and Gartshore, I. S., 1991, "Turbulent Flow Around a Bluff Rectangular Plate. Part I: Experimental Investigation," ASME J. Fluids Eng., **113**, pp. 51–59.
[11] Tillman, W., 1945, British Min. of Aircraft Prod. Volkenrode Translation MAP-VG 34-45T.
[12] Bergeles, G., and Athanassiadis, N., 1981, "The Flow Past a Surface-Mounted Obstacles," ASME J. Fluids Eng., **105**, pp. 461–463.
[13] Antoniou, J., and Bergeles, G., 1985, "Development of the Reattached Flow Behind Surface Mounted Two-Dimensional Prisms," ASME J. Fluids Eng., **110**, pp. 127–133.
[14] Tachie, M. F., Balachandar, R., and Bergstrom, D. J., 2001, "Open Channel Boundary Layer Relaxation Behind a Forward Facing Step a Low Reynolds Numbers," ASME J. Fluids Eng., **123**, pp. 539–544.
[15] Raffel, M., Willert, C. E., and Kompenhaus, J., 1998, *Particle Image Velocimetry: A Practical Guide*, Springer, New York.
[16] Nezu, I., and Rodi, W., 1986, "Open-Channel Flow Measurement With a Laser Doppler Anemometer," J. Hydraul. Eng., **112**, pp. 335–355.
[17] Tachie, M. F., Balachandar, R., and Bergstrom, D. J., 2003, "Low Reynolds Number Effects in Open Channel Turbulent Boundary Layers," Exp. Fluids, **34**, pp. 616–624.
[18] Coleman, H. W., and Steele, W. G., 1995, "Engineering Application of Experimental Uncertainty Analysis," AIAA J., **33**, pp. 1888–1896.
[19] Forliti, D. J., Strykowski, P. J., and Debatin, K., 2000, "Bias and Precision Errors of Digital Particle Image Velocimetry," Exp. Fluids, **28**, pp. 436–447.
[20] Brown, G. L., and Roshko, A., 1974, "On Density Effects of Large Structures in Turbulent Mixing Layers," J. Fluid Mech., **64**, pp. 775–816.
[21] Etheridge, D. W., and Kemp, P. H., 1978, "Measurement of Turbulent Flow Downstream of a Rearward Facing Step," J. Fluid Mech., **86**, pp. 545–566.
[22] Wygnanski, I., and Fiedler, H. E., 1970, "The Two-Dimensional Mixing Region," J. Fluid Mech., **41**, pp. 327–361.
[23] Simpson, R. L., Chew, Y. T., and Shivaprasad, B. G., 1981, "The Structure of Separating Turbulent Boundary Layer Part 2. Higher-Order Turbulence Results," J. Fluid Mech., **113**, pp. 53–73.
[24] Cutler, A. D., and Johnston, J. P., 1989, "The Relaxation of a Turbulent Boundary Layer in an Adverse Pressure Gradient," J. Fluid Mech., **200**, pp. 367–387.
[25] Tachie, M. F., Balachandar, R., and Bergstrom, D. J., 2001, "Open Channel Boundary Layer Relaxation Behind a Forward Facing Step at Low Reynolds Numbers," J. Fluids Eng., **123**, pp. 539–544.

Downloaded 03 Jun 2010 to 171.66.16.157. Redistribution subject to ASME license or copyright; see http://www.asme.org/terms/Terms_Use.cfm

Numerical Simulation of 3D Cavitating Flows: Analysis of Cavitation Head Drop in Turbomachinery

Benoît Pouffary
Centre National d'Etudes Spatiales,
Evry, 91023 France

Regiane Fortes Patella
INPG-LEGI,
Grenoble, 38041 France

Jean-Luc Reboud
CNRS-G2ELAB,
University of Grenoble,
Grenoble, 38042 France

Pierre-Alain Lambert
Snecma,
Vernon, 27208 France

The numerical simulation of cavitating flows in turbomachinery is studied at the Turbomachinery and Cavitation team of Laboratoire des Ecoulements Géophysiques et Industriels (LEGI), Grenoble, France in collaboration with the French space agency (Centre National d'Etudes Spatiales, CNES), the rocket engine division of Snecma and Numeca International. A barotropic state law is proposed to model the cavitation phenomenon and this model has been integrated in the CFD code FINE/TURBO™. An analysis methodology allowing the numerical simulation of the head drop induced by the development of cavitation in cold water was proposed and applied in the case of two four-bladed inducers and one centrifugal pump. Global results were compared to available experimental results. Internal flows in turbomachinery were investigated in depth. Numerical simulations enabled the characterization of the mechanisms leading to the head drop and the visualization of the effects of the development of cavitation on internal flows.
[DOI: 10.1115/1.2917420]

1 Introduction

Cavitation is an important phenomenon for the design of rocket engine turbopumps and remains a major issue for the space industry. That is why the CNES and the Rocket Engine Division of Snecma have supported research in order to make progress in the understanding and prediction of the mechanisms associated with cavitation for many years. In this frame, one main purpose of the research performed at the Turbomachinery and Cavitation team of *Laboratoire des Ecoulements Géophysiques et Industriels* (LEGI) consists in developing and validating a 3D Reynolds-averaged Navier–Stokes (RANS) code, enabling the simulation of the cavitating operation of turbopumps. Through collaboration between LEGI and Numeca International, a physical model of cavitation was implemented in the commercial code FINE/TURBO™ [1–3].

The applied numerical model is very similar to the one proposed by Kunz et al. [4,5] to calculate cavitating flows in centrifugal pumps. The main difference between the present work and those studies is the physical model applied to describe the cavitation phenomenon. In this study, the barotropic cavitation model initially proposed by Delannoy and Kueny [6] is considered and presented in the first section of this paper.

The 3D RANS code, described in Sec. 3, allows the steady and unsteady cavitating flow calculations in the 2D or 3D geometries, as presented in Refs. [1–3,7], and could be used as a tool to analyze inducer instabilities [8].

In complement to previous work [1,7,9], the main target of the present study is to propose a qualitative and quantitative analysis of the cavitation head drop in turbomachinery. As a matter of fact, some recent numerical works have been developed to predict cavitation inception, cavity dimensions, and/or the threshold corresponding to pump head drops. For example, Ait-Bouziad et al. [10,11] applied off-the-shelf software to investigate cavitating flows in a three-bladed industrial inducer. The authors present interesting global and local analyses of the cavitating flow field, but they noticed that the absolute value of head drop was not well predicted by the numerical simulations. Mejri et al. [12] applied the same off-the-shelf software to analyze the overall performances, as well as the location and sizes of blade cavities for the three three-bladed inducers identified by different blade angles at the leading edge. A qualitative agreement between the experimental and predicted results was found for two inducers. The authors concluded that the implemented cavitation model overpredicted the cavitating flow, mainly in partial load conditions.

We cite also the important numerical work developed by Hosangadi and Ahuja [13] concerning cavitating flows over a hydrofoil and a cylindrical headform. In Ref. [14], Hosangadi et al. presented a good comparison between the simulated and experimental data concerning breaking down of a helical flat-plate inducer configuration in cold water.

In spite of those relevant works, more studies are needed to improve and validate simulated and physical approaches in order to obtain reliable quantitative predictions of overall performances, especially in the case of inducer geometries. Moreover, detailed cavitating flow analyses are also required for the better understanding of the head drop hydrodynamic mechanism and of energy transfers in centrifugal and axial pumps.

In this context, the developed numerical model has been applied to calculate 3D steady cavitating flows in a centrifugal pump and in two rocket engine turbopump inducers, whose geometries are described in Sec. 4. The influence of steady cavitation behavior on the pump characteristics and on the final head drops has been simulated and compared to experimental results for different operating points. The observations of the pump global performances and associated local flow fields led us to carry out a detailed analysis of the influence of cavitation in the three different geometries (Sec. 5). From these results, the origin of the cavitation head drop is discussed and an analysis of its mechanism is proposed. The study is improved by the investigation of the repartition of the total pressure rise, the blade loads, as well as by the evaluation of cavitation influence on secondary flows.

2 Barotropic State Law

The considered numerical approach uses a single fluid model to describe the liquid-vapor mixture, with a mixture density ρ varying in the flow field between the vapor density and the liquid

Contributed by the Fluids Engineering Division of ASME for publication in the JOURNAL OF FLUIDS ENGINEERING. Manuscript received September 8, 2005; final manuscript received March 12, 2008; published online May 19, 2008. Review conducted by Joseph Katz.

 Copyright © 2008 by ASME

Downloaded 03 Jun 2010 to 171.66.16.157. Redistribution subject to ASME license or copyright; see http://www.asme.org/terms/Terms_Use.cfm

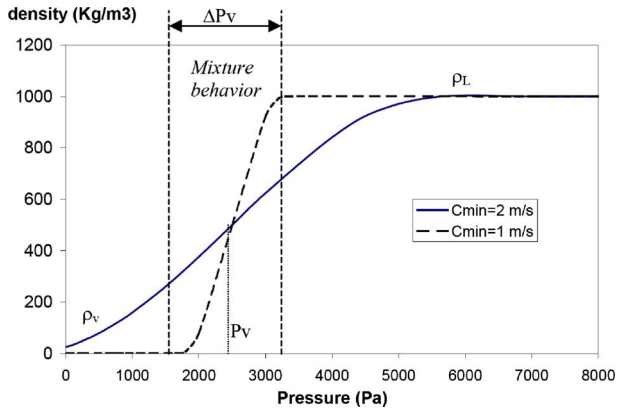

Fig. 1 Graph of the barotropic state law $\rho=\rho(P)$. Illustration of the speed of sound influence for water at 20°C. For more information, see Ref. [8].

density. The equivalent void ratio α of the liquid-vapor mixture relates to the varying specific mass by $\rho=\alpha\rho_v+(1-\alpha)\rho_l$. In the mixture, the velocities of liquid and vapor phases are the same and we obtain only one set of equations for the mixture mass, momentum, or turbulence (k-ε), written in their conservative form.

The void ratio α of the mixture depends on the local static pressure. As initially proposed by Delannoy and Kueny [6], we use a barotropic state law $\rho(P)$ to manage the relation between pressure and mixture density (Fig. 1). A smooth arbitrary law was chosen, ρ rapidly varying between liquid density ρ_l and vapor density ρ_v when the local static pressure P is around the vapor pressure P_v. The law is characterized by its maximum slope at $P=P_v$, which is related to the minimum speed of sound $c_{\min}$ in the two-phase homogeneous medium [8].

In the present work, based on experimental previous work concerning Venturi type sections (Stutz and Reboud [15,16]), the parameter $c_{\min}$ is taken equal to 2.35 m/s. The density ratio ρ_v/ρ_l is imposed to be 0.1. The compressibility of pure liquid and vapor phases is not taken into account. These choices were made to improve the robustness of the numerical code. Extensive numerical tests were carried out in other works to evaluate the influence of the speed of sound $c_{\min}$ and of the ratio ρ_v/ρ_l. Most important results obtained from these influence analyses are described in Refs. [17–19].

3 Numerical Model

The barotropic cavitation model was implemented in the commercial code FINE/TURBO™ developed by Numeca International. FINE/TURBO™ is a three-dimensional structured mesh code that solves the time dependent RANS equations, with artificial compressibility method. A detailed description of the initial code is given in Hakimi [20].

Time-accurate resolutions use the dual time stepping approach. Pseudotime derivative terms are added to the equations. They enable equation convergence at each physical time step. The initial set of mass and momentum equation can then be written under the following form:

$$\int\int\int_V \frac{\partial \mathbf{U}}{\partial \tau} dV + \frac{\partial}{\partial t}\int\int\int_V \mathbf{U} dV + \int\int_S \mathbf{F}\cdot\mathbf{dS} = \int\int\int_V ST dV \tag{1}$$

where

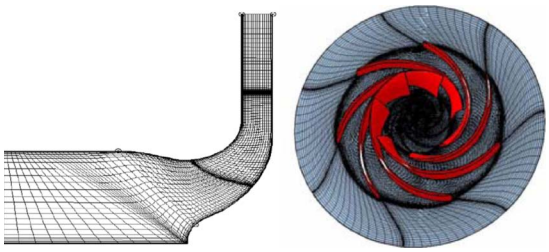

Fig. 2 Mesh of the SHF centrifugal pump

$$\mathbf{U} = \begin{pmatrix} \rho \\ \rho u \\ \rho v \\ \rho w \end{pmatrix}$$

is the vector of the conservative variables, $\mathbf{F}=\mathbf{F}_c-\mathbf{F}_v$ notes the convective and diffusive fluxes across the surface $\mathbf{dS}=\mathbf{n}\,dS$, ST is the source term, and τ the pseudotime.

The space discretization is based on a finite volume approach. A second order central scheme is associated with two artificial dissipation terms, respectively, of second and fourth orders. The first one is activated in the strong pressure and density gradient areas. The other one is used in the whole domain, and it results in a second order space accuracy.

In the case of low-compressible or incompressible flows, the pseudotime derivatives are multiplied by a preconditioning matrix, based on the studies of Turkel [21], Choi and Merkle [22]. The modifications of the preconditioning technique developed for cavitating flows are detailed in Refs. [2,23].

The pseudotime integration is made by a four-step Runge–Kutta procedure. In noncavitating conditions, the code resorts to a multigrid strategy to accelerate the convergence. The different computations presented hereafter have been performed in the steady case, without taking into account the real time derivative term.

A more detailed description of the code is given in Refs. [1–3]. A meaningful numerical work has been performed by Pouffary [23] to improve the preconditioner and the stability of numerical code for calculations of cavitating flows. It is worth noting that these numerical modifications led to major improvements in accuracy and numerical stability in comparison with our previous computations of cavitating flows in turbomachinery [7,9,24,25]. An illustration and quantification of these numerical improvements will be presented in Sec. 5.

4 Studied Geometries

Centrifugal Pump. The first considered geometry is the SHF centrifugal pump tested by Combes and Archer [26]. The SHF pump has a shrouded seven-bladed centrifugal impeller. The scale and the calculation configuration are chosen as close as possible to the experimental conditions to simplify comparisons in cavitating conditions. The outlet radius is 330 mm, the inlet pipe length is 200 mm, the rotation speed equals to 3000 rpm, and the nominal flow rate is 0.157 m^3/s. Grid resolution tests have been done in cavitation-free conditions. After comparing pump head and pressure distribution on the blade obtained with different multiblock structured meshes (I and H meshes with 170,000, 250,000 and 500,000 cells), an I mesh of 250,000 cells for one blade-to-blade channel was chosen (Fig. 2). Yang-Shih's k-ε turbulent model with extended wall functions is used [27].

Turbopump Inducers. To achieve high rotational speed and low inlet pressure, rocket engine pumps are equipped with an axial stage. Two different four-bladed inducers have been tested. Inducer 1 was designed by Snecma (Fig. 3(*a*)). The influence of

Downloaded 03 Jun 2010 to 171.66.16.157. Redistribution subject to ASME license or copyright; see http://www.asme.org/terms/Terms_Use.cfm

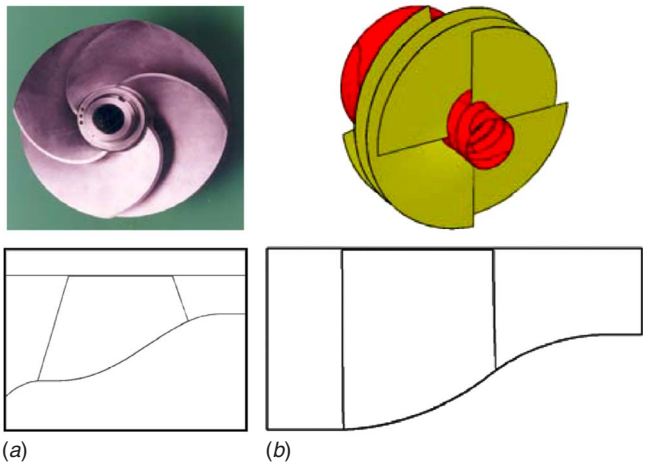

Fig. 3 Inducer geometries: (*a*) Inducer 1; (*b*) Inducer 2

the mesh and of the turbulence model (i.e., Baldwin–Lomax and three different k-ε models) was firstly studied in noncavitating conditions, mainly by comparing the static pressure profile at the shroud with experimental measurements performed at different flow rates at the CREMHyG Laboratory (Grenoble, France). An example at nominal flow rate is given on Fig. 4. From these comparisons, a mesh of about 500,000 cells for one blade-to-blade channel was chosen, associated with a k-ε model with wall functions [27]. Tip leakage was taken into account in noncavitating conditions, but to increase the numerical convergence speed, it was suppressed for the cavitating flow computations, by locally modifying the mesh. Analysis of the influence of the tip leakage on cavitating flows is in progress.

The geometry of Inducer 2 shows a pure radial leading edge shape (Fig. 3(*b*)) and has been experimentally studied at the University of Osaka [28]. The mesh has 250,000 cells for one blade-to-blade channel, and the tip leakage is not taken account of.

Simulation results presented in this paper for the three pump geometries are 3D and steady. Used meshes were chosen after a detailed study of mesh influence based on cavitation-free global performances of the inducer (head coefficient, torque, and efficiency).

5 Analysis of Cavitating Flows

Numerical Conditions. Steady calculations of cavitating and noncavitating flows were performed in these three geometries for different cavitation numbers.

In cavitation-free conditions, two sets of upstream and downstream boundary conditions have been compared in the case of Inducer 1 geometry: either the flow rate is imposed upstream and the static pressure downstream (with or without the radial equilibrium condition) or total pressure is imposed upstream and flow rate downstream. Influences of the rotation of hub and shroud boundaries upstream and downstream from the impeller have also been analyzed [23]. With a good convergence level of the computations, no major influences of the boundary conditions tested

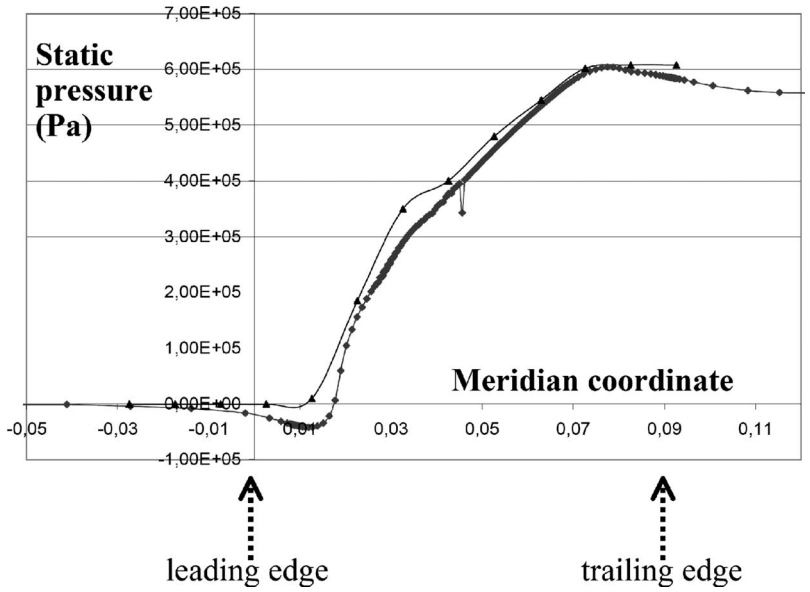

Fig. 4 Inducer 1 shroud static pressure at nominal flow rate (blue triangles, measurements; red rhombus, computation; k-ε+wall functions). Noncavitating condition. Meridian coordinate is nondimensional.

Downloaded 03 Jun 2010 to 171.66.16.157. Redistribution subject to ASME license or copyright; see http://www.asme.org/terms/Terms_Use.cfm

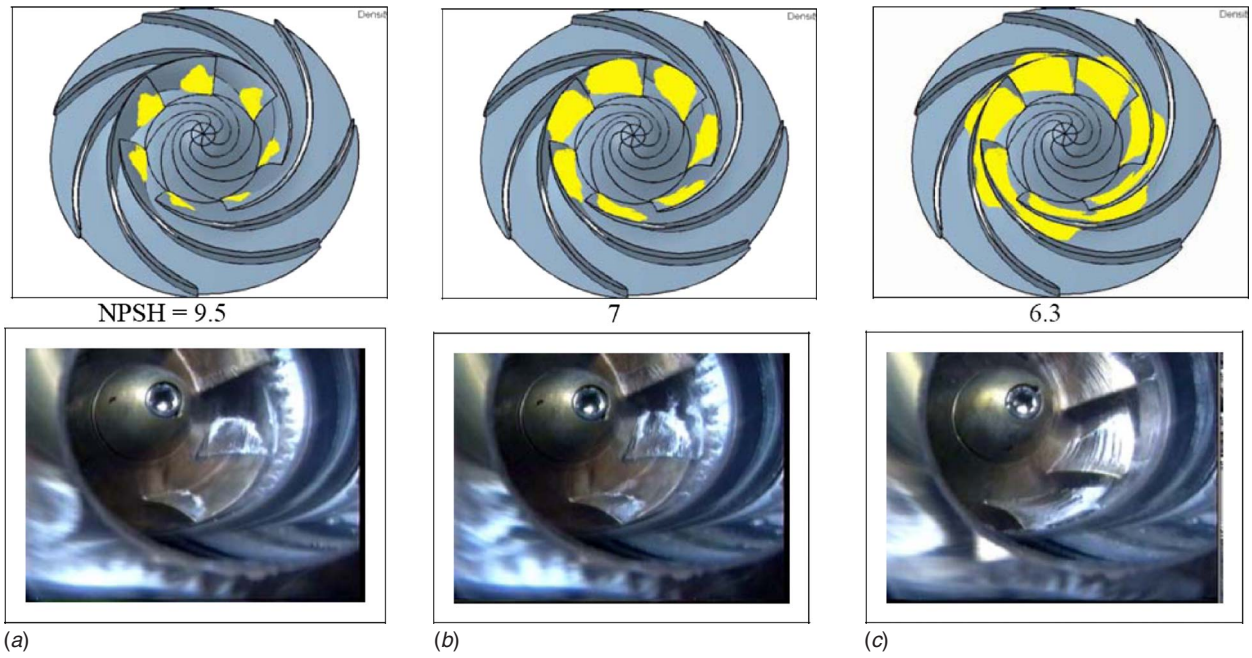

Fig. 5 SHF centrifugal pump, nominal flow rate, for decreasing NPSH=$(P_{ref}$-$P_v)/(\rho g)\approx$9.5 m, 7 m, and 6.3 m. The yellow color corresponds to a 5% equivalent void ratio. Comparison experiment/calculation of the suction side cavity extension. Experimental visualizations by Electricité de France [26].

were observed on the evaluation of global performances.

In cavitation conditions, the flow rate is imposed upstream and the static pressure downstream. The different analyzed cavitation numbers (or corresponding NPSH) are obtained by varying the pseudovapor pressure P_v involved in the definition of cavitation number σ, while the downstream pressure is kept constant.

It is worth noting that each calculated steady state solution was carefully converged. Convergence criteria of cavitating flow calculations were based on the comparisons between inlet and outlet mass-flow rates (allowed maximum error $<0.4\%$), on the analyses of the torque, the static and total heads obtained through numerical iterations (pseudotime integrations), and on the verification of the mass-flow rate through different sections inside the pumps, located in cavitating flow areas.

In relation to previous work [2], numerical modifications were performed by Pouffary [23], on the preconditioning technique and associated stability of the numerical algorithms, to deal with very large variations of compressibility of the liquid-vapor mixture in cavitating conditions. "Local velocity scaling" strategy was used for SHF pump calculations. For inducer computations, preconditioning coefficients were calculated as a function of the reference velocity U_{ref} and of the barotropic state law. These improvements allowed a very good convergence level, even in the cases of very large cavitation structures and associated strong modifications of the pump head. Indeed, operating points in cavitating regime leading to a 10% head drop or more could be accurately simulated in the three pump geometries considered in this paper.

Centrifugal Pump. For the SHF centrifugal pump, the cavitating behavior obtained at nominal flow rate *Qn* shows thin attached sheet cavities on the suction side of the impeller blades, their length increasing with the decreasing cavitation number (Fig. 5). Head begins to approximately drop when the cavitation sheet reaches the throat between two adjacent blades and rapidly decreases by more than 10% of its noncavitating value (Fig. 6). The simulated prediction of head breakdown is found for the critical NPSH close to 6.3 m, which corresponds to the $NPSH_{3\%}$ experimentally found at Electricité de France [26]. Flow rates superior to the nominal flow rate lead to larger critical NPSH, head breakdown being observed at 1.22*Qn* and 1.3*Qn* for NPSH values, respectively, of about 18 m and 26 m.

Simulation results obtained at nominal flow rate were analyzed in detail. It can be seen on Fig. 7 that the head drop can be mainly associated with a decrease of the torque (at the NPSH with 7% total head decrease, the calculated torque decreases by about 5% and the efficiency by 2%).

The torque decrease can be illustrated by Fig. 8, where the static pressure distributions around a blade section at midspan are drawn for different NPSH values. When the net pressure P_{ref}-P_v becomes smaller, a long sheet cavity develops along the blade suction side, reducing the suction effect near the blade leading edge, without significantly modifying the pressure distribution along the wetted surfaces, and thus clearly reducing the blade load. At head breakdown, it can be observed that cavitation also appears on the upstream part of the blade pressure side (NPSH $\sim$6.3). Such observations can also be made along other sections of the pump blades.

To study the energy transfers within the pump, an analysis of

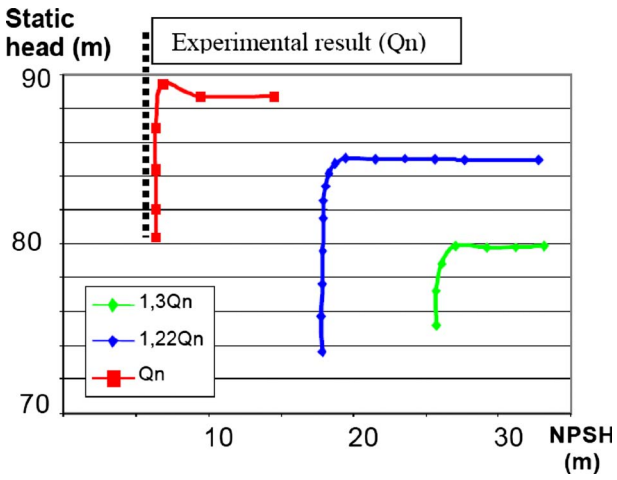

Fig. 6 Cavitation head drop curves at different flow rates

Downloaded 03 Jun 2010 to 171.66.16.157. Redistribution subject to ASME license or copyright; see http://www.asme.org/terms/Terms_Use.cfm

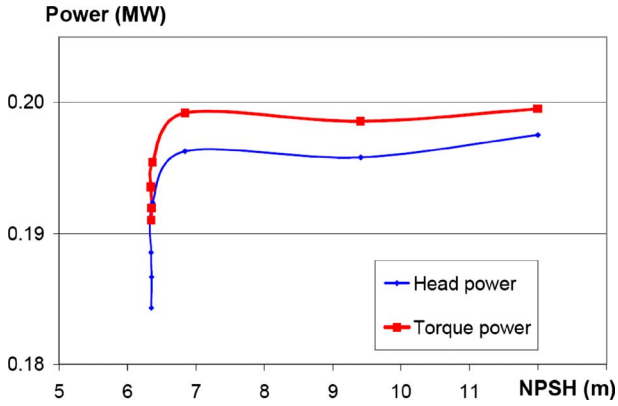

Fig. 7 Nominal flow rate. Evolution of mechanical and hydraulic power calculated; mechanical power $= T\omega$ **hydraulic power** $= \Delta P_{tot}.Q$.

the flow has been performed in eight different flow sections, from Cut I near the blade leading edge to Cut VIII near the trailing edge (Fig. 9). First of all, the mass-flow averaged total pressure rise between successive sections is drawn. One can clearly see on Fig. 10 that the total pressure breakdown principally occurs in the upstream Sections I–III, while the downstream ones (IV–VIII) approximately remain unaffected by the development of cavitation. During the beginning of the head drop (Calculations 1 and 2), the total pressure rise between Cuts I and III increases, leading to the rise of global performance observed in Fig. 6 for these NPSH values. This phenomenon seems to be related to an incidence effect: The meridional flow velocity decreases due to the blockage effect of cavitation and this leads to a local rise of the effective angle of attack.

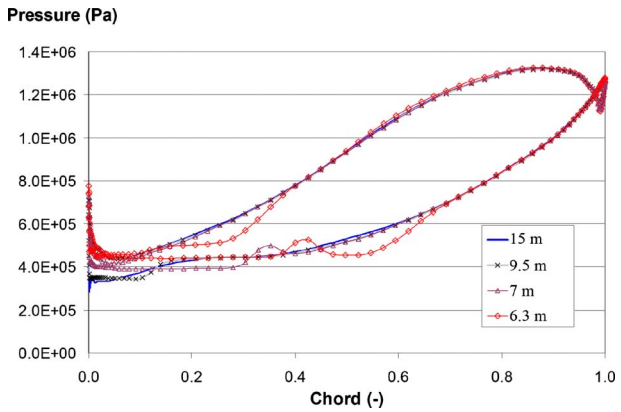

Fig. 8 Nominal flow rate. Blade load at midspan, for decreasing NPSH ≈15 m, 9.5 m, 7 m, and 6.3 m (with about 7% total head drop).

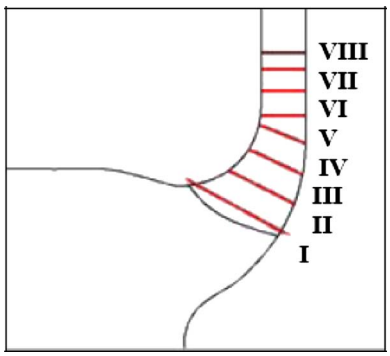

Fig. 9 Location of the analyzed flow sections in the SHF pump

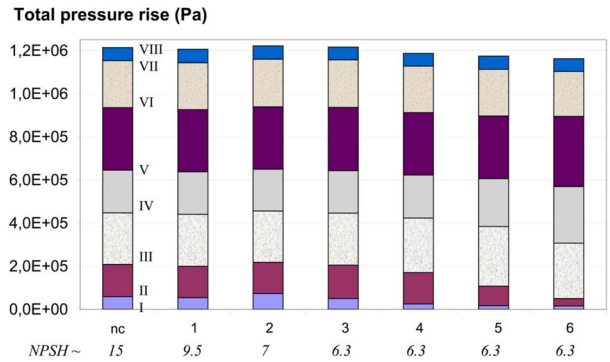

Fig. 10 Repartition of the total pressure rise between Sections 1 and VIII of the SHF pump, in noncavitating conditions (nc: left) and with decreasing downstream cavitation numbers (1–6). Total pressures are evaluated by mass-flow averaging in the cut plane. As the NPSH is calculated a posteriori from the upstream pressure resulting from the cavitating flow simulation, it takes into account the decreasing pump head associated with cavitation breakdown. The last four NPSH values, during final head drop, are found nearly constant, whereas the net downstream pressure continues to be decreased.

If one observes the meridian repartition of the total pressure rise corresponding to Calculations 3–6, one can note also, downstream of the cavitation sheet, an augmentation of the total pressure rise. This phenomenon of compensation is mainly observed between Cuts IV and VI.

For a better understanding, a local analysis of the influence of cavitation on the flow structure in the different sections has been also performed. In the present paper, the analysis of the secondary flows is based on the dimensionless relative helicity, drawn for the four upstream sections (I–IV): Fig. 11(*a*) illustrates the results concerning cavitation-free condition and Fig. 11(*b*) corresponds to a regime close to the cavitation breakdown. The blue colors represent the anticlockwise vorticity and the yellow to red ones indicate the clockwise vorticity. In noncavitating conditions, one can observe that the secondary flows in the rotating frame mainly develop along the blade suction side (blue color), progressively evolving to a hub vortex (Section IV). Clockwise vorticity (red color) can also be observed along the shroud.

In cavitating conditions (Fig. 11(*b*)), secondary flows are strongly modified along the cavitation sheet surface: in Section I, at the suction side, one observes a well organized structure of clockwise vorticity corresponding to the region of the cavitation sheet. In Section II, this structure disappears. The cavity wake generates a large anticlockwise structure, which seems to be related to the centrifugation of the cavity wake. In Sections III and IV, these vorticity structures due to the presence of the cavity sheet progressively dissipate.

Inducer 1. An analogous analysis has been performed for the Inducer I geometry. Development of cavitation structures starts from the blade tip and rapidly extends along the leading edge to the hub side. Then the cavitation sheet length progressively increases until it reaches the throat (Fig. 12). The head drop abruptly occurs when the cavity enters into the blade-to-blade channel.

Comparison of the simulated cavitation performance chart with experiments performed at the CREMHyG Laboratory is drawn on Fig. 13. For a high cavitation number, the obtained simulated value is found about 5% higher than the experimental inducer head, which can be mainly attributed to the fact that the tip leakage flow is not taken into account by numerical calculations. Successive cavitating flows were computed and a good convergence

Downloaded 03 Jun 2010 to 171.66.16.157. Redistribution subject to ASME license or copyright; see http://www.asme.org/terms/Terms_Use.cfm

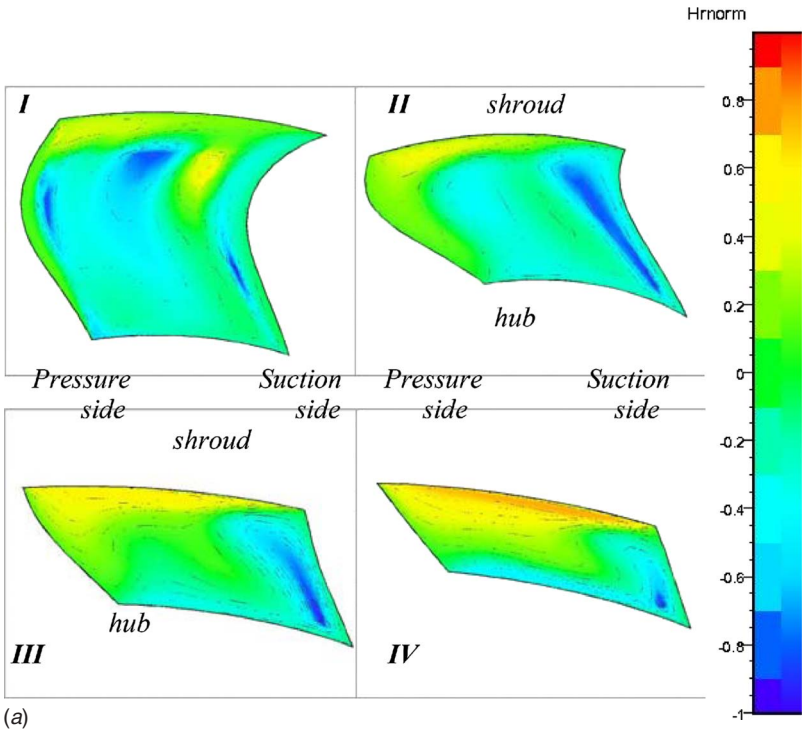

(*a*)

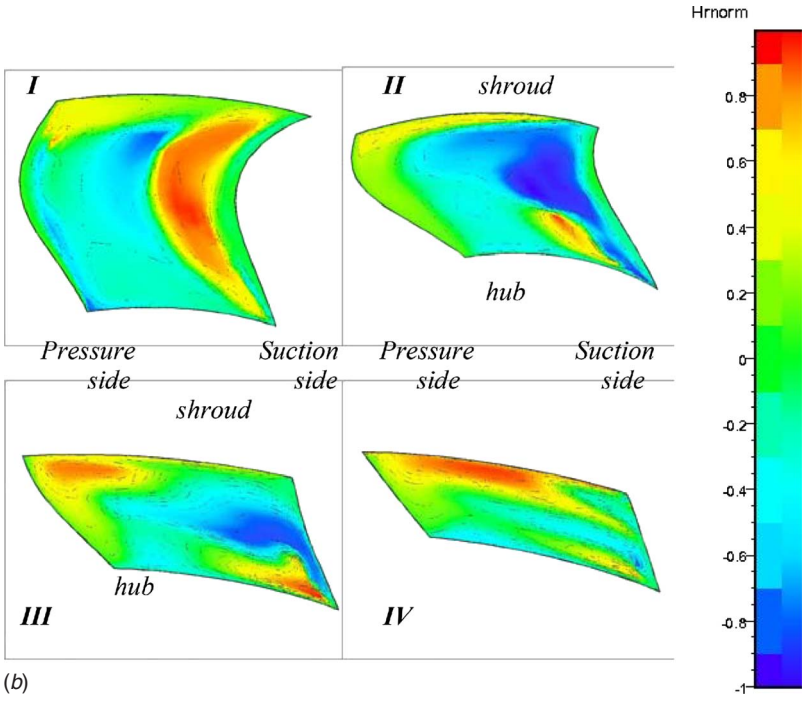

(*b*)

Fig. 11 (*a*) **Secondary flows: Dimensionless relative helicity, varying from –1 (blue, maximum anticlockwise vorticity) to 1 (red, maximum clockwise vorticity). Noncavitating flow. Planes I to IV.** (*b*) **Secondary flows (dimensionless relative helicity). Cavitating flow corresponding to 7% total head decrease. Planes I to IV.**

could be obtained even with more than 10% head loss. The critical cavitation number is very well predicted (Fig. 13) and the improvement of this prediction is significant with respect to the preceding code version [29].

According to the analyses done, detailed in Ref. [23], the inducer head drop seems to be mainly associated with a drop of the torque: For the critical cavitation number, the calculated torque decreases by about 10% of the noncavitating value, while hydraulic efficiency decreases by about 3%.

Static pressure distributions around the blade are drawn on Fig. 14 in noncavitating and strongly cavitating conditions: The blade load decrease is mainly due to the modification of the pressure

Downloaded 03 Jun 2010 to 171.66.16.157. Redistribution subject to ASME license or copyright; see http://www.asme.org/terms/Terms_Use.cfm

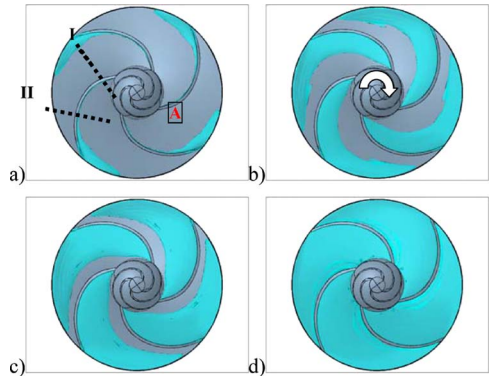

Fig. 12 Inducer 1, nominal flow rate, for decreasing cavitation number. The blue color corresponds to a 5% equivalent void ratio. Upstream cavitation numbers: (*a*) 0.0196; (*b*) 0.016; (*c*) 0.014; (*d*) 0.012.

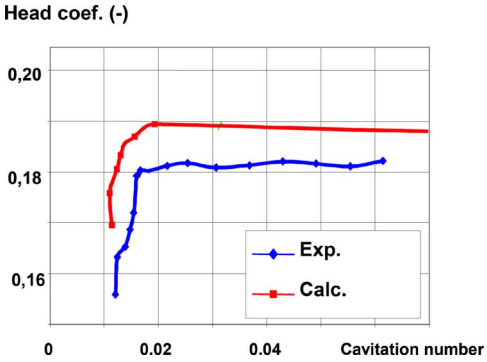

Fig. 13 Cavitation head drop curves at nominal flow rates. Comparisons between computations and experiments performed at the CREMHyG Laboratory (upstream cavitation number).

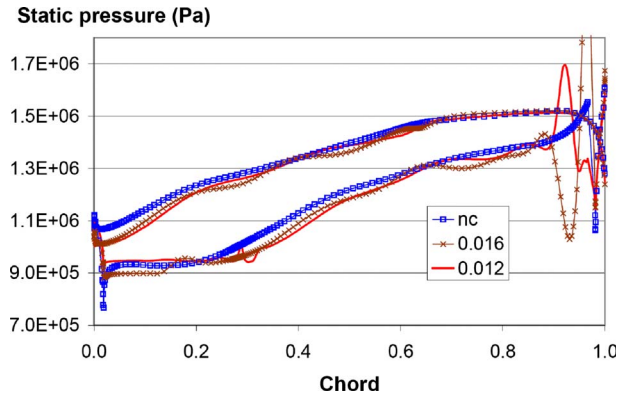

Fig. 14 Nominal flow rate. Inducer 1. Blade load at midspan, for decreasing cavitation numbers.

side distribution near the leading edge. The load reduction is observed when the cavitation sheet developed on the upstream blade suction side reaches the entry of the blade-to-blade channel. Perturbations of the trailing edge pressure distribution can also be observed. These perturbations can be associated with noticeable modifications of secondary flows, as will be discussed hereafter.

The mass-flow averaged total pressure rise between successive sections in Inducer 1 is drawn on Fig. 15. Analyzed sections are perpendicular to axial direction, as schematized in Fig. 21 for the Inducer 2 geometry. One can observe that the head decrease is mainly caused by the decrease in the upstream region.

The secondary flows in cut Sections I and II (presented in Fig. 12) are analyzed in Fig. 16. In noncavitating condition, an intense anticlockwise vorticity structure near the shroud is observed, which seems to be mainly due to the kinetic energy of the tip leakage flow. Another anticlockwise vorticity structure is observed near the suction side and a clockwise one is present close to the pressure side; both structures are related to the centrifugation of the boundary layer along the blades. There is no relevant vorticity effect in the middle of the analyzed sections.

In cavitating conditions (Fig. 16(*b*)), near the head breakdown, the secondary flow in Section I is slightly modified. On the other

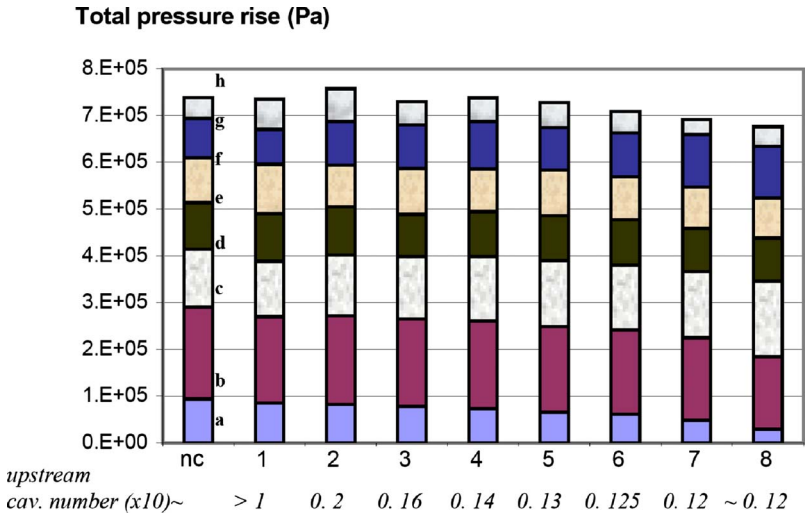

Fig. 15 Repartition of the total pressure rise between Sections "a" and "h" of Inducer 1, in noncavitating conditions (nc: left) and with decreasing downstream cavitation numbers (1–8). Total pressures are evaluated by mass-flow averaging in the cut plane. Sections "a"–"h" are perpendicular to the axial direction, as schematized in Fig. 21 for the Inducer 2 geometry. As in Fig. 10, the last two upstream cavitation number values are found nearly constant for decreasing values of the downstream cavitation number.

Downloaded 03 Jun 2010 to 171.66.16.157. Redistribution subject to ASME license or copyright; see http://www.asme.org/terms/Terms_Use.cfm

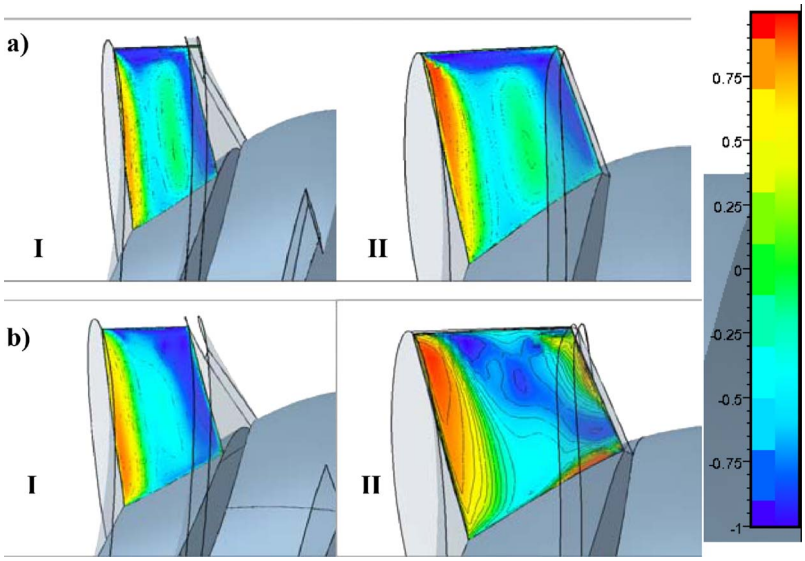

Fig. 16 Secondary flows (dimensionless relative helicity), and noncavitating (*a*) and cavitating (*b*) flows. Planes I and II.

hand, the outlet flow is highly influenced by the important cavity wake structure. This can be seen in Section II: the clockwise vorticity structure observed near the pressure side is amplified; the vorticity structure close to the suction side is convected through the middle of the section; a small secondary structure appears near the hub. Figure 16 shows that the downstream flow is highly influenced by the cavitation development: Increasing vorticity observed near the pressure side (left part of Plane II in Fig. 16(*b*)) interacts with the suction side in the trailing edge region of the inducer (right part of Plane II), and seems to lead to pressure distribution perturbations observed in Fig. 14 in this zone.

It is worth reminding that calculations performed under cavitating conditions do not take into account tip leakage. It is the reason why intense anticlockwise vorticity structure observed near the shroud in noncavitation condition (Fig. 16(*a*)) does not appear on Fig. 16(*b*). Improvements of methodology for tip leakage meshing, in association with multigrid strategy to accelerate the convergence of cavitating flow calculations, are needed to progress on secondary flow analyses and on the evaluation of the tip clearance effect for cavitating cases. Such improvements are still in progress.

Inducer 2. The second analyzed inducer geometry shows a quite different behavior in cavitating conditions. According to our numerical study, as illustrated by Fig. 17, the development of the cavitation structures appears much more pronounced at the inducer periphery. We can observe also a large backflow structure in front of the blades. On the blade suction side, the cavitation sheets show a triangular shape, increasing from hub to periphery, and merging with the cavitating backflow structure.

On the performance chart, illustrated by Fig. 18, the head drop much more gradually appears than for Inducer 1. The last point calculated shows a 20% head drop, mainly due to the drop of the torque. The efficiency decreases by about 3%.

The fact that the cavitation head drop is less abrupt can be explained by analyzing the blade load evolution drawn on Fig. 19, and comparing it to Fig. 14. In noncavitating condition, the blade loads of the two inducers appear very different: Inducer 2 blades are mainly loaded near the leading edge, while the load remains approximately constant along the Inducer 1 blades. In cavitating regime, the development of the sheet cavity from the leading edge of the Inducer 2 blade suction side gradually modifies the blade load, while in Inducer 1, the blade load decreases only when the cavity closure reaches the blade-to-blade passage.

It can be clearly seen on Fig. 20 that the main part of the total pressure rise in Inducer 2 is provided by the upstream part of the inducer. As a consequence, cavitation head drop mainly occurs due to a progressive decrease of the pressure rise between Sections I and II. The blade load at the downstream part of the inducer is not very significant and a compensation phenomenon cannot appear with this inducer design.

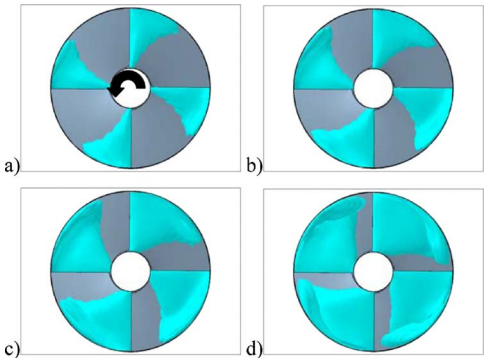

Fig. 17 Inducer 2, nominal flow rate, for decreasing upstream cavitation numbers: (*a*) 0.12; (*b*) 0.08; (*c*) 0.05; (*d*) 0.03. The blue color corresponds to a 5% equivalent void ratio.

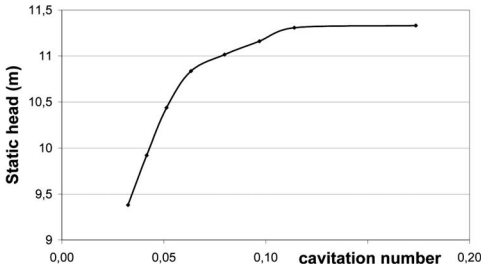

Fig. 18 Cavitation head drop curve. Nominal flow rate, Inducer 2.

Downloaded 03 Jun 2010 to 171.66.16.157. Redistribution subject to ASME license or copyright; see http://www.asme.org/terms/Terms_Use.cfm

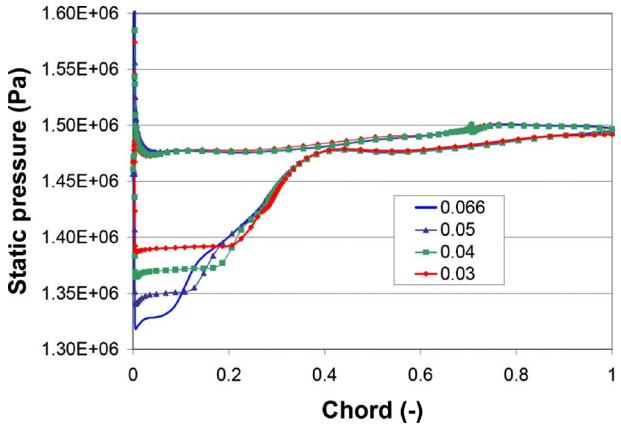

Fig. 19 Nominal flow rate. Inducer 2. Blade load at mid span, for decreasing cavitation numbers.

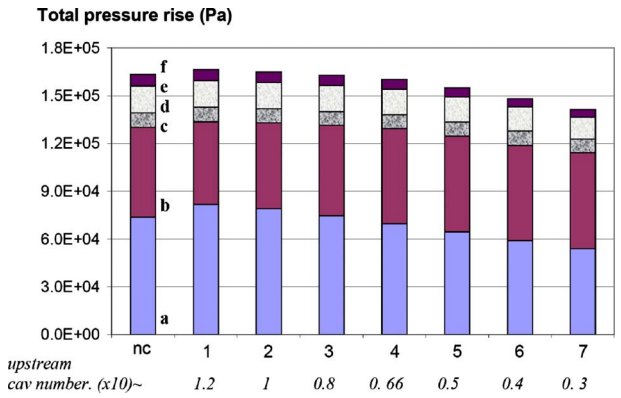

Fig. 20 Repartition of the total pressure rise between Sections "a"–"f" of Inducer 2, in noncavitating condition (nc: left) and with decreasing downstream cavitation numbers (1–7). Total pressures are evaluated by mass-flow averaging in the cut plane. Sections "a"–"f" locations are presented in Fig. 21.

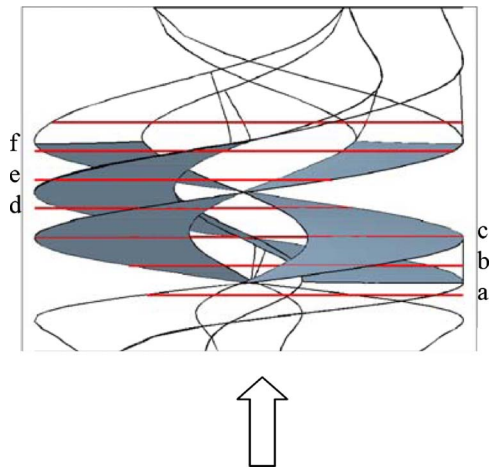

Fig. 21 Illustration of Planes "a"–"f" in the meridian view of Inducer 2

6 Conclusion

A numerical model of 3D cavitating flows has been developed to predict the cavitation behavior in turbomachinery. Compared to the previous studies [7,9,24,25], thanks to recent improvements of numerical stability and algorithm reliability, very good convergence and accuracy of the simulation of cavitating flows in turbomachinery can now be obtained, even for operating conditions very close to the machine head drop (Fig. 13).

Simulation results were presented and analyzed for a centrifugal pump and two different four-bladed inducers. Noncavitating and cavitating conditions were investigated and compared. The vapor structure extensions and associated pump head breakdowns seem to be correctly simulated by the numerical model and favorably compare with available experimental results.

Local analyses of the results provide interesting information on the breakdown mechanisms.

- In the three geometries, head breakdown is clearly associated with a decrease of the torque provided by the impeller, through a strong variation of the blade load. Otherwise, only a small decrease of the machine efficiency can be associated with the development of the cavitation structures.
- An important difference between the cavitation behaviors of the two inducers can be observed, which can be explained by an analysis of their respective blade load and total pressure rise repartition.
- Local visualizations of the flow fields and their evolution with cavitation can also be obtained. For example, the analysis of dimensionless relative helicity maps gives useful information about secondary flows in the machines and enables the identification of the location and influence of the cavity wakes in the blade-to-blade channels.

The methodology of analysis proposed in the present paper shows that numerical simulation can provide useful information for the design of turbomachinery, and more particularly of inducers. Applications performed on unsteady flows are in progress and the first results presented in Refs. [8,17] are very promising for the analysis and prediction of unstable cavitation behavior in turbomachinery.

Improvements of the cavitation model are also in development, mainly to take into account the thermodynamic behavior of fluids, such as hydrocarbons or cryogenic propellants.

Acknowledgment

This research was supported by the French space agency *Centre National d'Etudes Spatiales* (CNES) and Snecma. The authors wish also to express their gratitude to *Electricité de France* and CREMHyG for providing experimental results, to Professor Tsujimoto for providing the Inducer 2 geometry, and to Numeca International for its cooperation to the development of the numerical code.

Nomenclature

c_{min} = minimum speed of sound in the medium (m/s)

$Hr_{norm} = \dfrac{\mathbf{W} \cdot \mathbf{rot}(\mathbf{W})}{\|\mathbf{W}\| \cdot \|\mathbf{rot}(\mathbf{W})\|}$ = dimensionless relative helicity

L_{ref} = geometry reference length (m)

P_{ref} = reference pressure=total upstream pressure (Pa)

$P_{up}(P_{dw})$ = static upstream (downstream) pressure (Pa)

P_v = vapor pressure (Pa)

Q = flow rate (m^3/s)

t = physical time (s)

T = torque (N m)

u, v, w = velocity components (m/s)

U_{ref} = reference velocity (generally U_{blade_tip}) (m/s)

$\mathbf{W}$ = relative velocity vector (rotating frame) (m/s)

α = void ratio

Downloaded 03 Jun 2010 to 171.66.16.157. Redistribution subject to ASME license or copyright; see http://www.asme.org/terms/Terms_Use.cfm

ΔP_{tot} = total pressure rise in the pump (Pa)

$\rho = \alpha\rho_v + (1-\alpha)\rho_l$ = mixture density (kg/m^3)

$\rho_l (=\rho_{ref})$, ρ_v = liquid (=ref), vapor density (kg/m^3)

$\sigma_{up} = (P_{up} - P_v)/(\rho V_{ref}^2/2)$ = upstream cavitation number

$\sigma_{dw} = (P_{dw} - P_v)/(\rho V_{ref}^2/2)$ = downstream cavitation number

ω = pump rotation speed (rad/s)

NPSH = Net pressure suction head $(P_{ref} - P_v)/(\rho g)$ (m)

τ = pseudotime (s)

References

[1] Coutier-Delgosha, O., Fortes-Patella, R., Reboud, J. L., Hakimi, N., and Hirsch, C., 2005, "Numerical Simulation of Cavitating Flow in 2D and 3D Inducer Geometries," Int. J. Numer. Methods Fluids, **48**(2), pp. 135–167.

[2] Coutier-Delgosha, O., Fortes-Patella, R., Reboud, J. L., Hakimi, N., and Hirsch, C., 2005, "Stability of Preconditioned Navier–Stokes Equations Associated With a Cavitation Model," Comput. Fluids, **34**(3), pp. 319–349.

[3] Pouffary, B., Fortes-Patella, R., and Reboud, J. L., 2003, "Numerical Simulation of Cavitating Flow Around a 2D Hydrofoil: A Barotropic Approach," *Fifth International Symposium on Cavitation*, Osaka, Japan.

[4] Kunz, R. F., Boger, D. A., Stinebring, D. R., Chyczewski, T. S., Lindau, J. W., and Gibeling, H. J., 2000, "A Preconditioned Navier–Stokes Method for Two-Phase Flows With Application to Cavitation," Comput. Fluids, **29**(8), pp. 849–875.

[5] Medvitz, R. B., Kunz, R. F., Boger, D. A., Lindau, J. W., Yocum, A. M., and Pauley, L. L., 2001, "Performance Analysis of Cavitating Flow in Centrifugal Pumps Using Multiphase CFD," *ASME-FEDSM '01*, New Orleans.

[6] Delannoy, Y., and Kueny, J. L., 1990, "Two Phase Flow Approach in Unsteady Cavitation Modelling," *Cavitation and Multiphase Flow Forum, ASME-FED*, Vol. 98, pp. 153–158.

[7] Coutier-Delgosha, O., Fortes-Patella, R., Reboud, J. L., Hofmann, M., and Stoffel, B., 2003, "Experimental and Numerical Studies in a Centrifugal Pump With 2D-Curved Blades in Cavitating Conditions," ASME J. Fluids Eng., **125**(6), pp. 970–978.

[8] Pouffary, B., Fortes-Patella, R., Reboud, J. L., and Lambert, P. A., 2008, "Numerical Analysis of Cavitation Instabilities in Inducer Blade Cascade," ASME J. Fluids Eng., **130**, p. 041302.

[9] Coutier-Delgosha, O., Morel, P., Fortes-Patella, R., and Reboud, J. L., 2005, "Numerical Simulation of Turbopump Inducer Cavitating Behavior," Int. J. Rotating Mach., **2**, pp. 135–142.

[10] Ait-Bouziad, Y., Farhat, M., Guennoun, F., Kueny, J. L., Avellan, F., and Miyagawa, K., 2003, "Physical Modelling and Simulation of Leading Edge Cavitation, Application to an Industrial Inducer," *Fifth International Symposium on Cavitation*, Osaka, Japan.

[11] Ait-Bouziad, Y., Farhat, M., Kueny, J. L., Avellan, F., and Miyagawa, K., 2004, "Experimental and Numerical Cavitation Flow Analysis of an Industrial Inducer," *22th IARH Symposium on Hydraulic Machinery and Systems*, Stockholm, Sweden.

[12] Mejri, I., Bakir, F., Rey, R., and Belamri, T., 2006, "Comparison of Computational Results Obtained From a Homogeneus Cavitation Model With Experimental Investigations of Three Inducers," ASME J. Fluids Eng., **128**, pp. 1308–1323.

[13] Hosangadi, A., and Ahuja, V., 2001, "Simulations of Cavitating Flows Using Hybrid Unstructured Meshes," ASME J. Fluids Eng., **123**, pp. 331–340.

[14] Hosangadi, A., Ahuja, V., and Ungewitter, R. J., 2006, "Numerical Study of a Flat Plate Inducer: Comparison of Performance in Liquid Hydrogen and Water," *Sixth International Symposium on Cavitation, CAV2006*, Wageningen, The Netherlands, September.

[15] Stutz, B., and Reboud, J. L., 1997, "Two-Phase Flow Structure of Sheet Cavitation," Phys. Fluids, **9**(12), pp. 3678–3686.

[16] Stutz, B., and Reboud, J. L., 2000, "Measurements Within Unsteady Cavitation," Exp. Fluids, **29**, pp. 545–552.

[17] Fortes-Patella, R., Coutier-Delgosha, O., Perrin, J., and Reboud, J. L., 2007, "A Numerical Model to Predict Unsteady Cavitating Flow Behaviour in Inducer Blade Cascades," ASME J. Fluids Eng., **129**, pp. 128–135.

[18] Rolland, J., Boitel, G., Barre, S., and Fortes-Patella, R., 2006, "Experiments and Modelling of Cavitating Flows in Venturi, Part I.: Stable Cavitation," *Sixth International Symposium on Cavitation, CAV2006*, Wageningen, The Netherlands, September.

[19] Fortes-Patella, R., Barre, S., and Reboud, J.-L., 2006, "Experiments and Modelling of Cavitating Flows in Venturi, Part II: Unsteady Cavitation," *Sixth International Symposium on Cavitation, CAV2006*, Wageningen, The Netherlands, September.

[20] Hakimi, N., 1997, "Preconditioning Methods for Time Dependent Navier–Stokes Equations," Ph.D. thesis, Vrije University, Brussels.

[21] Turkel, E., 1987, "Preconditioning Methods for Solving the Incompressible and Low Speed Compressible Equations," J. Comput. Phys., **72**, pp. 277–298.

[22] Choi, D., and Merkle, C. L., 1993, "The Application of Preconditioning in Viscous Flows," J. Comput. Phys., **105**, pp. 207–223.

[23] Pouffary, B., 2004, "Simulation Numérique D'écoulements 2d/3d Cavitants, Stationnaires et Instationnaires: Analyse Spécifique Pour Les Turbomachines," Ph.D. thesis, Grenoble, France.

[24] Coutier-Delgosha, O., Pouffary, B., Fortes-Patella, R., Reboud, J. L., Archer, A., and Combes, J.-F., 2002, "Cavitation Performance of a Centrifugal Pump: Numerical and Experimental Investigations," *21st IAHR Symposium on Hydraulic Machinery and Systems*, Lausanne, September.

[25] Pouffary, B., Coutier-Delgosha, O., Fortes-Patella, R., Reboud, J. L., Laffite, S., and Nguyen Duc, J.-M., 2002, "Evaluation of the Effects of Cavitation on the Flow in a Centrifugal Pump: Analysis of the Breakdown Mechanisms," *21st IAHR Symposium on Hydraulic Machinery and Systems*, Lausanne, September.

[26] Combes, J. F., and Archer, A., 2000, "Etude de la cavitation dans la pompe SHF," *Coll. Machines Hydrauliques: Instationnarités et Effets Associés*, Société Hydrotechnique de France, Chatou, France.

[27] Hakimi, N., Hirsch, C., and Pierret, S., 2000, "Presentation and Application of a New Extended k-ε Model With Wall Functions," *ECCOMAS*, Barcelona, September.

[28] Yoshida, Y., Tsujimoto, Y., Kataoka, D., Horiguchi, H., and Wahl, F., 2001, "Effects of Alternate Leading Edge Cutback on Unsteady Cavitation in 4-Bladed Inducers," ASME J. Fluids Eng., **123**, pp. 762–770.

[29] Coutier-Delgosha, O., 2001, "Modélisation des écoulements cavitants: Etude des comportements instationnaires et application aux turbomachines," Ph.D. thesis, Grenoble, France.

Downloaded 03 Jun 2010 to 171.66.16.157. Redistribution subject to ASME license or copyright; see http://www.asme.org/terms/Terms_Use.cfm

A Runback Criterion for Water Drops in a Turbulent Accelerated Boundary Layer

Edward B. White

Jason A. Schmucker

Department of Aerospace Engineering,
Texas A&M University,
College Station, TX 77840

Predicting the runback threshold for liquid drops in aerodynamic boundary layers is a challenging problem with numerous applications including aircraft icing simulations. The critical parameters that govern drop runback are investigated in this experiment by using a wind tunnel that provides a turbulent accelerated flow similar to flows near an unswept wing's leading edge. The experiments feature water drops on aluminum with a contact angle of 70 ± 5 deg. Results show that significant water/air interface unsteadiness precedes drop runback. This is likely due to air-flow separation in the drop wakes. For displacement-thickness-scaled Reynolds numbers ranging from 348 to 429, a constant-Weber-number runback threshold We = 3.45 ± 0.09 is found to adequately correlate the runback results. [DOI: 10.1115/1.2917429]

Keywords: drop, runback, boundary layer

1 Introduction

When a liquid drop rests on an aerodynamic surface such as a wing, aerodynamic forces act to drive the drop downstream while surface tension and contact angle hysteresis act to keep the drop fixed at its original position. Whether or not a drop runs back depends on numerous factors such as its size, the air speed, the boundary-layer thickness, and surface roughness. Predicting a drop's behavior is difficult, particularly for large drops in high-Reynolds number boundary layers in which the flow is likely to be separated in the drop's wake. Shear stress also provides a downstream force but is less important than pressure at high Reynolds numbers.

Despite the difficulty, predicting whether a drop remains static or runs back has numerous important applications, notably for aircraft icing predictions. Icing prediction codes such as LEWICE [1] attempt to simulate the entire aircraft-icing process from the Lagrangian motion of water drops in the freestream, to the collection and movement of liquid water on the surface, to freezing and ice growth [2]. To do this successfully, the simulations must include accurate but computationally tractable models for liquid water motion on the surface. An early model by Messinger [3] assumes that liquid surface water runs back as a uniform film and this approach remains in use in modern engineering calculations [1]. However, experiments by Olsen and Walker [4] in the mid-1980s demonstrated that much of the liquid surface water exists as static drops near the stagnation line. Eventually, drops do run downstream once they grow sufficiently large and aerodynamic forcing overcomes the forces that keep the drops affixed to a point on the surface. These observations lead Olsen and Walker to conclude that the uniform-film model used in icing prediction codes must be modified to reflect actual icing behavior [4].

Critical conditions for drop runback have been predicted by using a variety of approaches. Kirchner [5] developed a phenomenological model that balances a presumed aerodynamic force against a correlation-based resisting force [6]. Dussan [7] and Myers et al. [8] used asymptotic models in the small-drop, lubrication-theory regime. Rothmayer and Tsao [9] used an asymptotic approach in the small-drop regime and also considered larger drops that generate separated wakes. Dimitrakopoulos and Higdon [10] used a Stokes-flow simulation for large drops with arbitrary contact angles in low-Reynolds number shear flow. However, none of these approaches are satisfactory as practical engineering calculations, especially for design-related parameter studies. As increased computational power becomes available, higher Reynolds number and higher fidelity models may become practical. However, for now, experimental correlations remain necessary for predicting runback behavior.

Working from this perspective, the objective of the current study is to gain an engineering-level understanding of the water-drop runback threshold on a smooth aluminum surface in an accelerated turbulent boundary layer. The flow field is representative of boundary layers near the leading edge of unswept wings where most ice accretion occurs. Although the experiments are inspired by the icing problem, they are not intended to be directly applicable to icing simulations. Instead, the broad objectives are to develop experience that will enable future experiments on ice substrates and also to provide experimental data against which emerging runback simulations may be compared.

2 Experimental Facility and Boundary-Layer Flow Measurements

The experiments were conducted in the NASA Glenn Icing Physics Flow Laboratory (the Flow Lab) while it was located at Case Western Reserve University. This facility is a vertical wind tunnel designed to produce boundary-layer air flows characteristic of an unswept wing's leading edge. The Flow Lab's main feature is a horizontal, aluminum flat plate that measures 1524 × 762 mm^2. The test surface is polished to a near-mirror finish. Air impinges on the test plate from above and flows across its two sides in a symmetric fashion. Curved walls above the plate are designed to enforce an inviscid 2D stagnation-point flow field in which the flow accelerates away from the symmetry line. Figure 1 is a schematic of this layout. Flat acrylic walls (parallel to the plane of the page) allow optical access to the test section. Above the test section are multiple flow conditioners that reduce the freestream turbulence intensity of the incoming flow. Flow through the facility is driven by a centrifugal fan located downstream of the test section. The maximum velocity at the test section exit planes ($x = \pm 762$ mm) is about 24 m/s. Further details on the facility's design are given in Refs. [11,12].

Contributed by the Fluids Engineering Division of ASME for publication in the JOURNAL OF FLUIDS ENGINEERING. Manuscript received June 22, 2007; final manuscript received March 10, 2008; published online May 19, 2008. Assoc. Editor: Theodore Heindel.

 Copyright © 2008 by ASME

Downloaded 03 Jun 2010 to 171.66.16.157. Redistribution subject to ASME license or copyright; see http://www.asme.org/terms/Terms_Use.cfm

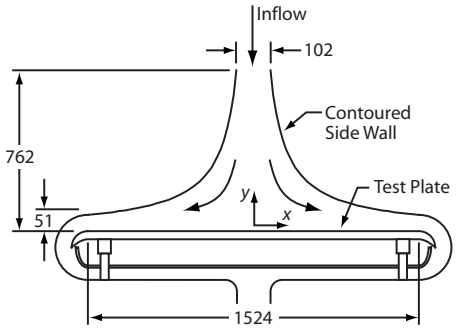

Fig. 1 Schematic of the Flow Lab test section. Dimensions are in millimeters.

At the time just following the Flow Lab's initial construction when these experiments were conducted, flow in the test section was turbulent. The boundary layers on the upper portion of the curved sidewalls separated near the inlet (near the top of Fig. 1) and reattached near $x \approx \pm 250$ mm. The measurement station used in these experiments was $x=635$ mm. At that point, the flow was attached but highly turbulent, as is shown below.

Air velocities in the tunnel are measured by using a Pitot/static tube and a single-element hotwire anemometer. The Pitot/static tube is used to calibrate the hotwire and to provide motor feedback; the hotwire is used for detailed boundary-layer velocity measurements. Because of the nature of the calibration, the hotwire's accuracy is limited by the accuracy of the differential pressure transducer used with the Pitot/static tube. This yields hotwire velocity uncertainties of 1.4% at 6.3 m/s and 0.3% at 12.8 m/s, the lowest and highest edge velocities used in the experiments, respectively. The overall lowest velocity measured during the experiments is 2.8 m/s (the point nearest the plate in the $U_e=6.3$ m/s experiment). This point has an uncertainty of 7% or ± 0.2 m/s.

The hotwire's position is manually controlled and its distance from the plate is measured by using a side-view camera mounted outside the wind tunnel. The camera is oriented with its optical axis a few degrees above the test plate so that both the hotwire probe and its reflection on the plate are visible. The image scale is calibrated so that video recordings of the hotwire and its reflection can be used to determine the hotwire's position relative to the surface. Calibration images of a scale placed at the camera's focal plane are judged to be accurate to about 2%. Additionally, a position uncertainty of about two pixels is associated with identifying the tip of the hotwire. When the hotwire is close to the plate, this uncertainty dominates and position uncertainties of about 75 μm are estimated. Farther from the plate, the 2% scale uncertainty becomes more important. When the hotwire is 5 mm from the plate, its position is judged to be accurate to within 125 μm.

In order to characterize the turbulent boundary layer, hotwire measurements were performed to give boundary-layer velocity profiles in the absence of water drops. These measurements give the time-mean streamwise velocity distribution $U(y)$, the turbulent velocity distribution $u'_{\text{rms}}(y)$, the displacement thickness δ^*, and the momentum thickness θ, all as functions of the boundary-layer edge velocity U_e. For these measurements, the hotwire was positioned at $x=635$ mm near the test plate's spanwise centerline and was scanned in the y direction from the inviscid freestream, $y>5$ mm, to within about 200 μm of the test plate surface. The edge velocities used for these measurements were $U_e=6.3$ m/s, 8.8 m/s, and 11.1 m/s at the measurement station. For each measurement, 1.0 s of hotwire and mean Pitot tube data were acquired, and the steady and unsteady streamwise velocities measured by the hotwire were normalized by the Pitot velocity. The U and u'_{rms} profiles resulting from these measurements are shown in Fig. 2.

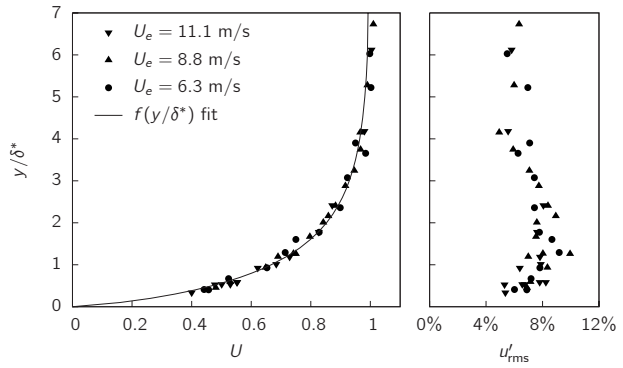

Fig. 2 Boundary layer velocity profiles, $U(y/\delta^*)$ and $u'_{\text{rms}}(y/\delta^*)$; $f(y/\delta^*)$ is an arbitrary fit used to calculate U_h

The boundary-layer displacement thickness δ^* and the momentum thickness θ are calculated as integrals of $U(y)$ from the surface to the freestream [13]. To generate these quantities from the experimental data, integrals are replaced by trapezoid-rule sums from $y_0=0$ where the no-slip condition requires $U_0=0$ to a point y_N in the freestream where $U_N \approx 1.0$. This approach gives

$$\delta^* \approx \sum_{n=0}^{N-1} \left(1 - \frac{U_{n+1}+U_n}{2}\right)(y_{n+1}-y_n) \tag{1}$$

and

$$\theta \approx \sum_{n=0}^{N-1} \left(\frac{U_{n+1}(1-U_{n+1})+U_n(1-U_n)}{2}\right)(y_{n+1}-y_n) \tag{2}$$

The displacement thickness, momentum thickness, and shape factor, $H=\delta^*/\theta$, for each of the three edge velocities are given in Table 1. The shape factors are consistent with the fact that the boundary layer is turbulent and accelerated.

Because the displacement thickness is used to generate drop runback correlations, it is important to know its uncertainty, σ_{δ^*}. This quantity is expected to be dominated by measurement errors so the numerical error associated with performing a trapezoid-rule integration rather than some higher-order scheme is ignored. Velocity and position errors are uncorrelated so σ_{δ^*} is given by [14]

$$\sigma_{\delta^*}^2 = \sum_{n=1}^{N} \left[\left(\frac{\partial \delta^*}{\partial U_n}\right)^2 \sigma_{U_n}^2 + \left(\frac{\partial \delta^*}{\partial y_n}\right)^2 \sigma_{y_n}^2\right] \tag{3}$$

The derivatives with respect to each of the U_n and y_n (except $n=N$) involve two terms:

$$\frac{\partial \delta^*}{\partial U_n} = -\frac{y_{n+1}-y_{n-1}}{2} \tag{4}$$

and

Table 1 Boundary-layer properties at $x=635$ mm

U_e	δ^*	θ	H	$C=\delta^* U_e^{1/2}$
6.3 m/s	726 ± 35 μm	387 ± 48 μm	1.87	1820 ± 90 μm(m/s)$^{1/2}$
8.8 m/s	649 ± 27 μm	348 ± 46 μm	1.86	1925 ± 80 μm(m/s)$^{1/2}$
11.1 m/s	582 ± 26 μm	321 ± 55 μm	1.81	1935 ± 85 μm(m/s)$^{1/2}$
Mean	—	—	1.85	1895 ± 50 μm(m/s)$^{1/2}$

Downloaded 03 Jun 2010 to 171.66.16.157. Redistribution subject to ASME license or copyright; see http://www.asme.org/terms/Terms_Use.cfm

$$\frac{\partial \delta^*}{\partial y_n} = \frac{U_{n+1} - U_{n-1}}{2} \tag{5}$$

The momentum thickness uncertainty is generated in a similar fashion but is somewhat more complex because U appears nonlinearly.

For both types of terms, uncertainties near the wall dominate. Near the wall, the velocity uncertainties are largest and the largest velocity uncertainty, σ_{U_1}, is multiplied by the largest derivative weighting factor because the distance between y_2 and y_0 is large. The uncertainty in y is smallest near the wall. However, its derivative weighting factor, the difference between adjacent velocities, is largest at the wall and σ_{y_n} only increases slightly over the boundary layer. The δ^* and θ uncertainties that result from these calculations are indicated in Table 1. The nature of the uncertainties and the measurement capabilities lead to smaller relative and absolute uncertainties for δ^* than for θ. This situation is the opposite of what can occur when the y_1 location is not known with good accuracy but all the other y_n locations are known with good accuracy relative to y_1 [15].

With the displacement thicknesses calculated, it is of interest to determine whether the boundary layers obtained at different U_e are self-similar and all collapse to a single curve when y is made dimensionless by using δ^*. Figure 2 shows the velocity and velocity fluctuation profiles plotted against y/δ^* and, indeed, the profiles do appear self-similar. The figure reveals $U(y/\delta^*)$ and $u'_{\text{rms}}(y/\delta^*)$ profiles typical of a strongly accelerated high-turbulence flow. There is relatively low scatter in the U data and what scatter exists falls within the measurement uncertainty.

In order to proceed to the runback experiments, it is necessary to characterize the experimentally determined U profiles by using a fitting function $f(y/\delta^*)$. This function provides estimated velocities in the boundary layer without requiring hotwire measurements to be made while drops are present. By using a strictly trial-and-error approach, the function

$$f\left(\frac{y}{\delta^*}\right) = 1 - \exp\left[-1.1\left(\frac{y}{\delta^*}\right)^{0.8}\right] \tag{6}$$

is found to adequately represent the U profiles. As y/δ^* becomes large, this function approaches one more slowly than the measured data. However, at the edge of the boundary layer and at all other points, the difference between the function and the data is less than the data scatter and is quite a bit less than the underlying uncertainty in U. Therefore, the adjustable parameters in this function are assumed to be exact.

In order to use this function in the drop runback experiments, it is necessary to know δ^* as a function of U_e. The laminar-flow similarity solution [13], suggests a boundary-layer thickness proportional to $U_e^{-1/2}$ and, by using this as a guide, the relationship $\delta^* = CU_e^{-1/2}$ was attempted as a δ^* correlation. Values of C were computed for all three U_e's considered; these values are given in Table 1 along with their uncertainties that arise from uncertainties in δ^* and U_e. The C values are quite consistent and the mean value $C = 1895 \pm 50$ μm$(\text{m/s})^{1/2}$ is used in the runback experiments to estimate δ^*.

3 Drop Runback Experiments

The main objective of the experiments is to develop a database of water-drop runback behavior and to determine the critical dimensionless drop-size and boundary-layer parameters under which a drop remains attached to a single point on the test plate and the conditions under which it runs downstream. All the tests were conducted at $x = 635$ mm, the point on the test plate where the boundary-layer scans were performed and the flow is well characterized. The drop runback tests consisted of placing distilled water drops of various volumes on the test plate surface by using a graduated syringe, initiating air flow so that a certain U_e was achieved, and observing which drops ran back at that speed.

Table 2 Dimensional stresses related to the drop runback threshold

Stagnation pressure (inviscid reference)	$\rho_{\text{air}} U_e^2$
Stagnation pressure (drop-height reference)	$\rho_{\text{air}} U_h^2$
Air shear (boundary-layer reference)	$\mu_{\text{air}} U_e / \delta^*$
Air shear (drop-height reference)	$\mu_{\text{air}} U_h / h$
Global pressure gradient	$\rho_{\text{air}} U_e^2 h / x$
Surface tension	σ / h

The runback data consist of drop heights that do and do not run back at a particular U_e. To make the results more broadly useful, these dimensional parameters are recast in a nondimensional form that reflects the appropriate physical mechanisms. The forcing that tends to move a drop downstream includes the difference between stagnation pressure on the drop's windward side and static pressure in the (presumably) separated region on the drop's leeward side, air shear that acts over the drop's surface, and the global pressure field imposed by test module's contoured sidewalls. The force resisting movement is provided by surface tension σ and the advancing and receding contact angles. In these experiments, the contact angle was only observed prior to initiating air flow. Its value was consistently observed to be $\theta = 70 \pm 5$ deg. No surface treatments that would vary θ were used so θ is not a variable in these experiments.

Casting the forcing and resisting mechanisms in terms of stresses gives a variety of dimensional terms from which to construct appropriate nondimensional groups. The dimensional stresses are given in Table 2. Most of these are familiar and can take two forms depending on whether the U_e or U_h is selected as a velocity scale. (U_h is the streamwise velocity that would exist at $y = h$ if a drop were not present.) The "global pressure gradient" term results from the freestream pressure gradient multiplied by a drop's height h that is taken as the characteristic drop size. This gives an appropriate measure of the pressure difference across the drop due to the contoured sidewalls.

In the experiment, h and U_e are varied independently, δ^* is a known function of U_e, $x = 635$ mm, and the physical properties (the air and water viscosities and densities, the air/water surface tension, and the contact angle) are constant. By using these parameters, three dimensionless groups are constructed. These are given in Table 3. Re_{δ^*} compares the stagnation pressure stress associated with U_e to boundary-layer shear, Re_h does the same by using U_h and shear across the drop height, and We compares the effect of stagnation pressure stress associated with U_h (a pressure that would tend to deform the drops) to σ/h (the surface tension effect that acts to maintain a spherical-cap shape). For all the drops tested, $h > 2\delta^*$ so $U_h/U_e \geq 0.85$. Therefore, the ratio of the global pressure stress to the stagnation pressure stress reduces to a term of order h/x. Because this ratio is always small, 5×10^{-3} or less, the global pressure gradient is judged to be insignificant relative to local pressure variations about the drop.

By using Re_{δ^*} as the primary measure of U_e, either Re_h or We may be used to parametrize h. In fact, because all other param-

Table 3 Dimensionless parameters related to the drop movement threshold

Boundary-layer-scale Reynolds number	$\text{Re}_{\delta^*} = \rho_{\text{air}} U_e \delta^* / \mu_{\text{air}}$
Drop-scale Reynolds number	$\text{Re}_h = \rho_{\text{air}} U_h h / \mu_{\text{air}}$
Weber number	$\text{We} = \rho_{\text{air}} U_h^2 h / \sigma$

Downloaded 03 Jun 2010 to 171.66.16.157. Redistribution subject to ASME license or copyright; see http://www.asme.org/terms/Terms_Use.cfm

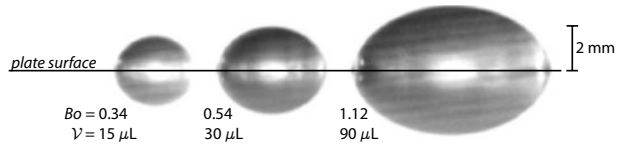

Fig. 3 Characteristic images of drops in still air. The plate surface is superposed; the drops' reflections are seen below this line.

eters are constant, Re_h may be written as a function of We, Re_{δ^*}, and other dimensionless parameters. By using the previous finding that $\delta^* \approx CU_e^{-1/2}$, Re_h may be written as

$$\mathrm{Re}_h = \kappa \frac{\mathrm{We}}{\mathrm{Re}_{\delta^*}^2} \frac{U_e}{U_h} \tag{7}$$

where $\kappa = C^2 \sigma \rho_{\mathrm{air}}^2 / \mu_{\mathrm{air}}^3 = (5.7 \pm 0.3) \times 10^7$. This relationship indicates that if there is a certain critical We beyond which drop movement is observed, the critical Re_h should decrease as $\mathrm{Re}_{\delta^*}^{-2}$ with a small correction for variations in U_h / U_e.

Although the drop height is the key size parameter, it was found most straightforward to apply drops of particular volumes $\mathcal{V}$ to the test plate. Then, instead of directly measuring h by using side-view images, the drop height was calculated from $\mathcal{V}$ and the contact angle. Drops ranged in volume from 5 μl to 150 μl and were applied with an accuracy of 0.5 μl. These small volumes were selected as they maintained the drops in the low-Bond-number regime, $\mathrm{Bo} = (\rho_{\mathrm{water}} - \rho_{\mathrm{air}}) g h^2 / \sigma$. With some practice, it was possible to produce drops whose contact line was circular when viewed from above. Viewed from the side, the drops appeared as indicated in Fig. 3. When Bo approaches zero, the contact angle is constant and the contact line is circular, the Young–Laplace equation indicates that drops take the shape of spherical caps [16]. Therefore, the height can be calculated as

$$h = \left[\frac{3\mathcal{V}(1 - \cos\theta)}{\pi(2 + \cos\theta)} \right]^{1/3} \tag{8}$$

Drop heights calculated by using this approach ranged from $h = 1.10$ mm to 3.43 mm and Bond numbers ranged from $\mathrm{Bo} = 0.16$ to 1.58.

Instead of calculating h by using Eq. (8), direct measurements of drop heights via side-view video would have also been possible. This approach was not used, primarily for convenience. Using the volume-based technique allowed several drops to be tested simultaneously while side-view height measurements would have restricted tests to single drops. Beyond convenience, however, the volume-based approach actually yields more accurate heights than direct measurements for small-volume drops. By assuming that deviations from the spherical-cap approximation can be neglected, the sources of uncertainty in Eq. (8) are the 0.5 μl volume uncertainty and the 5 deg contact angle uncertainty. These uncertainty sources yield

$$\sigma_h^2 = \left[\left(\frac{\partial h}{\partial \mathcal{V}} \right)^2 \sigma_{\mathcal{V}}^2 + \left(\frac{\partial h}{\partial \theta} \right)^2 \sigma_\theta^2 \right] \tag{9}$$

where

$$\frac{\partial h}{\partial \mathcal{V}} = \frac{1}{3} \frac{h}{\mathcal{V}} \tag{10}$$

and

$$\frac{\partial h}{\partial \theta} = \frac{h \sin\theta}{(2 + \cos\theta)(1 - \sin\theta)} \tag{11}$$

With the given uncertainties on $\mathcal{V}$ and θ, the 5 μl drops have $h = 1.10 \pm 0.07$ mm. This uncertainty is somewhat less than what would have been obtained for the same drop by using side-view imaging. The 150 μl drops have $h = 3.43 \pm 0.18$ mm. This uncertainty is somewhat greater than what would have been obtained from a side-view imaging, but not by a significant margin. Thus, operating strictly on the basis of drop volumes was deemed adequate.

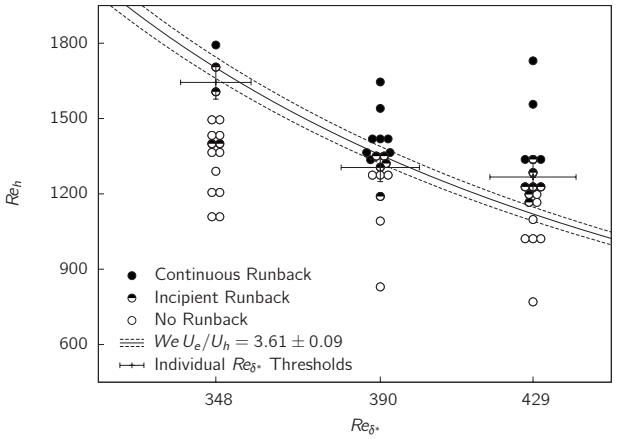

Fig. 4 Drop runback behavior. Each point represents a single drop with some drops offset from their correct Re_{δ^*} value where multiple data points would overlap.

Tests were conducted for a variety of drop sizes at three U_e settings: 8.4 m/s, 10.6 m/s, and 12.8 m/s. For each test, several drops of different volumes were placed along the line $x = 635$ mm, the drive fan was brought to its set point within 1–2 s, and the behavior of each drop was recorded. Three different outcomes were observed. First, once a test began, drops beyond the runback threshold underwent continuous motion along the plate. These drops began to move downstream almost immediately and their motion continued throughout a test. Second, drops below the runback threshold remained at their starting position for the duration of the test. Third, some drops near the runback threshold would break from their initial positions, move a short distance (less than 20 mm) downstream, and then stop and remain at their new positions. Sometimes, these drops would move again very slowly but would never exceed 20 mm of travel over the duration of a test.

Results of the runback tests are given in Fig. 4 and Table 4. In Fig. 4, individual drops are plotted based on the Re_{δ^*} of the particular test and the drop's Re_h value. Drops are coded as closed symbols for continuous runback, open symbols for no runback, or

Table 4 Summary of runback threshold parameters. "A" rows refer to the smallest drops at each Re_{δ^*} to run back, "B" rows refer to the largest drops not to run back, and "T" (threshold) rows are the mean of the A and B rows.

Re_{δ^*}		h/δ^*	Re_h	We	We U_e/U_h
348 ± 9	A	5.24 ± 0.31	1793 ± 102	3.37 ± 0.23	3.80 ± 0.22
	B	4.42 ± 0.26	1495 ± 87	3.08 ± 0.20	3.17 ± 0.19
	T	4.83 ± 0.20	1644 ± 67	3.41 ± 0.15	3.48 ± 0.15
390 ± 10	A	3.59 ± 0.21	1336 ± 80	3.40 ± 0.23	3.57 ± 0.22
	B	3.44 ± 0.21	1275 ± 77	3.23 ± 0.22	3.41 ± 0.21
	T	3.52 ± 0.15	1305 ± 56	3.32 ± 0.16	3.49 ± 0.15
429 ± 11	A	3.31 ± 0.20	1337 ± 82	4.07 ± 0.28	4.31 ± 0.27
	B	3.00 ± 0.18	1198 ± 76	3.59 ± 0.26	3.86 ± 0.25
	T	3.15 ± 0.13	1267 ± 56	3.83 ± 0.19	4.09 ± 0.18
All				3.45 ± 0.09	3.61 ± 0.09

Downloaded 03 Jun 2010 to 171.66.16.157. Redistribution subject to ASME license or copyright; see http://www.asme.org/terms/Terms_Use.cfm

half-open symbols for "incipient runback," the third case described above in which movement of less than 20 mm was observed. At each of the three Re_{δ^*} settings, there is a reasonably clear boundary between the runback and no-runback cases with incipient-runback cases in between. As Re_{δ^*} increases, the critical Re_h decreases. In all cases, the Re_h threshold for runback is quite large. This indicates that the forcing mechanism driving the runback is dominated by the stagnation pressure on the drops' windward side rather than by viscous shear.

Table 4 gives values of the nondimensional parameters of interest. For each Re_{δ^*}, three classes of data are given: *A*, *B*, and *T*. The *A* data refer to the smallest drop to run back and the *B* data refer to the largest drop not to not run back at a certain Re_{δ^*}. The *T* (for threshold) data are the mean of the *A* and *B* data. The tabular data confirm that a runback threshold given in terms of the h/δ^* or Re_h would be a decreasing function of Re_{δ^*}. The runback criterion appears to be well represented by a constant critical Weber number that varies from 3.32 to 3.83 for the three Re_{δ^*} settings. This variation is not unreasonable given the underlying uncertainty in the data. A modified Weber number, $\mathrm{We}U_e/U_h$, could also be used as a constant runback criterion. The last row of Table 4 gives a runback criterion based on the Weber number and modified Weber number that is the average of the three Re_{δ^*} settings. The critical values for We and $\mathrm{We}U_e/U_h$ are 3.45 ± 0.09 and 3.61 ± 0.09, respectively.

The runback threshold based on the modified Weber number is plotted in Fig. 4. This curve matches the three individual runback thresholds reasonably well, especially when the threshold points *T* are plotted with appropriate error bars. It should be noted that the uncertainties in all of these quantities include some correlated and some uncorrelated contributions. That is, every quantity plotted in Fig. 4 (as well as the Weber number) is calculated by using the *C* value obtained from the boundary-layer scans. Therefore, the difference between the estimate of *C* and its true value affects the Reynolds numbers and Weber numbers in a similar fashion. So, although the Re_{δ^*} error bars appear fairly large, their true values are all likely to be shifted in the same direction and by about the same distance from the plotted values. The Re_h and We values have less strongly correlated errors. These are driven more by drop-to-drop variations in the contact angle than by *C*.

In all of the cases considered, significant interface unsteadiness was observed for the continuous-runback, incipient-runback, and some of the no-runback cases. An example of this is given in Fig. 5 that shows a large oscillation of a drop's surface prior to runback followed by two frames showing the drop's movement during which there continue to be large surface oscillations. The large deviations from the spherical-cap shape before and during runback make it clear that the parameters generated by using the spherical-cap approximation do not fully capture the mechanisms of drop motion because instantaneous values of *h* may exceed the nominal *h* by a significant margin and, somehow, unsteady dynamics should be considered.

The cause and detailed characteristics of these oscillations have not been investigated in detail. It is possible that they are driven at least in part by the turbulent fluctuations in the boundary layer. However, the oscillations increase markedly with increasing Re_h. Therefore, it is suspected that the oscillations are most strongly associated with separated air flow in the drop wakes. Solid hemispherical roughness elements in laminar boundary layers are known to have unsteady separated regions in their wakes at Re_k (equivalent to Re_h here) values as low as 120 [17]. So, the very large values of Re_h used in this experiment almost certainly lead to unsteady separations even for the smallest drops considered.

4 Conclusion

The experiments presented here are intended to provide a basis for engineering predictions of drop runback behavior in a turbulent, accelerated boundary layer. The experiments consisted of measurements of a turbulent stagnation-point boundary-layer flow followed by runback tests in that boundary layer. Hotwire measurements confirm self-similar turbulent boundary layers for which $\delta^* \approx CU_e^{-1/2}$. By using the δ^* estimates this model provides, as well as drop-height estimates based on drop volumes, Reynolds numbers based on δ^* and the drop height and drop Weber numbers were generated to correlate the runback behavior.

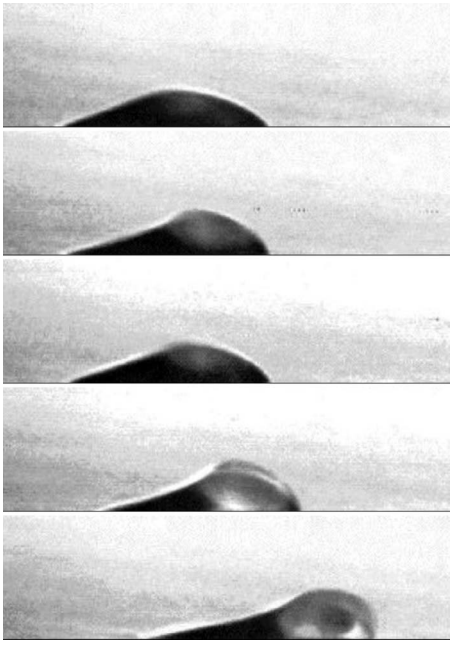

Fig. 5 Video images of a typical drop movement initiation

A runback threshold based on Re_h decreases as $\mathrm{Re}_{\delta^*}^{-2}$. Drops near and above the runback threshold all had Re_h values of 1336 or higher, so runback in these experiments is thought to be driven by the unsteady pressure difference between the windward and separated leeward sides of the drops. A runback threshold based on We does not appear to depend on Re_{δ^*}; it is a constant 3.45 ± 0.09. A modified Weber number We U_e/U_h might also provide a useful runback criterion; that threshold is 3.61 ± 0.09. Given the violent oscillations that precede runback (see Fig. 5), it is somewhat surprising that the data can be correlated by using static drop heights. A constant-We runback threshold is consistent with observations by Olsen and Walker [4].

Whichever drop runback criterion is applied, it is important to emphasize that the results should not be extended beyond conditions of the present experiment. That is, these results apply to drop with contact angles near $\theta = 70$ deg, with small Bond numbers, in turbulent boundary layers with shape factors near 1.85, and with Re_{δ^*} values of a few hundreds. If the flow were not as strongly accelerated or not turbulent, the $U(y)$ profile would be different and this would alter the aerodynamic forcing on the drop. Similarly, if θ or the contact angle hysteresis were different, the drops' resistance to motion would be affected and the results could be quite different. Finally, it is noted that drop runback always seems to be associated with large Re_h values that presumably lead to separated flow in a drop's wake. If Re_{δ^*} were larger than the values investigated here, the Re_h required for runback would be smaller and the lee-side separation might be less severely unsteady. It is unknown that as Re_{δ^*} increases and the Re_h threshold decreases, the runback threshold would change from what is observed here.

Downloaded 03 Jun 2010 to 171.66.16.157. Redistribution subject to ASME license or copyright; see http://www.asme.org/terms/Terms_Use.cfm

Acknowledgment

This work was supported by Grant No. NNC05GA39G from the Icing Branch at the NASA Glenn Research Center. J.A.S. received support through a fellowship from the Case School of Engineering at Case Western Reserve University. The authors wish to thank Professor J. Iwan Alexander at Case Western Reserve University for assistance with imaging and other matters.

References

[1] Wright, W., 2002, "User Manual for the NASA Glenn Ice Accretion Code LEWICE: Version 2.2.2," NASA Report No. CR 211793.
[2] Kind, R., Potapczuk, M., Feo, A., Golia, C., and Shah, A., 1998, "Experimental and Computational Simulation of In-Flight Icing Phenomena," Prog. Aerosp. Sci., **34**, pp. 257–345.
[3] Messinger, B., 1953, "Equilibrium Temperature of an Unheated Icing Surface as a Function of Airspeed," J. Aeronaut. Sci., **20**, pp. 29–41.
[4] Olsen, W., and Walker, E., 1986, "Experimental Evidence for Modifying the Current Physical Model of Ice Accretion on Aircraft Surfaces," NASA Report No. TM 87184.
[5] Kirchner, R. D., 1995, "Water Bead Formation in Glaze Icing Conditions," AIAA Paper No. 95-0593.
[6] Bikerman, J., 1950, "Sliding of Drops From Surfaces of Different Roughnesses," J. Colloid Sci., **5**, pp. 349–359.
[7] Dussan, V. E. B., 1987, "On the Ability of Drops or Bubbles to Stick to Solid Surfaces. Part 3. The Influences of the Motion of the Surrounding Fluid on Dislodging Drops," J. Fluid Mech., **174**, pp. 381–397.
[8] Myers, T., Charpin, J., and Chapman, S., 2002, "The Flow and Solidification of a Thin Film on an Arbitrary Three Dimensional Surface," Phys. Fluids, **14**(8), pp. 2788–2803.
[9] Rothmayer, A. P., and Tsao, J., 2001, "On the Incipient Motion of Air Driven Water Beads," AIAA Paper No. 2001-0676.
[10] Dimitrakopoulos, P., and Higdon, J., 1998, "On the Displacement of Three-Dimensional Fluid Droplets From Solid Surfaces in Low-Reynolds-Number Shear Flows," J. Fluid Mech., **377**, pp. 189–222.
[11] White, E. B., and Oliver, M. J., 2005, "Experiments on Surface Roughness Effects in Ice Accretion," AIAA Paper No. 2005-5190.
[12] Rabbitt, W. E., 2006, "Design and Construction of an Icing Physics Flow Laboratory," M.S. thesis, Case Western Reserve University, Cleveland, Ohio.
[13] Schlichting, H., 1979, *Boundary-Layer Theory*, 7th ed., McGraw-Hill, New York.
[14] Bevington, P. R., 1969, *Data Reduction and Error Analysis for the Physical Sciences*, McGraw-Hill, New York.
[15] White, E. B., and Ergin, F. G., 2004, "Using Laminar-Flow Velocity Profiles to Locate the Wall Behind Roughness Elements," Exp. Fluids, **36**, pp. 805–812.
[16] Dussan, V. E. B., 1979, "On the Spreading of Liquids on Solid Surfaces: Static and Dynamic Contact Lines," Annu. Rev. Fluid Mech., **11**, pp. 371–400.
[17] Acarlar, M., and Smith, C., 1987, "A Study of Hairpin Vortices in a Laminar Boundary Layer. Part 1. Hairpin Vortices Generated by a Hemisphere Protuberance," J. Fluid Mech., **175**, pp. 1–41.

Downloaded 03 Jun 2010 to 171.66.16.157. Redistribution subject to ASME license or copyright; see http://www.asme.org/terms/Terms_Use.cfm

Effervescent Atomization of Viscoelastic Liquids: Experiment and Modeling

S. C. Geckler[1]

P. E. Sojka[2]
e-mail: sojka@ecn.purdue.edu

Maurice J. Zucrow Laboratories,
School of Mechanical Engineering,
Purdue University,
West Lafayette, IN 47907-2014

The effervescent atomization of viscoelastic liquids is reported. A total of 23 fluids, formulated from a 60 wt % glycerine/40 wt % water solvent to which were added varying concentrations (0.001–0.5 wt %) of poly(ethylene oxide) polymers whose molecular weights ranged from 12,000 to 900,000, were sprayed through a conventional effervescent atomizer. Mean drop sizes were measured using a forward light scattering instrument. The drop size (D_{32}) data show the expected decrease with an increase in air-liquid ratio by mass (ALR), the expected increase with an increase in polymer concentration, plus an increase with an increase in polymer molecular weight for most cases. However, no significant change in D_{32} was observed for polymer solutions whose molecular weights ranged from 12,000 to 35,000, suggesting the presence of a critical molecular weight below which spray performance is unaltered. This argues for two different factors controlling drop size: Polymer molecular weight is most influential at the highest polymer concentrations while polymer concentration is most influential at the lowest polymer concentrations. Analysis of the spray formation process was carried out using a ligament formation model previously developed for the effervescent atomization of Newtonian liquids coupled with a linear stability model for the breakup of viscoelastic liquid jets. The jet breakup model assumes that an unrelaxed axial tension exists within the fluid. A comparison of model predictions and experimental data indicates that the model predicts the observed dependencies of mean drop size on ALR, polymer concentration, and polymer molecular weight. Quantitative agreement is within 10–50% of experimental values in all cases. Finally, a shortcoming of the model is noted and a means of avoiding this limitation reported. [DOI: 10.1115/1.2917430]

Introduction

Atomization is important in many industrial processes, including IC and gas turbine engines, industrial furnaces, consumer product sprays, paints/coatings, pharmaceutical/medicinal sprays, and agricultural sprays. Many of these applications rely on low viscosity liquids to produce the desired spray performance. However, it is increasingly difficult to atomize fluids from the noncombustion group for two reasons. First, consumer products manufacturers are subject to increasingly tighter regulations on the amount of volatile organic compounds (VOC's) that may be present in the liquids to be sprayed. Second, water-based paints and coatings are becoming more prevalent. Third, pharmaceutical/medicinal sprays are now being formulated with water as the primary solvent. As such, the inherent viscoelastic nature of the active ingredient in these liquids (typically a long-chain polymer) is dominating the Newtonian behavior of the solvent. This indicates that the effects of viscoelasticity will play a larger role when spraying such liquids in the future.

Effervescent atomization is one possible method for successfully spraying viscoelastic liquids. This area has not been studied in detail. In fact, previous researchers have considered non-Newtonian effervescent atomization only to the extent that they demonstrated the performance of this technology and qualitatively described how the process differs from its Newtonian counterpart. Buckner and Sojka [1] sprayed purely viscous fluids that varied in both consistency and flow behavior index and observed the expected increase in mean drop size for the non-Newtonian fluids relative to their Newtonian counterparts (having comparable low-shear viscosity). Jardine [2] also studied effervescent atomization of purely viscous non-Newtonian fluids, varying the fluid behavior index from 0.81 to 0.20 and the consistency index from 270 mPa s^n to 40,000 mPa s^n. However, the non-Newtonian parameters n and K failed to indicate how the atomizer would perform when fluid formulation was altered. Lee and Sojka [3] extended the purely viscous studies of Buckner and Sojka [1] and Jardine [2] by investigating the effervescent atomization of viscoelastic liquids that exhibited no shear thinning or shear thickening at strain rates up to 10,000 s^{-1}. They used a high speed rotating drum camera to examine the structure of the spray near the nozzle exit, and noted that while the internal flow remained unchanged from the previous investigations of Lund et al. [4], long ligaments were produced outside the exit orifice and substantially larger mean drop sizes were measured than for Newtonian liquids of equivalent shear viscosity. Lee and Sojka [3] then developed a correlation based on the work of Matta [5] in an attempt to relate their drop size data to the fluid relaxation time. They were able to correlate their mean drop size data, but the correlation coefficient was unique for each of the four fluids tested and no scaling laws were provided to describe how it depended on polymer molecular weight or polymer concentration.

Geckler and Sojka [6] used an effervescent atomizer to spray solutions of glycerin and water with dissolved poly(ethylene oxide). Their study included mean drop size measurements to illustrate the effect of viscoelasticity on spray performance, plus flow visualization using holographic imaging to provide a detailed description of the near nozzle spray structure. The holograms showed that the external two-phase structure is annular, and that it does not undergo significant change with increasing air-liquid ra-

[1]Present address: FEV, Auburn Hills, MI.
[2]Corresponding author.
Contributed by the Fluids Engineering Division of ASME for publication in the JOURNAL OF FLUIDS ENGINEERING. Manuscript received June 29, 2007; final manuscript received March 1, 2008; published online May 22, 2008. Assoc. Editor: Theodore Heindel.

Downloaded 03 Jun 2010 to 171.66.16.157. Redistribution subject to ASME license or copyright; see http://www.asme.org/terms/Terms_Use.cfm

tio by mass (ALR). Furthermore, the holograms showed that viscoelasticity delays breakup of the annular sheet with the result that a "net" of ligaments is present immediately downstream of the nozzle exit orifice instead of the clearly distinct ligaments observed in the Newtonian case. While Geckler and Sojka [6] presented mean drop size as a function of ALR, polymer concentration, and polymer molecular weight, their ranges of polymer concentration and molecular weight are limited and they provide no analytical model to explain their results.

The four previous studies indicate that (1) the decrease in nozzle performance observed upon the addition of polymer is not a strictly viscous phenomenon, (2) there is some causal link between the viscoelastic behavior of the fluid to be sprayed and spray mean drop size, (3) there is little difference between the two-phase flow at the nozzle exit when comparing Newtonian and viscoelastic fluids, and (4) the influence of liquid formulation can be overcome by increasing ALR. The first three points indicate that familiarity with viscoelastic ligament breakup is important to our understanding of the effervescent atomization of such fluids.

Experimental studies of viscoelastic ligament breakup date back to the work of Goldin et al. [7], who showed the effects of polymer addition on jet breakup by spraying both Newtonian and polymeric solutions through a capillary tube. The appearance of viscoelastic jets was remarkably different than Newtonian ones in two respects. First, the growth of disturbances on the jet surface appeared to occur faster than for the Newtonian liquids at short times. Second, and in marked contrast to Newtonian behavior, was the rapid decrease in disturbance growth rate at long times.

Hoyt et al. [8] also studied viscoelastic jets and noted that large scale disturbances eventually develop into a drop-thread configuration, as observed by Goldin et al. [7]. In addition, because the technique of Hoyt et al. [8] allowed more surface detail to be observed, they reported the absence of small scale disturbances that occur in Newtonian jets where the Weber number is high. Evidently, damping occurring in the viscoelastic jet eliminates the stripping effect that is often apparent in fast Newtonian jets. These authors also point out that polymer solutions exhibit slightly smaller values of surface tension. To investigate this, they sprayed a Newtonian jet with reduced surface tension and reported that surface tension variations were not the cause of the anomalous viscoelastic jet behavior.

Subsequent to this, Ferguson et al. [9] performed an experimental investigation into what they termed breakup in an "extensional flow field." They first studied eight Newtonian solutions over a wide range of compositions, developing a correlation between spray mass mean diameter (MMD) and fluid steady shear viscosity. Ferguson et al. [9] then proceeded to spray solutions of four different polymer types in water. Their results showed that the low molecular weight polymer solutions fit their correlation, but deviations appeared as the polymer molecular weight increased. Since their first correlation contained no description of the polymer molecular weight, a new form was introduced to account for molecular weight and concentration.

Correlations containing adjustable parameters that are fitted to experimental data, such as those proposed by Lee and Sojka [3] and Ferguson et al. [9], are of limited use for two reasons. First, they are valid only over the range of experimental conditions for which they were derived. Second, they provide limited physical insight into the spray formation process. A better understanding, and a more widely applicable model, must be based on first principles analysis.

The first analytical attempt to predict viscoelastic jet disintegration was undertaken by Middleman [10], who performed a linearized stability analysis similar to those of Rayleigh [11] and Weber [12]. The key difference was that the constitutive relationship Middleman [10] used to characterize the fluid was developed by Oldroyd [13]. Middleman developed a relationship for the axial shear stress

$$T_{rz}(r) = -\mu_1 \left[ikU_r(r) + \frac{dU_z(r)}{dr} \right] \tag{1}$$

where the new viscosity is given by

$$\mu_1 = \mu \frac{1 + \gamma\lambda_2}{1 + \gamma\lambda_1} \tag{2}$$

in terms of the low-shear viscosity μ, the growth rate γ, the relaxation time λ_1, and the retardation time λ_2. From this, he deduced a new dispersion relationship by substituting the expression for μ_1 into Weber's dispersion relationship,

$$\gamma^2 + \frac{3\mu k^2}{\rho}\gamma\left(\frac{1 + \gamma\lambda_2}{1 + \gamma\lambda_1}\right) - \frac{\sigma k^2(1 - k^2a^2)}{2\rho a} = 0 \tag{3}$$

where k is the wave number, ρ is the density, and a the jet initial radius.

It is interesting to note that the dispersion relation given by Eq. (3), which describes viscoelastic jet breakup, yields a shorter optimum wavelength than Weber's analysis for Newtonian liquids. This prediction is contrary to available experimental data for viscoelastic jet breakup.

Four years later, Goldin et al. [7] attempted to determine if Middleman's [10] choice of constitutive relation was responsible for his model's unphysical optimum wavelength prediction. To do so, they also performed a linearized stability analysis including a constitutive equation for the general viscoelastic fluid. Upon completing the analysis, they obtained results identical to Middleman's [10], but that were more general. They then concluded that nonlinear phenomena dominated the breakup of jets exhibiting elastic behavior.

Goren and Gottlieb [14] revisited the linear stability analysis for a viscoelastic fluid to show that the presence of an unrelaxed axial tension normal to the direction of the flow would cause a viscoelastic jet to be stabilized and, therefore, exhibit optimum disturbance wavelengths longer than their Newtonian counterpart. The most important result of their study is the dispersion equation. Following the lead of Bousfield [15], the Goren and Gottlieb [14] nondimensional dispersion relation may be rewritten as

$$\beta\gamma^2 + \frac{3\pi^2\gamma(1 + \phi_1\gamma)}{(1 + \phi_2\gamma)} - \frac{\pi^2(1 - \pi^2\alpha^2)}{2} - \frac{T_e\pi^2(1 - \phi_1\gamma)}{(1 + \phi_1\gamma)} = 0 \tag{4}$$

after small argument approximations are made for the Bessel functions and only terms from the Oldroyd B constitutive relation are retained. In this expression, β is a measure of inertial forces relative to surface tension forces, ϕ_1 and ϕ_2 are measures of viscoelasticity that include the fluid relaxation time, γ is the nondimensional growth rate, and α is the dimensionless wave number. The solution for the amplification factor in terms of the wave number is then straightforward, once a value is assigned to the unrelaxed axial tension T_e.

Results from solving Eq. (4) show a number of important points. First, the dispersion relation reduces to that of previous efforts such as [10] in the limit of T_e equal to zero. Second, the amplification factor is reduced as the value of the unrelaxed axial tension increases. Third, when the product $\phi_1\gamma$ is greater than 1, the growth rate predicted by Eq. (4) is smaller than that predicted by the Newtonian dispersion relation of Weber. This indicates that the jet is more stable than its Newtonian counterpart. Fourth, the wave number corresponding to the maximum growth rate decreases as the unrelaxed tension is increased. This means the dominant wavelength responsible for jet breakup is increasing, which leads directly to the formation of larger drops. Unfortunately, Goren and Gottlieb [14] provided no method for determining the magnitude of the unrelaxed axial tension; they only undertook a parametric study using this quantity.

Downloaded 03 Jun 2010 to 171.66.16.157. Redistribution subject to ASME license or copyright; see http://www.asme.org/terms/Terms_Use.cfm

Bousfield et al. [16] performed the first numerical simulation of the nonlinear surface tension driven breakup of Newtonian and non-Newtonian liquid jets, using two different solution strategies. The first was a two-dimensional, transient, finite element approach that was computationally intensive. The second was a one-dimensional approximation to the first case. Results from the one-dimensional approximation were compared to the two-dimensional counterpart and deviations shown to be small.

Bousfield et al. [16] used their one-dimensional model to calculate the entire development of the jet profile on its way to breakup. They report that growth rates of disturbances on a viscoelastic jet do grow more rapidly than their Newtonian counterparts at short times, in agreement with previous linear stability analyses. However, unlike any of the linear studies, Bousfield et al. [16] predicted the formation of the aforementioned droplet-thread configuration where the nonlinear buildup of extensional stresses becomes dominant. They reported that at times beyond this point, the final breakup distance is governed by the thinning of the connecting threads that were previously observed experimentally by Goldin et al. [7].

It is important to note that Bousfield et al. [16] also investigated cases that included an unrelaxed tensile stress in the jet. To do this, they first performed an analysis to predict the value of the axial tension in a jet that is issuing from a small pipe. They nondimensionalized this axial tension by the ratio of the surface tension to the exit orifice radius and obtained

$$T_e = \frac{32(1-\Lambda)}{3\phi_1}\left(\frac{\lambda_1 \bar{V}}{R_o}\right)^2 \tag{5}$$

This expression contains Λ, the ratio of the fluid relaxation time to the retardation time λ_1/λ_2, and ϕ_1, the previously noted nondimensional viscoelastic parameter,

$$\phi_1 = \frac{\lambda_1 \sigma}{\eta_o R_o} \tag{6}$$

Appearing in Eq. (6) are the fluid relaxation time λ_1, the fluid surface tension σ, the low-shear rate viscosity η_o, and the exit orifice radius R_o. Also included in Eq. (5) is the average velocity of the liquid in the pipe, $\bar{V}$. To derive Eq. (5), the authors were forced to assume that pipe flow upstream of the orifice was fully developed so characterized by a parabolic velocity profile.

In agreement with Goren and Gottlieb [14], Bousfield et al. [16] found that using Eq. (5) in their one-dimensional approximation resulted in a reduction of the disturbance growth rate. In fact, the linearized results of Goren and Gottlieb [14] were identical to those from the one-dimensional theory of Bousfield et al. [16] at short times. Since the analyses are identical at short times, the wavelength corresponding to the fastest growing disturbance is given correctly by Goren and Gottlieb's [14] linear theory. Moreover, while the time for this disturbance to cause jet breakup is misrepresented, the Goren and Gottlieb [14] result has practical utility since the droplet size is dependent primarily on the wavelength of the disturbance and less so on the breakup time.

In summary, the results of previous experimental and modeling studies on viscoelastic jet breakup indicate that the viscoelastic dispersion relationship of Goren and Gottlieb [14] and the unrelaxed axial tension expression of Bousfield et al. [16] can be combined to estimate viscoelastic ligament breakup length. Furthermore, previous experimental work [3,6] indicates that the geometric model for ligament formation provided by Lund et al. [4] is applicable to viscoelastic liquid spray formation. We therefore conclude that experimental mean drop size data for the effervescent atomization of viscoelastic liquids can be interpreted from first principles. That interpretation is the goal of this study.

Given that goal, the first step was to experimentally quantify the performance of an effervescent atomizer when spraying viscoelastic fluids, and to do so in a way that describes how changing viscoelastic fluid properties impact spray performance. The next step was to use holography to investigate the near nozzle region of the effervescent spray in order to elucidate the mechanisms responsible for atomization of these liquids and to identify differences in spray structure as compared to Newtonian effervescent atomization. The third step was to develop an analytical model to predict mean drop size, and its dependence on atomizer operating conditions (ALR) and fluid viscoelasticity. The final step was to compare model predictions with nozzle performance data, and use the former to help explain the latter.

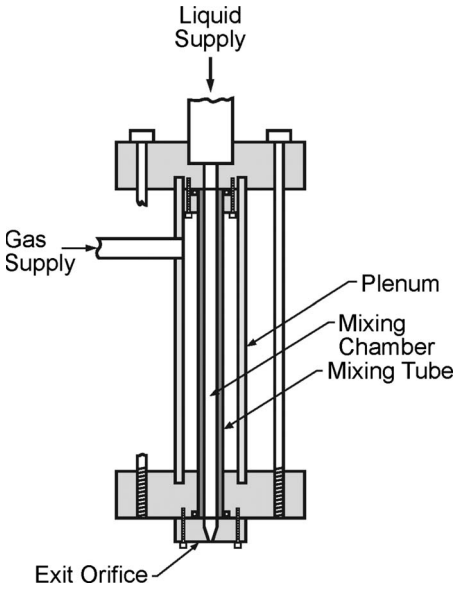

Fig. 1 Effervescent atomizer. The exit orifice is 1 mm in diameter; the full included cone angle of the contraction is 118 deg.

Method of Approach

Experimental Apparatus. A schematic of the effervescent atomizer used during this study appears in Fig. 1. Liquid enters the atomizer from above, and then flows into the mixing chamber. Air flows into the plenum and through the mixing tube. The resulting two-phase mixture exits through the bottom orifice.

Sprays were characterized by their mean drop size (D_{32}). All drop sizing was done using a Malvern 2600 particle analyzer equipped with a 300 mm focal length receiving lens. Drop size data were taken on the spray centerline at a distance of 25 cm from the nozzle exit. This value was chosen because it is a representative of consumer product, painting/coating, and pharmaceutical manufacturing atomizer-to-target distances. Key conclusions from this work are expected to be valid for distances greater than 25 cm because drop evaporation is low (vapor pressures are significantly below those of water), drop number densities are low so collisions/coalescence are minimal, and drop trajectory calculations suggest that size-velocity correlations are absent. Decreasing the measurement distance would alter these conclusions, as would be expected when the drop number densities are high (so collisions/coalescence are important) and when size-velocity correlations are significant.

Spray data were reduced using the Malvern software operating in model independent mode. Since obscurations were always well below 50%, multiple scattering corrections were unnecessary.

The accuracy of the Malvern was confirmed using a reticule and the procedure suggested by Hirleman [17]. The instrument reported a reticule Rosin–Rammler mean diameter parameter X that was within 2% of the reticule's value and a spread parameter q that was within 5% of the reticule's value.

Downloaded 03 Jun 2010 to 171.66.16.157. Redistribution subject to ASME license or copyright; see http://www.asme.org/terms/Terms_Use.cfm

Table 1 Summary of fluid physical properties

	η_0, low shear viscosity (mPa-s)	θ, characteristic time (s)	σ, surface tension (dynes/cm)
NO POLYMER	10.3 ± 0.02	0.0	67.8 ± 1.59
0.001%; 100,000	11.0 ± 0.03	2.8E-07	65.1 ± 0.29
0.01%; 35,000	10.6 ± 0.00	4.2E-06	62.6 ± 0.31
0.01%; 100,000	11.1 ± 0.02	1.4E-05	62.6 ± 0.31
0.01%; 900,000	11.0 ± 0.00	4.12E-06	62.6 ± 0.31
0.15%; 35,000	12.2 ± 0.01	6.18E-05	62.6 ± 0.31
0.15%; 100,000	15.4 ± 0.00	2.06E-4	62.6 ± 0.31
0.15%; 900,000	17.7 ± 0.00	1.03E-03	62.6 ± 0.31
0.5%; 35,000	14.1 ± 0.05	1.14E-03	62.6 ± 0.31
0.5%; 100,000	18.2 ± 0.02	17.1E-3	62.6 ± 0.31

Qualitative information concerning the breakup mechanisms responsible for viscoelastic liquid effervescent atomization was obtained using the holographic system of Santangelo and Sojka [18]. The interference pattern was developed and saved using the process discussed by Bjelkhagen [19]. At a later time, the spray image was reconstructed by expanding a 10 mW He–Ne laser beam to the same diameter as the original reference wave and illuminating the holographic plate at the same incident angle.

Solutions to be sprayed were formulated by adding poly(ethylene oxide) to solvents having a common composition of 60% glycerin-40% water solution by mass. PEO molecular weights of 12,000, 35,000, 100,000, 300,000 and 900,000 were used at mass concentrations of 0.001%, 0.01%, 0.15%, and 0.5%, (the 900,000 and 300,000 molecular weight polymers were not studied at a concentration of 0.5% because these solutions would not form a spray for the ALRs of interest). A base line case consisting of pure solvent was also prepared.

Model calculations require five physical properties for each liquid: density, surface tension, low-shear viscosity, solvent viscosity, and relaxation time. Density had the same value for all liquids ($1.2\ \mathrm{g/cm^3}$), as did the solvent viscosity (10.3 ± 0.02 mPa s). Surface tension, low-shear viscosity, and relaxation time were separately determined for each case. All data were acquired at 25°C. Uncertainties represent one standard deviation from a sample set of at least three trials.

A Du–Nuoy style surface tensiometer was used to determine surface tension. It was calibrated by suspending a known mass on its platinum-iridium ring. Once the instrument was calibrated, the surface tension of distilled water was measured. The accepted value, as reported by the manufacturer (77.5 dynes/cm), was reproduced to within 0.5 dynes/cm.

Polymer solution surface tensions were expected to be somewhat lower than that of the pure solvent [8]. As shown in Table 1, results obtained here are in agreement with previous work.

A Bohlin VOR concentric cylinder rheometer, equipped with a constant temperature circulating bath, was used to measure the low-shear viscosity. Its calibration was checked using standard silicone oil solutions; agreement was within 5%. Table 1 data are included for only those liquids that exhibited significant viscoelastic behavior.

It is difficult to experimentally determine relaxation times for liquids having polymer concentrations below 0.1% [20,21]. An alternative approach, use of molecular theory, was employed instead.

In his review, Williams [22] noted that the characteristic time is a measure of the relaxation time in the limit of small shear rates. Bird et al. [20] provided an expression for the characteristic time

$$\theta = \frac{2}{5}\frac{\eta_s [\eta]_o^2 M}{\rho_s R T} c \tag{7}$$

where η_s is the solvent shear viscosity, $[\eta]_o$ the intrinsic viscosity, M the polymer molecular weight, R the gas constant, T the fluid temperature, and c the polymer concentration in dimensionless form. Each of the quantities in Eq. (7) is known except the intrinsic viscosity, which is defined as

$$[\eta]_o = \lim_{c \to 0} \frac{(\eta_o - \eta_s)}{c\,\eta_s} \tag{8}$$

Here, η_o is the solution low-shear viscosity. Kalashnikov and Askarov [21] provided a standard form correlation for intrinsic viscosity in terms of polymer molecular weight

$$[\eta]_o = 1.25 \times 10^{-2} M^{0.78} \tag{9}$$

Characteristic times for each solution were calculated and are included in Table 1.

Theoretical Analysis. The analysis outlined here draws heavily upon the work of Lund et al. [4], but differs in that it is applicable to fluids with non-Newtonian (viscoelastic) rheological properties. It assumes that the drop formation process proceeds through two steps: liquid exits the atomizer such that an annular sheet is present in the exit orifice; the sheet then breaks up into a number of contiguous ligaments. The ligaments are assumed to be entirely liquid, a presumption supported by the holographic images.

Applying continuity to the liquid and gas phases exiting the nozzle and then defining the velocity slip ratio, sr,

$$\mathrm{sr} = \frac{V_A}{V_L} \tag{10}$$

gives a relation for the thickness of the annular sheet at the exit orifice in terms of the diameter of the air core, d_A,

$$d_A = \left(\frac{\rho_L \mathrm{ALR} d_o^2}{\rho_L \mathrm{ALR} + \rho_A \mathrm{sr}} \right)^{0.5} \tag{11}$$

The diameter of the individual ligaments is calculated by placing an integral number of ligaments around the annular ring of liquid that exits the atomizer, then applying liquid continuity to match the total of the ligament cross-sectional areas to that of the annular ring

$$d_l = \frac{2}{\sqrt{\pi}}(d_o - d_A) \tag{12}$$

where d_A is determined from Eq. (11).

Equation (11) requires knowledge of the velocity slip ratio. Fortunately, Panchagnula [23] has measured this quantity for similar nozzles using the two-phase momentum rate probe developed by Bush et al. [24]. Panchagnula's experimental data indicate that the slip ratio is approximately constant and equal to 2 for the conditions considered in this study.

Once the diameter of the ligaments separating from the annular sheet is determined, the optimum wavelength for ligament breakup can be found. The linearized stability analysis of Goren and Gottlieb [14] for viscoelastic jets is used for this purpose, in the simplified form suggested by Bousfield [15], and presented above as Eq. (4). The unrelaxed axial tension is evaluated using Eq. (5).

The dispersion relation, Eq. (4), is rewritten, after some effort, as a fourth order polynomial in γ. Once the polynomial coefficients, which are functions of fluid properties and flow conditions, are determined, the dispersion relation is solved by computing growth rates for a range of wave numbers and the maximum growth rate identified via a search. The wavelength corresponding to the maximum growth rate is equal to the optimum wavelength for jet breakup.

The model has now predicted the diameter and length of each

Downloaded 03 Jun 2010 to 171.66.16.157. Redistribution subject to ASME license or copyright; see http://www.asme.org/terms/Terms_Use.cfm

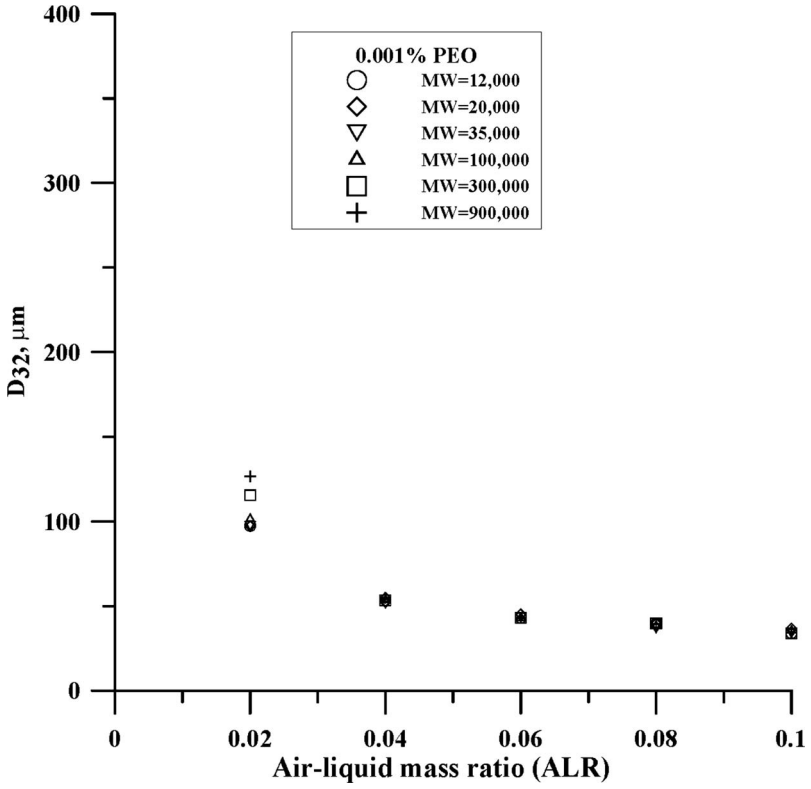

Fig. 2 D_{32} versus ALR for six different polymer molecular weights and a common polymer concentration of 0.001% by mass

ligament produced during the atomization process. Assuming no secondary atomization, justified by the small relative velocities between the liquid and surrounding gas, the volume of each ligament is equated to the volume of a single corresponding drop and mean drop size calculated directly.

Results and Discussion

Drop Size Measurements. Experimental drop size data are presented for all 23 fluids in Figs. 2–5. Results are reported as mean drop size (D_{32}) versus ALR. Each data point is the average of three measurements with a mean statistical error of less than 0.5% and a maximum statistical error of 3.4%. Uncertainty bars are not included in the figures because the maximum standard deviation for any of the data points was less than 5 μm, making the statistical deviation smaller than the height of the symbols.

Figure 2 contains data taken at the smallest polymer concentration, 0.001%. These dilute solutions might be expected to atomize as though there were no polymer present. This is nearly the case for the lower molecular weights with D_{32} values for the 12,000, 20,000, and 35,000 molecular weight solutions falling quite close to values for the Newtonian solvent. However, even at this concentration, differences in D_{32} can be detected if the molecular weight is sufficiently high ($>$100,000) and the ALR is sufficiently low ($\leq$0.02).

Comparison of Figs. 2 and 3 illustrates the effect of increasing polymer concentration. Unlike Fig. 2, the effect of polymer addition is clearly evident in Fig. 3 with data for an ALR of 0.02 indicating how sensitive the performance of the atomizer can be to changes in polymer molecular weight.

Figure 3 illustrates another effect of ALR on spray performance. Although D_{32} is a relatively strong function of polymer molecular weight at lower ALRs, atomizer performance is much less dependent on polymer molecular weight at the highest ALR tested. This insensitivity to fluid properties at higher ALRs has been reported by Buckner and Sojka [25] and Santangelo and Sojka [26] who noted the diminishing effect of liquid viscosity as ALR was increased.

Another aspect not apparent for the lower concentration data of Fig. 2, which becomes evident when considering the data of Fig. 3, is that the three lowest polymer molecular weight solutions atomize in such a way that their D_{32} values are virtually indistinguishable. This observation suggests the possibility of a threshold value for some fluid property associated with the polymer solutions used in this investigation, such as the characteristic time. Support for a critical characteristic time is provided by the spray work of Ferguson et al. [9] and the flow through porous media work of Kalashnikov and Askarov [21].

As the polymer concentration is increased to 0.15%, as shown in Fig. 4, the behavior discussed in the preceding paragraph becomes even more evident. In particular, the effect of an increase in polymer concentration for the three highest molecular weights results in continuing degradation of spray performance. While the spread in the D_{32} data diminishes with increasing ALR, as in Figs. 2 and 3, the effect of polymer molecular weight is still clearly evident at an ALR of 0.10. Note that the three lowest polymer molecular weight solutions still maintain a nearly constant level of atomization quality, although D_{32} does increase slightly relative to the no polymer base case.

Figure 5 contains data from solutions with the highest polymer concentration of 0.5%. Only data for four molecular weights are presented in this figure because the 300,000 and 900,000 molecular weight solutions would not form a spray at this concentration. As Fig. 5 shows, even at this concentration D_{32} for the three lowest molecular weight solutions are still nearly equal, although again somewhat higher than the pure solvent case. This is not true for the 100,000 molecular weight solution, which experiences a marked increase in D_{32} relative to the base case. Note that D_{32} still decreases with an increase in ALR and that the spread between molecular weights diminishes with ALR.

Downloaded 03 Jun 2010 to 171.66.16.157. Redistribution subject to ASME license or copyright; see http://www.asme.org/terms/Terms_Use.cfm

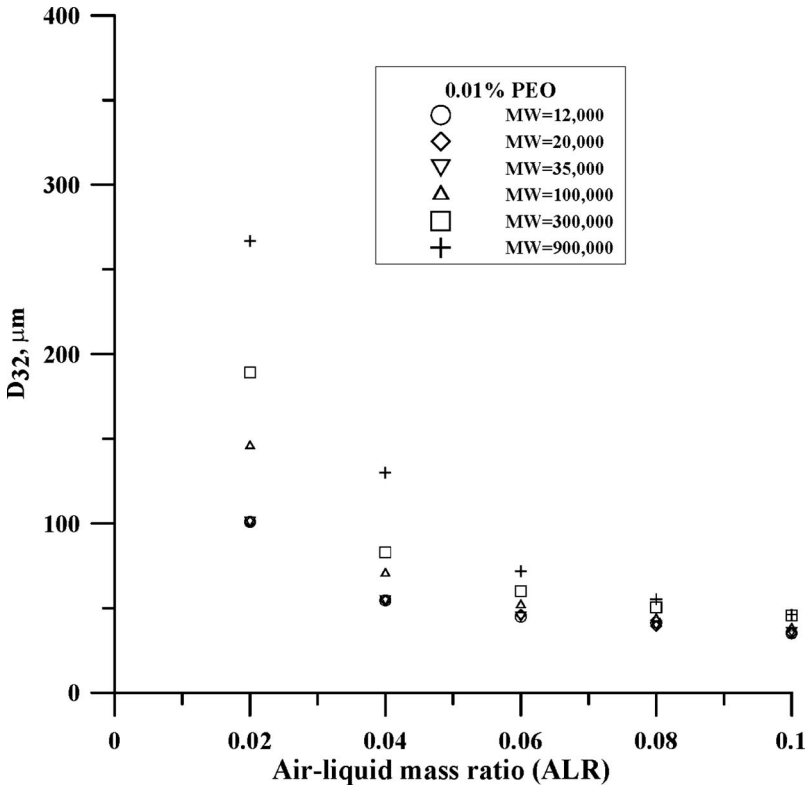

Fig. 3 D_{32} **versus ALR for six different polymer molecular weights and a common polymer concentration of 0.01% by mass**

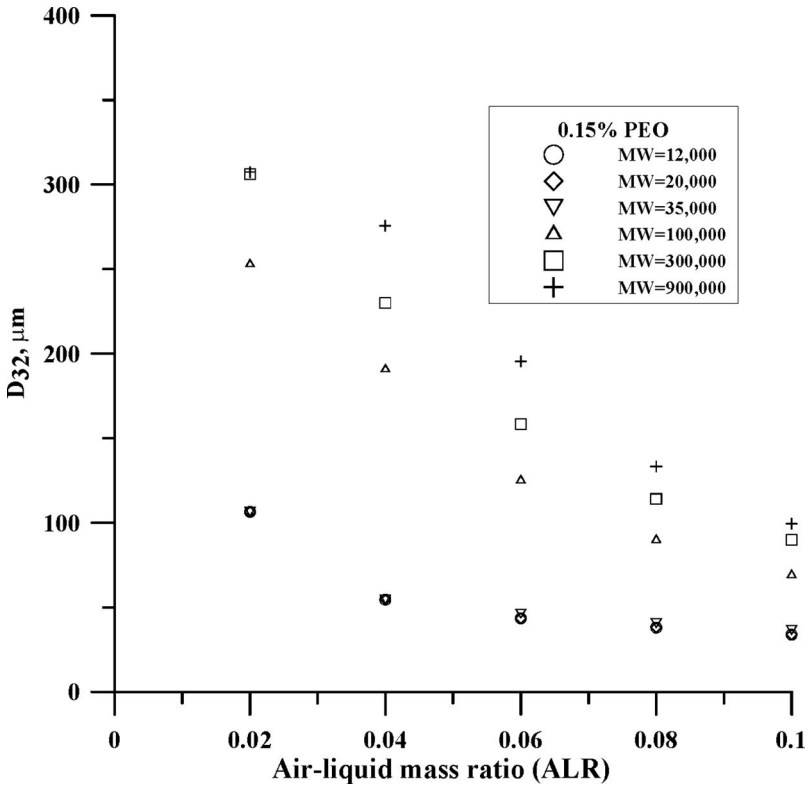

Fig. 4 D_{32} **versus ALR for six different polymer molecular weights and a common polymer concentration of 0.15% by mass**

Downloaded 03 Jun 2010 to 171.66.16.157. Redistribution subject to ASME license or copyright; see http://www.asme.org/terms/Terms_Use.cfm

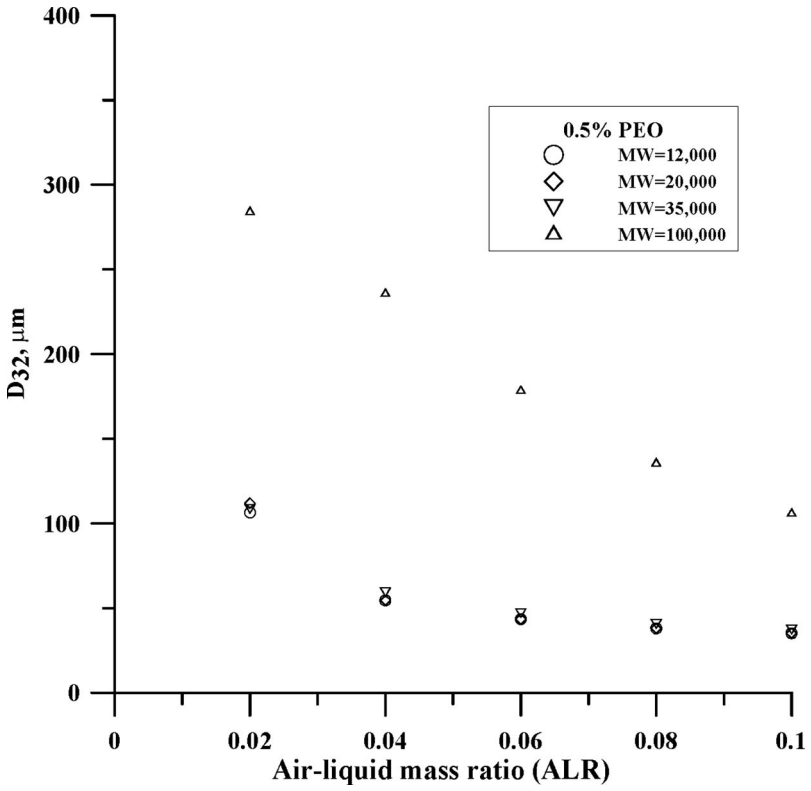

Fig. 5 D_{32} **versus ALR for four polymer molecular weights and a common polymer concentration of 0.5% by mass**

Figure 6 provides a qualitative indication of how polymer addition affects atomization. It is a black and white photograph made from a hologram constructed using the system of Santangelo and Sojka [18]. Upon comparison with the corresponding Newtonian case data, the viscoelastic spray formation process differs in several important ways. First, the presence of polymer in the solution delays the breakup of the sheet, thereby increasing the physical distance required to form ligaments. Furthermore, the ALR required to produce ligaments in the near nozzle region is increased. These observations may be explained by noting that the polymer acts to delay the growth of disturbances on the liquid sheet. As ALR increases, the energy available to those disturbances increases so that they grow more quickly. Consequently, ligaments are seen to form nearer the nozzle exit.

Second, having polymer in a solution increases the length of the ligaments produced from the sheet and the time required for those ligaments to break up and form drops. This may also be explained by noting that polymer addition delays the growth of disturbances on the liquid sheet.

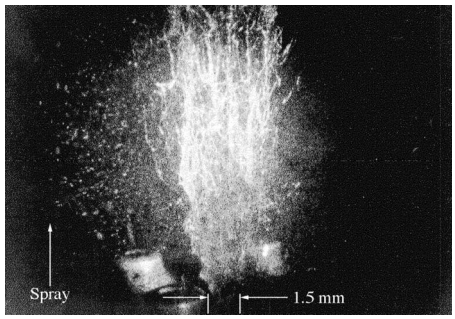

Fig. 6 Near nozzle spray structure of the 100,000 molecular weight polymer at a concentration of 0.15% and an ALR of 0.10

The qualitative observations listed above suggest that a polymer solution will produce a larger mean drop size than its Newtonian counterpart when used in an effervescent atomizer. This is in agreement with the mean drop size measurements presented here.

Comparison of Simulations and Experiments. The model developed here was used to predict the mean drop size produced by an effervescent atomizer using the selected set of fluids listed in Table 1. The results of these predictions appear in Figs. 7–9, along with corresponding measured D_{32} values.

Figure 7 contains experimental data and model predictions for solutions having three different concentrations of the 35,000 molecular weight polymer. Note that the model predicts that drop size will change rapidly with ALR at lower ALRs, but will vary more slowly at higher ALRs. Qualitative agreement between model predictions and experimental data is therefore excellent.

One difference between model predictions and experimental data in Fig. 7 is a weak dependence of model D_{32} on polymer concentration. The model predicts differences in mean drop size because, as Table 1 shows, the 35,000 molecular weight solutions have a characteristic time value proportional to their polymer concentrations. These differences in characteristic time translate into differences in unrelaxed axial tension, as given by Eq. (5), with the result that the optimum wavelengths provided by the dispersion equation reflect the differences in fluid properties. This discrepancy may be due to the use of calculated characteristic times as opposed to the measured values.

A second difference between model predictions and experimental data is the surprising behavior exhibited by the simulations for the smallest polymer concentration and the lowest ALR. In this case, the mean drop size predicted for the 0.01% solution is larger than that predicted for the 0.15% solution. This observation, while counter to the accepted view of viscoelastic ligament breakup

Downloaded 03 Jun 2010 to 171.66.16.157. Redistribution subject to ASME license or copyright; see http://www.asme.org/terms/Terms_Use.cfm

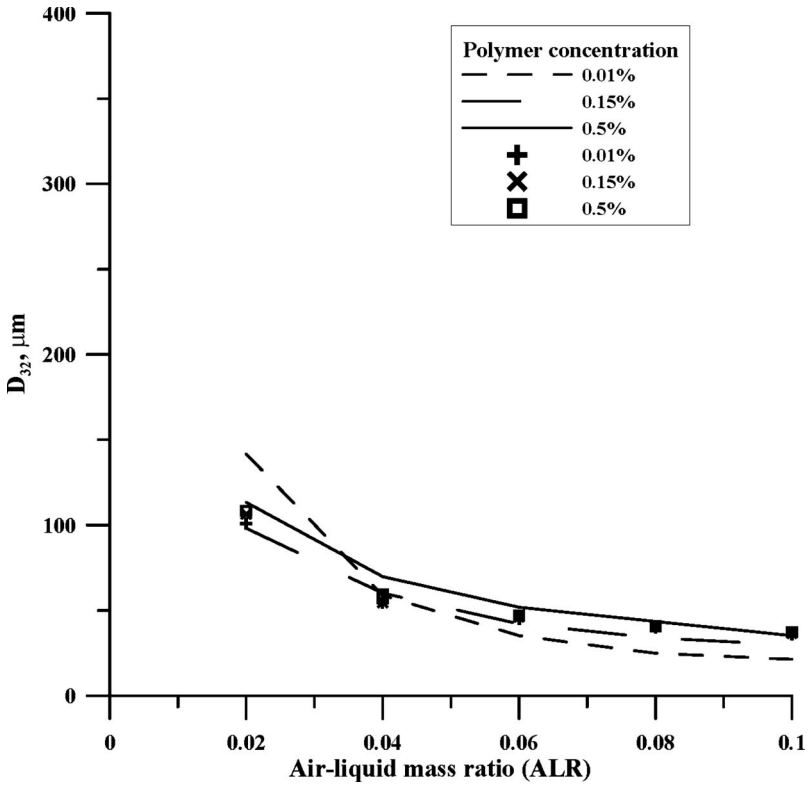

Fig. 7 Measured and predicted D_{32} versus ALR for solutions having 60% glycerine–40% water solvent and containing 35,000 molecular weight polymer in various concentrations

[9,16], is not surprising for two reasons. First, Goren and Gottlieb [14] indicated that under some conditions linear stability models will predict shorter breakup wavelengths for viscoelastic fluids than for their Newtonian counterparts. Second, Bousfield et al. [16] pointed out that linear stability analysis based models, such as the one developed here, cannot be expected to accurately describe the nonlinear viscoelastic breakup processes under all conditions. Fortunately, the occurrence of this behavior corresponds to a condition involving the viscoelastic parameter ϕ_1 and the dimensionless growth rate γ. The unphysical increase in predicted mean drop size with decreasing polymer concentration occurs only when $\phi_1\gamma \ll 1$. This criterion may therefore be used to evaluate the model's validity for small liquid characteristic times.

Model predictions for the 100,000 molecular weight polymer, presented in Fig. 8, are again in qualitative agreement with the experimental data. The model estimates mean drop size accurately for the two lower concentrations, but as concentration is increased the model predicts a smaller increase in mean drop size than that demonstrated by the data. It is therefore evident that liquid physical property estimates are not scaling properly with polymer concentration. One explanation for this discrepancy is a failure of the method used to evaluate the solution characteristic time, i.e., Eq. (7). Figure 8 also shows that the model predicts a larger mean drop size at the lowest polymer concentration, 0.001%, than at the next higher value (0.01%). This corresponds to the $\phi_1\gamma \ll 1$ condition mentioned in the previous paragraph.

Figure 9 shows that qualitative agreement between predicted trends and measurements continues when the polymer weight is increased to 900,000. In this figure, we see that the model generally overpredicts mean drop size at the lower polymer concentration with an average difference of 38%. However, quantitative agreement is quite good for the higher concentration of 0.15% with the average difference between the measured and predicted mean drop sizes being 14%.

To interpret the information that is present in Figs. 7–9, one must understand which model inputs are changing and to what degree. The viscoelastic fluid properties enter through Eq. (5). In particular, all viscoelastic parameters, ϕ_1, ϕ_2, and T_e, depend on the fluid characteristic time, θ. If evaluation of this property fails to accurately reflect changes in bulk fluid properties with variations in polymer molecular weight and concentration, then the model is destined to be inaccurate to some extent. One point, however, is clear. Application of viscoelastic jet stability analysis to the two-phase flow geometry observed at the exit orifice of an effervescent atomizer does describe the qualitative behavior observed in the laboratory.

In summary, the model developed here does predict the mean drop size of an effervescent atomizer spraying viscoelastic liquids. It qualitatively predicts the shape of the D_{32} versus ALR curves by showing a sharp drop, and then an asymptotic leveling as ALR increases. In addition, the influence of polymer molecular weight and polymer concentration is qualitatively demonstrated. Model predictions in some cases agree with experimental data to within 10%. The differences between model predictions and experimental data are never more than 50% of the experimental values.

A limitation of the model has been observed for weakly elastic fluids. Model predictions for liquids whose characteristic time is small enough to satisfy the condition $\phi_1\gamma \ll 1$ are not physically correct. Therefore, this condition serves as a criterion for identifying model limitations.

Summary and Conclusions

The effervescent atomization of viscoelastic fluids was studied using a total of 23 fluids formulated from a 60 wt % glycerine-40 wt % water solvent to which were added varying concentrations (0.001–0.5 wt %) of poly(ethylene oxide) poly-

Downloaded 03 Jun 2010 to 171.66.16.157. Redistribution subject to ASME license or copyright; see http://www.asme.org/terms/Terms_Use.cfm

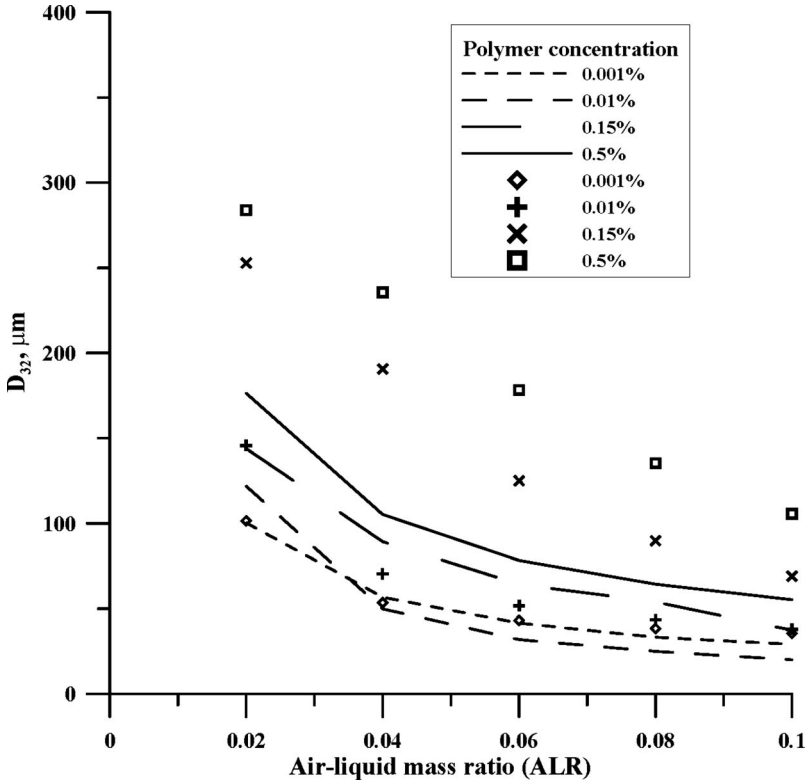

Fig. 8 Measured and predicted D_{32} versus ALR for solutions having 60% glycerine–40% water solvent and containing 100,000 molecular weight polymer in various concentrations

mers whose molecular weights ranged from 12,000 to 900,000. Measurements of spray mean drop size (D_{32}) as a function of ALR show the following characteristics.

- As expected, D_{32} decreases as ALR increases.
- Also as expected, solutions containing polymer in general produce a D_{32} that is larger than that obtained by spraying the pure solvent. However, no significant increase in D_{32} was observed for polymer solutions with molecular weights of 35,000 and below.
- Another expected observation was a decrease in the difference in mean drop size between solutions with common polymer concentrations, but differing polymer molecular weights, as ALR increased.
- Of more interest was the observation that D_{32} scales in two distinctly different fashions, depending on polymer concentration and molecular weight. This suggests two different controlling factors. At low concentration, D_{32} is a strong function of polymer concentration and only weakly dependent on polymer molecular weight. In contrast, at high concentration, D_{32} is a strong function of polymer molecular weight and only a weak function of concentration.

Qualitative information gained from the holograms allows interpretation of the D_{32} data in terms of the spray structure in the near nozzle region during the breakup process. As expected, the addition of polymer to the solvent changes the external spray structure in two distinct ways. First, the liquid exits the atomizer in the form of an annular flow and the addition of polymer to the solvent retarded the growth of disturbances that induce the formation of ligaments from the sheet. The diameter of the ligaments produced increases with polymer concentration and/or polymer molecular weight. Second, once the ligaments are separated from the liquid sheet, the presence of polymer in the solutions increases the wavelength of the disturbances responsible for jet breakup. These factors combine and manifest themselves as measured increases in D_{32}.

Analysis of the spray formation process was carried out in the spirit of previous effervescent spray models. We have determined that the ligament formation geometry of Lund et al. [4] can be combined with the linear stability analysis for viscoelastic ligament breakup of Goren and Gottlieb [14] and the unrelaxed axial tension expression of Bousfield et al. [16] to predict mean drop size. The jet breakup model assumes that an unrelaxed axial tension exists within the fluid. It is determined from a knowledge of the solvent viscosity, fluid low-shear viscosity, fluid surface tension, liquid jet velocity, ligament diameter, and fluid characteristic time. The viscosities and surface tensions are measured experimentally, while the jet velocity and ligament diameter come from the ligament formation model. The fluid characteristic time is estimated using a correlation for poly(ethylene oxide) in water.

A comparison of model predictions and experimental data indicates that the model predicts the observed dependencies of D_{32} on ALR, polymer concentration, and polymer molecular weight. Quantitative agreement is within 10–50% of experimental values in all cases. Finally, a shortcoming of the model is noted: it provides unphysical results for weakly elastic fluids. Fortunately, this limitation can be overcome if model predictions are ignored when $\phi_1 \gamma \ll 1$.

We believe improvements in model predictions could be made by substituting experimentally measured fluid characteristic time data for the calculated values used during this study. This will be the topic of a future program.

Downloaded 03 Jun 2010 to 171.66.16.157. Redistribution subject to ASME license or copyright; see http://www.asme.org/terms/Terms_Use.cfm

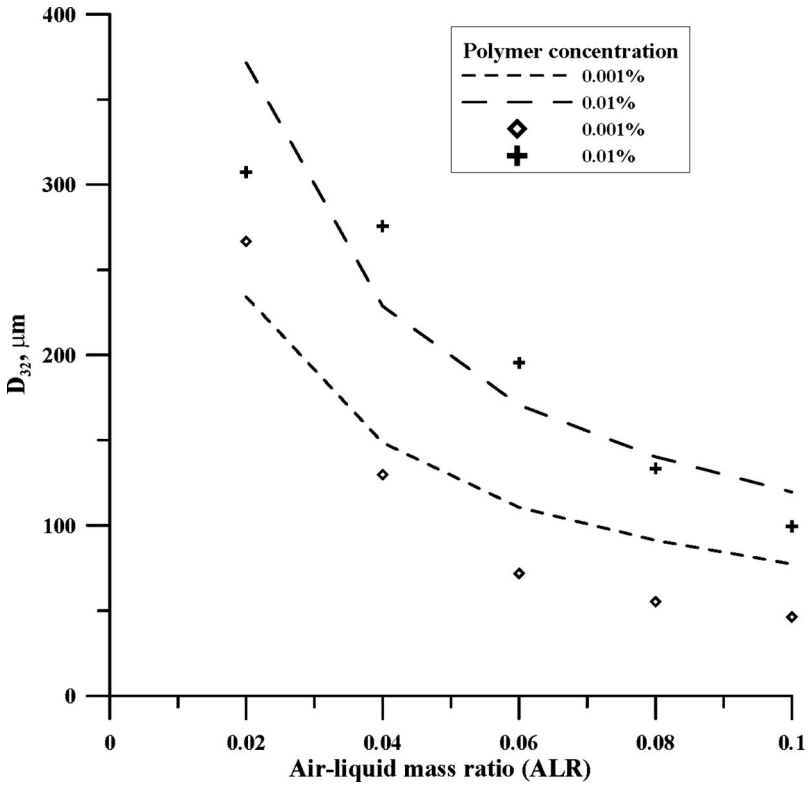

Fig. 9 Measured and predicted D_{32} versus ALR for solutions having 60% glycerine–40% water solvent and containing 900,000 molecular weight polymer in various concentrations

Acknowledgment

We gratefully acknowledge P. J. Santangelo's assistance with the linear stability analysis and the holograms, and Professor D. Bousfield's enlightening comments about viscoelastic jet breakup.

Nomenclature

a = jet radius, m
ALR = air-liquid mass flow rate ratio
c = polymer concentration, dimensionless
d_A = diameter of the air core at the atomizer exit orifice, m
d_l = ligament diameter, m
d_o = exit orifice diameter, m
K = consistency index, mPa s^{n-1}
k = wave number, $1/m$
M = polymer molecular weight, kg/kmol
n = flow behavior index, dimensionless
R = gas constant, kJ/kg K
R_o = jet radius, m
sr = velocity slip ratio, dimensionless
D_{32} = Sauter mean diameter, μm
T = temperature, K
T_e = unrelaxed axial tension, dimensionless
T_{rz} = axial shear stress, Pa
U_r = jet radial velocity, m/s
U_z = jet axial velocity, m/s
$\bar{V}$ = ligament velocity at the inception of breakup, m/s
V_A = air velocity, m/s
V_L = liquid velocity, m/s
α = dimensionless wave number
β = viscoelastic fluid parameter, dimensionless
η_o = low-shear viscosity, mPa s
η_s = solvent shear viscosity, mPa s
$[\eta]_o$ = solution intrinsic viscosity, dimensionless
γ = growth rate, dimensionless
λ_1 = relaxation time, s
λ_2 = retardation time, s
Λ = viscoelastic fluid parameter, dimensionless
μ = low-shear viscosity, mPa s
μ_1 = viscoelastic low-shear viscosity, mPa s
ϕ_1 = viscoelastic fluid parameter, dimensionless
ϕ_2 = viscoelastic fluid parameter, dimensionless
ρ = density, kg/m^3
ρ_A = air density, kg/m^3
ρ_L = liquid density, kg/m^3
ρ_s = solvent density, kg/m^3
σ = surface tension, dynes/cm
θ = fluid characteristic time, s

References

[1] Buckner, H. N., and Sojka, P. E., 1993, "Effervescent Atomization of High Viscosity Fluids: Part II. Non-Newtonian Liquids," Atomization Sprays, **3**, pp. 157–170.
[2] Jardine, K. J., 1991, M.S.M.E. thesis, Purdue University.
[3] Lee, W. Y., and Sojka, P. E., 1993, "The Influence of Fluid Viscoelasticity on Low Mass Flowrate Effervescent Atomization," J. W. Hoyt, T. J. O'Hern, C. Presser, A. K. Gupta, and R. L. Alpert, eds., ASME FED Vol. 178/HTD Vol. 270, pp. 129–134.
[4] Lund, M. T., Sojka, P. E., and Lefebvre, A. H., 1993, "Effervescent Atomization at Low Mass Flow Rates. Part I: The Influence of Surface Tension," Atomization Sprays, **3**, pp. 77–89.
[5] Matta, J. E., 1980, "Nonlinear Visco-Elastic Breakup in a High-Velocity Airstream," U.S. Army Technical Report No. ARCSL-TR-80067.
[6] Geckler, S. C., and Sojka, P. E., 1993 "High Mass Flowrate Effervescent Atomization of Visco-Elastic Fluids," J. W. Hoyt et al., eds., ASME FED Vol. 178/HTD Vol. 270, pp. 109–115.
[7] Goldin, M., Yerushalmi, J., Pfeffer, R., and Shinnar, R., 1969, "Breakup of a Laminar Capillary Jet of a Visco-Elastic Fluid," J. Fluid Mech., **38**, pp. 689–711.

Downloaded 03 Jun 2010 to 171.66.16.157. Redistribution subject to ASME license or copyright; see http://www.asme.org/terms/Terms_Use.cfm

[8] Hoyt, J. W., Taylor, J. J., and Runge, C. D., 1974, "The Structure of Jets of Water and Polymer Solutions in Air," J. Fluid Mech., **63**, pp. 635–640.
[9] Ferguson, J., Hudson, N. E., and Warren, B. C., 1992, "The Break-Up of Fluids in an Extensional Flow Field," J. Non-Newtonian Fluid Mech., **44**, pp. 37–54.
[10] Middleman, S., 1965, "Stability of a Visco-elastic Jet," Chem. Eng. Sci., **20**, pp. 1037–1040.
[11] Rayleigh, Lord, 1879, Proc. R. Soc. London, **A29**, pp. 71–97.
[12] Weber, C., "Disintegration of Liquid Jets," 1931, Z. Angew. Math. Mech., **11**, pp. 136–159.
[13] Oldroyd, J. G., 1950, Proc. R. Soc. London, Ser. A, **200**, pp. 523–541.
[14] Goren, S., and Gottlieb, M., 1982, "Surface-Tension Driven Breakup of Visco-Elastic Liquid Threads," J. Fluid Mech., **120**, pp. 245–266.
[15] Bousfield, D. W., 1986, Ph.D. thesis, University of California, Berkeley.
[16] Bousfield, D. W., Keunings, R., Marrucci, G., and Denn, M. M., 1986, "Nonlinear Analysis of the Surface Tension Driven Breakup of Visco-Elastic Filaments," J. Non-Newtonian Fluid Mech., **21**, pp. 79–97.
[17] Hirleman, H. D., 1983, "On Line Calibration Techniques for Laser Diffraction Droplet Sizing Instruments," ASME Paper No. 83-GT-232.
[18] Santangelo, P. J., and Sojka, P. E., 1994, "Focused Image Holography as a Dense Spray Diagnostic," Appl. Opt., **33**(19), pp. 4132–4136.
[19] Bjelkhagen, H. I., 1992, *Tutorial V: Pulse Holography*, Lake Forest College, Lake Forest, IL.
[20] Bird, R. B., Armstrong, R. C., and Hasseger, O., 1987, *Dynamics of Polymeric Liquids*, Wiley, New York.
[21] Kalashnikov, V. N., and Askarov, A. N., 1989, "Relaxation Time of Elastic Stresses in Liquids with Small Additions of Soluble Polymers of High Molecular Weights," J. Eng. Phys. Thermophys., **57**, pp. 874–878.
[22] Williams, M. C., 1975, "Molecular Rheology of Polymer Solutions: Interpretation and Utility," AIChE J., **21**, pp. 1–25.
[23] Panchagnula, M. V., 1994, M.S.M.E. thesis, Purdue University.
[24] Bush, S. G., Bennett, J. B., Panchagnula, M. V., Sojka, P. E., and Plesniak, M. W., 1996, "A Momentum Rate Probe for Use With Effervescent Sprays," Rev. Sci. Instrum., **67**(5), pp. 1878–1885.
[25] Buckner, H. N., and Sojka, P. E., 1991, "Effervescent Atomization of High Viscosity Fluids: Part I. Newtonian Liquids," Atomization Sprays, **1**, pp. 239–252.
[26] Santangelo, P. J., and Sojka, P. E., 1995, "The Near Nozzle Structure of an Effervescent Atomizer Produced Spray," Atomization Sprays, **5**, pp. 137–155.

Downloaded 03 Jun 2010 to 171.66.16.157. Redistribution subject to ASME license or copyright; see http://www.asme.org/terms/Terms_Use.cfm

Some Exact Solutions to Equations of Motion of an Incompressible Third Grade Fluid

Saif Ullah
School of Mathematical Sciences,
Government College University,
Lahore 54600, Pakistan
e-mail: saifullahkhalid75@yahoo.com

*This investigation deals with some exact solutions of the equations governing the steady plane motions of an incompressible third grade fluid by using complex variables and complex functions. Some of the solutions admit, as particular cases, all the solutions of Moro et al. [1990, "Steady Flows of a Third Grade Fluid by Transformation Methods," ZAMM, **70**(3), pp. 189–198]* [DOI: 10.1115/1.2928407]

Keywords: vorticity function, third grade fluid, stream function

1 Introduction

The governing equations that describe flows of Newtonian fluids are the Navier–Stokes equations. The mechanical behavior of many real fluids, especially those of low molecular weight, appears to be accurately described by these equations over a wide range of circumstances. There are, however, many real substances, which are capable of flowing but which are not at all well described by the Navier–Stokes theory. Due to this reason, many fluid models have been proposed and studied by different authors. Among these, the fluids of differential type have received much attention. Interesting studies of differential type fluids are given by Rajagopal [1], Erdogan [2], Rajagopal and Gupta [3], Bandelli [4], Siddiqui and Kaloni [5], Benharbit and Siddiqui [6], Ariel [7,8], Fetecau [9], and Hayat et al. [10–12]. The fluids of third grade, which form a subclass of the fluids of differential type, have been successfully studied in various types of motions.

Moro et al. [13] determined some exact solutions of the equations governing the steady plane motion of an incompressible third grade fluid employing hodograph and Legendre transformations.

The aim of this paper is to present some exact solutions for steady plane motions of incompressible third grade fluids. For this, the complex variables and complex functions are used. Some previous solutions can be obtained as special cases of our solutions. In Secs. 2 and 3 are presented the constitutive equations and the expression of the vorticity function ω. Section 4 contains solutions and their graphical illustrations.

2 Constitutive and Governing Equations

The fluids of grade n, introduced by Rivlin and Ericksen [14], are the fluids for which the stress tensor is a polynomial of degree n in the first n Rivlin–Ericksen tensors defined recursively by

$$A_1 = (\partial_i u_j + \partial_j u_i)_{i,j}; \quad A_n = \frac{d}{dt}A_{n-1} + A_{n-1}L + L^t A_{n-1}, \quad n > 1 \tag{1}$$

where $d/dt = \partial_t + u \cdot \nabla$ denotes the material derivative and

$$L = (\partial_j u_i)_{i,j}, \quad L^t = (\partial_i u_j)_{i,j}$$

Physical considerations were taken into account by Fosdick and Rajagopal [15] in order to obtain the following form of constitutive equation for the Cauchy stress T in a third grade fluid:

$$T = -pI + \mu A_1 + \alpha_1 A_2 + \alpha_2 A_1^2 + \beta_1 A_3 + \beta_2 [A_1 A_2 + A_2 A_1] + \beta_3 (\mathrm{tr}\, A_1^2) A_1 \tag{2}$$

where $-pI$ is the spherical stress due to the constraint of incompressibility, μ is the dynamic viscosity, $\alpha_i (i = 1, 2)$ and $\beta_i (i = 1, 2, 3)$ are the material constants, and the three Rivlin–Ericksen tensors A_1, A_2, and A_3 are given in Eq. (1).

Furthermore, a complete thermodynamic analysis of the constitutive equation (2) has been given by Fosdick and Rajagopal [15]. The Clausius–Duhem inequality and the assumption that the Helmholtz free energy is a minimum in equilibrium provide the following restrictions:

$$\mu \geq 0, \quad \alpha_1 \geq 0, \quad |\alpha_1 + \alpha_2| \leq \sqrt{24\mu\beta_3}, \quad \beta_1 = \beta_2 = 0, \quad \beta_3 \geq 0 \tag{3}$$

Thus, Eq. (2) becomes

$$T = -pI + \alpha_1 A_2 + \alpha_2 A_1^2 + [\mu + \beta_3 (\mathrm{tr}\, A_1^2)] A_1$$

where $\mu_{\mathrm{eff}} = \mu + \beta_3 (\mathrm{tr}\, A_1^2)$ is the effective shear-dependent viscosity. The velocity field corresponding to the motion is given as

$$v = v(x, y) = (u(x, y), v(x, y), 0)$$

3 Flow Equations

The basic equations governing the steady plane motion of a homogeneous incompressible fluid of third grade, in the absence of body forces, are [13]

$$\frac{\partial u}{\partial x} + \frac{\partial v}{\partial y} = 0 \tag{4}$$

$$\frac{\partial h}{\partial x} = \rho v \omega - \mu \frac{\partial \omega}{\partial y} - \alpha_1 v \nabla^2 \omega - \beta_3 \frac{\partial (\omega M)}{\partial y} + 2\beta_3 \left(\frac{\partial u}{\partial x}\frac{\partial M}{\partial x} + \frac{\partial v}{\partial x}\frac{\partial M}{\partial y} \right) \tag{5}$$

$$\frac{\partial h}{\partial y} = -\rho u \omega + \mu \frac{\partial \omega}{\partial x} + \alpha_1 u \nabla^2 \omega + \beta_3 \frac{\partial (\omega M)}{\partial x} + 2\beta_3 \left(\frac{\partial u}{\partial y}\frac{\partial M}{\partial x} + \frac{\partial v}{\partial y}\frac{\partial M}{\partial y} \right) \tag{6}$$

where

Contributed by the Fluids Engineering Division of ASME for publication in the JOURNAL OF FLUIDS ENGINEERING. Manuscript received May 2, 2007; final manuscript received January 24, 2008; published online May 19, 2008. Assoc. Editor: Dimitris Drikakis.

Downloaded 03 Jun 2010 to 171.66.16.157. Redistribution subject to ASME license or copyright; see http://www.asme.org/terms/Terms_Use.cfm

$$\omega = \frac{\partial v}{\partial x} - \frac{\partial u}{\partial y}$$

$$h = \frac{\rho q^2}{2} - \alpha_1(u\nabla^2 u + v\nabla^2 v) - (3\alpha_1 + 2\alpha_2)\frac{M}{4} + p$$

$$M = 4\left(\frac{\partial u}{\partial x}\right)^2 + 4\left(\frac{\partial v}{\partial y}\right)^2 + 2\left(\frac{\partial v}{\partial x} + \frac{\partial u}{\partial y}\right)^2 \tag{7}$$

$$q^2 = u^2 + v^2$$

Equations (5) and (6) are nonlinear partial differential equations for three unknowns u, v, and ρ as functions of x and y. In Eqs. (5)–(7), the viscosity μ and the material constants α_1, α_2, β_1, β_2, and β_3 satisfy the constraints given in Eq. (3) [15,16].

Equation (4) implies the existence of a stream function $\psi(x,y)$ such that

$$u = \frac{\partial \psi}{\partial y} \text{ and } v = -\frac{\partial \psi}{\partial x} \tag{8}$$

Equations (4) and (5), on utilizing Eq. (8) and the compatibility condition $\partial^2 h/\partial x \partial y = \partial^2 h/\partial y \partial x$, yield

$$\rho\left(\frac{\partial \psi}{\partial y}\frac{\partial \omega}{\partial x} - \frac{\partial \psi}{\partial x}\frac{\partial \omega}{\partial y}\right) - \alpha_1\left\{\frac{\partial \psi}{\partial y}\frac{\partial(\nabla^2\omega)}{\partial x} - \frac{\partial \psi}{\partial x}\frac{\partial(\nabla^2\omega)}{\partial y}\right\} - \beta_3\left\{\frac{\partial^2(\omega M)}{\partial x^2} + \frac{\partial^2(\omega M)}{\partial y^2}\right\} + 2\beta_3\left\{2\frac{\partial^2 \psi}{\partial x \partial y}\frac{\partial^2 M}{\partial y \partial x} - \frac{\partial^2 \psi}{\partial x^2}\frac{\partial^2 M}{\partial y^2} - \frac{\partial^2 \psi}{\partial y^2}\frac{\partial^2 M}{\partial x^2}\right\} - \mu\nabla^2\omega = 0 \tag{9}$$

where

$$\omega = -\left(\frac{\partial^2 \psi}{\partial x^2} + \frac{\partial^2 \psi}{\partial y^2}\right)$$

$$M = 8\frac{\partial^2 \psi^2}{\partial y \partial x} + 2\left(\frac{\partial^2 \psi}{\partial y^2} - \frac{\partial^2 \psi}{\partial x^2}\right)$$

Let

$$z = x + \iota y \text{ and } \bar{z} = x - \iota y$$

Then, from Stallybrass [17],

$$2\frac{\partial(\bullet)}{\partial \bar{z}} = \frac{\partial(\bullet)}{\partial x} + \iota\frac{\partial(\bullet)}{\partial y}, \quad 2\frac{\partial(\bullet)}{\partial z} = \frac{\partial(\bullet)}{\partial x} - \iota\frac{\partial(\bullet)}{\partial y}$$

$$4\,\mathrm{Im}\left\{\frac{\partial(\bullet)}{\partial \bar{z}}\frac{\partial(\circ)}{\partial z}\right\} = \frac{\partial(\bullet)}{\partial y}\frac{\partial(\circ)}{\partial x} - \frac{\partial(\bullet)}{\partial x}\frac{\partial(\circ)}{\partial y} \tag{10}$$

Equation (9), on utilizing Eq. (10), becomes

$$\mathrm{Im}\left\{\frac{\partial \psi}{\partial \bar{z}}\left(\rho\frac{\partial \omega}{\partial z} - \alpha_1\frac{\partial^3 \omega}{\partial z^2 \partial \bar{z}}\right)\right\} - \mu\frac{\partial^2 \omega}{\partial z \partial \bar{z}} - 2\beta_3\left\{\frac{\partial^2 \psi}{\partial \bar{z}^2}\frac{\partial^2 M}{\partial \bar{z}^2} + \frac{\partial^2 \psi}{\partial z^2}\frac{\partial^2 M}{\partial z^2}\right\} - \beta_3\left\{\frac{\partial^2 \omega}{\partial z \partial \bar{z}}M + \frac{\partial \omega}{\partial z}\frac{\partial M}{\partial \bar{z}} + \frac{\partial \omega}{\partial \bar{z}}\frac{\partial M}{\partial z}\right\} = 0 \tag{11}$$

where

$$\omega = -4\frac{\partial^2 \psi}{\partial z \partial \bar{z}}$$

$$M = 32\frac{\partial^2 \psi}{\partial \bar{z}^2}\frac{\partial^2 \psi}{\partial z^2} \tag{12}$$

4 Solutions

On integrating Eq. (12), we obtain the general form of the exact solutions

$$\psi = -\frac{1}{4}\int\int \omega dz d\bar{z} + A + \bar{A} \tag{13}$$

where A and $\bar{A}$ are complex functions and $\bar{A}$ is the complex conjugate of A.

To determine the solution of Eq. (11), our strategy will be to specify the vorticity function ω and determine the condition, which the functions A and $\bar{A}$ must satisfy. The condition is obtained from Eq. (11) utilizing Eq. (13).

I. When vorticity ω is constant, say, ω_o, then Eq. (13) yields

$$\psi = -\tfrac{1}{4}\omega_{\bigcirc} z\bar{z} + A + \bar{A} \tag{14}$$

Equation (11), on utilizing Eq. (14), yields

$$\beta_3\left(\frac{\partial^4 A}{\partial z^4} + \frac{\partial^4 \bar{A}}{\partial \bar{z}^4}\right) = 0, \quad \frac{\partial^2 A}{\partial z^2} \neq 0, \quad \frac{\partial^2 \bar{A}}{\partial \bar{z}^2} \neq 0$$

When $\beta_3 \neq 0$, then

$$A = \frac{\iota a_1 z^4}{24} + \frac{a_2 z^3}{6} + \frac{a_3 z^2}{2} + a_4 z + a_5 \tag{15}$$

where a_i's are all complex constants. The velocity components u and v are given by

$$u = \frac{\iota\omega_o}{4}(z - \bar{z}) - \iota\left\{-\frac{\iota\overline{a_1 z^3}}{6} + \frac{\overline{a_2 z^2}}{3} + \overline{a_3 z} + \overline{a_4} - \frac{\iota a_1 z^3}{6} - \frac{a_2 z^2}{3} - a_3 z - a_4\right\}$$

$$v = \frac{\omega_o}{4}(z + \bar{z}) - \left\{\frac{\iota a_1 z^3}{6} + \frac{a_2 z^2}{3} + a_3 z + a_4 - \frac{\iota\overline{a_1 z^3}}{6} + \frac{\overline{a_2 z^2}}{3} + \overline{a_3 z} + \overline{a_4}\right\}$$

Equation (14), on utilizing Eq. (15), yields

$$\psi = -\frac{\omega_o z\bar{z}}{4} + \frac{\iota(a_1 z^4 - \overline{a_1 z^4})}{24} + \frac{(a_2 z^3 + \overline{a_2 z^3})}{6} + \frac{(a_3 z^2 + \overline{a_3 z^2})}{2} + (a_4 z + \overline{a_4 z}) + a \tag{16}$$

where $a = a_5 + \overline{a_5}$.

The stream function ψ in Eq. (16) is represented graphically in Fig. 1 with $\omega_0 = -1$, $a_1 = 1 + 2\iota$, $a_2 = 1 + \iota$, $a_3 = 1 + 5\iota$, $a_4 = 2 + 0.5\iota$, $a = 2$, and $x, y \in [-1, 1]$.

When $\beta_3 = 0$, then Eq. (15) is identically satisfied and the complex A becomes arbitrary, due to which A enables us to construct a large number of stream function ψ and hence a large number of solutions to the flow equations. We mention that by taking $\omega = 0$ or appropriately choosing complex constants a_3, a_4, a_5, and $a_1 = 0 = a_2$ in Eq. (15), or by taking $A = \iota a \log z$ (for $\beta_3 = 0$), we get all the solutions of Moro et al. [13].

Furthermore, if we take the function $A = (c_1 + \iota c_2)z^2$ or $A = (c_1 + \iota c_2)\ln z$ and choose appropriately the constants or apply the appropriate boundary conditions, we get the plane Couette flow, the flow due to a spiral vortex at the origin and the flows having streamlines as a family of ellipses, concentric circles, and rectangular hyperbolas.

Downloaded 03 Jun 2010 to 171.66.16.157. Redistribution subject to ASME license or copyright; see http://www.asme.org/terms/Terms_Use.cfm

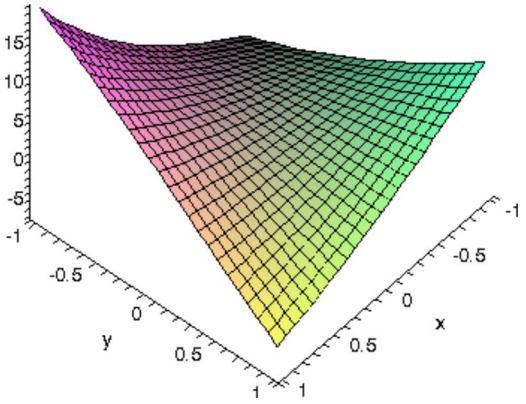

Fig. 1 Graphical representation of Eq. (16)

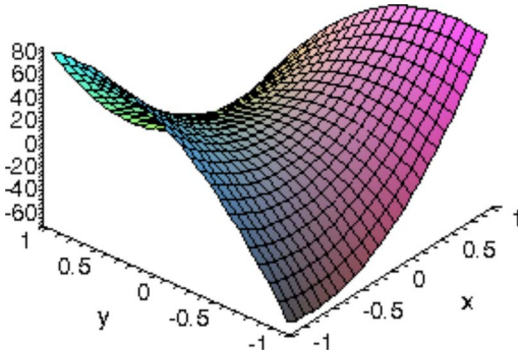

Fig. 2 Graphical representation of Eq. (19)

II. When ω is nonconstant, the solutions of Eq. (11) are determined as follows:

(i) When $\omega = m_1 z + \overline{m_1 z}$, Eq. (11) yields

$$\begin{aligned}\mathrm{Im}\left\{-\frac{m_1^2 z^2}{8}+m_1\frac{\partial \bar{A}}{\partial \bar{z}}\right\} &= \lambda\left\{6m_1\overline{m_1}(m_1 z+\overline{m_1}\bar{z})-8\left(m_1^2\frac{\partial^2\bar{A}}{\partial\bar{z}^2}+\overline{m_1^2}\frac{\partial^2 A}{\partial z^2}\right)\right.\\ &-16\left(m_1^2\bar{z}\frac{\partial^3\bar{A}}{\partial\bar{z}^3}+\overline{m_1^2}z\frac{\partial^3 A}{\partial z^3}\right)+64\left(m_1\frac{\partial^3\bar{A}}{\partial\bar{z}^3}\frac{\partial^2 A}{\partial z^2}\right.\\ &\left.\left.+\overline{m_1}\frac{\partial^3 A}{\partial z^3}\frac{\partial^2\bar{A}}{\partial\bar{z}^2}\right)+64\frac{\partial^3 A}{\partial z^3}\frac{\partial^3\bar{A}}{\partial\bar{z}^3}(m_1 z+\overline{m_1 z})\right\}\end{aligned} \tag{17}$$

where $\lambda = \beta_3/\rho$, and m_1 is the complex constant. The left-hand side (LHS) of Eq. (17) suggests to assume

$$\frac{\partial \bar{A}}{\partial \bar{z}} = \lambda_1\bar{z}^2+\lambda_2\bar{z}+\lambda_3$$

This, on putting in Eq. (17), gives

$$\lambda_1 = -\frac{\overline{m_1^2}}{8m_1},\quad \lambda_2 = 40\iota\lambda\overline{m_1^2},\quad \lambda_3 = 0$$

The solution of Eq. (17), therefore, is

$$A = -\frac{m_1^2 z^3}{24\overline{m_1}} - 20\iota\lambda m_1^2 z^2 + m_2 \tag{18}$$

where m_2 is a complex constant. Equation (13), using Eq. (18), becomes

$$\begin{aligned}\psi = &-\frac{z\bar{z}}{8}(m_1 z+\overline{m_1 z})-\frac{(m_1^3 z^3+\overline{m_1^3 z^3})}{24m_1\overline{m_1}}\\ &+20\iota\lambda(\overline{m_1^2 z^2}-m_1^2 z^2)+m\end{aligned} \tag{19}$$

where $m = m_2 + \overline{m_2}$.

The stream function ψ in Eq. (19) is represented graphically in Fig. 2 with $m_1 = 1+2\iota$, $m=1$, $\lambda = 0.3$, and $x, y \in [-1, 1]$.

(ii) For $\omega = B(z+\bar{z})$, the constant B being real, Eq. (11) becomes

$$\begin{aligned}\mathrm{Im}\left\{-\frac{Bz^2}{8}+\frac{\partial\bar{A}}{\partial\bar{z}}\right\} &= \lambda\left\{6B^2(z+\bar{z})-8B\left(\frac{\partial^2 A}{\partial z^2}+\frac{\partial^2\bar{A}}{\partial\bar{z}^2}\right)\right.\\ &-16B\left(\bar{z}\frac{\partial^3\bar{A}}{\partial\bar{z}^3}+z\frac{\partial^3 A}{\partial z^3}\right)\\ &+64\left(\frac{\partial^2 A}{\partial z^2}\frac{\partial^3\bar{A}}{\partial\bar{z}^3}+\frac{\partial^2\bar{A}}{\partial\bar{z}^2}\frac{\partial^3 A}{\partial z^3}\right)+64\frac{\partial^3 A}{\partial z^3}\frac{\partial^3\bar{A}}{\partial\bar{z}^3}(z+\bar{z})\\ &-4B\left(z^2\frac{\partial^4 A}{\partial z^4}+\bar{z}^2\frac{\partial^4\bar{A}}{\partial\bar{z}^4}\right)+32\left(z\frac{\partial^2\bar{A}}{\partial\bar{z}^2}\frac{\partial^4 A}{\partial z^4}\right.\\ &\left.\left.+\bar{z}\frac{\partial^2 A}{\partial z^2}\frac{\partial^4\bar{A}}{\partial(\bar{z})^4}\right)-\frac{64}{B}\left(\frac{\partial^2 A^2}{\partial z^2}\frac{\partial^4\bar{A}}{\partial\bar{z}^4}+\frac{\partial^2\overline{A^2}}{\partial\bar{z}^2}\frac{\partial^4 A}{\partial z^4}\right)\right\}\end{aligned} \tag{20}$$

The LHS of Eq. (20) suggests $\partial\bar{A}/\partial\bar{z}$ to be a polynomial in $\bar{z}$ of degree 2 and therefore on substituting

$$\frac{\partial\bar{A}}{\partial\bar{z}} = l_1\bar{z}^2+l_2\bar{z}+\lambda_4$$

In Eq. (20), we get

$$l_1 = -\frac{B}{8},\quad l_2 = 40\iota\lambda B^2,\quad \lambda_4 = 0$$

Hence,

$$\bar{A} = -\frac{B\overline{z^3}}{24}+20\iota\lambda B^2\bar{z}+m_3 \tag{21}$$

where m_3 is an arbitrary complex constant.

Using Eq. (21), Eq. (13) implies

$$\psi = -\frac{Bz\bar{z}}{8}(z+\bar{z})-\frac{B}{24}(z^3+\overline{z^3})+20\iota B^2\lambda(\bar{z}-z)+n \tag{22}$$

where $n = m_3 + \overline{m_3}$.

The stream function ψ in Eq. (22) is represented graphically in Fig. 3 with $B=-2$, $\lambda=2$, $n=1$, and $x \in [-10, 10]$, $y \in [0, 10]$.

(iii) When $\omega = D(z+\bar{z}+E)$, D and E being real, then Eq. (11) yields

Downloaded 03 Jun 2010 to 171.66.16.157. Redistribution subject to ASME license or copyright; see http://www.asme.org/terms/Terms_Use.cfm

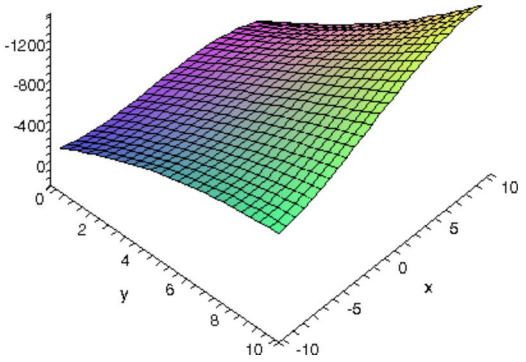

Fig. 3 Graphical representation of Eq. (22)

$$\mathrm{Im}\left\{-\frac{Dz^2}{8}-\frac{DEz}{4}+\frac{\partial\bar{A}}{\partial\bar{z}}\right\}$$
$$=\lambda\left\{6D^2(z+\bar{z})-8D\left(\frac{\partial^2 A}{\partial z^2}+\frac{\partial^2\bar{A}}{\partial\bar{z}^2}\right)-16D\left(z\frac{\partial^3 A}{\partial z^3}+\bar{z}\frac{\partial^3\bar{A}}{\partial\bar{z}^3}\right)+64\left(\frac{\partial^2 A}{\partial z^2}\frac{\partial^3\bar{A}}{\partial\bar{z}^3}+\frac{\partial^2\bar{A}}{\partial\bar{z}^2}\frac{\partial^3 A}{\partial z^3}\right)\right.$$
$$+64\left(z\frac{\partial^3 A}{\partial z^3}\frac{\partial^3\bar{A}}{\partial\bar{z}^3}+\bar{z}\frac{\partial^3 A}{\partial z^3}\frac{\partial^3\bar{A}}{\partial\bar{z}^3}\right)+4D^2E$$
$$+64E\frac{\partial^3 A}{\partial z^3}\frac{\partial^3\bar{A}}{\partial\bar{z}^3}-4D\left(\bar{z}^2\frac{\partial^4\bar{A}}{\partial\bar{z}^4}+z^2\frac{\partial^4 A}{\partial z^4}\right)$$
$$-\frac{64}{D}\left(\frac{\partial^2 A^2}{\partial z^2}\frac{\partial^4\bar{A}}{\partial\bar{z}^4}+\frac{\partial^2\overline{A^2}}{\partial\bar{z}^2}\frac{\partial^4 A}{\partial z^4}\right)$$
$$\left.+32\left(\frac{\partial^2\overline{A^2}}{\partial\bar{z}^2}\frac{\partial^4 A}{\partial z^4}+\frac{\partial^2 A^2}{\partial z^2}\frac{\partial^4\bar{A}}{\partial\bar{z}^4}\right)\right\}$$

Following the same procedure as that of the previous case, we find

$$\bar{A}=-\frac{D\overline{z^3}}{24}-\frac{DE\overline{z^2}}{8}+20\iota\lambda D^2\overline{z^2}+20\iota\lambda D^2E\bar{z}+m_4 \tag{23}$$

where m_4 is an arbitrary complex constant.

Using Eq. (23), Eq. (13) becomes

$$\psi=-\frac{Dz\bar{z}}{8}(z+\bar{z}+2E)-\frac{D}{24}(z^3+\overline{z^3})-\frac{DE}{8}(z^2+\overline{z^2})+20\iota\lambda D^2(\overline{z^2}-z^2)+20\iota\lambda D^2E(\bar{z}-z)+q \tag{24}$$

where $q=m_4+\overline{m_4}$.

The stream function ψ in Eq. (24) is represented graphically in Fig. 4 with $D=E=1$, $\lambda=2$, $q=-1$, and $x,y\in[-10,10]$.

(iv) When $\omega=B\iota(z-\bar{z})$, then Eq. (11) is satisfied provided

$$\bar{A}=-\frac{B\iota\overline{z^3}}{24}-20\iota\lambda B^2\overline{z^3}+m_5$$

where m_5 is an arbitrary complex constant and the stream function ψ is given by

$$\psi=-\frac{B\iota}{8}z\bar{z}(z-\bar{z})+\frac{B\iota}{24}(z^3-\overline{z^3})+20\iota\lambda B^2(z^3-\overline{z^3})+r \tag{25}$$

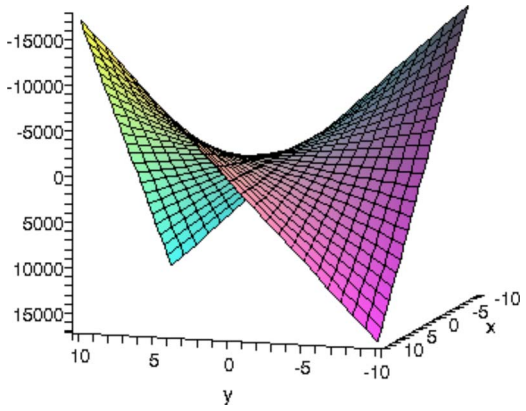

Fig. 4 Graphical representation of Eq. (24)

where $r=m_5+\overline{m_5}$.

The stream function ψ in Eq. (25) is represented graphically in Fig. 5 with $B=-5$, $\lambda=3$, $r=10$, and $x\in[-2,10]$, $y\in[0,8]$.

(v) For $\omega=B\ln(z\bar{z})+D_1$, Eq. (11) is satisfied provided

$$\bar{A}=m_6\ln\bar{z}+m_7 \tag{26}$$

where m_6, B, and D_1 are real constants and m_7 is a complex arbitrary constant.

According to Eq. (26), the stream function ψ becomes

$$\psi=-\frac{B}{4}z\bar{z}\{\ln(z\bar{z})-2\}-\frac{D_1}{4}z\bar{z}+m_6\ln(z\bar{z})+s \tag{27}$$

where $s=m_7+\overline{m_7}$.

The stream function ψ in Eq. (27) is represented graphically in Fig. 6 with $m_6=2$, $s=4$, and $x\in[-10,2]$, $y\in[-1,2]$.

The stream function ψ in Eq. (27) represents the motion whose streamlines are concentric circles with constant speed along each streamline for the appropriate choice of the constants.

(vi) When $\omega=Bz\bar{z}$, B being real constant, then Eq. (11) is satisfied provided

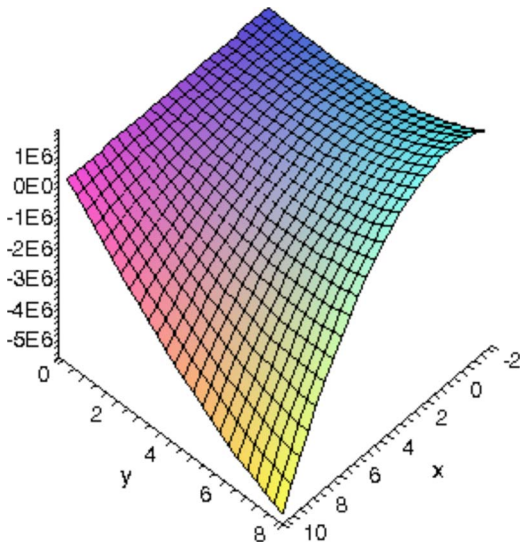

Fig. 5 Graphical representation of Eq. (25)

Downloaded 03 Jun 2010 to 171.66.16.157. Redistribution subject to ASME license or copyright; see http://www.asme.org/terms/Terms_Use.cfm

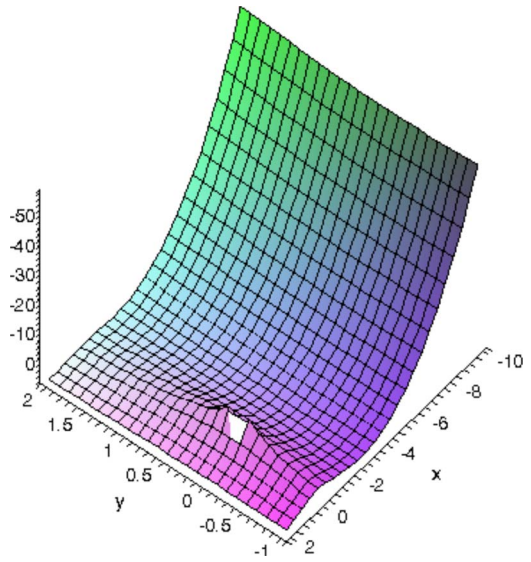

Fig. 6 Graphical representation of Eq. (27)

$$\bar{A} = \frac{\iota\mu}{\rho} \ln \bar{z} + m_8 \tag{28}$$

where m_8 is a complex constant.

According to Eq. (28), the stream function ψ becomes

$$\psi = -\frac{B}{16}(z\bar{z})^2 - \frac{\iota\mu}{\rho} \ln\left(\frac{z}{\bar{z}}\right) + t \tag{29}$$

where $t = m_8 + \overline{m_8}$.

The stream function ψ in Eq. (29) is represented graphically in Fig. 7 with $B=1$, $\mu=12$, $\rho=1$, $t=2$, and $x, y \in [-1, 10]$.

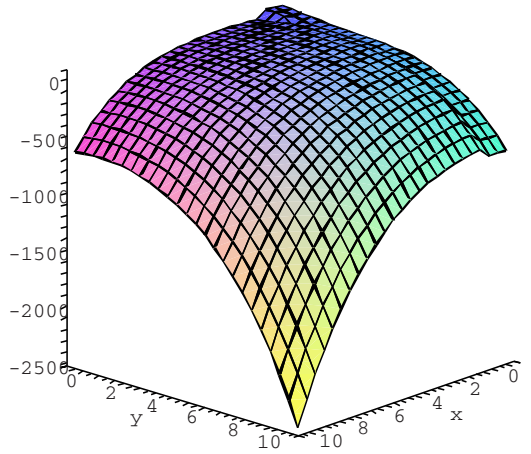

Fig. 7 Graphical representation of Eq. (29)

5 Conclusions

In this paper, we reconsidered the flow equations of Moro et al. [13] with the objective of determining some exact solutions.

For this purpose, the vorticity function ω and the stream function ψ are expressed in terms of complex variables and complex function. The condition which the complex functions must satisfy is determined through the equations for the generalized energy function h by using the compatibility condition $\partial^2 h/\partial x \partial y = \partial^2 h/\partial y \partial x$.

Some exact solutions to the flow equations are determined using the condition for the complex functions. The solutions presented in this paper admit, as particular cases, all the solutions of Moro et al. [13] by appropriately choosing the complex functions or the arbitrary constants therein.

Acknowledgment

I wish to thank the reviewers for their valuable comments and suggestions, which significantly improved this paper. I am also thankful to Professor C. Fetecau (Romania) and Professor D. Vieru (Romania) for productive scientific discussions and valuable suggestions.

References

[1] Rajagopal, K. R., 1984, "On the Creeping Flow of the Second-Order Fluid," J. Non-Newtonian Fluid Mech., **15**, pp. 239–246.
[2] Erdogan, M. E., 1995, "Plane Surface Suddenly Set in Motion in a Non-Newtonian Fluid," Acta Mech., **108**, pp. 179–187.
[3] Rajagopal, K. R., and Gupta, A. S., 1984, "An Exact Solution for a Flow of a Steady Flows of a Non-Newtonian Fluid Past an Infinite Porous Plate," Meccanica, **19**, pp. 158–160.
[4] Bandelli, R., 1995, "Unsteady Unidirectional Flows of Second Grade Fluids in Domains With Heated Boundaries," Int. J. Non-Linear Mech., **30**, pp. 263–269.
[5] Siddiqui, A. M., and Kaloni, P. N., 1986, "Certain Inverse Solutions of a Non-Newtonian Fluid," Int. J. Non-Linear Mech., **21**, pp. 459–473.
[6] Benharbit, A. M., and Siddiqui, A. M., 1992, "Certain Solutions of the Equations of the Planar Motion of a Second Grade Fluid for Steady and Unsteady Cases," Acta Mech., **94**, pp. 85–96.
[7] Ariel, P. D., 1994, "The Flow of a Viscoelastic Fluid Past a Porous Plate," Acta Mech., **107**, pp. 199–204.
[8] Ariel, P. D., 2003, "Flow of a Third Grade Fluid Through a Porous Flat Channel," Int. J. Eng. Sci., **41**, pp. 1267–1285.
[9] Fetecau, C., 1977, "Cone and Plate Flow of a Second Grade," Acta Mech., **122**, pp. 225–230.
[10] Hayat, T., Kara, A. H., and Momoniat, E., 2003, "Exact Flow of a Third Grade Fluid on a Porous Wall," Int. J. Non-Linear Mech., **38**, pp. 1533–1537.
[11] Hayat, T., Wang, Y., and Hutter, K., 2004, "Hall Effects on the Unsteady Hydromagnetic Oscillatory Flow of a Second Grade Fluid," Int. J. Non-Linear Mech., **39**, pp. 1027–1037.
[12] Hayat, T., Khan, M., Siddiqui, A. M., and Asghar, S., 2004, "Transient Flows of a Second Grade Fluid," Int. J. Non-Linear Mech., **39**, pp. 1621–1633.
[13] Moro, L., Siddiqui, A. M. and Kaloni, P. N., 1990, "Steady Flows of a Third Grade Fluid by Transformation Methods," ZAMM, **70**(3), pp. 189–198.
[14] Rivlin, R. S., and Ericksen, J. L., 1955, "Stress-Deformation Relations for Isotropic Materials," J. Rational Mech. Anal., **4**, pp. 323–425.
[15] Fosdic, R. L., and Rajagopal, K. R., 1980, "Thermodynamics and Stability of Fluids of Third Grade," Proc. R. Soc. London, Ser. A, **339**, pp. 351–377.
[16] Truessdell, C., and Noll, W., 1965, "The Non-Linear Field Theories of Mechanics," in *Handbuch der physik III, No. 3*, Springer, Berlin, pp. 494–513.
[17] Stallybrass, M. P., 1983, "A Class of Exact Solution of the Navier-Stokes Equations. Plane Unsteady Flow," Lett. Appl. Eng. Sci., **21**(2), pp. 179–186.

Downloaded 03 Jun 2010 to 171.66.16.157. Redistribution subject to ASME license or copyright; see http://www.asme.org/terms/Terms_Use.cfm

Passive Control of Transonic Cavity Flow

David G. MacManus
e-mail: d.g.macmanus@cranfield.ac.uk

Diane S. Doran

Department of Aerospace Sciences,
Cranfield University,
Wharley End,
Bedfordshire MK43 0AL, UK

Open cavities at transonic speeds can result in acoustic resonant flow behavior with fluctuating pressure levels of sufficient intensity to cause significant damage to internal stores and surrounding structures. Extensive research in this field has produced numerous cavity flow control techniques, the more effective of which may require costly feedback control systems or entail other drawbacks such as drag penalties or rapid performance degradation at off-design condition. The current study focuses on the use of simple geometric modifications of a rectangular planform cavity with the aim of attenuating the aeroacoustic signature. Experiments were performed in an intermittent suck-down transonic wind tunnel by using a typical open flow rectangular planform cavity, which was modularly designed such that the leading and trailing edge geometries could be modified by using a family of inserts. The current work focused on a variety of recessed leading edge step arrangements. Configurations were tested at transonic Mach numbers spanning the range Mach 0.7–0.9, and unsteady pressure measurements were recorded at various stations within the cavity in order to obtain acoustic spectra. The most effective configuration at Mach 0.9 was the leading edge step employing a step height to step length ratio of 0.4. This configuration achieved a tonal attenuation of up to 18.6 dB and an overall sound pressure level (OASPL) reduction of approximately 7.5 dB. This is a significant level of noise suppression in comparison with other passive control methods. In addition, it offers the additional benefits of being a simple geometric feature, which does not rely on placing flow effectors into the high-speed grazing flow.
[DOI: 10.1115/1.2917427]

Introduction

The high intensity resonant flow behavior inherent to the unsteady aerodynamics encountered within cavity flows under high-speed conditions is renowned to cause significant damage to internal stores and surrounding structures [1]. Indeed, for a typical open-cavity flow, the acoustic signature can achieve levels of over 165 dB [2–5]. The resulting impact on internal stores of high-speed aircraft has led to extensive studies to attenuate the unsteady flow and the examination of a broad range of flow control strategies [3,4,6–12]. These comprise both active and passive control methods and have met with mixed success. Indeed, some of these methods (such as spoilers) have been adopted in service. However, as there is an ever pressing drive for aircraft stealth and internalized stores, there remains an ongoing interest in furthering the understanding of open-cavity aerodynamics and potential robust flow control technologies.

Contributed by the Fluids Engineering Division of ASME for publication in the JOURNAL OF FLUIDS ENGINEERING. Manuscript received April 13, 2007; final manuscript received March 26, 2008; published online May 19, 2008. Assoc. Editor: Phillip M. Ligrani.

The flow physics fundamentally depends on the cavity length to depth aspect ratio (l/d) and encompasses closed, transitional, and open-cavity regimes [1,13,14]. The unsteady aerodynamics encountered for open flows, in which the shear layer bridges the cavity, is characterized by the presence of internal acoustic modes. The associated frequency peaks can be readily observed by investigating the acoustic spectra. The semi-empirical modified Rossiter equation (Eq. (1)) is used to predict the acoustic mode frequencies within a rectangular open-cavity flow [14,15]:

$$\mathrm{St} = f_m \frac{l}{U_\infty} = \frac{m-\alpha}{M_\infty \left(1+\frac{\gamma-1}{2}M_\infty^2\right)^{-0.5}} + \frac{1}{K} \tag{1}$$

where f_m is the frequency of a given longitudinal acoustic mode, m is the mode number, and α and K are empirical constants. α is a function of the cavity length to depth ratio and is related to the phase between the vortices within the shear layer and the upstream traveling pressure waves within the cavity. K is a function of freestream Mach number and is defined as the relative speed of the propagation of the vortices within the shear layer to the velocity of the freestream flow. Although this expression can be used to predict the modal frequencies, it does not predict the magnitude of the peaks. A variety of researchers have proposed models of the underlying flow physics, which generate such aeroacoustic characteristics [2,11,14,16,17]. Most of these highlight the interaction of the pressure waves within the cavity and the vortical structures within the cavity shear layer coupled with an internal feedback mechanism arising from the shear layer interaction with the cavity trailing edge.

Previous control technologies have delivered attenuation of both tonal peaks and broadband noise [3,4,14] although some of the most successful methods require complex flow modulation methods [9]. The aim of the current work is to assess the effect of novel modest geometric changes, which have the objective of disrupting the interaction of cavity internal and shear layer flow and the fundamental internal feedback mechanism. To this end, a variety of simple leading edge step configurations for a rectangular open cavity have been examined in this work.

Experimental Method

Facility and Instrumentation. The experimental work was conducted by using an intermittent suck-down transonic wind tunnel with working section dimensions of 63.5 mm wide and 60 mm high. The tunnel is connected to a vacuum tank, and the working section Mach number is controlled by using a downstream throat. The inlet air at atmospheric temperature and pressure is drawn through an alumina bed in order to dry the flow and the stabilised run time was typically 30 s. The cavity was built into the fixed working section upper liner. The lower liner contained slanted perforations providing 13% porosity leading to a ventilated lower cavity. The lower liner was inclined by 2 deg to counteract the boundary layer growth in the working section and to deliver a nominally pressure gradient. The static pressure gradient ($\Delta p/P_0$) in the working section was measured for the range of Mach numbers and was found to have a favorable pressure gradient of 0.5% in the worst case across the region of interest.

The operating Mach number was calibrated for a reference filled cavity configuration and determined from the working section total and static pressures. These pressures were measured by using a Druck PDCR22 15 PSI differential transducer, which was sampled at 300 Hz for 5 s to obtain an average reading. An array of up to six pressure transducers (Kulite XCS-190-15A 15 PSI absolute) was used to obtain the unsteady data, which was sampled at 20 kHz to obtain 2^{16} samples by using a 16 bit DAQ card. The Kulites are positioned on the cavity forward and rear faces and along the cavity floor centerline. The unsteady pressure signal is divided into 31 blocks of 4096 samples with a 50% overlap. Each block is windowed by using the Hanning function,

 Copyright © 2008 by ASME

Downloaded 03 Jun 2010 to 171.66.16.157. Redistribution subject to ASME license or copyright; see http://www.asme.org/terms/Terms_Use.cfm

Table 1 Working section boundary layer characteristics

Mach number	δ_{99} (mm)	δ^* (mm)	θ (mm)	H	$\mathrm{Re}_\delta{}^*$
0.90	3.28	0.76	0.44	1.72	13,500
0.86	3.35	0.75	0.44	1.71	12,500

and the resultant signal is analyzed by using a fast Fourier transform with a power correction to counteract the windowing. The 31 data blocks are then averaged to create an ensemble average for the entire signal. This provides a frequency resolution of 4.88 Hz.

The reference turbulent boundary layer was measured by using a flat-head Pitot probe (1.07 mm $\times$ 0.37 mm) in the tunnel working section without the cavity present. Boundary layer traverses were taken at a location that corresponds to a position of 36 mm behind the cavity leading edge. The measurements are summarized in Table 1 for which the average stagnation pressure and temperature in the settling chamber were 9.89×10^4 Pa and 298 K, respectively.

Experimental Accuracy. The Mach number is calculated from the total to static pressure ratio, and on average for the reported nominal Mach number, it is estimated to be within ±0.01. The unsteady pressure data were acquired by using the Kulite sensor, which the manufacturer quotes as having a natural frequency of approximately 200 kHz with valid data being obtainable from a static calibration at up to 20% of the resonant natural frequency, i.e., 40 kHz. The quoted typical transducer combined linearity, hysteresis, and repeatability error is $\pm0.1\%$ full-scale output. In addition, the static calibration standard was estimated to have an uncertainty of $\pm0.13\%$. Based on these bias errors and a statistical analysis of the measurements, the OASPL is estimated to have an uncertainty of ±0.4 dB, and the typical mode peaks have a SPL uncertainty of ±2.5 dB. The total uncertainty on the boundary layer traverse positioning was 0.11 mm.

Model Configurations. The cavity is of a modular construction enabling modification of the leading and trailing edge geometries by using a family of inserts. The datum rectangular cavity dimensions comprise length (l) 100 mm, width (w) 25 mm, and depth (d) 20 mm. For the Mach number range under consideration ($0.7<M<0.9$), the flow field was therefore classified as an open-cavity flow [1]. The inserts comprise leading edge steps employing step height (h) to cavity depth (d) ratios of 0.3, 0.145, and 0.1 for a fixed step length (s) of 15 mm. A schematic of the step configuration is illustrated in Fig. 1.

The step configurations were designed primarily to disrupt shear flow and internal cavity flow interaction at the leading edge at which the shear layer is most susceptible to disturbances [6]. Such disruption would minimize oscillatory shear layer excitement and hence disrupt the internal cavity oscillation feedback mechanism at the cavity trailing edge generated by oscillatory impingement of the shear layer on the cavity trailing edge.

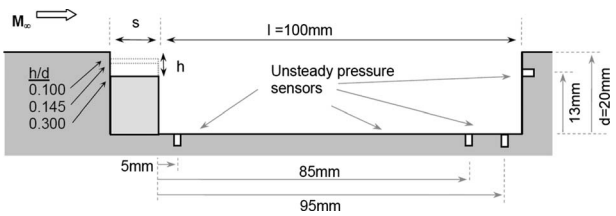

Fig. 1 Schematic of cavity streamwise cross section illustrating leading edge step cavity configuration and instrumentation positions

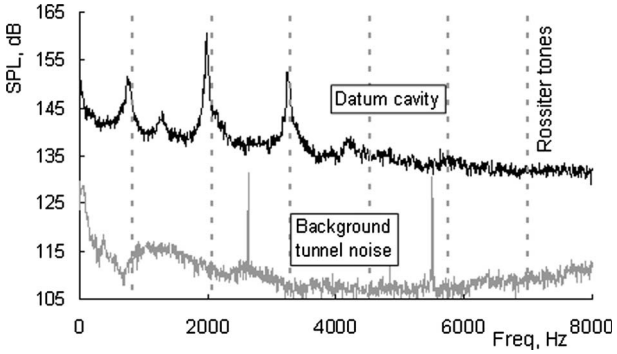

Fig. 2 SPL spectra for datum rectangular cavity ($l/d=5$, $w/d=1.25$) measured on the rear wall at Mach 0.9

The leading edge step configurations were designed based on the reattachment length characteristics for a backward facing step [1,18,19]. The designs are arranged to span the regime where, for a simple backward facing step, the flow would reattach onto the downstream face. Associated literature reports that for an isolated backward facing step, the reattachment line occurs at a downstream distance of approximately x/h of 6–9 [18,19]. However, this is dependent on Reynolds number, Mach number, and the approaching boundary layer characteristics [1]. Clearly, the proposed geometry is different for the cavity flow due to the forward propagating reflected pressure waves and the recirculating flow, which is characteristic of the datum cavity configuration. Nevertheless, these simple reattachment guidelines are used as a reference point for the leading edge steps. It is postulated that the depth to length ratio (h/s) of the step needs to be sufficiently large to avoid a simple reattachment on the step face to facilitate a disruption in the feedback mechanism. Based on these simple guidelines, a set of three step sizes was tested; $h/s=0.4$, in which the shear flow is not expected to reattach to the step face, and $h/s=0.193$ and 0.133, in which the shear flow may reattach on the step face according to a loose application of the backward facing step research mentioned above.

Results and Discussion

Datum Cavity. The SPL spectra obtained for the datum rectangular cavity configuration ($l/d=5$) show reasonable agreement with the estimated Rossiter frequencies based on $\alpha=0.32$ and $K=0.67$ (Fig. 2). The level of difference is similar to that reported by previous researchers under similar conditions [20]. As observed in previous research [2,3,5,21], the second mode has the highest SPL level of approximately 162 dB and in this case, the first three modes are clearly visible. Although the higher tones are not discernible, it is expected that the observed unsteady flow characteristics are sufficient to diagnose any notable effect of the geometric changes on the flow field. The minor resonance observed at 1200 Hz is not predicted by the Rossiter equation (Eq. (1)) and is currently unexplained although it is not observed for a reference working section study with no cavity present. The tunnel background noise signature was measured without the cavity present and the SPL spectrum at Mach 0.9 is also shown in Fig. 2. The background SPL across the spectrum is typically approximately 110 dB with two very narrow peaks at about 2600 Hz and 5500 Hz. These are not observed in the cavity case and Fig. 2 clearly highlights the relative effect of the cavity on the pressure signature. Similar levels of background noise were also found at Mach 0.7 and 0.86.

Effect of Leading Edge Steps. The two leading edge step configurations ($h/s=0.4$ and 0.193), distinguished by their expected shear layer step face reattachment characteristics, produce intrigu-

Downloaded 03 Jun 2010 to 171.66.16.157. Redistribution subject to ASME license or copyright; see http://www.asme.org/terms/Terms_Use.cfm

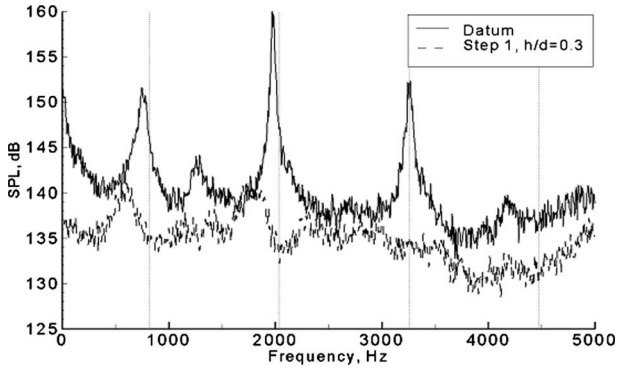

Fig. 3 Comparison of sound pressure level spectra obtained for the datum rectangular cavity and the leading edge step (h/s=0.4, h/d=0.3) configuration at Mach

ingly different sound pressure level attenuation characteristics. The largest leading edge step (h/s=0.4, h/d=0.3) has a significant effect on the unsteady aerodynamics with a notable attenuation of both the modal peaks and the broadband sound pressure level. This is most apparent at Mach 0.90 where all three observed tones are strongly attenuated by the step (Fig. 3). Superposition of the recorded spectra with those of the datum rectangular cavity illustrates the significant attenuation of sound pressure levels (Fig. 3). Indeed, the SPL peak for the second mode is reduced by 20 dB relative to the datum cavity, which, along with a reduction in broadband noise, results in an OASPL reduction of 7.6 dB. This is a significant level of noise attenuation achieved through a minor geometric modification. There are two pressure sensors on this face placed on either side of the centerline ($z/w = \pm 0.22$)—in these reported cases, there are no significant differences between the pair of pressure sensors. The step also has the effect of decreasing the frequency, and the fundamental first peak is reduced by approximately 19%. By considering the change in the maximum l/d when the step is included, the α term in the Rossiter equation is increased as well as the characteristic length in the Strouhal number. Relative to the datum cavity, both of these effects reduce the expected fundamental frequency by 19%, which is in agreement with the measured reduction.

Effect of Step Height. For the smallest step size of h/s =0.133 (h/s=0.1), in which the shear flow may be expected to reattach on the step face, the attenuation is less prodigious although there is still a 9.2 dB peak reduction in the largest tone SPL and a 3.1 dB reduction in the OASPL (Fig. 4(d)). However, the interaction of this smaller step with the flow field results in a curious SPL signature in which there is an additional SPL peak positioned at 4115 Hz. This does not exactly equate to a Rossiter tone and is not observed in the datum cavity (Fig. 4(a)) or background noise (Fig. 2). For this configuration, it is expected that the primary shear flow reattaches to the step face, which is confirmed by oil flow visualization studies. In addition, for a slightly larger step h/s=0.193 (h/d=0.145), the strongest second mode is almost completely attenuated although there are now a series of minor peaks between 1600 Hz and 2200 Hz. Furthermore, the third mode is unaffected, and the additional fourth SPL peak is also observed (Fig. 4(c)). Overall, the OASPL is reduced by 4.7 dB. The achieved mode peak attenuation mostly increases with increasing step size although there is a significant improvement in performance for the largest step (Table 2). In addition, the level of attenuation varies slightly along the length of the cavity although the relative ordinal performance of the steps remains unchanged (Fig. 5).

Oil flow visualization studies indicate that the smaller steps (h/d=0.1,0.145) do not significantly alter the flow field in comparison with the datum rectangular cavity. The visualizations indicate that the attenuation achieved by the largest step (h/d =0.30) may be related to a large recirculation bubble, which sits on top of the step. It is postulated that this separation bubble results in the outward deflection of the approaching boundary layer. It is known from previous flow control studies that an outward deflection of the shear layer can result in acoustic attenuation [22].

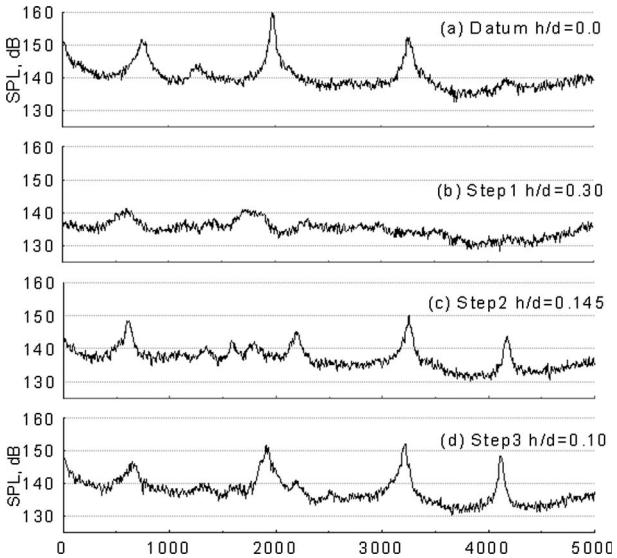

Fig. 4 Sound pressure level spectra for the datum rectangular cavity (a) and each of the leading edge step configurations (b)–(d) recorded at the cavity rear face for Mach 0.9

Effect of Mach Number. Although the large leading edge step (h/s=0.4, h/d=0.3), has a very notable impact on the unsteady flow characteristics at Mach 0.9, additional results at lower transonic speeds show that this attenuation mechanism is sensitive to Mach number. This is a little unexpected considering that the fundamental flow field associated with a backward facing step in

Table 2 Sound pressure level attenuation (dB) relative to the datum cavity at Mach 0.90

	Mode		
Configuration	1	2	3
Step 1, h/d=0.30	10.5	20.0	15.8
Step 2, h/d=0.15	3.1	17.1	2.2
Step 3, h/d=0.10	4.8	9.2	0.4

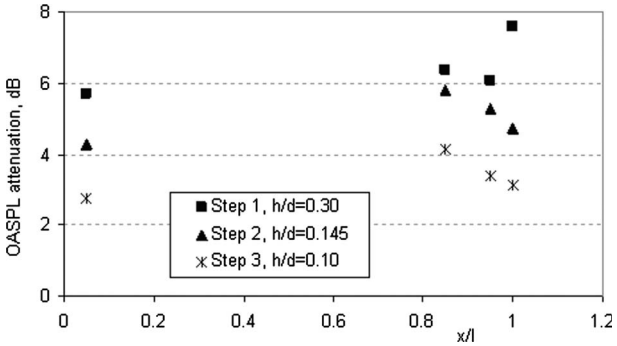

Fig. 5 OASPL attenuation relative to the datum cavity at Mach 0.90 for Steps 1–3

Downloaded 03 Jun 2010 to 171.66.16.157. Redistribution subject to ASME license or copyright; see http://www.asme.org/terms/Terms_Use.cfm

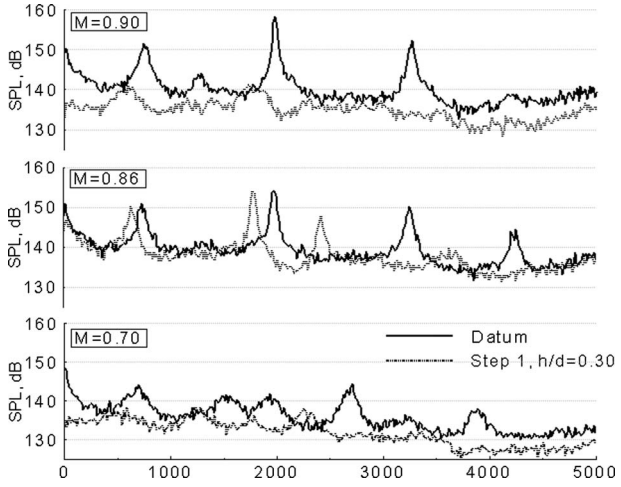

Fig. 6 Sound pressure level spectra obtained for the datum rectangular cavity and leading edge step (h/s=0.4, h/d=0.3) configurations at Mach 0.9, 0.86, and 0.7; measurements on the cavity rear face

transonic flow is primarily Mach number insensitive over the range tested [18,19]. Nevertheless, the effectiveness of the step is curtailed at lower Mach numbers. Overall, the largest step still has an impact on the SPL signature at the lower transonic Mach numbers but the peak attenuation is modest and the OASPL is only reduced by approximately 1.4 dB at Mach 0.86 (Fig. 6). However, at Mach 0.70, the OASPL attenuation improves to approximately 4.6 dB. Furthermore, at Mach 0.86, an additional peak occurs at approximately 2500 Hz when the step is included along with a reduction in the second tone frequency from approximately 200 Hz to 1800 Hz.

Conclusions

The datum rectangular cavity configuration exhibited the expected flow features with OASPLs of up to 174 dB recorded on the back wall at Mach 0.9. Results obtained for OASPL distributions along the cavity centerline and SPL spectra are consistent with results obtained in previous research.

The most effective geometric cavity modification was found to be the largest leading edge step (h/d=0.3, h/s=0.4) at Mach 0.9, which delivered up to a 20 dB attenuation in tone peaks together with a reduction in the broadband noise, which delivers an OASPL reduction of up to 7.6 dB. Leading edge step configuration performance was, however, found to be Mach number dependent with the greatest attenuation observed at Mach 0.9. Oil flow visualizations indicate that the most effective of the leading edge step configurations (h/d=0.30) may have a large recirculation bubble sitting on top of the step face, which results in a beneficial, outward deflection of the separated shear layer.

Nomenclature

d = cavity depth, Fig. 1
f = frequency
h = step depth, Fig. 1
H = boundary layer shape factor
K = empirical constant, Eq. (1)
l = cavity length, Fig. 1
M = mach number
m = mode number
P_0 = total pressure
Re_δ^* = Reynolds number based on boundary layer displacement thickness
s = step length, Fig. 1
St = Strouhal number
U = streamwise velocity
w = cavity width
α = empirical constant, Eq. (1)
δ_{99} = boundary layer thickness where $U=0.99U_e$
δ^* = boudary layer displacement thickness $\delta^* \equiv \int_0^\delta (1-(\rho U/\rho_e U_e))dy$
θ = boundary layer momentum thickness $\theta \equiv \int_0^\delta (\rho U/\rho_e U_e)(1-(\rho U/\rho_e U_e))dy$
γ = ratio of specific heats

Subscripts

∞ = freestream conditions

References

[1] ESDU, 2005, "Aerodynamics and Aero-Acoustics of Rectangular Planform Cavities, Part I: Time-Averaged Flow," Datasheet 02008.
[2] Heller, H., and Delfs, J., 1996, "Cavity Pressure Oscillations: The Generating Mechanism Visualised," J. Sound Vib., **196**(2), pp. 248–252.
[3] Vakili, A., and Gauthier, C., 1994, "Control of Cavity Flow by Upstream Mass-Injection," J. Aircr., **31**(1), pp. 169–174.
[4] McGrath, S., and Shaw, L., 1996, "Active Control of Shallow Cavity Acoustic Resonance," AIAA Paper No. 96-1949.
[5] Cattafesta, L., Williams, D., Rowley, C., and Alvi, F., 2003, "Review of Active Control of Flow-Induced Cavity Resonance," AIAA Paper No. 2003-3567.
[6] Ukeiley, L., Ponton, M., Seiner, J., and Jansen, B., 2003, "Suppression of Pressure Loads in Resonating Cavities Through Blowing," AIAA Paper No. 2003-0181.
[7] Sarno, R., and Franke, M., 1994, "Suppression of Flow-Induced Pressure Oscillations in Cavities," J. Aircr., **31**(1), pp. 90–96.
[8] Cabell, R., Kegerise, M., Cox, D., and Gibbs, G., 2002, "Experimental Feedback Control of Flow Induced Cavity Tones," AIAA Paper No. 2002-2497.
[9] Stanek, M., Raman, G., Kibens, V., Ross, J., Odedra, J., and Peto, J., 2000, "Control of Cavity Resonance Through Very High Frequency Forcing," AIAA Paper No. 2000-1905.
[10] Smith, B., Welterten, T., Maines, B., Shaw, L., Stanek, M., and Grove, J., 2002, "Weapons Bay Acoustic Suppression From Rod Spoilers," AIAA Paper No. 2002-0662.
[11] Rockwell, D., and Naudascher, E., 1978, "Review—Self-Sustaining Oscillations of Flow Past Cavities," ASME J. Fluids Eng., **100**(2), pp. 152–165.
[12] Sarohia, V., and Massier, P., 1977, "Control of Cavity Noise," J. Aircr., **14**(5), pp. 833–837.
[13] Charwat, A., Roos, J., Dewey, C., and Hiltz, J., 1961, "An Investigation of Separated Flows—Part II Flow in the Cavity and Heat Transfer," J. Aerosp. Sci., **28**(6), pp. 457–470.
[14] Rossiter, J., 1964, "Wind-Tunnel Experiments on the Flow Over Rectangular Cavities at Subsonic and Transonic Speeds," RAE Technical Report No. 64037.
[15] Heller, H., Holmes, D., and Covert, E., 1971, "Flow Induced Pressure Oscillations in Shallow Cavities," J. Sound Vib., **18**(4), pp. 545–553.
[16] Bilanin, A., and Covert, E., 1973, "Estimation of Possible Excitation Frequencies for Shallow Rectangular Cavities," AIAA J., **11**(3), pp. 347–351.
[17] Heller, H., and Bliss, D., 1975, "The Physical Mechanism of Flow-Induced Pressure Fluctuations in Cavities and Concepts for Their Suppression," AIAA Paper No. 75-491.
[18] Plentovich, E., Stallings, R., and Tracy, M., 1993, "Experimental Cavity Pressure Measurements at Subsonic and Transonic Speeds," NASA Technical Paper No. 3358.
[19] Zhang, J., Morishita, E., Okunuki, T., and Itoh, H., 2001, "Experimental and Computational Investigation of Supersonic Cavity Flows," AIAA Paper No. 87–0166.
[20] Tracy, M., and Plentovich, E., 1997, "Cavity Unsteady-Pressure Measurements at Subsonic and Transonic Speeds," NASA Technical Paper No. 3669.
[21] Komerath, N., Ahuja, K., and Chambers, F., 1987, "Prediction and Measurement of Flow Over Cavities—A Survey," AIAA Paper No. 87-0166.
[22] Ukeiley, L., Ponton, M., Seiner, J., and Jansen, B., 2003, "Suppression of Pressure Loads in Resonating Cavities Through Blowing," AIAA Paper No. 2002-0661.

Downloaded 03 Jun 2010 to 171.66.16.157. Redistribution subject to ASME license or copyright; see http://www.asme.org/terms/Terms_Use.cfm